THE UNIVERSITY
of EDINBURGH

High Pressure Synthesis and Neutron Diffraction Studies of New Magnetic Manganites

Graham M. McNally

Doctor of Philosophy

The University of Edinburgh

2017

I declare that this thesis was composed by myself, that the work contained herein is my own except where explicitly stated otherwise in the text, and that this work has not been submitted for any other degree or professional qualification except as specified. Parts of this work have been published in Angewandte Chemie – International Edition and Chemistry of Materials.

Graham M. McNally
29th November 2017

Lay Summary

The driving force behind much of scientific research is the desire to discover new technological advancements and to understand the fundamental science behind these advancements. This is particularly evident in materials research, which has a broad impact across every area of science and engineering. The research outlined in this thesis focuses on magnetic materials, a ubiquitous category of materials that have a profound effect on the way we live our lives. One important example of the appearance of magnetic materials in our day-to-day lives is in magnetic data storage, found in devices of all sizes. Binary information can be encoded in a magnetic material as bits, where a bit is either a 1 or a 0, these numbers referring to two distinct magnetic states. The ability to encode these bits as a 1 or a 0 (to write data), to identify if a bit is a 1 or a 0 (to read data) and to remove as form of encoding (to erase data) are essentially to the functioning of such a device. Generally, magnetic data is read through a phenomenon known as magnetoresistance, which is the response of a materials' electrical resistivity to changes in the magnetic field it is experiencing. Devices that utilise this phenomenon are now so prevalent that A. Fert and P. Grünberg were awarded the 2007 Nobel Prize in Physics for their discovery of Giant Magnetoresistance.

The work in this thesis focuses on the synthesis of novel magnetic materials which are found to possess interesting and novel magnetoresistance properties. These new materials are all of the perovskite family of minerals, and these syntheses utilise high-pressure techniques, with pressures exceeding 100,000 times earth's atmospheric

pressure and temperatures of approximately 1,400 °C, to force smaller cations into these structures in place of larger cations. This allows the substitution of, for example, non-magnetic calcium cations by smaller magnetic manganese cations. These modifications, made possible through high-pressure synthesis, cause new magnetic effects to be observed which dramatically change the magnetoresistance properties of these materials.

To analyse these materials, neutron diffraction has been used as a key experimental technique. Using a beam of neutrons, generated either by a nuclear reactor or a particle accelerator, materials can be analysed and their structures studied. Neutrons not only allow an analysis of the arrangement of atoms in a structure, but also of their magnetic structures. It is primarily through neutron diffraction that these materials have been able to be studied so thoroughly and an understanding of their physical properties can be made by considering their magnetic structures.

Abstract

With the discovery of appreciable room temperature magnetoresistance (MR) in high Curie temperature (T_c) ferrimagnetic double perovskites such as Sr_2FeMoO_6, research surrounding other materials of this type has expanded. Most ferrimagnetic double perovskites of the formula $A_2BB'O_6$ have non-magnetic A-site cations, such as Sr^{2+}, Ca^{2+} or Ba^{2+}. Replacing non-magnetic cations with magnetic variants offers further possibilities to tune magnetic effects. This thesis focuses on the substitution of non-magnetic A-site cations with relatively small magnetic Mn^{2+} cations. This substitution is made possible through the use of high-pressure/temperature (P/T) synthesis, and the characterisation of structural and magnetic properties of new phases discovered through these syntheses.

The first of these new phases to be reported herein is Mn_2FeReO_6, which can be described as the Mn analogue of the well-known ferrimagnetic double perovskite Ca_2FeReO_6. These materials are well ordered with Fe^{3+}/Re^{5+} on B-sites and crystallise in a $P2_1/n$ structure. Mn_2FeReO_6 shows a high T_c of 520 K due to ferrimagnetic Fe/Re magnetic order above RT, and a large saturated magnetisation of 5.0 μ_B, which peaks at 75 K. Interestingly, the A-site Mn^{2+} ($3d^5$) magnetic order has the effect of causing a spin reorientation of the Fe/Re sublattice observed by neutron powder diffraction (NPD) at temperatures below ~75 K. This causes the MR to exhibit the expected negative intergrain tunnelling behaviour above the transition and colossal positive behaviour below.

Also reported are a series of perovskite related structures with formulae $Ca_xMn_{2-x}FeReO_6$ (x = 0.5, 1.0, 1.5). Of particular note among these is $CaMnFeReO_6$, which exhibits 1:1 A-site ordering of Ca/Mn and adopts the $P4_2/n$ space group. This material

belongs to a family of newly discovered ‘double double’ perovskites, in which Ca/Mn order in columns pointing along the *c*-axis and Mn has alternating tetrahedral and square planar coordination environments. MR in this material remains negative down to 20 K, potentially due to the presence of Ca disrupting magnetic interactions between Mn^{2+} cations and suppressing the spin transition.

Alternating coordination environments in the double double perovskite structure type were exploited in the synthesis of $Ca(Mn_{0.5}Cu_{0.5})FeReO_6$. This material also crystallises in the $P4_2/n$ structure and is well ordered on B-sites, as evidenced by X-ray powder diffraction. Neutron diffraction yields, in addition to columnar order, a slight preference for Cu to occupy the square planar sites and for Mn to occupy tetrahedral sites. This doping of square planar sites with Cu has the effect of enhancing magnetic properties compared to $CaMnFeReO_6$, increasing the saturated magnetisation, raising the ferrimagnetic ordering temperature of the B-sites from 500 to 560 K, and also having a profound effect on the observed MR effects, as a switch in the sign of the MR is observed in this material through a magnetic transition.

Finally, B-site substitution has been experimented with in the synthesis of $CaMnMnReO_6$. This also possesses the combined A and B-site orders observed in $CaMnFeReO_6$ and an unusual magnetic structure, with perpendicular A and B-site magnetism due to frustration, deviating greatly from the magnetic structures of materials with B-site Fe/Re.

In summary, this thesis compiles the synthesis and analysis of a series of new double perovskites, double double perovskites and a new ‘triple double’ five-fold cation ordered structure with a general formula of $AA'_{0.5}A''_{0.5}BB'O_6$. These materials show that new types of structural ordering can be used to increase the number of degrees of freedom available for tuning the interplay between many different magnetic cations in different coordination environments.

Acknowledgements

The work contained in this thesis could not have been completed without the help, supervision and guidance of the individuals mentioned here.

First and most importantly, I must thank my supervisor Prof. J. Paul Attfield for the opportunity to enrol on this programme of study and for his many useful insights into all areas of my research. Paul has made enormous contributions to the direction of this work, as well as making my time spent in the Centre for Science at Extreme Conditions (CSEC) so delightful. This studentship is a joint project between the University of Edinburgh and the ISIS Neutron and Muon Facility and Dr. Pascal Manuel, my supervisor at ISIS, must also be recognised here for his provision of a large amount of practical experience of neutron diffraction and in aiding the understanding of these techniques, in particularly in the use of the WISH diffractometer and analysis of the data acquired from this instrument. My time spent at the Harwell site has been both productive and enjoyable, due in no small part to Pascal taking the time to make it so. I also must pay an enormous amount of gratitude to Dr. Ángel M. Arévalo-López. Through discussions in the office, work in our high-pressure laboratory, and by aiding in data analysis, has greatly contributed to all of the projects reported in this thesis. I know he will continue to have contributions to my future projects through the lasting impact of all he has taught me during these past three years. I am also grateful to the EPSRC and STFC for the provision of funding, enabling me to undertake this PhD studentship.

There any many others who have made contributions to the work in this thesis, with those in Edinburgh including: Dr. James Cumby, for his many useful and productive discussions and suggestions; Dr. Elise Pachoud, for maintaining the laboratories used throughout this work; Drs. Calum Lithgow, Xiao Wang, Michal Kepa and Rénald David, who have all had a hand in my training in the use of the magnetic instrumentation laboratory in CSEC and, of course, Dr. Gary S. Nichol, who has maintained the X-ray diffractometers in the School of Chemistry that have been so heavily used to carry out the phase analysis in this thesis.

A large amount of the data in this thesis is neutron diffraction data, for which the entire team on WISH at the ISIS Neutron and Muon Facility must be acknowledged, including Dr. Pascal Manuel as well as Drs. Fabio Orlandi and Dmitry Khalyavin. In addition, Dr. Clemens Ritter must also be thanked for his assistance in collection of neutron diffraction data on D20 at the Institut Laue Langevin reactor source. Dichroism and diffraction data from two synchrotron X-ray sources is also presented in this thesis. Dr. François Guillou is recognised here for assistance in the acquisition of dichroism data on ID12 at the European Synchrotron Radiation Facility (ESRF), as well as the time he has devoted to aiding with the analysis of this data, for which I am very grateful. The collection of X-ray diffraction data has been carried out on ID22 (also at the ESRF) with the assistance of Dr. Mauro Coduri, as well as on BL04-MSPD at the ALBA facility with assistance from Drs. Oriol Vallcorba and Catalin Popescu.

In addition to those mentioned above, I would like to thank the rest of the PhD students that I have been fortunate enough to work with in the Attfield group for their contributions, discussions and friendships over these years: Alex Browne, Giuditta

Perversi, Edward Pace, Jacky (Ka) Hong, Paul Sarte, Kunlang Ji, Hannah Johnston, Patricia Kloihofer and of course, Padraig Kearins, who was also a former project student and whose contributions to the work on $CaMnMnReO_6$ as part of his Master's degree have been invaluable in the production of this thesis. I have also had the pleasure to meet and work with many other project students and visitors: Frank Steigmann, Jingyi Ran, Yu Sun and Bruno Sousa Araújo.

On a personal note, I would like to thank my parents Brenda and Steve as well as my brother Richard, for their support throughout this work and who have always had nothing but encouragement for my academic pursuits. They have always somehow known that I have always had the potential to undertake this work. I would also like to thank those in CSEC, the School of Chemistry and School of Physics and Astronomy, for making me feel so welcome and the many friendships I have formed throughout my time at the University of Edinburgh. I would in particular like to name Dominic Pascoe, Rachel Fisher, Sara Schmidt, Toni Mey, Charlie McMonagle, Emily Macdonald, Fern Sinclair and Adam Michalchuk in the School of Chemistry; as well as Amy Coleman and Mary-Ellen Donnelly from the School of Physics and Astronomy. Thanks also to Helena, Flo, Sam, Holly, Gail, Adrian, Richard, Jeni, Rosie, Jonny and Peter for the many walks in the hills and breaks away from work, as well as the quiz team, who have all managed to keep me sane through these years. I must also give Emma my sincerest gratitude. Not only for being such an excellent friend but also for taking the time to proof read this thesis, despite being thirteen time zones away!

Lastly, I would also like to take the time to thank my examiners, Dr. Ingo Loa and Prof. Patrick Woodward, for their very useful constructive criticism that has helped me to improve my thesis.

Contents

Chapter 1. Introduction

1.1. Perovskites

1.1.1. Symmetry & Structure

Perovskites and their many related structures exhibit numerous properties useful for technological applications over a wide range of fields. This thesis will focus on materials that may find uses in the field of spintronics, the use of electron spin in the transport and storage of information.[1] The general formula for a perovskite is ABX_3, where A and B are different cations and X is an anion, usually O^{2-}. The name originates from Lev Perovski, the Russian mineralogist whom Gustav Rose named naturally occurring $CaTiO_3$ after, and which adopts the perovskite structure. While $CaTiO_3$ adopts an orthorhombic structure, the ideal structure of a perovskite is cubic, shown in **Fig. 1.1**.

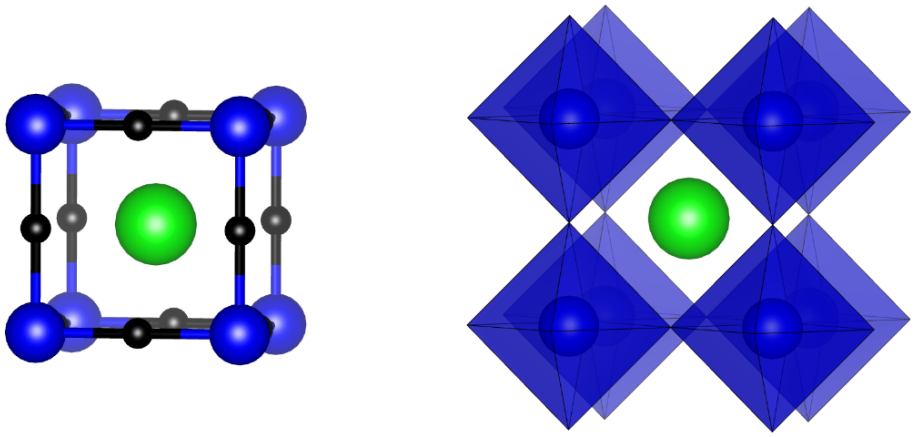

Figure 1.1 | ***Left****: The unit cell of an ideal crystal structure for a perovskite (ABX_3) in the cubic $Pm\bar{3}m$ space group. The central A cation (green) is surrounded by B cations (blue) at each unit cell corner. X anions are shown in black.* ***Right****: The coordination environments of the B cations to the X anions are shown as BX_6 octahedra (through the cell boundary). The X anions themselves are not shown, however these are present at each vertex of the octahedra.*

The B-X bonding network can be considered as corner sharing BX_6 octahedra and rotation/tilting of these octahedra can lead to distortion of the ideal perovskite structure away from the ideal cubic structure.[2] Typically, octahedral tilting arises in perovskite oxides when the A-cation is too small or too large for the 12-coordinate cavity created by the BO_6 network and these tilts can result in A-site coordination changes such that all A–O bond lengths are no longer equivalent. In discussions of perovskites in this thesis, it is useful to have methods of describing characteristics of these perovskites such as octahedral tilting and relative sizes of A, B and X ions with commonly understood terminology.

1.1.1.a Goldschmidt Tolerance Factor

The tolerance factor, *t* as defined by Goldschmidt, is a dimensionless quantity that can be calculated from the ionic radii of the constituent ions. This is shown as,

$$t = \frac{r_A + r_X}{\sqrt{2}(r_B + r_X)}, \qquad \textbf{(1.1)}$$

and this factor is an indication of the stability of the perovskite crystal structure. It can also be used to evaluate how compatible a particular ion might be with the structure or the degree to which BO_6 octahedra might have to tilt in order to compensate for an A-cation that is too large or small.

The value r_X is the radius of the anion and the radii of the A and B cations are represented by r_A and r_B, respectively. It should be noted that there may be more complex behaviours which cannot be simply predicted just by using the ionic radii,

such as the degree of covalency, metal-metal interactions as well as Jahn-Teller and lone pair effects.[3] Despite this, general rules for tolerance factors can be considered in that a tolerance factor of approximately 1 will yield a cubic perovskite (e.g. $SrTiO_3$),[4] while tolerance factors much greater than 1, with large A-cations (or conversely, small B-cations) tend to provide hexagonal structures (e.g. $BaMnO_3$)[5]. With tolerance factors less than 1, tilted perovskites are generally observed (e.g. $CaTiO_3$),[6] while if the tolerance factor is much less than 1 ($t < 0.8$), structure types related to perovskite are formed, such as the $LiNbO_3$-type.[7]

1.1.1.b Glazer Tilt Systems

The most common method of classifying these tilt systems is that defined by Glazer,[8] where a tilt system is classified by a rotation of the BO_6 octahedra around the *a*, *b* and *c* Cartesian axes of the cubic cell. In this system, a general case could be described where the octahedra are rotated by *x*, *y* and *z* degrees about the *a*, *b* and *c*-axes, respectively. The trivial case of the cubic $Pm\bar{3}m$ perovskite would be classified as $a^0a^0a^0$, signifying that there are no tilts along any axis. Represented as superscripts, a positive superscript indicates that layers of successive octahedra along that rotational axis are rotated in phase, whereas a negative superscript indicates that along that axis successive layers of octahedra are out of phase. In the case where no rotation about an axis is observed, the superscript of 0 is used. If tilts are equal, the letter is repeated in sequence. For example, following these rules a tilt system in which the tilt angles about the *a* and *b*-axes are equal and successive layers of BO_6 octahedra tilt in phase, while about the *c*-axis successive BO_6 layers tilt out of phase, would be classed as $a^+a^+c^-$

and, in this case, would correspond to the tetragonal space group $P4_2/nmc$. From symmetry analysis by C. Howard and H. Stokes,[9] the possible space groups that perovskites can adopt are shown in **Fig. 1.2**, along with their Glazer tilt systems and group-subgroup relationships.

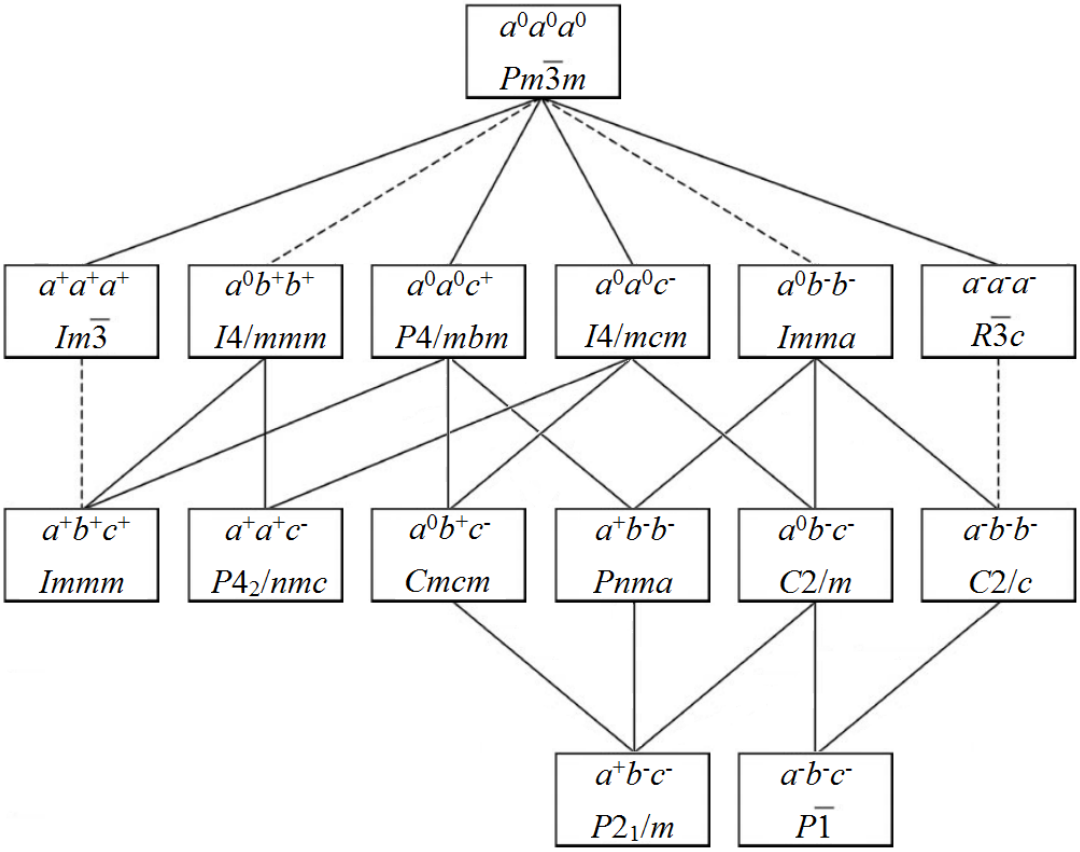

Figure 1.2 | *The possible space groups that a perovskite may take and the group-subgroup relationships between them. Two space groups connected by a dashed line are related by a first order transformation due to Landau theory. Figure from Howard and Stokes.*[9]

1.1.1.c Jahn-Teller Theorem

An important phenomenon to discuss is the Jahn-Teller effect.[10] In an octahedral crystal field the five sets of *d* orbitals are split into two degenerate groups of e_g (d_{z^2} and $d_{x^2-y^2}$, pointing directly at the surrounding anions) and t_{2g} (d_{xy}, d_{yz}

and d_{xz}, oriented between the surrounding anions). First Order Jahn-Teller (FOJT) effects arise from degenerate orbitals being unequally occupied by electrons. In particular, strong FOJT effects are commonly observed in materials containing an odd number of *d*-electrons in e_g orbitals, such as high spin $3d^4$ (e.g. Mn^{3+} or Fe^{4+}), low spin $3d^7$ (e.g. Co^{2+} or Ni^{3+}), or $3d^9$ systems (e.g. Cu^{2+}). This will remove the degeneracy of the e_g orbitals in a BO_6 octahedron, manifesting as a compression or elongation of two opposite bonds in the BO_6 octahedron, demonstrated in **Fig. 1.3**.

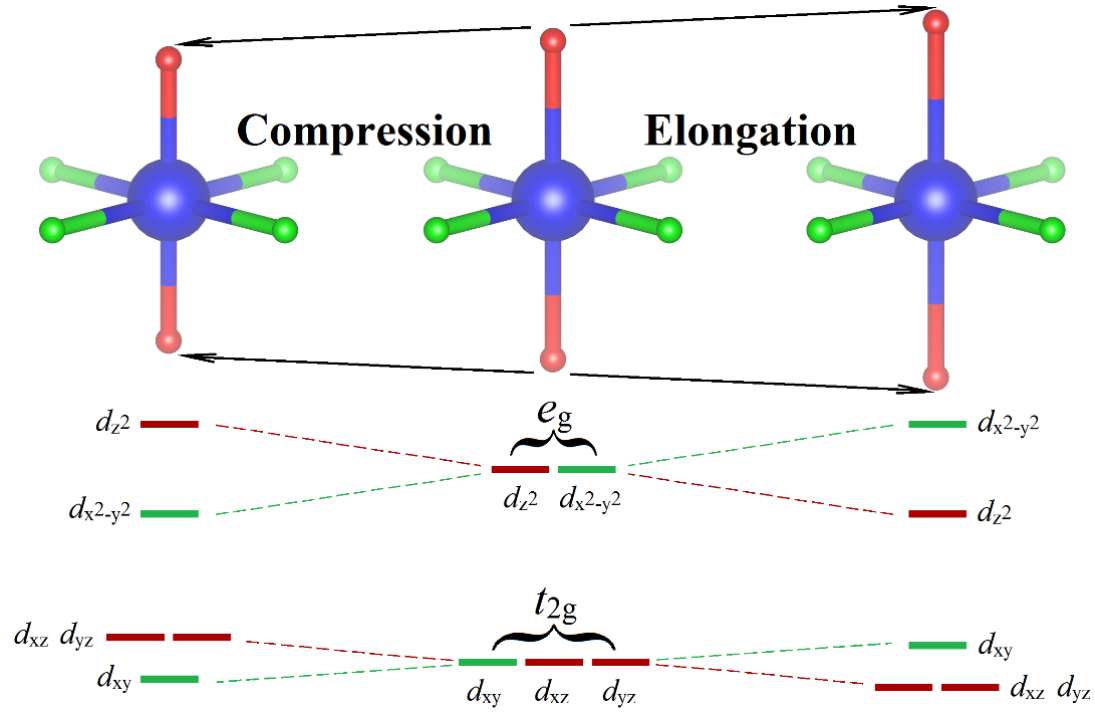

Figure 1.3 | *Schematic of the energy levels in an octahedral crystal field due to first order Jahn-Teller distortions, with pictorial representation of these distortions as elongation and compression when compared with the central regular octahedron.*[3]

The degeneracy of t_{2g} orbitals is also lifted, however as these orbitals are not oriented towards the anions, separation of these energy levels is smaller. In a perovskite, FOJT usually results in a simple cubic perovskite transforming to a tetragonal structure, with long and short bonds in the *ab*-plane and bonds along the *c*-

axis of intermediate length. Jahn-Teller distortion does not necessarily change the crystal structure other than to alter cation bond lengths to anions, however this effect is most often accompanied by tilts described above by Glazer. The Second Order Jahn-Teller effect (SOJT) is generally due to weak covalent bonding or lone pair effects and occurs when there is a small energy gap between the highest and lowest occupied molecular orbitals and, in this case, it is possible for mixing of these orbitals to occur.

1.1.2. Magnetic Order

Long-range order of magnetic moments in crystalline substances forms the basis for many of the physical properties of the materials in this thesis. Magnetic cations are those with unpaired electrons and both spin and orbital components of magnetic order can be significant. Spin, as a fundamental property of the electron, can only take discrete values of ±½ and generally referred to as spin up or spin down. Due to Hund's rules, unpaired electron spins on a single cation will preferentially align parallel to one another and the spins of these electrons are additive. Orbital moment however, is analogous to the magnetism generated from current travelling in a loop (i.e. in an electromagnet) as an electron orbits an ion, shown schematically in **Fig. 1.4**.

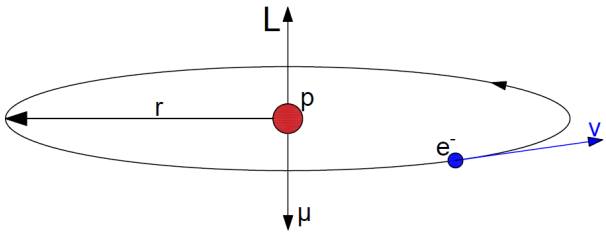

Figure 1.4 | *A schematic diagram of an electron (e^-) with velocity (v) orbiting a hydrogen nucleus (p). This produces an orbital magnetic moment (μ) due to current travelling in a circular motion, with angular momentum, L.*

In the presence of a magnetic field, this magnetic moment aligns antiparallel to the external field and, if this is the dominant effect in the material (such as in materials with no unpaired electrons), it can be considered a diamagnet and is repelled by magnetic fields (see '*1.1.3.c – Superconductivity*' for more regarding 'perfect diamagnetism' in superconductors). The orbital moment of a transition metal cation can often be considered to be quenched in cases where the symmetry of the coordination environment and electron count result in an angular momentum of zero, or even for non-zero values of *L* there are many magnetic 3*d* and 4*d* transition metal cations where in crystal fields the contribution from the orbital moment is often small enough to be negligible. However, there are cases where *L* is non-zero and the corresponding orbital moment is of a significant relative magnitude to the spin moment to necessitate that it be considered to explain the overall magnetic structure for transition metals in crystal fields. In particular, this is the case for many 5*d* or *f*-block elements where, due to the effects of lanthanide contraction and the higher effective nuclear charge, the valence electrons have a much greater velocity and as a result their angular momentum is more significant. When the orbital moment is non-zero this can add or subtract from the spin moment of the cation, depending on whether the orbitals are more or less than half-filled. In the case of many of these heavier transition metal cations or elements in the lanthanide or actinide series, spin-orbit coupling is a significant effect, where the total spin angular momentum *S* and total orbital angular momentum *L* are considered together as a total angular momentum, *J*. When orbitals are more than half-filled, $J = L + S$. If the orbitals are less than half-filled $J = |L - S|$.

Chapter 1. Introduction

In crystalline solids with repeating unit cells, coupling between cations in close proximity becomes significant. These couplings can cause the magnetic moments of neighbouring cations to be preferentially aligned parallel or antiparallel, based on the nature and magnitude of the many (potentially competing) couplings that can be present in the material. In metal oxides, the concept of superexchange is important to explain the origins of common types of coupling. Superexchange is the coupling of two magnetic cations (M_A and M_B) via a non-magnetic anion (X) in a M_A-X-M_B bond, first proposed by H. Kramers in 1934.[11] Based on the angle of the bond and the number of electrons in the bonding orbitals, this superexchange interaction can cause the spins of the two cations to be aligned parallel to one another (a ferromagnetic interaction) or antiparallel to one another (an antiferromagnetic interaction).

A set of rules outlined in the 1950s, known as the Goodenough-Kanamori rules, can be used to predict the nature of these superexchange interactions.[12–14] For a 180° M_A-X-M_B bond, with bonding orbitals on both M_A and M_B half-filled, the interaction will be strongly antiferromagnetic. Interactions between half-filled and vacant orbitals are likely to be ferromagnetic. In cases where one of these orbitals is filled, there is generally a much weaker superexchange interaction as the filled orbital in unable to have a preferred spin direction. However, deviating the M_A-X-M_B bond angle from 180° alters these rules, for example a 90° M_A-X-M_B bond with half-filled M_A/M_B orbitals leads to a strongly ferromagnetic interaction. These rules are sufficient in most cases, however when competing interactions exist, as can be the case when multiple cations with various magnetic states are present in more complex crystal structures, the type of interaction can be more difficult to predict or even lead to

'frustration',[15,16] where the criteria for ordering cannot be fulfilled for each cation, and the spin structure is required to compensate in some way to relieve the frustration. This is particularly notable effect in lattices with triangular motifs or networks of tetrahedra,[17,18] where moments must orientate to minimise the overall energy of the ground state.

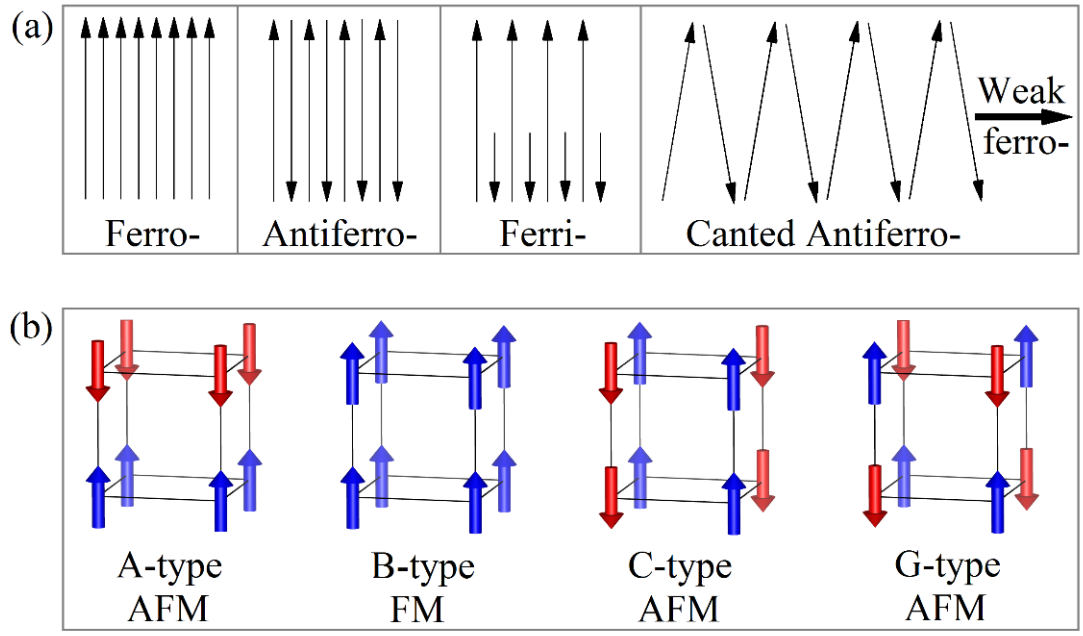

Figure 1.5 | *(**a**) Schematic showing possible types of common magnetic orders in materials, ferromagnetic, antiferromagnetic and ferrimagnetic. Also shown is canted antiferromagnetism, which results in a weak ferromagnetic component to the moment (Dzyaloshinsky-Moriya interactions).*[19,20] *(**b**) One octant of a magnetic unit cell is shown for common magnetic symmetries. A-type can be considered as layers of moments which are antiparallel to adjacent layers and results in antiferromagnetic order, B-type is the trivial ferromagnetic case where all spins are parallel, C-type consists of columns of parallel moments with adjacent antiparallel moments and G-type is analogous to rock salt order, where all nearest neighbours to a moment are antiparallel.*

With a framework of M-X-M bonds present in a metal oxide with magnetic M cations, the interactions between electron spins, whether anti- or ferromagnetic can create long range order of magnetic moments, shown in **Fig. 1.5a**. This results in a repeating magnetic unit cell analogous to long range periodic structural order one

would see from a repeating crystallographic unit cell. With ferromagnetic order, the symmetry of this magnetic unit cell is trivial as all moments are parallel. However, antiferromagnetic order can result in many inequivalent symmetries that still yield an overall moment of zero, shown in **Fig. 1.5b**, with antiferromagnetic symmetries that resemble layers, columns and rock salt, among some more complex orders.

Of note are cases where antiferromagnetic couplings can result in an overall magnetic structure that possesses a net moment. If the magnitude of up spins is not equivalent to the magnitude of down spins, an overall moment exists and the order is known as ferrimagnetic (**Fig. 1.5a)**. Alternatively, antiferromagnetic couplings can lead to small ferromagnetic components via Dzyaloshinsky-Moriya (D-M) interactions if there is an asymmetric exchange between two cations via an anion.[19,20] For D-M interactions to be possible there needs to be the absence of local inversion symmetry between the two cations, resulting in asymmetric coupling. In calculating the free energy of the system, the term which favours 'canted antiferromagnetism' (**Fig. 1.5a**) is described mathematically as $\boldsymbol{D_{1,2}} \cdot [\boldsymbol{S_1} \times \boldsymbol{S_2}]$, where $\boldsymbol{S_1}$ and $\boldsymbol{S_2}$ are the two interacting spins and $\boldsymbol{D_{1,2}}$ is the Dzyaloshinskii vector, describing the strength of the interaction based on properties of the crystal. This vector is equal to zero if a local inversion centre is present between the two interacting spins. It is also not necessary for a magnetic unit cell to have the same dimensions as the crystallographic unit cell, neither is it necessary that it be related to the crystallographic cell by an integer factor. Complex incommensurate magnetic orders involving rotations of moments as they propagate through the structure (such as helices), or spin density waves where the magnitude of magnetic moments vary sinusoidally through the structure with a set

wavelength are possible. Examples of these are given in section '**1.3. – High-Pressure A-site Manganite Perovskites and Related Structures**'.

Above a transition temperature, the Curie temperature (T_c) for ferro/ferrimagnets or Néel temperature (T_N) for antiferromagnets, the thermal energies of the system become significant enough that they exceed the energy of the spin-spin interactions and instead of being ordered, these spins are randomly oriented by the thermal energy leading to paramagnetism. Paramagnets will be attracted by magnetic fields as they cause their moments to co-align with the field, but upon removal of the field they return to their normal non-magnetised state. The Curie-Weiss law,

$$\chi = \frac{C}{T-\theta}, \quad \textbf{(1.2)}$$

is one of the most important relationships concerning magnetic order as it describes the predicted magnetic susceptibility (χ) of materials in the paramagnetic regime.

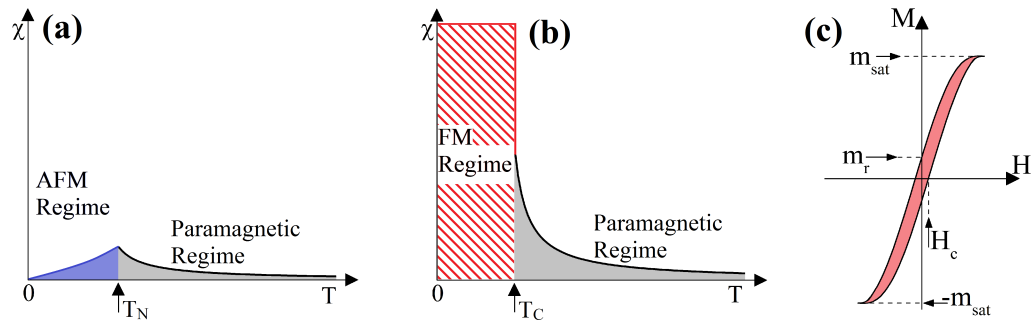

Figure 1.6 | *A schematic diagram of the magnetic susceptibility of* ***(a)*** *an antiferromagnet and* ***(b)*** *a ferro/ferrimagnet. The paramagnetic regime is shown shaded in grey and follows Curie-Weiss behaviour (**Equation 1.2**), while the antiferromagnetic (AFM) and ferromagnetic (FM) regimes are shown below their Néel (T_N) and Curie (T_c) temperatures, respectively. Also shown is a schematic of ferromagnetic magnetisation vs. field (M-H) hysteresis,* ***(c)****, with the coercive field (H_C), remanent magnetisation at zero-field (m_r) and saturation magnetisation (m_{sat}) indicated by arrows. The shaded region on this M vs. H plot is representative of the product of M and H within the loop, a measure of the energy required to change the magnetisation state of the material through one full hysteresis cycle.*

The value C is the Curie constant, specific to an individual material and θ is the Weiss constant. Schematic diagrams for the expected susceptibility of antiferromagnets and ferro/ferrimagnets are shown in **Fig. 1.6a** and **Fig. 1.6b**.

Ferro/ferrimagnets are arguably some of the most useful magnetic materials and find applications in many different areas. This can be due hysteretic effects when measuring their magnetisation in an applied field. Ferro/ferrimagnets possess characteristics which can change the potential applications of these materials. These include the ability of a ferro/ferrimagnet to switch the polarity of their magnetisation upon application of an opposing magnetic field, of a strength known as the coercive field strength H_C, specific to a particular material, and the ability to retain a high remanent magnetisation when the field is removed. Schematics of ferromagnetic hysteresis are shown in **Fig. 1.6c**, with points for coercive field strength and remanent magnetisation marked. As an example, a ferromagnet with a large coercive field and high remanent magnetisation would have suitable applications as a permanent magnet that would not be easily demagnetised by stray magnetic fields. However, where rapidly changing the polarity of magnetisation is desired, as in transformers, a very low coercive field would improve the efficiency of a material by reducing the energy loss due to repeated reversal of polarity.

1.1.3. Perovskite Case Studies & Applications

Perovskite materials exhibit many interesting and useful properties including magnetoresistance, ferroelectricity, superconductivity, charge order and negative thermal expansion. This section aims to highlight case studies of some materials which

display these features, as examples of the many reasons that perovskites are currently being pursued as a field of study for applications such as solar energy, solid-state magnetic memory storage or superconductivity. Additionally, many of the materials introduced here are not simple perovskites with ABX_3 structure, but are hybrid organic-inorganic perovskites (with organic cations occupying A-sites) or closely related defect structures (with regular, ordered arrangements of defects) that can be considered to be based on the simple perovskite structure. This section will be used to introduce these concepts with examples of these materials.

1.1.3.a Magnetoresistance

Mixed valence manganites $(R_{1-x}A_x)MnO_3$, with perovskite structures have a wide range of properties including differing magnetic, electronic and crystallographic phases. Particular attention has been paid to the mixed valence manganites of the form $(La_{1-x}A_x)MnO_3$, where A = Ca, Sr, Ba or Pb. These materials exhibit large negative magnetoresistance near the Curie temperature,[21] with magnetoresistance defined as,

$$\frac{R(H)-R(0)}{R(0)} \cdot 100 = MR\ (\%)\ , \qquad (\mathbf{1.3})$$

it is these materials for which the term 'colossal' magnetoresistance (CMR) was coined. These materials were first investigated in the 1950s,[22–24] with magnetoresistive effects first noted by J. Volger in 1954,[25] but it was not until the 1990s that these materials were re-examined and the magnitude of these effects were more appropriately appreciated.[26] This re-examination of manganites was after the discovery and widespread use of the giant magnetoresistance (GMR) effect for

magnetic data storage.[27] GMR is known to exist in layers of metallic films constructed as 'spin valves', but the magnetoresistance effect here is limited to a few percent. In $R_{1-x}A_xMnO_3$, insulating behaviour and antiferromagnetic order are found in end members when $x = 0$ and $x = 1$, however when $0.2 < x < 0.5$, these materials are ferromagnetic and their conductivity is metallic at low temperatures.[21] As an example, single crystals of $La_{0.65}(CaPb)_{0.35}MnO_3$ with T_c of 300 K have been measured to have CMR of almost -80 % at field strengths of 5.5 T and 300 K,[28] a significant increase compared with GMR effects seen in metallic multilayers.

To explain the field dependence of the resistivity, the concept of double exchange was developed by C. Zener in 1951.[29] Double exchange in this case refers to the simultaneous transfer of an electron from Mn^{3+} to a neighbouring oxygen and an electron from that oxygen to a neighbouring Mn^{4+}. In the case where the spins of the two *d*-shells are parallel, the two configurations: Mn^{3+}–O^{2-}–Mn^{4+} and Mn^{4+}–O^{2-}–Mn^{3+} are degenerate and the electron transfer is more favourable. If the spins are non-parallel, or if the Mn–O–Mn bond is bent, resistivity is increased. The effect on the probability of the exchange is generalised as,[29–31]

$$t = t_0 \cos\left(\theta/2\right), \qquad \textbf{(1.4)}$$

where the term t is the transfer integral, t_0 is the normal transfer integral dependent on spatial wavefunctions and θ is the angle between the two spin directions.

1.1.3.b Photovoltaics

Perovskites also find applications in the field of photovoltaics where they act as absorbers of solar energy, a topical issue in the current energy climate. The most common perovskites studied for this purpose are the methyl ammonium lead trihalides ($CH_3NH_3PbX_3$, where X = Cl, Br or I).[32] These are an example of organic-inorganic hybrid perovskites, where the A-cation in ABX_3 is an organic cation ($CH_3NH_3^+$) but the BX_6 octahedra remain as an inorganic framework (in this case PbX_6 octahedra). These materials can be printed on glass and films from solutions, making fabrication of devices using perovskite solar cells relatively simple.[33]

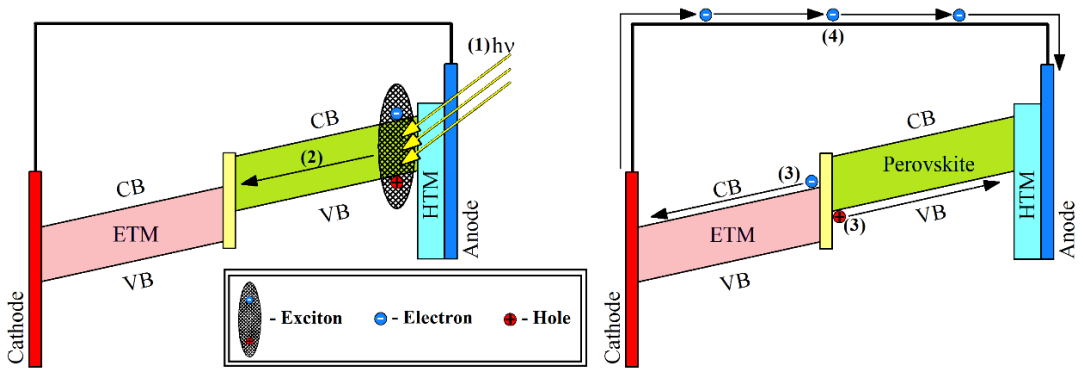

Figure 1.7 | *A schematic representation of the mechanism by which a perovskite solar cell generates an electric current. (1) an incident photon (hv) excites an electron from the valence band of a perovskite, generating an exciton. This exciton moves (2) towards an interface between the perovskite and an electron transport material (ETM, e.g. TiO_2). At this interface the exciton is able to charge separate (3) and the electron can move towards the cathode while the hole moves towards the anode through a hole transport material (HTM, e.g. Spiro-OMeTAD). This leads to the generation of a current (4).*

Perovskite solar cells have a slightly different mechanism of action (**Fig 1.7**) than Si based solar cells due to fundamental differences in electronic behaviour.[34] In Si cells a photon is absorbed, exciting an electron across the bandgap from valence band to conduction band. This creates an 'exciton' or an electron-hole pair, with a

small binding energy, enabling the electron and hole to separate (charge separation) and generate a current.[35] Perovskite-based solar cells act similarly, but they differ in that the exciton formed generally has a much higher binding energy and as such, an interface is required to aid the dissociation of the electrons from holes. In the preparation of a device to harvest solar energy and transform it into electrical energy, usually doped TiO_2 is used as an electron accepting material to interface with the cathode, while a hole transporting material, such as Spiro-OMeTAD, is used to interface with the anode.[36]

The first perovskite-based photovoltaics had photon efficiencies of 2.2 % in 2006, but by 2016 this figure had increased to 22.1 %, exceeding typical efficiencies of silicon solar cells (16-20 %).[33] However, these materials are not without their drawbacks. Perovskite solar cells are sensitive to extreme light levels as well as temperature and particularly moisture. Moisture can quickly render these solar cells ineffective by reacting with the perovskite surface and forming hydrates that hinder light absorption by the perovskite. Lifetimes of these solar cells can be up to 6 months, which is inferior to the longevity of silicon solar cells with typical life expectancies of up to 25 years. Attempts are being made to solve this drawback to perovskite solar cells. To prolong the lifetime of these solar cells there is ongoing research into encapsulating the devices in an inert environment to minimise their exposure to extreme temperature, moisture and UV light. One method is to use coatings made of luminescent photopolymers that absorb UV light and emit visible light, an interesting option to simultaneously encapsulate and improve the efficiency of the solar cell.[37]

1.1.3.c Superconductivity

Superconductivity is another important property that perovskite-type materials can possess. Below a certain superconducting critical temperature (often referred to as T_c and not to be confused with the Curie temperature, so will be referred to here as T_{sc}) some metallic materials become superconducting. As the name suggests this is characterised by resistivity dropping to zero, as well as perfect diamagnetism, with an onset at T_{sc}. This is an exciting phenomenon and has many potential uses in the transport of electrical energy or for generating high magnetic fields commonly used in equipment such as Nuclear Magnetic Resonance (NMR) machines and high magnetic fields in magnetometers, however superconductivity also finds uses in the medical sector in Magnetic Resonance Imaging (MRI) devices. Another characteristic property of superconductors is the expulsion of magnetic flux from the bulk of the material, known as the Meissner effect.[38] This effect is a result of perfect diamagnetism and opens many other potential applications for superconductors, as a superconductor below T_{sc} will levitate above (or hang below) a permanent magnet (or vice versa). This is a phenomenon that can be used, for example in levitating train technologies, notably the Central Japan Railway Company's L0 Series that passed the speed record with a speed of 603 $km.h^{-1}$.[39]

The best-known theory of superconductivity is BCS theory, named after Bardeen, Cooper and Schrieffer.[40] This relies on the formation of 'Cooper pairs' of electrons, with equal and opposite momenta and spin values, acting together as bosons rather than individually as fermions. This allows these Cooper pairs to move through

the material with the same wavefunction and zero resistance. This is known to be a result of electron-phonon interactions. As an electron moves through a lattice, it will displace cations towards it, creating a region of relative positive charge in the structure. This relative positive charge can then act to attract another electron, and results in the coupling of electron motion with lattice vibrations. This is one theory that accurately describes the behaviour of some of the low-temperature superconductors at $T_{sc} < 35$ K. However, materials with T_{sc} exceeding 35 K have also been found. In particular, cuprate superconductors are a well-studied category of high-T_{sc} superconductors such as $YBa_2Cu_3O_{7-x}$ (x ~0) or 'YBCO', the structure of which is shown in **Fig. 1.8**.

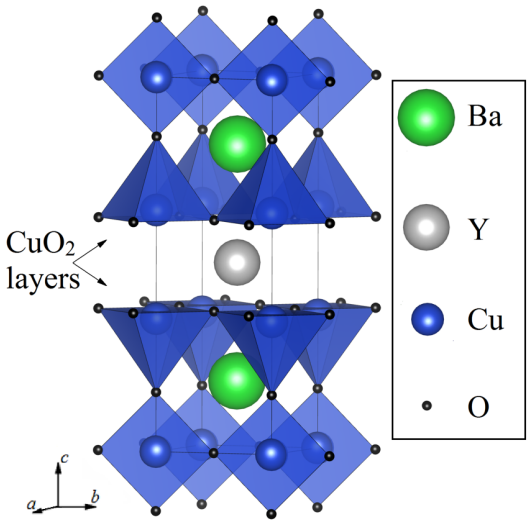

Figure 1.8 | *The crystal structure of $YBa_2Cu_3O_7$ (YBCO), which can be considered a defect perovskite with oxygen deficiencies. Indicated are CuO_2 layers, between which sit the Y atoms.*

YBCO is known to have a T_{sc} of 93 K,[41] exceeding the boiling point of liquid nitrogen and allowing this to be used as a relatively cheap cryogen to achieve a superconducting state. This is an example of a defect perovskite-type material with a layered structure of CuO_2 planes that have Y atoms sandwiched between these planes. Ba atoms occupy sides between square planar CuO_4 units perpendicular to the CuO_2

planes. This is another example of the variation in the properties of perovskites resulting from modifications of the basic structure.

1.1.3.d Ferroelectrics & Multiferroism

Ferroelectricity is a physical phenomenon that bears some analogies to ferromagnetism. If an electric field (E) is applied to a ferroelectric material then a polarisation (P) will result with a non-linear dependence of P on the magnitude of E, shown schematically in **Fig. 1.9**.

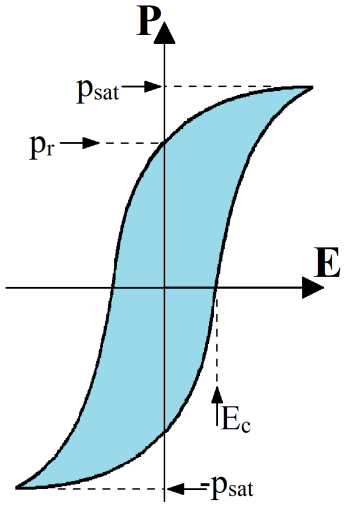

Figure 1.9 | *A ferroelectric polarisation-electric field hysteresis. Marked are the saturation polarisation (p_{sat} at high field) and retained polarisation (p_r, at zero-field). Also shown is the coercive field (E_C), required to depolarise the material after an electric field of opposite sign has been applied. These properties are analogous to those of ferromagnetism in **Fig.1.6c**. The shaded region on this plot is representative of the product of P and E within the loop, a measure of the energy required to change the polarisation state of the material through one full hysteresis cycle.*

In a paraelectric material this polarisation returns to zero if the electric field is removed, while in a ferroelectric a remanent polarisation is still present even in the absence of an electric field. This polarisation can be reversed with an electric field of the opposite direction yielding a ferroelectric P-E hysteresis resembling that of a

ferromagnetic M-H hysteresis. Typical ferroelectrics that have been widely studied include $BaTiO_3$ and $PbTiO_3$ (also $Pb(Ti_xZr_{1-x})O_3$, known as PZT and commonly used as a piezoelectric).[42,43] For both of these materials, hybridisation of the Ti 3*d* and O 2*p* states is critical for ferroelectricity.[44] Below the ferroelectric Curie temperature there is a structural distortion to a non-centrosymmetric lower symmetry, which is characterised by a shift of the Ti cation away from the ideal position, creating the spontaneous polarisation. In $PbTiO_3$ above 766 K, a non-centrosymmetric cubic symmetry exists but below this temperature transitions to a non-centrosymmetric tetragonal structure with a polarisation along [100]. $BaTiO_3$ has several transitions: from cubic to tetragonal at 393 K, to orthorhombic at 278 K and to rhombohedral at 183 K, with polarisation along [100] in the tetragonal phase (as in $PbTiO_3$), along [110] in the orthorhombic phase and [111] in the rhombohedral phase.[44,45]

Multiferroic materials, with simultaneous magnetic order and ferroelectric ordering are of great interest, especially in recent years as advancements in thin-film growth techniques have allowed the synthesis of extremely high quality thin-film materials. Ferromagnetic ferroelectrics are a rare class of materials due to the conventional mechanism for ferroelectricity involving cation displacement due to empty *d*-orbitals, while ferromagnetism is generally the result of partially filled *d*-orbitals. For this reason, multiferroics have often been designed as composites, with a ferroelectric material in contact with a ferromagnet.[46] Application of an electric field on the ferroelectric will induce a strain on the ferromagnet, causing a magnetic response (e.g. ferroelectric $PbZr_{1-x}Ti_xO_3$ in contact with ferromagnetic $Tb_{1-x}Dy_xFe_2$). Multiferroism can be achieved in a single phase by these two properties originating

from different cations in the structure, usually with a large A-site cation that possesses a lone pair of electrons, such as Bi or Pb, while a small transition metal B-site cation can provide the magnetic order, such as Fe or Cr.[45]

1.2. Double Perovskites

1.2.1. Symmetry & Structure

An important variation on the perovskite structure is the double perovskite.[47] This is the result of 1:1 cation ordering at one site (either A or B-sites, but most commonly between two different B cations labelled B and B′, with general formula: $A_2BB'O_6$). It is possible for ordering to occur in other ratios, the most common are termed quadruple perovskites due to 1:3 order on A-sites (general formula: $AA'_3B_4O_{12}$),[48] however 1:1 cation order will be the focus of this thesis. The different types of 1:1 order possible for double perovskites are depicted in **Fig. 1.10;** rock salt, columnar and layered.[49] The magnitude of the differences between B and B′ often determines the degree of ordering with charge difference, size and bonding character all playing a significant role. Arguably, charge difference between B-site cations is the factor that will most often cause a structure to adopt a crystallographically ordered state. Due to thermodynamic benefits of locating these differently charged cations as far away from one another as possible, rock salt order is most likely as all BO_6 octahedra are separated from each other by a $B'O_6$ octahedron, minimising the energy penalty of having two highly charged (or low-charged) chemical species in close proximity. By categorising these orders by degree of thermodynamic stability in separating electrostatically-alike nearest neighbours, these decrease in the order of

rock salt, columnar and layered. If electrostatics alone governed the type of ordering a double perovskite would crystallise with, then rock salt would always be the most favourable structure. However, when differences in ionic size and bonding characteristics start to become significant, columnar and layered orders can exist.

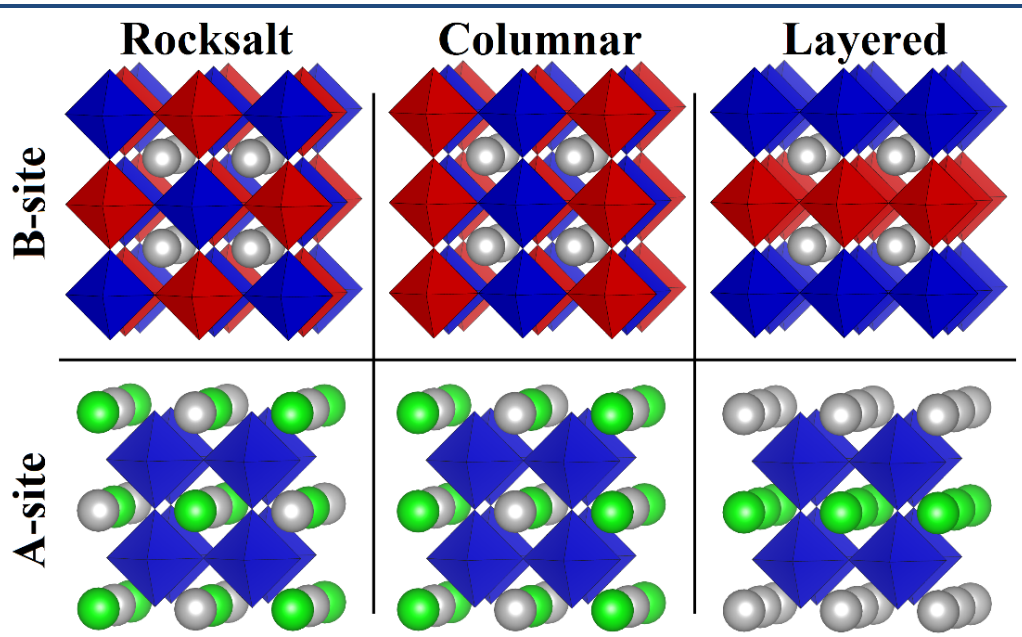

Figure 1.10 | *The types of ordering that are possible in double perovskites on both A and B-sites, shown here as completely ordered. In most real materials some degree of disorder can be observed. Rock salt orders occur when each B cation has 6 nearest neighbours of only B' and no B nearest neighbours. With columnar ordering, each B cation has 4 nearest neighbours of B' and 2 nearest neighbours of B. Layered order results in each B cation only having 2 nearest neighbours of B' but 4 of B. Figure adapted from G. King and P. M. Woodward.*[49]

Some of these types of order have many examples, such as the B-site rock salt order in Ba_2MgWO_6, which adopts the aristotype cubic space group $Fm\bar{3}m$. The main driving force for this order is the charge difference of Mg^{2+} and W^{6+}.[49] Columnar and layered order are less common for B-site order, but examples of these exist in columnar $LaCaMn^{3+}Mn^{4+}O_6$,[50] $NdSrMn^{3+}Mn^{4+}O_6$,[51] stabilised by charge order and Jahn-Teller distortions of Mn^{3+}/Mn^{4+} and in layered La_2CuSnO_6,[52] also stabilised by Jahn-Teller distortions of Cu/Sn. The situation is different with A-site order, where layered order

is actually most common, usually stabilised by size differences between the A-site cations, such as between Na^+ and La^{3+} in $NaLaMgWO_6$.[53] Rock salt order is rare but can also be observed, such as in A-site rock salt ordered $NaBaLiNiF_6$ stabilised by the A-site charge difference between Na^+ and Ba^{2+}. However, rock salt order is often destabilised by A-site cation size differences.[54] Columnar ordering on A-sites is also rare but can be exemplified by $CaMnTi_2O_6$ and $CaFeTi_2O_6$, which has a large A-site cation size difference and octahedral tilting to accommodate columns of large 10-coordinate Ca^{2+} cations and small 4-coordinate Mn^{2+}/Fe^{2+} cations.[55,56] Interestingly, this material crystallises in the $P4_2/nmc$ space group with $a^+a^+c^-$ tilt system, the only space group identified that actually requires octahedral distortions in order to maintain the connectivity of octahedra after tilting.[3] Doubly ordered 1:1 $AA'BB'O_6$ materials also exist, however these are very rare and have been termed 'double-double' perovskites. Materials where rock salt 1:1 B-site order combined with layered 1:1 A-site order is found are limited to: $NaRMgWO_6$ (R = La, Ce, Pr, Nd, Sm, Eu, Gd, Tb, Dy or Ho),[57,58] $NaRMnWO_6$ (R = La, Ce, Pr, Nd, Sm, Gd, Dy or Ho),[57–59] $NaLaNiWO_6$,[60] $NaNdCoWO_6$,[60] $NaLiMgWO_6$,[61] $NaLaScNbO_6$,[53] $KLaMnWO_6$,[57] $KLaMgWO_6$.[62,63] All of these materials possess a common motif of a large size difference between monovalent Na^+/K^+ (A^+) and trivalent R^{3+} (A'^{3+}) cations across A-sites and a high degree of charge difference on B-sites. Until very recently, layered A and rock salt B was the only combination of 1:1 order on both A and B-sites found in perovskites. A series of perovskites with general formula $RMnMnSbO_6$ (R = La, Pr, Nd or Sm) have been found to possess 1:1 columnar A-site order of Mn^{2+}/R^{3+} stabilised by a large size difference, with 1:1 rock salt B-site order of Mn^{2+}/Sb^{5+}, stabilised by a

large charge difference.[64] While the B-site order in this material is the commonly observed B/B′ rock salt order,[47] the A-site order resembles that of the columnar $CaMnTi_2O_6$ or $CaFeTi_2O_6$,[55,56] with 10-coordinate R^{3+} and 4-coordinate Mn^{2+}.

When evaluating the structure of a double perovskite and defining the Goldschmidt tolerance factor, a slightly modified version of **Equation 1.1** is useful as generally an average value of r_B and $r_{B'}$ is used,

$$t = \frac{r_A + r_X}{\sqrt{2}(0.5\, r_B + 0.5\, r_{B'} + r_X)}. \quad \textbf{(1.5)}$$

As has been explained above in relation to the potential orders in double perovskites, the situation is far more complicated than the Goldschmidt tolerance factor suggests when determining the likely structure of these ordered perovskites, due to the extra complexity offered by two different B cations.

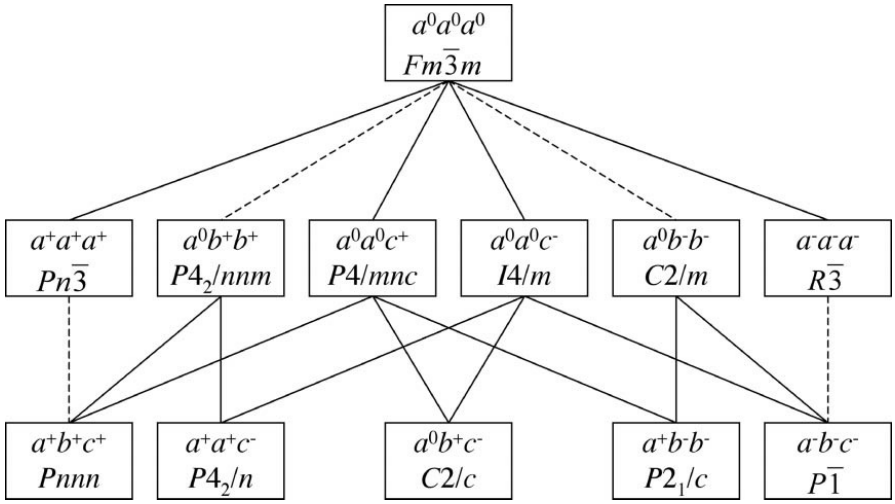

Figure 1.11 | *The possible space groups that 1:1 B-site rock salt ordered double perovskites may adopt and the group-subgroup relationships between them. Two space groups connected by a dashed line are related by a first order transformation due to Landau theory. Figure from Howard et al.*[65]

There are many possibilities for the space group of a double perovskite. As an example, a 1:1 double perovskite of the form $A_2BB'X_6$ with rock salt order can adopt

the groups shown in **Fig. 1.11**.[65] These space groups are generated from the potential tilting regimes of the $BO_6/B'O_6$ octahedra, without considering different types of B-site order or additional A-site orders. The common space groups for the ordering of $A_2BB'O_6$ double perovskites are the cubic space group $Fm\bar{3}m$ and the monoclinic group $P2_1/n$ (a non-standard setting of $P2_1/c$), but there are many examples of the other space groups listed in the figure above, such as Sr_2NiWO_6 crystallising in the tetragonal $I4/m$ space group,[66] or Ba_2LaRuO_6 in the triclinic $P\bar{1}$ space group.[67]

One interesting example of a double perovskite, demonstrating the importance of charge in the ordering of B and B′ cations, is $BaBiO_3$.[68] This exhibits a charge disproportionated structure ($Ba_2Bi^{3+}Bi^{5+}O_6$) and orders in a rock salt type arrangement of Bi^{3+} and Bi^{5+}.[68] This material adopts an $I2/m$ structure (non-standard setting of $C2/m$) at room temperature but discontinuously transitions to a rhombohedral $R\bar{3}$ structure at 405 K and then continuously transitions to a cubic $Fm\bar{3}m$ structure at 750-800 K. At low temperatures, of approximately 140 K, $BaBiO_3$ undergoes a continuous transition from its $I2/m$ structure to a monoclinic $P2_1/n$ structure. Not only does this show the importance of charge in ordering of double perovskites, but also the possible transformations that these structures will undergo. This material is also of particular interest when doped with K/Rb (A-sites) or Pb (B-sites).[69] For example when doped with K, this structure in the form of $Ba_{1-x}K_xBiO_3$, is noted to be superconducting, with the superconducting phase found to possess cubic symmetry (which forms only for $x > 0.25$) and with the highest values of T_{sc} found for compositions near this structural phase transition where $x \sim 0.25$.[70] Values of T_{sc} for these materials are reported up to 30 K, higher than those of most conventional superconductors but surpassed by values

of T_{sc} for the cuprates. However, the cubic symmetry excludes a two-dimensional metal-oxygen sublattice being responsible for high T_{sc} in these materials, as in the cuprates with CuO_2 planes being responsible for extremely high values of T_{sc}, explained in '*1.1.3.c – Superconductivity*'. The mechanism for superconductivity in these materials has been identified as BCS.[71]

1.2.2. Spin-Polarised Conduction

In the field of spintronics, Sr_2FeMoO_6 (SFMO),[72] which crystallises as a double perovskite in the *I*4/*m* space group,[73] is of particular note. This material has a Curie temperature $T_c = 410$ K and is a half metal with a high degree of spin polarisation at room temperature, exhibiting room temperature giant negative magnetoresistance of -9.5 % (as defined in terms of resistances measured at field, *R(H)*, and without field, *R(0)*, in **Equation 1.2**) under a field of 7 T.[72] The term half metal refers to the fact that one of the spin channels in the material is conducting, while the other is insulating, leading to a spin-polarised metallic conduction. This MR effect in SFMO is a result of negative tunnelling magnetoresistance (TMR),[74] where conduction across interfaces, such as intergrain conduction, is dependent on the alignment of magnetisation vectors in either grain, shown in **Fig. 1.12**. These effects have been exploited in trilayer magnetic tunnel junctions, such as $Sr_2FeMoO_6/SrTiO_3/Co$ and $Sr_2FeMoO_6/SrTiO_3/Sr_2FeMoO_6$.[75–77]

This discovery of MR in SFMO started a trend in research of similar materials which may also have spin-polarised conduction and ferrimagnetism at room temperature, such as Ba_2FeReO_6, Sr_2FeReO_6 and Ca_2FeReO_6,[78–80] which exhibit

negative magnetoresistance, however Ca_2FeReO_6 cannot be truly described as a half metal at low temperatures as it is in fact insulating.[81] In a simple TMR model, *MR* is given by **Equation 1.6**,

$$MR = -\frac{P^2M^2}{1+P^2M^2}, \quad \textbf{(1.6)}$$

where *P* and *M* are spin polarisation and magnetisation, respectively.[74] Thus, the search for new spintronic materials is a search for materials with high *P* and *M*.

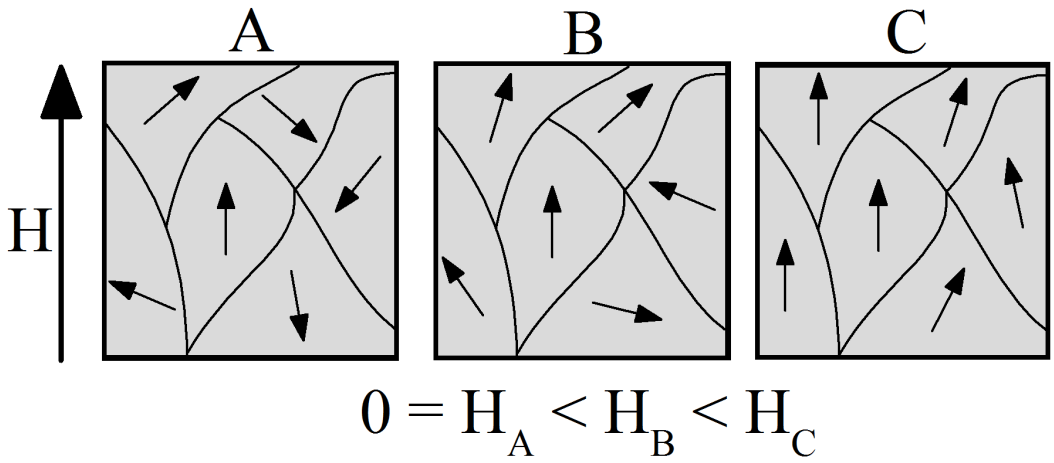

Figure 1.12 | *Schematic showing the relative orientations of moments in neighbouring grains of a polycrystalline substance. Magnetic field (H) increases from zero in A to a non-zero value in B and then to an even higher value in C. The stronger the applied field the greater the degree of co-alignment of moments in neighbouring grains.*

The rhenates are of most relevance to this thesis and, in particular, Ca_2FeReO_6. The crystal structure is described as monoclinic ($P2_1/n$, lattice at 300 K: a = 5.40078(5), b = 5.52525(5), c = 7.68390(7) Å and β = 90.0695(9)°)[82] with a rock salt order of magnetic Fe^{3+}/Re^{5+} B-site cations and non-magnetic Ca^{2+} A-site cations. The literature is generally agreed that Fe^{3+}/Re^{5+} are ferrimagnetically ordered in this structure at room temperature and the magnetisation saturates to a value of 2.1 μ_B f.u.$^{-}$

[1] at 4 K, with typical CMR values of -45 % reported at T = 9 K and $\mu_0 H$ = 7 T.[80] However, the Fe/Re moments orientations have been somewhat inconsistently reported. Most studies indicate that these spins order parallel/antiparallel with the *c*-axis, however others suggest that there may be an additional spin component along the *a*-axis to properly model the structure in Rietveld fits to powder neutron diffraction data.[82] This *a*-axis component results in moments in the *ac*-plane with polar angles of ϕ = 0° and θ ~35°, i.e. moments are 35° away from the *c*-axis. Below 140 K this material undergoes a phase transition from a ferrimagnetic metal to a ferrimagnetic insulating phase, with moments oriented on the *b*-axis and a larger monoclinic distortion (β = 90.02212(6)°). This transition has been attributed to orbital ordering of the 5*d* electrons in Re^{5+} and is evidenced by changes in the octahedral distortions at the metal-insulator transition.[82] These ReO_6 octahedra can be considered compressed at high temperature, but expanded at low temperature.

1.3. High-Pressure A-site Manganite Perovskites and Related Structures

Temperature is commonly used as the primary variable in synthesis to vary the products, yield and rate of a reaction. However, pressure is also an important variable that can be used to explore chemical synthesis and when used in combination with temperature variation, the phase space that can be explored widens so considerably that it could be considered naïve to only consider temperature when probing reaction conditions. The main reasons for a bias towards temperature as the preferred variable for most synthetic chemistry is due to the ease with which it can be measured and

altered, as well as being economically efficient. While low pressure/vacuums do find common uses in synthetic chemistry, high pressure normally involves high initial equipment costs that can be prohibitive. Nevertheless, pressure is an important variable to explore in chemical synthesis, particularly in solid-state sciences, when considering the typical pressures at which many naturally occurring minerals have formed on our planet, or indeed on other planetary bodies. These geological pressure ranges, from ambient pressure of 1 atmosphere (101 kPa) to pressures exceeding 3.6 million atmospheres (360 GPa) at the centre of the earth, are of interest for high-pressure synthesis and the study of high-pressure phases. Geological pressures used by our planet generate some of the most abundant known materials, such as silicate perovskite (bridgmanite) $(Mg,Fe)SiO_3$.[83] As such, pressure is an extremely important variable that synthetic science needs to utilise in the pursuit of novel materials.

While pressures at the high end of this range (360 GPa) are reserved for the particularly small sample sizes in diamond anvil cells, generally of the order of μm^3,[84] pressures on the order of tens of GPa can be achieved with relatively large sample sizes of tens of mm^3. The specific sample sizes that can be pressurised are dependent on the exact setup and target pressure, but in fact all of the A-site Mn^{2+} structures referenced in this section are synthesised by high-pressure techniques and quenched to ambient conditions as kinetically metastable phases.

Predominantly, perovskites consist of large non-magnetic cations at their A-sites and any magnetic properties usually originate from unpaired *d*-electrons on transition metal B-cations. It is however of fundamental physical interest to explore the electronic and magnetic phenomena that emerge from A-site magnetism and the

coupling of spin, charge and orbital degrees of freedom between these magnetic A and B-cations. A few factors make Mn^{2+} a viable transition metal (TM) candidate to replace non-magnetic A-site cations. Size and charge are important considerations when deciding on viable substitutions, and while Mn^{2+} is smaller than common non-magnetic A-site cations, for example Ca^{2+} (with an 8-coordinate cation radius of r_{Ca} = 1.12 Å), it is still relatively large for a $(TM)^{2+}$ cation (r_{Mn} = 0.96 Å).[85] Another important factor here is that the crystal field stabilisation energy must be considered when moving from A-site alkaline earth metals to A-site transition metals. However, for high spin Mn^{2+} ($3d^5$) the crystal field stabilisation energy is zero. These factors combined allow Mn^{2+} to readily occupy A-sites in these structures, and the largest difference between Mn^{2+} and Ca^{2+} as A-site cations is their relative sizes. However, the stability of other charge states, e.g. Mn^{3+}, can cause behaviour such as charge ordering that would not be observed with alkaline earth A-site cations. With regards to magnetic properties, A-site Mn^{2+} ($3d^5$, $S = {}^5/_2$) in the high spin state is also notable as having a large spin moment, which should lead to significant magnetic couplings to these cations. Mn^{2+} is therefore a good potential candidate to replace non-magnetic A-site cations in order to explore this interplay between A and B-site magnetism and several examples of materials with A-site Mn have been recently reported and are discussed in this section.

The Goldschmidt tolerance factor (**Equation 1.1** and **1.5**) can be used to rationalise why certain structures can only able be synthesised at high pressure.[86] When a particular perovskite is highly distorted and has a tolerance factor much less than 1, for example due to relatively small A-site cations, it may be that another

structure (such as $LiNbO_3$-type in **Fig. 1.13**) is more favourable at ambient pressures by a conventional high temperature solid-state synthesis route, e.g. the Ceramic Method. By synthesising materials at elevated pressures, the perovskite structure may be more favoured if it has a higher density and closer packing of atoms. High-pressure/temperature synthesis can therefore be used to access new phases, which after rapid cooling followed by a decompression stage may be metastable. These materials can then be analysed at ambient conditions and may have interesting new properties.

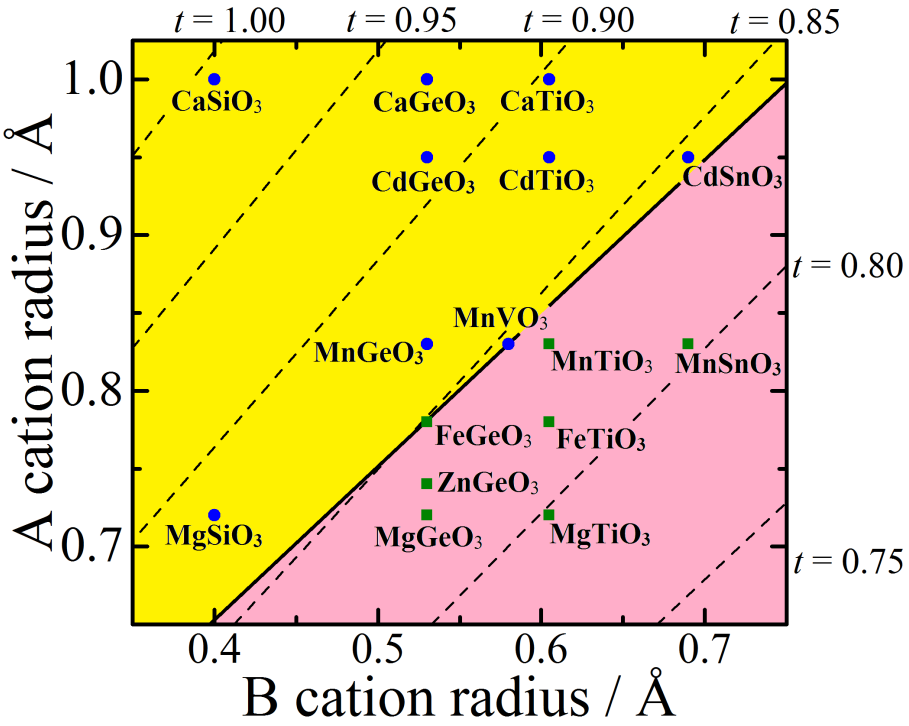

Figure 1.13 | *Goldschmidt plot for perovskite phases that are quenchable from high pressure (blue circles, yellow shaded area) and unquenchable from high pressure (green squares, pink shaded area). The unquenchable perovskite phases form $LiNbO_3$-type structures when quenched to ambient pressure. Plotted are A^{2+} and B^{4+} cation radii for a coordination number of 6. Goldschmidt tolerance factor contours (t) are also shown, calculated for 8-coordinate A^{2+} and 6-coordinate B^{4+}.*[85] *Figure adapted from Perovskites: Modern and Ancient.*[3]

Shown in **Fig. 1.13** is a Goldschmidt plot of various ABO_3 phases synthesised at high pressures and temperatures before being quenched to room temperature and decompressed to ambient pressure. Some of these phases are recovered as perovskite

structures (yellow shaded region) and some are recovered as $LiNbO_3$-type structures, a corundum derivative explained in detail in the following section (pink shaded region), with a rough cut-off point between the stability of these two structure types being t ~0.85. Tolerance factors lower than this cut-off tend to produce $LiNbO_3$-type structures, while above this point perovskite structures are favoured. However, using high pressure these corundum derived phases can be transformed to perovskite-type phases, effectively shifting the cut-off line between perovskite and corundum derivatives to lower tolerance factors as pressure is increased. As an example, $MnVO_3$-I (ilmenite-type) can be made at atmospheric pressure, however this phase transforms to $MnVO_3$-II (perovskite-type) at high pressures of ~5 GPa.[87] This phase can then be recovered as a metastable phase by quenching the reaction at 5 GPa. Examples of both corundum derived and perovskite-type structures are provided in this section.

1.3.1. Corundum Derivatives

Other notable examples of materials with A-site Mn are the series of perovskite-related materials Mn_2FeMO_6 that adopt the $LiNbO_3$ (when M = Nb or Ta)[88] and Ni_3TeO_6 (when M = W or Mo)[89,90] structure types. The corundum structure A_2O_3, exemplified by Al_2O_3, is a hexagonal close packed structure of oxygen atoms with metal atoms occupying two thirds of the octahedral sites, with the remaining one third left as vacancies (shown in **Fig. 1.14**). Within layers in the *ab*-plane, AO_6 octahedra are edge sharing. Between these layers AO_6 octahedra are face sharing to their adjacent layers along the *c*-direction. With the inclusion of two or more different cations,

ordering can occur as demonstrated in **Fig. 1.14**, with the structure type based on the ordering scheme.

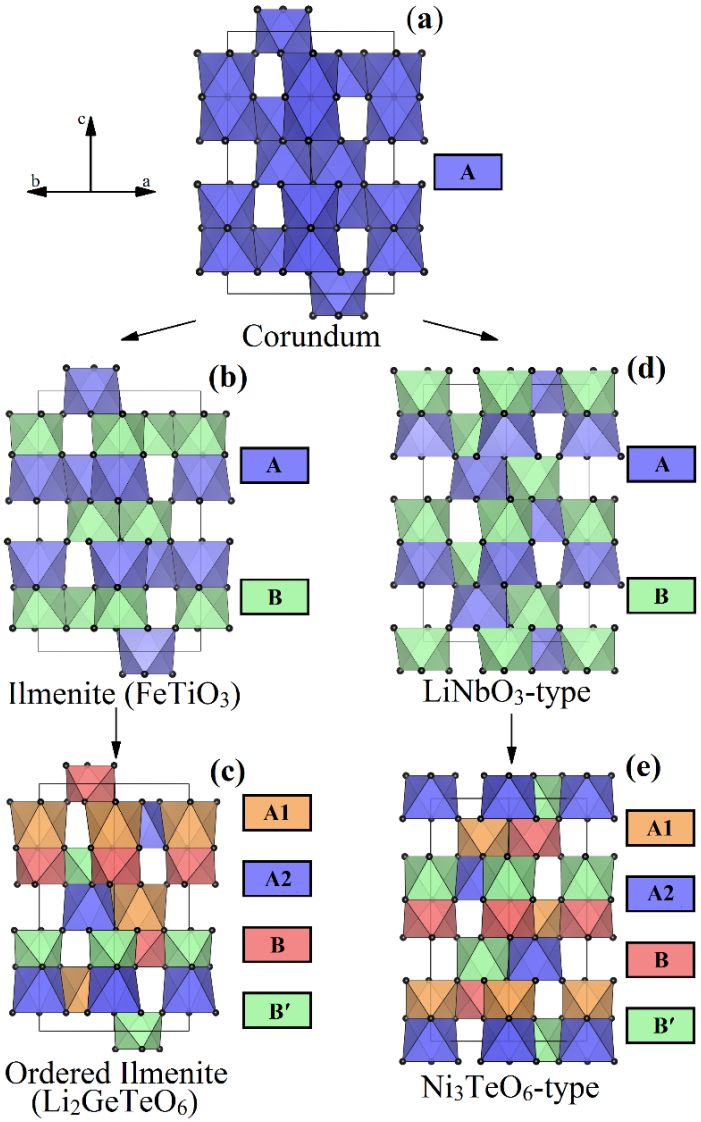

Figure 1.14 | ***(a)*** *The corundum structure (general formula: A_2O_3, space group: $R\bar{3}c$, archetype: Al_2O_3) and the structure of the archetypal materials of some of its derivatives.* ***(b)*** *Ilmenite (general formula: ABO_3, space group: $R\bar{3}$, archetype: $FeTiO_3$).* ***(c)*** *Ordered Ilmenite (general formula: $A_2BB'O_6$, space group: R3, archetype: Li_2GeTeO_6).* ***(d)*** *Lithium niobate-type (general formula: ABO_3, space group: R3c, archetype: $LiNbO_3$).* ***(e)*** *Trinickel tellurate-type (general formula: $A_2BB'O_6$, space group: R3, archetype: Ni_3TeO_6). Figure adapted from Li et al.*[90]

Within their octahedral coordination environments, cations in these structures tend to displace away from neighbouring face sharing octahedra towards vacancies in order to minimise electrostatic repulsion. This generates significant differences

between the thermodynamic stability of locating cations in neighbouring edge sharing octahedra versus neighbouring face sharing octahedra. The ilmenite structure type has layers of alternating AO_6 and BO_6 octahedra, such that all AO_6 share an edge with other AO_6 (likewise for BO_6), but all face sharing consists of an AO_6 and BO_6 octahedron sharing a face. On the other hand, the $LiNbO_3$ structure type also has alternating AO_6/BO_6 octahedra in the plane as well as between planes, such that all edge sharing and face sharing occurs between AO_6/BO_6 pairs and no like-cations are adjacent. The ordered ilmenite and Ni_3TeO_6-type structures are yet more complicated, as additional ordering across B-sites is now present, illustrated in **Fig. 1.14**.

The resulting structure type is generally difficult to predict with these order types and the relative stabilities of these structures are dominated by competition between the favourability of edge- and face-sharing of different A, B and B′O_6 octahedra.[90] Mn_2FeMO_6 (M = Nb and Ta), adopt the $LiNbO_3$-type structure described above, with Fe/M disordered across B-sites. Both these materials are synthesised by high-pressure methods at 7 GPa and 1300 °C, with a rhombohedral cell in the *R*3*c* space group (*a* ~5.27 and *c* ~13.9 Å).[88] As in the other A-site Mn materials shown above, the oxidation state of Mn is found to be Mn^{2+}, with B-site cations Fe^{3+} and M^{5+}, which is consistent with X-ray Absorption Near Edge Spectroscopy (XANES) as well as Bond Valence Sum (BVS)[91] calculations. Despite the charge difference between these B-cations, no further B-site ordering is observed. Calculations on these materials suggest that there should be a polarisation from the presence of non-magnetic Ta^{5+} ($5d^0$) or Nb^{5+} ($4d^0$) cations, with the magnetic behaviour arising from magnetic Mn^{2+} ($3d^5$) and Fe^{3+} ($3d^5$) cations.[88] When M = Ta, an antiferromagnetic transition is

evidenced at 200 K, below which *M-H* curves show a deviation from linear behaviour with a magnetic moment less than 0.05 μ_B·f.u.$^{-1}$ at 90 K, likely due to canted antiferromagnetism resulting in a weak ferromagnetic contribution.[88] A second transition is observed at 80 K, where a strongly antiferromagnetic state is stabilised and the *M-H* hysteresis returns to a linear form, suggesting that the canted ferromagnetism is lost. For the case where M = Nb, the *M-H* curves deviate from a linear form even at 300 K and persist down to at least 5 K, suggesting that this canted ferromagnetism is stabilised when M = Nb. Despite the absence of an inversion centre (*R*3*c*), no evidence of ferroelectricity is found and ferroelectric hysteresis and dielectric measurements show that these materials are paraelectrics.[88] These materials have however been noted to be pyroelectric at low temperatures (when their resistivities are high),[88] presenting an example of combinations of useful properties that materials of this structure type can possess when modified by inserting magnetic cations into the A-sites.

$MnTiO_3$-II is another example of a material with A-site Mn with a $LiNbO_3$-type structure.[92] An antiferromagnetic structure with weak Dzyaloshinsky-Moriya (DM) exchange leading to a small weak ferromagnetic component is observed in this material. Spin order in $MnTiO_3$-II exists below a 28 K antiferromagnetic transition with $\boldsymbol{k}$ = (0 0 0) and spins are oriented in the *ab*-plane with magnitudes of Mn^{2+} ($3d^5$) moments of 3.9(1) μ_B at 2 K.[92] The small ferromagnetic moment from DM exchange (0.0014 μ_B) is observed at 2 K from remanent moments in *M-H* hysteresis.

Mn_2FeMO_6 (M = W or Mo) are examples of structures with A-site Mn that adopt the Ni_3TeO_6-type structure described above and crystallise in the non-

centrosymmetric *R*3 space group.[89,90] Mn cations occupy the two independent A-sites (Mn1 and Mn2) while Fe and M cations occupy the B and B′-sites. These materials were both reported to be synthesised at 8 GPa and 1400 °C / 1350 °C, for M = W and M = Mo, respectively. Charge states in these materials are confirmed by XANES and BVS to be $Mn_2^{2+}Fe^{2+}W^{6+}O_6$ and $Mn_2^{2+}Fe^{3+}Mo^{5+}O_6$. A small amount of B-antisite disorder of 7 % is observed in the Fe^{3+}/Mo^{5+} material from X-ray diffraction, but no antisite disorder is observed in the Fe^{2+}/W^{6+} material. This preference for greater order in the W^{6+} material likely arises from the greater size and charge difference between B and B′.

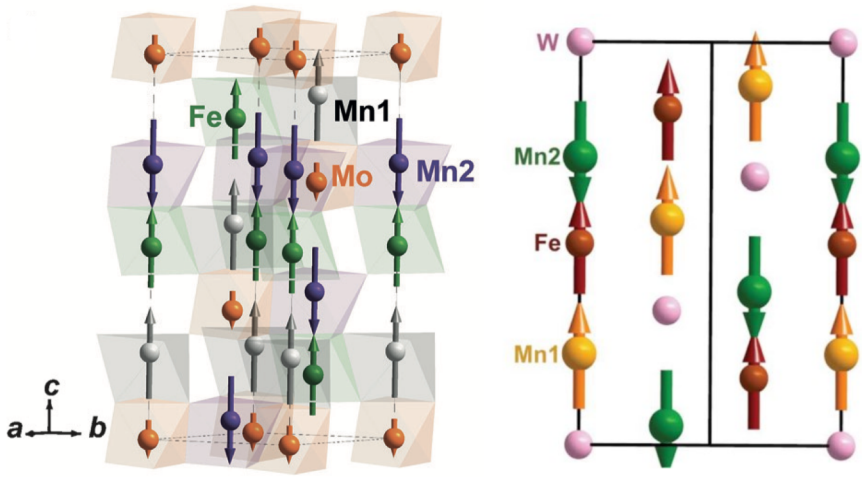

Figure 1.15 | *Left*: *Spin structure of Mn_2FeMoO_6 at 10 K from powder neutron diffraction data. Figure from Li et al.* ***Right***: *Ground state spin structure of Mn_2FeWO_6 from DFT + U spin polarisation calculations. Figure from Li et al.*[89,90]

Neutron diffraction was also used in the study of Mn_2FeMoO_6 to determine the degree of disorder between Mn and Fe, however no disorder was found.[90] Neutron diffraction also yields information about the magnetic structures of Mn_2FeMoO_6, shown in **Fig. 1.15**. These magnetic structures are rather similar, when M = Mo B-site Fe^{3+}/Mo^{5+} spin order yields a ferrimagnetic sublattice with moments oriented along

the *c*-axis. A-site Mn adopts a ferrimagnetic order collinear with the Fe^{3+}/Mo^{5+} spin order, with Mn1 moments oriented parallel to Fe^{3+} moments and Mn2 moments antiparallel. In the M = W case the ground state spin order from DFT + U spin polarisation calculations follows the same symmetry, with the exception that Mo^{5+} ($4d^1$) is replaced with non-magnetic W^{6+} ($5d^0$) and Fe^{3+} ($3d^5$) is replaced with Fe^{2+} ($3d^6$). Spin order is observed from *M-T* measurements to be complex and with an onset at 70 K, from calculations a two-cell antiferromagnetic state is likely the zero-field structure and the ground state under field is likely a ferrimagnetic structure.

First principles calculations suggest that Mn_2FeMoO_6 and Mn_2FeWO_6 should have a spontaneous electric polarisation of ~68 $\mu C.cm^{-2}$.[89,90] However, when M = W, no ferroelectric switching is observed in dielectric and polarisation measurements. In the M = Mo material ferrimagnetic order is observed at T_c = 337 K, no ferroelectricity is observed from dielectric or polarisation measurements. However, it is possible that while no ferroelectric effects are observed in bulk polycrystalline samples, thin films or single crystals of these materials may exhibit some ferroelectric and multiferroic behaviour, as has been seen in thin films of $ZnSnO_3$ samples with $LiNbO_3$ structure types (but not in polycrystalline samples).

1.3.2. Simple ABO_3 Perovskite Manganites

While $MnVO_3$ adopts an ilmenite structure (known as $MnVO_3$-I) when synthesised at ambient pressure, a perovskite phase, $MnVO_3$-II, can be formed by quenching the material at pressures of ~5 GPa.[87,93] This material shows metallic conduction and possesses a complex incommensurate magnetic structure.

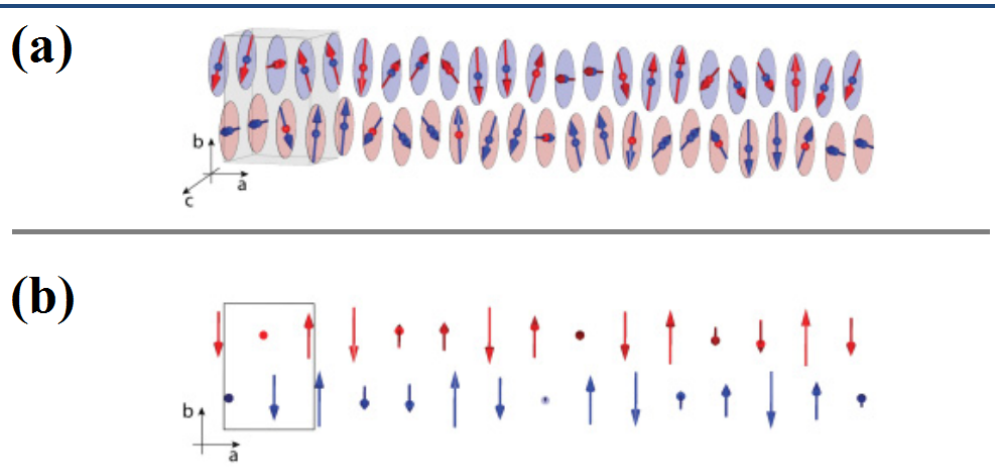

Figure 1.16 | *Example of (**a**) helical magnetic order in $MnVO_3$ (or a potential SDW, (**b**)). From neutron diffraction of polycrystalline samples, helical and SDW orders are mathematically equivalent. Figures from Markkula et al.*[93]

The magnetic structure of $MnVO_3$-II can be described by a magnetic propagation vector of $\boldsymbol{k}$ = (0.29 0 0) below a 46 K spin ordering transition. From fits to neutron diffraction data, the incommensurate magnetic intensities can be modelled equally well at 1.7 K with a helimagnetic spiral of Mn moments that all have equivalent magnitudes of 3.5(1) μ_B (**Fig. 1.16a**), or using a spin density wave (SDW) with collinear moments parallel to the (001) plane with an amplitude of 4.9(2) μ_B (**Fig. 1.16b**).[93] No B-site spin order on V^{4+} has yet been observed in this material.

1.3.3. Quadruple 134-Type Perovskite Manganites

The quadruple perovskite $(NaMn_3)Mn_4O_{12}$ is one example of perovskites commonly referred to as 134-type, with a general formula of $AA'_3B_4O_{12}$.[94] This material exists as a cubic structure in space group *Im*3 (a = 7.3043(3) Å) at room temperature but undergoes a transition to a charge ordered monoclinic *I*2/*m* structure below 176 K (a = 7.3527(6), b = 7.1986(5), c = 7.3493(6) Å and β = 90.558(3)°), with B-site columns of Mn^{3+}/Mn^{4+}, described as $(Na^+Mn_3^{3+})(Mn_2^{3+}Mn_2^{4+})O_{12}$. Two

magnetic ordering transitions are observed, one at 125 K at the onset of antiferromagnetic order of octahedrally coordinated Mn_B cations, with a second transition at 90 K, below which the dodecahedrally coordinated $Mn_{A'}$ orders. The simple binary oxide Mn_2O_3 transforms to a perovskite-type structure (ζ-Mn_2O_3) under high *P*/*T* conditions of approximately 18-22 GPa and temperatures of 700-1000 °C.[95] This is a highly distorted triclinic perovskite ($P\bar{1}$, a = 14.6985(2), b = 14.6482(2) and c = 14.6705(2) Å; α = 89.2108(8), β = 89.2031(9) and γ = 89.196(1)°) and is more accurately described as $(Mn^{2+}Mn_3^{3+})Mn_4^{3.25+}O_{12}$ ($AA'B_4O_{12}$-type) rather than simply $MnMnO_3$ (ABO_3-type), bearing striking similarity to the aforementioned perovskite $(NaMn_3)Mn_4O_{12}$. As the A-sites of perovskites generally require larger cations relative to the B-sites it is not entirely surprising that the Mn A-sites in ζ-Mn_2O_3 are partially reduced from Mn^{3+} (0.65 Å) to Mn^{2+} (0.93 Å) to compensate for this when compared with the Na^+ (1.39 Å) containing material.[85]

Another example of a 134-type perovskite with A-site Mn^{2+}, $MnCu_3V_4O_{12}$, can be synthesised at 12 GPa and 1000 °C, adopting the cubic $Im\bar{3}$ space group (a = 7.26684(10) Å).[96] This structure is notable for maintaining cubic symmetry while, unusually, Mn^{2+} is able to occupy 12-coordinate environment in the form of a regular icosahedron. In $MnCu_3V_4O_{12}$ a formal charge state of $Mn^{2+}Cu_3^{2+}V_4^{4+}O_{12}$ is found, where the 3*d* electrons of Cu^{2+} and V^{4+} are delocalised and provide a metallic conduction, while Mn^{2+} electronic states. Other A-sites are occupied by Cu^{2+} with square planar coordination environments, another example of transition metals occupying A-sites in perovskites. This is also observed in other 134-type materials such as $CaCu_3Fe_2Re_2O_{12}$,[97] that has 1:3 A-site order as well as 1:1 rock salt B-site

order and exhibits magnetoresistance through the Fe^{3+}/Re^{5+} ferrimagnetic structure, however A-site Mn shall be the focus of this section.

1.3.4. Double Perovskite Manganites

Two examples of double perovskites with A-site Mn^{2+} are Mn_2FeSbO_6 and Mn_2MnReO_6. The double perovskite Mn_2FeSbO_6, synthesised at 5.5 GPa and 1250 °C, adopts the monoclinic $P2_1/n$ space group (a = 5.234(1), b = 5.389(1), c = 7.7642(1) Å and β = 90.372° at 300 K),[98] with a formal charge distribution of $Mn_2^{2+}Fe^{3+}Sb^{5+}O_6$ and a rock salt order of Fe^{3+}/Sb^{5+}. The spin structure of Mn_2FeSbO_6 is complex. Spin order occurs below 200 K with an incommensurate magnetic propagation vector of $\boldsymbol{k}$ = (0 0.426 0). The orientations of moments of both Fe and Mn lie in the *ac*-plane and have been determined to propagate as an elliptical helix (**Fig. 1.17**).[98]

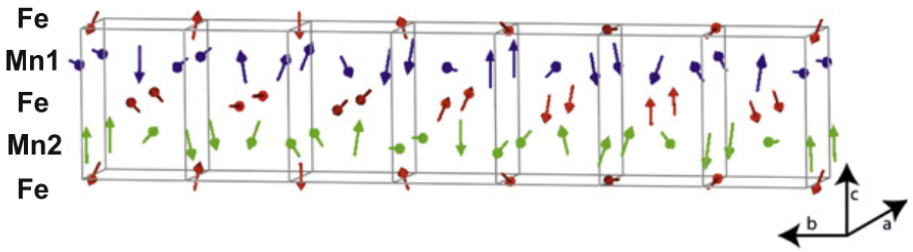

Figure 1.17 | *Example of helical magnetic order observed in Mn_2FeSbO_6, with both the Mn^{2+} and Fe^{3+} spins propagating as helices. Figure from Dos Santos-García et al.*[98]

Mn_2MnReO_6 adopts a double perovskite structure, with rock salt ordering of Mn/Re cations across B/B′-sites in the commonly adopted monoclinic space group $P2_1/n$ (a = 5.275(1), b = 5.400(1) and c = 7.710(1) Å; β = 90.02(1)° at 300 K).[99,100] This has been synthesised under conditions of 5-8 GPa and 1400 °C and is shown to have a charge distribution of $Mn_2^{2+}Mn^{2+}Re^{6+}O_6$ by BVS and X-ray absorption near-

edge spectroscopy, similar to that of $Ca_2^{2+}Mn^{2+}Re^{6+}O_6$.[101] Mn^{2+} spin order occurs at 109 K across both the A and B-sites, with Mn_A and Mn_B moments oriented in the *ab*-plane perpendicular to one another. A second magnetic transition is observed at 99 K by the temperature variation of magnetic intensities in the neutron data and attributed to the onset of Re^{6+} spin order, constrained in refinements of the magnetic structure to be to be collinear with Mn_B spins. These magnetic structures are shown in **Fig. 1.18** at 100 K (above the Re ordering transition) and at 10 K (below the Re ordering transition).

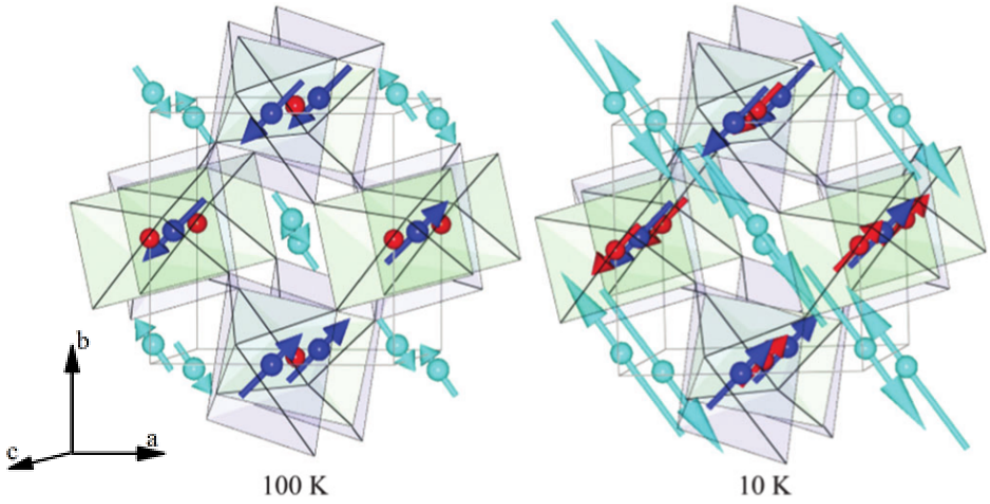

Figure 1.18 | *Spin structures of Mn_2MnReO_6 at 100 K (**left**) and at 10 K (**right**), indexed with a propagation vector of **k** = (½ ½ 0). Mn_A sites are coloured cyan. Mn_B and Re sites are coloured blue and red, respectively. Figure from Arévalo-López et al.*[99]

The successive transitions reveal interesting behaviour relating to frustration in this system. The Mn_B moment initially rises more rapidly than the Mn_A moment below 109 K and saturates at 99 K. This indicates a partial frustration of the Mn_A moment and full frustration of the Re moment (which does not begin to order until 99 K) by the dominant Mn_B spin order. However, at this point Mn_B saturates at 2.0 μ_B, well below the theoretical maximum of 5 μ_B. Mn_A/Re moments then rise below 99 K

from 1.1 and 0 μ_B to saturate at values of 4.5 and 1.0 μ_B, respectively (close to ideal values of 5 and 1 μ_B). The 99 K transition is therefore accompanied by a switch from frustrated Mn_A/Re spin order to frustration of further Mn_B order above a saturated value: 2.0 μ_B.

The monoclinic lattice distortion is suggested to somewhat relieve the frustration in this system and a change in thermal expansion of the *c*-axis from positive above 109 K and negative below 109 K increases the monoclinic distortion further, helping to remove frustration. Below the 99 K magnetic transition and the onset of Re spin order, another lattice anomaly is observed in the β lattice parameter, suggesting that these magnetoelastic couplings are linked to the mechanism of relieving magnetic frustration in the system.

1.3.5. Double Double Perovskite Manganites

The double double perovskite series $RMnMnSbO_6$ (R = La, Pr, Nd, Sm, Eu and Gd) has been previously discussed in '*1.2.1 – Symmetry and Structure*' as, when R is large (R = La, Pr, Nd or Sm), a rather unique simultaneous order of 1:1 columnar order across A-sites and 1:1 rock salt order across B-sites is observed.[64] It is also notable as another set of materials with A-site Mn^{2+}. As an example of the magnetic behaviour of these materials, the $NdMnMnSbO_6$ will be discussed further.

$NdMnMnSbO_6$ is synthesised under conditions of 10 GPa and 1200 K, and adopts the tetragonal $P4_2/n$ space group (a = 7.8295(3) and c = 7.9117(5) Å at 200 K).[64] Mn^{2+}/Nd^{3+} are ordered in (110) columns across A-sites, with Mn^{2+} occupying small 4-coordinate sites and Nd^{3+} occupying large 10-coordinate sites. The octahedral

B-sites are occupied by Mn^{2+}/Sb^{5+} with (111) rock salt order. With regard to the magnetic structure, powder neutron diffraction data and *M-T* curves reveals two distinct magnetic transitions.

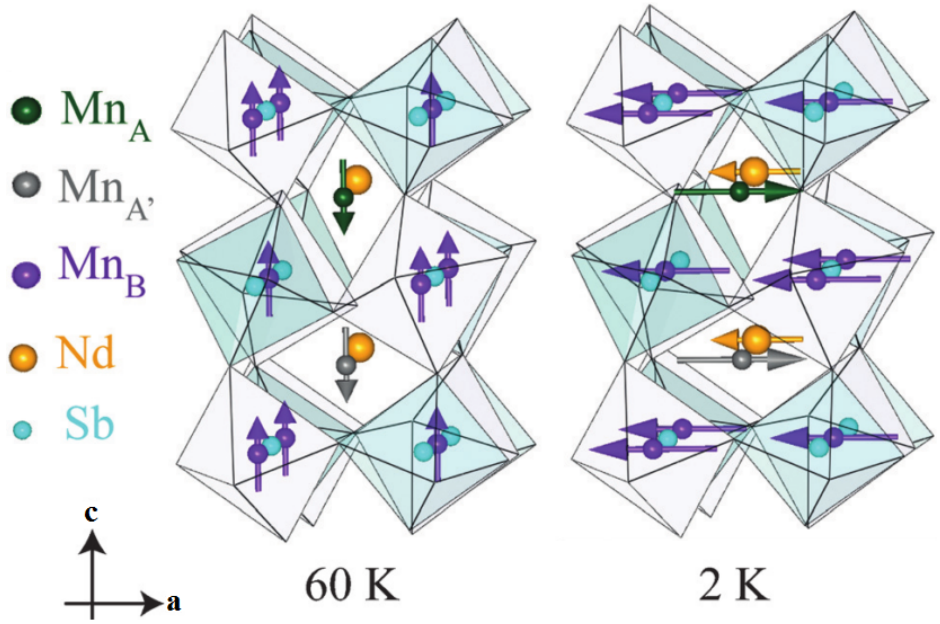

Figure 1.19 | *The spin structures of $NdMnMnSbO_6$ at 60 K, above the Nd^{3+} ordering transition (**left**) and at 2 K, below the Nd^{3+} ordering transition (**right**). Figure from Solana-Madruga et al.*[64]

The first magnetic transition is the ferrimagnetic spin order of Mn_B^{2+} and Mn_A^{2+} sites along the *c*-axis at 76 K.[64] Another magnetic transition occurs at 42 K, identified as the onset of Nd^{3+} spin order. Nd^{3+} spins orientate along the *a*-axis at this temperature and as they order, the Mn_A/Mn_B ferrimagnetic sublattice reorientates by rotating from the *c*-axis on to the *a*-axis, suggested to be driven by the single-ion anisotropy of the Nd^{3+} cation. These magnetic structures are shown in **Fig. 1.19** at 60 K (with Mn_A^{2+}/Mn_B^{2+} along the *c*-axis, before the spin order of Nd^{3+}) and at 2 K (after Nd^{3+} spin order and the reorientation of Mn_A^{2+}/Mn_B^{2+}, when all spins are along the *a*-axis).

The results of this study on $RMnMnSbO_6$ materials show that high pressure can be used to stabilise new types of structural ordering in perovskites which show interesting magnetic behaviour. In this case, the unusual structural order is due to a large size difference between the two A-cations, e.g. Mn^{2+}/Nd^{3+} (0.66 Å/~1.2 Å).[85] By placing magnetic cations at the A-sites of perovskite structures as well as B-sites, the A–O–B interactions are significant and as such new types of structural order provide different A–O–B pathways, as well as methods of controlling these interactions by varying cation size.

1.4. Research Outline

The research in this thesis focuses on using high-pressure techniques to combine the novel effects that can be realised with magnetic A-site transition metal cations, with the half-metallicity that double perovskites such as Sr_2FeMoO_6 with ordered B/B′ site cations possess. Strong antiferromagnetic couplings between B and B′ spins leads to ferrimagnetism with above-room-temperature Curie transitions. The synthesis of materials investigated as part of this work uses large volume (sample sizes of ~10 mm^3) multianvil equipment to generate pressures of ~10 GPa and temperatures of up to 1500 °C in order to attempt to synthesise high-pressure phases near the perovskite-$LiNbO_3$ cut-off line (**Fig. 1.13**), with the motivation being that many of the ABO_3 phases with tolerance factors near this boundary may be novel phases worthy of further study. A combination of magnetometry, resistivity and X-ray magnetic circular dichroism measurements as well as neutron and X-ray diffraction has been used to analyse the materials made throughout this work. The theory explaining these

techniques and practical aspects in carrying out the measurements are described in detail in the following section.

The materials investigated here focus primarily on the use of A-site Mn^{2+} with ferromagnetically ordered Fe/Re B-site cations and comparisons between these materials and the materials with Fe/Re and Fe/Mo rock salt B-site order presented in previous sections, such as Sr_2FeMoO_6 and Ca_2FeReO_6,[74] will be made. B-site order of Mn/Re has also been experimented with, yielding results that build upon the catalogue of Mn/Re materials that have been previously reported, notably with direct comparisons that can be made to the Mn_2MnReO_6 double perovskite discussed previously.[99,100] The materials discovered throughout this work will be shown to have interesting properties in terms of their structures and cation orders, notably with structures resembling the $RMnMnSbO_6$ series of double double perovskites discussed in the previous section.[64] The magnetic structures and properties of these materials will also be shown to have many variations, but with a common theme of contributions to magnetic properties from the presence of magnetic Mn^{2+} ($3d^5$, $S = {}^5/_2$) on A-sites as well as magnetic B/B′ couplings across B-sites. Significant couplings between magnetic A and B-site cations are also evident for some of these materials, complicating the magnetic interactions observed.

Chapter 2. Experimental Techniques

2.1. Preparation of Solid-State Materials

2.1.1. The Ceramic Method

Solid-state synthesis encompasses many methods of making solid materials for use further in characterisation or device fabrication. Of the many methods of solid-state synthesis, the ceramic method, involving the reaction of all reagents in their solid state, is most common. A mixture of solids is finely ground and pelleted before being heated at high temperature. If one or more of the components of the reaction are volatile or sensitive to the atmosphere, the reaction can be conducted in an evacuated sealed ampoule to prevent loss of reagent(s) or the formation of by-products. Alternatively, the reaction atmosphere can be controlled, for example by using N_2 or Ar to provide an inert atmosphere. Reducing or oxidising conditions can also be provided by using a flow of H_2 (often 5-10 % in Ar or N_2) or O_2, respectively. Encapsulating materials are also often used in the synthesis of metal oxides such as platinum, gold, silica or alumina, however the exact material chosen is dependent on the reagents used and the desired synthetic conditions.[102]

Temperature limits for synthesis by the ceramic method are typically of magnitudes of 2000 °C for resistive heating which is sufficient for the majority of metal oxide syntheses, however methods of heating using electric arcs or CO_2 lasers have been developed to access far higher temperatures of 3000 °C or 4000 °C. While these temperatures can be considered extreme in the context of synthesis in many other chemistry fields, solid-state synthesis routinely requires temperatures of this

magnitude. In general, the particle sizes of the finely ground powders are of the order of 10 μm when using a pestle and mortar. Reactions between powdered solids are diffusion limited and follow an Arrhenius rate law. As such, the temperatures required to achieve any significant ionic diffusion between solid particles in a pelleted sample are greater than 500 °C, but attention is needed to ensure that the temperature does not exceed the melting point of any of the reactants (or the product). Due to this diffusion limitation the cycle of grinding powdered reagents, pelleting and heating is often repeated several times, with the sample being reground and re-pelleted between heating steps. This facilitates the completion of the reaction and improves the homogeneity of the final sample. Particle sizes can be reduced by various methods, such as freeze-drying, spray-drying, co-precipitation or sol-gel techniques. This reduction in particle size can be of ~2 orders of magnitude, increasing the interfacial surface areas of neighbouring solid grains and leading to shorting diffusion path lengths for the reaction to proceed. This can then enable the synthetic route to proceed at lower temperatures, faster rates or reducing the number of intermediate grinding/re-heating/re-pelleting steps that are required for a homogeneous product.

2.1.2. High-Pressure Solid-State Synthesis

2.1.2.a Methods of Pressure Generation

The ceramic method can also be carried out at high pressures to stabilise dense structures. Historically, the synthesis of synthetic diamond drove the development of high-pressure techniques and diamond was first successfully synthesised in 1955 by the General Electric Company. The techniques and equipment developed for this

purpose were then used to explore the *P-T* phase diagrams of common elements such as Si, Ge and Bi.[102] The equipment to generate the high pressures required for these syntheses is quite varied in terms of the sample sizes able to be compressed and the pressures achievable by these different methods. In general, a device which is designed to compress a larger sample size will require a greater force to achieve the same pressure as a device designed to compress smaller samples. This follows from the simple relationship of pressure, force and area:

$$P = {}^{F}/_{A} . \qquad (\mathbf{2.1})$$

For pressures below approximately 1 GPa, hydrothermal synthesis can be used, while there are various techniques to achieve pressures exceeding this. Piston-cylinder devices are perhaps one of the simpler designs of high-pressure apparatus, generally consisting of a tungsten carbide chamber/piston shown in **Fig. 2.1a**. The precursor sample to be reacted is encapsulated within a metal suitable for the synthesis and placed inside the chamber, surrounded by a pressure transmitting material such as pyrophyllite. Pressure is generated by pressing the piston into the chamber and an internal graphite sleeve can be placed around the medium encapsulating the sample to act as a resistive heater by the application of a high current. In this setup, conditions of ~5 GPa and 1500 °C can be achieved, with relatively large sample volumes of 100 mm^3.[103] A popular alternative to the piston-cylinder apparatus is the belt apparatus, which can be considered a hybrid of the piston-cylinder and opposed anvil setup (**Fig. 2.1b**).[103] The belt apparatus consists of the precursor sample being encapsulated by a noble metal and again surrounded by pyrophyllite and a graphite sleeve. With this

apparatus there are two conical tungsten carbide pistons which are pressed from opposite sides into a tungsten carbide chamber, shown in **Fig. 2.1c**.

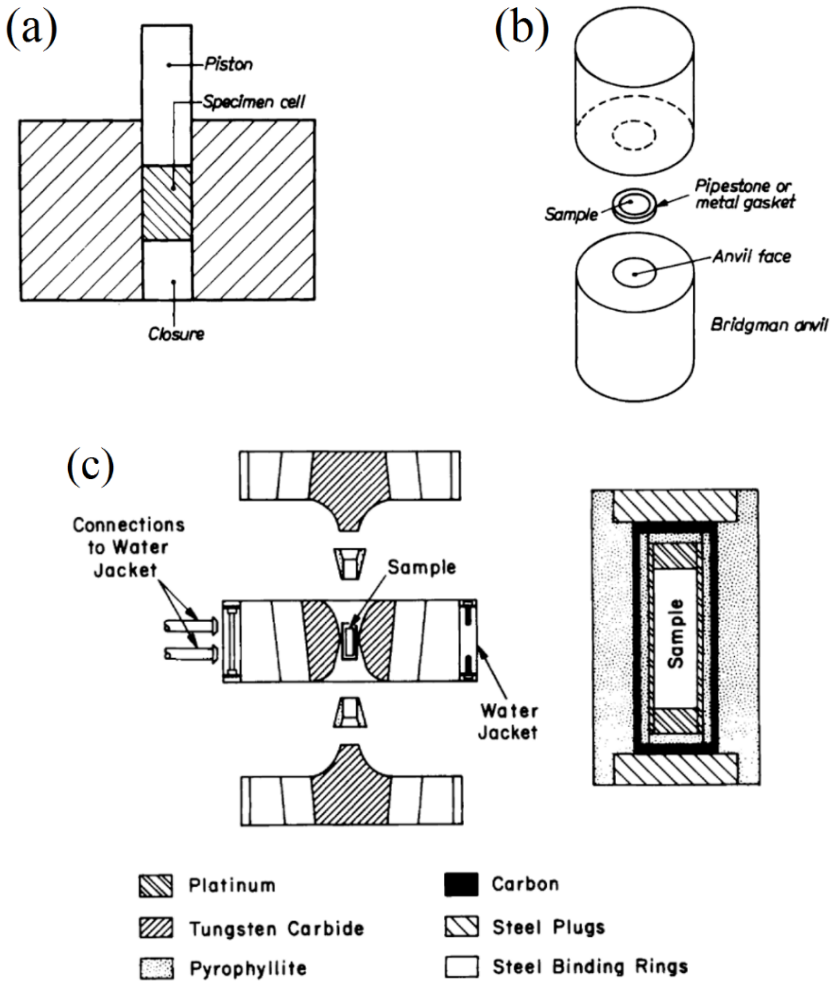

Figure 2.1 | *Examples of high-pressure cells for synthesis: (a) Piston-Cylinder, (b) Opposed Anvil and (c) 'Belt'-type apparatus. Figures from Preparative Methods in Solid-State Chemistry.*[104,105]

The entire belt assembly is supported by stainless steel rings or 'belts'. The belt apparatus is generally capable of reaching maximum pressures of ~15 GPa with temperatures of 2000 °C.[104,105] The popularity of this technique is due to the large sample sizes that can be pressurised, which can be over 100 mm^3 for pressures of ~6 GPa. In both of these setups, the piston(s) and supporting

tungsten carbide/steel are kept cold by water cooling, such that only the sample containing area reaches the high temperatures required for synthesis. This ensures that the mechanical properties of the metals used to generate high pressures do not alter significantly while heating is taking place.

2.1.2.b Multianvil Pressure Generation

Other means of producing high-pressure conditions include many different variations on multiple anvil setups. The opposed anvil design from **Fig. 2.1b** can be regarded as the simplest of these, of which the diamond anvil cell is a well-known example. However, setups utilising multiple anvils, and also with successive stages of multiple anvils exist. Various geometries of anvil assemblies have been used for this purpose, with many tetrahedral and cubic assembly designs, examples of which are shown in **Fig. 2.2**.[103] Support is provided to the anvils by surrounding rings of steel and preparation of sample precursors generally use noble metal encapsulating materials, with pyrophyllite as a pressure transmitting material.

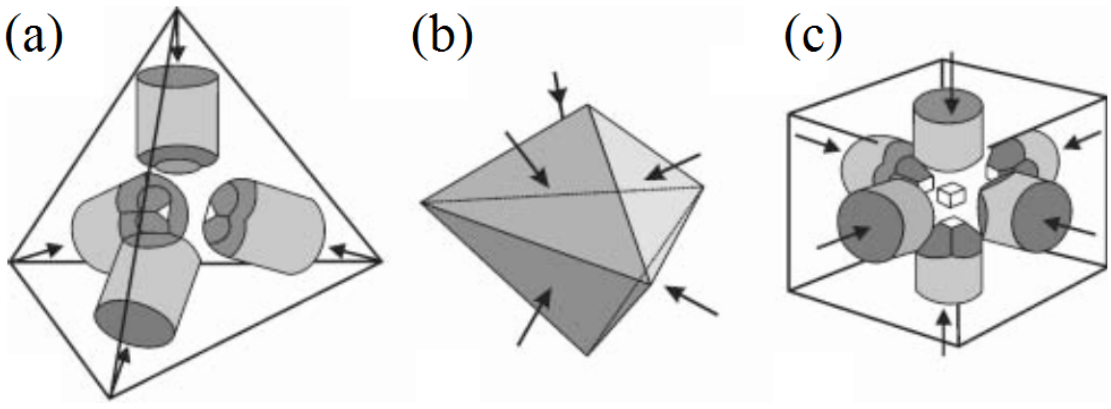

Figure 2.2 | *Examples of various multianvil geometries: (a) tetrahedral, (b) trigonal bipyramidal and (c) cubic. Figure from H. Huppertz.*[103]

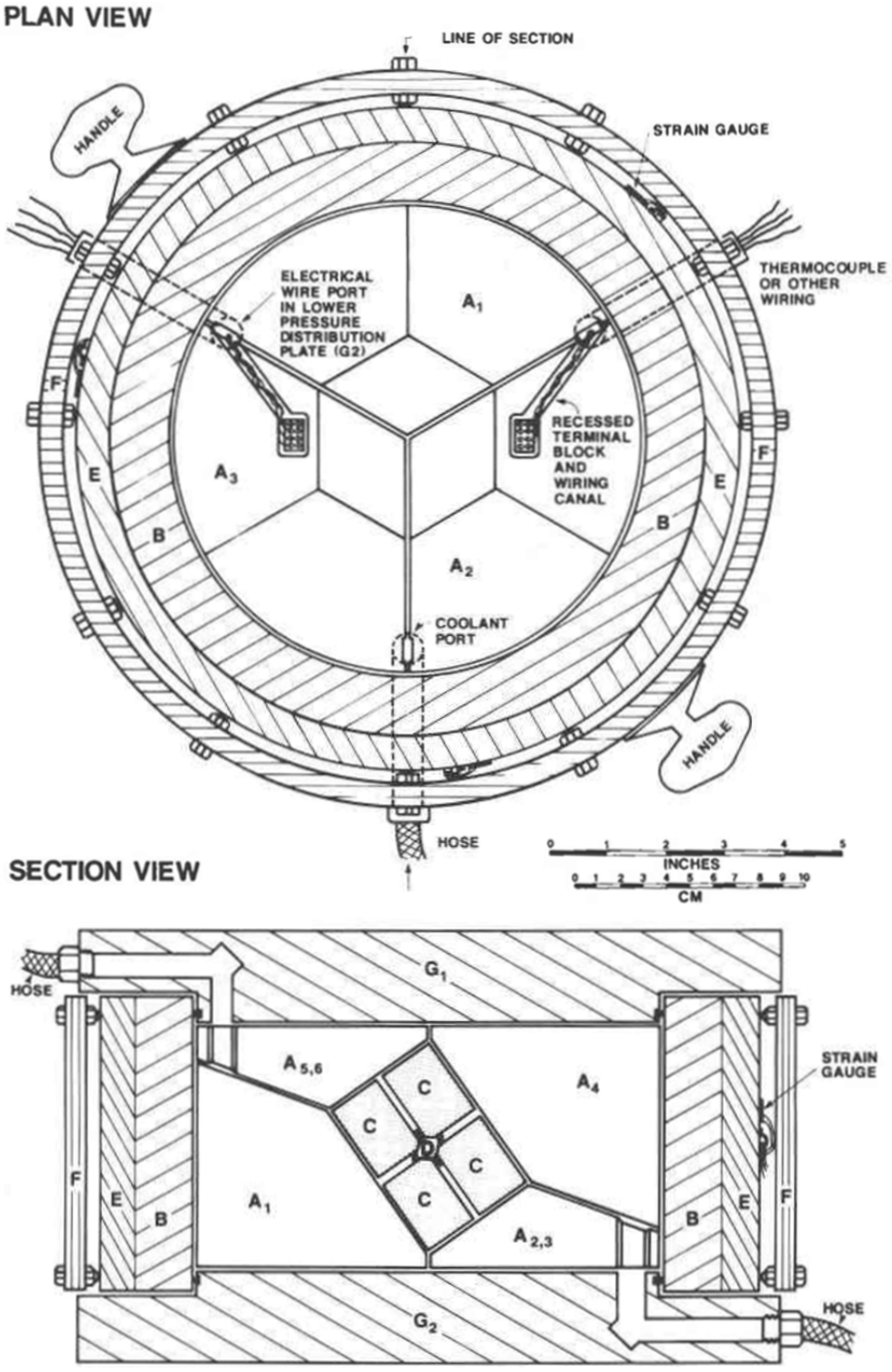

Figure 2.3 | *Plan view of Walker module (top) and section view (bottom). (A) Tool-steel wedges (set of 6 anvils), (B) tool-steel stress ring, (C) WC cubes with corner truncations, (D) chrome magnesia octahedron, (E) mild steel safety ring, (F) polycarbonate scatter shield and (G) tool steel pressure distribution plates. Figure from D. Walker et al.*[106]

As with the other setups, graphite sleeves can be incorporated around the encapsulated sample in order to provide a means to resistively heat the sample while at pressure. **Fig. 2.3** shows both a plan view and a section view of the original designs for a new two stage multianvil assembly, designed by D. Walker and now commonly known as the Walker Module.[106] The high-pressure synthesis conducted for the work in this thesis has been carried out using a module of this type. The Walker-type multianvil apparatus consists of a well-known octahedron-within-cubes geometry, where the sample containing setup including resistive heater, is seated within a set of eight cube-shaped anvils, each with a truncated corner in contact with one face of the octahedron (as in **Fig. 2.4**).

Compared with other octahedron-within-cubes designs, the Walker module features a supporting ring that surrounds a cylindrical assembly of steel wedges (that form a negative cube geometry able to accommodate the cube of eight anvils). This supporting ring allows a large amount of elastic strain when the module is pressurised, as well as providing a simple method of applying pressure to the sample.

2.1.2.c Walker Module Experimental Technique

The high-pressure techniques used for synthesis in this thesis use a 1000 ton hydraulic press, combined with the Walker module described earlier, to achieve pressures and temperatures of up to 22 GPa and 2000 °C. A well-mixed and finely ground sample precursor mixture resides in the centre of the multianvil assembly within a chrome magnesia (95 % MgO and 5 % Cr_2O_3) octahedron. This octahedron is placed at the centre of the set of eight WC cubes (each with a truncated corner), shown in **Fig. 2.4**.

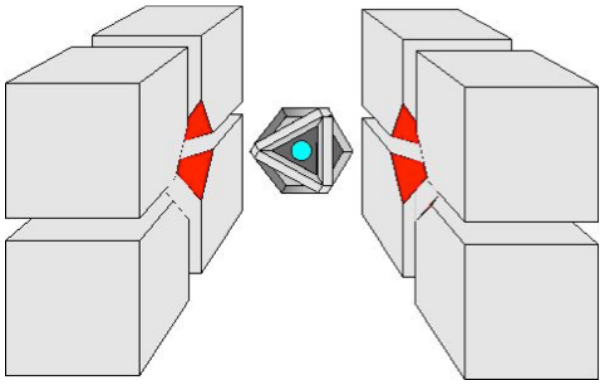

Figure 2.4 | *The octahedron sits between eight truncated WC anvils (truncated faces in red). The location of the cylindrical assembly is highlighted in blue, shown in detail in* ***Fig. 2.5****. Pyrophyllite gaskets are depicted on the edges of the octahedron. Figure from H. Huppertz.*[103]

The set of materials surrounding the sample capsule itself is also complex, consisting of materials with low thermal conductivity, to allow the sample to be heated while keeping the anvils cool. Another consideration is that the temperature gradient across the sample be minimal, with uniform heating of the entire bulk of the sample often being important in synthetic procedures. The chrome magnesia octahedron is typically a regular octahedron with octahedral edge length (OEL) of 14 mm and the truncation edge length (TEL) of tungsten carbide cubes used is 8 mm. However, variations on this exist, with the assemblies described by their OEL/TEL. In the high-pressure work in future chapters, the 14/8 setup is used exclusively, which is capable of reaching pressures of up to ~13 GPa with sample sizes of ~10 mm^3. Common measurements for OEL/TEL include: 25/17, 19/12, 18/11, 14/8, 10/5, 10/4 and 7/3.[103] Of these OEL/TEL measurements the 14/8 and 7/3 setups are used in the high-pressure lab in Edinburgh, capable of achieving pressures of up to ~22 GPa with the 7/3 setup (albeit with smaller sample sizes of ~1 mm^3). A 5.6 mm diameter hole is drilled into the chrome magnesia octahedron, allowing the sample and surrounding materials required for heating to be located at the centre. These materials are shown in **Fig. 2.5**.

Heating is achieved by passing a current through the octahedron assembly, with the graphite sleeves acting as the heating element. Two sleeves are used, with the interior sleeve acting as a heat exchanger to ensure a more uniform temperature gradient across the sample space. Zirconia and magnesia are also used in this assembly for their thermal properties, as well as their compressibility. With this setup the temperature can reach as high as 1500 °C, if higher temperatures are desired other materials such as Re or $LaCrO_3$ can be used as resistive heaters to push the temperature limit over 2000 °C. These heaters are also necessary when the pressure is ~20 GPa, as graphite sleeves will begin to transform into amorphous diamond when heated, preventing their use as a resistive heater.

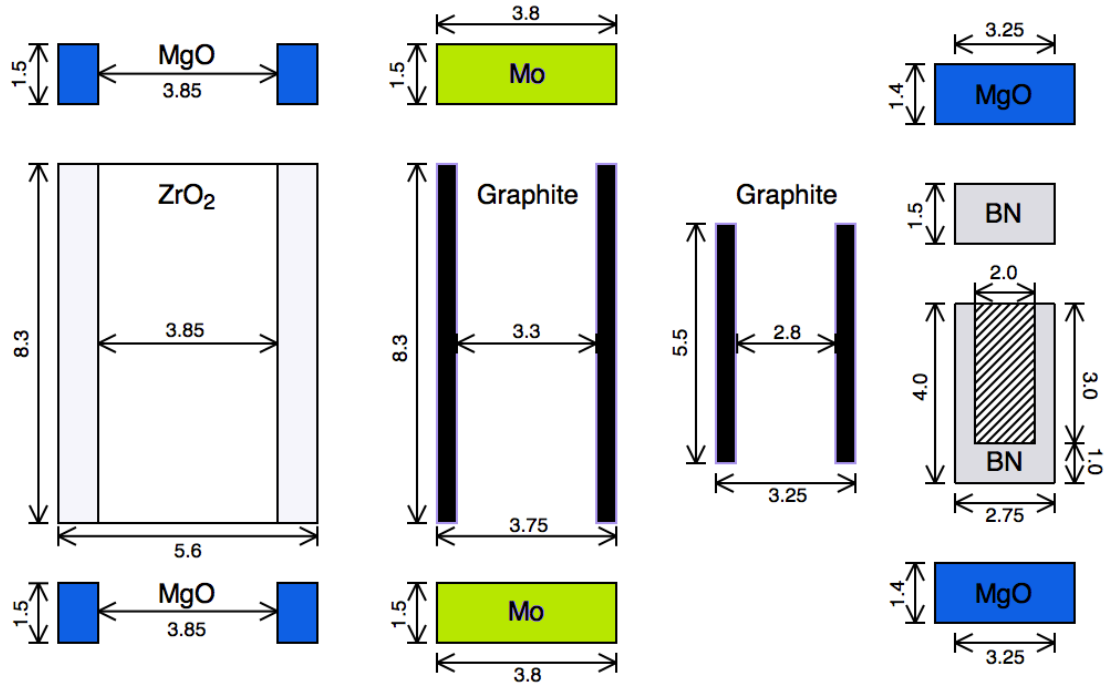

Figure 2.5 | *Diagram showing the materials that occupy the 5.6 mm diameter hole in the chrome magnesia octahedron. All measurements are in millimetres. The sample area is shown within a BN capsule. Not shown is the optional metal capsule (Au/Pt) between the BN and sample.*

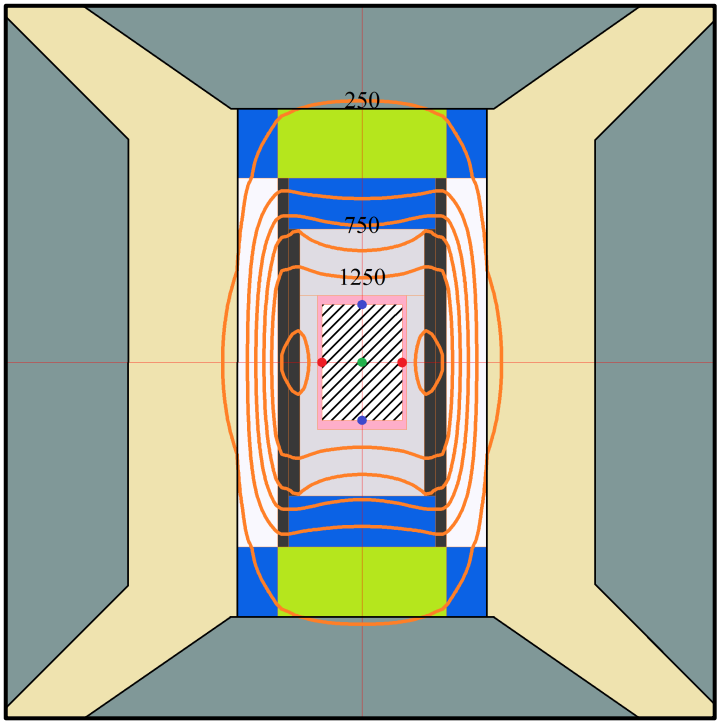

Figure 2.6 | *Schematic showing a model of the heating gradient around the sample space. The blue, green and red points shown in the figure indicate points on the sample with temperatures of 1400, 1440, 1466 °C, respectively. WC anvils in contact with the Mo discs of the sample assembly reach temperatures of ~250 °C. The truncated surface of other WC anvils maintains temperatures < 150 °C. Colours of materials are as **Fig. 2.5**. Figure adapted from output of Cell Assembly (Hernlund et al.).*[107]

Mo discs are used to provide the electrical contact between the graphite sleeves and the WC cube truncations. WC cubes are themselves electrically insulated from one another by PTFE tape and insulated from the steel anvils by fibreglass sheets, with the exception of the two WC cubes in contact with the Mo discs. The WC cubes in contact with Mo discs are contacted with the set of outer steel anvils by copper strips, one of the cubes to the upper set of three steel anvils and the other to the lower set of three steel anvils. The entire setup described allows the transport of current through the pressure assembly, passing through the graphite heater and resistively heating the sample. A temperature profile from a typical 1400 °C synthesis is modelled in **Fig. 2.6**,[107] showing a temperature gradient of less than 100 °C.

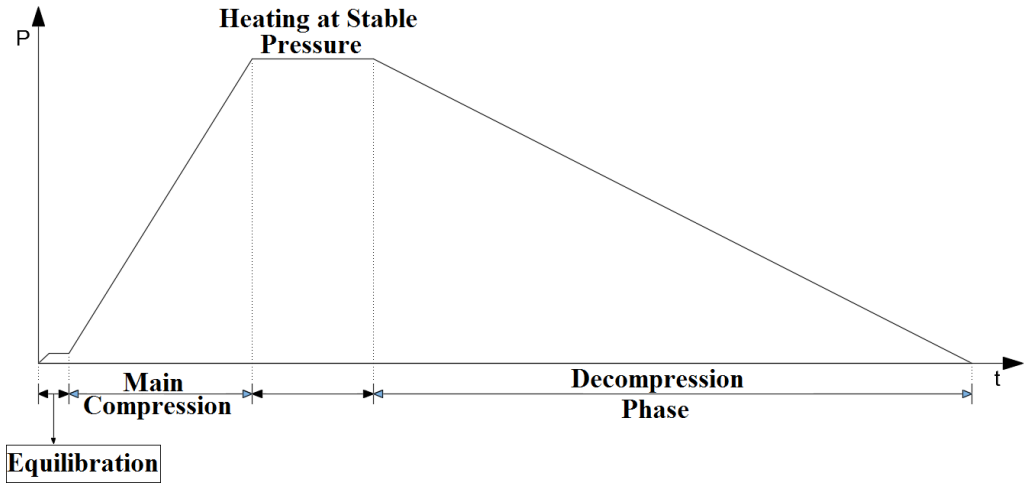

Figure 2.7 | *A schematic showing a typical profile of pressure versus time for a high-pressure synthesis using a Walker module.*

The sample itself is contained within a boron nitride capsule, However a secondary interior capsule (e.g. Au/Pt, dependent on the conditions of the synthesis) can be used to provide a secondary inert container for the synthesis. The pressure profile (**Fig. 2.7**) is monitored by the press control system, which transmits status messages to a computer. Typical syntheses consist of an equilibration stage, where a low load (approximately 10 tons) is applied to the module over a 10-minute compression and held for a duration of 20 minutes. After this initial stage the main compression stage can commence (calibrated using well-known phase transitions in a Bi standard: as 300 tons for a pressure of 10 GPa on a 14/8 - OEL/TEL set up) over a period of ~100 tons per hour. This pressure is held for up to two hours, during which time a current can be applied to heat the sample. The sample is then decompressed over a period of time that is three times the duration of the main compression stage to allow internal stresses in the WC anvils to relax gradually, preventing unnecessary damage to the anvils. Samples recovered from within Au/Pt capsules are typically hard, dense, polycrystalline pellets.

2.2. Structural Characterisation

2.2.1. Theory of Diffraction

Diffraction is the scattering of radiation from a periodic array of atoms and the resulting interference of the scattered radiation forms a diffraction pattern. A diagram of this phenomenon is shown in **Fig. 2.8**.

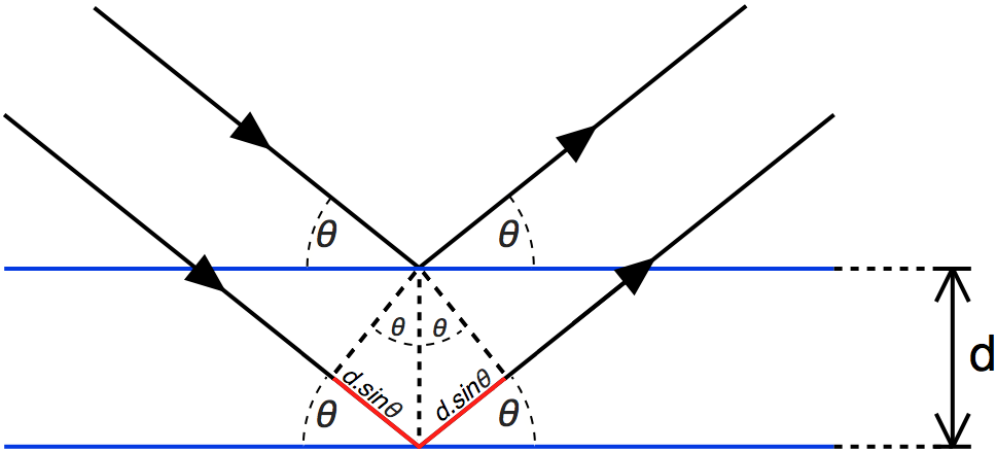

Figure 2.8 | *Diagram of the derivation of Bragg's Law, nλ = 2dsinθ, where λ is the wavelength of the incident radiation. The extra path length that the lower beam traverses is highlighted in red. The outgoing waves are in phase if this extra path length equals an integer number of wavelengths.*

When planes of atoms, separated by a distance, *d*, are considered as the diffraction planes, the extra path that a wave must travel into a deeper layer can be shown from trigonometric relationships to be *2dsinθ*. When this extra path distance is equal to an integer number of wavelengths, *nλ*, the outgoing diffracted waves will be in phase with one another and lead to constructive interference. These directions of high intensity are known as Bragg peaks after the Braggs who developed this theory. Bragg's Law,

$$n\lambda = 2d_{hkl}sin\theta, \qquad (2.2)$$

where d_{hkl} refers to the *d*-spacings for specific lattice planes denoted by the Miller indices *h*, *k* and *l*. The Braggs won the 1915 Nobel Prize in Physics, is now regarded as an extremely important relationship in crystallography.[108]

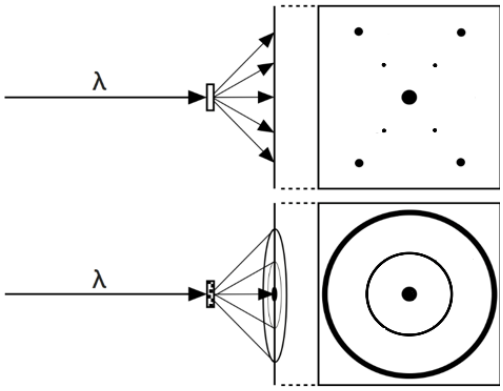

Figure 2.9 | *Schematic showing the difference in the diffraction patterns between a single crystal (**top**) and polycrystalline (**bottom**) samples. The conical diffraction features observed in the polycrystalline sample (that results in a series of concentric circles) are known as Debye-Scherrer cones.*

When examining single crystal structures in this manner, the diffraction pattern formed from the scattered radiation allows the elucidation of the crystal structure. A single crystal diffraction experiment can be considered in three-dimensions, where two dimensions referring to the orientation of the crystal that is under study and the diffraction angle being the third. When conducting diffraction experiments on polycrystalline powder samples two dimensions of information are lost in the experiment (as no crystal orientation information is present). This loss of dimensionality can be explained by thinking of the polycrystalline sample as being a collection of a large number of randomly oriented single crystals. By superimposing diffraction patterns obtained from every possible single crystal orientation the result is a set of concentric rings.[109] This is in essence how the Debye-Scherrer cone is produced by the randomly oriented particles in a powder, shown in **Fig. 2.9**.

This produces a problem when, due to the loss of all orientation information, multiple Bragg peaks originating from different reflections can overlap. This issue is overcome by allowing multiple reflections to contribute to the same intensity in a diffraction pattern using the Rietveld method (see '*2.2.6 - Rietveld Refinement*'). For this relationship to be of practical use, the wavelength of radiation used must be of a magnitude comparable to the atomic spacings in a crystal, usually in the order of Ångströms (Å). For electromagnetic radiation, these wavelengths correspond to X-rays of E ~10 keV, while the de Broglie relationship shows that neutrons with this wavelength have energies of ~100 meV. The use of neutrons or X-rays for a diffraction experiment generally depends on the information desired from the outcome of the experiment, as well as the ease of obtaining a source of X-rays/neutrons. One of the main benefits of X-rays that has aided in their widespread use in research laboratories, is the relative ease of their generation with X-ray tubes, but for many experiments brighter synchrotron sources of X-rays are required, e.g. the European Synchrotron Radiation Facility (ESRF).[110] By contrast, the generation of neutrons with high enough flux for diffraction experiments is exclusive to central facilities, using either a reactor source or a spallation source.[111,112]

X-rays and neutrons differ significantly in the way they interact with matter. With respect to diffraction, X-rays interact with the electrons in a material, while neutrons typically interact with the nuclei of the atoms. The intensity of X-ray diffraction from a particular atom is proportional to the square of the number of electrons in the atom, such that heavy atoms are stronger scatterers, as well as being proportional to a form factor that falls off with increasing angle.[109] In contrast,

neutrons do not have a distinct relationship with the atomic size of the element that are interacting with, but rather a complex relationship and can scatter very differently even from different isotopes of the same element. The form factor for nuclear neutron diffraction is a constant, as the nucleus can be considered a point scatterer that is far smaller than the wavelength of the incident neutrons.[107]

2.2.2. X-ray Diffraction

The development of easy generation of X-rays in the laboratory is one of the main contributors to the wide variety of applications for X-rays in modern science, such as X-ray powder diffraction (XRPD). Modern X-ray generators work by using an electron emitting filament. A positive voltage, *V*, is applied to a metal target (e.g. Cu, Mo) and electrons emitted from the filament are accelerated towards the target. On impact, the conversion of the electron kinetic energy into X-ray photons occurs by two different mechanisms. The Bremsstrahlung mechanism is a result of the rapid deceleration of electrons, emitting a continuum of wavelengths. The second mechanism is due to electrons being ejected from an inner energy level of the metal atom by the impact of the high energy electrons. On relaxation of an electron in an upper energy level to the newly created vacant site, an X-ray is emitted of an energy equal to the difference, ΔE, between these two energy levels. As such, the wavelength of this radiation can be calculated as,

$$\lambda = \frac{hc}{\Delta E}. \qquad (\mathbf{2.3})$$

This results in sharp features corresponding to specific wavelengths for different metal targets. Of these characteristic energies, the K_α emission, as labelled in **Fig. 2.10**, is typically the most intense emission. For Cu K_α, this emission corresponds to X-rays of wavelength 1.541(5) Å. Sample preparation for powder X-ray diffraction typically requires a finely ground and mixed (in a case where multiple phases are present) sample. In the case of magnetic powders, care must be taken to ensure that the sample is not exposed to magnetic fields during preparation, as this can cause a preferred orientation of individual sample grains. Depending on the diffractometer setup, the powder is either evenly distributed on a silica slide in methanol (and the methanol allowed to evaporate) or the sample is packed into a silica capillary.

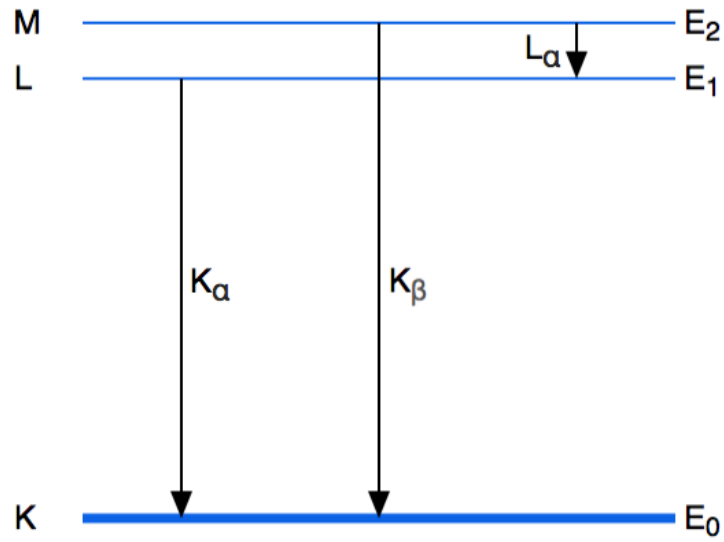

Figure 2.10 | *Schematic of the emission lines for X-rays. An electron is ejected from E_0 and the X-ray emission is caused by an electron from E_1 relaxing to E_0 (K_α) or relaxation from E_2 to E_0 (K_β). Also shown is L_α, however this involves the electron initially being ejected from E_1.*

When electrons impact the metal target during generation of X-rays, most of their kinetic energy is converted into heat, rather than useful X-rays. This limits the intensity of the X-ray source by the rate at which the target can be cooled and maintain

maximum X-ray output. To utilise X-rays of higher intensity a synchrotron source is required.

X-rays can be generated in large particle accelerator facilities known as synchrotrons.[109,110] A synchrotron is designed to accelerate particles, in this case electrons, to very high energies and guide them on a circular path. By accelerating electrons in a circle, energy is emitted in the form of X-rays in a direction that is tangential to the circle. In practice, a synchrotron is actually made up of many straight sections separated by curved sections. The curved sections consist of magnets referred to as bending magnets which direct the beam to the next straight section by bending the path of the electrons (producing intense X-rays in the process). The straight sections contain magnets known as undulators or wigglers that cause the beam to undergo rapid oscillatory motions. This produces an extremely intense X-rays parallel to the straight section of the synchrotron ring. At either a 'bending magnet' (BM) station or an 'insertion device' (ID) station, these intense synchrotron X-rays can be filtered and focussed using a combination of mirrors and diffraction gratings and used for diffraction or spectroscopy, with the benefit that the extreme flux provided will allow faster measurements with greater signal-to-noise ratios than those possible at a lab X-ray source.

For elastic X-ray diffraction we can define a scattering vector, $\boldsymbol{Q}$, from the incident ($\boldsymbol{k}_i$) and diffracted ($\boldsymbol{k}_f$) wavevectors:

$$\boldsymbol{Q} = \boldsymbol{k}_f - \boldsymbol{k}_i \quad (2.4)$$

While X-ray diffraction patterns are often presented as intensity versus scattering angle, as the scattering angle is wavelength dependent it is often helpful to present these patterns as intensity versus scattering vector (or *d*-spacing), as data acquired from different instruments with different incident wavelength radiation can be more easily compared. The scattering vector and scattering angle can be related mathematically as,

$$Q = \frac{4\pi \sin(\theta)}{\lambda} \quad , \qquad (\mathbf{2.5})$$

and the scattering vector is helpful to describe the atomic form factor for X-rays,

$$f_j(\lambda, \theta) = z \cdot r_e \cdot g_j(Q) \qquad (\mathbf{2.6})$$

where f_j is a function of Q and therefore depends on $sin\theta/\lambda$, which causes a fall off of the observed intensity of reflections with increasing 2θ. The constant r_e is the radius of the electron and $g_j(Q)$ is a decaying function, dependent on the specific atom, j, being studied. This function has a maximum of 1 at Q = 0 and tends to 0 as Q approaches infinity. The structure factor for X-ray scattering from a periodic lattice is shown as,

$$F_{hkl} = \sum_j f_j e^{2\pi i(hx_j + ky_j + lz_j)} . e^{-B_{iso,j} sin^2\theta/\lambda^2} \quad , \qquad (\mathbf{2.7})$$

which includes this form factor term and where $B_{iso,j}$ is the isotropic thermal factor for atom j; h, k and l are the Miller indices for specific lattice planes and x, y and z are the atomic coordinates. The arrangement of atoms in the crystal is related to the intensities of the diffraction pattern by a Fourier transform of the electron density distribution around the atoms and the diffracted intensities (I_{hkl}) are related to the structure factor

as: $I_{hkl} \propto |F_{hkl}|^2$. The main obstacle with the analysis of diffraction data arises because if the structure factor is known, the crystal structure can be determined, however the intensities in a diffraction pattern only give us information about $|F_{hkl}|^2$ and not F_{hkl}. There is a problem here as F_{hkl} is a complex number and cannot be determined simply from $|F_{hkl}|^2$,

$$F_{hkl} = A_{hkl} + iB_{hkl} \quad \textbf{(2.8)}$$

$$|F_{hkl}|^2 = (A_{hkl} + iB_{hkl})(A_{hkl} - iB_{hkl}) = {A_{hkl}}^2 + {B_{hkl}}^2 , \qquad \textbf{(2.9)}$$

and this has come to be known as the phase problem in crystallography. There are many methods that have been employed to overcome the phase problem, amongst these methods are Patterson maps, heavy-atom methods and direct methods.[109] Often, it is helpful to have some initial information about the crystal being studied, such as the elements present and their likely mole ratios or even some expected likely structure types, in order to solve the structure quickly. In addition to the structure factor there are many other factors which influence the intensity of a particular reflection, such as the length of time that the sample is exposed to incident radiation or the absorption of radiation by the sample. These factors must also be taken in to account in order to fully characterise a crystalline material by diffraction methods.

2.2.3. Neutron Diffraction

The 1935 Nobel Prize in Physics was awarded to J. Chadwick for the discovery of the neutron (1932),[113] and the first self-sustaining nuclear reaction was initiated in 1942 by a group led by E. Fermi with the fission of ^{235}U at Chicago Pile-1.[114] Today, nuclear reactors are not only widely used for energy generation, but are also commonly

used in research to generate neutrons for scattering experiments. Brockhouse and Shull were awarded with the 1994 Nobel Prize in Physics for developing neutron scattering techniques in condensed matter studies,[115] and these techniques rely on the fundamental properties of the neutron, with a mass of 1.675×10^{-27} kg, half-life when free of 610.0(8) s, zero charge (to which it owes its name), and a spin value of ½ with magnetic moment of -1.913 μ_N.[116] It is these properties of the neutron and how it contrasts with other forms of radiation, such as X-rays, which make the neutron so useful as a structural probe.[117]

In general, the neutron interacts strongly with atomic nuclei but not with paired electrons. This is in contrast to X-rays, which interact primarily with electrons in a material and the strength of these interactions are proportional to z^2 (the square of an elements' proton number). Neutrons however have no clear relationship between the strength of interactions and the proton number of an element. In fact, even different isotopes of the same element may have widely varied scattering power, as the interaction of neutrons is dependent on the specific nucleus. These properties lead to many unique characteristics of neutron scattering, such as adjacent elements having high contrast, or the potential to gain extra structural information by comparing diffraction patterns of isotopically substituted materials to those with elements in their natural abundances. In practice, the differences between the ways in which neutrons and X-rays interact with matter mean that these two techniques are often complementary techniques rather than substitutes for one another. Potentially the most important difference between X-rays and neutrons is the spin number of ½ that the neutron possesses. This magnetic moment of the neutron allows it to interact strongly

with unpaired electrons in a material and, if magnetic order is present, neutron diffraction can be used to obtain diffraction patterns that have contributions from repeating magnetic order in a material. This enables the magnetic unit cell, symmetry and magnitude of moments to all be determined from diffraction. For neutrons, as is the case with X-rays, the diffracted intensity is proportional to the square of the structure factor.[109] For an unpolarised source of neutrons, the square of the measured intensity for a reflection that has combined nuclear and magnetic contributions is proportional to the square of the modulus of the total structure factor. This is a simple sum of the squares of the moduli of the nuclear and magnetic components of the structure factors, shown as,[118]

$$|F_{hkl}|^2 = |F_{nuc}|^2 + \left|\boldsymbol{F}_{mag}\right|^2. \qquad \textbf{(2.10)}$$

The separate components for nuclear and magnetic scattering of neutrons have different forms,

$$F_{nuc} = \sum_j b_j \,.\, e^{2\pi i(hx_j+ky_j+lz_j)}.\, e^{-B_{iso,j}sin^2\theta/\lambda^2} \qquad \textbf{(2.11)}$$

$$\boldsymbol{F}_{mag} = p\sum_j f_j \boldsymbol{q}_j e^{2\pi i(hx_j+ky_j+lz_j)}.\, e^{-B_{iso,j}sin^2\theta/\lambda^2}, \ \textbf{(2.12)}$$

here x, y and z are the coordinates of atoms within the unit cell and the value b_j is the scattering length for the particular atom, j. The structure factor, $\boldsymbol{F}_{mag}$ for magnetic scattering of neutrons, is proportional to the magnetic moment of the involved atoms. $\boldsymbol{F}_{mag}$ is therefore dependent on a magnetic interaction vector, $\boldsymbol{q}_j = \widehat{\boldsymbol{Q}}\left(\widehat{\boldsymbol{Q}} \cdot \widehat{\boldsymbol{\mu}}_j\right) - \widehat{\boldsymbol{\mu}}_j$, (where $\widehat{\boldsymbol{Q}}$ and $\widehat{\boldsymbol{\mu}}_j$ are the unit scattering vector and atom j's magnetic moment vector, respectively). This magnetic interaction vector is an important aspect of magnetic neutron diffraction as only the component of $\boldsymbol{\mu}$ perpendicular to $\boldsymbol{Q}$ contributes to

magnetic intensity. The magnetic structure factor is also proportional to the magnetic cross section, *p,* and the magnetic form factor, f_j. The magnetic form factor reduces with increasing scattering angle as with the X-ray scattering form factor. This is in contrast to the nuclear neutron structure factor, which is independent of 2θ.[109]

2.2.4. Neutron Generation

2.2.4.a Reactors – The Institut Laue-Langevin

Since the 1940s reactors have been used to generate neutrons (e.g. by fission of ^{235}U).[114] Neutrons produced by nuclear fission are considered 'fast' and have energies of MeV, however, the cross section of fission for ^{235}U (absorption of ^{1}n and subsequent fission) is low for high-energy neutrons in the MeV range. For a self-sustaining nuclear reaction it is necessary to use slow neutrons with meV energies, for which the cross section of fission for ^{235}U is very high.[117] In practice, this is overcome in reactors by collisions of neutrons with a moderator to thermally equilibrate neutron energies,

$$E_K = {}^{1}/_{2}\, m_n v_n^2 = k_B T\,, \qquad \textbf{(2.13)}$$

where E_K is the kinetic energy, m_n the mass of the neutron, v_n the velocity of the neutron, k_B is Boltzmann's constant and T is the temperature of the moderator (to which the neutrons will be equilibrated to).

Using light elements (close in mass to the neutron) to moderate their energy, the neutrons in a reactor can be equilibrated to the temperature of the moderator (T), where v_p is the velocity of the neutron at the peak flux of the reactor. In this manner, a chain reaction can be sustained and it is fortuitous that the energy of neutrons required

to sustain a fission reaction are in the meV range and correspond with wavelengths that are of similar order of magnitude to lattice spacings in a crystal (~2 Å) and are therefore suitable to use for diffraction.

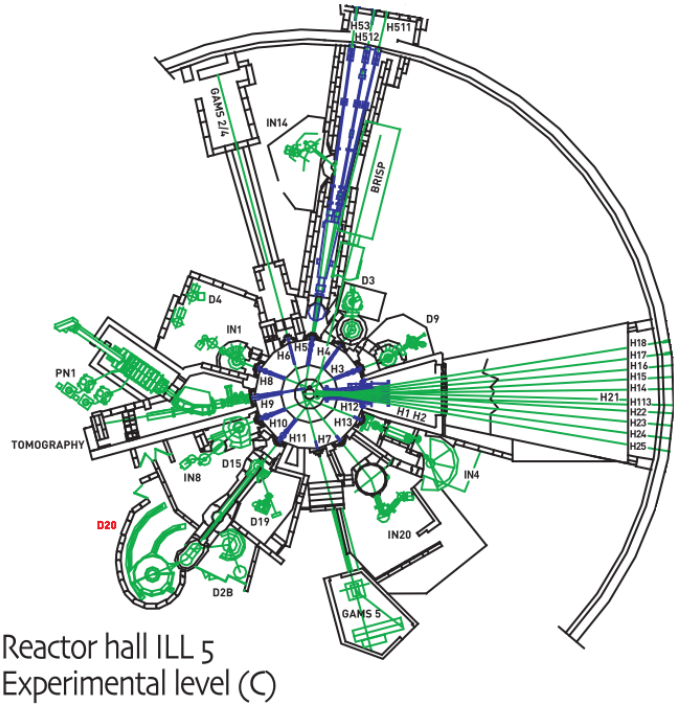

Figure 2.11 | *The main reactor hall of the Institut Laue Langevin (ILL). Highlighted in red is the D20 diffractometer (shown in detail in* ***Fig. 2.12****). Not shown are the guide halls to the top and right of the main reactor hall. Figure adapted from The Yellow Book: Guide to neutron research facilities at the ILL.*[111]

In a reactor neutron diffraction setup however, monochromation of the neutron beam is required to produce a beam of a very narrow range of wavelengths. This cuts the available neutron flux down considerably from the raw flux that is produced from the reactor. The Institut Laue-Langevin (ILL) reactor in Grenoble, France (shown in **Fig. 2.11)**, produces a raw flux of neutrons of 1.5 x 10^{15} s^{-1} cm^{-2}, with a thermal power of 58.3 MW.[111,117] The on-sample flux is significantly lower than this raw flux produced by the reactor.

2.2.4.b D20 – The Institut Laue-Langevin

Neutron diffraction data from the D20 diffractometer at the ILL (**Fig. 2.12**), a reactor source of neutrons, features in one of the publications resulting from the work in this thesis. This is an extremely high flux (10^7 $s^{-1}cm^{-2}$ to 10^8 $s^{-1}cm^{-2}$)[119] 2-axis diffractometer. The high flux allows the examination of small (~50 mg) powdered samples, such as those generated by high-pressure synthesis. An angular scattering range of 153.6° is covered by the microstrip detector on D20 and the sample container can be cryogenically cooled to 1.7 K. This makes this diffractometer a good instrument for collecting data for small sample sizes and, in particular, when examining magnetic structure at temperatures approaching absolute zero.

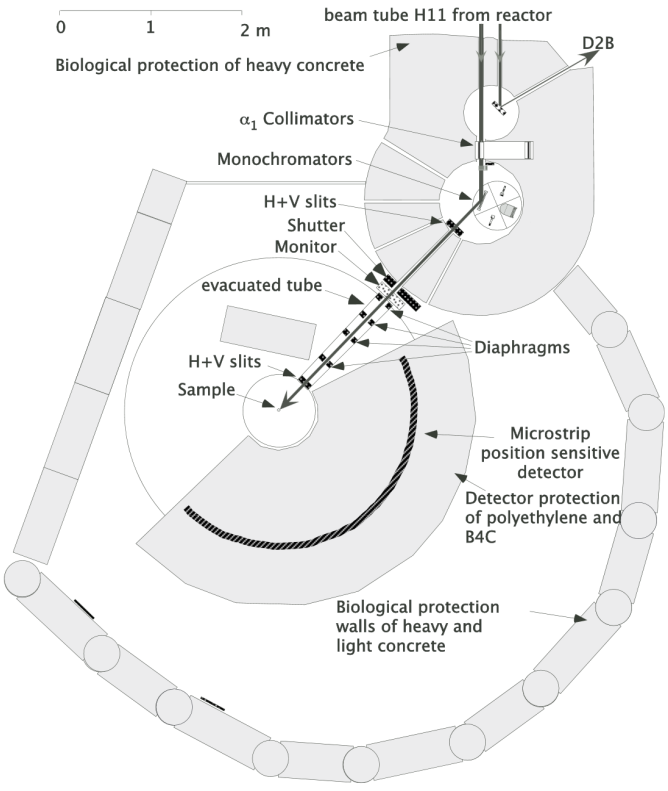

Figure 2.12 | *The D20 diffractometer at the ILL. The monochromators mounted on a carousel, such that the incident wavelength can be easily altered. The (002) face of highly oriented pyrolithic graphite (HOPG), which monochromates neutrons to 2.41 Å, provides an on-sample flux of 4.2 10^7 s^{-1} cm^{-2} and an average resolution of $^{\Delta d}/_{d} = 1.6\times10^{-2}$. Figure from Hansen et al.*[119]

As with powder X-ray diffraction, the sample preparation for powder neutron diffraction requires a finely ground sample. The sample holder used is generally made of thin vanadium due to its low neutron scattering length (b = -0.3824 fm).[118] The sample can be examined as a function of temperature from 1.7 K to 300 K, and diffraction patterns collected over a period of hours at regular temperature intervals. Typical collection times per pattern range from one to two hours for these small sample sizes.

2.2.4.c Accelerator-Based Sources – ISIS Neutron Facility

Since the 1960s accelerator-based sources have been used for the generation of neutrons.[117] These techniques began with the use of electron linear accelerators (LINACs) of ~50 MeV energies in the 60s and 70s. Electrons were accelerated towards heavy targets of uranium and the rapid deceleration of electrons as they impacted the target, through interaction with the electromagnetic field of U nuclei, was used to create a high intensity of Bremsstrahlung photons. These high-intensity photons produce neutrons via the excitation of a nucleus and its subsequent decay, causing neutrons to be emitted. This process produces neutrons at an efficiency of ~1 neutron per 20 electrons. More modern accelerator facilities use a combination of a LINAC with a synchrotron to produce neutrons. Protons, rather than electrons, are accelerated to energies of ~800 MeV and impact a heavy metal target such as tantalum, uranium or tungsten. For example, the ISIS Neutron and Muon Facility uses tantalum-clad-tungsten targets to generate neutrons in this manner. The layout of the ISIS facility is shown in **Fig. 2.13**.

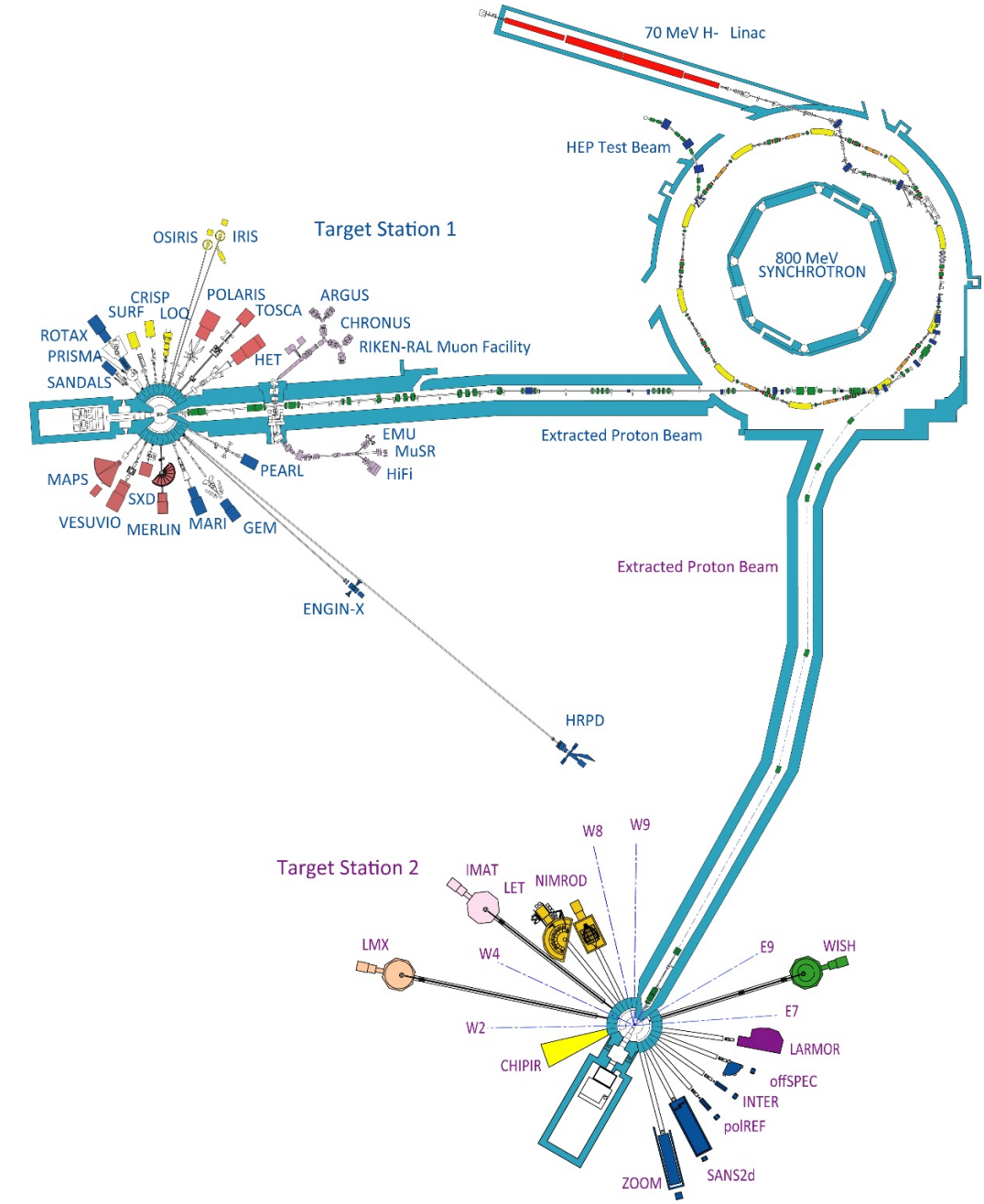

Figure 2.13 | *The ISIS Pulsed Neutron and Muon Facility. Target station 1 (TS1, consisting of the first tantalum-clad-tungsten target, as well as the graphite muon target) is shown to the top left of the figure. Target station 2 (TS2, the second tantalum-clad-tungsten target) is shown at the bottom of the figure, with the WISH diffractometer (shown in detail in **Figs. 2.15** and **2.16**) highlighted in green. Figure from ISIS Neutron and Muon Source Annual Review 2015.*[112]

The interaction of high-energy protons with the nuclei of the target causes spallation – so called because it results in violent spalling of light nuclear fragments

from the nuclei of the target. Along with these light fragments are neutrons, (~15 neutrons per proton, or ~25 for a fissile target) with the ejected neutrons having a polychromatic energy spectrum. Accelerator neutron sources are pulsed with a repetition rate of ~50 Hz for the proton beam. This produces a pulsed polychromatic neutron flux at the same frequency, which can then be used for neutron scattering. While the neutron source is polychromatic, monochromation is not necessary for a diffraction experiment as it is in X-ray diffraction or with reactor-based sources, as neutrons with varying energies can be separated temporally by time-of-flight techniques (**Fig. 2.14**) and the use of the pulsed structure of the beam. As long as there is no frame overlap, i.e. the slowest (least energetic, long wavelength) neutrons of a pulse are detected prior to the fastest (most energetic, short wavelength) neutrons of the following pulse, then based on the time of flight between the impact of the proton beam and the detection of a neutron, its wavelength can be calculated,

$$t = \frac{m_n}{h} L\lambda \,, \qquad \textbf{(2.14)}$$

where t is the time of flight and L is the path length).[117]

While the initial neutron flux generated by reactor sources is far in excess of that generated by spallation sources, monochromation is required for a reactor source. After the necessary monochromation of a reactor source the time averaged flux available from these different methods of neutron generation are comparable to one another. An advantage of spallation sources for neutron generation rather than reactor sources includes the fact that lower minimum values of *d*-spacing can be measured. To measure lower values of *d*, high angle scattering or low wavelength (high energy)

neutrons are required. Spallation sources have this advantage due to the significant flux available in the more energetic thermal neutron range when compared with the relatively narrow energy of neutrons available from a reactor post-monochromation.

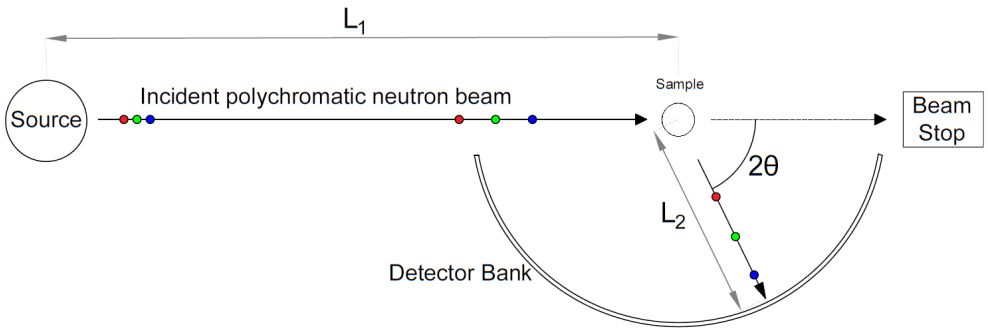

Figure 2.14 | *Schematic of time-of-flight neutron diffraction. A pulse of polychromatic neutrons is produced and travels down a guide towards the sample. Red, green and blue signify low, intermediate and high energy neutrons, respectively. After being diffracted by the sample the neutrons can be detected as a function of time as well as angle. Neutron wavelengths can be determined from their time-of-flight (using known flight-path lengths L_1 and L_2). Based on the diffraction angle and wavelength of neutrons, the d-spacing in the crystal can be calculated based on Bragg's law.*

2.2.4.d WISH – ISIS Neutron Facility

The time-of-flight neutron diffractometer used to obtain the majority of neutron diffraction data in this thesis is the WISH diffractometer, shown in **Fig. 2.15**, at the ISIS Neutron and Muon Facility (Oxfordshire, UK).[120] WISH is situated on the second target station at ISIS (TS2), which has a pulse frequency of 10 Hz. The design of WISH utilises the low pulse frequency in conjunction with a dedicated solid-methane moderator (kept at 50 K) in order to access a very broad *Q*-range in a single run. The divergence of the incident beam can be controlled as it reaches the sample by use of five sets of piezoelectric slits, allowing a resolution/flux trade off to be chosen with the highest resolution setting (HR mode) resulting in a 0.2° beam divergence. The

detector array consists of 760 ^{3}He tubes on either side of the instrument, with their long axis perpendicular to the scattering plane and arranged in a cylindrical geometry around the sample space, covering in-plane scattering angles of $10° \leq 2\theta \leq 170°$ and $-170° \leq 2\theta \leq -10°$. These tubes are 8 mm in diameter, with no gaps between them, and are located 2.2 m from the sample point (i.e. the angle covered by beam divergence in HR mode matches the angle covered by a single tube). The tubes are 1 m long and position sensitive (i.e. extending 0.5 m above and below the scattering plane), allowing out of plane scattering of ±12.80° to be recorded.

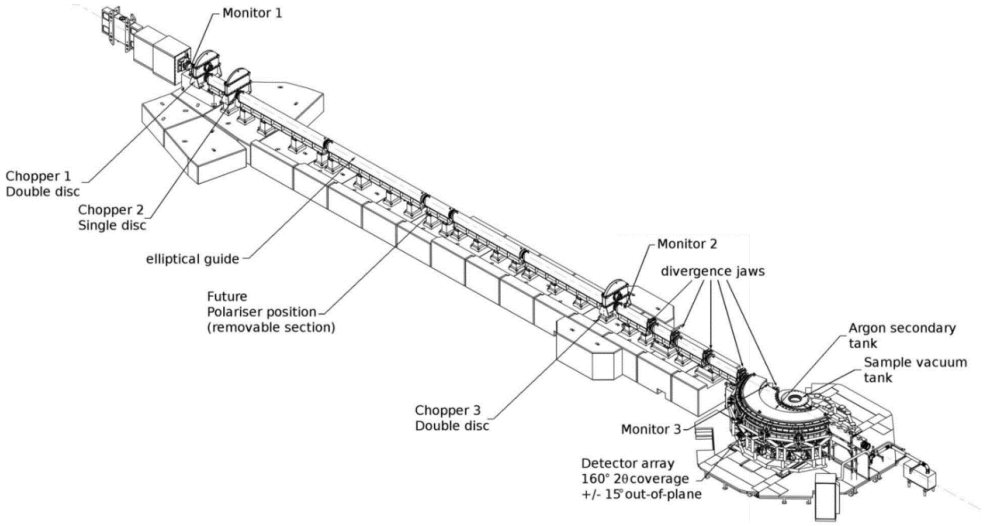

Figure 2.15 | *The WISH diffractometer and guide, showing the chopper set-up, one side of the detector array, the location of divergence jaws (piezoelectric slits) and an argon tank to reduce the potential for air scattering. Figure from Chapon et al.*[120]

It is important to note that while WISH has the capability to generate a single histogram, and indeed is described as 'Wide angle In a Single Histogram', the ^{3}He detectors are currently grouped and divided into ten banks of 152 tubes for data processing, each bank covering an in-plane angle of 32° (shown schematically in **Fig. 2.16**).

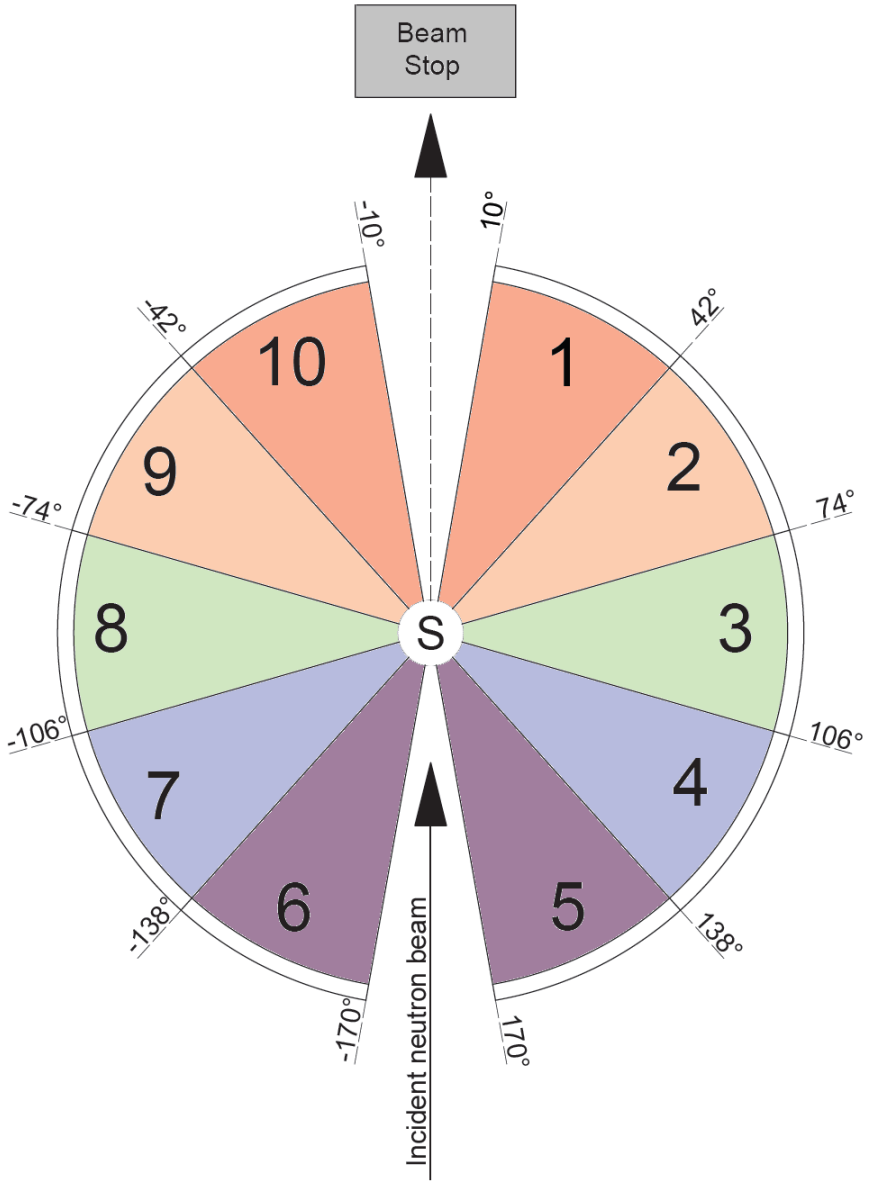

Figure 2.16 | *A birds-eye-view of the WISH diffractometer centred on the sample space. The two 160° detector arrays to the left and right of the instrument are separated into banks #1 to #10 and cover scattering angles of 32° with 152 ^{3}He tubes each. Bank #1 (+10 to +42°), bank #2 (+42° to +74°), bank #3 (+74 to +106°), bank #4 (+106° to +138°) and bank #5 (+138° to +170°) are located on the right side of the instrument. These banks are mirrored and averaged with bank #10 (-10 to -42°), bank #9 (-42° to -74°), bank #8 (-74 to -106°), bank #7 (-106° to -138°) and bank #6 (-138° to -170°), respectively, which are located on the left side of the instrument. The collimated sample environment is labelled S.*

Another important feature to note is the collimation on WISH. The oscillating radial collimator (ORC) is made from mylar blades painted with Gd_2O_3 and separated

by 0.75°. The collimated area is a 20 mm diameter cylinder at the centre of the sample space. To remove shadows on the detectors that would be present from a stationary collimator, the ORC oscillates at a low frequency (on the order of 1 Hz) by ±1°. The efficiency of the collimation is such that few corrections and subtractions for the various sample environments are required, as any non-sample scattering is removed from the measurement at its source by collimation the oscillating nature of the collimator ensures that the entire angular range of WISH is used to its full potential. Sample environments available on WISH include cryostats and cryofurnaces, pressure cells, dilution refrigerators and a dedicated magnet designed for WISH.

All of these features combined lead to WISH being one of the leading neutron diffractometers. High quality data can be obtained on sample sizes of less than 100 mg in under an hour of collection time (< 40 μA.h of total proton beam charge impacting the neutron target when TS2 is operating at its intended efficiency with a 40 μA proton beam) and Rietveld fits using data obtained on high-pressure products with sample sizes of ~50-100 mg are shown in this thesis. Using larger sample sizes, a collection time of only a few minutes provides data with statistics suitable for Rietveld refinement. Ordered magnetic moments of 0.1 μ_B have been resolved using WISH.[121] A wide range of *d*-spacings from 0.7 to up to ~50 Å can be examined (as ISIS is a pulsed source, choppers can be run at half frequency in order to skip every second neutron pulse, doubling the accessible *Q*-range in a 'double frame mode' and enabling the *d* ~50 Å upper limit). In all WISH data shown in this thesis, Rietveld fits to diffraction data will be shown simply for a single bank of detectors for clarity, however all Rietveld refinements have been conducted by considering all histograms

simultaneously in the refinement, with the exception of the average of the forward scattering banks (1_10), as this pair of banks have the lowest available resolution. These forward scattering banks have only been used throughout this work to identify whether any long *d*-spacing reflections could be observed (due to these banks being able to access the highest values of *Q*). WISH banks will be denoted as averaged banks on either side of the instrument e.g. 1_10, 2_9, 3_8, 4_7 or 5_6. The geometry of these banks is explained more thoroughly in **Fig. 2.16**.

2.2.5. Neutron Detection

As there is no charge on a neutron, the easiest method of neutron detection is to use a nuclear reaction to generate a detectable electrical signal. As such, the materials used to provide a means for the reaction to take place are carefully designed and often consist of ^{3}He, ^{10}B or ^{6}Li isotopes as neutron absorbers,[117]

$$^{3}_{2}He + ^{1}_{0}n \rightarrow ^{3}_{1}H + ^{1}_{1}p + 0.77\ MeV \qquad \textbf{(2.15a)}$$

$$^{10}_{5}B + ^{1}_{0}n \rightarrow ^{7}_{3}Li + ^{4}_{2}He + 2.3\ MeV \qquad \textbf{(2.15b)}$$

$$^{6}_{3}Li + ^{1}_{0}n \rightarrow ^{4}_{2}He + ^{3}_{2}He + 4.79\ MeV\ . \qquad \textbf{(2.15c)}$$

Ideal qualities for a detector include high neutron detection efficiency, low intrinsic background, low sensitivity to non-neutron impacts (particularly from penetrating radiation that is difficult to shield against, such as γ-rays) and a good stability. Both gas and scintillator detectors are widely in use for detection of neutrons.

2.2.5.a Gas Detectors

^{3}He or $^{10}BF_3$ gas (p ~10 bar) can be contained in a canister with a high voltage wire anode. Absorption of a neutron produces enough energy to ionise the gas, produce a current that is carried along the anode and this electrical signal can be detected. A benefit of this method is that ^{3}He is self-regenerating,

$$^{3}_{1}H \rightarrow {}^{3}_{2}He + e^{-} + \bar{\nu}_e + 18.6\ keV \quad \textbf{(2.16)}$$

and that ^{3}He detectors can discriminate well between neutrons and non-neutron events (typically γ-rays, and ^{3}He has a high ratio of neutron to γ-ray energy deposition) leading to a low intrinsic background for these types of detectors.[117]

Newer gas detectors can use multiple wires to cover more solid angle and can use resistive-wire position-sensitive detectors to determine the position along the length of a detector that a neutron has been detected, allowing the out-of-plane angle to be determined.

2.2.5.b Scintillator Detectors

Scintillator detectors combine a neutron absorber with a scintillating phosphor.[117] Products from the nuclear reaction that occurs due to neutron absorption strike the phosphor and produce light that is then detected via a photomultiplier tube. Older scintillators use a ^{6}Li/Ce glass, while more modern designs use granular ZnS(Ag)/^{6}Li. In both of these designs, ^{6}Li absorbs neutrons and causes a large amount of energy to be deposited in the scintillator by γ-rays, resulting in the formation of an

exciton. The exciton propagates through the material until it encounters an impurity 'activator' atom, which has energy levels between the conduction band (CB) and valence band (VB) of the bulk of the material. This exciton can then decay and produce light with energy lower than that of the VB to CB gap, which therefore cannot be readily reabsorbed by the material and is emitted and then detected by a photomultiplier. ZnS(Ag)/^{6}Li scintillators are capable of detector efficiencies exceeding that of gas detectors, with comparably low γ-sensitivities (intrinsic backgrounds of ~12 counts per hour). Other benefits of these scintillator detectors include the ease of which the size and geometry can be modified and the density of ^{6}Li that can be achieved. High ^{6}Li density is capable of improving the performance of the detection of high-energy neutrons with low absorption cross sections.

2.2.6. Rietveld Refinement

The Rietveld method is a powerful technique for obtaining structural information from powder diffraction data. This is a least-squares method of computationally fitting the positions, as well as the heights and widths of peaks, in a powder diffraction pattern, such that the crystal structure of a material may be elucidated. In order to effectively make use of this technique, some prior information about the structure is required such as the space group, approximate atomic positions, lattice parameters and instrument parameters. As such, the Rietveld method is not a structural solution method, but a structural refinement method. The method described by Rietveld in 1969 is a curve fitting procedure, where calculated intensities are

compared to the experimentally observed intensities.[122] The least-squares difference between a calculated and an observed pattern, S_y, is computed as shown,

$$S_y = \sum_i w_i (y_i - y_{ci})^2 , \qquad (2.17)$$

here, w_i is a statistical weight factor and the values y_i and y_{ci} are the observed and calculated intensities, respectively, at point i. This least-squares difference is minimised while refining structural parameters. Typical of powder diffraction is that Bragg peaks can overlap with one another if they are within half a peak width of one another. This potential problem is resolved by the Rietveld method as many reflections are allowed to contribute to the calculated intensity, y_{ci}. This calculated intensity,

$$y_{ci} = s \sum_K L_K |F_K|^2 \phi(2\theta_i - 2\theta_K) P_K A + y_{bi} , \qquad (2.18)$$

contains a factor from the square of the absolute value of the structure factor, $|F_K|^2$, where K refers to the miller indices, h, k and l. For the case of neutron experiments on magnetic structures, this structure factor also contains the component due to magnetic diffraction. Here, s is the scale factor; L_K contains the Lorentz, polarisation and multiplicity factors; ϕ is the reflection profile function; P_K is the preferred orientation function; A is an absorption factor specific to each phase that contributes to the intensity and y_{bi} is the background intensity at step i.

Another important aspect of the Rietveld method is the calculation of peak shape. This is generally described quite adequately for a constant wavelength neutron experiment, as the peak shape is almost perfectly Gaussian. The Full-Width-at-Half-Maximum (FWHM) is given by H_G,

$$H_G{}^2 = U tan^2\theta + V tan\theta + W , \qquad (2.19)$$

and this form is often known as the Caglioti Equation.[123] The values *U*, *V* and *W* are refinable parameters and for medium resolution diffractometers this function holds quite well. With higher resolution diffractometers the peaks become sufficiently narrow that defects in the sample become a significant factor in determining the peak shape and the peak shape deviates from being Gaussian. This issue can be resolved by modifying the above equation, for example by allowing peak width to vary with θ,

$$H_L = \frac{X}{cos\theta} + Ytan\theta \ , \qquad (\mathbf{2.20})$$

here the FWHM is given by H_L in the above equation and *X* and *Y* are refineable parameters describing strain and particle size, respectively. Differences arise when time-of-flight neutron diffraction is considered and the typical peak shapes deviate from the expected Gaussian distribution. The resolution function for a time-of-flight neutron diffraction intensity is given as,[117]

$$\frac{\Delta d}{d} = \left[\left(\frac{\Delta t}{t}\right)^2 + \left(\frac{\Delta L}{L}\right)^2 + (\Delta\theta cot\theta)^2\right]^{1/2} \qquad (\mathbf{2.21})$$

this resolution function contains terms relating to the uncertainty arising from the moderation of the source (Δt), the flight path uncertainty (ΔL) and a $cot\theta$ dependent angular dispersion term that arises from the finite angular widths of the moderator, sample and detector (a small distribution of wavelengths satisfy the Bragg condition for each of these). At low angles, the $cot\theta$ term dominates the resolution, while at higher backscattering angles the resolution of time-of-flight scattering improves dramatically as $cot\theta$ tends to zero. This resolution function leads to a rather unusual peak shape for time-of-flight diffraction, which can be described by the Ikeda-Carpenter function. It is essentially a convolution of a Gaussian shape from the

instrumental contribution with a sharp leading edge (due to rapid initial flux from the pulse structure of the beam) with a long trailing edge to the peak (due to the slowing processes in the moderation of the source). This is illustrated in **Fig. 2.17**.

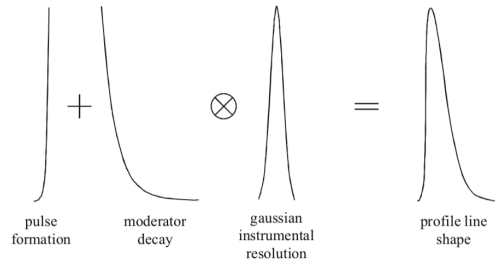

Figure 2.17 | *A typical Ikeda-Carpenter peak shape, shown here to be a convolution of a Gaussian (from instrumental contributions) with sharp leading and long trailing edges (that are observed from time-of-flight neutron diffraction conducted on pulsed sources). Figure from the ISIS Neutron Training Handbook.*[117]

After refining the structural parameters such as the lattice parameters, atomic positions, occupancies, thermal factors, background, peak shape and phase fractions, the final refinement can be evaluated and the fit to the observed diffraction data can be assessed. This is generally measured by the values for the weighted pattern R-index, R_{wp} and the 'goodness of fit' χ^2,

$$R_{wp} = \left[\frac{\sum_{i=1}^{n} w_i[y_i - y_{ci}]^2}{\sum_{i=1}^{n} w_i y_i^2}\right]^{1/2} \qquad (2.22)$$

$$\chi^2 = \frac{{R_{wp}}^2}{{R_e}^2} = \frac{\sum_{i=1}^{n} w_i[y_i - y_{ci}]^2}{n-p}, \quad (2.23)$$

here n is the number of observations and p the number of refined parameters. R_e is the expected R index defined as,

$$R_e = \left[\frac{n-p}{\sum_{i=1}^{n} w_i y_i^2}\right]^{1/2}. \qquad (2.24)$$

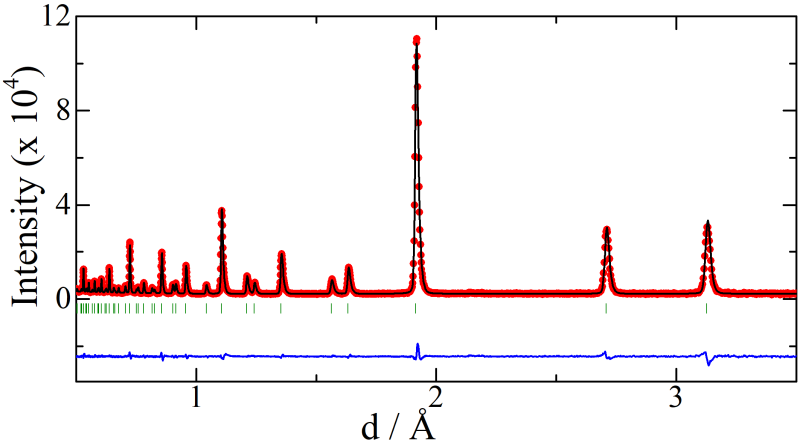

Figure 2.18 | *A Rietveld plot of intensity versus d-spacing for a CeO_2 standard measured on Pearl at the ISIS Neutron Facility. The observed intensities are shown as red point; the calculated pattern based on the refined structure model is shown as a black line; green tick marks indicate the calculated position for specific values of hkl and the blue line is the difference plot, determined by subtracting the calculated pattern from the observed pattern.*

Polycrystalline diffraction results, whether from X-ray or neutron scattering, are often presented in the form of a Rietveld plot of diffracted intensity versus one of the diffraction variables: e.g. scattering angle, *d*-spacing, momentum transfer, time-of-flight or wavelength. These plots consist of the observed diffraction intensities, the calculated pattern based on the crystal structure model, tick marks referring to specific values of *hkl* indicating the calculated positions of these Bragg reflections and lastly a difference plot (the calculated profile subtracted from the observed data). An example of a typical Rietveld plot is shown in **Fig. 2.18** to illustrate this. In this case, the data shows a CeO_2 standard that was measured on Pearl at the ISIS Neutron Facility, with intensity plotted against *d*-spacing.

2.2.7. Magnetic Symmetry Analysis

If we have a crystalline material with a known structural symmetry (known space group) solved by diffraction techniques, the magnetic structure of such a

material can be determined by the magnetic intensities in neutron diffraction profiles. Structurally, a space group is able to describe the arrangements of atoms in a unit cell of a crystal. However, magnetic moments must be considered differently to atomic positions with regards to symmetry operations, as these moments are axial vectors. This can be visualised as a current loop in a plane perpendicular to the direction of the vector. Some symmetry operations will act to reverse the direction of the current in this loop, such as a mirror plane parallel to the axial vector. The position of this current loop is mapped correctly by such operations but, because its direction changes, there is said to be a time reversal. A new type of symmetry operation known as 'priming' or 'time reversal' is introduced to allow for operations that leave these axial vectors unchanged. This priming operation inverts only the axial vectors and a symmetry operation combined with time reversal is known as a primed operation. All possible combinations of priming some or all of the symmetry operations in the 230 space groups generate a total of 1651 magnetic space groups or 'Shubnikov groups'.[124]

Representation theory is a means to simplify the selection of possible magnetic symmetries and reduce the number of potential structures. Essentially representation analysis involves the determination of a set of linear operations, Γ, which correspond with the symmetry elements in a given space group. Each operator in this representation of the group is defined by a matrix and by applying rotations to these matrices it is possible to reduce this representation into a set of lower dimensional irreducible representations (IrReps). These IrReps (Γ_n) describe magnetic symmetry in terms of the crystallographic symmetry operations and whether moments are parallel or antiparallel to their orientation before and after the symmetry operation. For

an adequate description of symmetry in a magnetic structure, a single IrRep may be required or a combination of many may be necessary to describe order on multiple cation sites or multiple orders operating on a single site.

In practice, an IrRep is itself composed of a set of basis vectors, the relative ratios of these basis vectors being the refined parameters in Rietveld fits to magnetic diffraction data. References to tables containing these IrReps and sets of basis vectors will be made in discussions of magnetic structure solutions for the materials analysed throughout this work. Magnetic representation theory in this work has been conducted using BasIreps in the FullProf Suite,[125] as well as using ISODISTORT, part of the Isotropy suite.[126]

2.3. Magnetic Measurements

2.3.1. Magnetometry

In order to probe the magnetic properties of a sample, a known magnetic field is applied to the sample and the magnetic response recorded. To achieve this a Superconducting Quantum Interference Device (SQUID) magnetometer is used. In this thesis magnetic measurements were done using a Quantum Design Magnetic Property Measurement System XL (QD-MPMS XL). A SQUID magnetometer (**Fig. 2.19**) is able to resolve tiny changes in the measured magnetic field of a sample.

The Josephson junction is the key component that allows the detection of small magnetic fields.[127] In the simplest terms, the Josephson junction is a superconductor with a ‘weak link’. This weak link is a gap in the superconducting material, made of

either an insulator (a few tens of ångströms thick) or a non-superconducting metal (a few microns thick). Up to a certain critical current a supercurrent is able to flow through this weak link. Above the critical current, a voltage develops across the junction. In a SQUID, there is a superconducting loop, interrupted by two Josephson junctions. In this system, the voltage across the junctions is extremely sensitive to the total magnetic flux that penetrates the area of the loop.

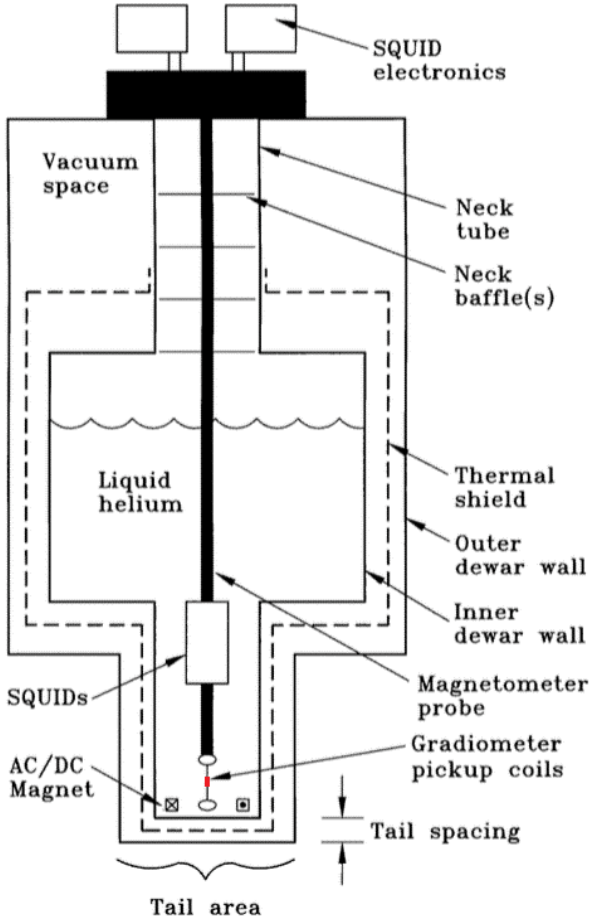

Figure 2.19 | *Schematic of a SQUID magnetometer. The input coils and Josephson junctions, which allow accurate magnetic measurements, are contained within the device labelled 'SQUIDs'. The sample is located at the centre of the gradiometer pickup coils (shown in red). Figure from Jenks et al.*[127]

In a SQUID magnetometer the sample to be studied is moved through superconducting 'pickup' coils. The movement of the sample induces a supercurrent

in these coils. These pickup coils are connected to 'input' coils that are located above the Josephson Junction containing superconducting loop . In this manner, an electric current generated by moving a magnetic sample through the pickup coils will generate a magnetic field at the input coils. This field will then influence the voltage across the Josephson Junctions. This change in voltage can be measured and is proportional to the magnetic moment of the sample. By having this arrangement of pickup and input coils, it is possible to separate these two parts of the device. The input coil and Josephson Junction part of the device (the SQUID) is encased in a superconducting niobium canister that shields the Josephson Junctions from external magnetic fields. This allows magnetic fields to be applied to the sample without affecting the SQUID.

SQUID magnetometers can be used to measure the magnetic properties of materials over a wide range of different conditions. Using liquid helium it is possible to measure these properties down to low temperatures of 2 K, and the QD-MPMS XL used in this work is capable of applying magnetic fields of up to 7 T to the sample. It is also possible, by using an optional oven module, to measure magnetic properties of materials up to temperatures of 650 K by using this equipment. The magnetisation measurements in this work also utilise DC magnetisation measured with a Quantum Design Physical Property Measurement System (QD-PPMS), capable of measuring magnetisation similarly by moving a sample through pickup coils. However, the sensitivity of this instrument is not as high as is possible by using a SQUID magnetometer, as the induced current is measured by conventional methods rather than utilising a superconducting loop with Josephson Junctions.

2.3.2. Magnetoresistance

Simply put, magnetoresistance is a measure of the effect an applied field has on the electronic transport properties of a material, defined previously in **Equation 1.3**. This is an important phenomenon in modern technologies, for instance in data storage and magnetic read-heads for hard drives. This phenomenon is deemed to be so important to modern technology that, for their discovery of Giant Magnetoresistance (GMR) in layered magnetic thin films,[128,129] A. Fert and P. Grünberg were awarded the Nobel Prize in Physics in 2007.

In order to measure magnetoresistance (MR), resistivity needs to be measured as a function of magnetic field at constant temperature and also as a function of temperature at constant field. To achieve this, a Quantum Design Physical Property Measurement System (PPMS) in the resistivity option is used. A superconducting 7 T magnet is cooled with liquid helium and provides the external magnetic field on the sample. The sample itself can be cooled to ~2 K using liquid ^{4}He (or ^{3}He for temperatures down to 0.5 K).

To prepare samples for measuring resistivity in the PPMS, pelleted samples recovered from high-pressure synthesis (as described in '*2.1.2.c Walker Module Experimental Technique*') are used. A 'four-probe' geometry is used for magnetoresistance measurements in this work, where four micrometre-diameter copper wires are connected to the sample pellet using silver paint as a conducting adhesive. Two wires on either end of the sample pellet are connected to an ammeter and power supply, with two wires between these connected to a voltmeter. This pellet

is then wired to a 'puck', able to accommodate up to three samples, before being placed in the PPMS. The sample sits within a superconducting magnet inside the device allowing the measurement of the resistance of a sample while being able to alter temperature and/or external magnetic field.

2.3.3. X-Ray Magnetic Circular Dichroism

X-Ray Magnetic Circular Dichroism (XMCD) is the difference between two X-ray Absorption Spectra (XAS), both measured in a magnetic field, one with right circularly polarised light (μ^+, helicity +1) and the other with left circularly polarised light (μ^-, helicity -1), shown as,[130]

$$XMCD = \mu^- - \mu^+. \quad (\mathbf{2.25})$$

XMCD became a far more useful technique as a means of probing magnetic properties in an element selective manner after magneto-optical sum rules were derived by Thole et al. (orbital sum rule)[131] and Carra et al. (spin sum rule).[132] These sum rules for L_2 and L_3 absorption edges are shown below, along with a ratio of orbital to spin moment, as functions of integrals A, B and C which are themselves defined here,

$$A = \int_{L_3} (\mu^- - \mu^+)\, dE \qquad (\mathbf{2.26})$$

$$B = \int_{L_2} (\mu^- - \mu^+)\, dE \qquad (\mathbf{2.27})$$

$$C = \int_{L_3+L_2} (\mu^- + \mu^+ + \mu^0)\, dE \qquad (\mathbf{2.28})$$

$$\frac{m_L}{n_h} = -\frac{2(A+B)}{C}\mu_B \qquad (\mathbf{2.29})$$

$$\frac{m_S}{n_h} = -\frac{3(A-2B)}{2C}\mu_B \qquad (\mathbf{2.30})$$

$$\frac{m_L}{m_S} = \frac{4(A+B)}{3(A-2B)}\mu_B\,, \qquad (\mathbf{2.31})$$

terms μ^0 and n_h refer to XAS measured in an unpolarised X-ray beam and the number of *d*-state holes, respectively. These sum rules not only allow the calculation of magnetic moments of a specific element in a material by measuring XAS with left and right circularly polarised light, but also allow this moment to be separated into orbital and spin contributions.

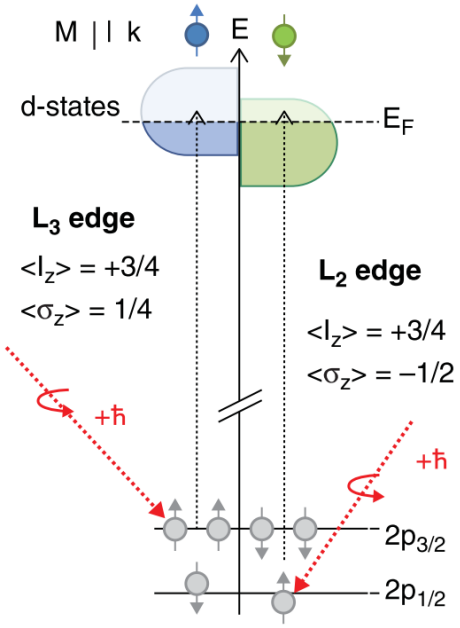

Figure 2.20 | *Schematic illustrating the absorption of circularly polarised light by electrons originating from 2p½ and 2p³⁄₂ states and the final d-states above the Fermi level that these electrons occupy. Figure from Rogalev et al.*[130]

Circularly polarised light of opposite helicity can result in differing XAS due to a two-step process. The first step involves the excitation of a core electron with right (helicity +1) or left (helicity -1) circularly polarised light, light that carries an angular momentum. Due to conservation of momentum, the angular momentum of the incident photon is transferred to the electron. By spin-orbit coupling this angular momentum is converted to a combination of spin and orbital momentum of the electron (if the electron is excited from a spin-orbit split energy level). In the case of 2*p* orbitals split

into $2p_{½}$ and $2p_{3/2}$ ($J = L + S$, $L = 1$, $S = \pm ½$), then the expectation values of spin and orbital polarisations with respect to the X-ray trajectory are -½ and +¾ for $2p_{½}$ (L_2-edge), and +¼ and +¾ for $2p_{3/2}$ (L_3-edge).[130] This is known as the Fano effect, illustrated schematically in **Fig. 2.20**, and provides a means to produce spin-polarised photoelectrons from circularly polarised light.[133] The second step in the process of XMCD requires that there be an imbalance of the empty spin up and spin down *d*-states as, due to spin conservation in optical transitions the photoelectrons excited from $2p_{3/2}$ (L_3-edge) are more likely to be excited to spin up *d*-states, while from $2p_{½}$ (L_2-edge) they are more likely to be excited to spin down *d*-states. Experimentally, the XAS are measured on samples in a magnetic field oriented parallel to the X-ray vector to maximise XMCD effects by aligning the spin orientation of *d*-states with the X-ray vector.

Measuring XAS under intense magnetic fields using circularly polarised light is possible at X-ray synchrotron sources, with insertion devices being particularly well suited to this purpose. The ID12 beamline at the ESRF, which is able to quickly switch between linear and circularly polarised beams from helical undulator devices, is used to measure XAS from which XMCD is calculated in this work. Energy selection here (2 to 15 keV) is in the hard X-ray range, suitable for probing the L-edges of 4*d* and 5*d* transition metals or the K-edges of 3*d* transition metals.[130]

To summarise, if the spin moment of the *d*-states is aligned parallel to the X-ray vector, absorption of left circularly polarised light is enhanced at the L_3-edge while being reduced at the L_2-edge (compared to an unpolarised beam). The opposite is true

for right circularly polarised light. XMCD can also be calculated by reversing the direction of the magnetic field to be antiparallel to the X-ray vector instead of reversing the polarisation of the light. The same XAS should be observed with right polarised light in a positive field as with left polarised light in a negative field ($\mu^+(B) = \mu^-(-B)$), and vice versa. Due to this, it is often practical to measure XAS with both left and right circularly polarised light, in both parallel and antiparallel applied magnetic fields as,

$$XMCD = \mu^-(B) - \mu^+(B) = \mu^+(-B) - \mu^-(-B)\,, \qquad (\mathbf{2.32})$$

the final XMCD can then be calculated as an average of the XMCD measured in positive and negative fields.

Chapter 3. Mn_2FeReO_6 – Magnetoresistance Switching Due to Frustration

3.1. Introduction

The field of spintronics relies on using the spin of electrons as a means to transmit information, not just the charge of electrons (as in electronics). By encoding information as up or down spins (ones and zeroes), this magnetic data can be read by a device that is sensitive to the polarisation of these spins. A magnetoresistive read-head in a hard disk drive can do exactly this, allowing a current to pass when the polarisation in the read-head and the electron spin direction of the datum are parallel, while hindering the flow of a current when these polarisations are antiparallel. In this manner, an up spin (which can be defined as a 1) results in a current while a down spin (defined as a 0) results in no current. The synthesis of new magnetoresistive materials with greater sensitivity to smaller magnetic fields allows the magnetic domain size of each datum to be reduced, densifying the information that a device can contain. This highlights the technological importance of new magnetoresistive materials.

Materials with particularly large magnetoresistance effects include those of the double perovskite structure type, the best-known of these being Sr_2FeMoO_6 (SFMO). The rock salt order here of the B/B′ cations (Fe/Mo) and the G-type ferrimagnetism results in a spin-polarised conduction pathway and, in polycrystalline SFMO, the intergrain tunnelling magnetoresistance exists at room temperature and 7 T, showing a rather large effect of -4 %.[72] This effect is also noted in other double perovskites with

B-site rock salt structural order and G-type ferrimagnetism, with both A and B-site cation variations on SFMO, such as Sr_2FeReO_6 and Ca_2FeReO_6,[78,80,82] discussed in '*1.2.2 – Spin-Polarised Conduction*'.

Enhancing the polarisation (*P*) and magnetisation (*M*) of the material should increase the magnetoresistive effects of a material, based on **Equation 1.6**. Considering the double perovskites discussed previously, such as SFMO, one method of enhancing *P* and *M* is to substitute the non-magnetic cations in these materials, such as Sr or Ca, for a magnetic cation. This research will focus on the substitution of non-magnetic A^{2+} cations for magnetic Mn^{2+} ($3d^5$). Prior to the start of the work in this thesis, Mn_2FeMoO_6 was synthesised by Li et al. and determined to adopt the Ni_3TeO_6-type structure rather than the double perovskite-type structure which would be expected to exhibit magnetoresistance.[90] As such, this chapter focuses on the Fe/Re system and substitution of non-magnetic A-site cations for Mn^{2+} in the synthesis of Mn_2FeReO_6. The Goldschmidt tolerance factor of this material is calculated as 0.83 (for Mn^{2+}, Fe^{3+}, Re^{5+} and O^{2-} with ionic radii of 0.96, 0.645, 0.58 and 1.4 Å respectively),[85] and should therefore adopt a double perovskite-type structure based on '*1.1.1.a Goldschmidt Tolerance Factor*'.

3.2. Experimental

3.2.1. Synthesis of Mn_2FeReO_6

The synthesis of Mn_2FeReO_6 has been conducted using the techniques outlined in '*2.12. High-Pressure Solid-State Synthesis*'. Two different solid-state precursors have been used, referred to here as precursor A (2 MnO + ¼ Fe + ¼ Fe_3O_4 + ReO_3) and B (2 Mn_3O_4 + Fe_3O_4 + 3 ReO_2). These metal oxides were combined in the

stoichiometric ratios listed and ground together in a pestle and mortar several times to generate thoroughly mixed precursors. The precursors were then loaded inside Au or Pt encapsulating metal and then loaded inside the Walker module assembly. Conditions used for the synthesis of samples of Mn_2FeReO_6 were explored between 5 GPa and 13 GPa, with temperatures between 1200 and 1400 °C.

3.2.2. Structural Characterisation of Mn_2FeReO_6

Initial X-ray patterns of products of high-pressure synthesis were all collected using a Bruker D2 Phaser diffractometer with Cu K_α/K_β X-ray source (15-minute scans of $5° \leq 2\theta \leq 70°$). A longer X-ray diffraction pattern was collected on sample #4 using a Bruker D8 Advance diffractometer with a Cu K_α X-ray source (8-hour scan of $5° \leq 2\theta \leq 140°$).

Samples #1-5 were combined and well ground to provide a sample size of approximately 50 mg. Neutron diffraction patterns were collected on D20 at the ILL on this combined sample at five different temperatures (1.7, 50, 100, 150 and 300 K) for 2.5 hours at each temperature step over a range of angle $0° \leq 2\theta \leq 150°$. The (002) face of highly oriented pyrolithic graphite (HOPG) was used as the monochromator during data collection, with a neutron wavelength of 2.41 Å. The flux-on-sample provided by this setup is 4.2×10^7 $s^{-1}.cm^{-2}$, with an average resolution of $^{\Delta d}/_{d} = 1.6\times10^{-2}$. A 70 mg sample of Mn_2FeReO_6 (samples #1-5 and #13) was also measured in high resolution single frame mode on WISH at the ISIS Neutron Facility at 14 temperatures and with data collected for varying amounts of beam current (T = 1.5 (60 μA), 20 (40 μA), 40 (40 μA), 60 (40 μA), 80 (40 μA), 100 (29 μA), 125 (25 μA), 150 (25 μA), 175

(25 μA), 200 (25 μA), 225 (25 μA), 250 (25 μA), 275 (24 μA), 300 K (22 μA)). Data from D20 was used in a publication relating to this material,[134] but the more rigorous analysis of this material using data acquired on WISH shall be presented in this thesis. The structures responsible for these X-ray and neutron diffraction patterns were solved using the FullProf Suite and refined by the Rietveld method.[122,125]

3.2.3. Magnetic Measurements of Mn_2FeReO_6

Magnetometry measurements were carried out on samples #4 and #6 using a Quantum Design MPMS XL Superconducting Quantum Interference Device (SQUID) magnetometer. Magnetisation versus field hysteresis loops were recorded for sample #4 ($-7 \leq \mu_0 H$ (T) ≤ 7) at temperatures of 2 and 300 K and magnetisation versus temperature was measured zero-field cooled and field cooled ($\mu_0 H = 0.5$ T) from 2 K to 650 K. Additionally, magnetisation at 7 T was measured on sample #6 at temperatures of 20, 50, 75, 100 and 150 K.

Magnetoresistance was also measured on a pelleted portion of sample #3, as described in '*2.3.2. Magnetoresistance*'. This was measured on a Quantum Design Physical Property Measurement System (PPMS). Resistivity versus field hysteresis loops ($-7 \leq \mu_0 H$ (T) ≤ 7) were measured at constant temperatures of 20, 50, 75, 100, 150, 200, 250 and 300 K, from which the magnetoresistance was calculated as a percentage based on **Equation 1.3**. The resistance of Mn_2FeReO_6 versus temperature between 20 and 300 K was also measured at fields of $\mu_0 H = 0$, 3.5 and 7 T.

In order to determine X-ray Magnetic Circular Dichroism (XMCD) on Re, X-ray Absorption Near-Edge Spectra (XANES) were measured on Mn_2FeReO_6 in the

ranges 10.511-10.605 keV (Re L_3 edge) and 11.934-12.055 keV (Re L_2 edge). These measurements were conducted at ID12 at the European Synchrotron Radiation Facility. These spectra were measured using circularly polarised X-rays of helicity +1 and -1, as well as in magnetic fields of +2 and -2 T. In addition, XMCD versus field hysteresis measurements were performed at 11.969 keV, at the Re L_2-edge maximum, between fields of ±17 T. These measurements were carried out at temperatures of 2.2, 100 and 290 K.

3.3. Results & Discussion

3.3.1. Phase Analysis & X-ray Crystal Structure: Mn_2FeReO_6

Initial phase analysis was conducted using X-ray diffraction data from samples of Mn_2FeReO_6 recovered from high-pressure syntheses. These raw data files obtained from the Bruker D2 Phaser are shown stacked in **Fig. 3.1**.

The main phase in Mn_2FeReO_6 syntheses is consistently the desired double perovskite phase with rock-salt Fe/Re B-site cation order. The main impurity phase identified by X-ray analysis is ReO_2 that, while ReO_2 is used as a reagent in precursor B, is present even in syntheses using precursor A (which uses ReO_3 as the source of Re). This suggests that ReO_2 is inherently stable under the synthetic pressure and is present as a by-product in syntheses using precursor B, rather than as unreacted material. This is supported by another by-product containing Mn and Fe being detected by neutron diffraction: $MnFe_3O_5$.[135] This phase is consistently present in low quantities (< 1 % by weight) and is identified as isostructural to $CaFe_3O_5$. This phase can be identified rather easily with neutron data from WISH however, in the neutron data

from D20 as well as in X-ray data, this phase is almost undetectable. The results Rietveld refinements of these syntheses, including the degree of B-site disorder and weight percentage of ReO_2 impurity, are shown in **Table 3.1**.

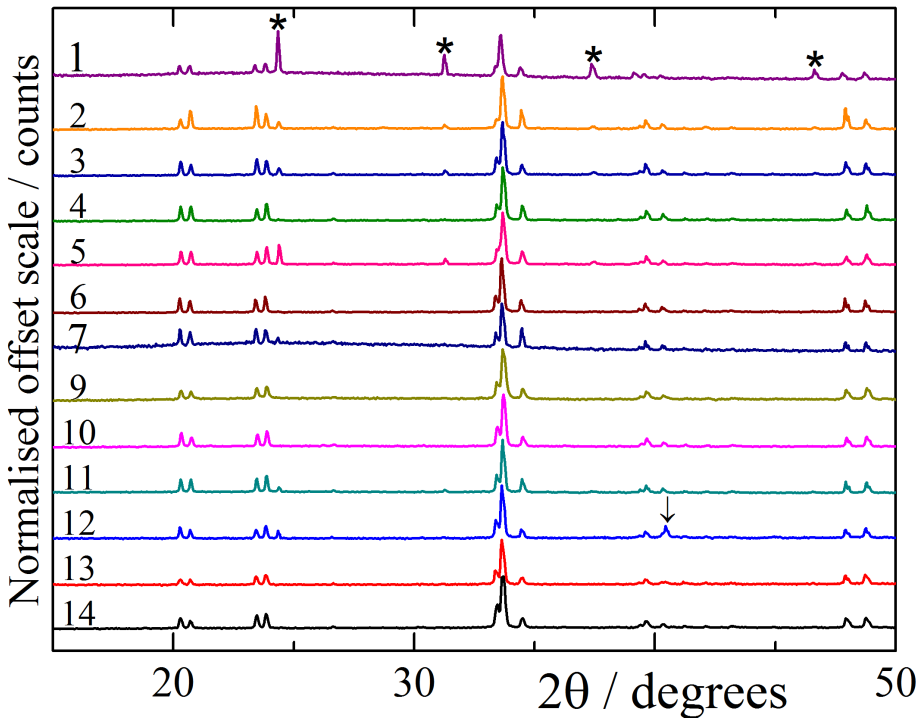

Figure 3.1 | *A stacked plot of the raw powder X-ray data initially collected on samples of Mn_2FeReO_6 for phase analysis (in the 2θ range 15-50°). Asterisks mark the main ReO_2 impurity reflections. The arrow in pattern #12 marks the location of the main Pt reflection, a rarely observed impurity from the encapsulating material.*

While it may be possible in some cases to infer the stoichiometry of the main phase by identifying the quantity of particular elements in impurities, in practice this often is not possible and it is far more reliable to simply determine the stoichiometry of the main phase by Rietveld refinement of the occupancies of particular atomic positions. This is likely the case here, where ReO_2 impurities can be observed (often in low proportions when compared to the main phase). It could be assumed that the main phase is therefore Re deficient, however another explanation is that further Mn, Fe or Mn/Fe oxide impurities are also present in the samples under study. These further

impurities may simply be at a level that is below the detection limits of the diffraction experiment, and the Re impurities are observed due to the high z^2 for this element.

The 300 K crystal structure of Mn_2FeReO_6, synthesised at 11 GPa and 1400 °C (sample #4) was solved and refined using the FullProf Suite.[125] Data collected for 8 hours using a Bruker D8 Advance diffractometer was used for this purpose. The unit cell is monoclinic and adopts the space group $P2_1/n$, with parameters a = 5.1958(1), b = 5.3562(1), c = 7.5822(1) Å and β = 89.914(3)°. Refined fractional coordinates and occupancies are shown in **Table 3.2** and a Rietveld fit to this pattern using this structure is shown in **Fig. 3.2**.

Table 3.1 | A collection of the synthesis conditions and measure of the resulting purity and B-site disorder in the Mn_2FeReO_6 double perovskite product.

Sample no.	Precursor *	Pressure / GPa	Temp. / °C	Wt. ReO_2 / %	B-Antisite Disorder / %	χ^2	R_{wp} / %
1	A	10	1200†	29(1) †	8(1)	1.36	3.49
2	A	10	1400	4.3(1)	4.3(5)	2.33	6.36
3	A	11	1400	5.3(3)	5.8(5)	1.86	5.60
4‡	B	11	1400	1.1(1)	2.3(4)	1.89	5.16
5	B	11	1400	11.7(8)	5.0(5)	2.03	5.51
6	B	11	1400	0.4(1)	5.3(5)	1.93	5.69
7	B	8	1400	1.9(5)	6(1)	1.85	4.87
9	B	10	1400	0	10.7 (8)	2.06	7.77
10	B	10	1400	0	8.2(3)	2.10	3.99
11	B	10	1400	3.3(2)	6.8(4)	1.64	3.54
12	B	10	1400	1.4(3)	3.8(8)	2.48	6.29
13	B	10	1400	0	14.0(8)	1.75	5.76
14	B	10	1400	0	10.6(4)	2.56	4.41

Samples 1-5 were mixed and examined on D20 at the ILL and samples 1-5 and 13 on WISH at the ISIS Neutron Facility. The measures of the fit, χ^2 and R_{wp}, are shown for X-ray patterns collected over 15 minutes using a Bruker D2 Phaser diffractometer with Cu K_α radiation. *Precursor A (2·MnO + FeO + ReO_3) or Precursor B (2·Mn_3O_4 + Fe_3O_4 + 3·ReO_2). †A gold capsule was used for synthesis 1 at 1200 °C, this product also contains an unidentified phase. All other syntheses used platinum capsules and reasonable fits are achieved only including Mn_2FeReO_6 and ReO_2 phases. ‡Sample #4 underwent a slow cooling step for 50 minutes from 1400 to 1000 °C before being quenched.

Table 3.2 | Refined structure parameters for Mn_2FeReO_6 at 300 K in space group $P2_1/n$ using powder X-ray data.

Atom	*x*	*y*	*z*	Occupancy
Mn	0.517(2)	0.553(1)	0.751(1)	1
Fe/Re	0	½	0	0.986(6)/0.014
Re/Fe	½	0	0	0.986/0.014
O1	0.324(4)	0.353(4)	0.977(8)	1
O2	0.337(4)	0.320(4)	0.545(5)	1
O3	0.877(3)	0.463(5)	0.764(4)	1

B_{iso} = 0.375(4) Å^2; lattice parameters a = 5.1958(1), b = 5.3562(1), c = 7.5822(1), β = 89.914(3); residuals R_{wp} = 2.20 % and χ^2 = 3.76 for Mn_2FeReO_6.

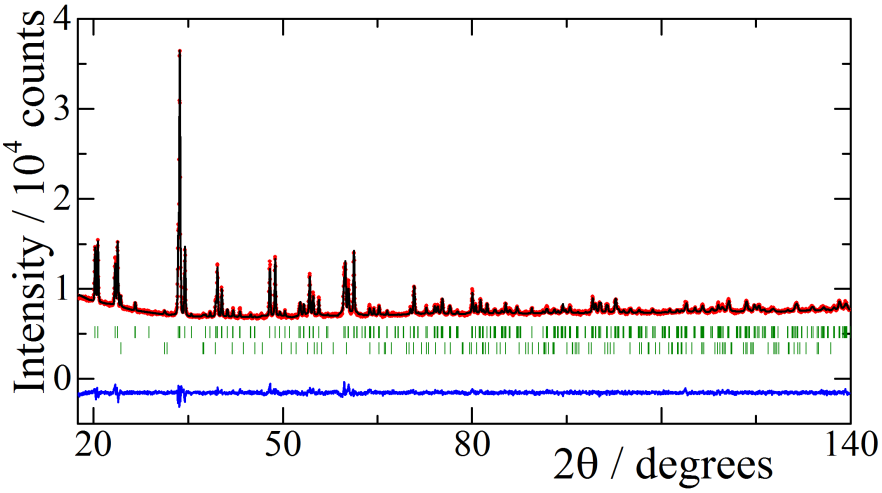

Figure 3.2 | *Rietveld fit to a Cu K_α X-ray pattern at 300 K of Mn_2FeReO_6 in the $P2_1/n$ space group, lower tick marks index an ReO_2 impurity phase.*

This $P2_1/n$ monoclinic structure is one of the expected space groups for double perovskites with rock-salt order and the highly distorted structure is one that can be rationalised by the low Goldschmidt tolerance factor of 0.83 for Mn_2FeReO_6.[85] The tilting distortions, shown in the structure of Mn_2FeReO_6 (**Fig. 3.3**), of the $BO_6/B'O_6$ octahedra cause the size of the A-site cavity to be reduced relative to that of the simple cubic structure. This compensates somewhat for the small size of Mn^{2+} as an A-cation. X-rays provide good contrast between Fe and Re cations (but little contrast between Mn/Fe), allowing the B-site rock-salt order to be accurately determined (for sample #4, with antisite disorder as low as 1.4(6) %). To determine whether any Mn/Fe

disorder exist, reference must be made to the neutron data, which also allows accurate location of O^{2-} anions to be determined, as well as the magnetic structure.

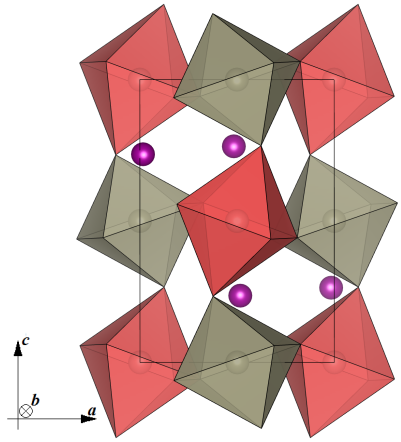

Figure 3.3 | *The monoclinic $P2_1/n$ crystal structure of Mn_2FeReO_6. The 8-coordinate A-site Mn^{2+} cations are shown in purple. The B-site Fe and Re cations are shown in red and grey, respectively. Image generated using VESTA.*[136]

3.3.2. Neutron Crystal & Magnetic Structure of Mn_2FeReO_6

Using extensive data collected by the WISH diffractometer on Mn_2FeReO_6 (a mixture of samples #1-5 (the samples initially studied on D20) and #13, total sample size of 70 mg) the crystal and magnetic structure has been analysed at multiple temperatures from 1.5 to 300 K. The $P2_1/n$ monoclinic structure obtained from X-ray diffraction was used as a starting point for neutron refinements. Trends in lattice parameters show that the *b*-axis exhibits no significant thermal dependence on cooling below 80 K, while the monoclinic angle β slightly increases as the sample is cooled. By refining Mn/Fe cation occupancies, no site disorder was found and these site occupancies were fixed to the ideal values of A-sites being fully occupied by Mn. Due to the lack of contrast between Fe and Re by neutron diffraction, B/B′-site occupancies were also fixed to be fully occupied by Fe/Re. Results of the crystal structure from these neutron refinements are shown in **Table 3.4** and in **Appendix A**. In addition to

the crystal structure parameters, Mn_2FeReO_6 exhibits magnetic order above room temperature and in all neutron diffraction patterns collected, magnetic diffraction intensity must be considered during Rietveld refinements. These magnetic intensities can be described by the symmetry operations shown in **Table 3.3**.

Table 3.3 | Irreducible representations from BasIreps for Mn^{2+}, Fe^{3+} and Re^{5+} spin ordering in Mn_2FeReO_6 using the $\boldsymbol{k}$ = (0, 0, 0) propagation vector in space group $P2_1/n$.[125]

IrRep:	Γ_1			Γ_3		
Basis Vector:	ψ_1	ψ_2	ψ_3	ψ_4	ψ_5	ψ_6
Atoms	m_x	m_y	m_z	m_x	m_y	m_z
Mn1, Mn2, Fe1, Re1[a]	+	+	+	+	+	+
Mn3, Mn4, Fe2, Re2[b]	-	+	-	+	-	+

[a] Mn1=(0.490, 0.560, 0.755); Mn2=(0.510, 0.440, 0.245); Fe1=(0, 0.5, 0); Re1=(0.5, 0, 0).
[b] Mn3=(0.010, 0.060, 0.745); Mn4=(0.990, 0.940, 0.255); Fe2=(0.5, 0, 0.5); Re2=(0, 0.5, 0.5).
Coordinates at 1.5 K. Further details of magnetic structure solution are provided in '*2.2.7 – Magnetic Symmetry Analysis*'.

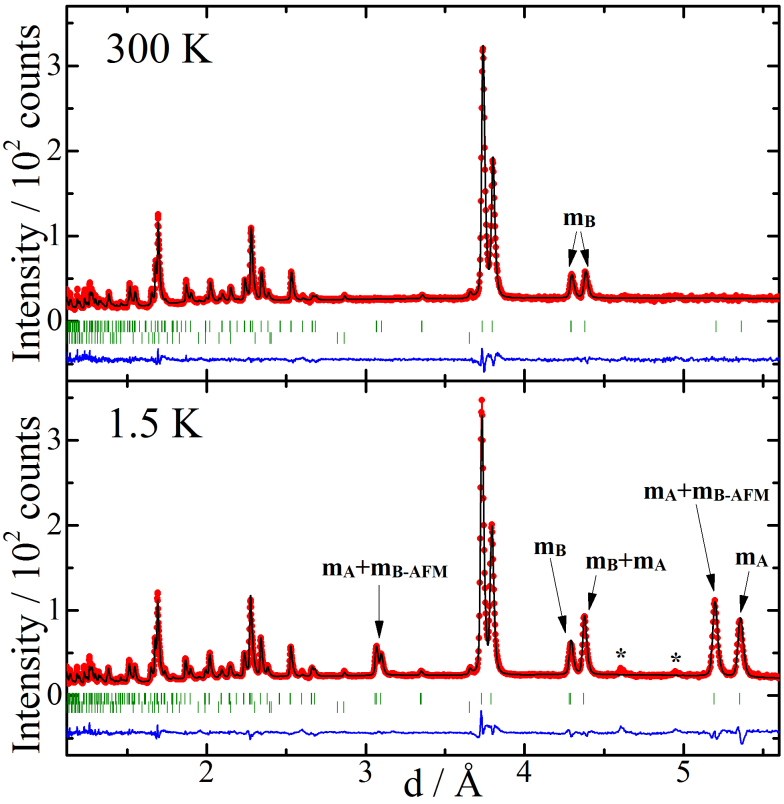

Figure 3.4 | *Combined nuclear and magnetic Rietveld fits to neutron diffraction data on Mn_2FeReO_6, collected on the WISH diffractometer at the ISIS Neutron Facility. The patterns shown are from an average of bank 3 and 8.* ***Top****: 300 K.* ***Bottom****: 1.5 K. The markers m_A and m_B refer to magnetic reflections with contributions from A and B-site spin order, respectively. Lower markers index ReO_2, with asterisks marking $MnFe_3O_5$ reflections.*

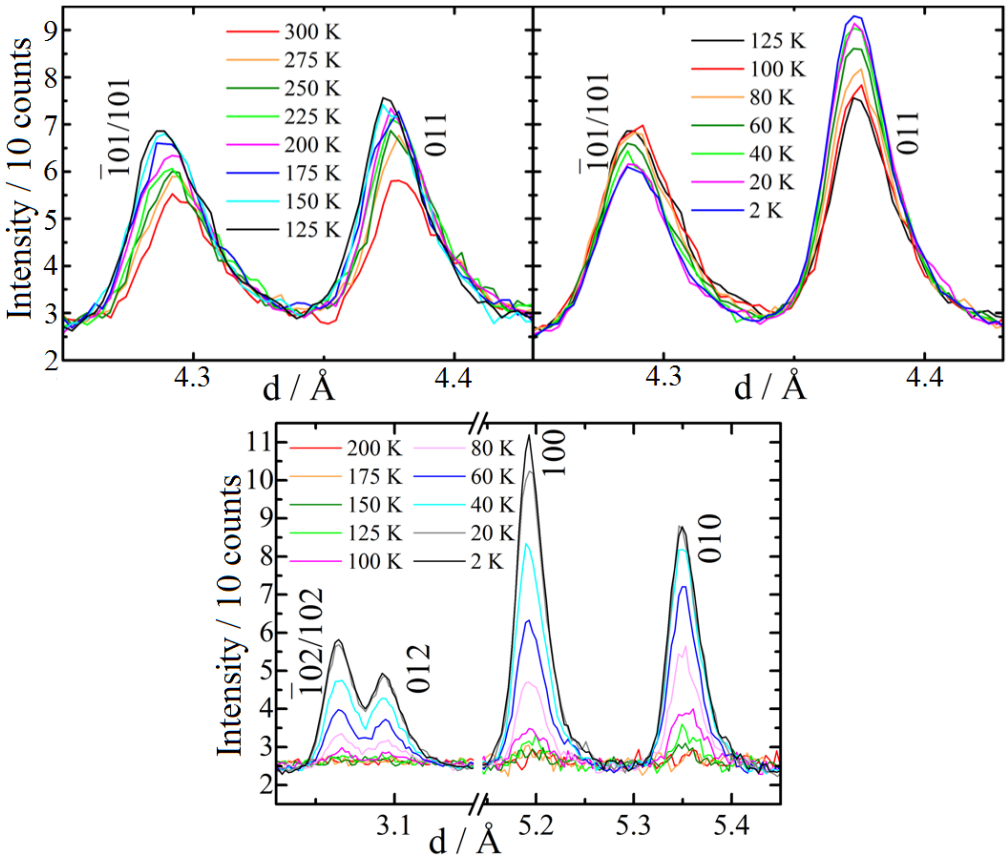

Figure 3.5 | *Diffracted neutron intensities are shown for Fe/Re spin order in the region d ~4.35 Å between 300 and 125 K (**top left**) and between 125 and 1.5 K (**top right**). Diffracted neutron intensities for Mn spin order are shown in the regions d ~3.1 and 5.3 Å between 200 and 1.5 K (**bottom**). The miller indices are shown beside each reflection. A particularly notable feature is the relative rate of evolution of reflections $\bar{1}$01/101 and 011 and that the intensity of the 101 reflection reduces with decreasing temperature below 80 K.*

Rietveld fits to the neutron patterns obtained from an average of banks 3 and 8 shown in **Fig. 3.4** at both 1.5 and 300 K. Comparing the patterns between these temperatures shows clear magnetic intensities on the $\bar{1}$02/102, 012, $\bar{1}$01/101, 011, 100 and 010 reflections (*d* ~3.1, 4.35 and 5.3 Å). The evolutions of magnetic intensities in neutron diffraction patterns of this material are shown in **Fig. 3.5** (*d* ~4.35 Å are intensities mainly attributed to Fe/Re spin order; *d* ~3.1 and 5.3 Å are intensities mainly attributed to Mn spin order).

Several symmetry operations are required to accurately describe the magnetic structure used in the Rietveld fits above (**Fig. 3.4**). It is found that good fits to the

neutron data can be achieved by using $\Gamma_3\psi_4$ and $\Gamma_3\psi_6$ in the high-temperature regime (up to at least 300 K) to describe Fe/Re ferrimagnetic order (with negative coefficients of these symmetry operations for Re). These operations provide intensity on the $\bar{1}01/101$ and 011 reflections (d ~4.3 and 4.4). When the sample is cooled below approximately 175 K, Mn spin order begins to be observed and can be described by a combination of three operations: $\Gamma_1\psi_1$, $\Gamma_1\psi_3$ and $\Gamma_3\psi_5$. These operations account for intensity observed on the $\bar{1}02/102$, 012, 100 and 010 reflections (d ~3.1, 5.2 and 5.35 Å), as well as an additional component to the 011 reflection (d ~4.4 Å, mainly attributed to Fe/Re spin order).

Another transition is observed at temperatures between 60 and 80 K, which can only be adequately fit by Fe/Re spins gaining a more substantial component along the *a*-axis as well as an antiferromagnetic component along the *b*-axis described by $\Gamma_3\psi5$. This operation provides intensity on the $\bar{1}02/102$, 012 and 100 reflections (d ~3.1 and 5.2 Å, reflections that are mainly attributed to Mn spin order). It is also important to note that in these refinements Re moments have been constrained to be $^1/_5$ of the moment of Fe to ensure stable refinement. This fits with values of Re moments expected from previous refinements using D20 data (independently refining Re moments) and with XMCD data at 300 K (*3.3.5 – X-ray Magnetic Circular Dichroism*) that show Re moments to be close to $^1/_5$ of the Fe moment in the high-temperature regime. Full refined magnetic parameters of this combined crystal and magnetic structure are shown in **Table 3.6**. In addition, the BO_6 octahedral tilt angles are tabulated here and are approximately 25° (tilting from the *c*-axis on to the *a*-axis) and 12° (tilting from the *c*-axis on to the *b*-axis).

Table 3.4 | Refined structural parameters for Mn_2FeReO_6 in space group $P2_1/n$ from neutron data collected on the WISH diffractometer at the ISIS Neutron Facility. Sample size 70 mg.

T / K		1.5	20	40	60	80	100	125	150	175	200	225	250	275	300
Cell	a / Å	5.1985(4)	5.1988(4)	5.1989(4)	5.1991(4)	5.1995(4)	5.2002(4)	5.2004(4)	5.2011(4)	5.2020(4)	5.2027(4)	5.2041(4)	5.2051(4)	5.2066(4)	5.2087(4)
	b / Å	5.3590(4)	5.3593(4)	5.3589(4)	5.3589(4)	5.3589(4)	5.3597(5)	5.3600(5)	5.3611(5)	5.3624(5)	5.3634(4)	5.3650(4)	5.3660(4)	5.3670(4)	5.3687(5)
	c / Å	7.5867(6)	7.5871(6)	7.5878(6)	7.5890(6)	7.5902(6)	7.5913(6)	7.5914(6)	7.5925(6)	7.5935(6)	7.5941(6)	7.5956(5)	7.5964(5)	7.5979(6)	7.5998(6)
	β / °	90.114(8)	90.110(8)	90.098(9)	90.08(1)	90.07(1)	90.08(1)	90.08(1)	90.07(1)	90.07(1)	90.06(1)	90.06(1)	90.05(1)	90.06(1)	90.06(2)
	V / Å^3	211.36(3)	211.39(3)	211.40(3)	211.44(3)	211.49(3)	211.58(3)	211.60(3)	211.71(3)	211.82(3)	211.91(3)	212.07(3)	212.17(3)	212.31(3)	212.52(3)
Mn	x	0.490(2)	0.490(2)	0.490(2)	0.486(2)	0.483(2)	0.480(2)	0.478(2)	0.479(2)	0.479(2)	0.477(2)	0.481(2)	0.482(2)	0.482(2)	0.484(2)
	y	0.560(2)	0.560(2)	0.559(2)	0.560(2)	0.560(2)	0.560(2)	0.560(2)	0.560(2)	0.558(2)	0.559(2)	0.558(2)	0.556(2)	0.555(2)	0.553(2)
	z	0.755(3)	0.756(4)	0.756(4)	0.761(4)	0.761(4)	0.761(4)	0.759(4)	0.759(4)	0.761(4)	0.758(4)	0.755(4)	0.763(4)	0.768(3)	0.764(4)
O1	x	0.308(3)	0.308(3)	0.307(3)	0.307(3)	0.309(3)	0.306(3)	0.307(3)	0.305(2)	0.305(2)	0.304(2)	0.306(3)	0.305(3)	0.304(2)	0.310(4)
	y	0.317(3)	0.317(3)	0.318(3)	0.318(3)	0.320(3)	0.321(3)	0.322(3)	0.321(3)	0.320(3)	0.321(2)	0.320(3)	0.318(3)	0.315(3)	0.314(4)
	z	0.946(2)	0.946(2)	0.945(2)	0.943(2)	0.942(2)	0.942(2)	0.942(2)	0.943(2)	0.943(2)	0.943(2)	0.944(2)	0.940(2)	0.940(2)	0.941(3)
O2	x	0.329(3)	0.329(3)	0.331(3)	0.331(3)	0.330(3)	0.330(3)	0.330(3)	0.331(2)	0.332(2)	0.331(2)	0.329(3)	0.330(3)	0.332(2)	0.326(4)
	y	0.298(3)	0.299(3)	0.298(3)	0.299(3)	0.299(3)	0.297(3)	0.297(3)	0.298(3)	0.299(3)	0.299(3)	0.300(3)	0.302(3)	0.305(3)	0.309(4)
	z	0.568(2)	0.567(2)	0.566(2)	0.563(2)	0.562(2)	0.561(2)	0.561(2)	0.562(2)	0.562(2)	0.563(2)	0.565(2)	0.562(2)	0.562(2)	0.564(3)
O3	x	0.879(1)	0.879(1)	0.878(1)	0.879(1)	0.878(1)	0.876(1)	0.876(1)	0.876(1)	0.877(1)	0.876(1)	0.877(1)	0.878(1)	0.878(1)	0.876(1)
	y	0.439(1)	0.439(1)	0.439(1)	0.439(1)	0.441(1)	0.442(1)	0.442(1)	0.443(1)	0.443(1)	0.444(1)	0.444(1)	0.444(1)	0.444(1)	0.445(1)
	z	0.735(2)	0.734(2)	0.733(2)	0.731(2)	0.728(2)	0.729(2)	0.728(2)	0.727(2)	0.727(2)	0.726(1)	0.730(2)	0.730(2)	0.732(2)	0.734(2)
Mn, B_{iso} / Å^2		1.51(5)	1.52(5)	1.58(5)	1.4(3)	1.5(3)	1.4(3)	1.5(3)	1.6(3)	1.7(3)	1.9(3)	1.9(3)	1.8(3)	1.8(3)	2.3(3)
Fe/Re, B_{iso} / Å^2		1.67(2)	1.64(2)	1.67(2)	1.67(8)	1.64(8)	1.69(9)	1.69(9)	1.66(9)	1.75(9)	1.77(9)	1.81(9)	1.74(8)	1.74(8)	1.76(8)
O, B_{iso} / Å^2		0.86(2)	0.85(2)	0.81(2)	0.76(9)	0.69(9)	0.62(9)	0.58(9)	0.60(9)	0.62(9)	0.56(8)	0.70(8)	0.78(8)	0.94(9)	1.14(9)
R_{wp} / %		4.00	3.88	4.10	3.99	3.98	4.14	4.18	4.12	4.04	3.87	3.77	3.71	3.67	3.73
χ^2		5.01	3.57	3.47	3.31	3.32	2.58	2.31	2.27	2.19	2.03	1.93	1.88	1.77	1.67
Q / μA·h		60	40	40	40	40	29	25	25	25	25	25	25	24	22

Fe atoms are located at (0, ½, 0), with Re atoms at (½, 0, 0). Antisite disorder of Fe/Re is not refined due to poor neutron contrast. No site mixing between A and B-sites was found. Q, a measure of the total length of exposure of the sample to the neutron beam ($Q = I \cdot t$), is also tabulated.

Table 3.5 | Refined magnetic parameters for Mn_2FeReO_6 in space group $P2_1/n$ from neutron data collected using the WISH diffractometer at the ISIS Neutron Facility. Magnetic symmetry operations are those as described in **Table 3.3**. Sample size 70 mg.

	T / K	1.5	20	40	60	80	100	125	150	175	200	225	250	275	300
Fe	mFe / μ_B	4.86(4)	4.82(4)	4.84(4)	4.77(4)	4.63(4)	4.54(4)	4.43(4)	4.33(5)	4.22(5)	4.04(4)	3.92(4)	3.78(4)	3.62(4)	3.39(5)
	φ_{Fe} / degrees	8(1)	8(1)	9(1)	8(2)	0	0	0	0	0	0	0	0	0	0
	θ_{Fe} / degrees	49(1)	49(1)	45(1)	38(1)	29(2)	24(2)	21(3)	23(3)	25(3)	24(2)	28(2)	29(2)	30(3)	18(4)
	φ_{FeFe} / degrees	16(2)	16(2)	17(3)	16(4)	0	0	0	0	0	0	0	0	0	0
	m_x / μ_B (FM)	3.64(6)	3.59(6)	3.41(7)	2.90(9)	2.3(1)	1.8(2)	1.6(2)	1.7(2)	1.8(2)	1.7(2)	1.9(1)	1.8(1)	1.8(2)	1.1(3)
	m_y / μ_B (AFM)	0.52(6)	0.50(6)	0.52(8)	0.4(1)	0	0	0	0	0	0	0	0	0	0
	m_z / μ_B (FM)	3.18(8)	3.19(9)	3.40(8)	3.77(8)	4.05(8)	4.15(8)	4.12(8)	3.97(8)	3.82(8)	3.68(8)	3.45(8)	3.31(9)	3.1(1)	3.22(9)
	θ_{Tilt} / degrees	24.5(1)	24.5(1)	24.5(1)	24.3(1)	24.1(1)	24.5(1)	24.6(1)	24.5(1)	24.3(1)	24.3(1)	24.5(1)	24.4(1)	24.5(1)	25.0(1)
	φ_{Tilt} / degrees	13.0(2)	12.9(2)	12.8(2)	12.7(2)	12.3(2)	12.1(2)	12.0(2)	11.7(2)	11.8(2)	11.5(2)	11.7(2)	11.8(2)	11.9(2)	11.8(2)
Mn	mMn / μ_B	3.84(3)	3.74(3)	3.31(3)	2.71(3)	2.06(4)	1.42(5)	1.10(6)	0.74(9)	0.6(1)	0	0	0	0	0
	φ_{Mn} / degrees	58(1)	58(1)	53(1)	46(2)	39(2)	40(4)	39(6)	50(20)	60(20)	-	-	-	-	-
	θ_{Mn} / degrees	55(1)	55(1)	51(2)	47(2)	49(3)	51(5)	54(9)	50(20)	60(30)	-	-	-	-	-
	m_x / μ_B (AFM)	1.67(8)	1.64(8)	1.56(8)	1.39(8)	1.20(7)	0.84(9)	0.7(1)	0.3(2)	0.3(3)	0	0	0	0	0
	m_y / μ_B (AFM)	2.65(4)	2.58(4)	2.06(5)	1.42(6)	0.98(8)	0.7(1)	0.6(1)	0.5(1)	0.5(1)	0	0	0	0	0
	m_z / μ_B (AFM)	2.22(6)	2.15(7)	2.07(6)	1.84(7)	1.35(6)	0.89(9)	0.6(1)	0.5(2)	0.3(3)	0	0	0	0	0
m_{tot} / μ_B f.u.$^{-1}$		3.87(8)	3.84(9)	3.9(1)	3.8(1)	3.7(1)	3.6(2)	3.5(2)	3.5(2)	3.4(2)	3.2(2)	3.1(2)	3.0(2)	2.9(2)	2.7(2)
R_{wp} / %		4.00	3.88	4.10	3.99	3.98	4.14	4.18	4.12	4.04	3.87	3.77	3.71	3.67	3.73
χ^2		5.01	3.57	3.47	3.31	3.32	2.58	2.31	2.27	2.19	2.03	1.93	1.88	1.77	1.67
Q / μA·h		60	40	40	40	40	29	25	25	25	25	25	25	24	22

Magnetic vectors for Fe and Mn are tabulated in both polar and Cartesian coordinate systems, in the polar system φ denotes the angle between the a and b axes (0° defined as parallel to a) and θ denoting the angle between the c and a axes (0° defined as parallel to c). The angles θ_{Tilt} and φ_{Tilt} reference the FeO_6 octahedra tilt angles between the c-axis and the a and b-axes, respectively. The angle φ_{FeFe} denotes the angle between Fe moments due to the antiferromagnetic component of Fe spin order along the b-axis. Magnitudes of Re moments are constrained as $-0.2 \times mFe$, with the same magnetic symmetry as Fe. Total magnetisation due to ferrimagnetic Fe/Re order is shown as m_{tot}.

Table 3.6 | Bond lengths, angles and BVS values for Mn_2FeReO_6 in space group $P2_1/n$ from the neutron profile fit at 1.5 K.

Bond	M – O length / Å	Bond	M – O length / Å
Mn – O1	2.17(1)	Fe – O1	1.92(2) × 2
Mn – O1	2.57(2)	Fe – O2	1.90(2) × 2
Mn – O1	2.58(3)	Fe – O3	2.13(1) × 2
Mn – O2	2.16(2)	**<Fe – O>**	1.98(1)
Mn – O2	2.49(2)		
Mn – O2	2.73(2)	Re – O1	2.01(2) × 2
Mn – O3	2.13(1)	Re – O2	2.09(2) × 2
Mn – O3	2.14(1)	Re – O3	1.92(1) × 2
<Mn – O>	2.371(7)	**<Re – O>**	2.01(1)
Cation	**BVS**	**B – O# – B′**	**Angle / degrees**
Mn	1.83	Fe – O1 – Re	143.2(7)
Fe	3.38	Fe – O2 – Re	138.8(6)
Re	4.12	Fe – O3 – Re	138.9(6)

The program BondStr in the FullProf Suite was used to compute this data.[125] The parameters used in BondStr for Re are not well defined and so the BVS computed is slightly lower than the expected value of 5.

Table 3.7 | Bond lengths, angles and BVS values for Mn_2FeReO_6 in space group $P2_1/n$ from the neutron profile fit at 300 K.

Bond	M – O length / Å	Bond	M – O length / Å
Mn – O1	2.07(3)	Fe – O1	1.95(2) × 2
Mn – O1	2.59(3)	Fe – O2	1.95(2) × 2
Mn – O1	2.59(3)	Fe – O3	2.14(1) × 2
Mn – O2	2.17(3)	**<Fe – O>**	2.01(1)
Mn – O2	2.49(3)		
Mn – O2	2.78(4)	Re – O1	2.01(2) × 2
Mn – O3	2.14(1)	Re – O2	2.04(2) × 2
Mn – O3	2.23(1)	Re – O3	1.92(1) × 2
<Mn – O>	2.38(1)	**<Re – O>**	1.99(1)
Cation	**BVS**	**B – O# – B′**	**Angle / degrees**
Mn	1.83	Fe – O1 – Re	141.9(9)
Fe	3.09	Fe – O2 – Re	138.9(9)
Re	4.30	Fe – O3 – Re	138.9(6)

The program BondStr in the FullProf Suite was used to compute this data.[125] The parameters used in BondStr for Re are not well defined and so the BVS computed is slightly lower than the expected value of 5.

Bond lengths, B – O – B′ angles and bond valence sum (BVS) values for Mn, Fe and Re are tabulated for temperatures of 1.5 (**Table 3.6**) and 300 K (**Table 3.7**). This data helps to confirm formal charge states of cations in the material as Mn^{2+}, Fe^{3+} and Re^{5+}, however it is notable that the BVS for Re is rather low. The R_0 values for Re used in this BVS calculation are those from IUCr tables and may have a large unknown uncertainty associated with them.[91]

Also of note are Jahn-Teller (J-T) distortions of ReO_6 octahedra (compressions along the *c*-axis). This J-T compression of ReO_6 octahedra is consistent with that observed by Oikawa et al. at high temperatures in $Ca_2Fe^{3+}Re^{5+}O_6$.[82] However, in the Ca material a switch from J-T compression at high temperature to J-T elongation at low temperature (with long Re–O2 bonds) is attributed to Re^{5+} orbital ordering, accompanied by a switch from a ferrimagnetic metallic phase to a ferrimagnetic insulating phase (transition temperature ~140 K). Oikawa et al. also suggest that this change in J-T distortion of ReO_6 octahedra should be accompanied by a rotation of the spin structure by 90°, which they observe to be true as the Fe/Re spins reorientate from being parallel to the *c*-axis to being parallel to the *b*-axis. In Mn_2FeReO_6, Re^{5+} orbital ordering is not observed and the Fe/Re spins do not reorientate by 90° on to the *b*-axis. However, the Fe/Re spin structure does gain a magnetic mode acting along the *b*-axis at a transition below 80 K. It could be speculated that in $Mn_2^{2+}Fe^{3+}Re^{5+}O_6$ the $Re^{5+}O_6$ ($5d^2$) octahedra are attempting to distort as J-T elongated octahedra at this transition due to a propensity to orbitally order (note that at 2 K, the Re–O2 bonds do seem expanded relative to their lengths at 300 K, essentially resulting in pairs of short, medium and long bonds). However, to do this the Fe/Re spin structure must also

reorientate by 90° and this is prevented by the presence of antiferromagnetic Mn^{2+} spin order which causes frustration. This may explain why orbital ordering is not observed in Mn_2FeReO_6.

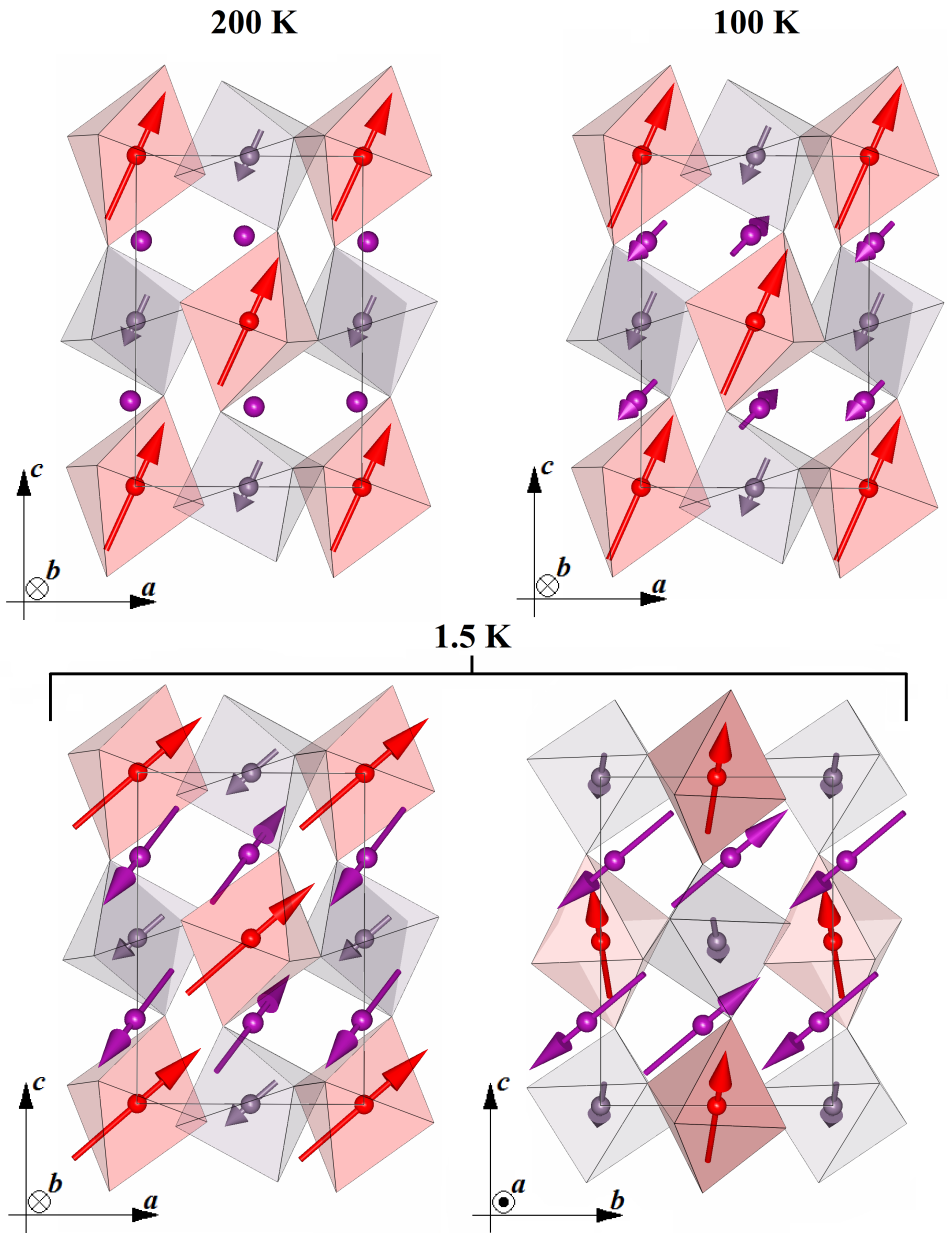

Figure 3.6 | *Magnetic structures of Mn_2FeReO_6 at 200 K (with ferrimagnetic Fe/Re spin order in the ac-plane), at 100 K (with ferrimagnetic Fe/Re spin order in the ac-plane and antiferromagnetic Mn spin order with x, y and z components) and at 1.5 K (with ferrimagnetic Fe/Re spin order in the ac-plane and antiferromagnetic layers of Fe/Re that cant along ±b, as well as Mn spin order with x, y and z components). Fe shown as red, Re as grey and Mn as purple. Images generated using FPStudio.*[125]

The magnetic structure of Mn_2FeReO_6, as determined by refinement of data acquired from WISH is depicted in **Fig. 3.6**, with two orientations of the low-temperature (1.5 K) structure shown to clearly illustrate the antiferromagnetic B cation order along the *b*-axis. The data presented so far has been that obtained from the WISH diffractometer, however this is not the only source of neutron data collected on Mn_2FeReO_6, five patterns at varying temperature were also collected on the D20 diffractometer.

Analysis of D20 data differs somewhat from analysis of data collected on WISH, with main differences including the fact that the small *a*-axis Fe/Re component of the high-temperature structure is not resolved with D20 data and only a component along the *c*-axis can be determined. It should also be noted here that in refinements of neutron data collected on Ca_2FeReO_6, it was found by Oikawa et al. that better Rietveld fits were obtained by orientating Fe/Re moments in the *ac*-plane,[82] however their fit was not improved enough to reliably ascertain whether an *a*-axis component was truly present (much in the same manner as our analysis of Mn_2FeReO_6 at high temperature using D20 data). However, the data obtained from WISH seems to clarify that there is indeed an *a*-axis component, at least in Mn_2FeReO_6. Additionally, by analysis of D20 data Mn spin order appears to first occur along the *c*-axis at 100 K, before tilting and acquiring components along all three axes at lower temperatures of 50 and 1.7 K. Data from WISH however, yields a higher temperature of the onset of Mn spin order of 175 K, with evidence that there are components in *x*, *y* and *z* of Mn spin order that persist up to this temperature.

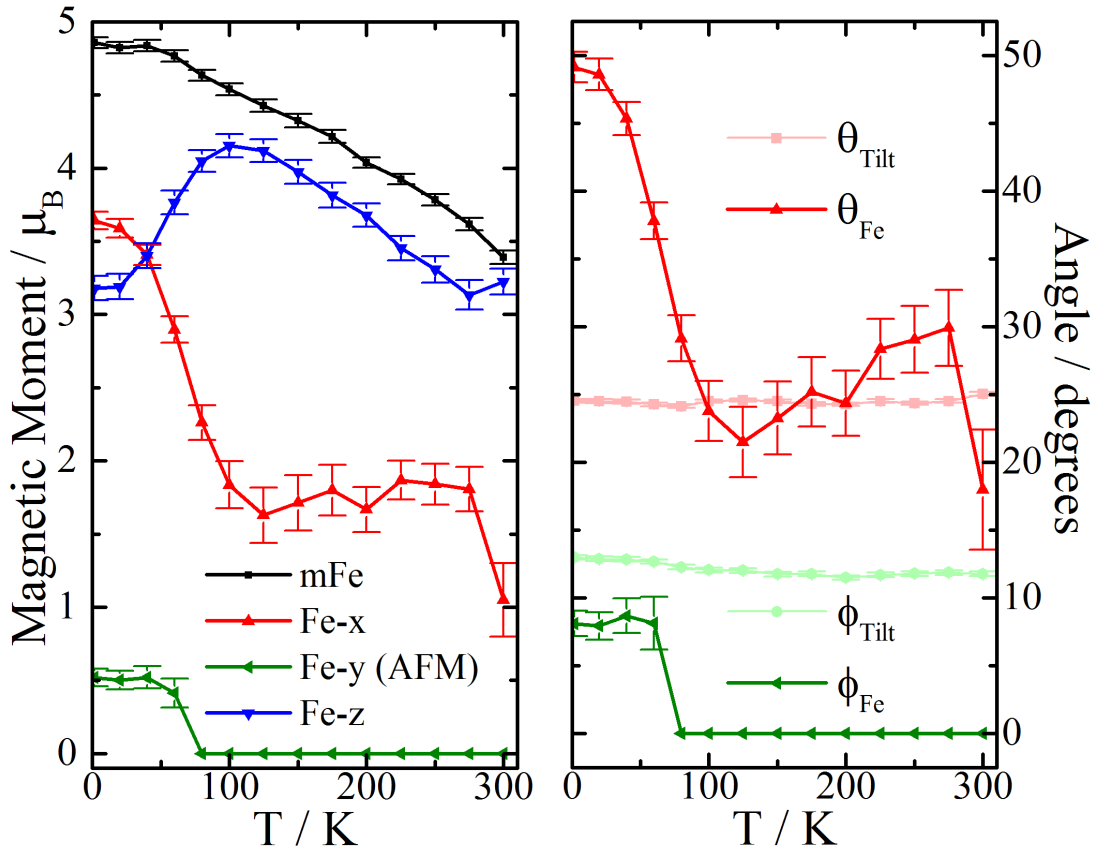

Figure 3.7 | *Magnetic structure data for Mn_2FeReO_6.* ***Left****: Magnetic components in the Cartesian coordinate system for Fe, as well as the total magnetic moment for the Fe site.* ***Right****: Polar angles for Fe, as well as FeO_6 octahedra tilts.*

Other interesting features of these magnetic structures are the tilting angles of Fe magnetic moments when compared to the tilting of FeO_6 octahedra (**Fig. 3.7**). Magnetic structures at 100 K and above show that the Fe spins with magnetic components in *x* and *z* are oriented at a similar angle from the *c*-axis toward the *a*-axis (defined as θ_{Fe}) as the FeO_6 octahedra tilt from the *c*-axis toward the *a*-axis (defined as θ_{Tilt}). In the low-temperature regime, however θ_{Fe} and θ_{Tilt} no longer follow one another, the angle of Fe moments from the *c*-axis toward the *b*-axis (defined as ϕ_{Fe}) begins to approach the angle of the FeO_6 octahedra tilts from the *c*-axis toward the *b*-axis (defined as ϕ_{Tilt}), with the same symmetry as the octahedral tilts. It could be

concidence that these angles of magnetic moments and octahedral tilts are similar, but this could also be an indication of local structural considerations driving the orientation of magnetic moments. However, the data available is not substantial enough to determine any significant implications of similarities between these angles.

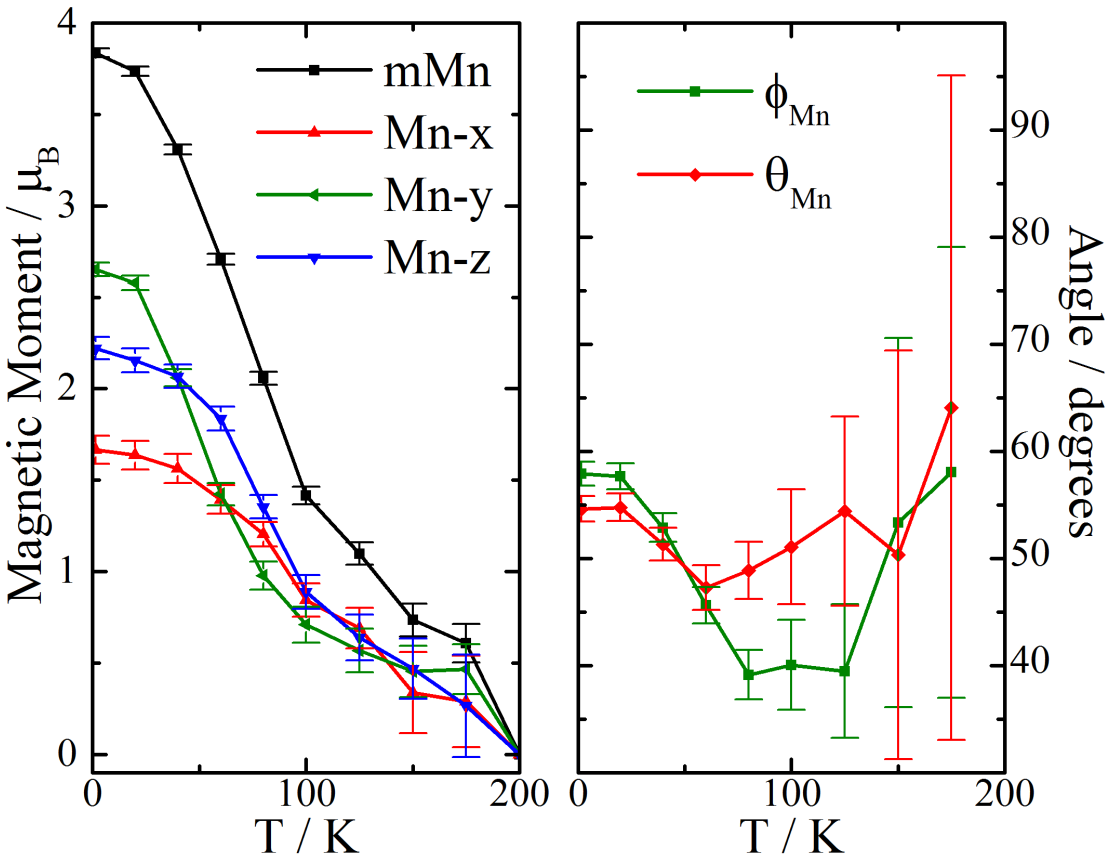

Figure 3.8 | *Magnetic structure data for Mn_2FeReO_6.* ***Left****: Magnetic components in the Cartesian coordinate system for Mn with antiferromagnetic components in x, y and z, as well as the total magnetic moment for the Mn site.* ***Right****: Polar angles for Mn.*

The Cartesian and polar coordinates for Mn spin order are also displayed in **Fig. 3.8**. This plot shows that the onset of antiferromagnetic Mn spin order occurs at higher temperatures (< ~175 K) than the onset of Fe/Re *b*-axis antiferromagnetic order (< 80 K), and possesses components along all three Cartesian axes.

3.3.3. Magnetometry Measurements of Mn_2FeReO_6

Magnetometry data collected on Mn_2FeReO_6 shows behaviour that is consistent with the magnetic structures obtained from analysis of neutron diffraction data. Magnetisation vs. temperature in **Fig 3.9** shows the presence of a transition at 520 K, associated with the T_c of the material and the ferrimagnetic ordering of Fe/Re above room temperature. A second transition is observed at approximately 75 K, indicative of the antiferromagnetic component of Fe/Re spin order, accompanied by a reduction in the overall magnetisation of the material.

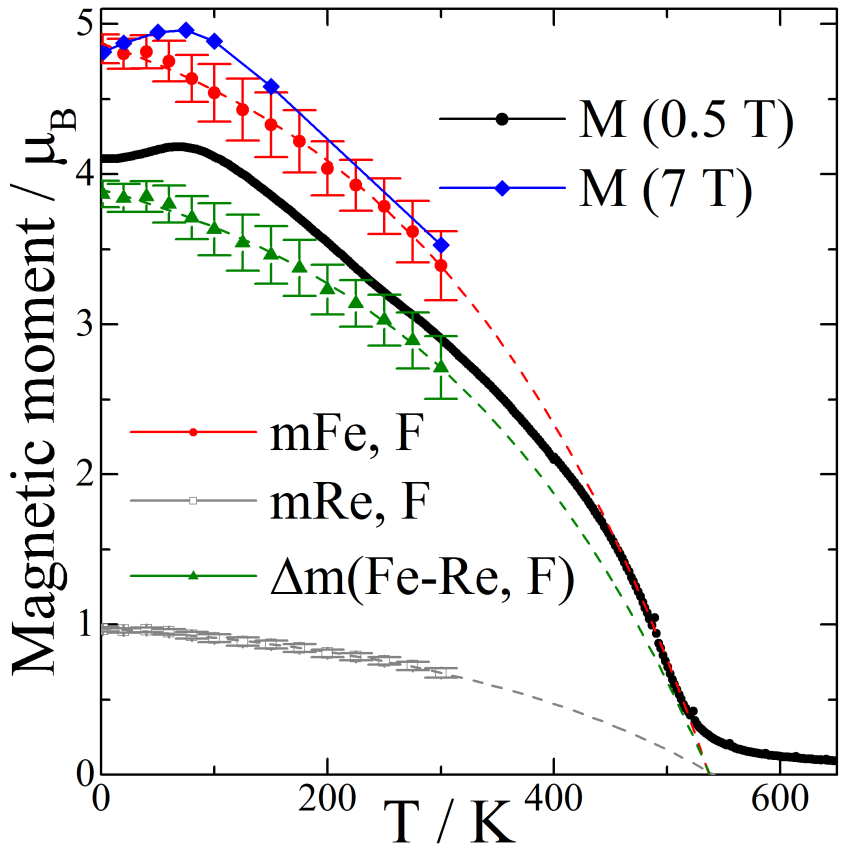

Figure 3.9 | *Magnetisation vs. temperature obtained from SQUID magnetometry from T = 0-650 K of Mn_2FeReO_6. Overlaid on this plot are also the ferrimagnetic components of magnetic moments for Fe and Re (i.e. neglecting the antiferromagnetic y-component of magnetic moment), as well as the difference between these two moments, represented as Δm(Fe-Re, F). This difference should follow the overall magnetisation of the sample at zero-field.*

Based on neutron diffraction analysis an antiferromagnetic transition associated with Mn spin order should be visible above approximately 175 K, however this transition is subtle and could be evidenced by anomalies in the gradient of magnetisation at approximately 210 K or potentially even higher, at 285 K (zero-field cooled *M* versus *T*, **Appendix A**). The refined ferrimagnetic component of the magnetic moment of Fe and Re is also shown in **Fig. 3.9**, overlaid on top of the magnetisation data. This shows a reasonably clear trend for the difference in ferrimagnetic components between Fe and Re to follow the overall magnetisation as would be expected from the magnetic structures. Extrapolation of these refined moments using an exponential decay function leads to *x*-axis intercepts of approximately 540 K, predicting a slightly higher T_c than that observed from magnetometry data (520 K).

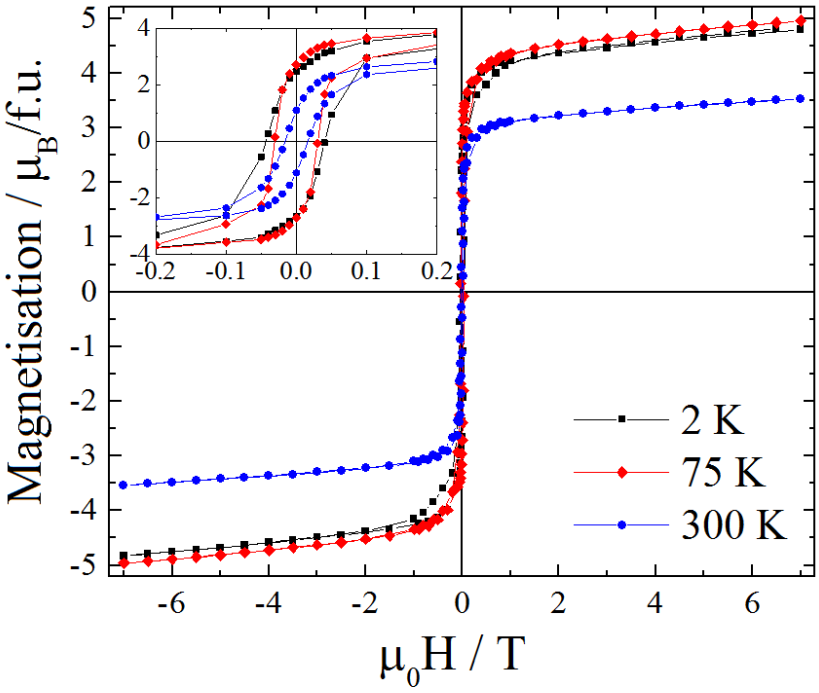

Figure 3.10 | *Magnetisation versus field hysteresis measurements for Mn_2FeReO_6. The low field region is shown in the inset, where a low coercivity (~400 Oe at 2 K) can be seen.*

3.3.4. Magnetoresistance of Mn_2FeReO_6

Particularly interesting phenomena are observed in polycrystalline pellets of Mn_2FeReO_6 when the resistivity of the material is measured with and without the presence of an applied magnetic field. In zero-field, bulk semiconducting behaviour is observed, shown in the magnitude and trend in resistivity in **Fig. 3.11**. This is expected as a trend to shift from metallic to semiconducting behaviour has been noted to occur as the A^{2+} cation size decreases across the A_2FeReO_6 series.[74]

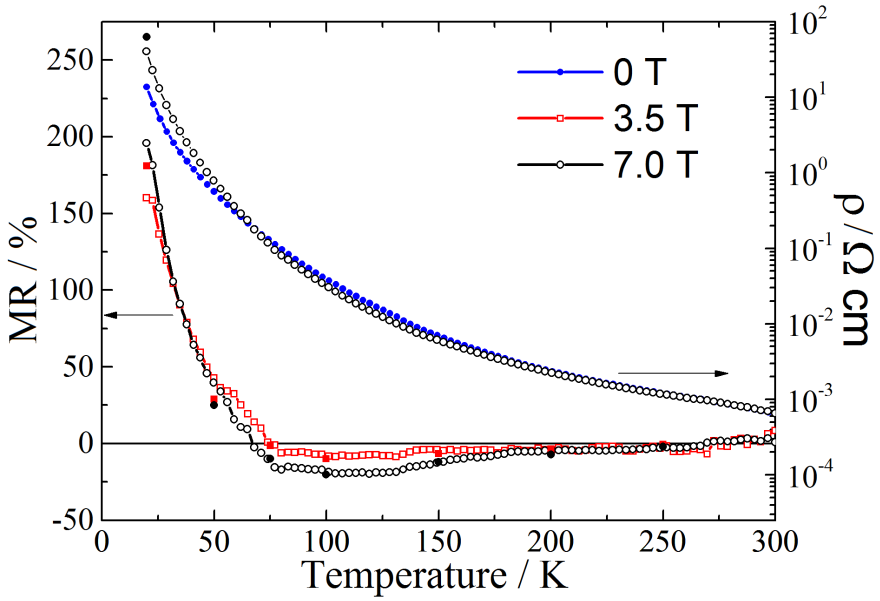

Figure 3.11 | *Resistivity (0 and 7 T) and magnetoresistance (3.5 and 7 T) of Mn_2FeReO_6, showing a change in the sign of the magnetoresistance. Solid black/red points are taken from M vs. H measurements at constant temperature.*

Comparison of resistivity measurements in applied magnetic fields to those at zero-field show expected negative magnetoresistance (MR) effects (as seen in other double perovskites with Fe/Re B-site order) at high temperature, e.g. *MR* = -19 % at 100 K and 7 T. However, at low temperatures the MR adopts large positive values of up to 265 % at 20 K and 7 T. This crossover transition between negative and positive

MR occurs at approximately 75 K, as seen in **Fig. 3.11**. MR versus field hysteresis loops shown in **Fig. 3.12** also show this positive to negative transition to occur at approximately 75 K. The loop at 75 K also shows a positive low field response, with a negative high field response, indicating that the mechanisms that are providing these very different effects may be in competition with one another and have different field dependencies.

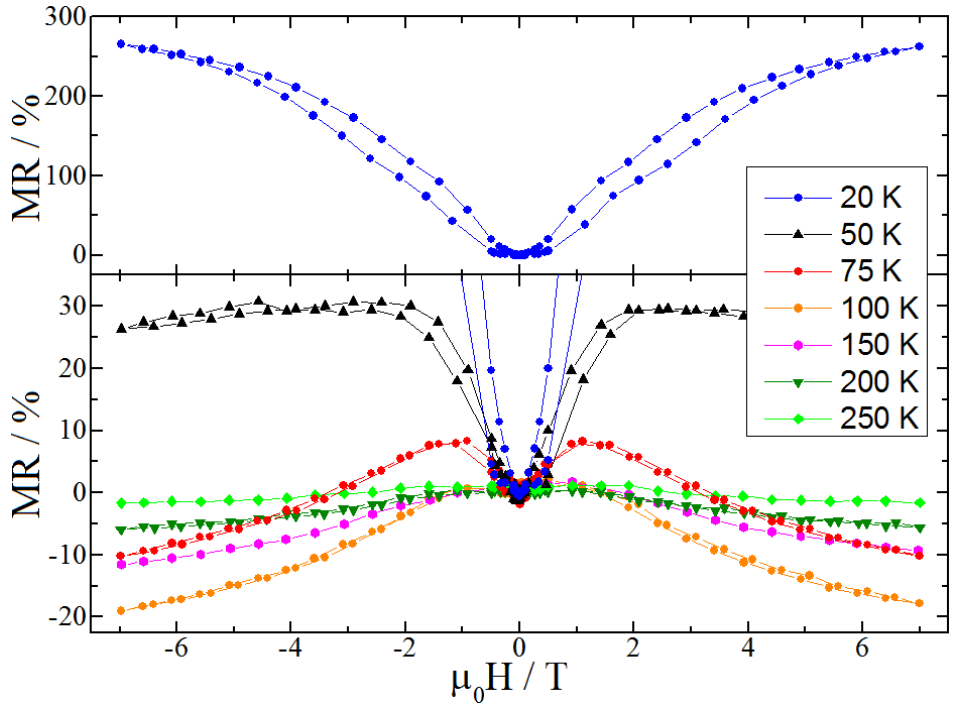

Figure 3.12 | *Magnetoresistance vs. field (-7 T to +7 T) at constant temperatures for Mn_2FeReO_6. The 20 K magnetoresistance is clearly seen to be positive (+265 %) while the magnetoresistance at 100 K is negative (-19 %). Of particular note is that at 75 K, around the spontaneous spin ordering of Mn^{2+} positive magnetoresistance is observed at low fields of 0 to 3 T but at higher fields negative magnetoresistance is observed.*

In $A_2FeB'O_6$ double perovskites the probability of electron transfer between cations via a double exchange mechanism is dependent on the alignment of Fe spins and follows $\cos(\frac{1}{2}\cdot\theta_{FeFe})$ as in **Equation 1.4**.[137–140] The magnetic structure in the temperature range above ~75 K possesses parallel Fe spins which provide this bulk

conduction pathway. In the intergrain tunnelling mechanism of magnetoresistance, the enhancement of polarisation (*P*) and magnetisation (*M*) of a polycrystalline material result in an increased MR effect, as described in **Equation 1.6**.[74] The co-alignment of spins in adjacent polycrystalline grains is necessary to promote the conduction pathway, which is improved by the application of a field resulting in negative MR. This intergrain tunnelling explains the negative magnetoresistance observed in Mn_2FeReO_6 in the high-temperature range above ~75 K.

In the positive MR temperature range, below ~75 K, the magnetic structure no longer possesses parallel Fe spins, with a θ_{FeFe} canting angle of ~16° (**Table 3.5**). This canting angle corresponds to a 1 % decrease in the probability of electron transfer via double exchange, only slightly increasing the resistivity of the material. Our MR measurements indicate an extremely large positive MR effect of +265 % at 20 K and 7 T, however we cannot determine exactly how this applied field changes the magnetic structure. The application of a magnetic field must act to change the magnetic structure of Mn_2FeReO_6 in such a way as to increase the resistivity further. This could be by affecting the orientation of Fe/Re sublattice, the orientation of the Mn sublattice, or some combination of both and thereby increasing the bulk resistivity. These two separate mechanisms of MR, with intergrain tunnelling providing negative MR from interfacial effects and magnetic structure modifications providing positive MR from bulk effects seem to be supported by the different MR responses with varying field strength at 75 K. At this temperature the magnetic structure reorientation would appear to occur easily with a low field strength providing positive MR before the intergrain tunnelling MR becomes dominant at high fields resulting in the negative MR.

3.3.5. X-ray Magnetic Circular Dichroism: Mn_2FeReO_6

X-ray Absorption Near-Edge Spectra (XANES) and calculated X-ray Magnetic Circular Dichroism (XMCD) are shown in **Fig. 3.13** and **Fig. 3.14** for the Re L_2 and L_3-edges, respectively. From the integrals of XANES and XMCD in the range of the absorption edge, and the application of the sum rules described in '*2.3.3. X-ray Magnetic Circular Dichroism*', ratios between spin and orbital moments for Re can be calculated (**Equation 2.31**).

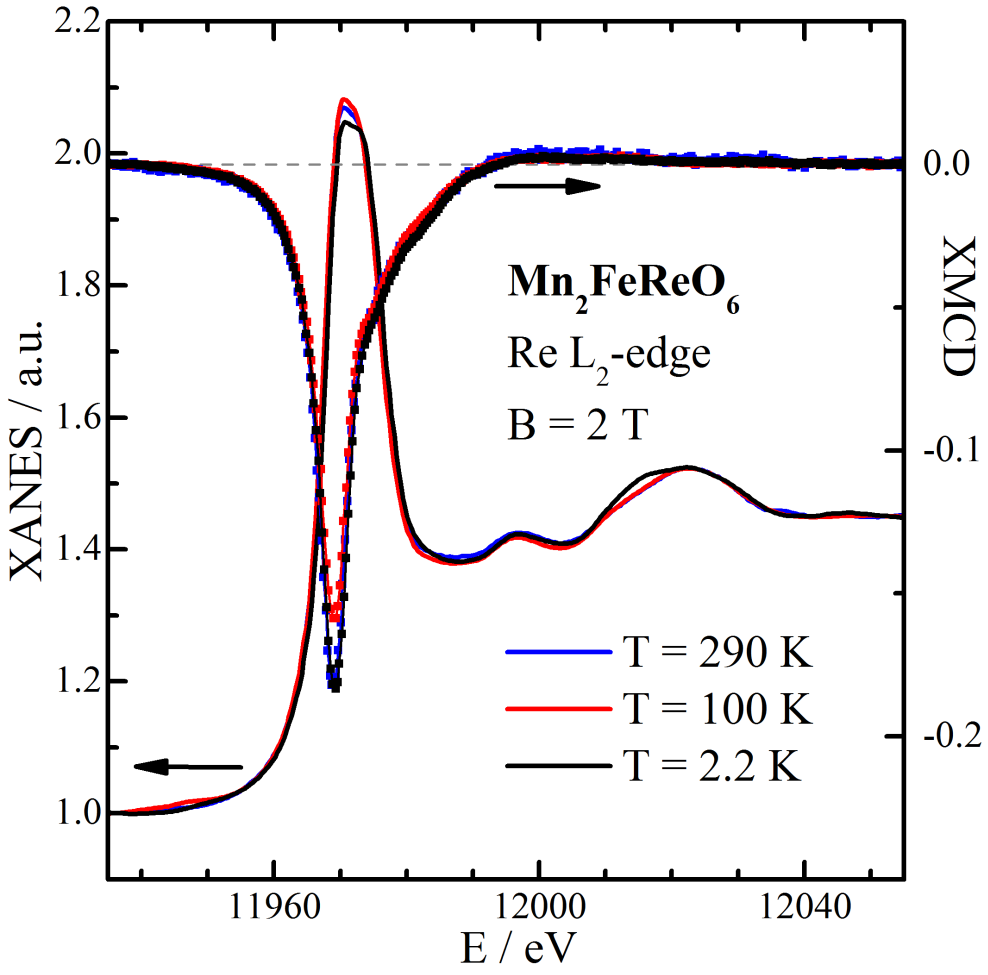

Figure 3.13 | *X-ray Absorption Near-Edge and X-ray Magnetic Circular Dichroism on Mn_2FeReO_6, Re L_2-edge.*

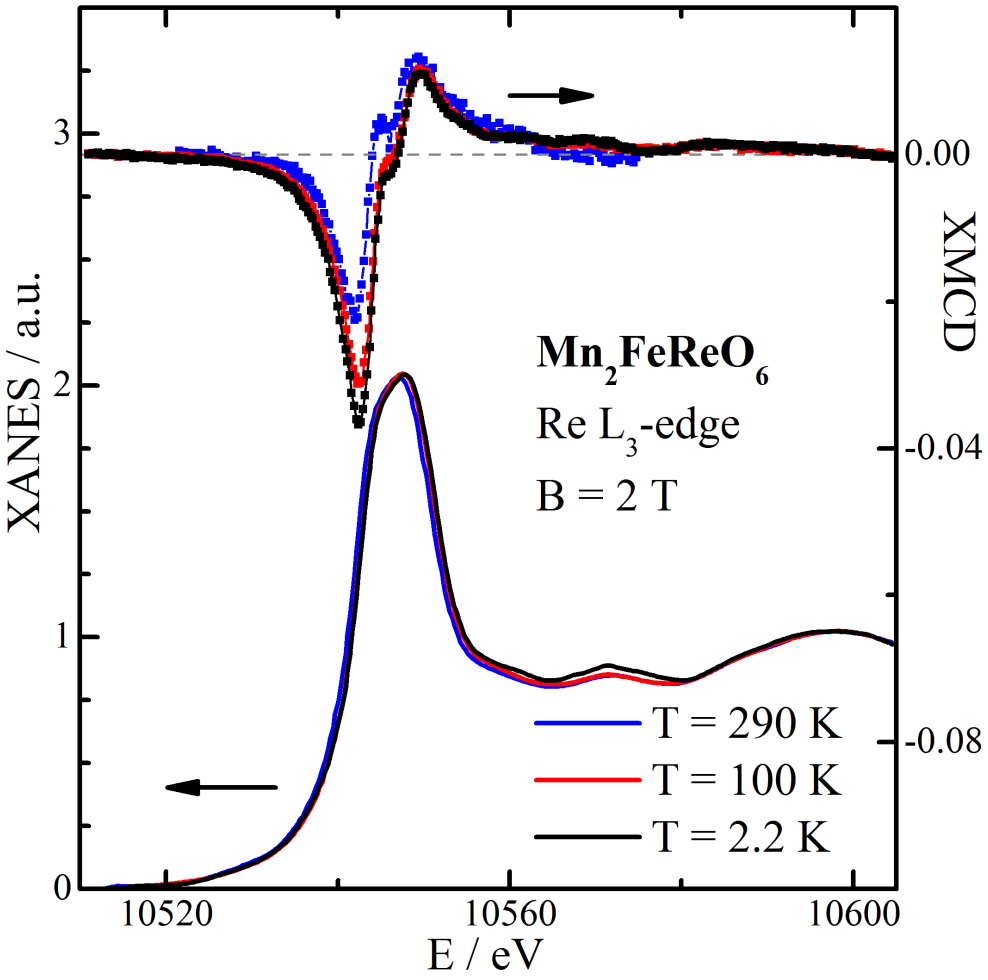

Figure 3.14 | *X-ray Absorption Near-Edge and X-ray Magnetic Circular Dichroism on Mn_2FeReO_6, Re L_3-edge.*

In addition to calculating the ratio between spin (m_S) and orbit (m_L) moments of Re, absolute values of m_L (**Equation 2.29**) and m_S (**Equation 2.30**) can be estimated by using values of n_h, the number of *d*-state electron holes. In a mixed valence state between Re^{5+} and Re^{6+}, n_h can take values between 8 and 9. As such, values of m_S and m_L for Re (**Table 3.8**) have been calculated to have lower (n_h = 8) and upper (n_h = 9) bounds, with a true value lying somewhere between these.

Table 3.8 | XMCD of Mn_2FeReO_6. Calculated orbit (m_L) and spin (m_S) moments from XMCD data at B = 2 T for Re at n_h values of 8 and 9, their ratio: m_S/m_L and the total Re moment: mRe.

	m_S/m_L	m_L / μ_B		m_S / μ_B		mRe / μ_B	
T / K	n_h:	8	9	8	9	8	9
290	-3.51	0.21	0.24	-0.74	-0.81	-0.53	-0.60
100	-2.71	0.24	0.26	-0.64	-0.72	-0.40	-0.45
2.2	-2.61	0.28	0.31	-0.72	-1.09	-0.45	-0.50

Negative moments refer to antiparallel alignment to Fe moments.

Values of total Re moment (mRe) saturate at values lower than 1 μ_B, however XMCD shows a minimum in $|mRe|$ at 100 K, close to the reorientation transition of the Fe/Re sublattice determined by neutron diffraction and at the onset of the magnetoresistance switching. This minimum is shown in XMCD field dependence measurements of the Re L_2-edge in **Fig. 3.15**.

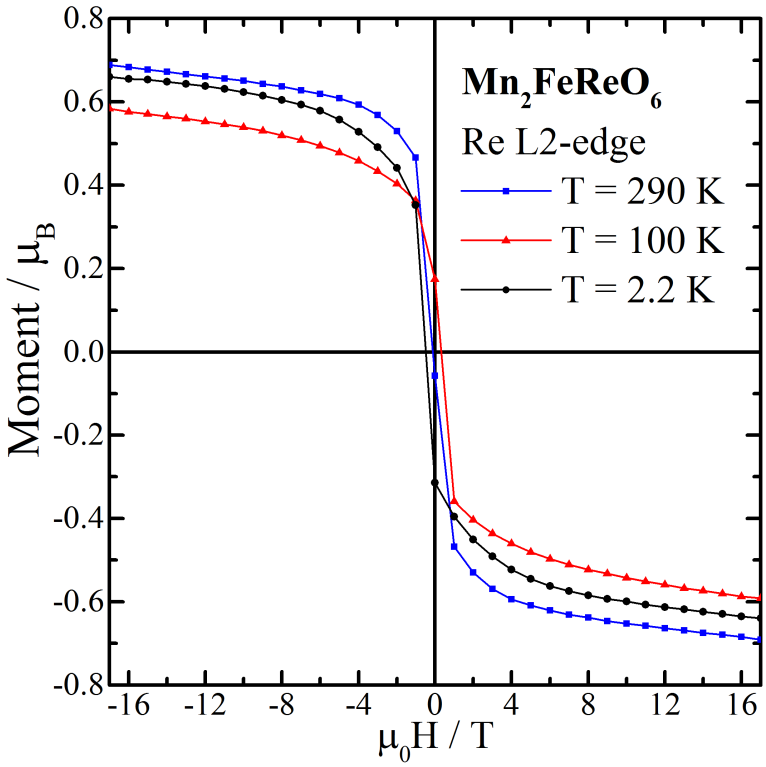

Figure 3.15 | *XMCD moment vs. field from the Re L_2-edge at field strengths in the range of ±17 T for Mn_2FeReO_6. These measurements have been normalised to values of m_{Re} (n_h = 8) calculated from sum rules at each temperature.*

This minimum at 100 K is likely to be a result of the canted Fe/Re spin structure, as to maximise XMCD effects the spin orientation of *d*-states need to be co-aligned with the X-ray vector. The additional antiferromagnetic *b*-axis component of Re at low temperatures results in the orientation of *d*-states no longer being perfectly aligned with the X-ray vector, reducing the measured value of *mRe*. This provides further evidence for the canting of the Fe/Re sublattice and may suggest that absolute values of *mRe* could be unreliable below the canting transition.

3.4. Conclusions

Using high-pressure techniques to stabilise small Mn^{2+} cations at the A-site of the $A_2BB'O_6$ double perovskite structure a new material of this type has been synthesised: Mn_2FeReO_6 (P = 10 GPa, T = 1400 °C). This material is the first all transition metal double perovskite and polycrystalline samples have been studied using X-ray and neutron diffraction, magnetometry, resistivity measurements and X-ray magnetic circular dichroism. Mn_2FeReO_6 combines the spin-polarised conduction of rock salt ordered Fe^{3+}/Re^{5+} that has been observed in other double perovskites with ferrimagnetic G-type B/B′ spin order,[74] with an interesting magnetic transition observed due to the presence of magnetic A-sites in the form of Mn^{2+} ($3d^5$). Cations Mn^{2+}, Fe^{3+} and Re^{5+} are well ordered across A, B and B′ sites in the material respectively, as a combination of X-ray (high contrast between Mn/Fe and Re) and neutron diffraction (high contrast between Mn and Fe/Re) allows accurate determination of occupancies of all sites in Mn_2FeReO_6.

Chapter 3. Mn_2FeReO_6

Mn_2FeReO_6 possesses a high T_c of 520 K at the onset of Fe^{3+}/Re^{5+} ferrimagnetic G-type order, well above room temperature, with record high magnetisation of 5.0 μ_B f.u.$^{-1}$ at 75 K, exceeding magnetisations of other similar double perovskites.[47,74] At temperatures lower than ~175 K Mn^{2+} spin order is antiferromagnetic but frustrated with respect to the Fe^{3+}/Re^{5+} spin sublattice, and presumably the magnetisation is enhanced by the A-site Mn^{2+}, with the applied field aligning fluctuating Mn^{2+} spins. Another transition below ~75 K signifies the onset of a reorientation of the Fe^{3+}/Re^{5+} sublattice, where an antiferromagnetic component to Fe^{3+}/Re^{5+} spin order along the *b*-axis can be refined using neutron diffraction, giving rise to non-collinear Fe^{3+} spins, with Re^{5+} constrained to be antiparallel to Fe^{3+}. This transition is likely due to the frustration between Fe^{3+}/Re^{5+} spin order and Mn^{2+} spin order.

The low-temperature Fe^{3+}/Re^{5+} spin reorientation transition at ~75 K is accompanied by interesting magnetoresistance changes. At high temperature above this transition negative magnetoresistance, where *MR* = -19 % at 100 K and 7 T, is observed. However, below this transition positive magnetoresistance, up to *MR* = +265 % at 20 K and 7 T, is observed. There is no precedence for magnetoresistance switching among double perovskites, and magnetoresistance switching transitions with temperature variation are extremely rare. Notable examples of this are in $Zn_{0.85}Cu_{0.05}Cr_2Se_4$ (at 25 K)[141] and in GdSi single crystals (at 50 K)[142] due to 4*f* spin transitions of magnetopolarons. This transition occurs in Mn_2FeReO_6 at higher temperature (~75 K), approaching temperatures of liquid N_2 (77 K), with a different mechanism of magnetoresistance switching due to interaction between B-site

Fe^{3+}/Re^{5+} ferrimagnetic and A-site Mn^{2+} antiferromagnetic spin orders. Presumably this is due a switch in the dominant mechanism of magnetoresistance from negative intergrain tunnelling magnetoresistance above ~75 K. This causes a reduction in interfacial resistance with an applied field in polycrystalline samples, to a mechanism where the applied field increases the bulk resistivity of the material, through a reorientation of the spin structure.

In summary, high pressure can be a useful means to improve the stability of structures that would otherwise be unstable due to unideal cation size differentials in the perovskite structure. This can be exploited to force small Mn^{2+} cations on to the A-sites of perovskites and may lead to enhancement of existing properties of a material, such as magnetisation, or even to magnetic transitions due to the presence of Mn^{2+} spin order that can completely alter the physical properties of the material. Further exploration of possible perovskite-type phases with A-site Mn^{2+} is therefore an interesting avenue to pursue in order to discover materials with novel properties. This discovery of Mn_2FeReO_6 and analysis of the material using data collected on D20 at the ILL has been published in Angewandte Chemie – International Edition (*Large Magnetization and Frustration Switching of Magnetoreistance in the Double-Perovskite Ferrimagnet Mn_2FeReO_6*)[134] back-to-back with another publication on the discovery of Mn_2FeReO_6 by Li et al. (*Giant Magnetoresistance in the Half-Metallic Double-Perovskite Ferrimagnet Mn_2FeReO_6*),[143] demonstrating that this is an extremely active area of research and developments are always being made. Additional data for Mn_2FeReO_6 is provided in '**Appendix A**'.

Chapter 4. $Ca_xMn_{2-x}FeReO_6$ – Discovery of Double Double Cation Order in Ca-Based Perovskites

4.1. Introduction

With the successful synthesis of Mn_2FeReO_6 described in '**Chapter 3. Mn_2FeReO_6 – Magnetoresistance Switching Due to Frustration**', and the knowledge that this material crystallises in the same monoclinic $P2_1/n$ space group as the well-studied Ca_2FeReO_6 analogue, a natural progression of this research is to expand the number of systems studied by including solid solutions between Ca and Mn on A-sites. These solid solutions take the general form $Ca_xMn_{2-x}FeReO_6$, of which the aforementioned materials Mn_2FeReO_6 (x = 0) and Ca_2FeReO_6 (x = 2) are end members. While sharing similar crystallographic structures, these end members have distinctly different magnetic properties and a study of these intermediate materials may provide an interesting insight into the way these differences develop as x is varied and Mn^{2+} is diluted by Ca^{2+}.

Other studies of similar solid solutions such as $Ca_xSr_{2-x}FeReO_6$ are focussed on the difference in cation size between eight coordinate Ca^{2+} (r_{Ca} = 1.12 Å) and Sr^{2+} (r_{Sr} = 1.26 Å), and the way that the variation of average A-cation size (as x is varied) alters other properties of the material.[80] This is also a factor in this proposed study of $Ca_xMn_{2-x}FeReO_6$, as the relative cation sizes of eight coordinate Ca^{2+} (r_{Ca} = 1.12 Å) and Mn^{2+} (r_{Mn} = 0.96 Å) are also expected to have similar effects as the average cation size is varied with differing values of x. However, this study differs dramatically in

that Mn^{2+} is also a magnetic cation ($3d^5$, $S = {}^5/_2$) and the effects that A-site magnetic order has on the overall properties of the materials can be the most significant factor, as already seen in Mn_2FeReO_6, where competing A and B-site spin orders result in a low-temperature magnetic transition that reverses the sign of magnetoresistance from negative values above to positive values below the transition. As these $Ca_xMn_{2-x}FeReO_6$ materials are to be synthesised with high-pressure techniques and studied by neutron diffraction, a limited number of values for x have been selected: 0.5, 1.0, 1.5 (in addition to the x = 0 and 2.0 materials that have already been studied). A set of materials in this series is found to possess tetragonal symmetry (denoted in this chapter by 'T-' preceding the structural formula), with another set of materials found to possess monoclinic symmetry (denoted in this chapter by 'M-' preceding the structural formula).

4.2. Experimental

4.2.1. Synthesis of $Ca_xMn_{2-x}FeReO_6$

The synthesis of $Ca_xMn_{2-x}FeReO_6$ has been conducted using the techniques outlined in '*2.12. High-Pressure Solid-State Synthesis*' for values of x = 0.5, 1.0 and 1.5. To provide the correct ratio of elements for these various values of x, complex mixtures of metal oxides are required as precursors: x = 0.5 (½ $CaMnO_3$ + ${}^1/_3$ Mn_3O_4 + ${}^1/_3$ Fe_3O_4 + ReO_2); x = 1.0 (½ $CaMnO_3$ + ¼ $Ca_2Fe_2O_5$ + ${}^1/_6$ Mn_3O_4 + ${}^1/_6$ Fe_3O_4 + ReO_2) and x = 1.5, ½ $CaMnO_3$ + ½ $Ca_2Fe_2O_5$ + ReO_2. Conditions used for the synthesis of samples of $Ca_xMn_{2-x}FeReO_6$ were kept relatively consistent at pressures of 10-11 GPa, with temperatures of 1400 °C.

The $Ca_2Fe_2O_5$ brownmillerite-type metal oxide used in these precursors was prepared from solid-state synthesis (2 $CaCO_3$ + Fe_2O_3) with two sintering steps of 1000 °C and 1100 °C, each for 24 hours and grinding the product in between these steps.[144] The $CaMnO_3$ metal oxide used in these precursors was prepared by the solid-state reaction of $CaCO_3$ and MnO_2, with two sintering steps of 1000 °C and 1100 °C each for 24 hours and grinding the product in between these steps.[145] These metal oxides were combined in the stoichiometric ratios listed and ground together in a pestle and mortar several times to generate thoroughly mixed precursors. The precursors were then loaded inside Pt capsules, before being loaded inside the Walker module assembly.

4.2.2. Structural Characterisation of $Ca_xMn_{2-x}FeReO_6$

Initial X-ray patterns of products of all high-pressure syntheses were collected using a Bruker D2 Phaser diffractometer with Cu K_α/K_β X-ray source (15-minute scans of $5° \leq 2\theta \leq 70°$) for phase analysis purposes. Laboratory X-ray diffraction was also carried out over 8 hours ($10° \leq 2\theta \leq 90°$) using a Bruker D8 Phaser diffractometer on $x = 1.0$ (sample #2). Synchrotron X-ray diffraction was performed on $x = 1.0$ (sample #6) at 304 K on BL04-MSPD at ALBA (wavelength, $\lambda = 0.44214$ Å). Synchrotron X-ray diffraction was also performed on $x = 0.5$ (sample #5) and $x = 1.5$ (sample #2) at ID22 at the ESRF (wavelength, $\lambda = 0.39987$ Å).

For each composition, a set of samples was combined and well ground to provide a sample size of approximately 50 mg to be used for neutron diffraction. For $x = 0.5$, 54 mg (samples #6–8); $x = 1.0$, 49 mg (samples #1 and #4–5) and $x = 1.5$, 49

mg, (samples #3–5). These samples were measured in high resolution single frame mode on WISH at the ISIS Neutron Facility at a range of temperatures between 2 and 300 K. Data was collected for a varying amount of beam current. For x = 0.5 (T = 2 (45 μA), 25 (45 μA), 50 (45 μA), 75 (45 μA), 100 (45 μA), 200 (45 μA) and 300 K (45 μA)). For x = 1.0 (T = 2 (51 μA), 20 (50 μA), 40 (50 μA), 60 (50 μA), 80 (50 μA), 100 (50 μA), 150 (50 μA), 200 (50 μA), 250 (50 μA) and 300 K (65 μA)). For x = 1.5 (T = 2 (36 μA), 25 (45 μA), 50 (45 μA), 75 (45 μA), 100 (45 μA), 200 (50 μA) and 300 K (50 μA)). These X-ray and neutron diffraction patterns were analysed and solved using the FullProf Suite and refined by the Rietveld method.[122,125]

4.2.3. Magnetic Measurements of $Ca_xMn_{2-x}FeReO_6$

Magnetometry measurements were carried out on samples of x = 0.5 (sample #4), x = 1.0 (sample #2) and x = 1.5 (sample #3) using a Quantum Design MPMS XL Superconducting Quantum Interference Device (SQUID) magnetometer. Magnetisation versus field hysteresis loops ($-7 \leq \mu_0 H$ (T) ≤ 7) for were recorded for these materials at temperatures of 2 and 300 K for x = 0.5; temperatures of 5, 25, 50, 75, 100 and 300 K for x = 1 and temperatures of 10 and 300 K for x = 1.5. Magnetisation versus temperature was measured zero-field cooled and field cooled at field strengths of $\mu_0 H$ = 0.5 T from 2 K to 650 K for each material.

Magnetoresistance was also measured on a pelleted portion of the x = 1.0 material, as described in '*2.3.2. Magnetoresistance*'. This was measured on a Quantum Design Physical Property Measurement System (PPMS). Resistivity versus field hysteresis loops ($-7 \leq \mu_0 H$ (T) ≤ 7) were measured at constant temperatures of 20, 50,

75, 100 and 150 K, from which the magnetoresistance was calculated as a percentage based on **Equation 1.3**.

In order to determine X-ray Magnetic Circular Dichroism (XMCD) on Re, X-ray Absorption Near-Edge Spectra (XANES) were measured on $Ca_xMn_{2-x}FeReO_6$, x = 1.0 and x = 1.5 in the ranges 10.511-10.605 keV (Re L_3 edge) and 11.934-12.055 keV (Re L_2 edge). XANES were measured and XMCD calculated at temperatures of 2 and 290 K for x = 1.0 and just at 290 K for x = 1.5. These measurements were conducted at ID12 at the European Synchrotron Radiation Facility. These spectra were measured using circularly polarised X-rays of helicity +1 and -1, as well as in magnetic fields of +2 and -2 T. In addition, XMCD versus field hysteresis measurements were performed at 11.969 keV, at the Re L_2-edge maximum, between fields of ±17.

4.3. Results & Discussion

For ease of discussion, the first of the $Ca_xMn_{2-x}FeReO_6$ materials to be mentioned here will be the x = 1.0 material. The reason for beginning the discussion of this series in the centre, with $CaMnFeReO_6$, is that this material exhibits a markedly different structure type than those materials on either end, where x = 0 or 2, which have monoclinic structures and crystallise in the $P2_1/n$ space group.

This central member of the series with nominal x = 1.0 will be shown to crystallise in the $P4_2/n$ space group, with additional columnar order of cations on the A-sites (as well as the rock salt order on B-sites). This characteristic of the x = 1.0

material helps to more easily explain the results from materials with nominal values of $x = 0.5$ and $x = 1.5$.

4.3.1. $Ca_xMn_{2-x}FeReO_6$: x = 1.0

4.3.1.a Phase Analysis & X-ray Crystal Structure: x = 1.0

Initial phase analysis on $x = 1.0$ was carried out using X-ray diffraction data collected with a Bruker D2 Phaser diffractometer. Syntheses of the $x = 1.0$ material are all relatively consistent (with the exception of synthesis 3, for which no Pt capsule was used and only metallic Re is observed in the diffraction pattern) and, while these patterns can be well fit with the $P2_1/n$ symmetry, comparisons to M-Mn_2FeReO_6 or M-Ca_2FeReO_6 show diffraction patterns which seem at first glance to be of a material with higher symmetry. However, testing of alternative space groups that allow for B-site double perovskite rock salt ordering (**Fig. 1.11**) yields no space group of higher symmetry that can fit this structure, in particular when considering several minor intensities that are allowed from the $P2_1/n$ symmetry. As such, an initial assessment of the structure concluded it to be likely that this structure possesses $P2_1/n$ symmetry, which coincidentally has a cell that is close to being metrically cubic (when transformed to a $2 \times 2 \times 2$ perovskite cell), such that these diffraction patterns appear to be of higher symmetry with the available resolution of the D2 diffractometer.

Primarily through neutron diffraction it can be deduced that the symmetry of this $x = 1.0$ material is actually $P4_2/n$, and there is a simultaneous columnar order of A-site cations as well as rock salt order of B-site cations. An example of Rietveld fits using this double double perovskite $P4_2/n$ structure compared with those using the

$P2_1/n$ structure is shown in **Fig. 4.1**, for laboratory X-ray diffraction data and for neutron diffraction data collected on WISH. This clearly shows that with laboratory X-ray data roughly equivalent fits are found using either structure, while with neutron data very poor fits are achieved using the $P2_1/n$ cell. This is particularly evident from the presence of structural intensity at d ~5.4 Å. This intensity can be indexed by a $P4_2/n$ (2 × 2 × 2) perovskite cell, corresponding to the 110 and 011 reflections, and is well fit by introducing columnar order, but the $P2_1/n$ cell cannot account for any structural intensity on this reflection.

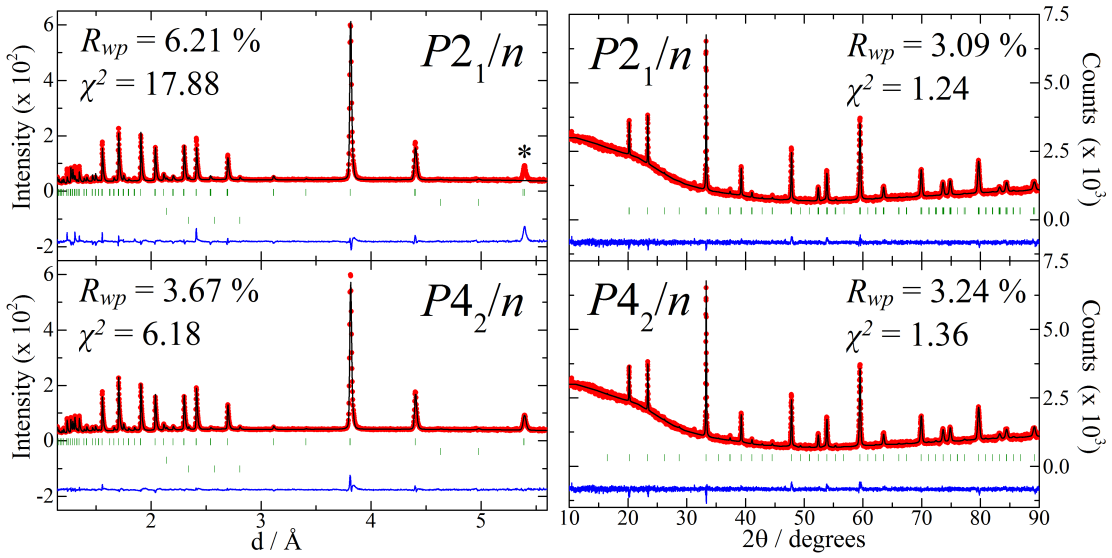

Figure 4.1 | *Fits to diffraction data collected on $CaMnFeReO_6$ at 300 K.* ***Left****: Neutron diffraction data collected on WISH.* ***Right****: Laboratory X-ray diffraction data collected using Cu K_α radiation. Two structural models are used: $P2_1/n$ cell* ***(top)*** *$P4_2/n$ cell* ***(bottom)****. Equivalent fits are found to X-ray data with these models, but the $P4_2/n$ cell provides a substantially better fit to neutron data. Structural intensity in neutron data at d ~5.4 Å, unexplained by a $P2_1/n$ cell, is marked by an asterisk. Additional phases indexed by tick marks in neutron fits in order: $MnFe_3O_5$, V, Cd.*

This columnar A-site order between Ca and Mn on A-sites is not entirely unprecedented. It is also observed in $CaMnTi_2O_6$,[55] as well as a similar order between Ca and Fe in $CaFeTi_2O_6$,[56] in addition to the simultaneous order of columnar A-site and rock salt B-site cations observed in $RMnMnSbO_6$ materials (which also crystallise

in the tetragonal $P4_2/n$ space group) that was recently discovered while this research was ongoing.[64] This symmetry explains these diffraction patterns well, as well as accounting for intensities in the neutron and synchrotron X-ray diffraction patterns that are not well fit by the $P2_1/n$ symmetry. Raw data files for X-ray diffraction data collected on all samples of $x = 1$ are shown stacked in **Fig. 4.2,** with results from fits to these patterns presented in **Table 4.1** using the $P4_2/n$ symmetry, showing the sample variation between syntheses.

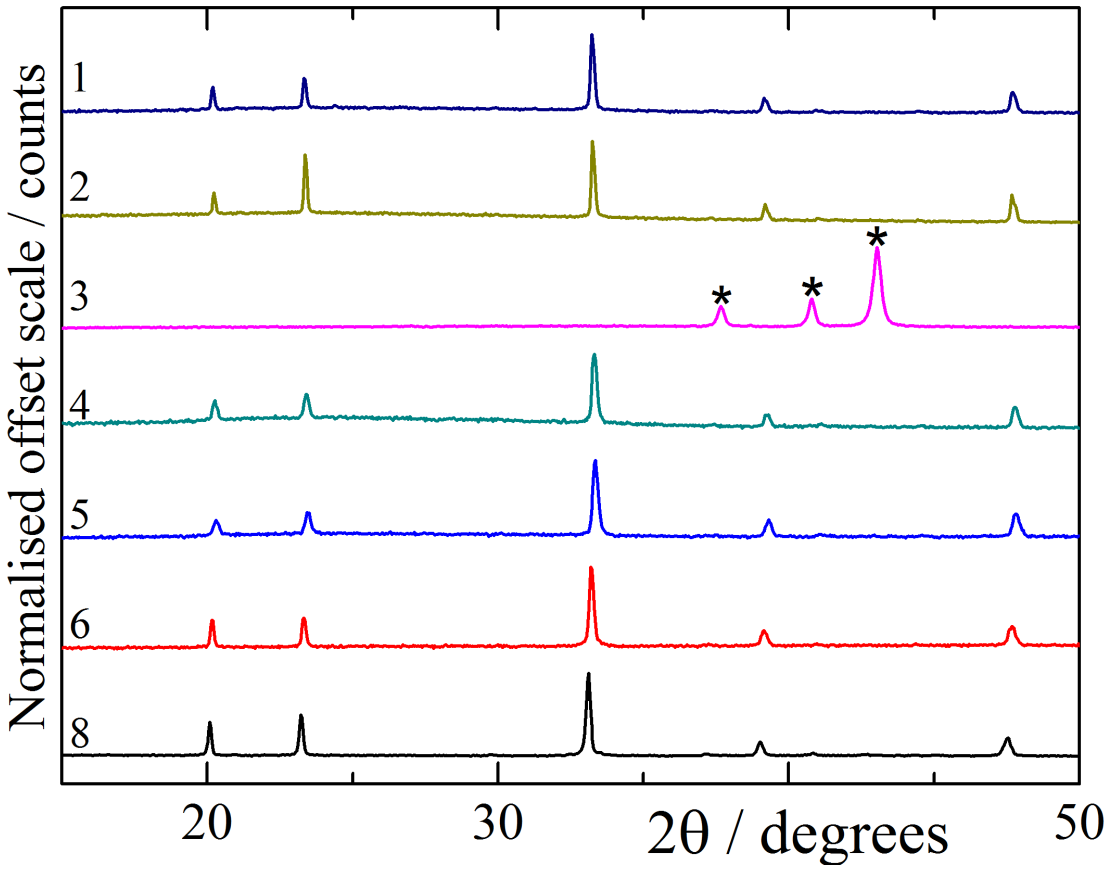

Figure 4.2 | *A stacked plot of the raw powder X-ray data initially collected on samples of T-$CaMnFeReO_6$ for phase analysis (in the 2θ range 15-50°). Asterisks mark metallic Re observed as the only identifiable product in synthesis 3, in which a Pt capsule was not used (BN container).*

Table 4.1 | A collection of the synthesis conditions and measure of the resulting purity and B-site disorder in the $P4_2/n$ $CaMnFeReO_6$ perovskite product.

Sample no.	Pressure / GPa	Wt. ReO_2 / %	B-Antisite Disorder / %	χ^2	R_{wp} / %
1	11	3.8(5)	5.0(4)	2.10	4.82
2	10	0	0.8(6)	1.92	4.75
3†	10	0	*n/a*	5.25	3.79
4	10	0	6.4(6)	1.70	4.72
5	10	0	2.4(6)	1.42	4.89
6‡	10	0	1.0(6)	1.49	6.63
8	10	0	2.4(6)	3.07	5.99

Samples 1, 4 and 5 were mixed to create a 49 mg aggregate and examined by neutron diffraction on WISH at the ISIS Neutron Facility. The measures of fit, χ^2 and R_{wp}, are shown for X-ray patterns collected over 15 minutes using a Bruker D2 Phaser diffractometer with Cu K_α radiation. †A Pt capsule was used for all syntheses except for synthesis 3, which simply used BN as the sample container. No perovskite product was observed in this sample and the only phase identifiable is Re metal. ‡All syntheses were conducted with heating at 1400 °C for 20 minutes before being quenched except for an additional slow cooling to 1000 °C over 50 minutes preceding the quench in synthesis 6.

In synchrotron X-ray data collected on $x = 1.0$, shown in **Fig. 4.3**, a good fit to the data is achieved by the use of the $P4_2/n$ symmetry with columnar A-site order. This columnar order provides a small intensity on the 110, 011 reflection, shown in the inset. While small due to the poor X-ray scattering contrast between Ca and Mn in the presence of Re (note the difference in scale by an order of magnitude between the 110, 011 and the 111 reflections), this reflection does provide evidence for this simultaneous order of A and B-site cations. The B-antisite disorder can be well defined by the contrast between Fe and Re, however the site occupancies of A-site Ca and Mn are fixed in this refinement to be fully occupied and no disorder can be reliably refined. This necessitates analysis by neutron diffraction to adequately characterise the structure of this material. Results from fits to the synchrotron X-ray data on $x = 1.0$ are shown in **Table 4.2**, a 3.0(1) % B-antisite disorder is found, and of particular note are the refined lattice parameters $a = 7.62825(6)$ and $c = 7.6267(1)$ Å, showing that the tetragonal distortion is indeed extremely small. The large TiO_2 intensities seen in the

diffraction pattern obtained from BL04-MSPD (**Fig 4.3**) are present from instrumental error and are not sample related.

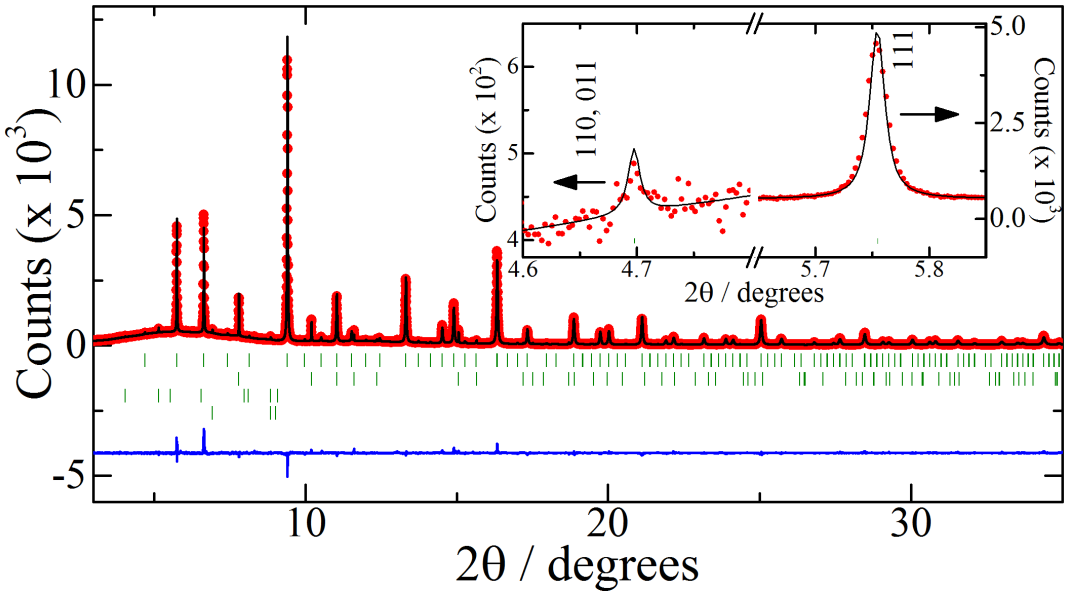

Figure 4.3 | *Rietveld fit to data collected from BL04-MSPD at ALBA 304 K of T-CaMnFeReO₆ in the P4₂/n space group (λ = 0.44214 Å). Occupancy of Ca and Mn$_{TD}$ and Mn$_{SP}$ are fixed to ideal occupancies. The inset shows the intensity of the 110 and 011 reflections (a result of columnar order between Ca and Mn) in comparison to the 111 reflection. Rows of indices indicate phase 1 as P4₂/n T-CaMnFeReO₆, phase 2 as parasitic scattering from TiO₂ in the measurement, phase 3 as MnFe₃O₅ and phase 4 as ReO₂.*

Table 4.2 | Refined structure parameters for T-CaMnFeReO$_6$ at 304 K in space group $P4_2/n$ using synchrotron powder X-ray data from BL04-MSPD at ALBA.

Atom	*x*	*y*	*z*	Occupancy	B_{iso} / Å^2
Ca	¼	¾	0.2969(4)	1	0.316(7)
Mn$_{TD}$	¾	¾	¾	1	0.316
Mn$_{SP}$	¼	¼	¾	1	0.316
Fe/Re	0	0	½	0.970(1)/0.030	0.316
Re/Fe	0	½	½	0.970/0.030	0.316
O1	0.960(5)	0.547(4)	0.257(4)	1	1.1(1)
O2	0.740(4)	0.979(2)	0.563(3)	1	1.1
O3	0.827(1)	0.015(3)	0.951(2)	1	1.1

Lattice parameters: $a = 7.62825(6)$ and $c = 7.6267(1)$ Å; residuals $R_{wp} = 5.49$ % and $\chi^2 = 2.55$. Ca, Mn$_{TD}$ and Mn$_{SP}$ are fixed at ideal site occupancies due to insufficient data to refine disorder.

4.3.1.b Neutron Crystal & Magnetic Structure: x = 1.0

Data from the WISH diffractometer has enabled structural and magnetic characterisation of an aggregate of samples #1, 4 and 5, with total sample size of 49 mg. X-ray diffraction is able to determine the degree of B-site order in T-$CaMnFeReO_6$ but determination of A-site order is inadequate. Conversely, neutron diffraction is unable to adequately distinguish Fe (b = 9.45 fm) from Re (b = 9.2 fm), however neutrons do reveals a high degree of A-site order due to the contrast between Ca (b = 4.7 fm) and Mn (b = -3.63 fm). The structure of x = 1.0, as determined by neutron diffraction, is shown in **Fig. 4.4**. Shown in this visualisation of the structure are projections in the *ab*-plane, looking down the *c*-axis along the A-site columns, as well as a projection in the *ac*-plane, showing the coordination environments of A-site Mn^{2+} cations. This shows that, in addition to the columnar A-site order between 10-coordinate Ca^{2+} and 4-coordinate Mn^{2+}, there are also alternating coordination environments for the 4-coordinate Mn^{2+} columns. These Mn^{2+} sites alternate between tetrahedra and square planes.

Table 4.3 | Magnetic modes in the Γ_1^+ irreducible representation (defined from the Isotropy Suite)[126] for the T-$CaMnFeReO_6$ magnetic structure. Propagation vector, $\boldsymbol{k}$ = (0 0 0) in space group $P4_2/n$.

B-sites mag. modes:	**A_g1**		**$A_g2^{\dagger}$**		**$A_g3^{\dagger}$**	**A-sites mag. modes:**	**$A^{\ddagger}$**
Atom	m_x	m_y	m_x	m_y	m_z	**Atom**	m_z
Fe1, Re1[a]	*n/a*	-	-	*n/a*	+	**$Mn_{TD}1$, $Mn_{TD}2$[e]**	+
Fe2, Re2[b]	*n/a*	+	+	*n/a*	+		
Fe3, Re3[c]	+	*n/a*	*n/a*	-	+	**$Mn_{SP}1$, $Mn_{SP}2$[f]**	+
Fe4, Re4[d]	-	*n/a*	*n/a*	+	+		

Magnetic mode A_g3 is used in magnetic structure refinements for B-sites of T-$CaMnFeReO_6$. †For Re sites, coefficients for A_g3 are negative. B-Sites: [a]Fe1 = (0, ½, 0), Re1 = (0, ½, ½); [b]Fe2 = (½, 0, 0), Re2 = (½, 0, ½); [c]Fe3 = (½, ½, ½), Re3 = (½, ½, 0); [d]Fe4 = (0, 0, ½), Re4 = (0, 0, 0). Magnetic mode A is used for magnetic structure refinements of A-Sites: [e]$Mn_{TD}1$ = (¼, ¼, ¼), $Mn_{TD}2$ = (¾, ¾, ¾); [f]$Mn_{SP}1$ = (¼, ¼, ¾), $Mn_{SP}2$ = (¾, ¾, ¼). ‡While these A-sites are independent, magnitudes of this ferrimagnetic order of Mn_{TD} and Mn_{SP} are constrained to be equal. Further details of magnetic structure solution are provided in '*2.2.7 – Magnetic Symmetry Analysis*'.

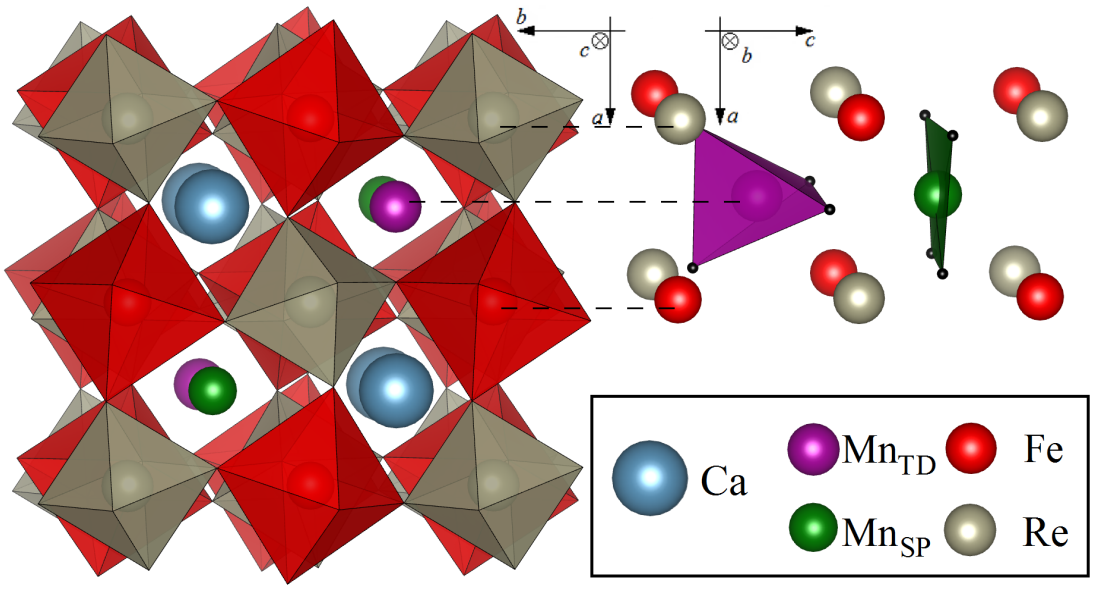

Figure 4.4 | *The tetragonal $P4_2/n$ crystal structure of T-$CaMnFeReO_6$. Columnar order between 10-coordinate Ca and 4-coordinate Mn is shown. Two different coordination environments for Mn are evident, with tetrahedra and square planes alternating along the c-axis. The B-site Fe/Re is also shown. Image generated using VESTA.*[136]

In addition to structural considerations, magnetic diffraction intensity must be considered during Rietveld refinements. The symmetry of magnetic order was solved in this material with a $\boldsymbol{k}$ = (0 0 0) propagation vector and the symmetry operations for this order are shown in **Table 4.3**, separated into the operations used for A-site order and for B-site order.[126] Rietveld fits to neutron diffraction patterns collected on x = 1.0 are shown in **Fig 4.5** at 300 K and at 2 K. Clearly observed are the 111 and the 110, 011 reflections due to rock salt (B-site) and columnar (A-site) orders, respectively. This allows the accurate determination of A-site disorder. Magnetic reflections are also observed on top of the 111 reflection at room temperature and on the 110, 011 reflections at ~40 K and below. These reflections can be attributed to the magnetic order described in **Table 4.3** and those reflections due to A and B-site magnetic orders are labelled by m_A and m_B. The thermal evolution of these magnetic reflections is shown in **Fig. 4.6**.

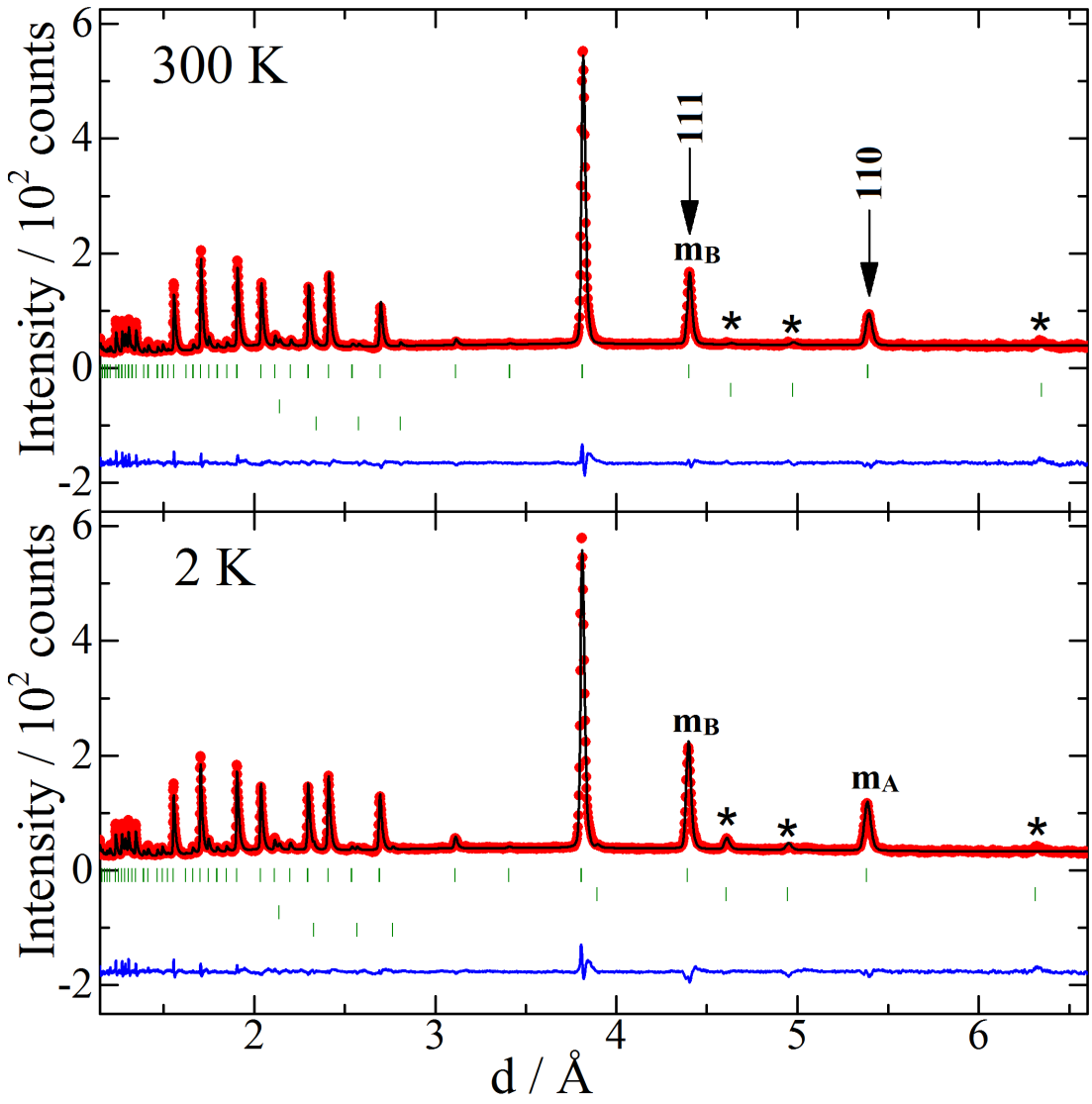

Figure 4.5 | *Combined nuclear and magnetic Rietveld fits to neutron diffraction data on T-CaMnFeReO₆, collected on the WISH diffractometer at the ISIS Neutron Facility. The patterns shown are from an average of bank 3 and 8.* ***Top****: 300 K.* ***Bottom****: 1.5 K. The markers m_A and m_B refer to magnetic reflections with contributions from A and B-site spin order, respectively. Lower markers index $MnFe_3O_5$ as well as V and Cd from the measurement.*

It is found that a G-type ferrimagnetic order of Fe/Re spins is responsible for the magnetic intensity on the 111 reflection (which can be described by the 'A_g3' magnetic mode in **Table 4.3**), and the lower temperature evolution of magnetic intensity on the 110, 011 reflections can be accounted for by a further A-site

ferrimagnetic order of tetrahedral Mn^{2+} and square planar Mn^{2+} sites (described by the 'A' magnetic mode in **Table 4.3**), where tetrahedrally coordinated Mn^{2+} is parallel to Fe (and therefore parallel to the net magnetisation of the material), and square planar Mn^{2+} is antiparallel to Fe. While this A-site order is ferrimagnetic due to the inequivalent Mn^{2+} sites, in Rietveld refinements of the structure to the powder neutron diffraction data these two sites have been constrained to be equal and opposite.

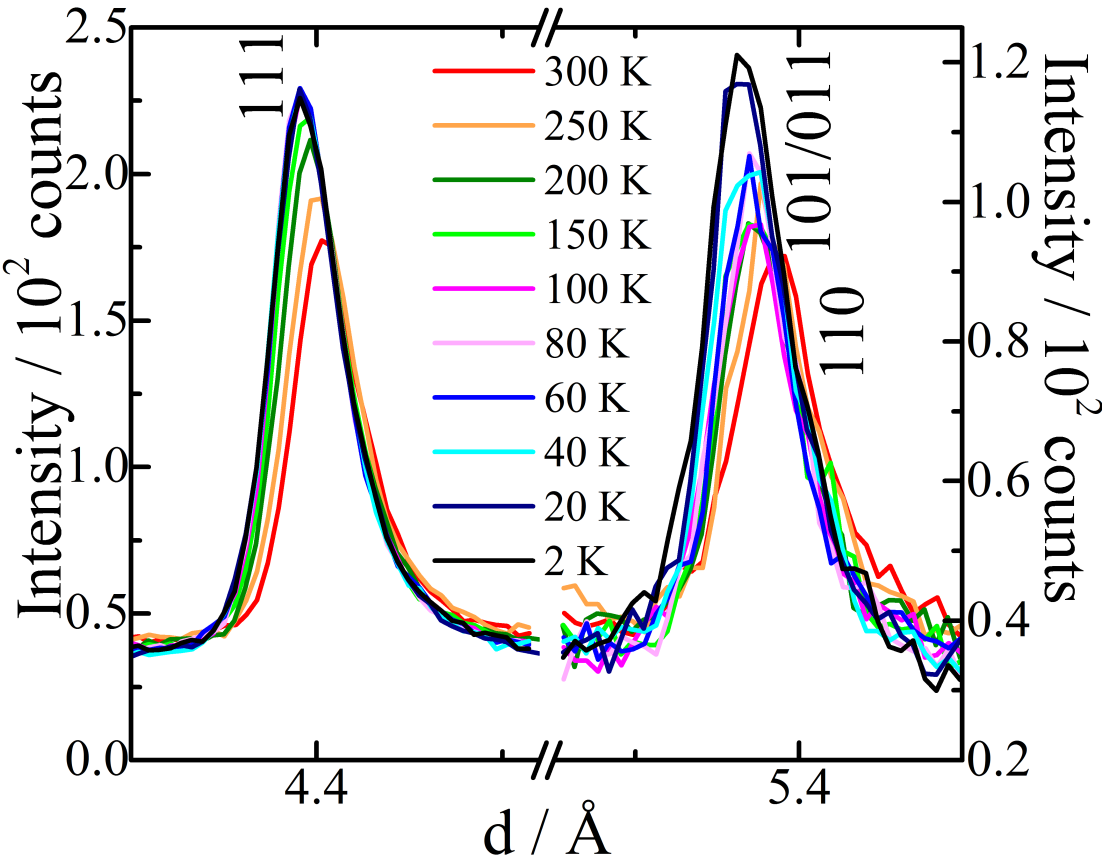

Figure 4.6 | *Intensity variations with temperature of the main magnetic reflections in T-$CaMnFeReO_6$: 111 (d ~4.4 Å), 110 and 101/011 (d ~5.4 Å).*

Table 4.4 | Refined structure parameters for x = 1.0 at 2-300 K in space group $P4_2/n$ using neutron powder diffraction data from the WISH diffractometer at the ISIS Neutron Facility. Magnetic symmetry follows the descriptions in **Table 4.3**. Sample size 49 mg. This phase is found to have a chemical formula of T-Ca($Mn_{0.88(4)}Fe_{0.12}$)$FeReO_6$.

T / K		2	20	40	60	80	100	150	200	250	300
Cell Param	a / Å	7.6197(5)	7.6202(6)	7.6209(5)	7.6218(5)	7.6222(5)	7.6224(5)	7.6241(5)	7.6255(5)	7.6285(5)	7.6311(5)
	c / Å	7.6166(8)	7.6162(8)	7.6149(8)	7.6139(7)	7.6142(7)	7.6154(7)	7.6174(7)	7.6195(7)	7.6241(6)	7.6266(7)
	V / Å^3	442.22(8)	442.25(8)	442.26(7)	442.31(7)	442.37(7)	442.47(7)	442.77(7)	443.05(7)	443.68(7)	444.12(7)
Ca	z	0.280(1)	0.278(1)	0.277(1)	0.276(1)	0.280(1)	0.284(1)	0.280(1)	0.277(1)	0.281(1)	0.276(1)
O1	x	0.937(2)	0.937(2)	0.938(3)	0.939(3)	0.937(2)	0.936(2)	0.937(3)	0.940(4)	0.937(3)	0.941(4)
	y	0.552(2)	0.552(2)	0.553(3)	0.552(3)	0.551(2)	0.551(2)	0.554(3)	0.556(4)	0.555(3)	0.555(4)
	z	0.245(4)	0.241(3)	0.240(3)	0.239(3)	0.241(3)	0.242(3)	0.242(3)	0.240(3)	0.241(3)	0.239(2)
O2	x	0.731(3)	0.731(3)	0.734(3)	0.736(3)	0.733(3)	0.733(3)	0.739(4)	0.738(3)	0.741(3)	0.741(4)
	y	0.9540(9)	0.956(1)	0.956(1)	0.9567(9)	0.9552(9)	0.9526(8)	0.9539(9)	0.9552(9)	0.951(1)	0.9531(9)
	z	0.563(1)	0.563(1)	0.5640(9)	0.5643(9)	0.5635(9)	0.5627(9)	0.5637(8)	0.5644(9)	0.5634(8)	0.5632(8)
O3	x	0.742(4)	0.741(4)	0.745(5)	0.741(4)	0.743(4)	0.744(4)	0.746(6)	0.753(7)	0.749(7)	0.751(8)
	y	0.0568(8)	0.0572(9)	0.0578(8)	0.0581(8)	0.0566(8)	0.0544(7)	0.0573(8)	0.0565(7)	0.0545(9)	0.0552(7)
	z	0.969(1)	0.959(1)	0.967(1)	0.967(1)	0.967(1)	0.970(1)	0.968(1)	0.967(1)	0.970(1)	0.968(1)
mFe / μ_B		4.54(3)	4.52(3)	4.52(3)	4.50(3)	4.50(3)	4.45(3)	4.33(3)	4.17(3)	3.81(3)	3.60(3)
mRe / μ_B		0.908(5)	0.905(5)	0.905(5)	0.901(6)	0.899(5)	0.889(5)	0.866(5)	0.834(5)	0.762(6)	0.719(5)
mMn / μ_B		1.54(5)	1.38(6)	0.92(9)	0	0	0	0	0	0	0
m_{tot} / μ_B f.u.$^{-1}$		3.63(1)	3.62(1)	3.62(1)	3.60(1)	3.60(1)	3.56(1)	3.46(1)	3.34(1)	3.05(1)	2.88(1)
A/B	B_{iso} / Å^2	0.91(5)	0.77(5)	0.87(5)	0.75(5)	0.92(5)	1.26(5)	1.11(5)	1.02(5)	1.29(7)	1.02(4)
O	B_{iso} / Å^2	0.78(6)	0.78(6)	0.80(6)	0.72(6)	0.68(6)	0.53(6)	0.69(6)	0.77(6)	0.76(7)	0.79(5)
R_{wp} / %		4.33	4.47	4.22	4.29	4.25	4.30	4.04	3.88	3.61	3.67
χ^2		6.60	6.96	6.09	6.32	6.21	6.33	5.63	5.31	4.67	6.18
Q / μA·h		51	50	50	50	50	50	50	50	50	65

Cation positions are as follows for A-sites: Ca (¼, ¾, z), Mn_{TD} (¾, ¾, ¾), Mn_{SP} (¼, ¼, ¾); and for B-sites: Fe (0, 0, ½) and Re (0, ½, ½). B-antisite disorder is not refined due to lack of contrast between Fe and Re. A 16(2) % occupancy of Fe^{2+} is found on the Mn_{SP}-site, with an 8(3) % occupancy of Fe^{2+} on the Mn_{TD}-site. The tabulated value of m_{tot} refers to the total magnetisation of T-$CaMnFeReO_6$, equivalent to: $m_{tot} = mFe - mRe$.

Table 4.5 | Bond lengths, angles and BVS values for T-$CaMnFeReO_6$ in space group $P4_2/n$ from the neutron profile fit at 2 K.

Bond	M – O length / Å	Bond	M – O length / Å
Ca – O1	2.71(2) × 2	Fe – O1	1.97(3) × 2
Ca – O1	2.84(2) × 2	Fe – O2	2.13(3) × 2
Ca – O2	2.558(9) × 2	Fe – O3	1.91(3) × 2
Ca – O3	2.40(1) × 2	**<Fe – O>**	2.00(2)
Ca – O3	2.42(1) × 2	Re – O1	2.04(3) × 2
<Ca – O>	2.58(2)	Re – O2	1.86(3) × 2
Mn_{TD} – O2	2.114(8) × 4	Re – O3	2.03(3) × 2
Mn_{SP} – O1	2.08(1) × 4	**<Re – O>**	1.98(2)

Cation	BVS	Cation	BVS	B – O# – B′	Angle / degrees
Ca	1.74	Fe	3.21	Fe – O1 – Re	144.0(9)
Mn_{TD}	1.54			Fe – O2 – Re	145.2(5)
Mn_{SP}	1.68	Re	4.52	Fe – O3 – Re	151.0(4)

The program BondStr in the FullProf Suite was used to compute this data.[125]

Table 4.6 | Bond lengths, angles and BVS values for T-$CaMnFeReO_6$ in space group $P4_2/n$ from the neutron profile fit at 300 K.

Bond	M – O length / Å	Bond	M – O length / Å
Ca – O1	2.75(4) × 2	Fe – O1	1.92(2) × 2
Ca – O1	2.80(4) × 2	Fe – O2	2.06(3) × 2
Ca – O2	2.576(9) × 2	Fe – O3	1.97(6) × 2
Ca – O3	2.39(1) × 2	**<Fe – O>**	1.98(2)
Ca – O3	2.45(1) × 2	Re – O1	2.08(2) × 2
<Ca – O>	2.59(2)	Re – O2	1.94(3) × 2
Mn_{TD} – O2	2.107(7) × 4	Re – O3	1.97(6) × 2
Mn_{SP} – O1	2.08(3) × 4	**<Re – O>**	2.00(2)

Cation	BVS	Cation	BVS	B – O# – B′	Angle / degrees
Ca	1.69	Fe	3.32	Fe – O1 – Re	144.2(2)
Mn_{TD}	1.57			Fe – O2 – Re	145.1(4)
Mn_{SP}	1.66	Re	4.19	Fe – O3 – Re	151.4(4)

The program BondStr in the FullProf Suite was used to compute this data.[125]

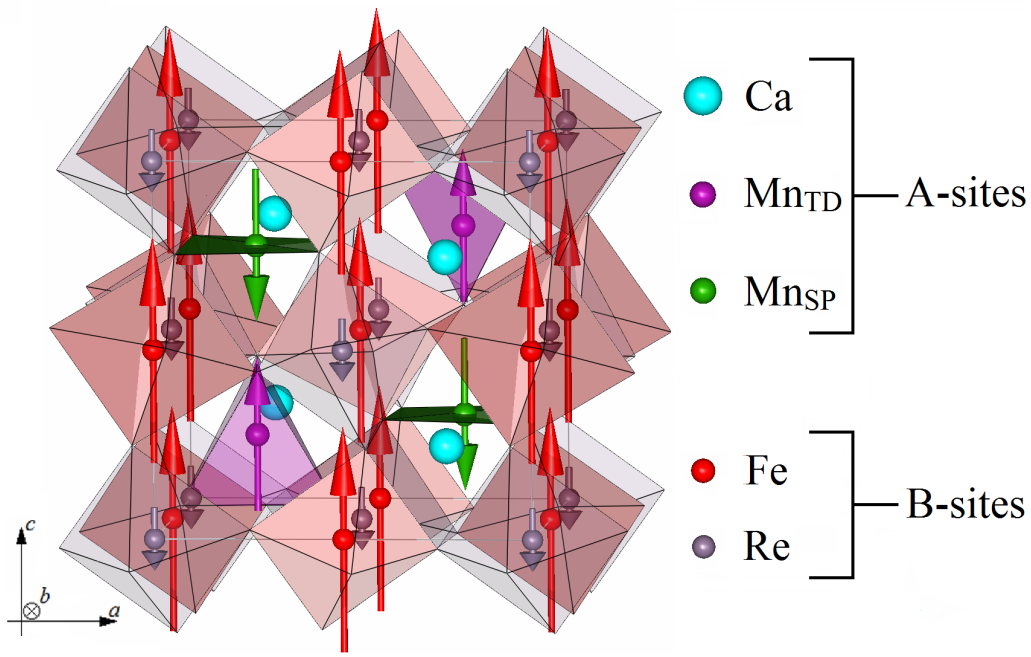

Figure 4.7 | *The crystal and magnetic structure at 2 K of T-$CaMnFeReO_6$. Columnar A-site order of Ca and Mn is shown, with the 4-coordinate sites further split into tetrahedral (Mn_{TD}) and square planes (Mn_{SP}). Rock salt B-site order is also observed between Fe and Re. G-type ferrimagnetism is seen on the Fe/Re sublattice, with an additional ferrimagnetic order of A-sites. The component of moment from Mn_{TD} is parallel to the total magnetisation, and component from Mn_{SP} is antiparallel, constrained here to be equal in magnitude. Image generated with FPStudio.*[125]

Results from Rietveld refinements of are shown in **Table 4.4**, with A/B–O lengths, B–O–B′ angles and BVS at 2 and 300 K in **Tables 4.5** and **4.6**, respectively. These suggest the formula of 'x = 1.0' to be: T-$Ca^{2+}(Mn_{0.88(4)}Fe_{0.12})^{2+}Fe^{3+}Re^{5+}O_6$. The magnetic structure at 2 K is shown in **Fig. 4.7**, illustrating the refined collinear structure of A and B-sites as well as the coordination environments of A-sites. Due to the very close lengths of the *a* and *c*-axes it is possible that there may be a component of the spin order along the *a*-axis that cannot be resolved in these neutron diffraction patterns. The magnitude of Re moments has been constrained here to be of one fifth the magnitude of Fe moments, as in refinements of the x = 0 sample against WISH data (determined to be a reasonable constraint based on previous refinements with D20 data and by X-ray Magnetic Circular Dichroism).

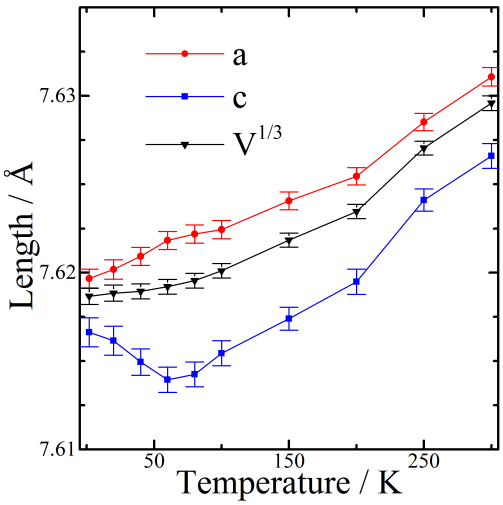

Figure 4.8 | *Lattice parameters: a, c and cube root of volume: $V^{1/3}$, for T-$CaMnFeReO_6$ in the tetragonal $P4_2/n$ space group versus temperature.*

Plots of the thermal evolution of lattice parameters of $x = 1.0$ in **Fig. 4.8** also show an interesting transition, with a negative thermal expansion of the *c*-axis which seems to have an onset temperature approximately at the A-site magnetic ordering transition. This evidence of magnetoelasticity suggests a coupling of magnetic ordering to the lattice. Tabulated bond lengths for the ReO_6 octahedra reveal that at 300 K there is a Jahn-Teller (J-T) expansion directed along the Re–O1 axis in the *ab*-plane (notably, O1 is the bonding pathway to the Mn_{SP}), yet at 2 K a J-T compression of ReO_6 octahedra is observed along the Re–O2 axis. The Re–O2 axis is also predominantly in the *ab*-plane, however O2 is the anion providing the bonding pathway to Mn_{TD}. In plots of the thermal evolution of Re–O bond lengths (**Appendix B**) this switch in distortion direction of ReO_6 octahedra occurs somewhere between 100 and 200 K, which is above the A-site ordering transition of ~70 K. This transition temperature of ~70 K is determined from the presented magnetometry data, however no A-site magnetic moment is observed in the 60 K neutron diffraction dataset. This could simply be that the magnitude of the ordered moment is too small to be detected

by neutron diffraction at this temperature. As in $x = 2.0$, the low-temperature distortion of ReO_6 is a compression, which would be expected for orbital ordering of $Re^{6+}O_6$ octahedra rather than the $Re^{5+}O_6$ octahedra that are suggested by BVS calculations. This J-T compression of $Re^{5+}O_6$ could be linked to the A-site magnetic order, however there is a considerable gap between the onset of this distortion (~100-200 K) and A-site magnetism (~70 K), as such this is unlikely. Another explanation could be due to mixed valences of Re^{5+}/Re^{6+} and electron delocalisation, contributing to an unusual orbital order.

4.3.1.c Magnetometry: x = 1.0

Magnetic moments of $x = 1.0$ extracted from Rietveld refinement (**Table 4.4**) are plotted in **Fig. 4.9**, overlaid on top of magnetisation measured by field cooled (0.5 T) magnetometry. This data shows a T_c due to ferrimagnetic Fe/Re spin order at 500 K, with a lower temperature transition at ~70 K due to A-site spin order.

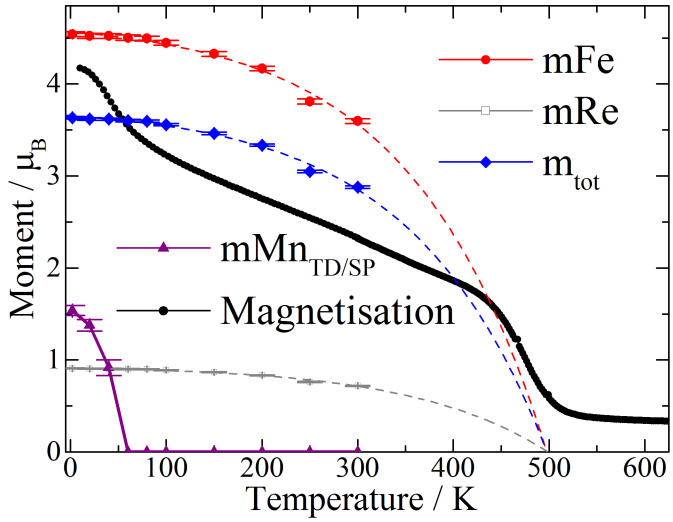

Figure 4.9 | *Magnetisation of T-CaMnFeReO₆ (field cooled, 0.5 T) with the magnetic moments from neutron refinements of Fe, Re and A-sites overlaid on this plot. Also plotted is the total magnetic moment observed, m_{tot}, from neutron diffraction, showing a similar temperature dependence to the overall magnetisation, with T_c of 500 K.*

Relatively close agreement can be seen between the thermal dependence of magnetisation from neutron diffraction and from magnetometry. Dependence of the magnetisation with field is shown in **Fig. 4.10**, with a narrow hysteresis of less than 0.05 T, similar to that of $x = 0$. Saturation values of 4.3 μ_B f.u.$^{-1}$ are found at 5 K (M at 7 T), which is reduced compared to the 4.8 μ_B f.u.$^{-1}$ of $x = 0$ at similar temperatures and fields.

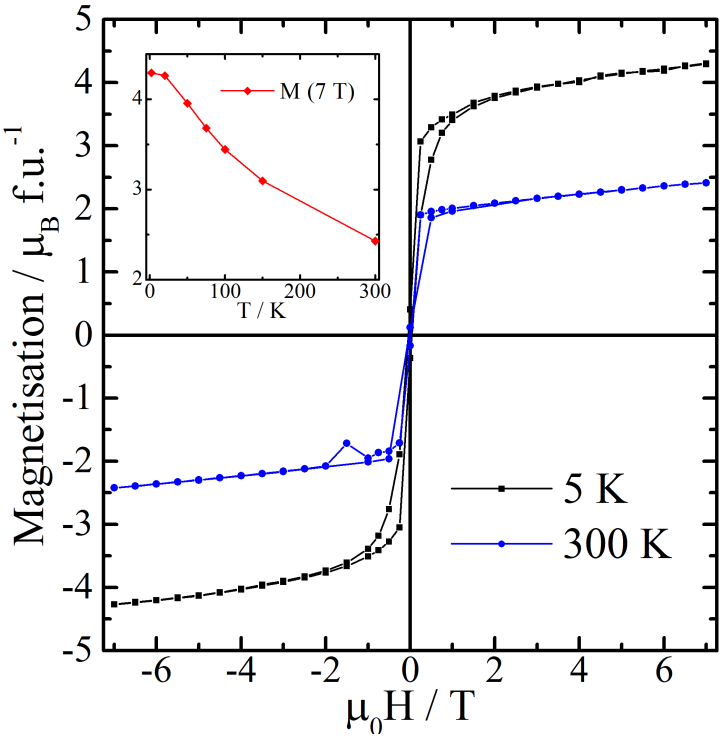

Figure 4.10 | *Magnetic hysteresis loops between fields of μ_0H = +7 and -7 T on T-$CaMnFeReO_6$ at constant temperatures of 2 and 300 K.*

4.3.1.d Magnetoresistance: x = 1.0

Resistivity for $x = 1.0$ has also been measured at constant temperature, between values of field μ_0H = -7 T and +7 T. The calculated magnetoresistance, as defined in **Equation 1.3** is shown in **Fig. 4.11**, which demonstrates a negative magnetoresistance

down to at least T = 20 K. When compared to the magnetoresistance of x = 0, which shows a switching transition at ~75 K from negative magnetoresistance in the high-temperature regime to positive in the low-temperature regime, it would seem that the dilution of A-site Mn^{2+} spin order with Ca^{2+} has suppressed the mechanism by which the positive regime becomes dominant. In fact, in x = 1.0, negative magnetoresistance is greatly enhanced when cooling through the A-site ordering transition, suggesting that A-site spin order in this material benefits the negative intergrain tunnelling mechanism of magnetoresistance. This phenomenon could be due to the collinear nature of spin order in x = 1.0 (**Fig. 4.11**), as solved by neutron diffraction, which enhances spin polarisation.

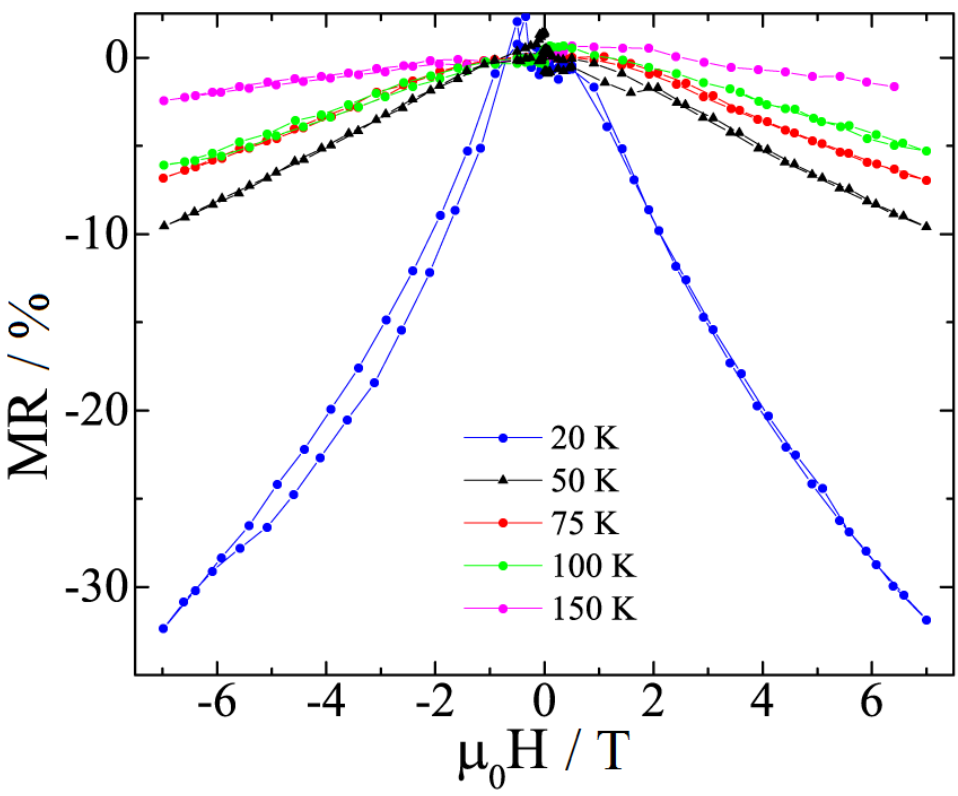

Figure 4.11 | *Magnetic hysteresis loops of the magnetoresistance of T-$CaMnFeReO_6$. Negative MR down to 20 K can be observed.*

4.3.1.e X-ray Magnetic Circular Dichroism: x = 1.0

X-ray Absorption Near-Edge Spectra (XANES) and calculated X-ray Magnetic Circular Dichroism (XMCD) are shown in **Fig. 4.12** and **Fig 4.13** for the Re L_2 and L_3-edges, respectively, in x = 1.0. Using **Equation 2.31** in '*2.3.3. X-ray Magnetic Circular Dichroism*' the ratio of spin to orbital moment for Re can be calculated from this data. This has been measured for x = 1.0 at temperatures of 2 and 290 K.

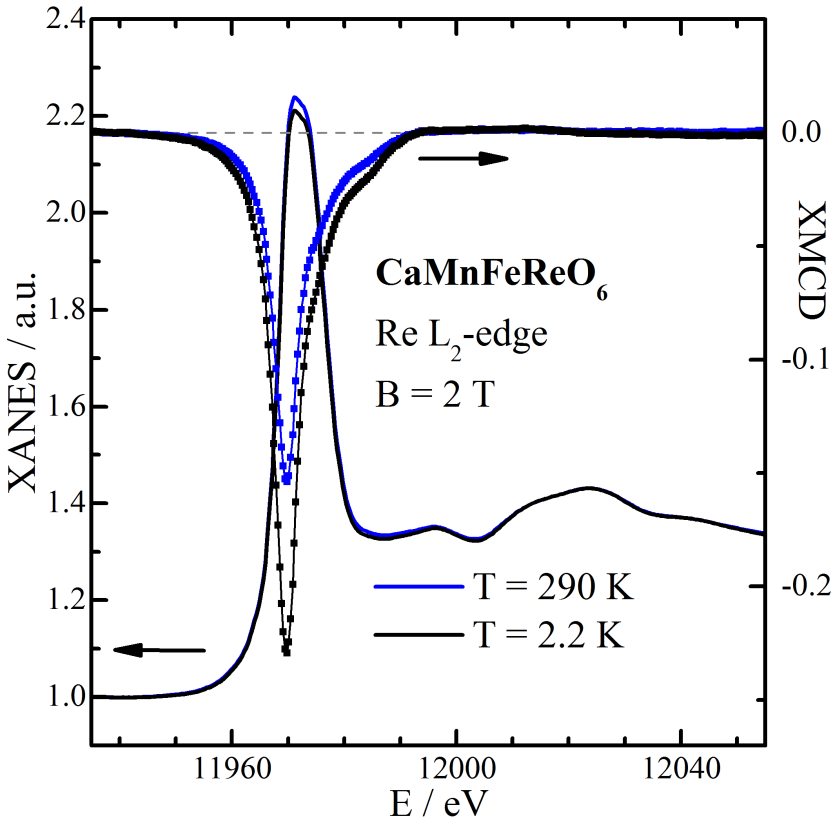

Figure 4.12 | *X-ray Absorption Near-Edge and X-ray Magnetic Circular Dichroism on T-$CaMnFeReO_6$, Re L_2-edge.*

As well as calculating the ratios of spin (m_S) to orbital (m_L) moments for Re, the absolute values of m_S and m_L can be estimated by an estimated value of n_h, the

number of *d*-state electron holes (**Equations 2.29** and **2.30**). In this case, absolute values for n_h are assumed to take values between 8 and 9, as in the analysis of XMCD data for the $x = 0$ sample (*3.3.5. X-ray Magnetic Circular Dichroism: Mn_2FeReO_6*).

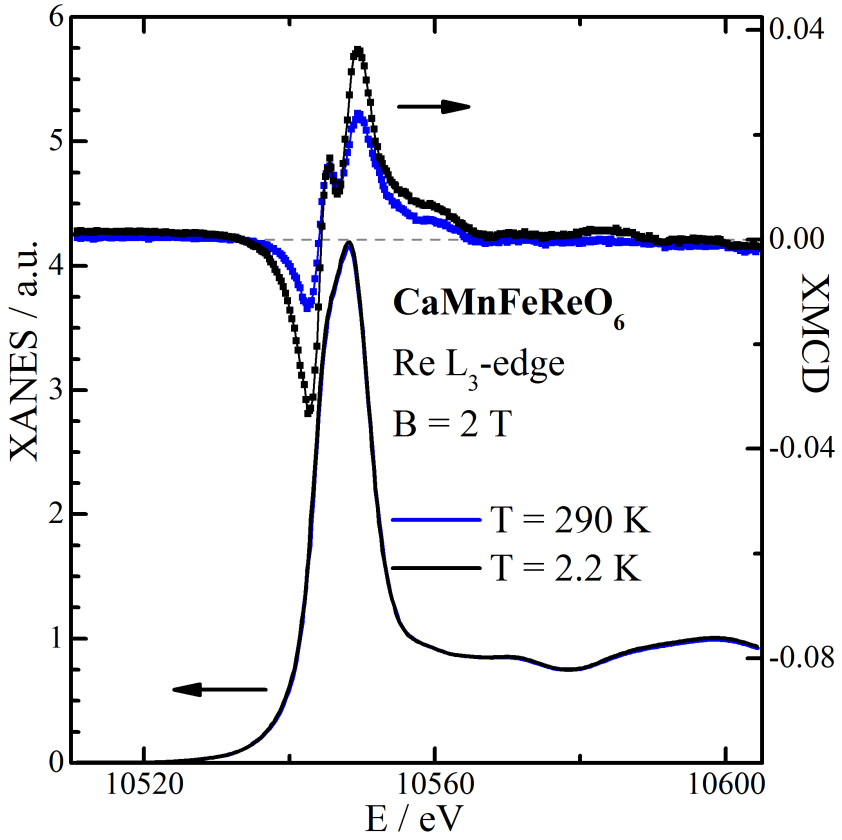

Figure 4.13 | *X-ray Absorption Near-Edge and X-ray Magnetic Circular Dichroism on T-$CaMnFeReO_6$, Re L_3-edge.*

Table 4.7 | Calculated orbit (m_L) and spin (m_S) moments from XMCD data at $B = 2$ T for Re at n_h values of 8 and 9, their ratio: m_S/m_L and the total Re moment: *mRe*.

	m_S/m_L	m_L / μ_B		m_S / μ_B		*mRe* / μ_B	
T / K	n_h:	8	9	8	9	8	9
290	-3.52	0.14	0.15	-0.48	-0.54	-0.34	-0.39
2.2	-3.39	0.21	0.24	-0.72	-0.81	-0.51	-0.57

Negative moments refer to antiparallel alignment to Fe moments.

Values for m_S, m_L and m_S/m_L, as well as the total Re moment from XMCD (*mRe*) are listed in **Table 4.7** for values of $n_h = 8$ and $n_h = 9$, which can be thought of as upper and lower bounds for this simple approximation of absolute values for m_S, m_L and *mRe*. Of particular note is that values of *mRe* are increased at 2 K versus those measured at 290 K. This is more clearly shown in plots of the magnetic hysteresis of *mRe* in **Fig. 4.14**. This plot clearly shows that *mRe* is oriented antiparallel to the net magnetisation in the material, as negative values of *mRe* are adopted in positive fields (and positive *mRe* in negative fields).

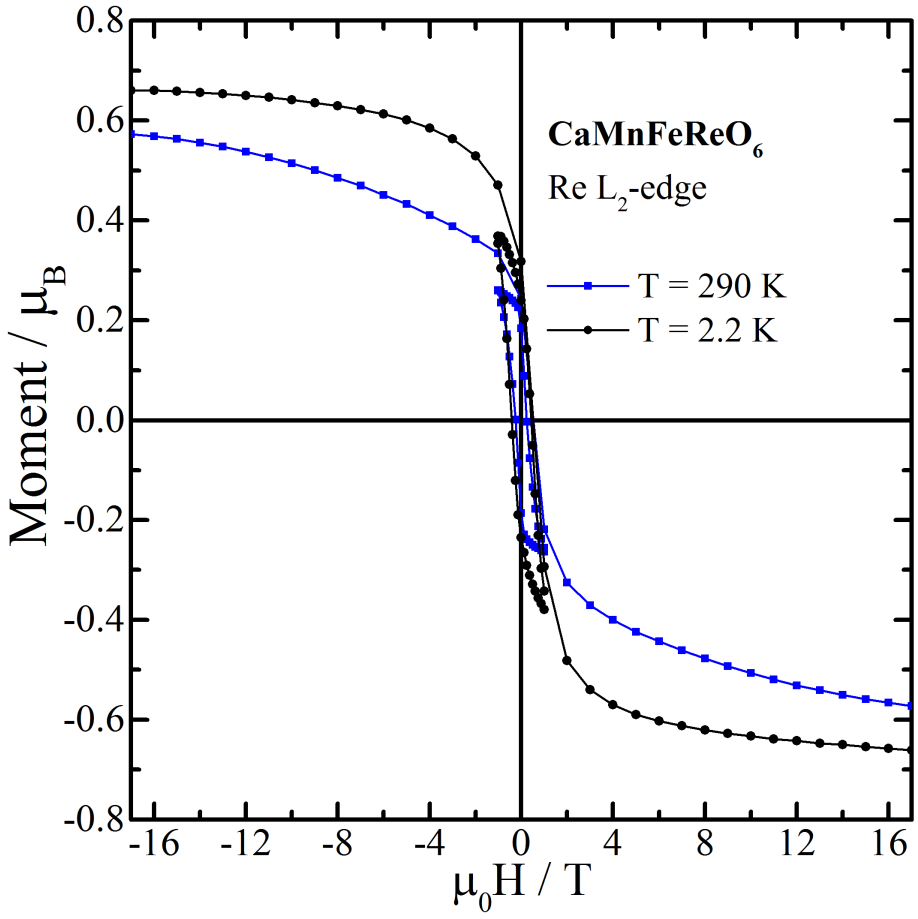

Figure 4.14 | *XMCD hysteresis of the Re L_2-edge (x = 1.0) at field strengths in the range of ±17 T. These measurements have been normalised to values of m_{Re} ($n_h = 8$) calculated from sum rules at each temperature. Plotted are two pairs of hysteresis loops, ±17 T in 1 T intervals and ±1 T in 0.125 T intervals.*

Returning to the analysis of the x = 0 material in '*3.3.5. X-ray Magnetic Circular Dichroism: Mn_2FeReO_6*', it was observed that there is a reduction in *mRe* as *T* is reduced (as measured by XMCD). From neutron diffraction studies, the known magnetic reorientation transition in the x = 0 material at low temperatures involves a spin canting of the Fe/Re sublattice. The reduction in *mRe* was hypothesised to be a result of *mRe* no longer being collinear with the X-ray vector, reducing the observed XMCD (a component of *mRe* due to antiferromagnetic order on the *b*-axis now lies perpendicular to the X-ray vector). In this x = 1.0 material no obvious spin reorientation is observed by neutron diffraction, and based on these structures, *mRe* should remain collinear with the X-ray vector when measuring XMCD. This explains why there is a reduction in *mRe* below the magnetic ordering transition in x = 0 (M-Mn_2FeReO_6) and not in x = 1.0 (T-$CaMnFeReO_6$).

4.3.2. $Ca_xMn_{2-x}FeReO_6$: x = 0.5

4.3.2.a Phase Analysis & Crystal Structure: x =0.5

Phase analysis on samples of the x = 0.5 material were conducted by X-ray diffraction using a Bruker D2 Phaser diffractometer. A stacked plot of these patterns is shown in **Fig. 4.15**. While these patterns seem relatively consistent, with some ReO_2 peaks noted in several syntheses (asterisks above pattern 2), there are difficulties in refining the structure of this material. As in the monoclinic x = 0 and x = 2 materials, the diffraction pattern of this material can be well indexed with a similar unit cell in the $P2_1/n$ space group. Accounting for peak intensities with this cell however, is rather problematic and results in poor fits. Taking into account the x = 1.0 phase discussed

earlier in this chapter which possesses a tetragonal $P4_2/n$ symmetry, this x = 0.5 material is found to be well fit with a phase mixture of the A-cation disordered $P2_1/n$ cell and the A-cation columnar ordered $P4_2/n$ cell. Results from Rietveld refinement with the inclusion of these two phases are shown in **Table 4.8**.

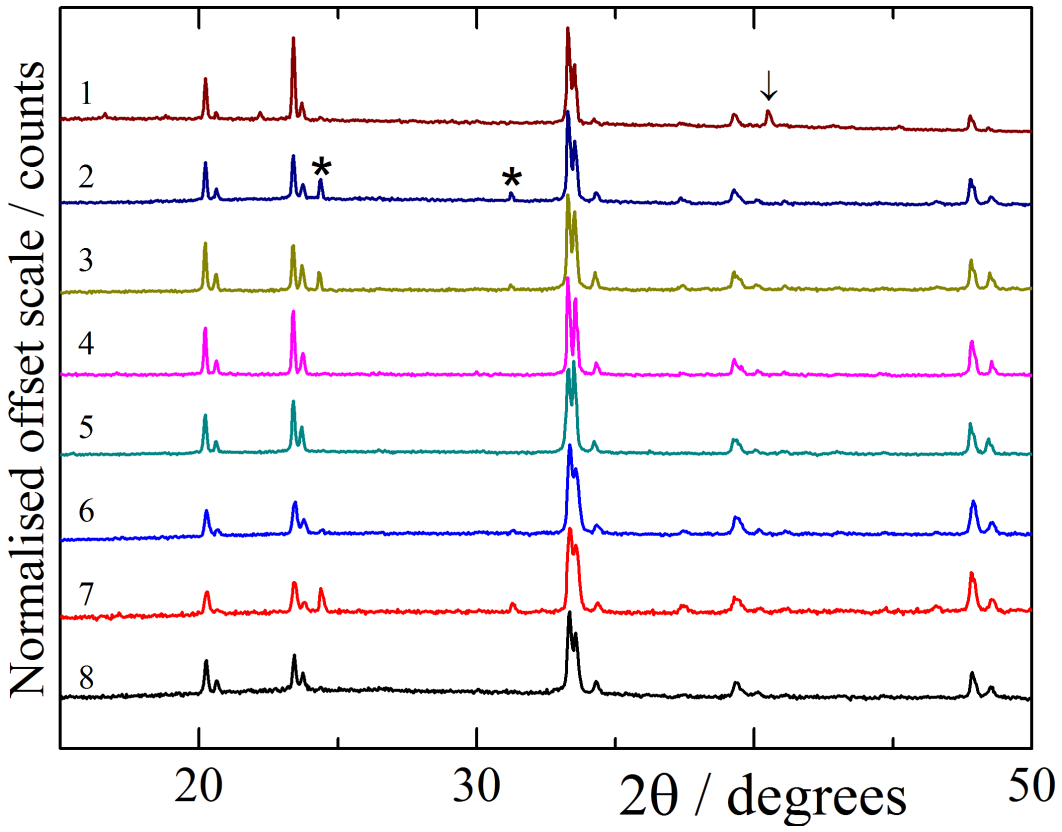

Figure 4.15 | *A stacked plot of the raw powder X-ray data initially collected on samples of $Ca_{0.5}Mn_{1.5}FeReO_6$ for phase analysis (in the 2θ range 15-50°). Asterisks mark the main ReO_2 impurity reflections. The product of synthesis 1 also contains other impurity phases. Of these phases MnO is able to be identified and is indicated by the arrow.*

This result is sensible as the x = 0.5 composition lies halfway between these two distinct structure types. This phase mixture was difficult to determine based on these initial phase analyses and was ultimately determined based on high resolution synchrotron X-ray diffraction data collected at the ESRF on ID22 (**Fig. 4.16**). However, these patterns obtained from laboratory X-ray diffraction have been

analysed here as phase mixtures to provide a sense of the variation between different syntheses. Notably, these syntheses seem to have rather consistent proportions of the two main perovskite-type phases. This could be an indication that these phases naturally separate at this composition, but it is more likely that varying *P* or *T* may favour one phase over the other as the synthesis conditions used for $x = 0.5$ have been extremely consistent and this possibility has not been explored. Potentially by increasing (or reducing) *P*, the fraction of monoclinic A-site disordered perovskite may be increased (or reduced) as this phase possess a lower volume ($V = 214.990(6)$ Å^3 at 300 K) when compared to the A-site ordered perovskite (when calculating volume with $\frac{a}{\sqrt{2}}$ in an $\frac{a}{\sqrt{2}} \times \frac{a}{\sqrt{2}} \times c$ perovskite cell: $V_{557} = 220.3189(8)$ Å^3 at 300 K).

Table 4.8 | A collection of the synthesis conditions and measure of the resulting purity and B-site disorder in $Ca_{0.5}Mn_{1.5}FeReO_6$ syntheses. Syntheses are found to be a phase mixture of monoclinic ($P2_1/n$) and tetragonal ($P4_2/n$) perovskite type phases, with percentages and ratio tabulated.

Sample no.	Pressure / GPa	Wt. Mon. / %	Wt. Tet. / %	Mon:Tet	Wt. ReO_2 / %	B-Antisite Disorder / %	χ^2	R_{wp} / %
1†	11	68(4)	29(1)	2.34	0.7(1)	24(2)	5.28	10.0
2	11	47(1)	47(1)	1.00	6.4(4)	11(1)	2.30	4.17
3	11	57(1)	39(1)	1.46	4.1(3)	8.2(8)	2.00	5.15
4	10	56(1)	44(1)	1.27	0	10.0(8)	1.81	5.05
5	10	57(1)	43(1)	1.33	0	13.6(8)	2.38	3.95
6	10	52(1)	45(1)	1.16	3.0(3)	16(1)	1.67	3.93
7	10	45(1)	43(2)	1.05	12.1(9)	18(2)	1.55	4.42
8	10	52(2)	47(2)	1.11	0.8(7)	8(1)	1.51	3.90

Samples 6, 7 and 8 were mixed to create a 54 mg aggregate and examined by neutron diffraction on WISH at the ISIS Neutron Facility. The measures of fit, χ^2 and R_{wp}, are shown for X-ray patterns collected over 15 minutes using a Bruker D2 Phaser diffractometer with Cu K_α radiation. A Pt capsule was used for all syntheses. All syntheses were conducted with heating at 1400 °C for 20 minutes before being quenched. †Synthesis 1 also contains 3.1(2) % by weight of MnO.

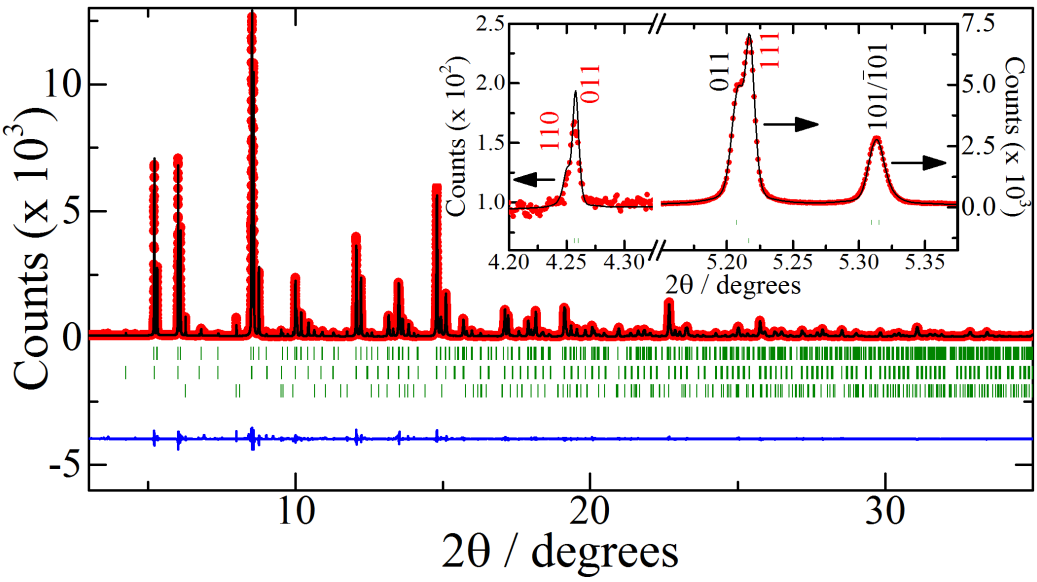

Figure 4.16 | *Rietveld fit to data collected from ID22 at the ESRF at 300 K for $Ca_{0.5}Mn_{1.5}FeReO_6$ (λ = 0.39987 Å). Ratios of Ca:Mn are fixed to the ratio of elements in the synthesis (1:3). The inset shows distinct reflections from the double perovskite monoclinic phase (indices in black) and the double double perovskite tetragonal phase (indices in red), including the characteristic 110 and 011 reflections from columnar A-site order in the tetragonal double double perovskite. Rows of indices indicate phase 1 (57.1(1) % by weight) as $P2_1/n$ M-$(Ca_{0.5}Mn_{1.5})FeReO_6$, phase 2 (41.7(1) % by weight) as $P4_2/n$ T-$(Ca_{0.5}Mn_{0.5})MnFeReO_6$ and phase 3 (1.14(1) % by weight) as ReO_2.*

Table 4.9 | Refined structure parameters for M-$(Ca_{0.5}Mn_{1.5})FeReO_6$ at 300 K in space group $P2_1/n$ using synchrotron powder X-ray data from ID22 at the ESRF.

Atom	*x*	*y*	*z*	Occupancy	B_{iso} / Å²
Ca/Mn	0.0089(4)	0.0522(2)	0.2486(2)	0.25/0.75	0.305(7)
Fe/Re	0	½	0	0.942(1)/0.058	0.305
Re/Fe	½	0	0	0.942/0.058	0.305
O1	0.32404(8)	0.30386(9)	0.05414(9)	1	0.45(6)
O2	0.30080(8)	0.2966(1)	0.43867(9)	1	0.45
O3	0.60834(6)	0.96246(8)	0.24577(8)	1	0.45

Lattice parameters: a = 5.23676(1), b = 5.39465(1) and c = 7.61015(2) Å with β = 90.0615(2)°; residuals R_{wp} = 7.47 % and χ^2 = 7.66. Ca:Mn occupancy is fixed to the synthesis composition of 1:3 This monoclinic A-site disordered phase constitutes 57.1(1) % by weight of the refined sample, with the tetragonal A-site ordered phase (parameters in **Table 4.10**) constituting 41.7(1) %. An impurity phase of 1.14 (1) % ReO_2 is also observed.

Table 4.10 | Refined structure parameters for T-$(Ca_{0.5}Mn_{0.5})MnFeReO_6$ at 300 K in space group $P4_2/n$ using synchrotron powder X-ray data from ID22 at the ESRF.

Atom	*x*	*y*	*z*	Occupancy	B_{iso} / Å^2
Ca/Mn	¼	¾	0.2804(5)	0.5/0.5	0.261(5)
Mn_{TD}	¾	¾	¾	1	0.261
Mn_{SP}	¼	¼	¾	1	0.261
Fe	0	0	½	0.950(1)/0.050	0.261
Re	0	½	½	0.950/0.050	0.261
O1	0.9323(2)	0.5410(2)	0.2568(1)	1	0.03(7)
O2	0.7291(1)	0.9581(1)	0.5734(1)	1	0.03(7)
O3	0.7444(1)	0.0572(1)	0.9584(1)	1	0.03(7)

Lattice parameters: a = 7.61368(1) and c = 7.60138(2) Å; residuals R_{wp} = 7.47 % and χ^2 = 7.66. Ca:Mn occupancy is fixed to the synthesis composition of 1:3. This tetragonal A-site ordered phase constitutes 41.7(1) % by weight of the refined sample, with the monoclinic A-site disordered phase (parameters in **Table 4.9**) constituting 57.1(1) %. An impurity of 1.14(1) % ReO_2 is also observed.

Synchrotron X-ray diffraction data in **Fig. 4.16** is well fit by this two-phase model of x = 0.5, with the results of these Rietveld refinements shown in **Table 4.9** (A-site disordered phase) and **Table 4.10** (A-site ordered phase). Due to lack of Ca/Mn contrast occupancies are fixed, such that each phase contains the same ratio of Ca:Mn, 1:3. It has been assumed here that in the A-site ordered phase some Mn^{2+} may occupy the 10-coordinate A-site, but that Ca^{2+} would be unlikely to occupy a small 4-coordinate A-site. This leads to a preliminary formula of T-$(Ca_{0.5}Mn_{0.5})MnFeReO_6$ for the A-site ordered phase.

As can be observed in **Fig. 4.16** (inset), the high resolution provided by synchrotron X-ray diffraction is required to observe the independent peaks from the $P2_1/n$ A-site disordered (black indices) and $P4_2/n$ A-site ordered (red indices) phases. The lower resolution in neutron diffraction patterns, as well as the necessity to mix samples (which may be slightly different compositionally) to provide a large enough

sample to study the $x = 0.5$ synthetic products, leads to an inability to clearly resolve these phases by neutron diffraction methods.

4.3.2.b Neutron Crystal & Magnetic Structure: x = 0.5

The two-phase mixture from $x = 0.5$ syntheses of an A-site disordered phase with an additional A-site ordered phase was studied on the WISH diffractometer at the ISIS Neutron Facility. The magnetic intensities from these diffraction patterns, shown in **Fig. 4.17**, can be qualitatively described by a superposition of magnetic intensities one might expect from spin structures similar to the $x = 0$ and $x = 1$ phases. Using this analysis from synchrotron X-ray diffraction in the evaluation of the neutron data, it is possible to fully explain this diffraction pattern. This results in good fits to the structure as well as the magnetic intensities. Fits at 300 and 2 K are shown in **Fig. 4.18**.

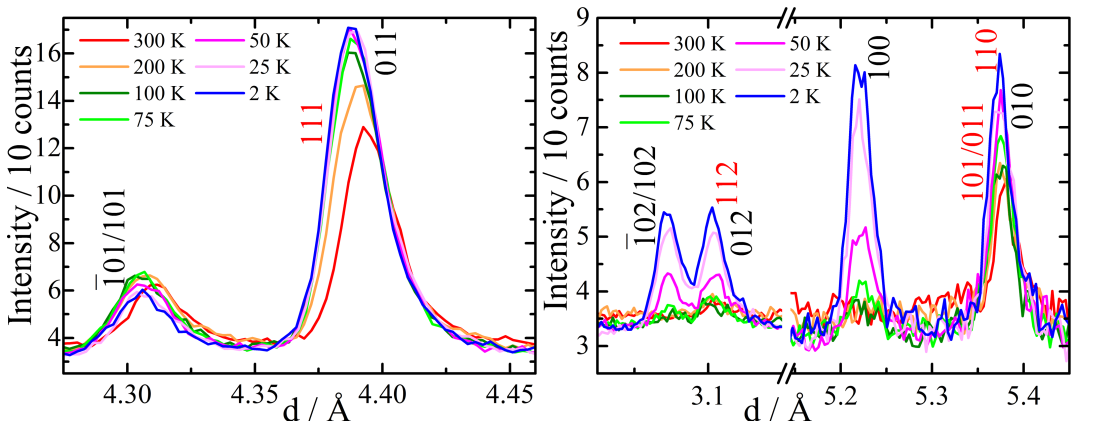

Figure 4.17 | *$Ca_xMn_{2-x}FeReO_6$, nominal x = 0.5. Diffracted neutron intensities are shown in the region d ~4.35 Å K (**left**) and in the regions d ~3.1 and 5.3 Å (**right**) between 300 and 2 K. The Miller indices are shown beside each reflection, with indices in black indicating those of the monoclinic double perovskite phase and those in red indicating those of the tetragonal double double perovskite phase.*

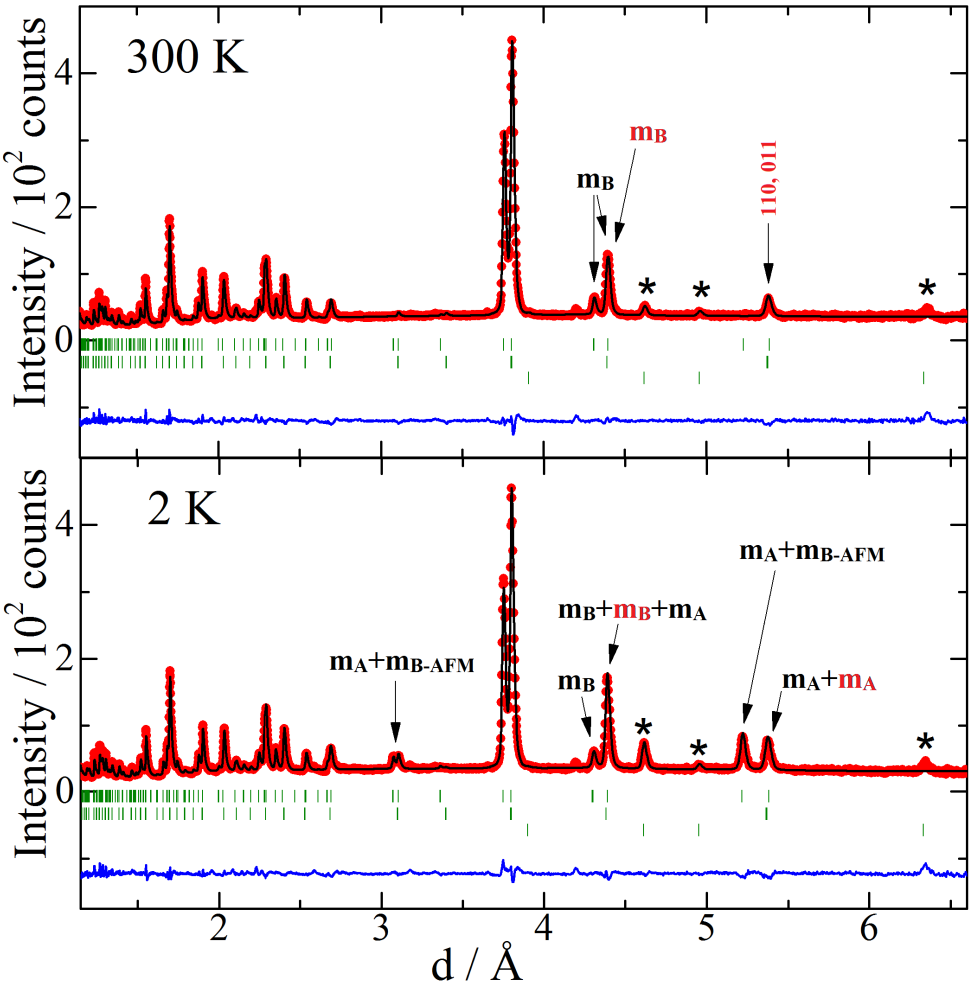

Figure 4.18 | *Combined nuclear and magnetic Rietveld fits to neutron diffraction data on* $Ca_xMn_{2-x}FeReO_6$ with nominal $x = 0.5$, *collected on the WISH diffractometer at the ISIS Neutron Facility. The patterns shown are from an average of bank 3 and 8.* ***Top****: 300 K.* ***Bottom****: 1.5 K. The markers* m_A *and* m_B *refer to magnetic reflections with contributions from A and B-site spin order, respectively, with black markers indicating reflections from the monoclinic phase and red markers from the tetragonal phase. Indices mark phase 1 as the* $P2_1/n$ *double perovskite, phase 2 as the* $P4_2/n$ *double double perovskite (intensity is observed on the 110 and 011 reflections at room temperature) and phase 3 as* $MnFe_3O_5$.

These magnetic intensities in $x = 0.5$ are essentially a superposition of the same intensities that were observed in the $x = 0$ (M-Mn_2FeReO_6) and the $x = 1.0$ (T-$CaMnFeReO_6$) materials. This suggests that the magnetic symmetry of the $P2_1/n$ phase in $x = 0.5$ is similar to the magnetic symmetry in M-Mn_2FeReO_6 (explained in '*3.3.2 Neutron Crystal & Magnetic Structure of* Mn_2FeReO_6') and the magnetic

symmetry of the A-site ordered $P4_2/n$ phase is similar to that in T-$CaMnFeReO_6$ (explained in '*4.3.1.b Neutron Crystal & Magnetic Structure: x = 1.0*').

The coexistence of these two phases makes structure refinement using the data collected on WISH difficult, nevertheless the structures of these two phases have been refined using the same magnetic symmetry as in $x = 0$ and $x = 1.0$. The results are shown in **Table 4.11** ($P2_1/n$ phase) and **4.14** ($P4_2/n$ phase), with bond lengths for these phases at 2 and 300 K shown in **Table 4.12** and **4.13** ($P2_1/n$ phase) and **Table 4.15** and **4.16** ($P4_2/n$ phase). Some of the parameters in these two phases correlate in Rietveld refinement, and ideally diffraction data would be collected on these two phases individually (if they could be isolated separately by varying the synthetic conditions). However, this analysis does provide some insight into the properties of these two phases. In addition, the occupancies of Ca/Mn can be refined due to good neutron scattering contrast and have been determined to be M-$(Ca_{0.17(3)}Mn_{1.83})FeReO_6$ for the A-site disordered phase and T-$(Ca_{0.74(2)}Mn_{0.26})MnFeReO_6$ for the A-site ordered phase. Indicating that the A-site ordered phase has $x = 0.74(2)$, 49(3) % by weight of the total sample, and the A-site disordered phase has $x = 0.17(3)$, 51(3) % by weight of the total sample, showing a separation in the $x = 0.5$ syntheses to preferentially form two distinct phases which are compositionally closer to the $x = 1.0$ or $x = 0$ type structures. A weighted mean of these phases results in a value of $x = 0.45(9)$, which when compared to the nominal value of $x = 0.5$, is in good agreement with this conclusion.

Table 4.11 | Refined structure parameters for $Ca_xMn_{2-x}FeReO_6$ with nominal $x = 0.5$ at 2-300 K in space group $P2_1/n$ using neutron powder diffraction data from the WISH diffractometer at the ISIS Neutron Facility. Magnetic symmetry follows the descriptions in **Table 3.3**. Sample size 54 mg. The composition of this material is a two-phase mixture, including this phase (51(3) wt.%) and the phase described in **Table 4.14** (49(3) wt.%). This phase is found to have a chemical formula of M-$(Ca_{0.17(3)}Mn_{1.83})FeReO_6$.

T / K		2	25	50	75	100	200	300
Cell	a / Å	5.2230(6)	5.2233(7)	5.2236(7)	5.2241(7)	5.2244(7)	5.2280(7)	5.2339(7)
	b / Å	5.3856(7)	5.3856(7)	5.3854(7)	5.3858(7)	5.3862(7)	5.3885(7)	5.3929(7)
	c / Å	7.5975(9)	7.5979(9)	7.5998(9)	7.602(1)	7.603(1)	7.606(1)	7.610(1)
	β / °	90.04(2)	90.03(2)	89.99(2)	89.96(2)	89.93(2)	89.92(2)	89.95(2)
	V / Å^3	213.71(5)	213.73(5)	213.79(5)	213.89(5)	213.95(5)	214.27(5)	214.80(5)
A	x	0.493(4)	0.495(4)	0.497(4)	0.492(4)	0.491(4)	0.496(4)	0.495(4)
	y	0.573(5)	0.571(5)	0.565(6)	0.564(6)	0.561(6)	0.554(6)	0.552(5)
	z	0.782(3)	0.784(3)	0.806(3)	0.821(3)	0.827(3)	0.828(3)	0.823(4)
O1	x	0.325(4)	0.323(4)	0.322(4)	0.320(4)	0.316(4)	0.315(5)	0.307(5)
	y	0.269(4)	0.269(4)	0.275(4)	0.274(4)	0.276(4)	0.288(5)	0.291(5)
	z	0.934(4)	0.935(4)	0.936(4)	0.938(3)	0.941(3)	0.937(4)	0.940(5)
O2	x	0.297(4)	0.297(4)	0.299(4)	0.301(4)	0.305(4)	0.311(5)	0.320(5)
	y	0.339(4)	0.340(4)	0.337(4)	0.338(3)	0.336(3)	0.325(4)	0.323(5)
	z	0.551(3)	0.553(3)	0.557(3)	0.559(3)	0.561(3)	0.564(4)	0.569(4)
O3	x	0.886(2)	0.885(2)	0.884(2)	0.881(2)	0.880(2)	0.880(2)	0.881(2)
	y	0.442(2)	0.442(2)	0.441(2)	0.441(2)	0.442(2)	0.444(2)	0.445(2)
	z	0.738(5)	0.738(5)	0.741(6)	0.742(5)	0.740(4)	0.740(4)	0.738(4)
θ_{Tilt} / degrees		23.6(1)	23.8(1)	24.1(1)	24.7(1)	24.8(1)	24.7(1)	24.3(1)
φ_{Tilt} / degrees		12.5(2)	12.5(2)	12.7(2)	12.8(2)	12.7(2)	12.1(2)	11.8(2)
mFe / μ_B		4.3(1)	4.3(1)	4.2(1)	3.9(1)	3.7(1)	3.56(1)	3.1(2)
φ_{Fe} / °		5(2)	8(2)	11(7)	21(31)	0	0	0
θ_{Fe} / °		63(4)	62(4)	48(5)	20(10)	9(11)	12(10)	14(18)
φ_{FeFe} / °		10(4)	15(5)	23(15)	42(63)	0	0	0
mFe_x / μ_B		3.8(2)	3.7(2)	3.1(3)	1.2(7)	0.6(7)	0.7(6)	0.7(10)
mFe_y / μ_B		0.3(1)	0.5(2)	0.6(4)	0.5(7)	0	0	0
mFe_z / μ_B		1.9(2)	2.0(3)	2.8(2)	3.6(2)	3.7(1)	3.5(1)	3.0(3)
mRe / μ_B		0.86(3)	0.85(3)	0.85(3)	0.77(3)	0.74(2)	0.71(2)	0.62(3)
m_{tot} / μ_B		3.4(4)	3.4(5)	3.3(6)	3.1(8)	3.0(3)	2.8(4)	2.5(10)
A/B	B_{iso} / Å^2	1.24(2)	1.25(2)	1.22(2)	1.24(2)	1.28(2)	1.30(2)	1.33(3)
O	B_{iso} / Å^2	0.35(2)	0.33(2)	0.46(2)	0.49(2)	0.55(2)	0.52(2)	0.69(3)
R_{wp} / %		3.61	3.61	3.52	3.43	3.42	3.47	3.44
χ^2		4.08	4.08	3.90	3.75	3.72	3.89	3.80
Q / μA·h		45	45	45	45	45	45	45

Fe atoms are located at (0, ½, 0), with Re atoms at (½, 0, 0). Antisite disorder of Fe/Re is not refined due to poor neutron contrast. Magnitudes of Re moments are constrained as $-0.2 \times mFe$, with the same magnetic symmetry as Fe. Total magnetisation due to ferrimagnetic Fe/Re order is shown as m_{tot}. No site mixing between A and B-sites was found. A-sites are found to be 91.5(14) % Mn, with 8.5(14) % Ca. Q, a measure of the total length of exposure of the sample to the neutron beam ($Q = I \cdot t$), is also tabulated.

Table 4.12 | Bond lengths, angles and BVS values for M-($Ca_{0.17(3)}Mn_{1.83}$)$FeReO_6$ in space group $P2_1/n$ from the neutron profile fit at 2 K.

Bond	A – O length / Å	Bond	B – O length / Å
Mn/Ca – O1	2.19(4)	Fe – O1	2.16(3) × 2
Mn/Ca – O1	2.51(4)	Fe – O2	2.15(3) × 2
Mn/Ca – O1	2.56(4)	Fe – O3	2.10(5) × 2
Mn/Ca – O2	2.44(4)	**<Fe – O>**	2.14(2)
Mn/Ca – O2	2.39(4)		
Mn/Ca – O2	2.8(4)	Re – O1	1.78(3) × 2
Mn/Ca – O3	2.19(3)	Re – O2	1.82(3) × 2
Mn/Ca – O3	2.09(3)	Re – O3	1.93(5) × 2
<Mn/Ca – O>	2.40(1)	**<Re – O>**	1.84(2)
Cation	**BVS**	**B – O# – B′**	**Angle / degrees**
Mn/Ca/<Mn/Ca>	1.82/2.94/1.78	Fe – O1 – Re	144(2)
Fe	2.17	Fe – O2 – Re	142(1)
Re	6.34	Fe – O3 – Re	140.8(6)

The program BondStr in the FullProf Suite was used to compute this data.[125]

Table 4.13 | Bond lengths, angles and BVS values for M-($Ca_{0.17(3)}Mn_{1.83}$)$FeReO_6$ in space group $P2_1/n$ from the neutron profile fit at 300 K.

Bond	A – O length / Å	Bond	B – O length / Å
Mn/Ca – O1	1.93(4)	Fe – O1	2.01(3) × 2
Mn/Ca – O1	2.25(5)	Fe – O2	2.05(3) × 2
Mn/Ca – O1	2.86(5)	Fe – O3	2.11(3) × 2
Mn/Ca – O2	2.35(4)	**<Fe – O>**	2.06(2)
Mn/Ca – O2	2.47(5)		
Mn/Ca – O2	3.21(5)	Re – O1	1.78(3) × 2
Mn/Ca – O3	2.20(3)	Re – O2	1.82(3) × 2
Mn/Ca – O3	2.26(3)	Re – O3	1.93(5) × 2
<Mn/Ca – O>	2.44(2)	**<Re – O>**	1.84(3)
Cation	**BVS**	**B – O# – B′**	**Angle / degrees**
Mn/Ca/<A>	2.03/3.28/1.98	Fe – O1 – Re	145(2)
Fe	2.7	Fe – O2 – Re	136(2)
Re	4.69	Fe – O3 – Re	140.2(6)

The program BondStr in the FullProf Suite was used to compute this data.[125]

Table 4.14 | Refined structure parameters for $Ca_xMn_{2-x}FeReO_6$ with nominal $x = 0.5$ at 2-300 K in space group $P4_2/n$ using neutron powder diffraction data from the WISH diffractometer at the ISIS Neutron Facility. Magnetic symmetry is follows the descriptions in **Table 4.3**. Sample size 54 mg. The composition in this material is a two-phase mixture, including this phase (49(3) wt.%) and the phase described in **Table 4.11** (51(3) wt.%). This phase is found to have a chemical formula of T-$(Ca_{0.74(2)}Mn_{0.26})MnFeReO_6$.

T / K		2	25	50	75	100	200	300
Cell Param	a / Å	7.600(1)	7.601(1)	7.602(1)	7.6035(9)	7.6040(9)	7.607(1)	7.612(1)
	c / Å	7.594(2)	7.594(2)	7.590(1)	7.590(1)	7.590(1)	7.594(1)	7.603(1)
	V / Å^3	438.6(2)	438.7(2)	438.7(1)	438.8(1)	438.9(1)	439.5(1)	440.5(1)
Ca/Mn	z	0.298(7)	0.301(7)	0.314(6)	0.331(7)	0.342(7)	0.358(7)	0.341(6)
O1	x	0.94(1)	0.94(1)	0.940(9)	0.93(1)	0.924(9)	0.915(4)	0.919(5)
	y	0.57(1)	0.57(2)	0.572(9)	0.57(1)	0.567(8)	0.555(3)	0.557(3)
	z	0.25(2)	0.25(2)	0.25(1)	0.265(5)	0.267(4)	0.266(4)	0.261(6)
O2	x	0.762(9)	0.76(1)	0.765(7)	0.76(1)	0.76(1)	0.749(8)	0.75(1)
	y	0.942(3)	0.941(3)	0.943(3)	0.948(2)	0.950(3)	0.951(2)	0.950(2)
	z	0.557(2)	0.558(2)	0.558(2)	0.555(2)	0.554(2)	0.553(2)	0.554(2)
O3	x	0.75(2)	0.75(2)	0.75(1)	0.74(1)	0.734(9)	0.731(6)	0.74(1)
	y	0.053(2)	0.052(2)	0.053(2)	0.054(2)	0.054(2)	0.053(2)	0.054(2)
	z	0.972(2)	0.972(2)	0.972(2)	0.970(2)	0.970(2)	0.972(2)	0.972(2)
mFe / μ_B		4.1(1)	4.2(1)	4.3(1)	4.5(1)	4.5(1)	4.22(9)	3.7(1)
mRe / μ_B		0.83(3)	0.83(3)	0.87(3)	0.90(2)	0.89(2)	0.84(2)	0.74(2)
mMn / μ_B		0.8(2)	0.8(2)	0.5(2)	0	0	0	0
m_{tot} / μ_B f.u.$^{-1}$		3.31(7)	3.33(8)	3.46(7)	3.60(5)	3.56(5)	3.37(4)	2.94(6)
A/B	B_{iso} / Å^2	1.24(2)	1.25(2)	1.22(2)	1.24(2)	1.28(2)	1.30(2)	1.33(3)
O	B_{iso} / Å^2	0.35(2)	0.33(2)	0.46(2)	0.49(2)	0.55(2)	0.62(2)	0.69(3)
R_{wp} / %		3.61	3.61	3.52	3.43	3.42	3.47	3.44
χ^2		4.08	4.08	3.90	3.75	3.72	3.89	3.80
Q / μA·h		45	45	45	45	45	45	45

Cation positions are as follows for A-sites: Ca/Mn (¼, ¾, z), Mn_{TD} (¾, ¾, ¾), Mn_{SP} (¼, ¼, ¾); and for B-sites: Fe (0, 0, ½) and Re (0, ½, ½). The 10-coordinate Ca/Mn site is found to have a site occupancy of 74(2) % Ca, 26 % Mn. Other sites are fixed at ideal occupancies of each ion. Magnitudes of Re moments are constrained as -0.2 × mFe, with the same magnetic symmetry as Fe. The tabulated value of m_{tot} refers to the total magnetisation of this phase, equivalent to: $m_{tot} = mFe - mRe$.

Table 4.15 | T-$(Ca_{0.74(2)}Mn_{0.26})MnFeReO_6$ bond lengths, angles and BVS values in space group $P4_2/n$ from the neutron profile fit at 2 K.

Bond	M – O length / Å	Bond	M – O length / Å
Ca/Mn – O1	2.76(10) × 2	Fe – O1	2.02(14) × 2
Ca/Mn – O1	2.85(10) × 2	Fe – O2	1.91(7) × 2
Ca/Mn – O2	2.59(4) × 2	Fe – O3	1.95(14) × 2
Ca/Mn – O3	2.30(5) × 2	**<Fe – O>**	1.96(7)
Ca/Mn – O3	2.54(5) × 2	Re – O1	2.04(14) × 2
<Ca/Mn – O>	2.61(5)	Re – O2	2.08(7) × 2
Mn_{TD} – O2	2.07(2) × 4	Re – O3	1.96(14) × 2
Mn_{SP} – O1	1.97(7) × 4	**<Re – O>**	2.03(7)

Cation	BVS	Cation	BVS	B – O# – B′	Angle / degrees
<Ca/Mn>	1.79	Ca/Mn	2.03/1.26	Fe – O1 – Re	139(5)
Mn_{TD}	1.73	Fe	3.50	Fe – O2 – Re	143.9(11)
Mn_{SP}	2.25	Re	3.85	Fe – O3 – Re	153.0(9)

The program BondStr in the FullProf Suite was used to compute this data.[125]

Table 4.16 | T-$(Ca_{0.74(2)}Mn_{0.26})MnFeReO_6$ bond lengths, angles and BVS values in space group $P4_2/n$ from the neutron profile fit at 300 K.

Bond	M – O length / Å	Bond	M – O length / Å
Ca/Mn – O1	2.78(4) × 2	Fe – O1	2.12(5) × 2
Ca/Mn – O1	2.98(4) × 2	Fe – O2	1.99(9) × 2
Ca/Mn – O2	2.42(3) × 2	Fe – O3	1.86(8) × 2
Ca/Mn – O3	2.06(4) × 2	**<Fe – O>**	1.99(4)
Ca/Mn – O3	2.81(5) × 2	Re – O1	1.97(5) × 2
<Ca/Mn – O>	2.61(4)	Re – O2	1.98(9) × 2
Mn_{TD} – O2	2.13(2) × 4	Re – O3	2.06(8) × 2
Mn_{SP} – O1	1.95(3) × 4	**<Re – O>**	2.00(4)

Cation	BVS	Cation	BVS	B – O# – B′	Angle / degrees
<Ca/Mn>	2.37	Ca/Mn	2.69/1.67	Fe – O1 – Re	136.7(18)
Mn_{TD}	1.47	Fe	3.37	Fe – O2 – Re	147.2(9)
Mn_{SP}	2.36	Re	4.12	Fe – O3 – Re	152.6(9)

The program BondStr in the FullProf Suite was used to compute this data.[125]

While there is difficulty in reliably extracting useful information from this data, results from Rietveld refinements will be discussed here, beginning with the monoclinic $P2_1/n$ A-site disordered phase, which can be likened to $x = 0$ (M-Mn_2FeReO_6).

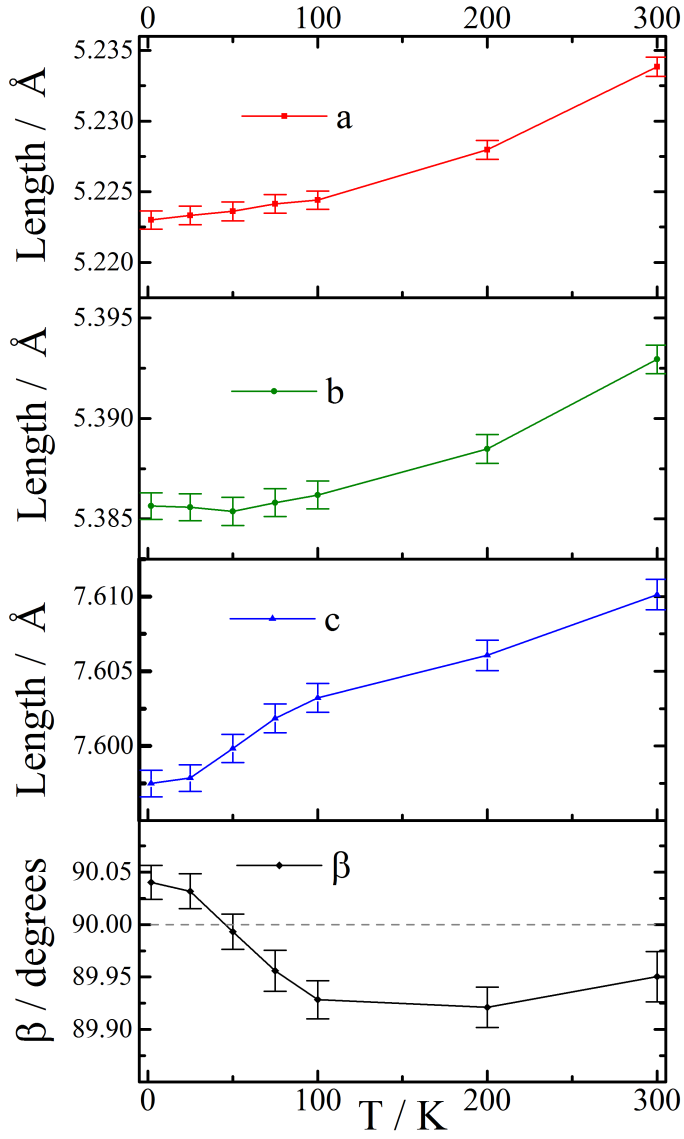

Figure 4.19 | *Thermal variation of the lattice parameters of M-($Ca_{0.17(3)}Mn_{1.83}$)$FeReO_6$ in the $P2_1/n$ space group (one of the observed phases from x = 0.5 syntheses). A switch from the monoclinic angle $\beta < 90°$ to $\beta > 90°$ is observed, where the onset of this increase appears around the magnetic reorientation temperature (~75 K in M-Mn_2FeReO_6). A plateauing of the b parameter is also observed around this temperature (as in M-Mn_2FeReO_6).*

In **Fig. 4.19**, a plot of the thermal variation of lattice parameters in this material is shown, where at the magnetic reorientation transition (~75 K in M-Mn_2FeReO_6, assumed to be similar here in M-$(Ca_{0.17(3)}Mn_{1.83})FeReO_6$, a few things can be noted to deviate from their trends above this temperature. The *b*-axis exhibits no considerable dependence on temperature below this reorientation transition, and the *c*-axis seemingly increasing in its rate of contraction (which is also observed in M-Mn_2FeReO_6). Most strikingly is the switch in the monoclinic angle, β, which is below 90° above the transition and takes values above 90° below the transition (note that this is not observed in M-Mn_2FeReO_6). This could be further indication of coupling of magnetic ordering to the lattice, however it is difficult to say with certainty that this is not an artefact of correlations with other parameters. Referencing comparisons to low and high-temperature BVS shown in **Table 4.12** and **4.13** respectively, it also seems to indicate valence states of Fe^{2+} and Re^{6+} at these low temperatures (versus Fe^{3+} and Re^{5+} at high temperature). It seems unlikely that a charge transfer is actually occurring in this material, and perhaps correlation of oxygen coordinates and monoclinic distortion with other parameters in the secondary phase may explain these unusual observations that are absent in Mn_2FeReO_6, unfortunately refining these parameters to give sensible results from Rietveld refinement is not possible with the available two-phase data.

Results from the magnetic data extracted from Rietveld refinement for this phase are shown in **Fig. 4.20** (for Fe moments) and in **Fig. 4.21** (for Mn moments). These refinements have been conducted to reflect the symmetry and temperature onsets of A-site magnetic order and reorientation observed in M-Mn_2FeReO_6, as

discerning any potential differences between this and M-$(Ca_{0.17(3)}Mn_{1.83})FeReO_6$ are difficult with the complexity of the patterns. In general, it can be seen that qualitatively the magnetic structure of M-$(Ca_{0.17(3)}Mn_{1.83})FeReO_6$ is extremely similar to that of the Mn pure material. Uncertainties in the values of some components on magnetic moment are rather large in this analysis, but this could be expected as the coexistence of this phase with the A-site ordered phase complicates the refinement. The magnitude of magnetic moments of both Fe and Mn are reduced when compared to the Mn pure material, however a reorientation of both Fe/Re and Mn spin lattices is still found to occur.

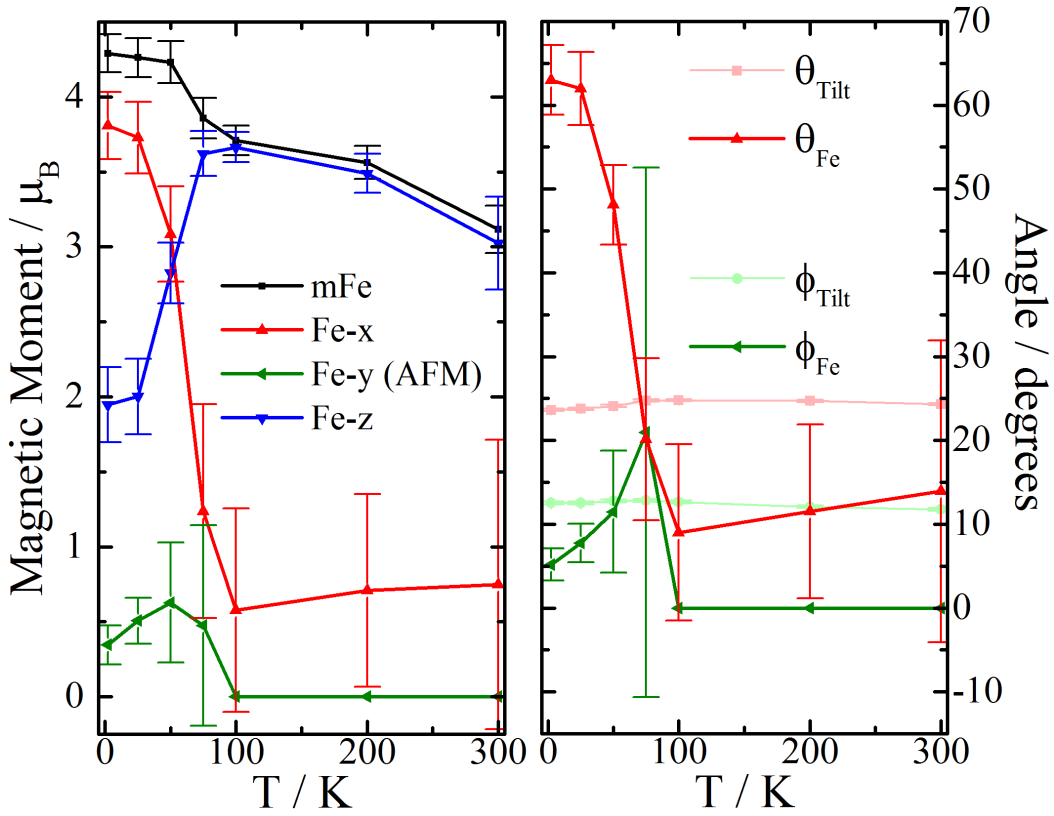

Figure 4.20 | *Refined magnetic moments for Fe in M-$(Ca_{0.17(3)}Mn_{1.83})FeReO_6$. Uncertainties are large for some components of magnetic moment because of correlations due to overlapping intensities with the A-site ordered phase, however these refinements have been conducted to mirror the symmetry found in M-Mn_2FeReO_6. Also shown are the tilt angles of FeO_6 octahedra.*

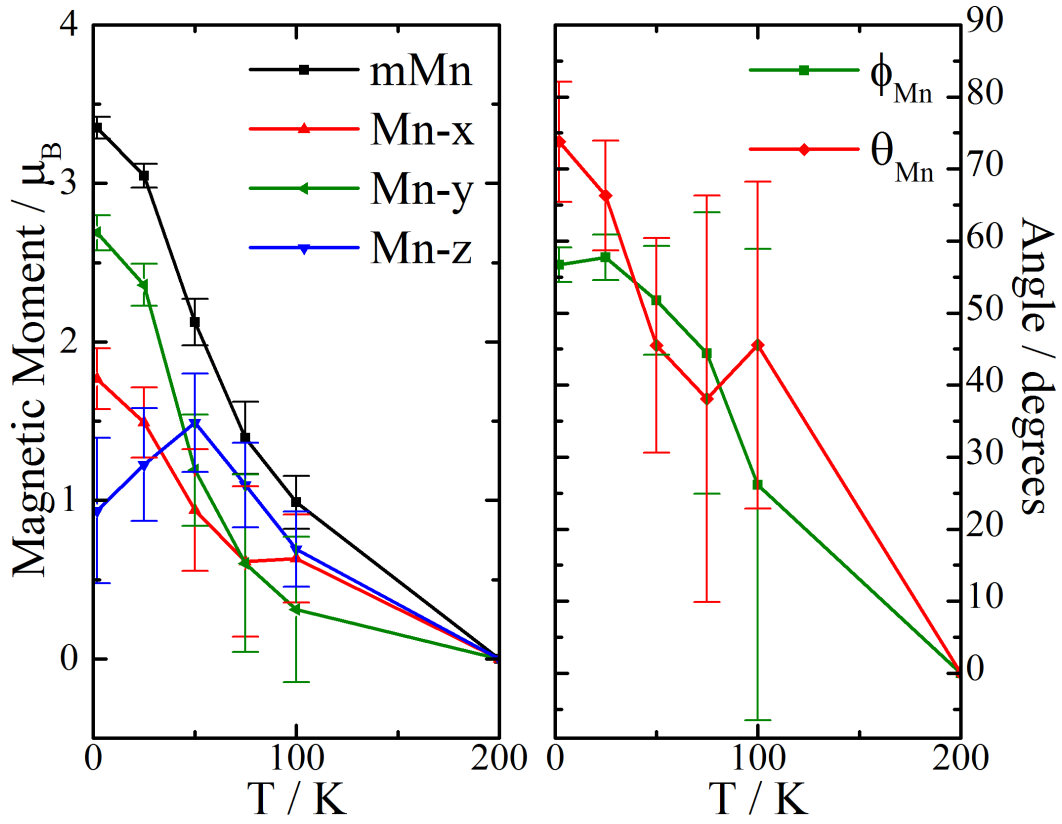

Figure 4.21 | *Refined magnetic moments for Mn in M-($Ca_{0.17(3)}Mn_{1.83}$)$FeReO_6$. The components shown all refer to antiferromagnetic order of Mn.*

The analysis of the tetragonal $P4_2/n$ A-site ordered phase can be discussed by making comparisons with the x = 1.0 (T-$CaMnFeReO_6$) phase. The thermal variation of the lattice parameters for this phase are shown in **Fig. 4.22**, where a clear negative thermal expansion of the *c*-axis is observed. This is very similar to what is observed in T-$CaMnFeReO_6$, with a similar onset temperature that coincides with A-site magnetic order, evidencing a coupling of the magnetic order to the lattice in this T-($Ca_{0.74(2)}Mn_{0.26}$)$MnFeReO_6$ material as well.

Other notable results that can be extracted from Rietveld analysis of this phase can be observed in the BVS values at 2 K (**Table 4.15**) for Fe and Re. These values

suggest BVS at 2 K of 3.5 (Fe) and 3.85 (Re). Perhaps initially surprising, this is likely an artefact of Rietveld refinement.

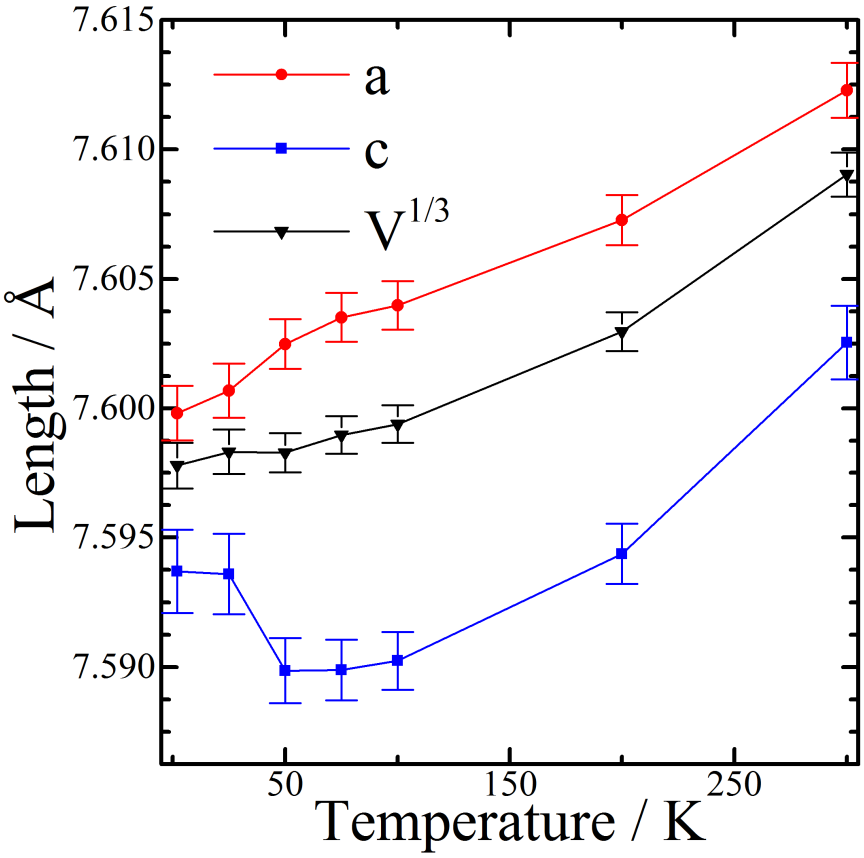

Figure 4.22 | *Thermal dependence of T-$(Ca_{0.74(2)}Mn_{0.26})MnFeReO_6$ lattice parameters a and c, as well as the cube root of volume, $V^{1/3}$. A negative thermal expansion of the c-axis can be noted that coincides with the onset of magnetic order.*

It is possible that a large amount of disorder between Fe and Re could cause the BVS result, but X-ray diffraction only yields a 5.0(1) % B-antisite disorder. This suggests that the peculiar Fe and Re BVS are due to correlations in refinements of this mixture of complex and rather similar structures resulting in difficulty in the accurate placement of the O^{2-} anions. Stable refinements which place reasonable coordination environments around Fe and Re for these phases cannot be reliably achieved.

4.3.2.c Magnetometry: x = 0.5

The temperature dependence of the magnetisation has been measured for samples of x = 0.5 and is shown in **Fig. 4.23** and reproduced in **Fig. 4.24**. Magnetic moments from neutron diffraction are overlaid on top of this M vs. T plot for the A-site disordered phase (**Fig. 4.23**) and for the A-site ordered phase (**Fig. 4.24**). In this sample (#4) a 1.27 ratio of monoclinic:tetragonal phases is present based on laboratory X-ray analysis.

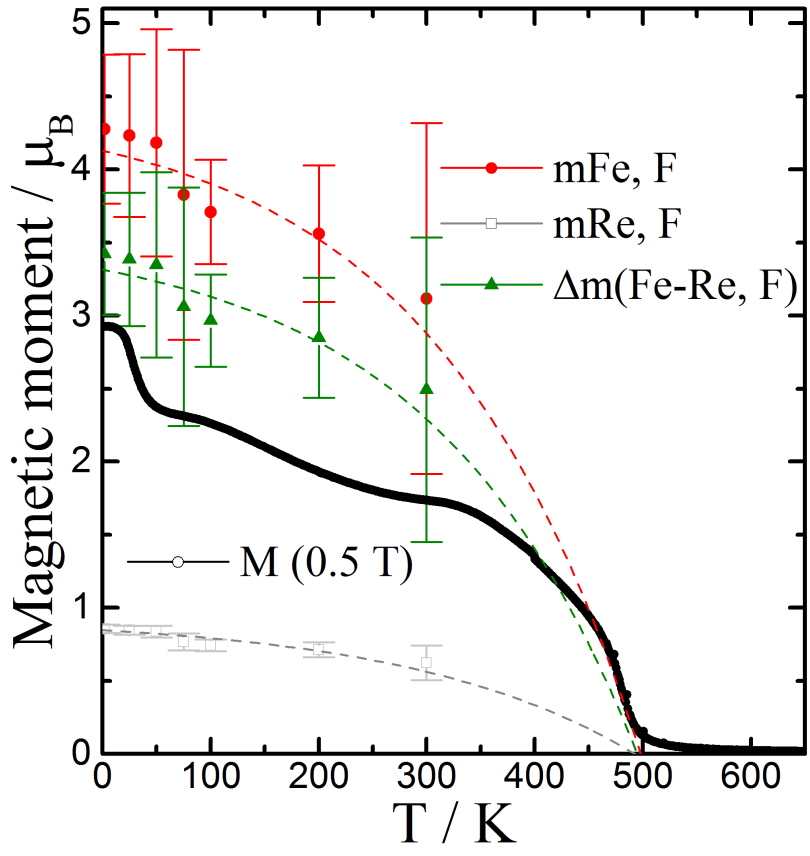

Figure 4.23 | *Magnetisation vs. temperature obtained from SQUID magnetometry from T = 0-650 K for $Ca_xMn_{2-x}FeReO_6$ with nominal x = 0.5 (field-cooled, 0.5 T). Overlaid on this plot are also the ferrimagnetic components of magnetic moments for Fe and Re (i.e. neglecting the antiferromagnetic y-component of magnetic moment) for M-$(Ca_{0.17(3)}Mn_{1.83})FeReO_6$, as well as the difference between these two moments, represented as Δm(Fe-Re, F). Also present in the magnetometry data is the T-$(Ca_{0.74(2)}Mn_{0.26})MnFeReO_6$ phase, explaining the appearance of many transitions.*

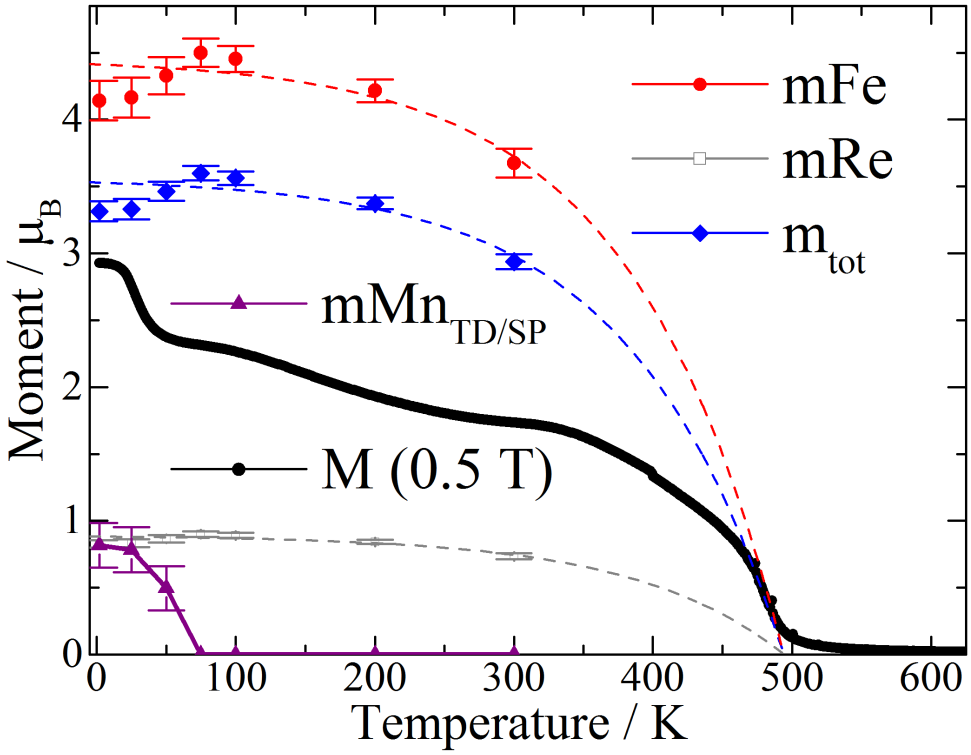

Figure 4.24 | *Magnetisation of $Ca_xMn_{2-x}FeReO_6$ with nominal x = 0.5 (field cooled, 0.5 T) with the magnetic moments from neutron refinements of the T-$(Ca_{0.74(2)}Mn_{0.26})MnFeReO_6$ phase: mFe, mRe and ferrimagnetic A-sites overlaid on this plot (constraint: mMn_{TD} = mMn_{SP}). Also plotted in the total magnetic moment observed of this phase, m_{tot}, from neutron diffraction. The onset of A-site Mn spin order also seems to coincide with a reduction in the observed B-site moments. A T_c of 498 K is found from the magnetometry data.*

When compared to the x = 0 and x = 1.0 materials on either side of this composition, the x = 0.5 biphasic material appears to have a comparable T_c to the x = 1.0 material of approximately 500 K. Neutron diffraction shows that the monoclinic A-site disordered phase follows a similar trend to that observed in M-Mn_2FeReO_6, however due to the data available and the complexity of this magnetic structure, the uncertainties associated with these moments are high and any deviations from this structure due to the Ca substitution cannot be reliably determined. The tetragonal A-site ordered phase does however show a peculiar reduction in B-site magnetic moment in the neutron diffraction analysis in datasets at 50 K and below, which coincides with

the A-site magnetic ordering temperature. This could be evidence of some form of a reorientation transition, perhaps similar to what is observed in the $x = 0$ (M-Mn_2FeReO_6) material, caused by the additional magnetic A-site Mn^{2+} occupying the 10-coordinate Ca^{2+} sites. It is also possible that this is simply another artefact of correlations between parameters in Rietveld refinements because of these biphasic neutron patterns, and an analysis of these materials as single phases would be required to evaluate this.

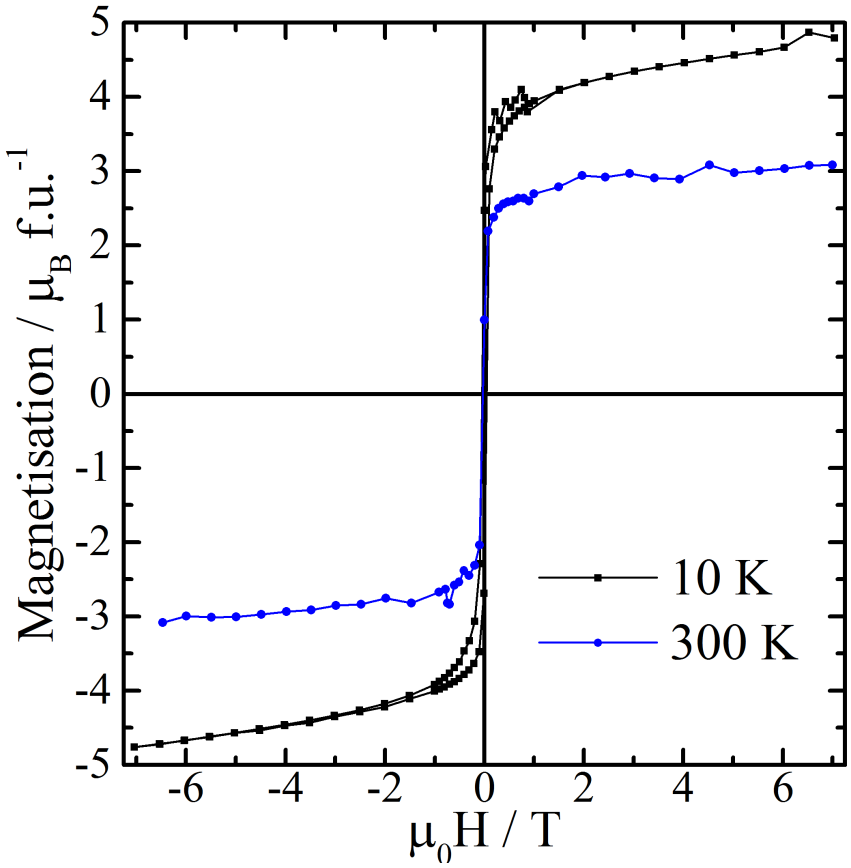

Figure 4.25 | *Magnetic hysteresis loops between fields of μ_0H = +7 and -7 T on $Ca_xMn_{2-x}FeReO_6$ with nominal x = 0.5 (biphasic mixture) at constant temperatures of 2 and 300 K.*

Magnetic hysteresis of the $x = 0.5$ sample shows an exceptionally high value of saturated magnetisation at low temperatures of 4.8 μ_B f.u.$^{-1}$. This is comparable to

the values of saturated magnetisation achieved in the x = 0 material (M-Mn_2FeReO_6: 5.0 μ_B f.u.$^{-1}$ at 75 K and 4.8 μ_B f.u.$^{-1}$ at 2 K) which was a record for an all transition metal double perovskite. Considering this is a two-phase mixture of perovskite-type phases in x = 0.5, and this 4.8 μ_B f.u.$^{-1}$ value of magnetisation is a weighted average of these two phases, it is likely that a pure sample of one of these phases may have saturated values of magnetisation that exceed those of M-Mn_2FeReO_6. The substitution of Mn by Ca causes the dilution of antiferromagnetic Mn spin order from M-Mn_2FeReO_6, which likely leads to paramagnetic A-site Mn spins being aligned by the applied magnetic field, enhancing magnetisation. A more thorough study of these materials could maximise the contribution to magnetisation from A-site Mn order by variation of the composition, diluting A-site antiferromagnetic interactions while maintaining some Mn to enhance magnetisation.

4.3.3. $Ca_xMn_{2-x}FeReO_6$: x = 1.5

4.3.3.a Phase Analysis & Crystal Structure: x = 1.5

Initial phase analysis on syntheses where x = 1.5 were carried out by X-ray diffraction using a Bruker D2 Phaser diffractometer. These patterns (shown as a stacked plot in **Fig. 4.26**) can be well fit by a monoclinic double perovskite phase with $P2_1/n$ symmetry. General characteristics of the products obtained from these x = 1.5 syntheses are shown in **Table 4.17**, with ReO_2 being the main impurity observed and can be detected in products 3, 4 and 5. There is also the presence of a small amount of Re metal that can be detected in synthesis 6.

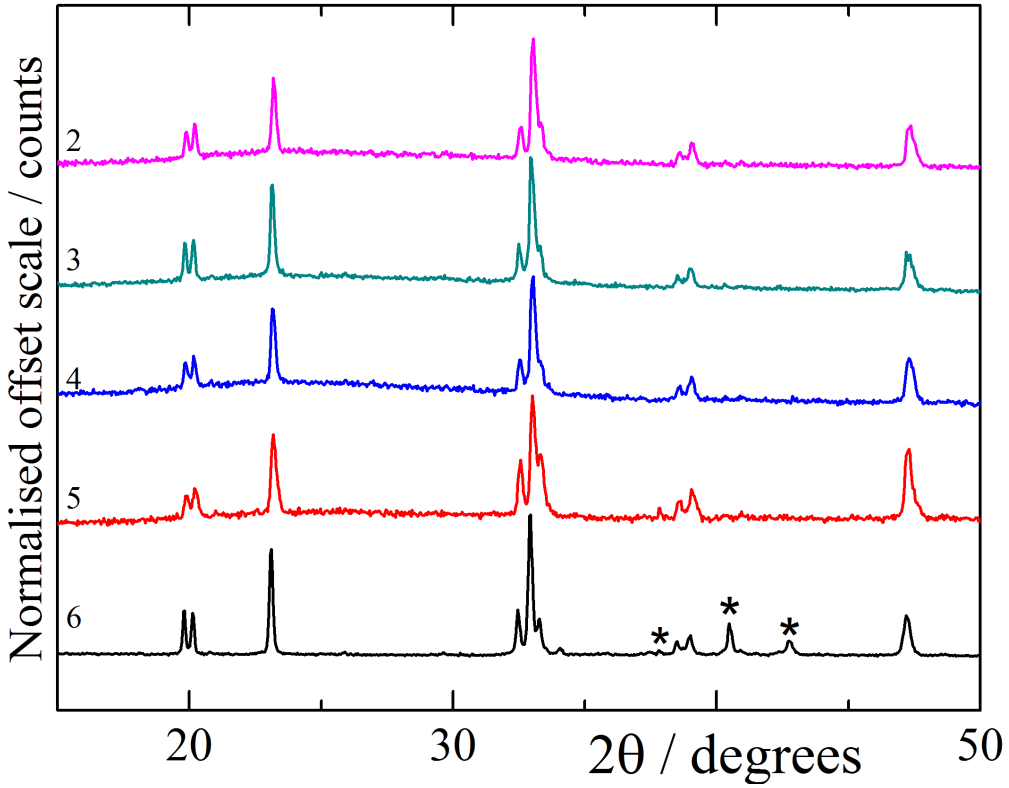

Figure 4.26 | *A stacked plot of the raw powder X-ray data initially collected on samples of synthetic products of $Ca_xMn_{2-x}FeReO_6$ with nominal x = 1.5 for phase analysis (in the 2θ range 15-50°). Asterisks mark the reflections due to metallic Re, present only in sample 6.*

Table 4.17 | A collection of the synthesis conditions and measure of the resulting purity and B-site disorder in the $P2_1/n$ M-$Ca_{1.5}Mn_{0.5}FeReO_6$ double perovskite product.

Sample no.	Pressure / GPa	Wt. ReO_2 / %	B-Antisite Disorder / %	χ^2	R_{wp} / %
2	10	0	11(1)	5.39	7.31
3	10	1.20(1)	7.4(6)	5.02	6.71
4	10	1.72(3)	12(1)	5.35	7.30
5	10	1.53(3)	12.0(8)	4.32	8.45
6	10	0	7.0(4)	5.13	5.38

Samples 3, 4 and 5 were mixed to create a 49 mg aggregate and examined by neutron diffraction on WISH at the ISIS Neutron Facility. The measures of fit, χ^2 and R_{wp}, are shown for X-ray patterns collected over 15 minutes using a Bruker D2 Phaser diffractometer with Cu K_α radiation. A Pt capsule was used for all syntheses. All syntheses were conducted with heating at 1400 °C for 20 minutes before being quenched.

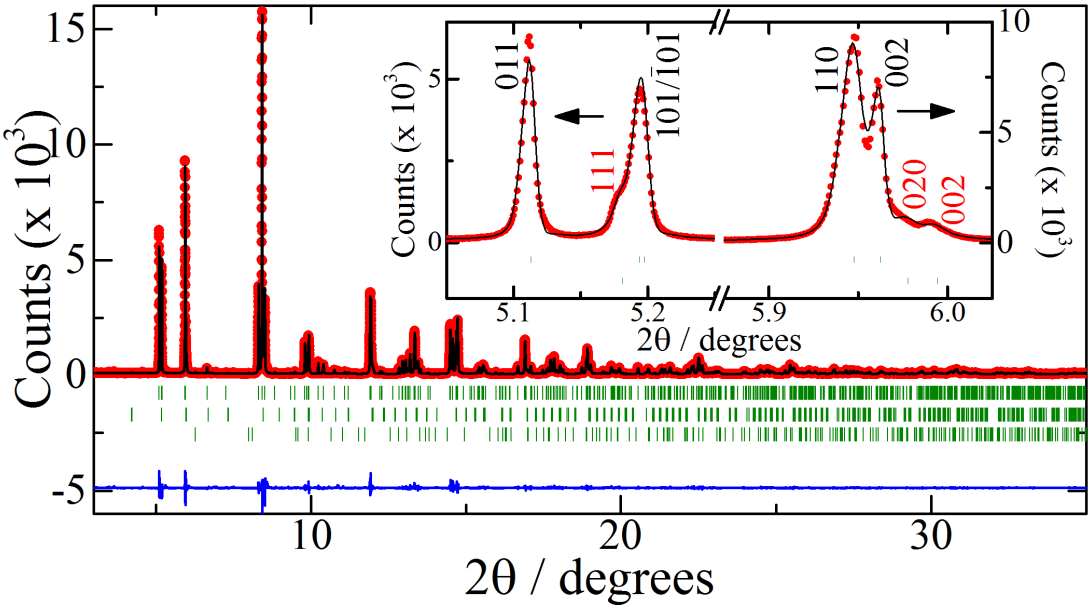

Figure 4.27 | *Rietveld fit to data collected from ID22 at the ESRF at 300 K for $Ca_xMn_{2-x}FeReO_6$ with nominal x = 1.5 (λ = 0.39987 Å). Ratios of Ca:Mn are fixed to the ratio of elements in the synthesis (3:1). The inset shows characteristic reflections from the double perovskite monoclinic phase (indices in black) and another perovskite-type phase fit with a tetragonal $P4_2/n$ double double structure (110 and 011 reflections due to columnar order are not observed due likely due to the small percentage of this phase). Rows of indices indicate phase 1 (88.0(2) % by weight) as $P2_1/n$ $Ca_{1.5}Mn_{0.5}FeReO_6$, phase 2 (11.88(6) % by weight) is fit with a $P4_2/n$ double double perovskite phase and phase 3 (0.09(1) % by weight) as a small quantity of ReO_2.*

Table 4.18 | Refined structure parameters for M-$Ca_{1.5}Mn_{0.5}FeReO_6$ at 300 K in space group $P2_1/n$ using synchrotron powder X-ray data from ID22 at the ESRF.

Atom	*x*	*y*	*z*	Occupancy	B_{iso} / Å²
Ca/Mn	0.0175(3)	0.0476(1)	0.2493(1)	0.75/0.25	0.270(3)
Fe/Re	0	½	0	0.948(2)/0.052	0.270
Re/Fe	½	0	0	0.948/0.052	0.270
O1	0.2978(7)	0.2918(7)	0.0520(7)	1	0.38(4)
O2	0.2959(7)	0.2944(7)	0.4524(7)	1	0.38
O3	0.5828(6)	0.9735(6)	0.2463(5)	1	0.38

Lattice parameters: $a = 5.38536(1)$, $b = 5.51731(1)$ and $c = 7.68841(1)$ Å with $\beta = 90.0456(2)°$; residuals R_{wp} = 3.75 % and χ^2 = 11.6. Ca:Mn occupancy is fixed to the synthesis composition of 3:1. This monoclinic phase constitutes 88.0(2) % by weight of the refined sample, with another minority phase observed 11.88(6) %. This is assumed to be a tetragonal $P4_2/n$ phase, (as observed in $x = 0.5$ and 1.0) this is fit with lattice parameters: $a = 7.66839(6)$ and $c = 7.64770(7)$ Å. Insufficient data is present to adequately refine the structure of this phase. An impurity phase of 0.09 (1) % ReO_2 is also observed.

Sample 2 of $x = 1.5$ was studied by synchrotron X-ray diffraction at the ESRF on ID22. A Rietveld fit of this pattern is shown in **Fig. 4.27**, using a double perovskite structure with $P2_1/n$ symmetry. This model provides a good fit to the patterns obtained on this material, however this synchrotron data does also suggest the presence of another perovskite-type phase. As the $x = 0.5$ phase exhibited a phase coexistence between the monoclinic A-site disordered and tetragonal A-site columnar ordered phases, this additional perovskite-type phase has been fit with a tetragonal double double perovskite cell that seems to provide a good account of the additional reflections observed. Unlike the $x = 0.5$ material, which exhibits approximately equal amount of these two distinctly different phases, this $x = 1.5$ material only contains small amounts of this secondary perovskite phase (11.88(6) % by weight based on Rietveld fits). Also unlike the $x = 0.5$ phase, the additional perovskite-type phase in $x = 1.5$ is far more clearly resolved. This is seen in the inset of **Fig. 4.27**, where the red indices refer to the tetragonal phase that these reflections have been fit with and the black indices refer to the main monoclinic $P2_1/n$ double perovskite phase. Results from Rietveld fits of these structures to the synchrotron patterns are shown in **Table 4.18**.

The low proportion of the double double perovskite phase can be rationalised by the ratio of Ca:Mn being 3:1 in this composition and, as discussed in '*4.3.2. $Ca_xMn_{2-x}FeReO_6$: $x = 0.5$*', it seems unlikely that the double double perovskite phase would be able to accommodate Ca^{2+} in either of the two 4-coordinated A-sites. It then follows that this $x = 1.5$ composition should have a greater propensity to form the double perovskite A-site disordered phase, rather than adopting the columnar order of the double double perovskite phase. This secondary phase could therefore be a material

close in composition to T-$CaMnFeReO_6$ (x = 1.0), and therefore the A-site disordered main phase would then be more Ca-rich than intended (x > 1.5). However, the lattice parameters of this secondary phase, fit with an A-site ordered structure (a = 7.66839(6) and c = 7.68841(1) Å), differ somewhat from the lattice parameters of x = 1.0 (a = 7.62825(6) and c = 7.6267(1) Å). This suggests that this phase, if it is indeed another A/B-site columnar/rock salt ordered phase, must be compositionally different to T-$CaMnFeReO_6$. However determining the exact composition, or whether this phase is a different structure type entirely, is not possible with the limited data available, as it constitutes only a small amount of the product with limited Ca/Mn contrast by X-rays.

4.3.3.b Neutron Crystal & Magnetic Structure: x = 1.5

An aggregate of products from synthesis 3, 4 and 5 of x = 1.5 (49 mg) was studied by neutron diffraction using the WISH diffractometer at the ISIS Neutron Facility. A secondary double double perovskite-type phase can be seen in synchrotron data obtained on sample 2, however this secondary phase is not observed in the neutron data of this aggregate. This could be due to the statistics involved, or perhaps this secondary phase is highly dependent on the synthetic procedure and is simply not present in samples 3, 4 and 5. Rietveld fits using a double perovskite phase with $P2_1/n$ symmetry are shown in **Fig. 4.28** at 300 K and at 2 K, with an impurity phase of $MnFe_3O_5$ fit using an intensity matching le Bail model. With regard to the A-site composition of x = 1.5 products, a formula of M-$(Ca_{1.73(8)}Mn_{0.27})FeReO_6$ is found by neutron diffraction, yielding a more Ca-rich A-site disordered product than intended

of x = 1.73(8), when compared to the nominal value of x = 1.5. The double double perovskite phase that was observed in synchrotron diffraction patterns is therefore likely to be Mn–rich, with a value of x in the range: $1.0 < x < 1.5$.

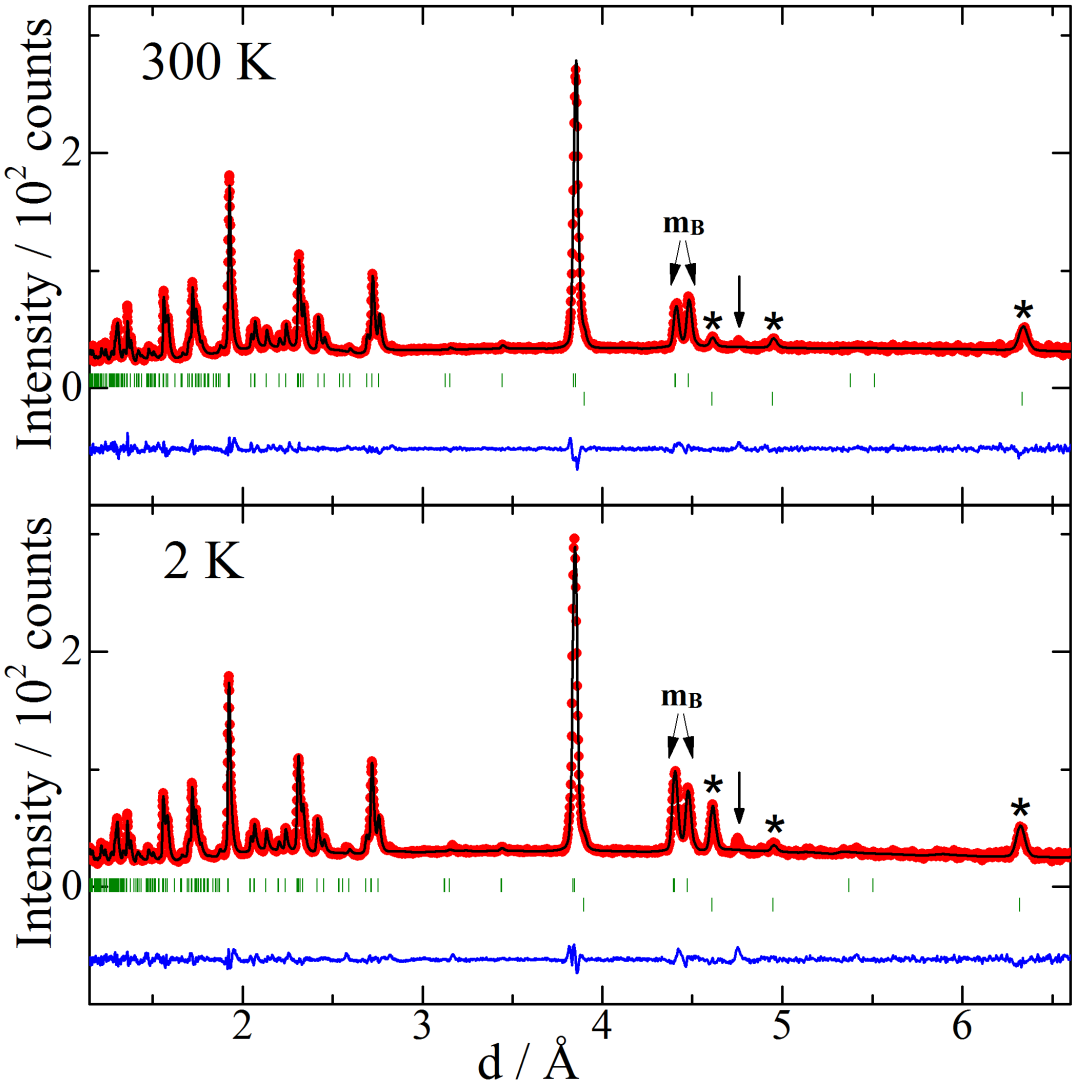

Figure 4.28 | *Combined nuclear and magnetic Rietveld fits to neutron diffraction data of $Ca_xMn_{2-x}FeReO_6$ with nominal x = 1.5, collected on the WISH diffractometer at the ISIS Neutron Facility. The patterns shown are from an average of bank 3 and 8.* ***Top****: 300 K.* ***Bottom****: 1.5 K. The markers m_B refer to magnetic reflections with contributions from B-site spin order. Lower markers index $MnFe_3O_5$, with the main reflections of this phase marked by asterisks. The arrow at d ~4.75 Å indicates an unknown impurity.*

There are magnetic reflections, marked m_B in **Fig. 4.28** and shown in more detail with their thermal evolution in **Fig. 4.29**, that can be determined to be due to ferrimagnetic Fe/Re spin order in M-$(Ca_{1.73(8)}Mn_{0.27})FeReO_6$. These magnetic reflections show a switch in intensity at a magnetic transition with an onset of approximately 75 K. The magnetic structures of M-$(Ca_{1.73(8)}Mn_{0.27})FeReO_6$ above and below this transition have been solved and determined to be due to a reorientation of the spin structure in this material.

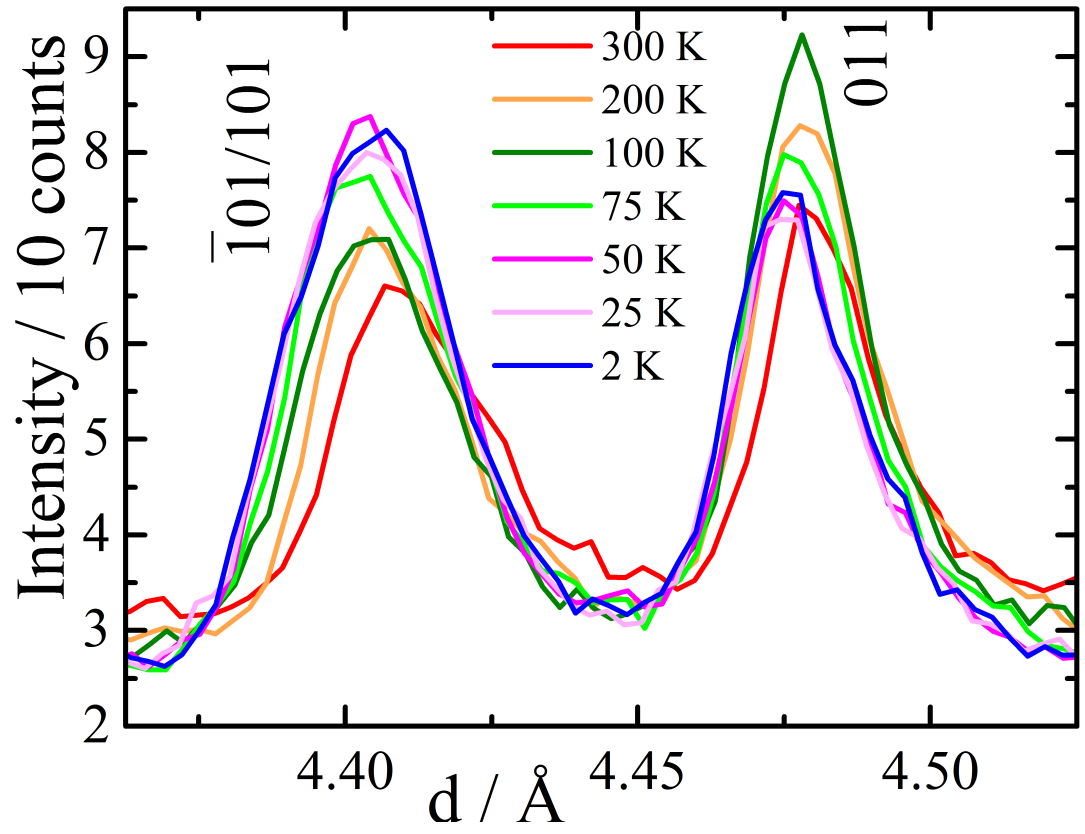

Figure 4.29 | *$Ca_xMn_{2-x}FeReO_6$, with nominal x = 1.5. Diffracted neutron intensities are shown for Fe/Re spin order in the region d ~4.35 Å between 300 and 2 K. The Miller indices are shown beside each reflection.*

The magnetic symmetry operations that describe the magnetic structures above and below this transition are shown in **Table 4.19** by the BasIreps definitions of

magnetic symmetry.[125] In the high-temperature regime, the basis vectors $\Gamma_3\psi_4$ and $\Gamma_3\psi_6$ describe ferrimagnetic G-type Fe/Re spin order in the *ac*-plane that adequately fits the neutron data. The low-temperature regime, after the spin reorientation, can be described with a combination of the two basis vectors present in the high-temperature regime, with an additional basis vector: $\Gamma_3\psi_4$. This additional basis vector preserves the G-type symmetry, but provides a substantial magnetic component along the *b*-axis. This change in spin direction corresponds with a 90° reorientation. Structural and magnetic results from Rietveld refinement are given here in **Table 4.20**, as well as A/B–O lengths, B–O–B′ angles and BVS at 2 and 300 K in **Table 4.21** and **4.22**.

Table 4.19 | Irreducible representations from BasIreps for Fe^{3+} and Re^{5+} spin ordering in M-$(Ca_{1.73(8)}Mn_{0.27})FeReO_6$ using the $\boldsymbol{k}$ = (0, 0, 0) propagation vector in space group $P2_1/n$.[125]

IrRep:	Γ_1			Γ_3		
Basis Vector:	ψ_1	ψ_2	ψ_3	ψ_4	ψ_5	ψ_6
Atoms	m_x	m_y	m_z	m_x	m_y	m_z
Fe1, Re1[a]	+	+	+	+	+	+
Fe2, Re2[b]	-	+	-	+	-	+

[a] Fe1 = (0, 0.5, 0); Re1 = (0.5, 0, 0). [b] Fe2 = (0.5, 0, 0.5); Re2 = (0, 0.5, 0.5). Coordinates at 2 K. Further details of magnetic structure solution are provided in '*2.2.7 – Magnetic Symmetry Analysis*'.

The magnetic structures of M-$(Ca_{1.73(8)}Mn_{0.27})FeReO_6$ above and below the reorientation transition are shown in **Fig. 4.30**. The high-temperature regime is notable for possessing the same structure identified in the $x = 0$ and the A-site disordered phase found in $x = 0.5$, where Fe^{3+} moments are oriented predominantly along the *c*-axis but with a small *a*-axis component, such that these moments are directed along the Fe–O3 bond. Re^{5+} moments are constrained to be antiparallel with a magnitude of one fifth of that of Fe^{3+} moments in these refinements. Cooling through the magnetic transition at approximately 75 K yields a low-temperature regime where spins are directed

predominantly in the *ab*-plane, making an angle of approximately 30° with the *b*-axis. There is a small, potentially negligible *c*-axis component of the magnetic moment. By also refining the *c*-axis component (rather than fixing it to zero), refinements converge with the direction of spins at 2 K along the (B/B′)–O1/O2 bonds, plotted in **Fig. 4.31** (albeit with large uncertainties in this *c*-component at temperatures of 25-75 K, but may be meaningful at 2 K).

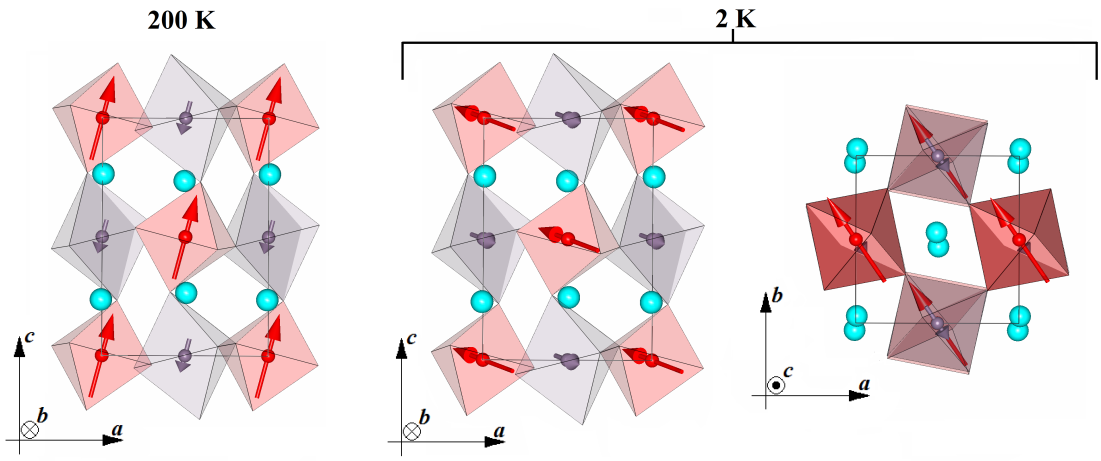

Figure 4.30 | *Magnetic structures of M-($Ca_{1.73(8)}Mn_{0.27}$)$FeReO_6$ at 200 K (with ferrimagnetic Fe/Re spin order in the ac-plane) and at 2 K (with ferrimagnetic Fe/Re spin order with large components on a and b. Fe ions shown as red, Re as grey and (Ca/Mn) as cyan. Images generated using FPStudio.*[125]

The magnetic reorientation and structural coupling in this material bear many similarities to that of the x = 2 material, M-Ca_2FeReO_6. In terms of the magnetic structures, the high-temperature regimes of these two materials are qualitatively the same with moments oriented in the *ac*-plane. Analysis by Oikawa et al. orientates these moments along the *c*-axis, however they do mention that better fits are achieved with moments in the *ac*-plane and indicate that their data may not have been sufficient to discern the small *a*-axis component.[82] The low-temperature magnetic structure of x = 2 was reported to have G-type symmetry, with moments oriented along the *b*-axis.

While this analysis finds that the magnetic structure of M-$(Ca_{1.73(8)}Mn_{0.27})FeReO_6$ consists of moments oriented in the *ab*-plane, with large components along both of these axes. This difference in the low-temperature magnetic structures of M-Ca_2FeReO_6 and M-$(Ca_{1.73(8)}Mn_{0.27})FeReO_6$, and the difference in ordering temperature (140 K in $x = 2$, ~75 K in $x = 1.73$) may be due to the variation in A-cation sizes between the two compositions, or this could be because of the effect of magnetic Mn^{2+} A-site cations.

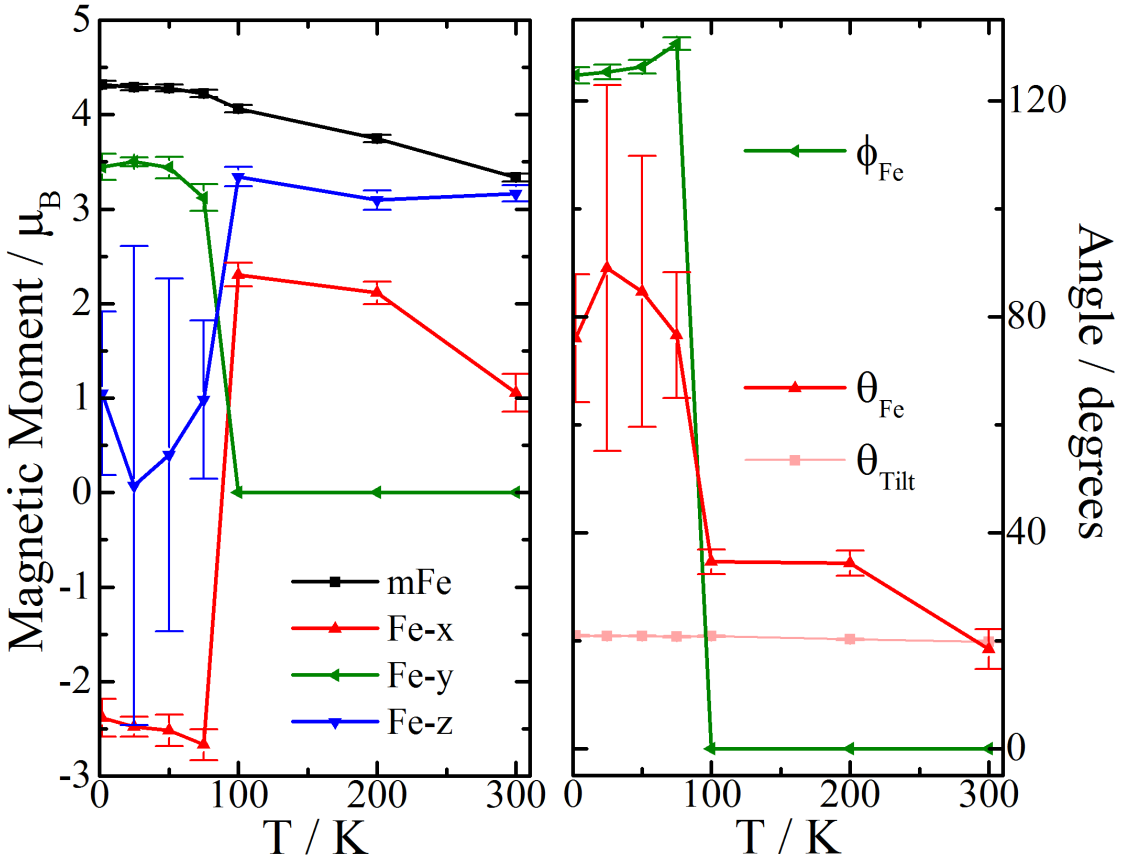

Figure 4.31 | *M-$(Ca_{1.73(8)}Mn_{0.27})FeReO_6$. **Left**: Magnetic components in the Cartesian coordinate system for Fe, as well as the total magnetic moment for the Fe site. **Right**: Polar angles for Fe, as well as FeO_6 octahedra tilts.*

Table 4.20 | Refined structure parameters for $Ca_xMn_{2-x}FeReO_6$ with nominal $x = 1.5$ at 2-300 K in space group $P2_1/n$ using neutron powder diffraction data from the WISH diffractometer at the ISIS Neutron Facility. Magnetic symmetry is follows the descriptions in **Table 4.19**. Sample size 49 mg. This phase is found to have a chemical formula of M-($Ca_{1.73(8)}Mn_{0.27}$)$FeReO_6$.

T / K		2	25	50	75	100	200	300
Cell	a / Å	5.3736	5.3738	5.3739	5.3738	5.3739	5.3782	5.3843
	b / Å	5.5094	5.5095	5.5102	5.5120	5.5153	5.5162	5.5168
	c / Å	7.6744	7.6747	7.6751	7.6745	7.6740	7.6771	7.6831
	β / °	89.9634	89.9957	89.9868	89.9687	90.0500	90.0402	89.9961
	V / Å^3	227.20(6)	227.22(6)	227.27(6)	227.32(6)	227.45(6)	227.76(6)	228.22(5)
A	x	0.991(3)	0.993(3)	0.995(3)	0.996(3)	0.994(3)	0.996(2)	0.997(2)
	y	0.958(2)	0.960(2)	0.959(2)	0.959(2)	0.957(2)	0.956(2)	0.957(2)
	z	0.263(4)	0.265(3)	0.267(3)	0.267(3)	0.267(3)	0.266(3)	0.264(3)
O1	x	0.301(3)	0.302(3)	0.302(3)	0.305(4)	0.313(3)	0.313(3)	0.305(6)
	y	0.300(4)	0.302(4)	0.303(4)	0.290(4)	0.288(3)	0.290(4)	0.293(6)
	z	0.945(2)	0.944(2)	0.946(2)	0.947(2)	0.949(2)	0.949(2)	0.961(2)
O2	x	0.308(3)	0.306(3)	0.306(3)	0.304(3)	0.294(3)	0.295(3)	0.305(6)
	y	0.291(4)	0.291(3)	0.291(3)	0.304(4)	0.303(3)	0.302(4)	0.299(7)
	z	0.534(2)	0.533(2)	0.533(2)	0.535(2)	0.537(2)	0.537(2)	0.550(2)
O3	x	0.912(1)	0.913(1)	0.913(1)	0.912(1)	0.911(1)	0.9118(9)	0.9125(9)
	y	0.464(1)	0.466(1)	0.467(1)	0.467(1)	0.466(1)	0.4665(9)	0.4668(9)
	z	0.730(2)	0.729(2)	0.729(2)	0.732(2)	0.735(2)	0.739(3)	0.743(4)
θ_{Tilt} / degrees		8.6(2)	8.4(2)	8.3(2)	8.1(2)	8.2(2)	8.0(2)	7.8(2)
φ_{Tilt} / degrees		20.9(1)	20.8(0)	20.8(1)	20.7(1)	20.8(1)	20.2(1)	19.8(1)
mFe / μ_B		4.32(4)	4.29(4)	4.28(4)	4.22(4)	4.06(4)	3.75(4)	3.34(4)
φ_{Fe} / °		125(1)	125(1)	126(1)	131(1)	0	0	0
θ_{Fe} / °		76(12)	89(33)	85(25)	77(12)	35(2)	34(2)	18(4)
mFe_x / μ_B		-2.4(2)	-2.5(1)	-2.5(2)	-2.7(2)	2.3(1)	2.1(1)	1.1(2)
mFe_y / μ_B		3.4(1)	3.50(5)	3.4(1)	3.1(1)	0	0	0
mFe_z / μ_B		1.0(9)	0.08(254)	0.4(19)	1.0(8)	3.3(1)	3.1(1)	3.16(9)
mRe / μ_B		0.864(7)	0.858(7)	0.856(7)	0.844(8)	0.812(8)	0.749(8)	0.667(8)
m_{tot} / μ_B		3.46(3)	3.43(3)	3.42(3)	3.38(3)	3.25(3)	3.00(3)	2.67(3)
A/B	B_{iso} / Å^2	0.756(1)	0.79(1)	0.78(1)	0.79(1)	0.82(1)	0.85(1)	0.95(2)
O	B_{iso} / Å^2	0.49(2)	0.51(2)	0.52(2)	0.56(2)	0.56(2)	0.60(2)	0.69(2)
R_{wp} / %		4.18	4.14	4.10	3.98	3.91	3.55	3.28
χ^2		3.33	4.10	4.03	3.83	3.74	3.52	3.12
Q / μA·h		36	45	45	45	45	50	50

Fe atoms are located at (0, ½, 0), with Re atoms at (½, 0, 0). Antisite disorder of Fe/Re is not refined due to poor neutron contrast. The total magnetic moment determined from neutron diffraction, m_{tot}, is defined as mFe - mRe. No site mixing between A and B-sites was found. A-sites are found to be 86.5(4) % Ca, with 13.5 % Mn. Q, a measure of the total length of exposure of the sample to the neutron beam ($Q = I \cdot t$), is also tabulated.

Table 4.21 | Bond lengths, angles and BVS values for M-($Ca_{1.73(8)}Mn_{0.27}$)$FeReO_6$ in space group $P2_1/n$ from the neutron profile fit at 2 K.

Bond	M – O length / Å	Bond	M – O length / Å
Ca/Mn – O1	2.19(3)	Fe – O1	2.00(2) × 2
Ca/Mn – O1	2.65(3)	Fe – O2	1.92(3) × 2
Ca/Mn – O1	2.65(4)	Fe – O3	2.14(1) × 2
Ca/Mn – O2	2.44(3)	**<Fe – O>**	2.02(1)
Ca/Mn – O2	2.62(3)		
Ca/Mn – O2	2.68(4)	Re – O1	2.01(3) × 2
Ca/Mn – O3	2.32(2)	Re – O2	2.03(2) × 2
Ca/Mn – O3	2.39(1)	Re – O3	1.83(1) × 2
<Ca/Mn – O>	2.49(1)	**<Re – O>**	1.96(1)
Cation	**BVS**	**B – O# – B′**	**Angle / degrees**
Ca/Mn/<Ca/Mn>	2.16/1.34/1.96	Fe – O1 – Re	147(1)
Fe	3.05	Fe – O2 – Re	153(1)
Re	4.73	Fe – O3 – Re	150.2(4)

The program BondStr in the FullProf Suite was used to compute this data.[125]

Table 4.22 | Bond lengths, angles and BVS values for M-($Ca_{1.73(8)}Mn_{0.27}$)$FeReO_6$ in space group $P2_1/n$ from the neutron profile fit at 300 K.

Bond	M – O length / Å	Bond	M – O length / Å
Ca/Mn – O1	2.29(4)	Fe – O1	2.02(4) × 2
Ca/Mn – O1	2.53(3)	Fe – O2	1.99(4) × 2
Ca/Mn – O1	2.75(4)	Fe – O3	2.04(3) × 2
Ca/Mn – O2	2.36(4)	**<Fe – O>**	2.02(2)
Ca/Mn – O2	2.59(4)		
Ca/Mn – O2	2.78(4)	Re – O1	1.95(4) × 2
Ca/Mn – O3	2.28(1)	Re – O2	2.02(4) × 2
Ca/Mn – O3	2.39(1)	Re – O3	1.93(3) × 2
<Ca/Mn – O>	2.50(1)	**<Re – O>**	1.97(2)
Cation	**BVS**	**B – O# – B′**	**Angle / degrees**
Ca/Mn/<Ca/Mn>	2.14/1.33/1.94	Fe – O1 – Re	152(2)
Fe	2.99	Fe – O2 – Re	148(2)
Re	4.51	Fe – O3 – Re	150.5(3)

The program BondStr in the FullProf Suite was used to compute this data.[125]

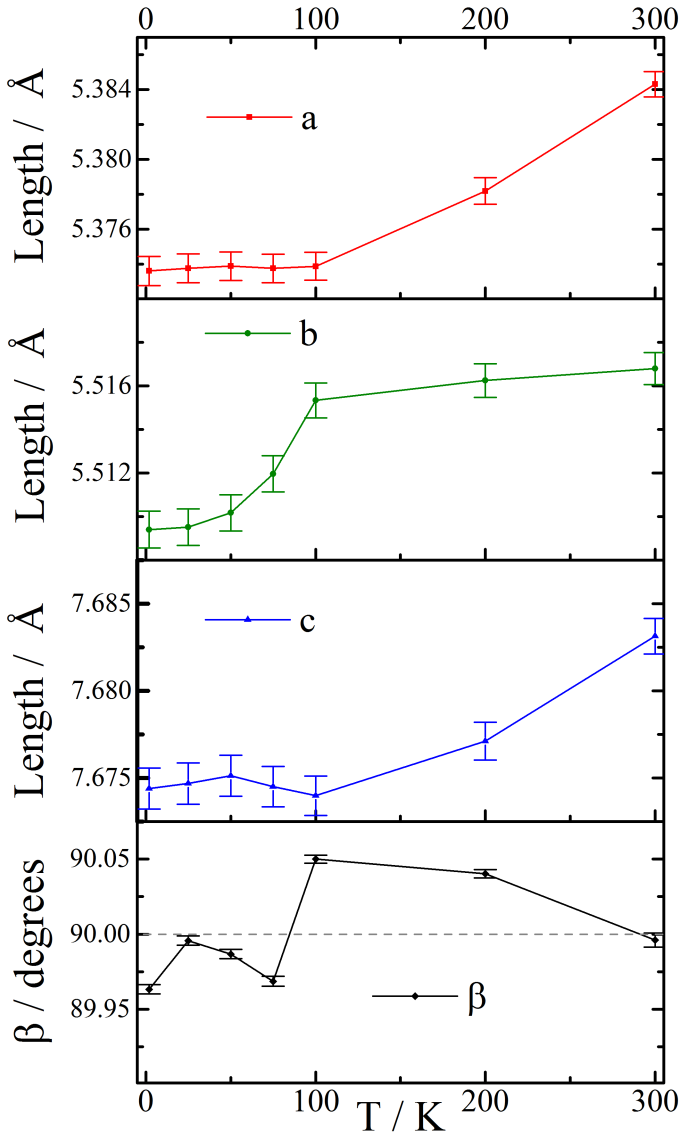

Figure 4.32 | *Temperature variation of M-($Ca_{1.73(8)}Mn_{0.27}$)$FeReO_6$ lattice parameters: a, b, c and β, from refined data obtained on WISH at the ISIS Neutron Facility.*

Coupling of magnetic order to the lattice in M-($Ca_{1.73(8)}Mn_{0.27}$)$FeReO_6$ is evident in the thermal evolution of lattice parameters (**Fig. 4.32**). Below 100 K a rapid contraction in the *b*-axis is observed, while the *a*/*c*-axes exhibit no significant thermal dependence below this temperature. An apparent switch in the *β* parameter is also evident at the magnetic transition, from values greater than 90° in the high-temperature regime to less than 90° below the transition. These effects are similar to those observed

in $x = 2$. The combination of magnetic reorientation and structural distortions observed in $x = 2$ are attributed to orbital ordering of Re^{5+} at low temperatures. As Re^{5+} is Jahn-Teller active, it would be expected that the ground state in these materials would consist of a J-T expansion of $Re^{5+}O_6$ octahedra, with a pair of long Re–O bonds and two pairs of short Re–O bonds. This is found in the $x = 2$ material, as at high temperature a compression is seen in the form of a pair of short Re–O3 bonds (along the *c*-axis) and at low temperatures a pair of long Re–O2 bonds is found (in the *ab*-plane).

In M-$(Ca_{1.73(8)}Mn_{0.27})FeReO_6$ a slight expansion of Re octahedra with pairs of long Re–O2 bonds is found in the *ab*-plane, which transform at low temperatures to compressed of ReO_6 octahedra, with the compressed pair of bonds being Re–O3 (along the *c*-axis), contrary to the expected expansion if orbital ordering were present. The change in ReO_6 distortion may be related to the lattice distortions of M-$(Ca_{1.73(8)}Mn_{0.27})FeReO_6$, however the lack of a ground state that contains expanded ReO_6 octahedra suggests that this is not orbital ordering of Re^{5+}. Other factors may be responsible for this change of distortion such as a mixed valence state of Re^{5+}/Re^{6+} or additional magnetic interactions due to A-site Mn^{2+}.

4.3.3.c Magnetometry: x = 1.5

Magnetometry vs. *T* performed on samples of $x = 1.5$ (**Fig. 4.33**) shows a similar T_c to that of previous samples studied in this series ($T_c = 490$ K). This transition is due to the G-type ferrimagnetic order of Fe/Re, as determined by neutron diffraction. A second transition can be observed at ~120 K, which could potentially be the onset

of the magnetic reorientation, where the spin structure reorientates away from the ac-plane and on to the ab-plane. A second transition below ~50 K could be the onset of magnetic effects due to the presence of paramagnetic A-site Mn^{2+}.

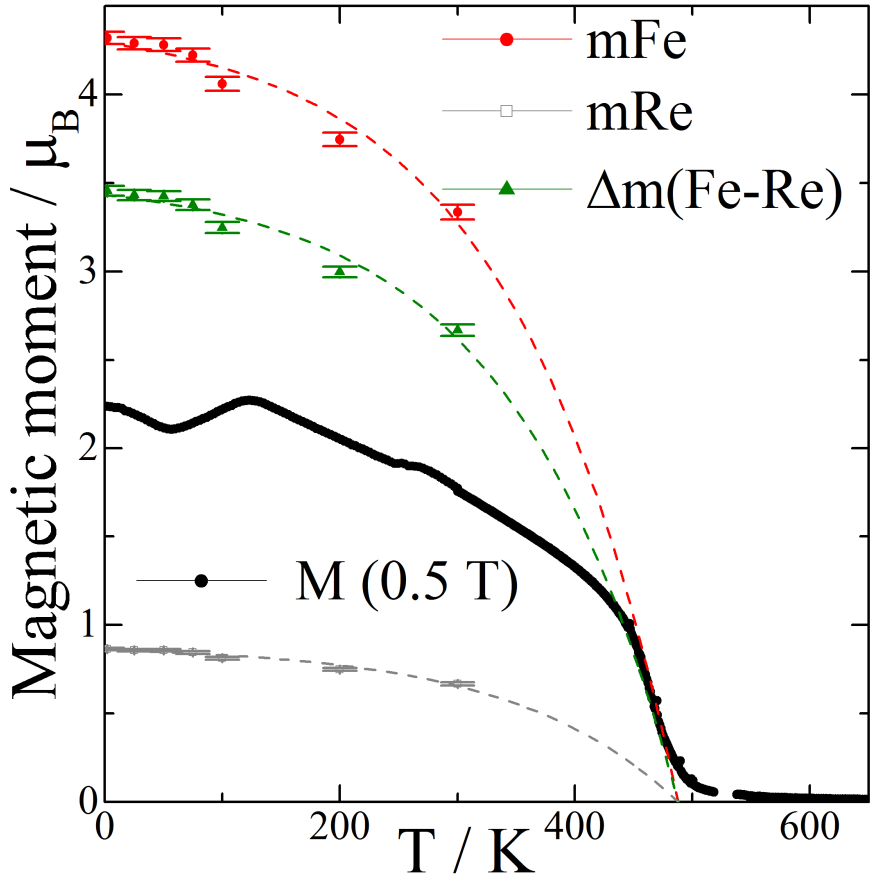

Figure 4.33 | *Magnetisation of M-$(Ca_{1.73(8)}Mn_{0.27})FeReO_6$ (field cooled, 0.5 T) with the magnetic moments from neutron refinements of Fe and Re overlaid on this plot. Also plotted is the total magnetic moment observed from neutron diffraction, equivalent to mFe - mRe. T_c = 490 K.*

Interesting behaviour can be observed from *M* vs. *H* hysteresis measurements (**Fig. 4.34**), as a coercive field of $\mu_0 H_c$ = 0.5 T emerges at low temperatures. Small coercive fields are found for all other members of the $Ca_xMn_{2-x}FeReO_6$ series but notably coercive fields of around 1 T have been found in M-Ca_2FeReO_6.[81] While the coercive field in this M-$(Ca_{1.73(8)}Mn_{0.27})FeReO_6$ material does not equal that of the x = 2 material, the fact that large coercive fields are emerging in this series at values closer

to x = 2 suggests that this M-$(Ca_{1.73(8)}Mn_{0.27})FeReO_6$ material must possess similar qualities to the Ca-pure analogue which provides this high coercivity.

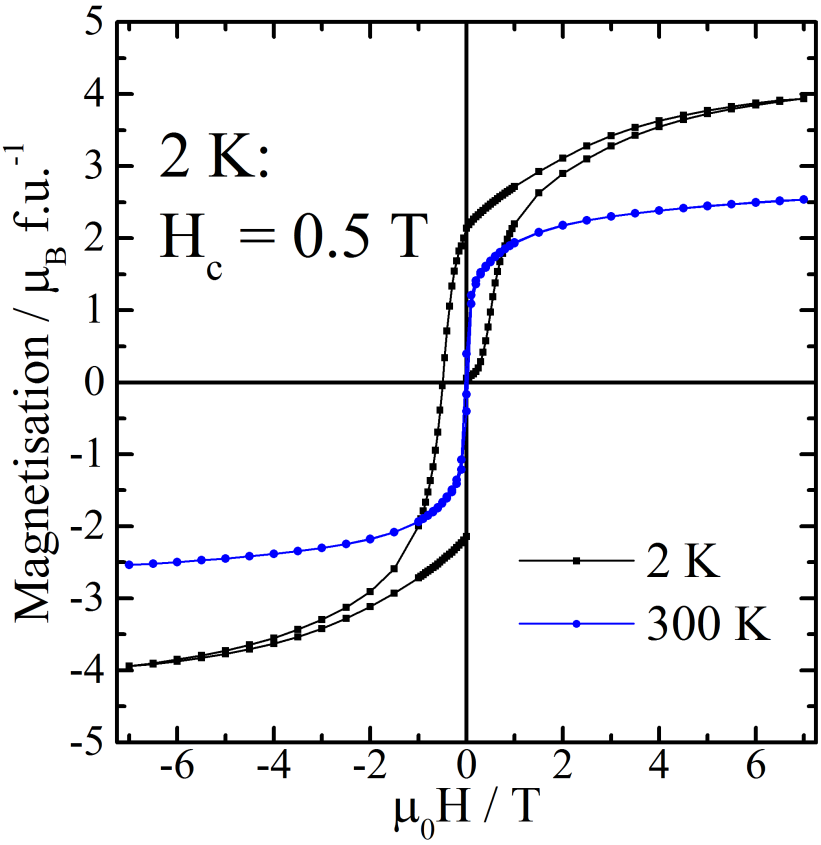

Figure 4.34 | *Magnetic hysteresis loops between fields of μ_0H = +7 and -7 T of $Ca_{1.5}Mn_{0.5}FeReO_6$ at constant temperatures of 2 and 300 K. At 2 K a large coercive field of H_c = 0.5 T can be observed.*

Differences in the coercivity of AA′$FeReO_6$ double perovskites are discussed by De Teresa et al.[81] They show that coercivities of ~0.4 T are found in samples of Sr_2FeReO_6 and $(Ca_{0.5}Sr_{1.5})FeReO_6$, but reducing the cation size further increases the coercivity to values of ~0.9 T in (CaSr)$FeReO_6$ and peaking at ~1.4 T in $(Ca_{1.5}Sr_{0.5})FeReO_6$, before decreasing to ~0.9 T in Ca_2FeReO_6. The finding here that by decreasing the cation size further in M-$(Ca_{1.73(8)}Mn_{0.27})FeReO_6$ results in coercivity of ~0.5 T (and of ~0.05 T in the case of T-$CaMnFeReO_6$ and materials with smaller cation size), suggests that the magnetic coercivity is related closely to the A-cation

size (and therefore tilts of BO_6 octahedra and the B–O–B′ connectivity), with maximum effect observed in the $(Ca_{1.5}Sr_{0.5})FeReO_6$ material. It is suggested that the high coercivities in these materials are related to the magnetostructural transition observed in Ca_2FeReO_6, and while the distortions found in the analysis of M-$(Ca_{1.73(8)}Mn_{0.27})FeReO_6$ here do not indicate an orbitally ordered expanded distortion of $Re^{5+}O_6$, a very similar magnetic transition is observed, along with a switch in the compressed axis of the $Re^{5+}O_6$ octahedra, suggesting this magnetostructural transition in M-$(Ca_{1.73(8)}Mn_{0.27})FeReO_6$ is likely to be linked to the high coercivity.

4.3.3.d X-ray Magnetic Circular Dichroism: x = 1.5

X-ray Absorption Near-Edge Spectra (XANES) and X-ray Magnetic Circular Dichroism (XMCD) have only been measured at 290 K for this sample (shown in **Fig. 4.35** and **4.46** for the Re L_2-edge and Re L_3-edge respectively), nevertheless this still provides an important insight into the magnetic behaviour of Re. As in the x = 1.0 material, this data has been interpreted by use of **Equation 2.31** in '*2.3.3. X-ray Magnetic Circular Dichroism*' and from this a ratio of spin to orbital moment can be calculated. The absolute values of spin (m_S) and orbital moment (m_L) can also be estimated by using a value of the number of d-state electron holes (n_h) of 8 and 9, which can be considered lower and upper bounds for the corresponding values of m_S and m_L. The total moment of Re, *mRe*, can also be estimated from this as the sum of m_S and m_L. These values are listed at 290 K in **Table 4.23**.

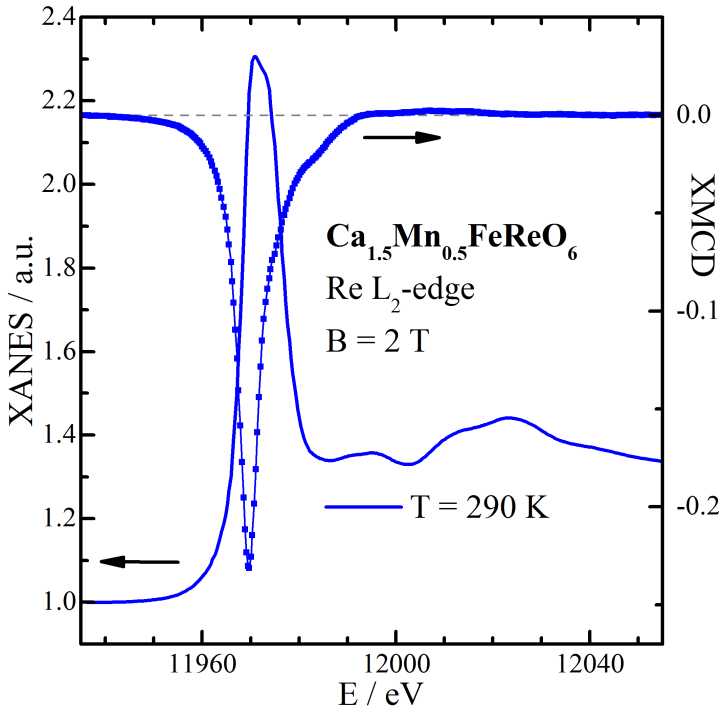

Figure 4.35 | *X-ray Absorption Near-Edge and X-ray Magnetic Circular Dichroism on $Ca_xMn_{2-x}FeReO_6$, x = 1.5, Re L_2-edge.*

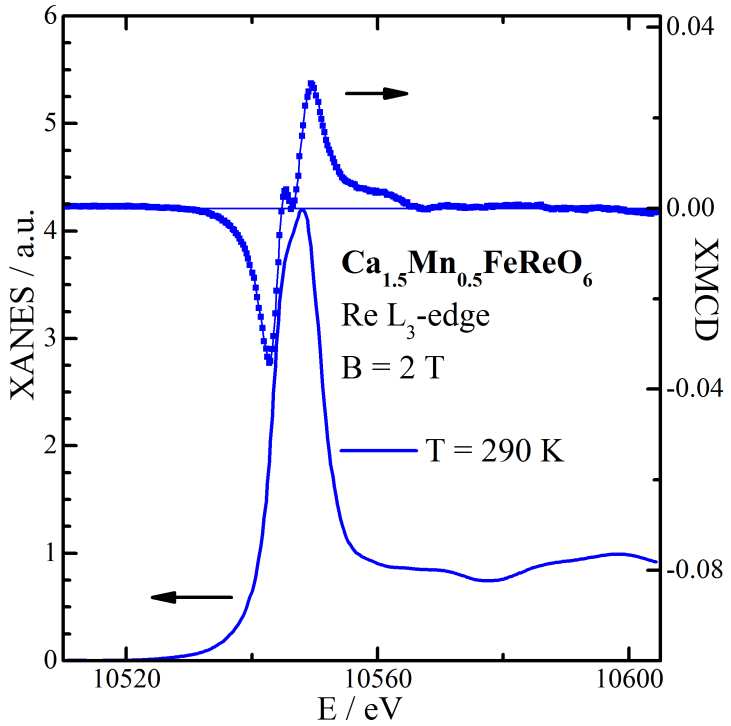

Figure 4.36 | *X-ray Absorption Near-Edge and X-ray Magnetic Circular Dichroism on $Ca_xMn_{2-x}FeReO_6$, x = 1.5, Re L_3-edge.*

Table 4.23 | Calculated orbit (m_L) and spin (m_S) moments from XMCD data at B = 2 T for Re at n_h values of 8 and 9, their ratio: m_S/m_L and the total Re moment: mRe.

	m_S/m_L	m_L / μ_B		m_S / μ_B		mRe / μ_B	
T / K	n_h:	8	9	8	9	8	9
290	-3.07	0.22	0.24	-0.66	-0.74	-0.45	-0.50

Negative moments refer to antiparallel alignment to Fe moments.

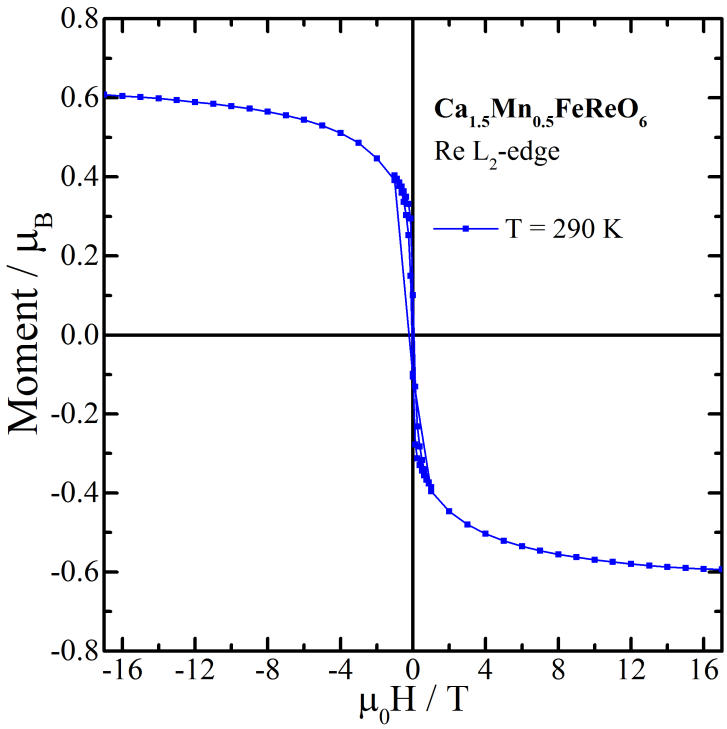

Figure 4.37 | *XMCD hysteresis of the Re L_2-edge ($Ca_xMn_{2-x}FeReO_6$ with nominal x = 1.5) at field strengths in the range of ±17 T. These measurements have been normalised to values of m_{Re} (n_h = 8) calculated from sum rules at each temperature. Two hysteresis loops are plotted, ±17 T in 1 T intervals and ±1 T in 0.125 T intervals.*

The XMCD hysteresis for Re in **Fig. 4.37** shows a similar saturation of the Re moment (~0.6 μ_B) as observed in the x = 1.0 material. Unfortunately, only high-temperature XMCD data was able to be collected for this material and comparisons of the Re coercive field in this material are not able to be made above and below the magnetic transition, where magnetometry shows a large coercive field emerge. Nevertheless, this XMCD data does indicate that a measurable unquenched Re orbital

moment is present and the values of m_S/m_L found here for M-$(Ca_{1.73(8)}Mn_{0.27})FeReO_6$ can be compared to those found for M-Mn_2FeReO_6 and T-$CaMnFeReO_6$, as well as to literature values of M-Ca_2FeReO_6, in the following section.

4.4. Comparisons & Conclusions

This study of $Ca_xMn_{2-x}FeReO_6$ set out to provide a means of understanding incremental changes between M-Ca_2FeReO_6 and M-Mn_2FeReO_6 by means of synthesising materials with nominal values of x = 0.5, 1.0 and 1.5. However, the discovery of a structure type with combined A and B-site orders amongst the materials in this series complicates analysis of clear trends due to simply changing the proportion of Mn to Ca. The phase fractions of these disordered monoclinic phases ($P2_1/n$) compared to the ordered tetragonal phases ($P4_2/n$) as the nominal value of x is varied are shown in **Fig. 4.38**, as found from X-ray diffraction. This plot includes data from x = 0, 1 and 2, which are found to only contain a single perovskite phase of M-Mn_2FeReO_6, T-$Ca(Mn_{0.88(4)}Fe_{0.12})FeReO_6$ and M-Ca_2FeReO_6, respectively. Also shown are the nominal x = 0.5 and x = 1.5 samples, which exist as phase mixtures of monoclinic and tetragonal perovskite phases. The refined values of x found from neutron diffraction for the monoclinic phase (x = 0.17(3)) and the tetragonal phase (x = 0.74(2)) in nominal x = 0.5 products are also plotted in blue. A straight line linking these two points passes through 0.5 (a 50:50 mixture of $P2_1/n$ and $P4_2/n$ phases) at x = 0.455, which is exactly halfway between the two values of x for these points. This strongly suggests that these points represent solubility limits in this phase diagram and solid grey lines are shown in **Fig. 4.38** to indicate these solubility limits.

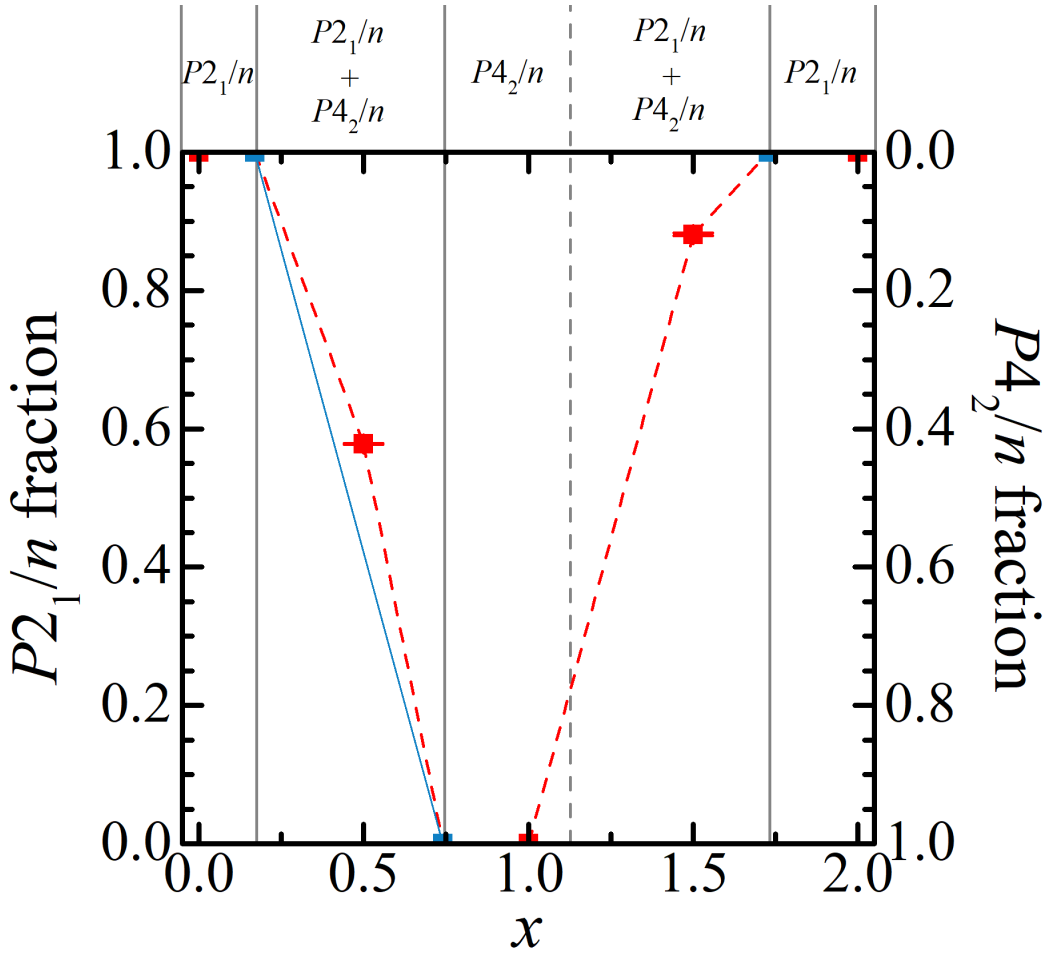

Figure 4.38 | *The fractions of double perovskite $P2_1/n$ (A-site disordered) and double double perovskite $P4_2/n$ (columnar A-site ordered) phases in syntheses of $Ca_xMn_{2-x}FeReO_6$ from synchrotron X-ray data. Points at x = 0, 1 and 2 are from syntheses where only a single perovskite phase of M-Mn_2FeReO_6, T-$Ca(Mn_{0.88(4)}Fe_{0.12})FeReO_6$ and M-Ca_2FeReO_6 are observed, respectively. Points at x = 0.5 and 1.5, show synthetic products with these nominal values of x that consist of mixtures between monoclinic and tetragonal perovskite phases. Points in blue show the refined values of x (from neutron diffraction) for the monoclinic and tetragonal phases in the x = 0.5 and 1.5 syntheses. The straight blue line linking the x = 0.17(3) and 0.74(2) points passes through a 50:50 mixture of monoclinic to tetragonal phases at x = 0.455, exactly halfway between the values of x for these two materials. Solubility limits are noted by solid grey lines at x = 0.17(3) and x = 0.74(2)). It is assumed that the x = 1.73(8) material also accounts for a solubility limit, however in this plot there is an absence of the tetragonal phase from the nominal x = 1.5 synthesis (this phase was not observed in neutron diffraction and x cannot be refined using X-ray data). The exact value of x for the solubility limit between x = 1.0 and x = 1.5 is not known and a dashed grey line is used here simply as a guide for the eye.*

Also shown is the refined value of x from neutron diffraction for the monoclinic phase (x = 1.73(8)) found in x = 1.5 products. However, the tetragonal phase observed in x = 1.5 products is only observed in synchrotron X-ray diffraction data and not in neutron data. The value of x for this phase cannot be determined using X-ray

diffraction and so it cannot be plotted here. As a result, it is assumed that x = 1.73(8) is also a solubility limit in this phase diagram and this is also marked with a solid grey line. Due to the absence of the tetragonal phase between x = 1.0 and x = 1.5, the solubility limit in this region is uncertain and is simply marked by a dashed grey line as a guide for the eye.

Syntheses of nominal x = 0.5 materials have yielded a biphasic mixture of an A-site disordered phase and an A-site ordered phase. The A-site disordered phase is monoclinic with $P2_1/n$ symmetry (similar to M-Mn_2FeReO_6), possesses rock salt B-site order and has experimentally determined formula of M-$(Ca_{0.17(3)}Mn_{1.83})FeReO_6$. The A-site ordered phase is tetragonal with $P4_2/n$ symmetry (similar to the nominal x = 1.0 material: T-$Ca(Mn_{0.88(4)}Fe_{0.12})FeReO_6$), possesses columnar A-site order with a simultaneous rock salt B-site order and has experimentally determined formula of T-$(Ca_{0.74(2)}Mn_{0.26})MnFeReO_6$. It has not been possible to explore how the synthetic procedure effects the coexistence of the A-site ordered and A-site disordered structure types in this x = 0.5 material, however it might be expected that increasing pressure would increase the fraction of the lower volume A-site disordered phase. The magnetic structure of the A-site disordered phase is found to be qualitatively similar to that of x-= 0 (M-Mn_2FeReO_6), with the A-site ordered phase qualitatively similar to that of the nominal x = 1.0 phase T-$(Ca(Mn_{0.88(4)}Fe_{0.12})FeReO_6)$. Magnetometry measurements of an approximately 1:1 ratio of these two phases is found to have an ordering temperature of T_c = 498 K.

Products of syntheses with nominal x = 1.0 have yielded a material with tetragonal $P4_2/n$ symmetry, columnar order of A-site cations with simultaneous B-site

rock salt order and an experimentally determined formula of T-$Ca(Mn_{0.88(4)}Fe_{0.12})FeReO_6$. This structure type is analogous to that of $RMnMnSbO_6$ materials, where R = Rare Earth.[64] The A-sites are divided into three distinct sites, with half of these being 10-coordinate sites occupied by Ca^{2+}, one quarter being tetrahedral sites and the final quarter, square planar sites. These tetrahedral and square planar sites alternate in along columns directed along the *c*-axis and are occupied by Mn^{2+} (with a small quantity of Fe^{2+}). The magnetic structure of this material has been solved as a G-type ferrimagnetic structure, with Fe moments parallel to the *c*-axis and Re moments antiparallel (T_c = 500 K). A second magnetic transition occurs at 70 K, at the onset of Mn ferrimagnetic spin order. Tetrahedral Mn moments are determined to be parallel to the *c*-axis, with square planar Mn moments antiparallel. While these sites are independent, in Rietveld refinements of this magnetic structure the magnitudes of moments on these two Mn sites are constrained to be equal.

Syntheses where x = 1.5 have yielded a monoclinic material, with $P2_1/n$ symmetry (similar to M-Ca_2FeReO_6) and rock salt order of B-site cations, with an experimentally determined A-site occupancy from neutron diffraction of M-$(Ca_{1.73(8)}Mn_{0.27})FeReO_6$. The magnetic structure of this material has been determined to be very similar to that of M-Ca_2FeReO_6, with G-type ferrimagnetism of the Fe/Re spin structure (T_c = 490 K) in the *ac*-plane that reorientates at ~75 K to the *ab*-plane, however it is noted that magnetic components along both the *a* and *b*-axes are present in the low-temperature structure of M-$(Ca_{1.73(8)}Mn_{0.27})FeReO_6$ (while moments are determined to be solely along the *b*-axis in M-Ca_2FeReO_6). In M-Ca_2FeReO_6 a low-temperature orbital ordering of Re was found to result in

expanded octahedra, with pairs of long Re–O2 bonds. However, a change in the distortion direction of ReO_6 octahedra is found when M-$(Ca_{1.73(8)}Mn_{0.27})FeReO_6$ is cooled, from expanded pairs of Re–O2 to compressed pairs of Re–O3.

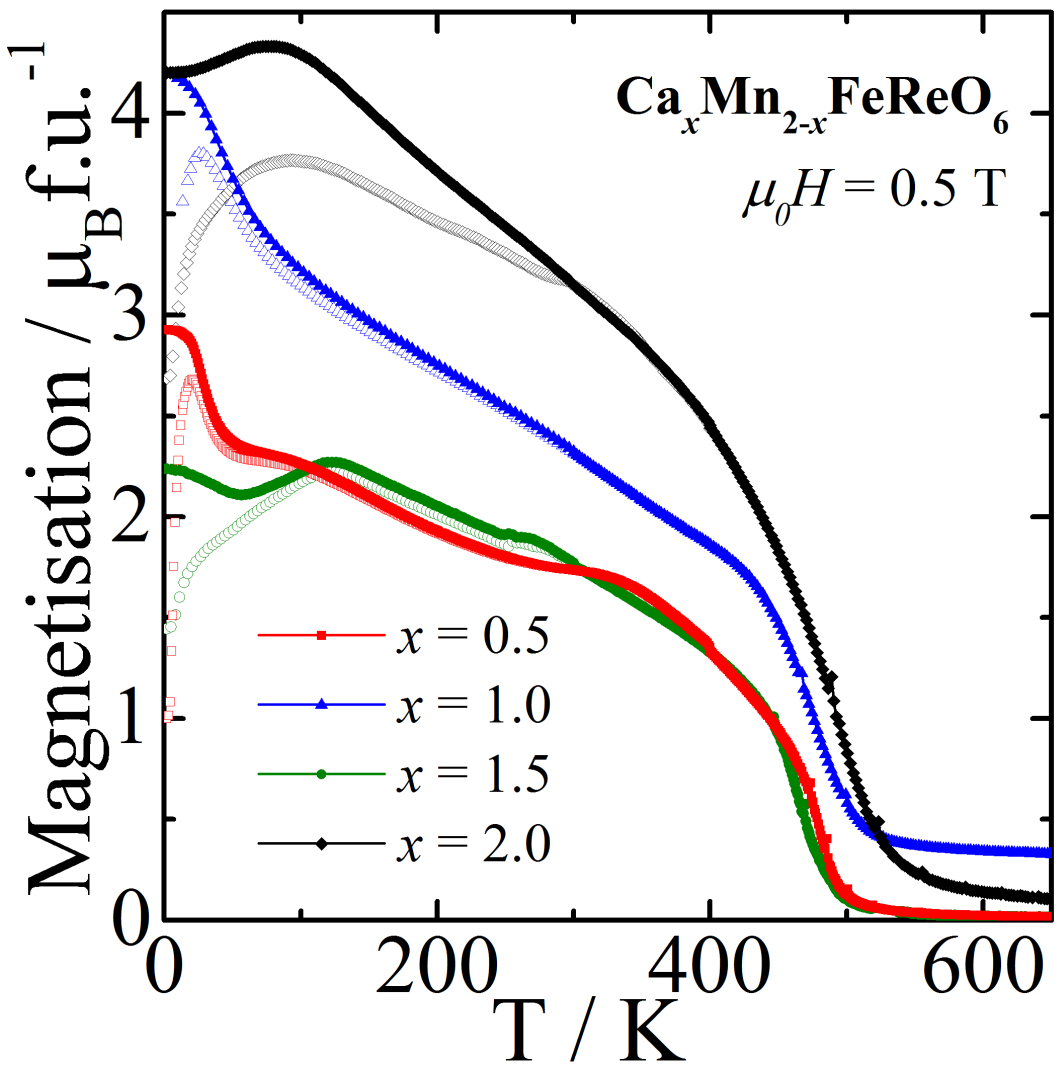

Figure 4.39 | *Field cooled (closed symbols) and zero-field cooled (open symbols) magnetisation versus temperature measured in applied fields of $\mu_0 H$ = 0.5 T, obtained from SQUID magnetometry from T = 0 to T = 650 K for samples of $Ca_xMn_{2-x}FeReO_6$ (x = 0.5, 1.0, 1.5, 2.0; T_c = 498, 500, 490, 520 K, respectively).*

Zero-field cooled and field cooled (0.5 T) magnetometry data on all of these samples of $Ca_xMn_{2-x}FeReO_6$ are shown in **Fig. 4.39** and a plot of the lattice parameters

of $Ca_xMn_{2-x}FeReO_6$ phases is shown in **Fig. 4.40**, using neutron diffraction data obtained from WISH at the ISIS Neutron Facility (x = 0, 0.17, 0.74, 1.0, 1.73) and from Oikawa et al.[82] from Sirius at the Pulsed Spallation Neutron Facility (KENS) at the National Laboratory for High Energy Physics (KEK) in Tsukuba, Japan (x = 2). Both the monoclinic (x = 0.17) and tetragonal (x = 0.74) products from syntheses with nominal x = 0.5 are shown plotted here. This compositional phase diagram is complicated as the central members of this series possess a different structure type, namely one with columnar A-site order of Ca/Mn in addition to the rock salt B-site order of Fe/Re that all of these materials possess, but it can be clearly seen that the volume of these phases generally decrease as Ca is further substituted by Mn to lower values of x. While most of these parameters exhibit clear trends, the variation in the β lattice parameter in the monoclinic materials seems rather unusual, where this monoclinic angle is < 90° for the nominal x = 1.5 sample, but > 90° for all other monoclinic materials. This peculiarity could be explained by differences in the low-temperature distortions of these various materials due to a combination of effects such as varied cation size and A-site magnetic contributions from Mn^{2+}.

Magnetic data for $Ca_xMn_{2-x}FeReO_6$ phases is shown in **Fig. 4.41**, where a clear trend towards higher magnetisation with further substitution of Ca by Mn is seen in SQUID data at 7 T. A similar trend is observed in the magnetisation determined by neutron diffraction, based on the refined magnetic structures found to fit this data. A greater separation between magnetisation measured by SQUID magnetometry and that calculated from magnetic structures appears to exist for materials with higher Mn content, perhaps explained by applied magnetic fields coaligning fluctuating Mn spins

in these samples with the axis of magnetisation and enhancing the magnetisation as measured by magnetometry. This would not be observed in zero-field neutron diffraction studies.

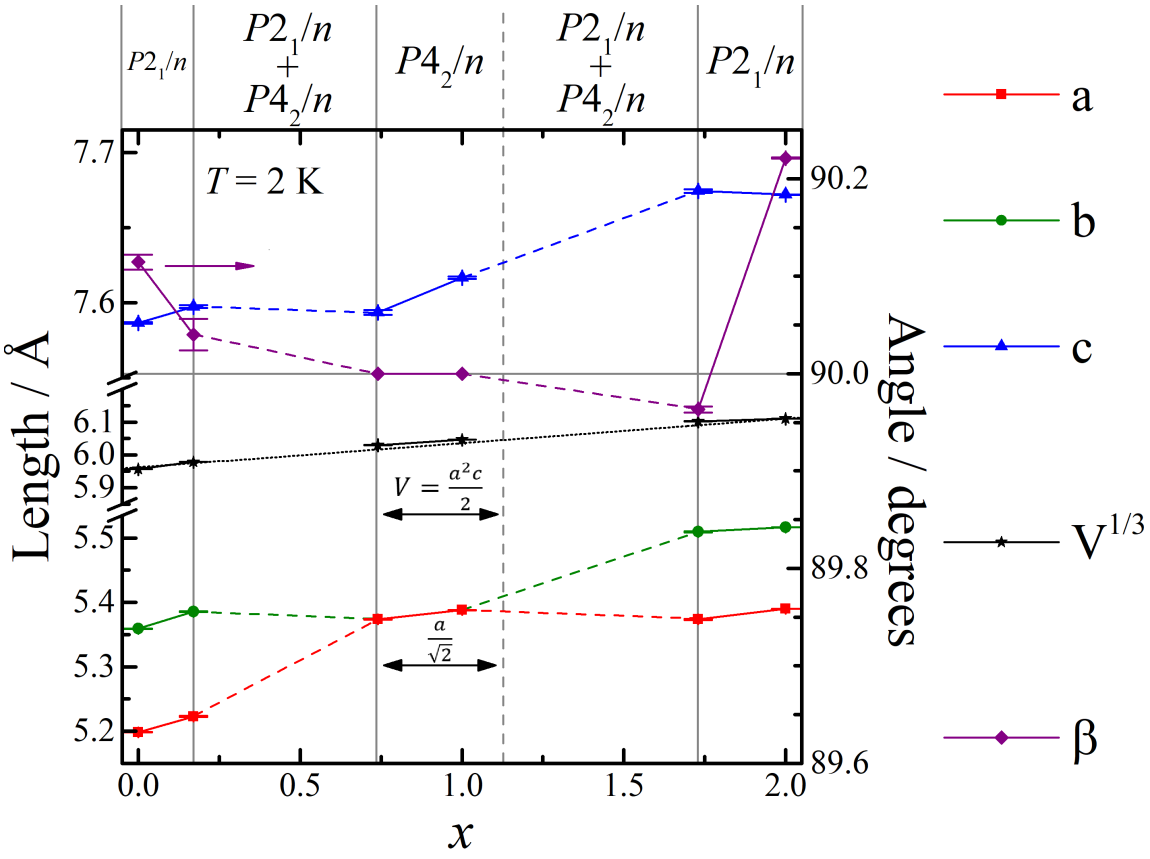

Figure 4.40 | *$Ca_xMn_{2-x}FeReO_6$ lattice parameters: a, b (for monoclinic materials), c and β. The cube root of volume, $V^{1/3}$, is also plotted. The a parameter for tetragonal $P4_2/n$ phases is shown divided by √2 to be comparable to those of the monoclinic phases. Similarly, the volumes of these tetragonal phases are calculated as: $V = ½a^2c$ (the $a/\sqrt{2} \times a/\sqrt{2} \times c$ cell volume), to be comparable to volumes of the monoclinic phases. The black dotted line is a linear best fit to the $V^{1/3}$ points. Other lines are a guide for the eye: vertical grey lines separate the general area of $P2_1/n$ (A-site disordered) and $P4_2/n$ (columnar A-site ordered) structure types, while dashed lines connect lattice parameters through these transitions. Data presented is at 2 K from neutron diffraction using WISH at the ISIS Neutron Facility, with the exception of x = 2 ($M\text{-}Ca_2FeReO_6$) which is data at 7 K (Sirius) from Oikawa et al.*[82]

The trend in coercive field, increasing with higher Ca content, can be explained here by a comparison to a study of the effects of cation size in $AA'FeReO_6$ double perovskites by De Teresa et al.[81] In particular, the series of $Ca_xSr_{2-x}FeReO_6$, which

shows a peak in coercive field in the $Ca_{1.5}Sr_{0.5}FeReO_6$ composition. The decrease in coercive field measured here by substituting Ca with Mn is a continuation of this trend by decreasing the cation size further and is the 'tail-end' of this peak in coercivity. De Teresa et al. relate these high coercive fields to a magnetostructural transition observed in materials such as M-Ca_2FeReO_6 and a similar transition is observed in this analysis of M-$(Ca_{1.73(8)}Mn_{0.27})FeReO_6$.

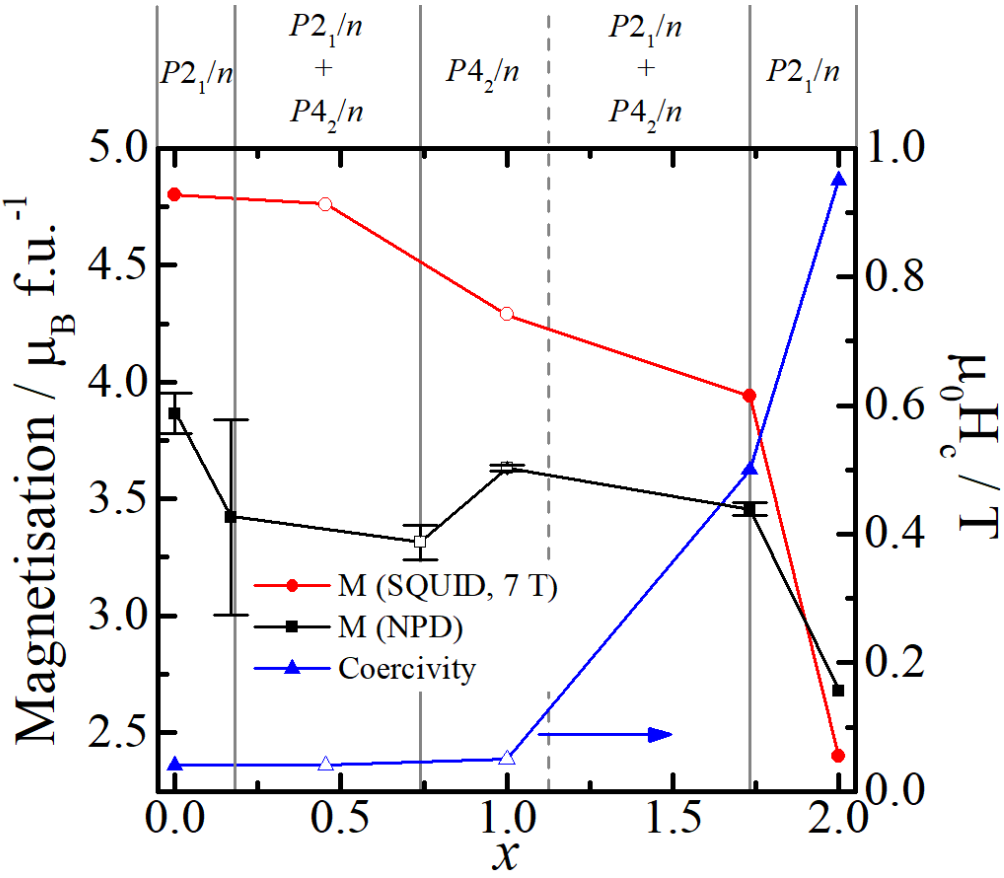

Figure 4.41 | *$Ca_xMn_{2-x}FeReO_6$ magnetic properties, with the magnetisation determined by refined magnetic structures from neutron diffraction data and magnetisation determined by SQUID magnetometry both shown. A general trend towards higher magnetisations by the further substitution of Ca with Mn is evidenced. The coercive field of these materials measured by SQUID magnetometry is also plotted, shown to be negligible for x = 0 to x = 1, but ~0.5 and 0.95 T for x = 1.73 and x = 2, respectively. Open symbols represent those points which contain an A-site ordered phase. As the x = 0.17 and x = 0.74 phases exist as a phase mixture, magnetometry data plotted here for these materials is at a value of x = 0.45, a weighted mean of these two values of x. Data for x = 2 from Oikawa et al.*[82]

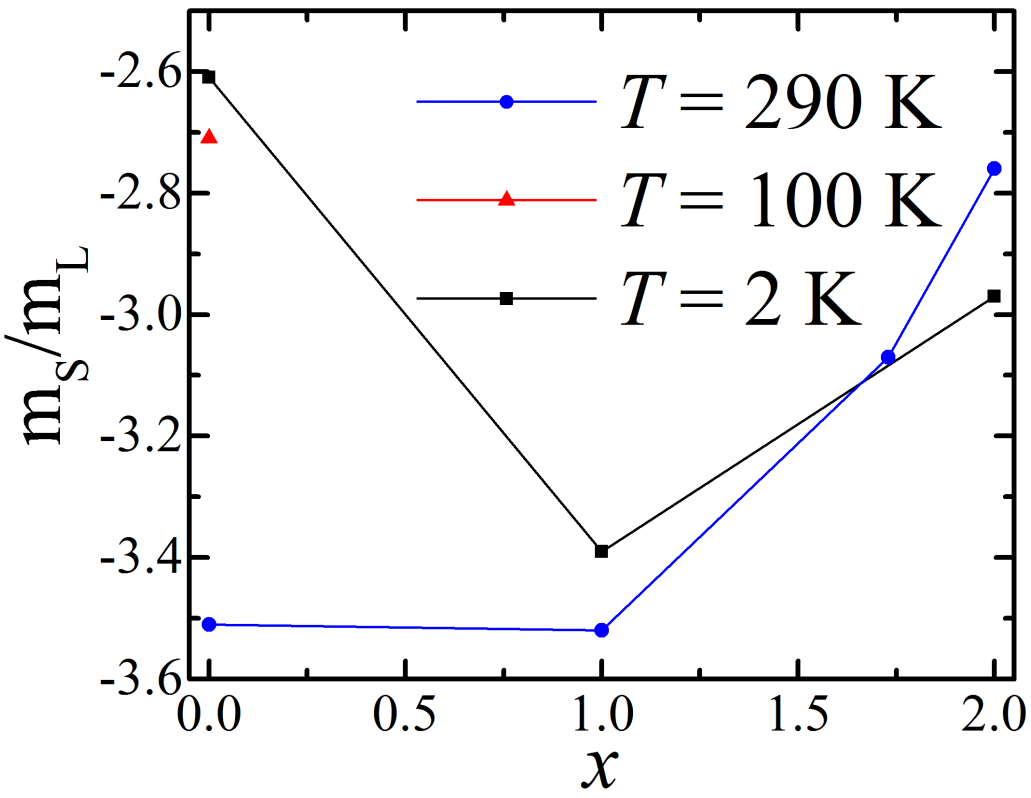

Figure 4.42 | *The ratio of spin to orbital moment, m_S/m_L, in $Ca_xMn_{2-x}FeReO_6$ as determined by X-ray Magnetic Circular Dichroism. In general, m_S/m_L decreases with decreasing cation size (lower values of x), however x = 0 (M-Mn_2FeReO_6) appears not to follow this trend. Data for x = 2 from Sikora et al.*[146]

Comparisons between the X-ray Magnetic Circular Dichroism (XMCD) data collected on these samples of $Ca_xMn_{2-x}FeReO_6$ are shown in **Fig. 4.42**, with a general decrease in the value of m_S/m_L observed as the cation size is further decreased with increasing Mn content (lower values of x). The $x = 0$ (M-Mn_2FeReO_6) material seems to not follow this trend. This is potentially due to the additional magnetic transition observed in this material, where an antiferromagnetic component to magnetic order of the Fe/Re spin lattice exists along the *b*-axis. This is discussed previously in '*3.3.5. X-ray Magnetic Circular Dichroism*' as an explanation as to why the Re moment, as measured by XMCD, appears to decrease on cooling. With the Re moment being non-

collinear to the axis of magnetisation, and therefore non-collinear to the X-ray vector, the effect of XMCD is reduced and the measured XMCD may not be accurately accounting for spin/orbital contributions due to Re.

In summary, perhaps one of the most interesting findings in the exploration in this series of $Ca_xMn_{2-x}FeReO_6$ perovskite-type materials is that the central member of the series, where $x = 1$, exhibits simultaneous columnar A-site (Ca/Mn) and rock salt B-site (Fe/Re) cation orders. This finding is remarkable as these combined types of order in a single material have only recently been discovered in the form of $RMnMnSbO_6$ (R = Rare Earth) materials.[64] The finding of this structure type in Ca-based materials will be exploited in subsequent chapters in this thesis: '**Chapter 5. $Ca(Mn_{0.5}Cu_{0.5})FeReO_6$ - Partial Triple Double Cation Order and Magnetoresistance Switching in a Perovskite**' and '**Chapter 6. $CaMnMnReO_6$ – Large Coercivity and Mutually Frustrated A and B-site Spin Orders in a Double Double Perovskite**'. Results presented in this chapter on the $x = 1$ material have been published in Angewandte Chemie – International Edition (*Large Magnetization and Frustration Switching of Magnetoreistance in the Double-Perovskite Ferrimagnet Mn_2FeReO_6*)[134] and in Chemistry of Materials (*Complex Ferrimagnetism and Magnetoresistance Switching in Ca-Based Double Double and Triple Double Perovskites*)[147]. Appended data on $Ca_xMn_{2-x}FeReO_6$ materials mentioned here is also provided in '**Appendix B**'.

Chapter 5. $Ca(Mn_{0.5}Cu_{0.5})FeReO_6$ - Partial Triple Double Cation Order and Magnetoresistance Switching in a Perovskite

5.1. Introduction

Following the discovery of double double cation ordering in $CaMnFeReO_6$, with columnar order of Ca and Mn across A-sites with simultaneous ordering of Fe/Re in a rock-salt structure across B-sites, the exploration of similar structures with these cation orders should yield further novel materials. $CaMnFeReO_6$ is itself an interesting material and is described in detail as the $x = 1$ material in '**Chapter 4. $Ca_xMn_{2-x}FeReO_6$ – Discovery of Double Double Cation Order in Ca-Based Perovskites**'. This material exhibits two types of structural order, room temperature ferrimagnetism, a high saturated magnetisation of 4.3 μ_B f.u.$^{-1}$ at 5 K and polycrystalline samples show substantial negative intergrain tunnelling magnetoresistance.

The magnetic structure of $CaMnFeReO_6$ consists of a ferrimagnetic B-site Fe^{3+}/Re^{5+} sublattice that orders at 500 K, with ferrimagnetic A-site Mn^{2+} order occurring at 70 K. A key detail of this double double (columnar-A, rock salt-B) perovskite structure type can be seen with further examination of the A-site columns, with one set of columns possessing 10-coordinate cavities (occupied in this case by Ca^{2+}) and the other set of columns possessing 4-coordinate cavities (occupied predominantly by Mn^{2+}). The driving force behind this order is the difference in cation size. The 4-coordinate cavities are further divided into two distinct coordination

environments of square planes and tetrahedra alternating along the column. The ferrimagnetic order of Mn^{2+} occurs with tetrahedral Mn^{2+} ordering parallel to Fe^{3+} and square planar Mn^{2+} ordering antiparallel. In neutron refinements of this magnetic structure it was necessary to constrain the magnitudes of these two unique Mn^{2+} sites together for stable refinements and as such no contribution to the overall magnetisation could be discerned from neutron diffraction. These two unique coordination environments for 4-coordinate A-sites are the inspiration for the synthesis of $Ca(Mn_{0.5}Cu_{0.5})FeReO_6$.

While Mn^{2+} is clearly able to occupy both the tetrahedral and square planar sites in this double double perovskite structure (as it does in $CaMnFeReO_6$ and in $RMnMnSbO_6$)[64] by substituting half of the Mn^{2+} ($3d^5$, $S = {}^5/_2$) for Cu^{2+} ($3d^9$, $S = {}^1/_2$), the higher preference for Cu^{2+} to adopt the square planar geometry than for Mn^{2+} should be a driving force for even further cation order. This would potentially be a 'triple double' perovskite, with Ca^{2+}, Mn^{2+} and Cu^{2+} occupying 10-coordinate, tetrahedral and square planar A-sites, respectively and Fe^{3+} and Re^{5+} occupying octahedral B and B′-sites.

Assuming a similar magnetic structure for $Ca(Mn_{0.5}Cu_{0.5})FeReO_6$ as is observed in $CaMnFeReO_6$, the Fe/Re ferrimagnetic sublattice would still be present providing room temperature ferrimagnetism. A similar low-temperature ferrimagnetic A-site transition would result in tetrahedral Mn^{2+} ($3d^5$, $S = {}^5/_2$) ordering parallel with Fe^{3+} ($3d^5$, $S = {}^5/_2$) and square planar Cu^{2+} ($3d^9$, $S = {}^1/_2$) ordering antiparallel. Theoretically, this structure results in saturated spin moments of up to 5 μ_B $f.u.^{-1}$. An

enhancement of the total magnetisation versus $CaMnFeReO_6$ and acts as further motivation for the synthesis of $Ca(Mn_{0.5}Cu_{0.5})FeReO_6$ in addition to the interesting cation ordering potential this structure possesses.

5.2. Experimental

5.2.1. Synthesis of $Ca(Mn_{0.5}Cu_{0.5})FeReO_6$

Synthesis of $Ca(Mn_{0.5}Cu_{0.5})FeReO_6$ has been conducted using techniques outlined in '*2.12. High-Pressure Solid-State Synthesis*'. A complex precursor (½ $Ca_2Fe_2O_5$ + ½ MnO_2 + ½ CuO + ReO_2) was prepared and used for all syntheses, with these metal oxides ground and combined in the stoichiometric ratio listed using a pestle and mortar to thoroughly mix these precursors. The $Ca_2Fe_2O_5$ brownmillerite-type metal oxide used in the precursor was prepared from solid-state synthesis (2 $CaCO_3$ + Fe_2O_3) with two sintering steps of 1000 °C and 1100 °C, each for 24 hours and grinding the product in between these steps.[144] The encapsulating material used around the sample in high-pressure experiments was Pt, with conditions chosen to be similar to that of $CaMnFeReO_6$. A pressure of 10 GPa was consistently used and not altered, with heating to 1400 °C. Cooling steps were however varied between syntheses. Several syntheses involved directly quenching the sample from 1400 °C to room temperature. Slow cooling procedures were used in many syntheses, cooling from 1400 to as low as 1000 °C for a duration of up to 50 minutes before quenching.

5.2.2. Structural Characterisation

X-ray data was collected on all products from high-pressure syntheses of $Ca(Mn_{0.5}Cu_{0.5})FeReO_6$ using a Bruker D2 Phaser diffractometer with a Cu K_α/K_β X-ray source (15-minute scans of $5° \leq 2\theta \leq 70°$). These diffraction patterns were used for phase analysis and to select syntheses for further characterisation by synchrotron X-ray diffraction and neutron diffraction. Sample #2 was analysed by synchrotron X-ray diffraction at 304 K on BL04-MSPD at ALBA (wavelength, $\lambda = 0.44214$ Å). A 56 mg aggregate of samples #5, 8 and 11 was used for powder neutron diffraction analysis in high resolution single frame mode on the WISH diffractometer at the ISIS Neutron Facility, with collections at 6 different temperatures (T = 2, 50, 100, 150, 200 and 300 K). Data was collected at T = 2 K for a total proton beam current of 79 μA. Datasets at all other temperatures were collected for total proton beam currents of 40 μA. These X-ray and neutron diffraction patterns were analysed and solved using the FullProf Suite and refined by the Rietveld method.[122,125]

5.2.3. Magnetic Measurements of $Ca(Mn_{0.5}Cu_{0.5})FeReO_6$

Magnetometry was carried out on sample #2 using a Quantum Design MPMS XL Superconducting Quantum Interference Device (SQUID) magnetometer. Magnetisation versus field hysteresis loops were recorded for sample #2 ($-7 \leq \mu_0 H$ (T) ≤ 7) at temperatures of 2 and 300 K and magnetisation versus temperature was measured zero-field cooled and field cooled ($\mu_0 H$ = 0.5 T) from 2 K to 650 K. Magnetoresistance was also measured for pellets of sample #14 and #15, as described in '*2.3.2. Magnetoresistance*'. These measurements were conducted using a Quantum

Design Physical Property Measurement System (PPMS). Resistivity versus field hysteresis ($-7 \leq \mu_0 H$ (T) ≤ 7) was measured at constant temperatures of 2.5, 20, 50, 100, 200 and 300 K, and magnetoresistance was then calculated as a percentage using **Equation 1.3**. Resistance versus temperature was also measured between 10 and 200 K at magnetic fields of $\mu_0 H = 0$ and 7 T.

X-ray Magnetic Circular Dichroism (XMCD) on Re was calculated from X-ray Absorption Near-Edge Spectra (XANES) measured on $Ca(Mn_{0.5}Cu_{0.5})FeReO_6$ at ID12 at the European Synchrotron Radiation Facility. XANES were measured in the ranges 10.511-10.605 keV (Re L_3-edge) and 11.934-12.055 keV (Re L_2-edge). These spectra were measured with circularly polarised X-rays of helicity +1 and -1, as well as in magnetic fields of +2 and -2 T. XMCD versus field hysteresis measurements were performed at 11.969 keV, at the Re L_2-edge maximum, between fields of ±17 T. Both XANES and hysteresis measurements were conducted at temperatures of 290 and 2.2 K.

5.3. Results & Discussion

5.3.1. Phase Analysis & X-ray Crystal Structure: $Ca(Mn_{0.5}Cu_{0.5})FeReO_6$

Initial phase analysis on $Ca(Mn_{0.5}Cu_{0.5})FeReO_6$ was carried out using X-ray diffraction data collected with a Bruker D2 Phaser diffractometer. Raw data files are shown stacked in **Fig. 5.1**. A large degree of sample variation is seen in these syntheses, with some syntheses appearing to have many complex and unknown phases.

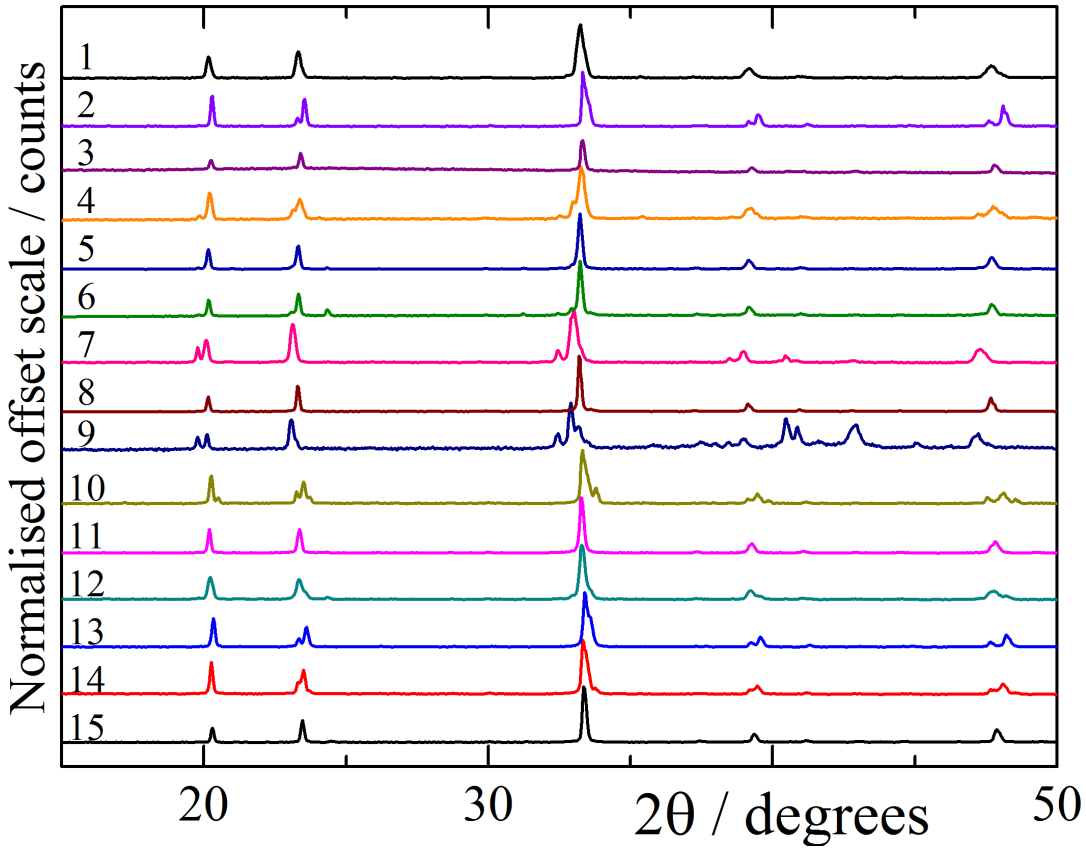

Figure 5.1 | *A stacked plot of normalised raw powder X-ray data initially collected on samples of $Ca(Mn_{0.5}Cu_{0.5})FeReO_6$ for phase analysis (in the 2θ range 15-50°). A high degree of sample variation can be seen and, based on the desired triple double perovskite structure type, samples 5, 8 and 11 were selected for neutron analysis. The characteristic peaks in the 15-25° range of 2θ suggest that many syntheses have additional unidentifiable phases.*

Variation between syntheses is not entirely unexpected; as this material is an attempt to order multiple cations across five cation sites and various slow cooling procedures were used to attempt to control this. **Table 5.1** shows key parameters of these $Ca(Mn_{0.5}Cu_{0.5})FeReO_6$ syntheses, such as the slow cooling duration and the final temperature the sample was cooled to before being quenched. All syntheses were conducted at 10 GPa and only temperature was varied. This procedure was chosen as

it is easier to maintain consistent pressures in many consecutive syntheses and vary temperature than it is to maintain a consistent temperature in each synthesis.

Table 5.1 | A collection of the initial Rietveld analysis of individual syntheses of $Ca(Mn_{0.5}Cu_{0.5})FeReO_6$, and the resulting purity and B-site disorder in the product. Syntheses were conducted at 10 GPa, using dwell temperatures of 1400 °C for 20 minutes and various slow cooling durations (t_{cool}) were used before the sample was quenched from the final heating temperature (T_f).

Sample no.	t_{cool} / minutes	T_f / °C	Unidentified phases, Y/N	Wt. ReO_2 / %	B-Antisite Disorder / %	χ^2	R_{wp} / %
1	0	1400	N	0	6.6(2)	5.92	7.86
2	30	1000	N	0	0	3.61	6.83
3	30	1000	Y	0	10.2(6)	1.72	4.44
4	50	1000	Y	0.7(2)	1.4(4)	5.07	3.67
5	30	1000	N	1.02(1)	7.0(4)	6.60	7.73
6	50	1000	Y	5.0(3)	9.4(4)	3.20	6.50
7	50	1000	Y	0	10.6(8)	25.1	15.7
8	12	1300	N	0	11.6(2)	3.13	5.45
9	35	1100	Y	0	20(10)	12.1	13.0
10	0	1400	Y	0	2.6(8)	13.5	12.2
11	0	1400	N	0.4(2)	4.8(2)	3.41	6.09
12	0	1400	N	1.0(2)	2.6(4)	6.35	7.32
13	50	1000	N	0	3.6(2)	4.01	5.41
14	0	1400	N	0	3.0(4)	4.47	6.88
15	0	1400	N	1.6(2)	12.0(2)	2.59	6.02

Samples 5, 8, and 11 were mixed and examined on WISH at the ISIS Neutron Facility. The measures of the fit, χ^2 and R_{wp}, are shown for X-ray patterns collected over 15 minutes using a Bruker D2 Phaser diffractometer with Cu K_α radiation. All syntheses used platinum capsules.

Multiple syntheses of this material show an additional reflection at 2θ = ~20°, such as syntheses 4, 7 and 9. This corresponds to the 111 reflection in the $P4_2/n$ tetragonal double double perovskite structure, suggesting that the origin of this additional peak in syntheses 4, 7 and 9 could be due to a further monoclinic distortion of the tetragonal lattice. Attempts to solve these structures in this way were unsuccessful. More likely sources for these reflections are additional compositionally different double perovskite or double double perovskite phases. However, with the

presence of five cations, identification of this phase is non-trivial as there are many possibilities.

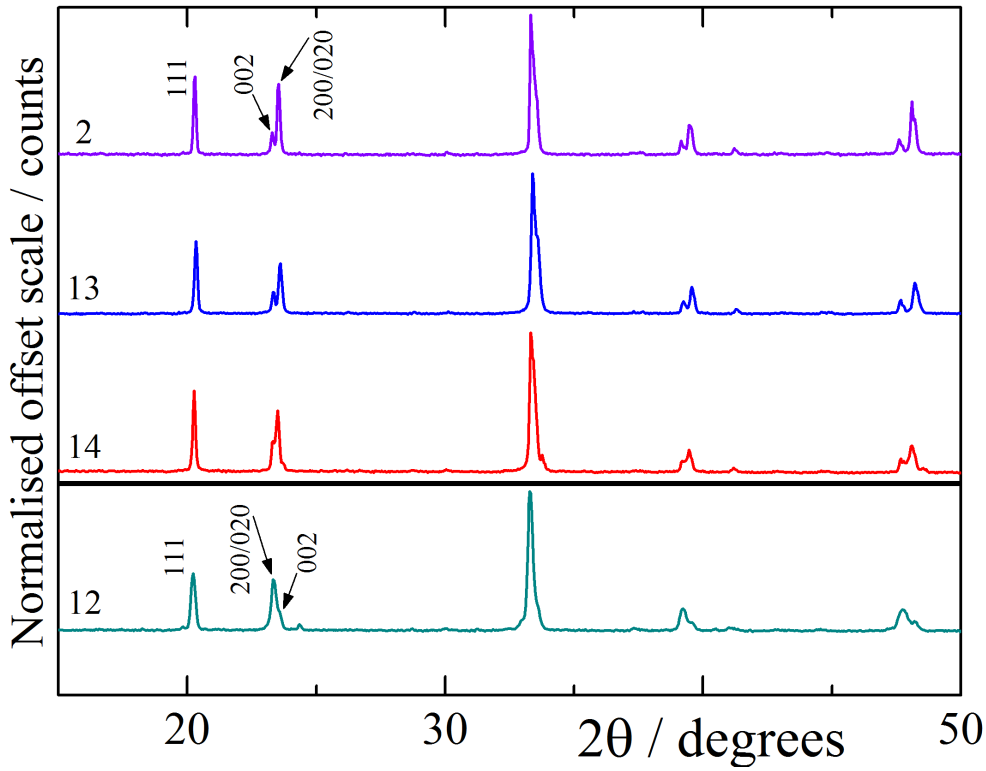

Figure 5.2 | *Top:* *Raw patterns for $Ca(Mn_{0.5}Cu_{0.5})FeReO_6$ samples 2, 13 and 14, showing tetragonal distortions where $a > c$.* ***Bottom:*** *Raw pattern for $Ca(Mn_{0.5}Cu_{0.5})FeReO_6$ sample 12, showing a tetragonal distortion where $a < c$.*

Another variation between syntheses is the magnitude of the tetragonal distortion. The reflections at $2\theta = \sim 23.5°$ correspond to the 200/020 and 002 reflections from the tetragonal $P4_2/n$ double double perovskite structure and are a good diagnostic for the degree of tetragonal distortion. In the vast majority of syntheses the tetragonal distortion is small and the 200/020 and 002 reflections cannot be reliably resolved, but refinements generally suggest that: $a > c$. The greatest distortion in this manner is noticeable in sample 12 (bottom of **Fig. 5.2**), with the 002 reflection shifted to higher 2θ and appearing as a shoulder on the 200/020 reflection. This pattern can be fit with

a single tetragonal phase, as well as a small quantity of ReO_2 (1.0(2) % by weight). Other samples such as samples 2, 13 and 14, also show tetragonally distorted unit cells, however these distortions are such that $a < c$ (top of **Fig. 5.2**) and can again be fit with a single tetragonal phase. This observation, coupled with the large variation in sample quality in the form of unidentified impurity phases, shows that the products must be very sensitive to the synthesis temperature and heating profile. A correlation seems to be present, where the most tetragonally distorted products possesses some of the highest B-cation order. However, these measurements give insufficient information to characterise A-site order. It could be possible that the undetectable variations in the further columnar order between Ca/(Mn/Cu), or square planar / tetrahedral order between Mn and Cu (with the possible presence of Fe on A-sites as well), contribute to the distortion direction of the lattice and account for differences between sample 12 ($a > c$) and samples 2, 13 and 14 ($a < c$).

Table 5.2 | Refined structure parameters for $Ca(Mn_{0.5}Cu_{0.5})FeReO_6$ at 304 K in space group $P4_2/n$ using synchrotron powder X-ray data from BL04-MSPD at ALBA. Two phases of $Ca(Mn_{0.5}Cu_{0.5})FeReO_6$ can be identified with differing magnitudes of tetragonal distortion.

Atom	*x*	*y*	*z*
Ca	¼	¾	0.2757(8)
Mn_{TD}	¾	¾	¾
Cu_{SP}	¼	¼	¾
Fe	0	0	½
Re	0	½	½
O1	0.9457(6)	0.5549(6)	0.2843(2)
O2	0.7292(3)	0.9586(3)	0.5653(2)
O3	0.7926(3)	0.0476(3)	0.9692(3)

B_{iso} = 0.77(2) Å^2; lattice parameters for phase #1: a = 7.56594(3) and c = 7.63983(4); lattice parameters for phase #2: a = 7.54804(5) and c = 7.64964(9); residuals R_{wp} = 15.3 % and χ^2 = 4.66. Ratio of phases #1:#2 is refined to 3:1. No Fe/Re site disorder was observed. Ca, Mn_{TD} and Cu_{SP} are fixed at ideal site occupancies due to insufficient data to refine disorder. The same fractional coordinates were used for both of these two phases and constrained in refinements to be equal.

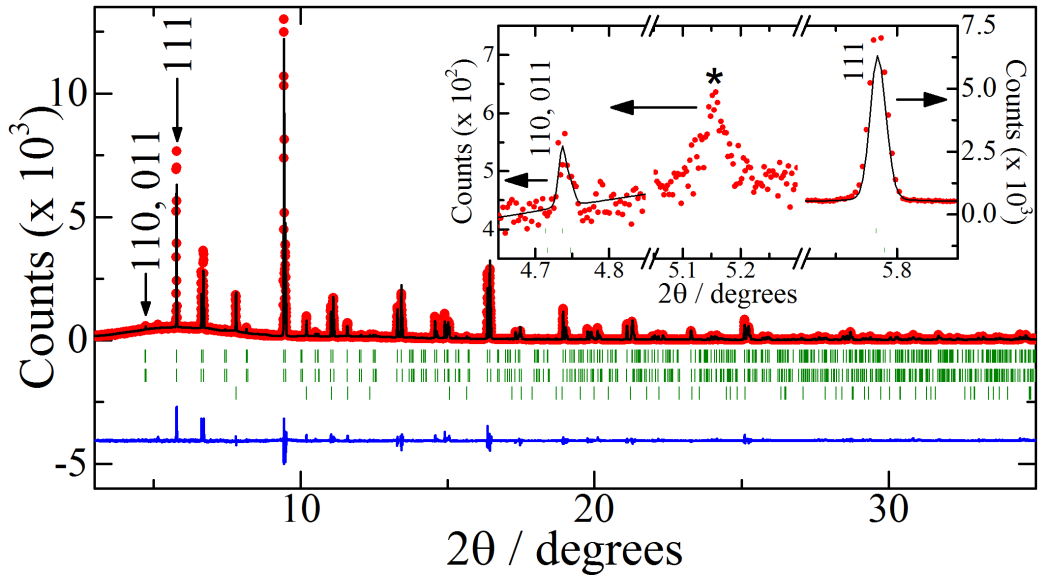

Figure 5.3 | *Rietveld fit to data collected from BL04-MSPD at ALBA 304 K of $Ca(Mn_{0.5}Cu_{0.5})FeReO_6$ in the $P4_2/n$ space group (λ = 0.44214 Å). Occupancy of Ca and Mn_{TD} and Cu_{SP} are fixed to ideal occupancies. The inset shows the intensity of the 110 reflection (a result of columnar order between Ca and (Mn/Cu)) in comparison to the 111 reflection. The asterisk indexes the most intense reflection (020) due to trace quantities of $MnFe_3O_5$. Rows of indices indicate phase 1 and phase 2 as $P4_2/n$ $Ca(Mn_{0.5}Cu_{0.5})FeReO_6$ and phase 3 as parasitic scattering from TiO_2 in the measurement.*

In synchrotron X-ray data collected on $Ca(Mn_{0.5}Cu_{0.5})FeReO_6$ (sample #2) using BL04-MSPD at ALBA (**Fig. 5.3**), a good Rietveld fit could only be obtained using two different tetragonal phases, both with short *a*-axes and long *c*-axes (this is shown more clearly in **Fig. 5.4**). To ensure stable refinements the structure parameters of these two phases have been constrained and are shown in **Table 3.2** above. No B-antisite order is observed in this sample and even using synchrotron X-rays the lack of contrast between Ca, Mn, Cu and Fe does not allow accurate refinement of the disorder between 10-coordinate Ca and 4-coordinate (Mn/Cu) or between tetrahedral Mn and square planar Cu (or B to A-site mixing of Fe). In **Fig. 5.3** a comparison is made between the 110 reflection due to columnar A-site order with the 111 reflection. The 110 reflection is of comparable intensity to that of trace $MnFe_3O_5$ (< 1 % by weight).

These observations reinforce the fact that the distortions in this material are very sensitive to the synthesis conditions as, even in a single sample, subtly different $Ca(Mn_{0.5}Cu_{0.5})FeReO_6$ phases can be identified, possibly due to temperature gradients across the sample space during synthesis.

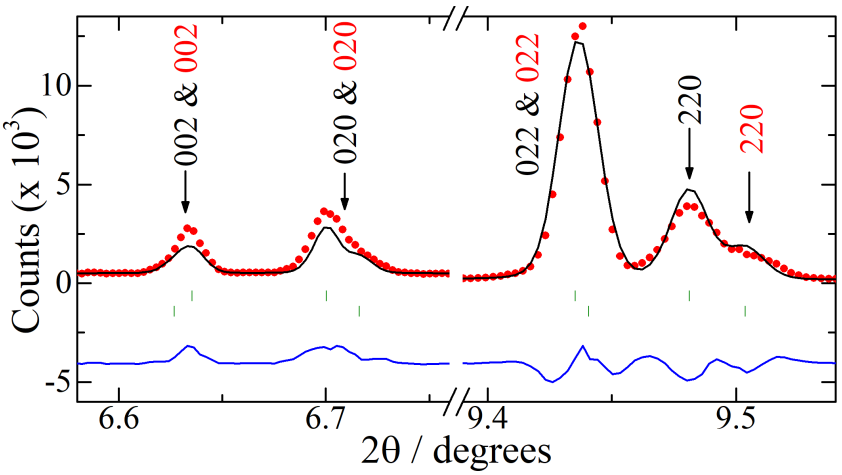

Figure 5.4 | *Rietveld fit to data collected from BL04-MSPD at ALBA 304 K of $Ca(Mn_{0.5}Cu_{0.5})FeReO_6$ in the $P4_2/n$ space group (λ = 0.44214 Å). The data shown in this range highlights the 002, 020, 022 and 220 reflections for both of the double double perovskite phases (the first phase of $Ca(Mn_{0.5}Cu_{0.5})FeReO_6$ is indicated by the upper row of tick marks and black hkl values, while the second $Ca(Mn_{0.5}Cu_{0.5})FeReO_6$ phase is indicated by the lower row of tick marks and red hkl values. These reflections more clearly show the presence of two similar phases, but with distinctly different lattice parameters.*

5.3.2. Neutron Crystal & Magnetic Structure of $Ca(Mn_{0.5}Cu_{0.5})FeReO_6$

Data from the WISH diffractometer has enabled structural and magnetic characterisation of an aggregate of samples #5, 8 and 11, with total sample size of 56 mg. From analysis using D2 X-ray data these samples contain very similar single tetragonal perovskite-type phases (with negligible quantities of ReO_2), that are likely to be the desired double double (or triple double) perovskite: $Ca(Mn_{0.5}Cu_{0.5})FeReO_6$. In addition to structural considerations, magnetic diffraction intensity must be

considered during Rietveld refinements of $Ca(Mn_{0.5}Cu_{0.5})FeReO_6$ as magnetic order above room temperature is present. This magnetic order was solved with a $\boldsymbol{k}$ = (0 0 0) propagation vector and the symmetry operations for this order as described by the Isotropy Suite ('*2.2.7 – Magnetic Symmetry Analysis*') are shown in **Table 5.3**.[126]

Table 5.3 | Magnetic modes in the Γ_1^+ irreducible representation (defined from the Isotropy Suite)[126] for the $Ca(Mn_{0.5}Cu_{0.5})FeReO_6$ magnetic structure. Propagation vector, $\boldsymbol{k}$ = (0 0 0) in space group $P4_2/n$.

B-sites mag. modes:	**A_g1**		**$A_g2^\dagger$**		**$A_g3^\dagger$**	**A-sites mag. modes:**	**$A^\ddagger$**
Atom	m_x	m_y	m_x	m_y	m_z	**Atom**	m_z
Fe1, Re1[a]	*n/a*	-	-	*n/a*	+	**$A_{TD}1$, $A_{TD}2$[e]**	+
Fe2, Re2[b]	*n/a*	+	+	*n/a*	+		
Fe3, Re3[c]	+	*n/a*	*n/a*	-	+	**$A_{SP}1$, $A_{SP}2$[f]**	+
Fe4, Re4[d]	-	*n/a*	*n/a*	+	+		

Magnetic mode A_g3 is used in magnetic structure refinements for B-sites of $Ca(Mn_{0.5}Cu_{0.5})FeReO_6$. †For Re sites, coefficients for A_g3 are negative. B-Sites: [a]Fe1 = (0, ½, 0), Re1 = (0, ½, ½); [b]Fe2 = (½, 0, 0), Re2 = (½, 0, ½); [c]Fe3 = (½, ½, ½), Re3 = (½, ½, 0); [d]Fe4 = (0, 0, ½), Re4 = (0, 0, 0). Magnetic mode A is used for magnetic structure refinements of A-Sites: [e]$A_{TD}1$ = (¼, ¼, ¼), $A_{TD}2$ = (¾, ¾, ¾); [f]$A_{SP}1$ = (¼, ¼, ¾), $A_{SP}2$ = (¾, ¾, ¼). ‡For A_S sites, moment is fixed to zero. Further details of magnetic structure solution are provided in '*2.2.7 – Magnetic Symmetry Analysis*'.

Neutron diffraction data can be well fit using the $P4_2/n$ structure of double double perovskites with refinements at 2 and 300 K shown in **Fig. 5.5**. Data collected at 300 K yields information of the cation ordering in this material. The 110 reflection shows an appreciable intensity at room temperature due to the high contrast between the neutron scattering lengths of Ca (b = 4.7 fm) and Mn/Cu (b = -3.63/7.718 fm), confirming the presence of columnar order. While columnar order is evidenced by the characteristic 110 reflection, further cation order between Mn (b = -3.63 fm) and Cu (b = 7.718 fm) is more subtle and revealed by minor intensity variations across the whole pattern. The occupancies of many cation sites are able to be refined, with the 10-coordinate A-site refined as fully occupied by Ca and fixed to this for further refinements. Refining the occupancies of 4-coordinate tetrahedral and square planar

sites between Mn and Cu does however reveal a significant amount of disorder. The tetrahedral site and square planar site do predominantly appear to be occupied by Mn and Cu, respectively. However, these ratios of Mn:Cu on tetrahedra or Cu:Mn on square planes only refine to approximately 3:2. The lack of neutron scattering contrast between Fe (b = 9.45 fm) and Re (b = 9.2 fm) requires their occupancies to be fixed as fully occupied to refine the structure. Full structural and magnetic information from these neutron refinements are tabulated in **Table 5.4**.

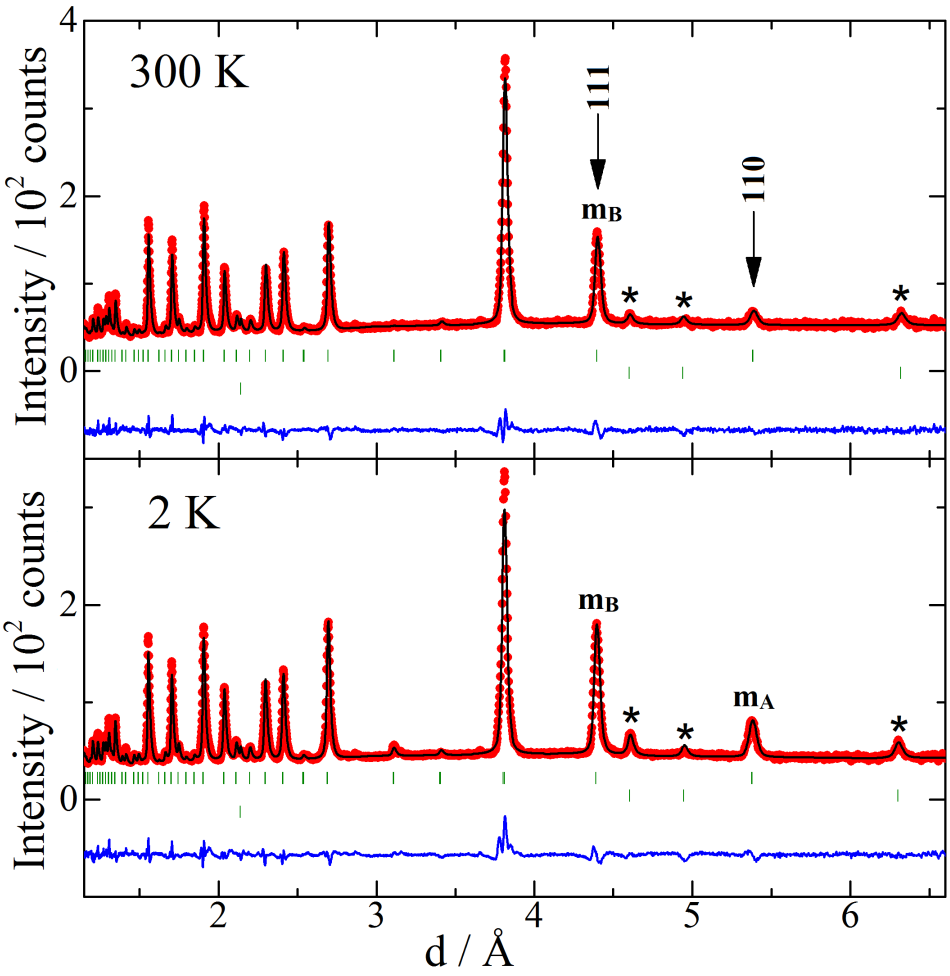

Figure 5.5 | *Combined nuclear and magnetic Rietveld fits to neutron diffraction data on $Ca(Mn_{0.5}Cu_{0.5})FeReO_6$ collected on the WISH diffractometer at the ISIS Neutron Facility. Patterns shown are from an average of bank 3 and 8.* ***Top****: 300 K.* ***Bottom****: 2 K. Markers m_A and m_B refer to magnetic reflections with significant contributions from A and B-site spin order, respectively. Asterisks mark $MnFe_3O_5$ reflections.*

Table 5.4 | Refined structure parameters for $Ca(Mn_{0.5}Cu_{0.5})FeReO_6$ at 2-300 K in space group $P4_2/n$ using neutron powder diffraction data from the WISH diffractometer at the ISIS Neutron Facility. Magnetic symmetry is follows the descriptions in **Table 5.3**. Sample size 56 mg.

T / K		2	50	100	150	200	300
Cell Param	a / Å	7.609(1)	7.610(1)	7.6104(9)	7.613(1)	7.615(1)	7.618(1)
	c / Å	7.622(1)	7.622(1)	7.622(1)	7.622(1)	7.625(1)	7.629(1)
	V / Å^3	441.3(1)	441.4(1)	441.5(1)	441.8(1)	442.2(1)	442.7(1)
Ca	z	0.284(1)	0.280(2)	0.283(2)	0.282(2)	0.283(2)	0.282(2)
O1	x	0.946(2)	0.935(5)	0.935(4)	0.934(3)	0.933(3)	0.935(3)
	y	0.567(2)	0.566(6)	0.566(5)	0.576(3)	0.574(4)	0.572(4)
	z	0.246(5)	0.248(4)	0.245(3)	0.244(4)	0.245(4)	0.247(4)
O2	x	0.758(4)	0.736(5)	0.731(3)	0.735(4)	0.734(4)	0.734(4)
	y	0.952(2)	0.951(2)	0.951(2)	0.951(2)	0.951(2)	0.949(2)
	z	0.5654(9)	0.5710(9)	0.5683(9)	0.5675(8)	0.5672(8)	0.5669(9)
O3	x	0.779(2)	0.767(3)	0.759(4)	0.756(6)	0.756(6)	0.759(5)
	y	0.049(1)	0.051(1)	0.048(1)	0.048(1)	0.049(1)	0.048(1)
	z	0.976(1)	0.973(1)	0.973(1)	0.975(1)	0.975(1)	0.975(1)
mFe / μ_B		4.31(3)	4.27(4)	4.22(4)	4.14(3)	4.00(4)	3.71(4)
mRe / μ_B		0.861(6)	0.854(8)	0.845(7)	0.828(7)	0.800(7)	0.742(8)
mTD / μ_B		2.67(8)	2.40(9)	1.8(1)	0	0	0
ΔB / μ_B		3.45(2)	3.42(2)	3.38(2)	3.31(2)	3.20(2)	2.97(2)
m_{tot} / μ_B f.u.$^{-1}$		4.78(4)	4.62(5)	4.28(5)	3.31(2)	3.20(2)	2.97(2)
A/B	B_{iso} / Å^2	0.51(5)	0.94(5)	0.80(5)	0.98(5)	0.96(5)	1.06(8)
O	B_{iso} / Å^2	1.11(8)	1.46(9)	1.22(8)	1.28(8)	1.25(8)	1.3(1)
R_{wp} / %		3.90	3.93	3.81	3.79	3.74	3.57
χ^2		10.31	5.24	4.99	5.08	5.05	4.69
Q / μA·h		79	40	40	40	40	40

Cation positions are as follows for A-sites: Ca (¼, ¾, z), A_{TD} (¾, ¾, ¾), A_{SP} (¼, ¼, ¾); and for B-sites: Fe (0, 0, ½) and Re (0, ½, ½). Occupancy of A_{TD} is refined to 64(1) % Mn (36 % Cu) and A_{SP} refined to 60(1) % Cu (40 % Mn), with The tabulated value of m_{tot} refers to the total magnetisation of $Ca(Mn_{0.5}Cu_{0.5})FeReO_6$, equivalent to:$m_{tot} = mFe + mTD - mRe$.

Shown in **Fig. 5.***6* is the magnetic evolution of the 111 (d ~4.4 Å) and 101/011 reflections (d ~5.4 Å). Intensity variations are seen on the 111 reflection cooling from 300 K and can be attributed to the G-type ferrimagnetic order of the Fe/Re sublattice. Refinements of this sublattice have used magnetic mode 'A_g3' from **Table 5.3**, with Re moments constrained to be antiparallel to those of Fe and of one fifth the magnitude, based on refinements of Mn_2FeReO_6 (from D20 data, with Re refined independently) and using XMCD data at 300 K (*5.3.4 – X-ray Magnetic Circular Dichroism*). This Fe/Re sublattice is refined to be collinear to the c-axis.

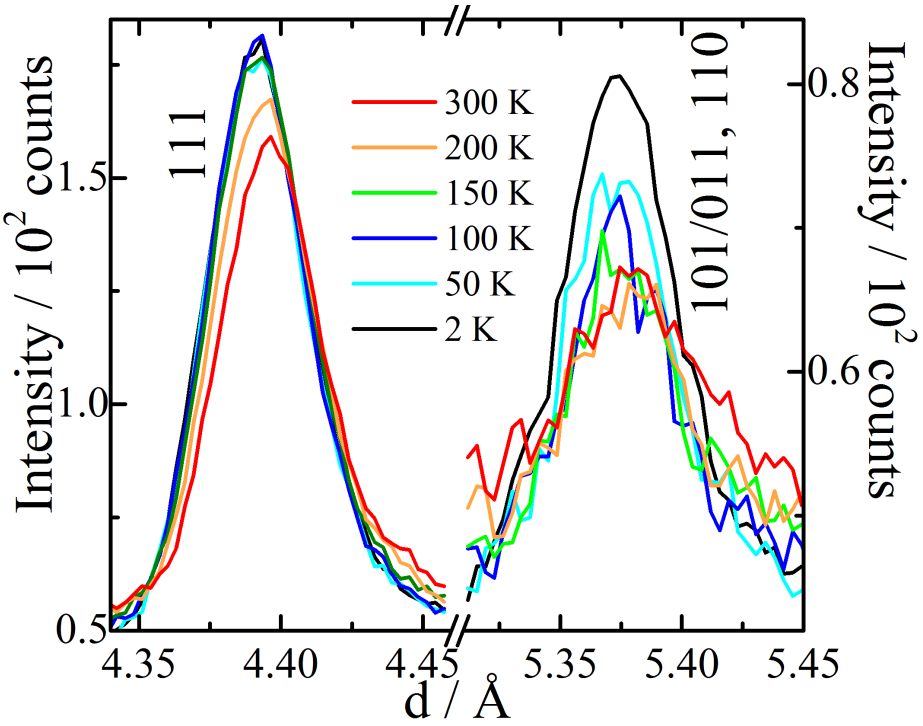

Figure 5.6 | *Intensity variations with temperature of the two main magnetic reflections in* $Ca(Mn_{0.5}Cu_{0.5})FeReO_6$*: 111 (d ~4.4 Å) and 101/011 (d ~5.4 Å).*

Intensity at 300 K is present on the 110 reflection and can be attributed to structural columnar order of Ca and (Mn/Cu). Due to the very small tetragonal distortion in this material ($a \sim c$), this reflection lies on top of the 101/011 reflections and we are unable to resolve them. At 100 K and lower, additional intensity is observed on the 101/011 reflection that can be attributed to A-site magnetic order, using magnetic mode 'A', defined in **Table 5.3**. Refinements of A_{TD} and A_{SP} independently result in moments for A_{SP} of zero and these were fixed as such. Moments of A_{TD} refine to positive values along the *c*-axis, parallel to moments of Fe, contributing to an increase in the overall magnetisation of the sample when compared to the Fe/Re sublattice alone, with calculated moments saturating at 4.78(4) μ_B $f.u.^{-1}$ with this magnetic structure. This overall crystal and magnetic structure is shown in **Fig. 5.7**.

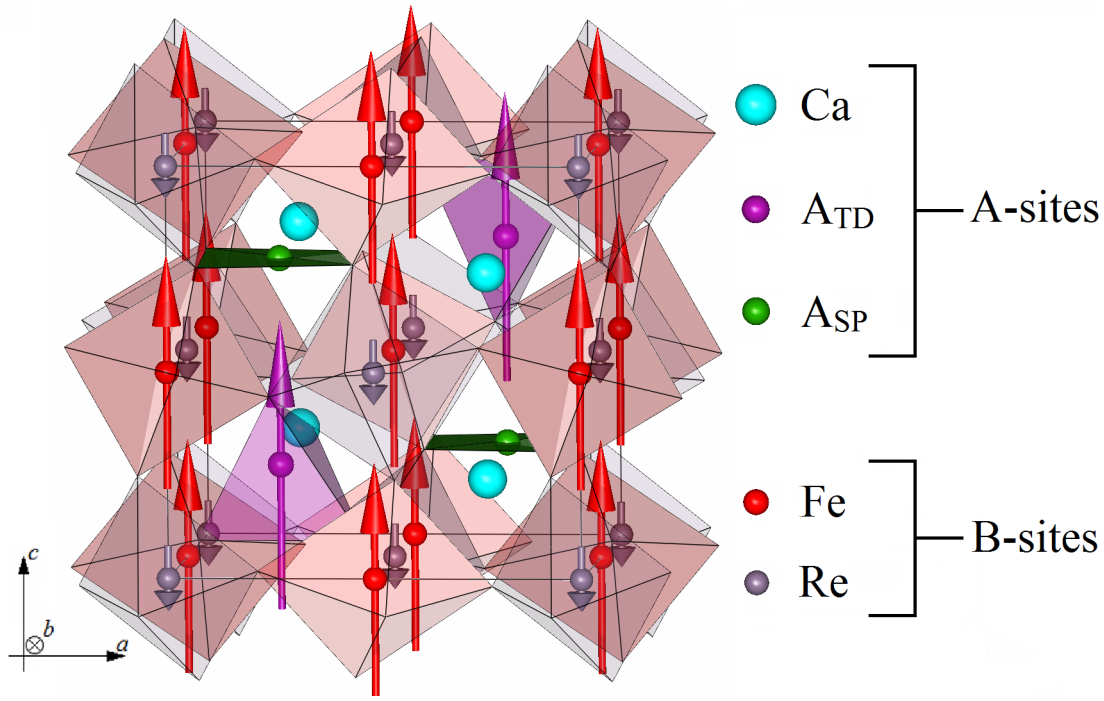

Figure 5.7 | *The crystal and magnetic structure at 2 K of $Ca(Mn_{0.5}Cu_{0.5})FeReO_6$. Columnar A-site order of Ca and (Mn/Cu) is shown, with the 4-coordinate sites further split into tetrahedral (A_{TD}) and square planes (A_{SP}). Rock salt B-site order is also observed between Fe and Re. G-type ferrimagnetism on the Fe/Re sublattice, with an additional component of moment from A_{TD} that is parallel to the total magnetisation and effectively enhances the total magnetisation of $Ca(Mn_{0.5}Cu_{0.5})FeReO_6$ when compared to $CaMnFeReO_6$. Image generated with FPStudio.*[125]

While there is a magnetic transition above 100 K, where A-site magnetic order occurs, there is no evidence for any transition similar to that seen in the $NdMnMnSbO_6$ double double perovskite, where the spin moments reorientate from the *c*-axis on to the *a*-axis at the onset of Nd spin ordering. However, due to the small tetragonal distortion it is possible that tilts on to the *a*-axis could occur and not be detectable by neutron diffraction, as in Rietveld fits a similar magnetic structure oriented along the *a*-axis results in almost equivalent fits to neutron data.

Table 5.5 | Bond lengths, angles and BVS values for Ca(Mn$_{0.5}$Cu$_{0.5}$)FeReO$_6$ in space group $P4_2/n$ from the neutron profile fit at 2 K.

Bond	M – O length / Å			Bond	M – O length / Å
Ca – O1	2.72(2) × 2			Fe – O1	1.99(4) × 2
Ca – O1	2.84(2) × 2			Fe – O2	1.94(3) × 2
Ca – O2	2.54(1) × 2			Fe – O3	2.16(1) × 2
Ca – O3	2.39(1) × 2			**<Fe – O>**	2.03(2)
Ca – O3	2.52(1) × 2			Re – O1	2.05(4) × 2
<Ca – O>	2.60(2)			Re – O2	2.06(3) × 2
A$_{TD}$ – O2	2.08(1) × 4			Re – O3	1.73(1) × 2
A$_{SP}$ – O1	2.04(1) × 4			**<Re – O>**	1.95(2)
Cation	**BVS**	**Cation**	**BVS**	**B – O# – B′**	**Angle / degrees**
Ca	1.63	<A$_{TD}$>/<A$_{SP}$>	1.67/1.90	Fe – O1 – Re	141.8(9)
Mn$_{TD}$/Cu$_{TD}$	1.82/1.34	Fe	2.97	Fe – O2 – Re	143.9(5)
Cu$_{SP}$/Mn$_{SP}$	1.53/2.06	Re	5.22	Fe – O3 – Re	155.2(6)

The program BondStr in the FullProf Suite was used to compute this data.[125]

Table 5.6 | Bond lengths, angles and BVS values for Ca(Mn$_{0.5}$Cu$_{0.5}$)FeReO$_6$ in space group $P4_2/n$ from the neutron profile fit at 300 K.

Bond	M – O length / Å			Bond	M – O length / Å
Ca – O1	2.77(7) × 2			Fe – O1	2.02(4) × 2
Ca – O1	2.84(3) × 2			Fe – O2	2.13(2) × 2
Ca – O2	2.57(3) × 2			Fe – O3	2.02(4) × 2
Ca – O3	2.41(2) × 2			**<Fe – O>**	2.06(2)
Ca – O3	2.49(3) × 2			Re – O1	2.07(4) × 2
<Ca – O>	2.62(4)			Re – O2	1.90(2) × 2
A$_{TD}$ – O2	2.06(2) × 4			Re – O3	1.88(4) × 2
A$_{SP}$ – O1	1.96(2) × 4			**<Re – O>**	1.95(2)
Cation	**BVS**	**Cation**	**BVS**	**B – O# – B′**	**Angle / degrees**
Ca	1.61	<A$_{TD}$>/<A$_{SP}$>	1.63/2.06	Fe – O1 – Re	137.6(5)
Mn$_{TD}$/Cu$_{TD}$	1.92/1.42	Fe	2.73	Fe – O2 – Re	142.5(4)
Cu$_{SP}$/Mn$_{SP}$	1.89/2.55	Re	4.85	Fe – O3 – Re	155.6(2)

The program BondStr in the FullProf Suite was used to compute this data.[125]

Bond lengths, B – O – B′ angles and bond valence sum (BVS) values for Ca, A_{TD}, A_{SP}, Fe and Re are tabulated for temperatures of 2 (**Table 5.5**) and 300 K (**Table 5.6**). These results help to confirm formal charge states of these cation sites, as well as demonstrate some interesting behaviour of this material at low temperatures. Many of the tabulated parameters remain largely unchanged between 2 and 300 K, however when examining the (Fe/Re)–O bond lengths a clear transition can be observed. These bond lengths are plotted in **Fig. 5.8**.

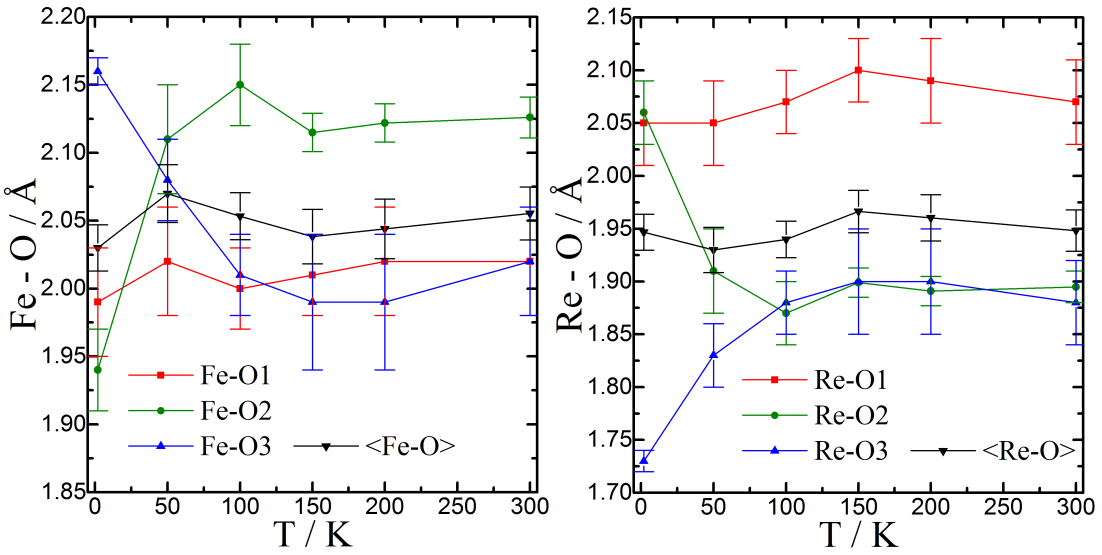

Figure 5.8 | *Bond lengths for Fe–O and Re–O versus temperature in $Ca(Mn_{0.5}Cu_{0.5})FeReO_6$. FeO_6 octahedra remain elongated (four short, two long bonds) at all temperatures, however the pair of long Fe–O bonds switch from being Fe–O2 at high temperatures to Fe–O3 at low temperatures. ReO_6 octahedra are elongated at high temperatures, switching to being compressed (four long, two short bonds) at low temperatures. The onset of these changes appears to be approximately at the A-site magnetic ordering transition.*

From neutron diffraction it can be determined that the A-site magnetic ordering transition occurs between 150 and 100 K. Examining the Fe–O and Re–O bond lengths determined by neutron diffraction shows a switch in the distortions of these octahedra with an onset that seems to coincide with this A-site ordering. In particular, the ReO_6

octahedra switch from being elongated at high temperatures (with long Re–O1 bonds and short Re–O2/O3 bonds) to compressed at low temperatures (with short Re–O3 bonds and long Re–O1/O2 bonds). Considering the expected Jahn-Teller (J-T) distortions (*1.1.1.c – Jahn Teller Theorem*), an orbitally ordered state of $Re^{5+}O_6$ ($5d^2$) would be expected to be an elongated octahedron, rather than the compressed $Re^{5+}O_6$ observed at low temperatures in this material. The $Fe^{3+}O_6$ ($3d^5$) octahedra are not expected to undergo any J-T distortion. These are expanded at all temperatures, but they do switch from being expanded along Fe–O2 at high temperatures to expanded along Fe–O3 at low temperatures. Another effect that arises at the A-site magnetic ordering transition may help explain this, as the *c*-axis ceases to contract when cooling $Ca(Mn_{0.5}Cu_{0.5})FeReO_6$ through this transition (**Fig. 5.9**).

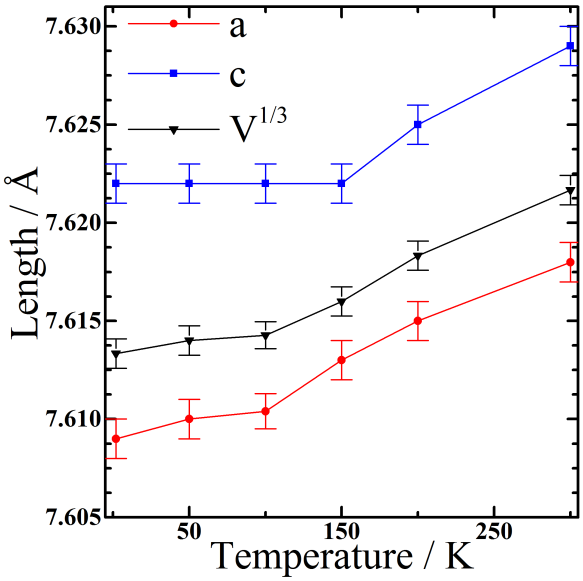

Figure 5.9 | *Lattice parameters: a, c and cube root of volume: $V^{1/3}$, for $Ca(Mn_{0.5}Cu_{0.5})FeReO_6$ in the tetragonal $P4_2/n$ space group versus temperature.*

This anomaly in the lattice contraction in $Ca(Mn_{0.5}Cu_{0.5})FeReO_6$ could be related to the changes in distortion of octahedra in the material. An important note is

that B/B′–O1 bonds are predominantly along the *c*-axis, while B/B′–O2 and B/B′–O3 bonds are predominantly in the *ab*-plane. A-site magnetic order could cause magnetoelasticity, as in order to minimise the energy of interaction between magnetic moments in A–O–B/B′ couplings bond lengths may also change to compensate and ultimately result in a change in the ratio *a*:*c*.

5.3.3. Magnetometry Measurements of $Ca(Mn_{0.5}Cu_{0.5})FeReO_6$

The SQUID magnetometry data collected on $Ca(Mn_{0.5}Cu_{0.5})FeReO_6$ is consistent with interpretations with neutron diffraction data. This magnetometry data is displayed in **Fig. 5.10**, with individual site moments determined by refinement to neutron diffraction data overlaid on top.

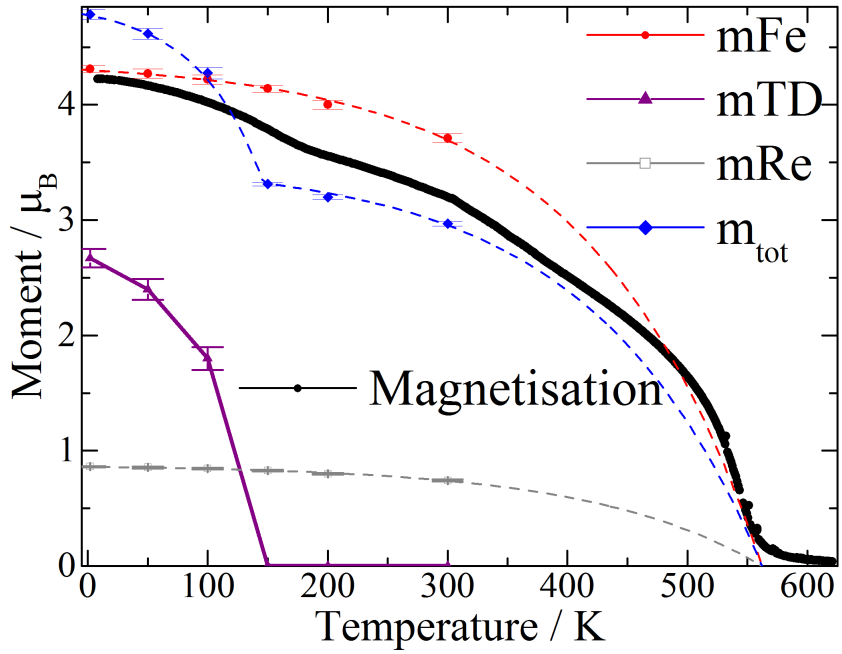

Figure 5.10 | *Magnetisation of $Ca(Mn_{0.5}Cu_{0.5})FeReO_6$ (field cooled, 0.5 T) with the magnetic moments from neutron refinements of Fe, Re and A_{TD} sites overlaid on this plot. Also plotted is the total magnetic moment per formula unit observed, m_{tot}, from neutron diffraction, showing a similar temperature dependence to the overall magnetisation, with T_c of 560 K. Note that there are only ½A_{TD} sites per formula unit, compared to 1 Fe and 1 Re site.*

The high-temperature ferrimagnetic ordering transition can be seen at T_c ~560 K, signifying the onset of G-type magnetic ordering of the Fe/Re sublattice. This is enhanced when compared to the ferrimagnetic ordering temperature of $CaMnFeReO_6$ (T_c ~500 K). Another transition can be observed at ~160 K, determined to be the onset of the A-site magnetic ordering, however this is not observed in the 150 K neutron dataset, presumably as moments on A_{TD} sites are too low to be discerned at this temperature. The total moment as determined by neutron diffraction is calculated by the moment due to ferrimagnetic Fe/Re order, with an additional moment from the tetrahedral A-site: $m_{tot} = mFe - mRe + ½\ mTD$. Magnetic hysteresis is also displayed in **Fig. 5.11**, showing low coercive fields of 600 Oe at 2 K and displaying a high saturated magnetisation of 4.8 μ_B f.u.$^{-1}$, consistent with 4.78(4) μ_B f.u.$^{-1}$ calculated from Rietveld analysis and enhanced compared to $CaMnFeReO_6$ (4.3 μ_B f.u.$^{-1}$).

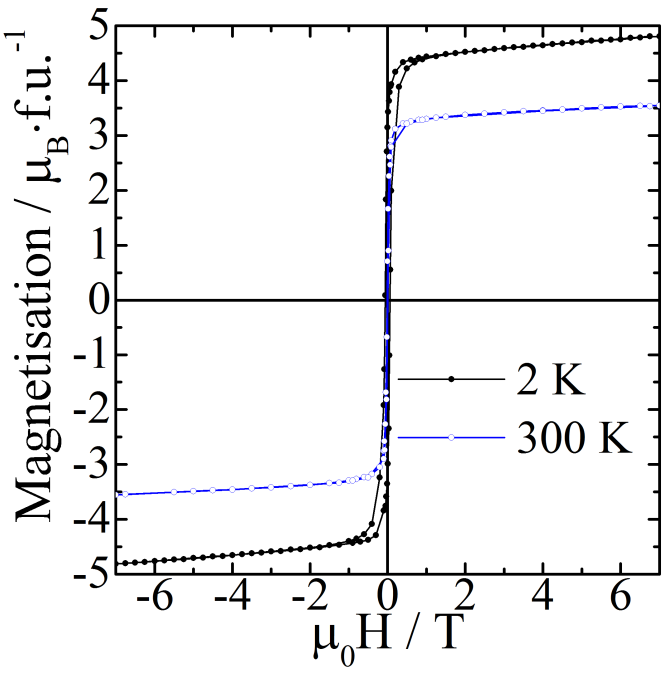

Figure 5.11 | *Magnetic hysteresis loops between fields of μ_0H = +7 and -7 T of $Ca(Mn_{0.5}Cu_{0.5})FeReO_6$ at constant temperatures of 2 and 300 K.*

5.3.4. Magnetoresistance of $Ca(Mn_{0.5}Cu_{0.5})FeReO_6$

Magnetoresistance (MR) measurements of $Ca(Mn_{0.5}Cu_{0.5})FeReO_6$ reveal unusual and unexpected behaviour, as shown in **Fig. 5.12**. There are many striking differences between the MR behaviour of this material when compared to that of $CaMnFeReO_6$.

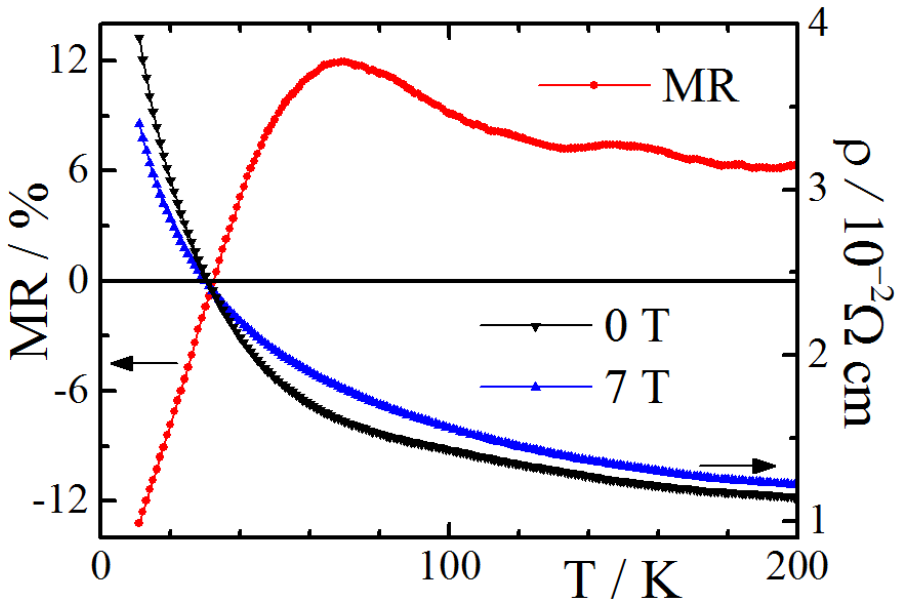

Figure 5.12 | *Resistivity of $Ca(Mn_{0.5}Cu_{0.5})FeReO_6$ versus temperature at constant fields of 0 and 7 T. Also shown is the calculated magnetoresistance, MR, at 7 T. A clear switch from positive MR at high temperatures to negative MR at low temperatures is observed, with the onset of this switch occurring at ~70 K and the sign change occurring at ~28 K.*

The magnitude of the resistivity in this material indicates that there is bulk metallic conductivity, with resistivity remaining on the order of 10^{-2} Ω cm between 10 and 200 K, and the temperature variation of this resistivity is consistent with what may be expected from interfacial resistance between adjacent grains in polycrystalline samples. This effect is observed in samples of Sr_2FeMoO_6, the first reported double perovskite with intergrain tunnelling MR.[72] The low magnitude of resistivity in

$Ca(Mn_{0.5}Cu_{0.5})FeReO_6$ combined with the small increase in resistivity on cooling (corresponding to a low activation energy of ~3 meV from an Arrhenius model) suggests that this is also the case here. This data shows a clear switch in the MR of this material between positive MR at high temperatures to negative MR at low temperatures.

This MR switching is also observed in MR versus field hysteresis measurements, displayed in **Fig. 5.13**. The onset of this transition appears to be at ~70 K, the temperature where the MR begins to decrease, with the sign of MR switching at ~40 K. This resistivity behaviour is distinctly different from that observed in $CaMnFeReO_6$, where MR remains negative down to 20 K and resistivity is much higher, spanning five orders of magnitude.

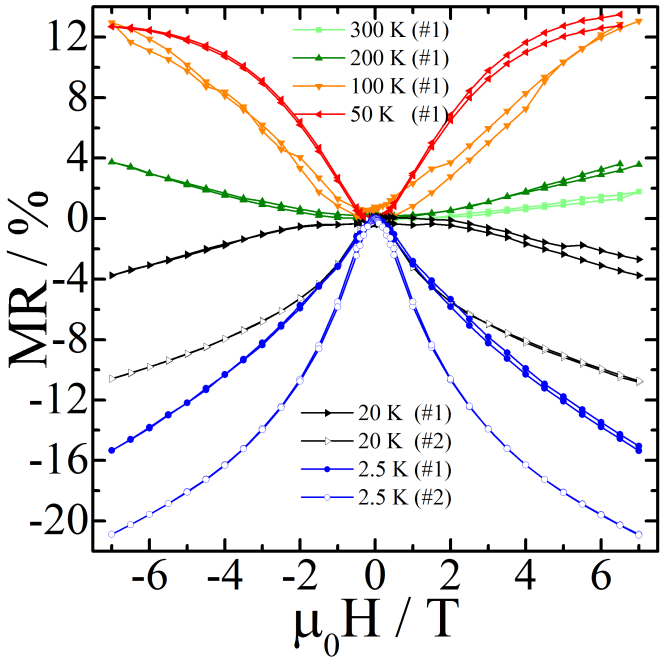

Figure 5.13 | *Magnetic hysteresis loops of the magnetoresistance, MR, in $Ca(Mn_{0.5}Cu_{0.5})FeReO_6$ sample-14 (#1). A switch from positive MR (> 50 K) to negative MR (20 K and 2.5 K) can be observed. Also shown are two other MR versus H loops at 20 and 2.5 K from sample-15 (#2), showing some variation between samples in the magnitude of MR in the low-temperature negative regime, possibly due to different sample morphologies.*

The MR switching transition is potentially the result of a spin reorientation transition of the magnetic structure, similar to the behaviour observed in Mn_2FeReO_6 at ~75 K. This transition in Mn_2FeReO_6 acts to provide a low-temperature positive MR mechanism that cancels out the higher temperature negative MR mechanism. If a spin reorientation transition is responsible for these effects in $Ca(Mn_{0.5}Cu_{0.5})FeReO_6$ then it must act to provide a negative MR mechanism that cancels out the positive MR of the high-temperature regime. It is possible that this is the case, as the orientation of magnetic moments in this material are unable to be defined accurately from powder neutron diffraction due to the small tetragonal distortion ($a \sim c$).

Another possibility here is that the square planar site, on which no ordered magnetic moment could be observed by neutron diffraction and which is occupied by Cu/Mn in an approximately 3:2 ratio, is affected by the application of magnetic field. If this square planar site was occupied solely by Cu^{2+} ($3d^9$, $S = {}^1/_2$), then it could be expected that the moment on this site may be small enough to not be detected by neutron diffraction. However, the significant amount of Mn^{2+} ($3d^5$, $S = {}^5/_2$) on this site should result in a magnetic moment that is detectable by neutron diffraction, if this site is magnetically ordered. It is therefore very likely that this site is magnetically frustrated, explaining the lack of ordered moment. The effect that a magnetic field would have on this frustrated site, and the effect this would have on the rest of the magnetic structure of $Ca(Mn_{0.5}Cu_{0.5})FeReO_6$ is unknown, however this could result in a mechanism for the observed MR effects.

Assuming that a transition in the magnetic structure is responsible for the MR switching mechanism, this could be explored by carrying out powder neutron

diffraction measurements under an applied magnetic field. If this affects the magnetic structure by influencing the frustrated A_{SP} site then it may be detectable in this manner. However, if the magnetic structure is modified by a subtle reorientation from the *c*-axis to the *a*-axis, this may not be resolved due to the small tetragonal distortion and single crystal neutron diffraction would be required to discern this, which would be difficult to carry out as growth of a large enough crystal of $Ca(Mn_{0.5}Cu_{0.5})FeReO_6$ under high pressure is not a trivial synthesis.

5.3.5. X-ray Magnetic Circular Dichroism: $Ca(Mn_{0.5}Cu_{0.5})FeReO_6$

X-ray Absorption Near-Edge Spectra (XANES) and calculated X-ray Magnetic Circular Dichroism (XMCD) at 2.2 and 290 K are shown in **Fig. 5.14** and **5.15** for Re L_2 and L_3-edges, respectively.

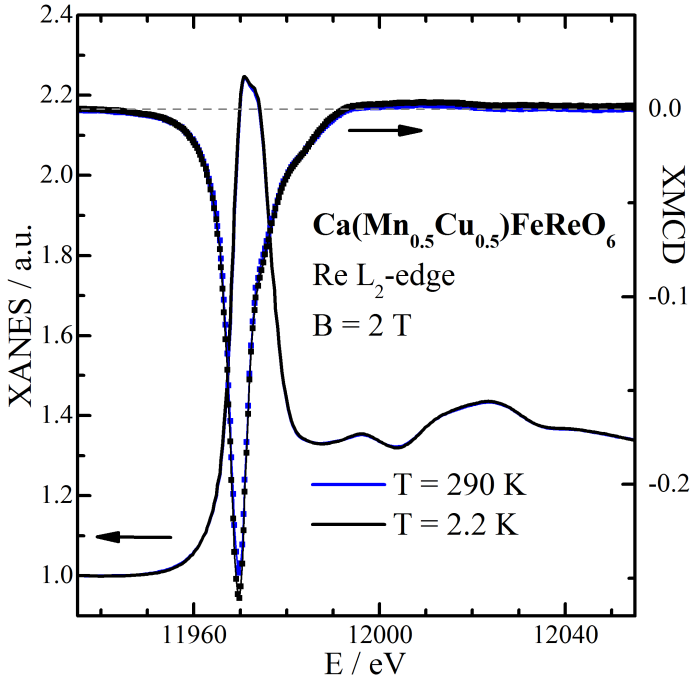

Figure 5.14 | *X-ray Absorption Near-Edge and X-ray Magnetic Circular Dichroism on $Ca(Mn_{0.5}Cu_{0.5})FeReO_6$ Re L_2-edge.*

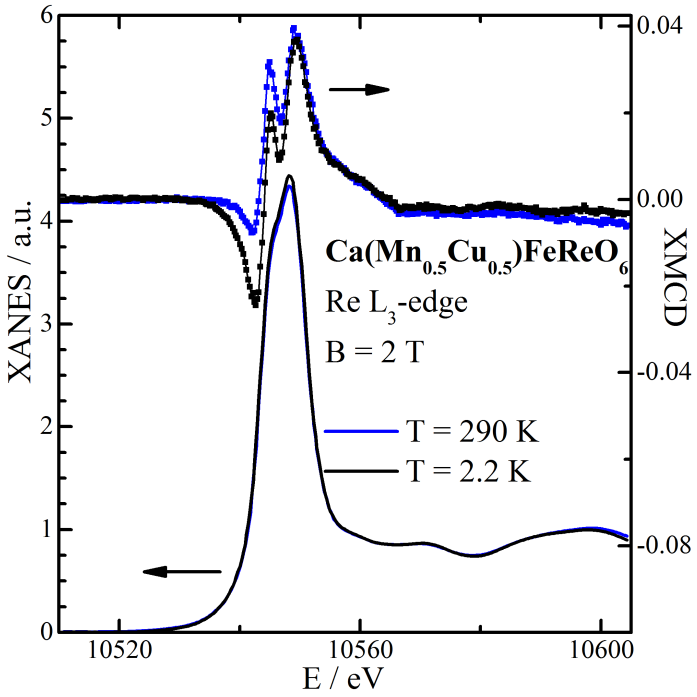

Figure 5.15 | *X-ray Absorption Near-Edge and X-ray Magnetic Circular Dichroism on $Ca(Mn_{0.5}Cu_{0.5})FeReO_6$ Re L_3-edge.*

From integrals of XANES and XMCD in the range of these absorption edges, the ratios between spin moment (m_S) and orbit moment (m_L) for Re can be calculated using **Equation 2.31**, derived from the sum rules defined in '*2.3.3. X-ray Magnetic Circular Dichroism*'. The magnitudes of moments can also be calculated using values of n_h, the number of *d*-state electron holes. A sensible value for n_h in the case of Re would be somewhere between 8 and 9, depending on the exact valence state (between Re^{5+} and Re^{6+}). Values for m_S, m_L and the total moment of Re (*mRe*) as calculated from this XMCD data are displayed in **Table 5.7** for values where $n_h = 8$ (lower bound) and $n_h = 9$ (upper bound). These values show that there is no significant change in *mRe* observed from XMCD as $Ca(Mn_{0.5}Cu_{0.5})FeReO_6$ is cooled from 290 to 2.2 K, and only a slight reduction in the m_S/m_L ratio.

Table 5.7 | Calculated orbit (m_L) and spin (m_S) moments from XMCD data at B = 2 T for Re in $Ca(Mn_{0.5}Cu_{0.5})FeReO_6$ at n_h values of 8 and 9, their ratio: m_L/m_S and the total Re moment: *mRe*.

	m_S/m_L	m_L / μ_B		m_S / μ_B		*mRe* / μ_B	
T / K	n_h:	8	9	8	9	8	9
290	-3.64	0.20	0.22	-0.71	-0.80	-0.51	-0.58
2.2	-3.30	0.22	0.25	-0.74	-0.83	-0.51	-0.58

Negative moments refer to antiparallel alignment to Fe moments.

These observations may suggest that, as in Mn_2FeReO_6, there could be a magnetic reorientation in $Ca(Mn_{0.5}Cu_{0.5})FeReO_6$ at low temperatures. As explained in '*2.3.3. X-ray Magnetic Circular Dichroism*' and '*3.3.5. X-ray Magnetic Circular Dichroism: Mn_2FeReO_6*', XMCD is maximised when the spin moment of *d*-states is aligned collinear to the X-ray vector. A reduction in the value of *mRe* that is observed by XMCD can be noted as the temperature is reduced in Mn_2FeReO_6. This is a material known to have a magnetic reorientation at ~75 K (that also causes a switch in the sign of the magnetoresistance). The lack of a considerable change in the value of *mRe* in $Ca(Mn_{0.5}Cu_{0.5})FeReO_6$ between 290 and 2.2 K suggests this could also be the case in this material (as we might expect this to increase towards lower temperatures), even if there is no reorientation resolved by neutron diffraction. This could be an explanation for magnetoresistance switching in $Ca(Mn_{0.5}Cu_{0.5})FeReO_6$, as a reorientation similar to that observed in Mn_2FeReO_6 would result in a non-collinear alignment of Re moments with the total magnetisation of the material, and hence a non-collinear alignment of Re moments with the X-ray vector. The XMCD sum rules require that the moment of the magnetic ion to be studied in the material and the X-ray vector are collinear to be truly valid, and if this is not the case then this would result in a reduction of the observed XMCD effect (and therefore a reduction in the calculated value of *mRe*). Unfortunately, it was not possible to acquire a detailed temperature dependence

of XMCD in this material, and as such this hypothesis cannot be confirmed. However, it remains a possibility that some form a spin reorientation is present (even if it is small). Shown in **Fig. 5.16** are XMCD moment vs. field measurements for $Ca(Mn_{0.5}Cu_{0.5})FeReO_6$, showing that the 17 T value of *mRe* is actually reduced at 2.2 K when compared to 290 K. There is also no significant change in the spin to orbital moment ratio (**Table 5.7**).

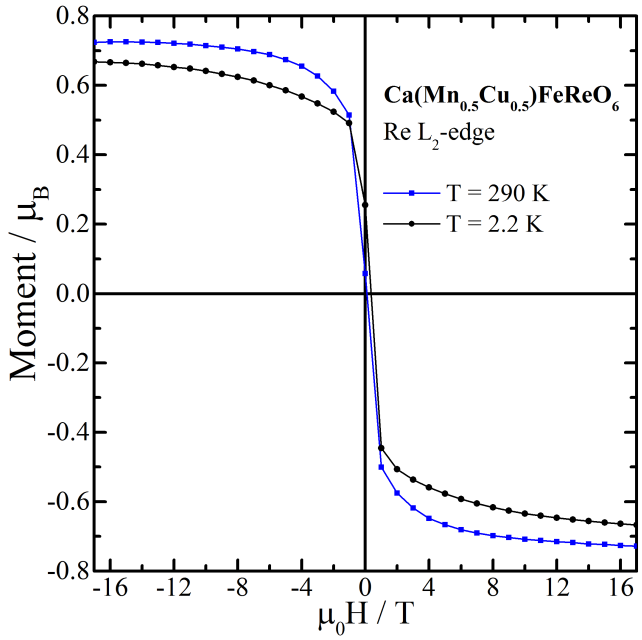

Figure 5.16 | *XMCD moment vs. field of the Re L_2-edge at field strengths in the range of ±17 T for $Ca(Mn_{0.5}Cu_{0.5})FeReO_6$. These measurements have been normalised to values of m_{Re} (n_h = 8) calculated from sum rules at each temperature.*

5.4. Conclusions

Following the discovery of double double cation ordering in $CaMnFeReO_6$, with 1:1 columnar A-site order and 1:1 rock salt B-site order, similar to that found in $RMnMnSbO_6$,[64] attempts to exploit the different coordination environments of the small 4-coordinated A-sites have been made. These 4-coordinated sites alternate down

the column between tetrahedral coordination and square planar coordination. By substitution of half the Mn in $CaMnFeReO_6$ by Cu, the synthesis of a triple double perovskite was attempted in the form of $Ca(Mn_{0.5}Cu_{0.5})FeReO_6$, with order of five different cations Ca^{2+} (10-coordinate A-sites), Mn^{2+} (tetrahedral A_{TD}-sites), Cu^{2+} (square planar A_{SP}-sites) and Fe^{3+}/Re^{5+} with rock salt order (octahedral $BO_6/B'O_6$).

Examination of $Ca(Mn_{0.5}Cu_{0.5})FeReO_6$ by laboratory X-ray diffraction has found that this material is tetragonal and can be well fit by the $P4_2/n$ columnar-A/rock salt-B double double perovskite space group of $RMnMnSbO_6$. The degree of cation order in these syntheses may vary significantly and result in different degrees of tetragonal distortion, with presumed monoclinic double perovskite impurity phases also noted in some syntheses. A high degree of rock salt order between Fe and Re is observed by X-ray analysis, but this is not sufficient to accurately determine the cation ordering between columns of Ca and (Mn/Cu) or between A_{TD} or A_{SP}. Analysis of neutron diffraction data collected on WISH at the ISIS Neutron Facility suggests that there is a preference for Mn^{2+} to occupy tetrahedral sites versus Cu^{2+} but this preference only results in a 3:2 ratio of Mn:Cu. A similar 3:2 ratio exists for Cu:Mn on square planar sites, suggesting that there is only a slight preference for this cation order.

Despite only a small preference for cation order between tetrahedral and square planar sites, there are distinct differences between this Cu^{2+} containing material when compared to that of the parent material: $CaMnFeReO_6$. Regarding the magnetic properties of $Ca(Mn_{0.5}Cu_{0.5})FeReO_6$, an enhanced T_c of 560 K for the onset of

ferrimagnetic Fe^{3+}/Re^{5+} spin order and an enhanced value of μ_{sat}, of 4.8 μ_B f.u.$^{-1}$, is found when comparing this material to $CaMnFeReO_6$, which has T_c = 500 K and μ_{sat} = 4.3 μ_B f.u.$^{-1}$. This can be explained by examination of the magnetic structure as determined by neutron diffraction. Neutron diffraction data of these two materials can be fit with magnetic structures containing similar ferrimagnetic G-type order of Fe/Re collinear with the *c*-axis. A_{TD} and A_{SP}-sites in $CaMnFeReO_6$ order ferrimagnetically at ~70 K, with A_{TD} spins parallel to Fe (A_{SP} antiparallel to Fe). In $Ca(Mn_{0.5}Cu_{0.5})FeReO_6$ A-site spin order occurs at higher temperatures of ~160 K, again A_{TD} spins order parallel to Fe, but no appreciable moment is detected on A_{SP}. While A_{SP} is occupied primarily by Cu^{2+} ($3d^9$, $S = {}^1/_2$), there is still a large amount of Mn^{2+} ($3d^5$, $S = {}^5/_2$) present which should still result in a detectable moment if there is long range magnetic order on this site. The lack of moment here suggests that this site is magnetically frustrated and results in the enhancement of the total magnetisation of $Ca(Mn_{0.5}Cu_{0.5})FeReO_6$ when compared to that of $CaMnFeReO_6$.

The resistivity of $Ca(Mn_{0.5}Cu_{0.5})FeReO_6$ also shows interesting behaviour when compared to that of $CaMnFeReO_6$, with the Cu^{2+} substitution appearing to change the material to have bulk metallic conductivity. The temperature dependence of the resistivity follows a behaviour consistent with a polycrystalline bulk metal possessing resistive grain boundaries. Magnetoresistance (MR) in $CaMnFeReO_6$ is negative at all temperatures down to 20 K, however the Cu^{2+} substituted material has positive MR at high temperatures, which is unusual in double perovskites with ferrimagnetic rock salt Fe/Re.[47,74] This MR then begins to reduce at ~70 K, before switching to negative at ~40 K. Different samples show a variation between the

magnitudes of MR in this low-temperature negative regime, suggesting this could be due to differences in sample morphology and grain sizes. This mechanism of negative MR could therefore be intergrain tunnelling MR. High-temperature positive MR could be explained by the spin-scattering of charge carriers by paramagnetic A_{TD} and A_{SP}, which is increased by the application of a field. At temperatures below A-site ordering (T_A ~160 K), this effect would be reduced and, in 7 T fields, the negative intergrain tunnelling mechanism starts to cancel out the paramagnetic scattering mechanism at ~70 K.

To summarise, samples of $Ca(Mn_{0.5}Cu_{0.5})FeReO_6$ have been synthesised and analysed by X-ray and neutron diffraction, magnetometry, X-ray magnetic circular dichroism and by resistivity measurements. X-ray diffraction shows that Fe/Re are ordered across B-sites in a rock salt manner, while neutron diffraction shows a columnar order of Ca/(Mn/Cu) and a further partial order of Mn^{2+}/Cu^{2+} across tetrahedral/square planar sites. This material can be considered a partial triple double perovskite. The magnetic structure is similar to that of the parent material ($CaMnFeReO_6$), but a significant ordered moment is not found on the square planar sites. This has the effect of enhancing the ordering temperature and saturated moment of $Ca(Mn_{0.5}Cu_{0.5})FeReO_6$. MR measurements of this material yield an interesting switch in the sign of MR, with positive MR above ~40 K and negative MR below. These results have been published in Chemistry of Materials (*Complex Ferrimagnetism and Magnetoresistance Switching in Ca-Based Double Double and Triple Double Perovskites*)[147] and appended data on $Ca(Mn_{0.5}Cu_{0.5})FeReO_6$ is provided in '**Appendix C**'.

Chapter 6. $CaMnMnReO_6$ – Large Coercivity and Mutually Frustrated A and B-site Spin Orders in a Double Double Perovskite

6.1. Introduction

The materials described in previous chapters all focus on rock salt order of Fe/Re with G-type ferrimagnetic order above room temperature. Several examples of perovskites with antiferromagnetic ordering also exist and, due to the fact that B (or B′) sites in perovskites can be considered as networks of edge sharing tetrahedra, this can lead to geometric frustration (e.g. in the spin liquid Ba_2YMoO_6).[144]

While Mn_2FeReO_6 was the first all transition metal double perovskite synthesised (described in '**Chapter 3. Mn_2FeReO_6 – Magnetoresistance Switching Due to Frustration**'), during the course of this work another all transition metal double perovskite was reported: Mn_2MnReO_6.[99,100] This material is described further in '*1.3.4. – Double Perovskite Manganites*'. This double perovskite adopts the monoclinic $P2_1/n$ structure, similar to that of Mn_2FeReO_6 and can be synthesised under similar high-pressure/temperature conditions. Mn_2MnReO_6 possesses a rock salt ordering of Mn^{2+}/Re^{6+} cations and two successive magnetic transitions are observed at 109 K (antiferromagnetic Mn_A and Mn_B spin order) and 99 K (Re spin order). Spin moments of Mn_A, Mn_B and Re are oriented in the *ab*-plane, with Mn_A perpendicular to Mn_B and Re constrained in fits to be collinear with Mn_B. These perpendicular orientations suggest that spin order of these sublattices are frustrated.

Chapter 6. $CaMnMnReO_6$

Described in '**Chapter 4. $Ca_xMn_{2-x}FeReO_6$ – Discovery of Double Double Cation Order in Ca-Based Perovskites**' is the A-site substitution of Mn with Ca in Mn_2FeReO_6. When $x = 1$ ($CaMnFeReO_6$) a recently discovered simultaneous cation order of 1:1 columnar A-site order (Ca^{2+}/Mn^{2+}) and 1:1 rock salt B-site order (Fe^{3+}/Re^{5+}) is observed, which changes the magnetic structure and properties of the material, but maintains the overall ferrimagnetic sublattice of Fe/Re spin order. A similar substitution of Mn with Ca in Mn_2MnReO_6 may yield an analogous material in the form of $CaMnMnReO_6$. This material could be expected to have same cation ordering while maintaining overall antiferromagnetic interactions, a well as a likelihood to exhibit magnetic frustration, producing an exotic magnetic structure or otherwise providing an insight into the exchange pathways in these double double perovskite materials. Large parts of this work, particularly with regards to synthesis and collection of magnetic data, were carried out with the aid of Padraig Kearins as part of his Master's project, who must be acknowledged here for these contributions.

6.2. Experimental

6.2.1. Synthesis of $CaMnMnReO_6$

As the synthetic conditions for $CaMnFeReO_6$ were $P = 10$ GPa, $T = 1400$ °C, this was deemed a good starting point for syntheses of a structural analogue in the form of $CaMnMnReO_6$. These syntheses were conducted using the techniques outlined in '*2.12. High-Pressure Solid-State Synthesis*'. The precursor used was a simple 1:1:1 mole ratio of $CaMnO_3$, MnO and ReO_2. The $CaMnO_3$ metal oxide used in this precursor was prepared by the solid-state reaction of $CaCO_3$ and MnO_2, with two

sintering steps of 1000 °C and 1100 °C each for 24 hours and grinding the product in between these steps.[145] Capsules made of Pt were used to contain the precursor during high-pressure synthesis in the Walker module setup.

6.2.2. Structural Characterisation of $CaMnMnReO_6$

X-ray data was collected on $CaMnMnReO_6$ using a Bruker D2 Phaser diffractometer with a Cu K_α/K_β source of X-rays (see **Fig. 2.10** in '*2.2.2 – X-ray Diffraction*' for clarification of K_α/K_β). Short 15-minute scans were collected for the purposes of phase analysis, to ensure consistency between different syntheses and to select products of high purity for further analysis by neutron diffraction.

A 100 mg aggregate of samples #2-6 was thoroughly mixed and ground for analysis by neutron diffraction on the WISH diffractometer at the ISIS Neutron Facility in high resolution single frame mode, with data collections at 8 different temperatures and varying amounts of proton beam current, measured in microamperes (T = 2 (60 μA), 20 (20 μA), 40 (40 μA), 60 (20 μA), 80 (40 μA), 100 (20 μA), 120 (20 μA), 150 (42 μA) and 300 K (20 μA)). These X-ray and neutron diffraction patterns were analysed and solved using the FullProf Suite and refined by the Rietveld method.[122,125]

6.2.3. Magnetic Measurements of $CaMnMnReO_6$

Magnetometry was carried out on sample #2 of $CaMnMnReO_6$ using a Quantum Design Physical Property Measurement System (PPMS). Zero-field cooled and field cooled magnetic susceptibility was measured from T = 3 to 300 K, in applied

fields of $\mu_0 H$ = 0.5 and 0.05 T. Magnetic hysteresis measurements ($-7 \leq \mu_0 H$ (T) ≤ 7) on $CaMnMnReO_6$ were also measured at temperatures of 80, 40 and 3 K.

6.3. Results & Discussion

6.3.1. Phase Analysis of $CaMnMnReO_6$ Syntheses

Initial phase analysis for $CaMnMnReO_6$ using X-ray diffraction data collected using a Bruker D2 Phaser diffractometer is shown in **Fig. 6.1**. All syntheses show a tetragonal perovskite-type product, with a high degree of rock salt Mn/Re cation order on B-sites. MnO is also observed as a minority phase in all samples. All products appear to be extremely consistent and no synthesis parameters were altered between all six syntheses.

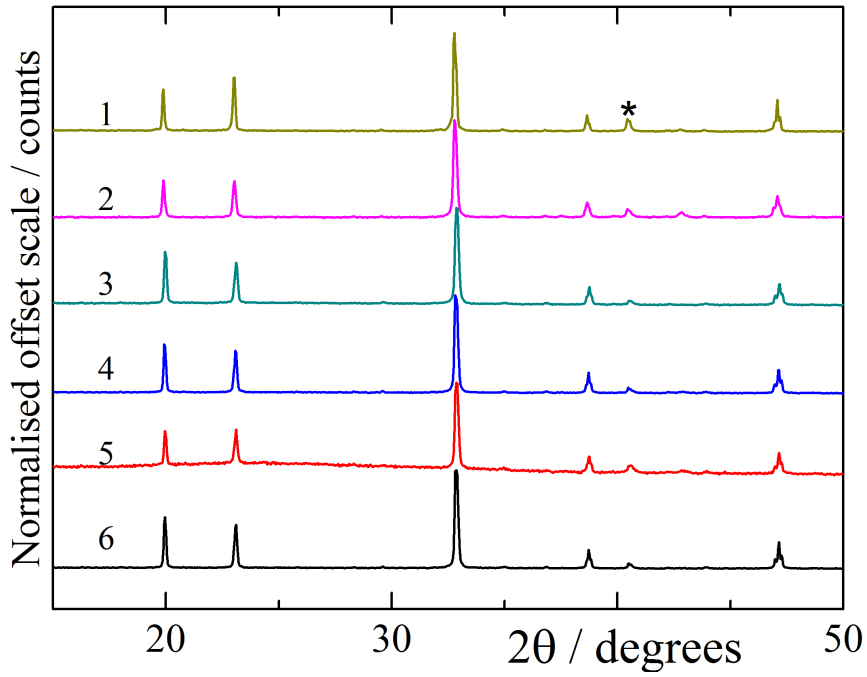

Figure 6.1 | *A stacked plot of normalised raw powder X-ray data initially collected on samples of $CaMnMnReO_6$ for phase analysis (in the 2θ range 15-50°). In general all samples are of high purity with high B-site order, but small, 3-10 % quantities of MnO can be refined. The main reflection for MnO is marked by the asterisk.*

Table 6.1 | A collection of the initial analysis of individual syntheses of $CaMnMnReO_6$, and of the resulting purity and B-site disorder in the double double perovskite product. All syntheses were conducted at 10 GPa and 1400 °C.

Sample no.	Wt. MnO / %	B-Antisite Disorder	χ^2	R_{wp} / %
1	10.6(6)	7.2(4)	6.20	7.71
2	7.4(6)	6.6(4)	2.60	6.42
3	3.4(4)	2.4(2)	2.44	4.70
4	3.6(4)	3.0(2)	2.83	5.02
5	9.3(7)	6.4(4)	1.41	3.91
6	4.1(3)	3.8(2)	3.13	5.09

Samples #2-6 were mixed and examined on WISH at the ISIS Neutron Facility. The measures of the fit, χ^2 and R_{wp}, are shown for X-ray patterns collected over 15 minutes using a Bruker D2 Phaser diffractometer with Cu K_α radiation. All syntheses used platinum capsules.

As with other double double perovskite type materials with columnar A-site order that have been discussed previously, order between A-site Ca and Mn is not able to be determined from this data due to the low X-ray contrast between Ca and Mn. The structure was able to be refined simply by fixing the occupancies of these cations to the ideal fully occupied 10-coordinate Ca^{2+} sites and 4-coordinate Mn^{2+} sites. Due to a high consistency between different syntheses, samples #2-6 were all selected and combined to provide a 100 mg sample for neutron diffraction studies.

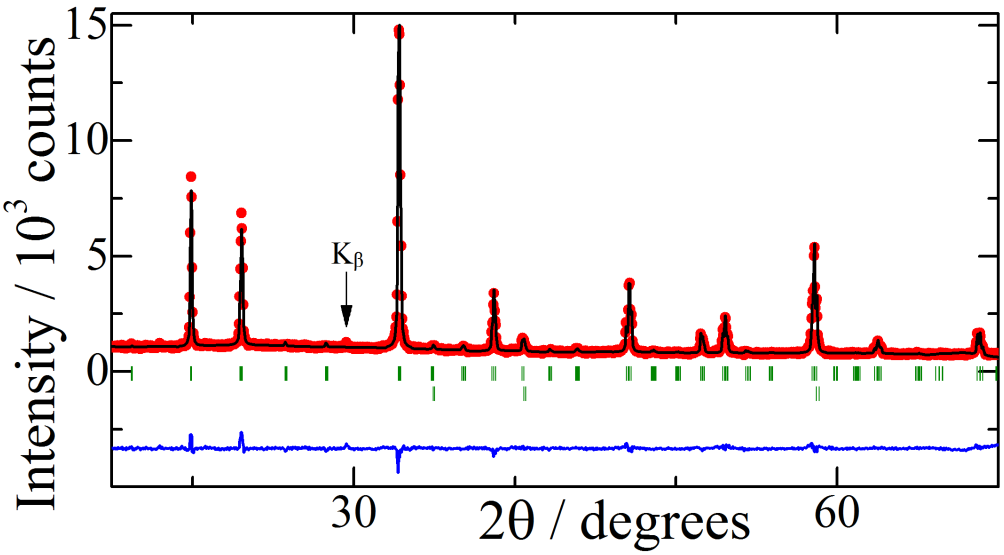

Figure 6.2 | *Rietveld fit to a Cu K_α X-ray pattern of $CaMnMnReO_6$-3 at 300 K (space group: $P4_2/n$). Lower tick marks indicate MnO reflection (3.4 % by weight). A minor intensity from Cu Kβ radiation can be observed, indicated by the arrow (this is explained in **Fig. 2.10** in '2.2.2. – X-ray Diffraction').*

6.3.2. Neutron Crystal & Magnetic Structure of $CaMnMnReO_6$

Rietveld analysis (**Fig. 6.3**) of neutron diffraction data collected on a 100 mg aggregate of samples #2-6 of $CaMnMnReO_6$ using the WISH diffractometer at the ISIS Neutron Facility allows for an accurate characterisation of both the columnar Ca/Mn (b = 4.7/-3.73 fm) A-site order, as well as the Mn/Re (b = -3.73/9.2 fm) B-site order, due to high contrast between these elements.

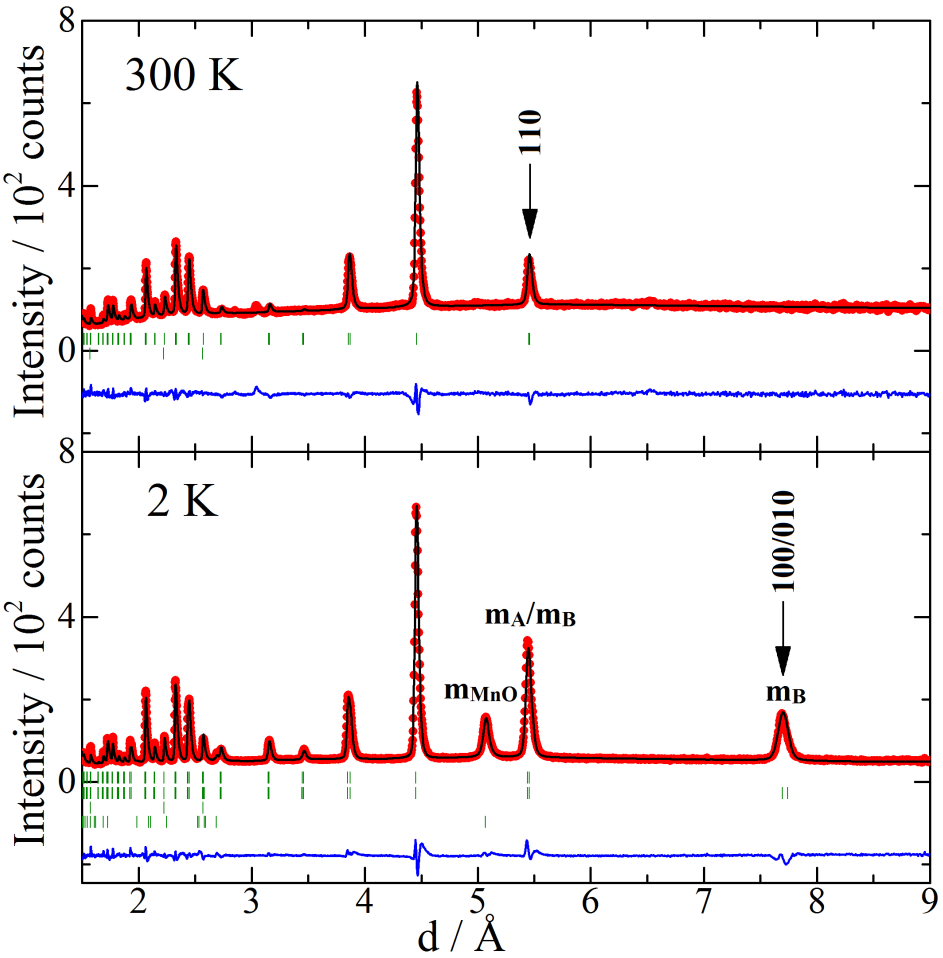

Figure 6.3 | *Neutron and Magnetic Rietveld fits to neutron diffraction data collected on $CaMnMnReO_6$ using the WISH diffractometer at the ISIS Neutron Facility. Patterns shown are from an average of bank 2 and 9.* ***Top****: 300 K.* ***Bottom****: 2 K. Markers m_A and m_B refer to magnetic reflections due to the A and B-site spin order respectively. Sets of tick marks at 300 K indicate nuclear CaMnMnReO6 (phase 1) and nuclear MnO (phase 2) contributions. Sets of tick marks at 2 K indicate nuclear and magnetic contributions from CaMnMnReO6 (phase 1 nuclear, phase 2 magnetic) and MnO (phase 3 nuclear, phase 4 magnetic).*

Columnar order between Ca and Mn is shown by presence of the characteristic 110 reflection at (d ~5.45 Å). These occupancies are able to be refined, showing that 4-coordinate A-sites are occupied solely by Mn^{2+}, and a 5.4(2) % occupancy of Mn^{2+} on the 10-coordinate A-site. Across B-sites, a 4.0(1) % Mn_B/Re antisite disorder is also found.

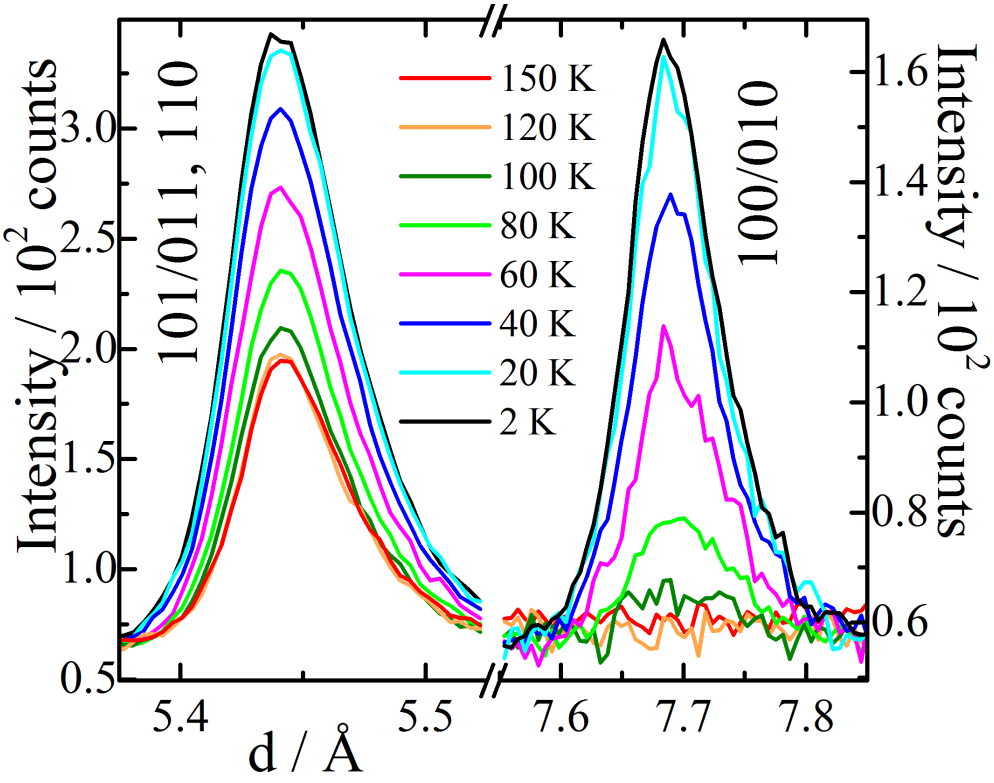

Figure 6.4 | *Evolution of magnetic intensities in $CaMnMnReO_6$. Intensity on the 100/010 reflection is attributed to B-site magnetic order of antiferromagnetic Mn_B^{2+} (and Re^{6+}). Intensity on the 110 reflection is observed at room temperature due to columnar A-site order. Magnetic intensity evolves on the 110 reflection below 120 K, and is attributed to ferromagnetic order of A-site Mn^{2+}.*

As well as revealing this structural order, neutron diffraction allows determination of long range magnetic order in $CaMnMnReO_6$, with magnetic reflections indexed by the propagation vector $\boldsymbol{k}$ = (0 0 0). The evolution of these magnetic intensities is displayed in **Fig. 6.4**. Also observed at d ~5.1 Å is a significant incommensurate magnetic intensity due to MnO as an impurity phase (3.6(2) % by

weight). Symmetry operations for magnetic order in $CaMnMnReO_6$ are shown in **Table 6.2**. There is intensity due to A-site columnar order observed on the 110 and 101/011 reflections (d ~5.45 Å) at all temperatures, but additional magnetic intensity evolves on these reflections below 120 K which can be partly attributed to ferromagnetic A-site order of Mn^{2+}, with Mn_{TD} sites aligning parallel to Mn_{SP} sites (fit with magnetic mode 'A'), as well as a component due to antiferromagnetic Mn_B^{2+} (and Re^{6+}) order. The antiferromagnetic B-site order also contributes to magnetic intensities on the 100/010 reflection (d ~7.7 Å) below 120 K. This is fit with a combination of magnetic mode 'A_g1' and 'A_g2'. Rietveld fits find Mn_B spin order in fits to patterns at 100 K and below, with a second transition at 80 K and below signifying A-site Mn spin order. These symmetry operations describe antiferromagnetic order of Mn_B sites, where moments are oriented in the *ab*-plane. Successive layers of Mn_B spins are oriented at 90° to one another, with Re moments constrained to the same symmetry. Full refined structural and magnetic parameters from Rietveld fits to neutron diffraction data on $CaMnMnReO_6$ are displayed in **Table 6.3**, with tables of bond lengths at 2 and 300 K shown in **Table 6.4** and **6.5**.

Table 6.2 | Magnetic modes in the Γ_1^+ irreducible representation (defined from the Isotropy Suite)[126] for the $CaMnMnReO_6$ magnetic structure. Propagation vector, $\boldsymbol{k}$ = (0 0 0) in space group $P4_2/n$.

B-sites mag. modes:	A_g1		$A_g2^{\dagger}$		$A_g3^{\dagger}$	A-sites mag. modes:	A
Atom	m_x	m_y	m_x	m_y	m_z	Atom	m_z
Mn_B1, Re1[a]	*n/a*	-	-	*n/a*	+	$Mn_{TD}1$, $Mn_{TD}2$[e]	+
Mn_B2, Re2[b]	*n/a*	+	+	*n/a*	+		
Mn_B3, Re3[c]	+	*n/a*	*n/a*	-	+	$Mn_{SP}1$, $Mn_{SP}2$[f]	+
Mn_B4, Re4[d]	-	*n/a*	*n/a*	+	+		

Magnetic modes A_g1 and A_g2 describe B-site magnetism in $CaMnMnReO_6$. [†]For Re, coefficients for A_g2 are negative. B-Sites: [a]Mn_B1 = (0, ½, 0), Re1 = (0, ½, ½); [b]Mn_B2 = (½, 0, 0), Re2 = (½, 0, ½); [c]Mn_B3 = (½, ½, ½), Re3 = (½, ½, 0); [d]Mn_B4 = (0, 0, ½), Re4 = (0, 0, 0). Mode A describes magnetism of A-Sites: [e]$Mn_{TD}1$ = (¼, ¼, ¼), $Mn_{TD}2$ = (¾, ¾, ¾); [f]$Mn_{SP}1$ = (¼, ¼, ¾), $Mn_{SP}2$ = (¾, ¾, ¼). Further details of magnetic structure solution are provided in '*2.2.7 – Magnetic Symmetry Analysis*'.

Table 6.3 | Refined structure parameters for $CaMnMnReO_6$ at 2-300 K in space group $P4_2/n$ using neutron powder diffraction data from the WISH diffractometer at the ISIS Neutron Facility. Magnetic symmetry is follows the descriptions in **Table 6.2**. Sample size 100 mg.

T / K		2	20	40	60	80	100	120	150	300
Cell Param	*a* / Å	7.6972(5)	7.6972(5)	7.6975(5)	7.6994(5)	7.7012(5)	7.7023(5)	7.7031(5)	7.7048(5)	7.7136(7)
	c / Å	7.7450(5)	7.7447(5)	7.7435(5)	7.7423(6)	7.7413(5)	7.7410(6)	7.7404(6)	7.7406(6)	7.7430(8)
	V / Å^3	458.87(7)	458.85(7)	458.86(7)	458.97(7)	459.12(7)	459.24(7)	459.30(7)	459.51(7)	460.7(1)
Ca	*z*	0.281(1)	0.280(1)	0.281(1)	0.280(1)	0.279(1)	0.281(1)	0.280(1)	0.279(1)	0.278(2)
O1	*x*	0.932(1)	0.932(1)	0.932(1)	0.932(1)	0.935(1)	0.939(2)	0.943(3)	0.943(3)	0.948(4)
	y	0.548(1	0.548(1)	0.548(1)	0.548(1)	0.550(1)	0.554(2)	0.559(3)	0.560(3)	0.560(4)
	z	0.2617(8)	0.2619(8)	0.2618(8)	0.2620(8)	0.2616(8)	0.2615(9)	0.2614(9)	0.2617(9)	0.258(1)
O2	*x*	0.741(2)	0.741(2)	0.740(1)	0.739(2)	0.738(2)	0.738(2)	0.739(2)	0.739(2)	0.738(3)
	y	0.9489(8)	0.9496(9)	0.9495(8)	0.9491(8)	0.9495(7)	0.9505(7)	0.9498(7)	0.9491(8)	0.948(1)
	z	0.5749(6)	0.5751(6)	0.5750(6)	0.5755(6)	0.5756(6)	0.5761(6)	0.5768(6)	0.5766(6)	0.5771(9)
O3	*x*	0.769(1)	0.769(1)	0.769(1)	0.768(1)	0.768(1)	0.768(2)	0.768(2)	0.769(2)	0.766(3)
	y	0.0587(8)	0.0590(9)	0.0600(8)	0.0606(8)	0.0615(7)	0.0616(6)	0.0605(7)	0.0607(8)	0.058(1)
	z	0.9670(8)	0.9668(8)	0.9668(8)	0.9672(8)	0.9672(8)	0.9674(8)	0.9690(8)	0.9692(8)	0.968(1)
mMn-B / μ_B		2.60(4)	2.51(4)	2.19(5)	1.65(5)	1.16(7)	0.6(1)	0	0	0
mRe / μ_B		0.258(4)	0.248(4)	0.215(5)	0.163(5)	0.114(7)	0.05(1)	0	0	0
mTD / μ_B		2.4(1)	2.3(1)	1.9(1)	1.5(2)	0.9(2)	0	0	0	0
mSP / μ_B		2.99(8)	2.90(9)	2.58(9)	2.1(1)	1.5(1)	0	0	0	0
m_{tot} / μ_B f.u.$^{-1}$		2.70(6)	2.60(7)	2.24(7)	1.8(1)	1.2(1)	0	0	0	0
A/B	B_{iso} / Å^2	0.52(6)	0.54(7)	0.56(6)	0.59(7)	0.59(6)	0.54(6)	0.55(6)	0.6(1)	1.31(9)
O	B_{iso} / Å^2	1.20(6)	1.19(7)	1.17(6)	1.17(6)	1.22(6)	1.29(6)	1.36(6)	1.3(1)	2.42(9)
R_{wp} / %		4.34	4.60	4.25	4.36	4.09	4.29	4.33	3.94	4.23
χ^2		11.85	4.44	7.91	3.96	6.99	3.87	3.94	6.95	5.76
Q / μA·h		60.00	20.00	40.00	20.00	40.00	20.00	20.00	42.00	20.00

Cation positions are as follows for A-sites: Ca (¼, ¾, *z*), Mn_{TD} (¾, ¾, ¾), Mn_{SP} (¼, ¼, ¾); and for B-sites: Mn_B (0, 0, ½) and Re (0, ½, ½). B-antisite disorder is refined to be 4.0(1) % between Mn_B and Re. A 5.4(2) % occupancy of Mn^{2+} is found on the 10-coordinate A-site, predominantly occupied by Ca^{2+}. The tabulated value of m_{tot} refers to the total magnetisation of $CaMnMnReO_6$, equivalent to the average of *mTD* and *mSP*.

Table 6.4 | Bond lengths, angles and BVS values for $CaMnMnReO_6$ in space group $P4_2/n$ from the neutron profile fit at 2 K.

Bond	M – O length / Å	Bond	M – O length / Å
Ca – O1	2.71(1) × 2	Mn_B – O1	2.125(7) × 2
Ca – O1	2.90(1) × 2	Mn_B – O2	2.115(7) × 2
Ca – O2	2.56(1) × 2	Mn_B – O3	2.14(1) × 2
Ca – O3	2.42(1) × 2	**<Mn_B – O>**	2.127(5)
Ca – O3	2.45(1) × 2	Re – O1	1.953(7) × 2
<Ca – O>	2.61(2)	Re – O2	1.981(7) × 2
Mn_{TD} – O2	2.46(6) × 4	Re – O3	1.85(1) × 2
Mn_{SP} – O1	2.10(1) × 4	**<Re – O>**	1.928(5)

Cation	BVS	Cation	BVS	B – O# – B′	Angle / degrees
Ca	1.94	Mn_B	2.24	Mn_B – O1 – Re	143.4(3)
Mn_{TD}	1.84			Mn_B – O2 – Re	139.9(3)
Mn_{SP}	1.62	Re	5.05	Mn_B – O3 – Re	149.6(3)

The program BondStr in the FullProf Suite was used to compute this data.[125]

Table 6.5 | Bond lengths, angles and BVS values for $CaMnMnReO_6$ in space group $P4_2/n$ from the neutron profile fit at 300 K.

Bond	M – O length / Å	Bond	M – O length / Å
Ca – O1	2.76(4) × 2	Mn_B – O1	2.09(2) × 2
Ca – O1	2.85(4) × 2	Mn_B – O2	2.146(9) × 2
Ca – O2	2.59(3) × 2	Mn_B – O3	2.11(3) × 2
Ca – O3	2.42(2) × 2	**<Mn_B – O>**	2.12(1)
Ca – O3	2.46(2) × 2	Re – O1	1.97(2) × 2
<Ca – O>	2.62(4)	Re – O2	1.972(9) × 2
Mn_{TD} – O2	2.03(1) × 4	Re – O3	1.87(3) × 2
Mn_{SP} – O1	2.12(3) × 4	**<Re – O>**	1.94(1)

Cation	BVS	Cation	BVS	B – O# – B′	Angle / degrees
Ca	1.72	Mn_B	2.30	Mn_B – O1 – Re	144.9(6)
Mn_{TD}	1.92			Mn_B – O2 – Re	138.9(4)
Mn_{SP}	1.52	Re	4.87	Mn_B – O3 – Re	150.4(3)

The program BondStr in the FullProf Suite was used to compute this data.[125]

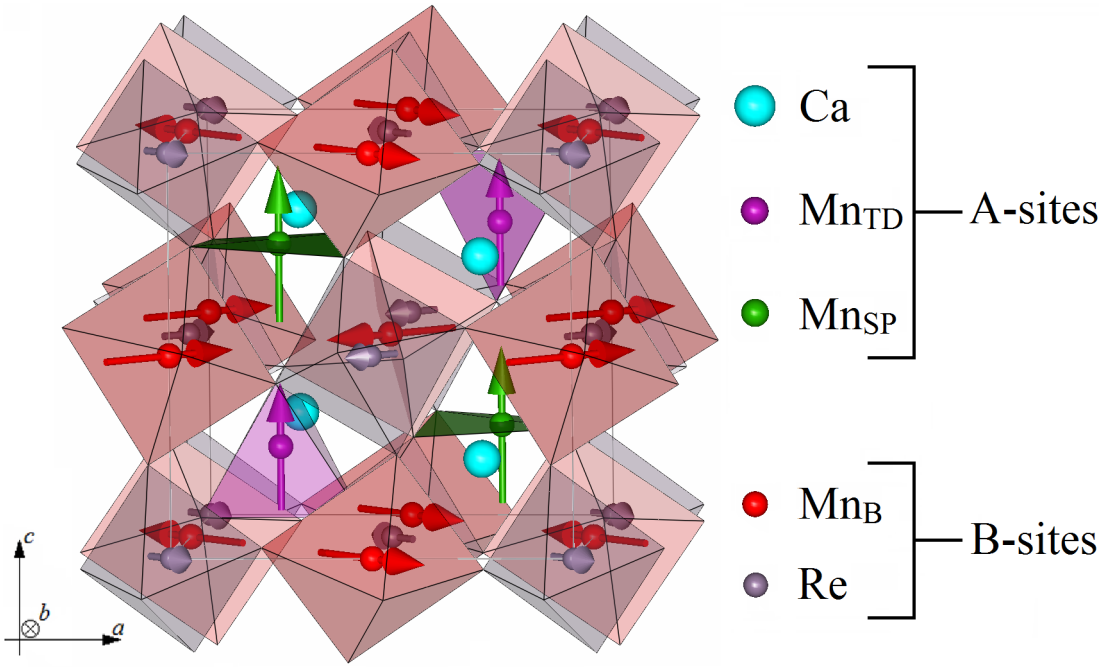

Figure 6.5 | *The crystal and magnetic structure of $CaMnMnReO_6$ at 2 K. Columnar A-site order of Ca and Mn is shown, with 4-coordinate sites further divided into tetrahedral (Mn_{TD}) and square planar (Mn_{SP}) geometries. Rock salt B-site order of Mn_B and Re is also shown. Spin order of B-sites consists of antiferromagnetic layers oriented in the ab-plane, with successive layers perpendicular to one another. A-site Mn_{TD} and Mn_{SP} order ferromagnetically along the c-axis, perpendicular to B-site spin order. Image generated with FPStudio.*[125]

The magnetic structure of $CaMnMnReO_6$, described by the symmetry operations in **Table 6.2**, is shown in **Fig. 6.5** at $T = 2$ K. This structure is notable for possessing antiferromagnetic order of Mn_B spins that are perpendicular in successive *ab*-layers, with Mn_{TD} and Mn_{SP} spins also perpendicular to Mn_B, oriented along the *c*-axis. These observations suggest a high degree of frustration in the system, with the perpendicular alignment of moments maximising antisymmetric Dzyaloshinskii-Moriya interactions. Each Mn_{TD} site is coupled to B-site cations through Mn_{TD}–O2–B bonds, with each Mn_{SP} site coupled to B-site cations through Mn_{SP}–O1–B bonds. From the visualisation of the spin structure above, it can be seen that these couplings are equivalent and frustration is minimised by these A-site moments adopting a spin

structure perpendicular to the B-site spin structure. The ferromagnetic A-site structure in $CaMnMnReO_6$ results in a magnetic moment of 2.70(6) μ_B f.u.$^{-1}$ as determined by Rietveld analysis. Coupling between magnetic ordering and the lattice in $CaMnMnReO_6$ is evidenced by the thermal variation of lattice parameters *a* and *c*, with the *c*-axis exhibiting a negative thermal expansion at the onset of magnetic ordering, shown in **Fig. 6.6**.

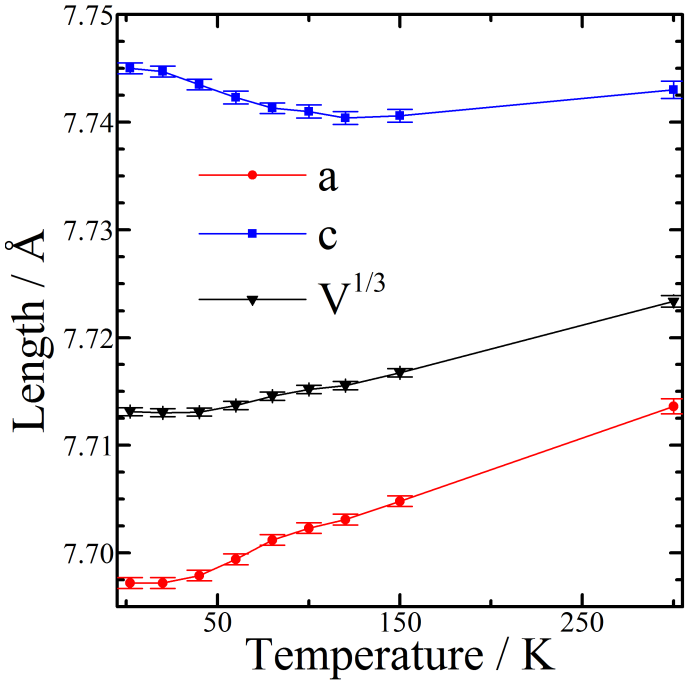

Figure 6.6 | *Temperature variation of lattice parameters a and c, and the cube root of volume, $V^{1/3}$ for $CaMnMnReO_6$. Negative thermal expansion of the c-axis is observed near the magnetic ordering transitions, below 120 K.*

Other significant structural distortions in the vicinity of the magnetic ordering temperature can be seen in the fractional coordinates of the O1 site. This anion site defines the geometry around the $Mn_{SP}O_4$ square plane, which seems to rotate slightly about the *c*-axis at the onset of magnetic order, as well as being the anion site through which Mn_BO_6 and ReO_6 octahedra point predominantly along the *c*-axis. It is likely

that these distortions in the positions of O1 are the mechanism by which the magnetic ordering couples to the lattice and causes the negative thermal expansion of the *c*-axis.

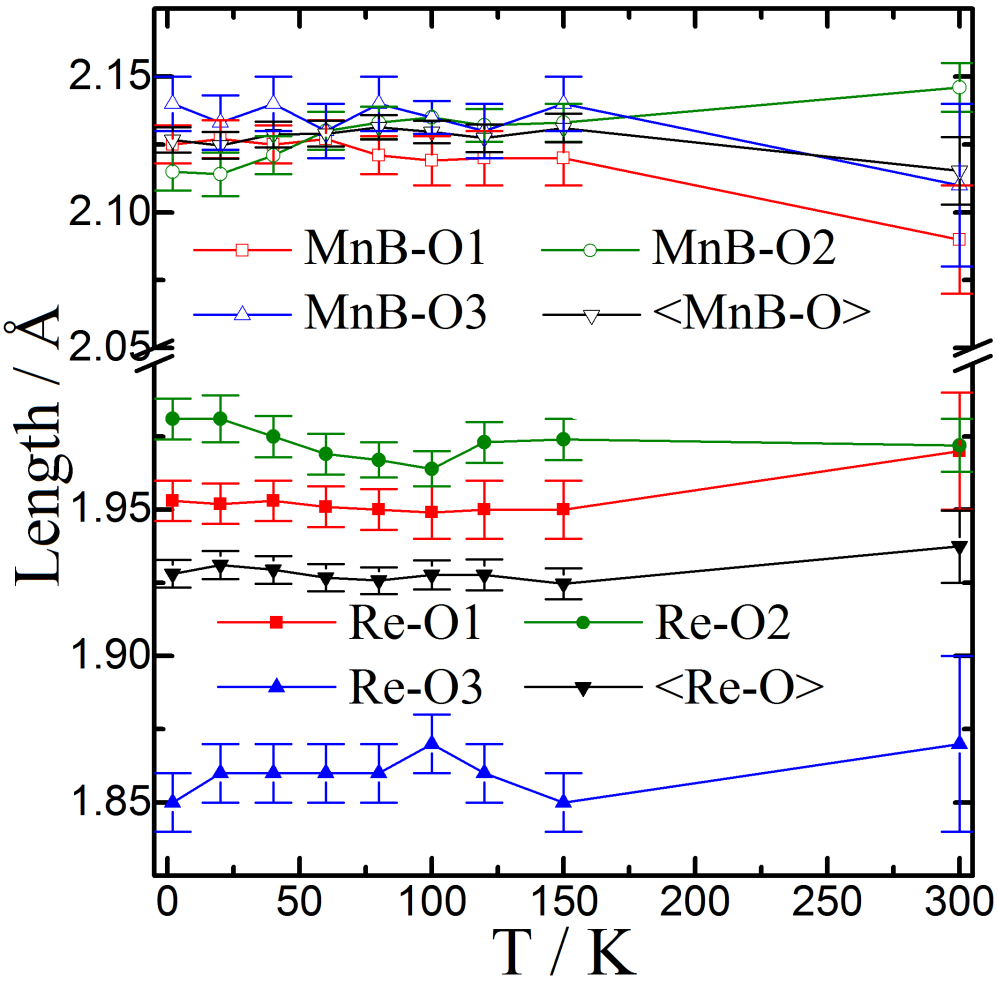

Figure 6.7 | *Thermal variation of Mn_B–O and Re–O bond lengths in CaMnMnReO6.*

Fig. 6.7 shows the temperature variation of B–O bond lengths in $CaMnMnReO_6$. Mn_BO_6 octahedra show no significant Jahn-Teller type distortions and appear as regular octahedra, which can be expected from the electronic configuration of Mn^{2+} ($3d^5$). ReO_6 octahedra are however highly compressed, with a pair of short Re–O3 bonds and two pairs of long Re–O1/O2 bonds. This distortion is consistent with

the ground state of Re^{6+} ($5d^1$), stabilising the J-T compression. Bond valence sum (BVS) calculations for cations in $CaMnMnReO_6$ suggest formal charge states of +2 for Ca and all Mn sites. BVS for Re however suggests a lower charge state than would be expected: Re^{5+}. This discrepancy can be explained by BVS being rather unreliable for Re, particularly as tabulated values for r_0 for Re^{6+} with O^{2-} ligands are not present amongst the tabulated r_0 values for various cations from the IUCr.[91] This absence has led to the BVS values for Re in **Tables 6.4** and **6.5** being calculated using the r_0 value of Re^{5+} bonded to O^{2-}. As such the likely formal charge distribution is $Ca^{2+}Mn^{2+}Mn^{2+}Re^{6+}O_6$.

6.3.3. Magnetometry Measurements of $CaMnMnReO_6$

Magnetometry measurements of $CaMnMnReO_6$ show behaviour that is consistent with the analysis by neutron diffraction. A broad magnetic transition is observed in the range of 150-100 K, which is likely the ordering of Mn_B (and Re) and Mn_A spin moments. The broadness of this transition would agree with the frustrated structure determined by neutron diffraction, however it is difficult to separate this feature into two distinct ordering transitions due to A and B-site magnetic sublattices from magnetometry data alone (**Fig. 6.8**). The overlaid moments determined from neutron diffraction show the evolution of moments on Mn_B, Mn_{TD} and Mn_{SP} sites, with the onset of Mn_B spin order occurring at approximately 120 K and Mn_{TD}/Mn_{SP} spin order occurring at approximately 100 K. The average of Mn_{TD} and Mn_{SP} moments yields the total magnetisation of $CaMnMnReO_6$, which saturates at 2.70(6) μ_B $f.u.^{-1}$ and follows the magnetometry data reasonably well.

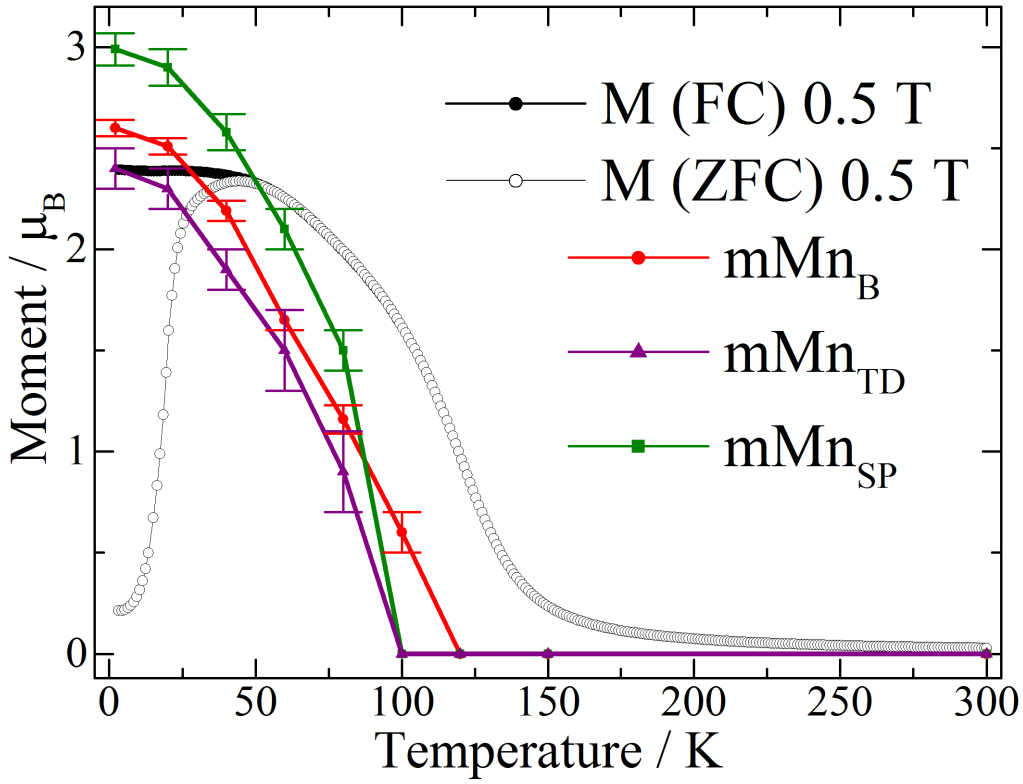

Figure 6.8 | *Zero-field cooled and field cooled magnetometry data on CaMnMnReO6, measured in applied magnetic fields of 0.5 T. Overlaid on this plot are the site moments for antiferromagnetic Mn_B and ferromagnetic Mn_{TD}/Mn_{SP}. The total magnetic moment determined by neutron diffraction is the average of mMn_{TD} and mMn_{SP}.*

Magnetic hysteresis measurements are shown in **Fig. 6.9** at 80, 40 and 3 K. These measurements show that at low temperatures $CaMnMnReO_6$ develops into a hard magnetic material. Coercive fields at 80 K are very low at 0.03 T, with higher coercive fields of 0.11 T developing at 40 K, before extremely high coercive fields of 1.3 T can be observed at 3 K. The saturated magnetisation peaks at 3.4 μ_B f.u.$^{-1}$ at 7 T and 3 K, higher than the predicted magnetic moment from neutron diffraction of 2.70(6) μ_B f.u.$^{-1}$, but still of comparable magnitude. High coercivity is a property of many Fe/Re double perovskites, such as the $Ca_xSr_{2-x}FeReO_6$ double perovskite series reported by De Teresa et al.[81] The authors attribute these high coercive fields to the

anisotropy of Re^{5+} and spin-orbit interactions in this case, however in the Fe^{3+}/Re^{5+} perovskite type materials discussed in previous chapters this is not observed and coercivities of only a few hundred Oersted are measured down to 2 K, likely as there is electron delocalisation accompanying the spin-polarised ferrimagnetic structure. However, a large coercivity is observed in $CaMnMnReO_6$ with Mn^{2+}/Re^{6+} B-site order, which possess mutually frustrated A and B-site magnetic sublattices, with Re^{6+} electron localised states that can provide a mechanism for high coercive fields due to spin orbit interactions.

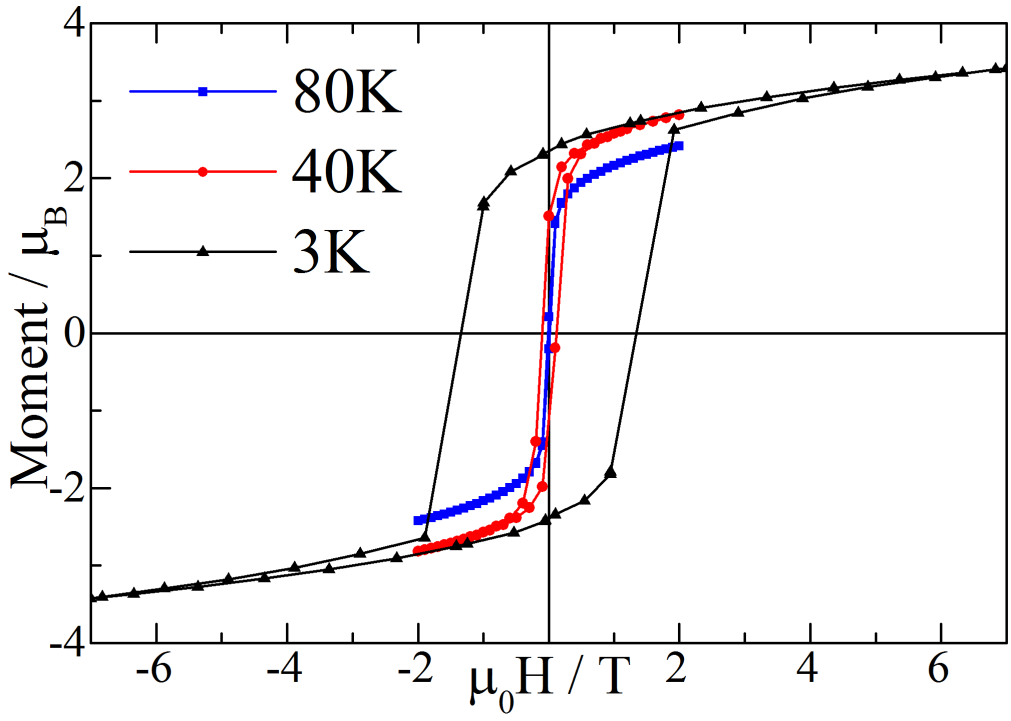

Figure 6.9 | *Magnetic hysteresis measurements between +7 and – 7 T on $CaMnMnReO_6$ at 80, 40 and 3 K. Measurements at lower temperatures show increasing coercive field values, up to 1.3 T at 3 K.*

Resistivity measurements on samples of $CaMnMnReO_6$ were also attempted which show that this material is insulating in nature. This data is shown in **Fig. 6.10** in the temperature range of 300 K to 160 K.

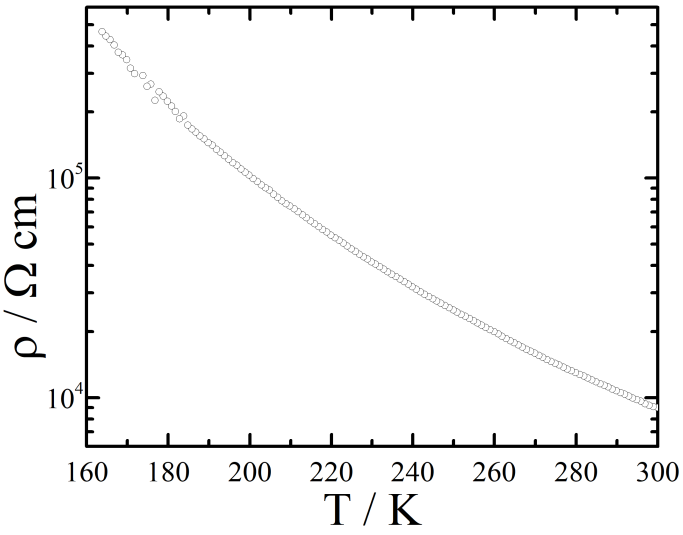

Figure 6.10 | *Resistivity versus temperature for CaMnMnReO6 between 160 and 300 K.*

6.4. Conclusions

In addition to the Ca-based double double ($CaMnFeReO_6$) and triple double ($Ca(Mn_{0.5}Cu_{0.5})FeReO_6$) perovskites reported in previous chapters, another new double double perovskite in the form of $CaMnMnReO_6$ has been synthesised. This material crystallises in the same $P4_2/n$ structure as $RMnMnNdO_6$ and $CaMnFeReO_6$ and can be synthesised under similar conditions of 10 GPa and 1400 °C. $CaMnMnReO_6$ possess the same columnar 1:1 A-site order of 10-coordinate Ca^{2+} and 4-coordinate Mn^{2+} as seen in $CaMnFeReO_6$, however rock salt 1:1 B-site order of Fe^{3+} and Re^{5+} is replaced with a similar order of Mn^{2+} and Re^{6+}. These formal charge states are the same as those seen for B-site rock salt order in the double perovskites Ca_2MnReO_6 and Mn_2MnReO_6.[99,101]

The degree of cation order in $CaMnMnReO_6$ is well characterised by neutron diffraction data collected on the WISH diffractometer at the ISIS Neutron Facility.

Rietveld refinement of this data yields a 5.4(2) % occupancy of Mn^{2+} on the 10-coordinate A-site (predominantly occupied by Ca^{2+}). A small antisite disorder of 4.0(1) % is also found between Mn_B^{2+} and Re^{6+}. The substitution of B-site Fe with Mn not only changes the formal charge states across B-sites, but also has profound effects on the magnetic interactions and the resultant magnetic structure of the material.

The materials reported in previous chapters all have spin-polarised ferrimagnetic G-type order of B-site Fe^{3+}/Re^{5+} spins, with large magnetisations at room temperature and values of T_c typically exceeding 500 K. The magnetic structure of $CaMnMnReO_6$ however has antiferromagnetic B-site order, with perpendicular Mn (and Re) moments stacked in layers and spins oriented in the *ab*-plane. The Fe^{3+}/Re^{5+} materials with A-site Mn^{2+} also display lower temperature A-site magnetic ordering transitions, with Mn_2FeReO_6 exhibiting antiferromagnetic Mn^{2+} order and $CaMnFeReO_6$/$Ca(Mn_{0.5}Cu_{0.5})FeReO_6$ exhibiting A-site ferrimagnetic order between the two inequivalent tetrahedral and square planar sites. $CaMnMnReO_6$ also shows a second lower magnetic transition due to A-site order at 100 K, however this is determined from neutron diffraction to be a ferromagnetic order of Mn_{TD} and Mn_{SP}. This ferromagnetic order occurs along the *c*-axis, perpendicular to B-site order and indicative of the potential frustration in this system, similar to the perpendicular orientations of A and B-site magnetic orders in the double perovskite Mn_2MnReO_6. This ferromagnetic A-site order gives rise to a saturated magnetisation of 2.70(6) μ_B f.u.$^{-1}$ as predicted by the magnetic structure refined against neutron data, and is observed to saturate at 3.4 μ_B f.u.$^{-1}$ by magnetic hysteresis measurements at $\mu_0 H = 7$ T and $T = 3$ K.

Magnetisation versus field hysteresis measurements also reveal other behaviour of $CaMnMnReO_6$ that deviates from that of the related Fe^{3+}/Re^{5+} materials. Magnetic hysteresis measurements of Fe^{3+}/Re^{5+} materials consistently show low coercive fields up to ~600 Oe down to 2 K. Small coercive fields are also measured for $CaMnMnReO_6$ at 80 and 40 K, comparable to those of the Fe^{3+}/Re^{5+} materials, however a large coercive field of 1.3 T is present at 3 K. At these temperatures $CaMnMnReO_6$ is a hard magnet with a large remanent magnetisation of 2.3 μ_B $f.u.^{-1}$. The large coercivity of $CaMnMnReO_6$ is rationalised by this material possessing electron localised Re^{6+} ($5d^1$) states, deviating from the electron delocalisation that the Fe^{3+}/Re^{5+} spin-polarised materials exhibit.

In summary, the successful synthesis of $CaMnMnReO_6$ demonstrates that the recently discovered $P4_2/n$ double double perovskite structure has a versatile chemistry, able to accommodate the charge configuration of $A^{2+}A'^{2+}B^{2+}B'^{6+}O_6$, as well as the previously known charge configurations of $A^{2+}A'^{2+}B^{3+}B'^{5+}O_6$ (in $CaMnFeReO_6$ and $Ca(Mn_{0.5}Cu_{0.5})FeReO_6$) and $A^{3+}A'^{2+}B^{2+}B'^{5+}O_6$ (in $RMnMnSbO_6$, R = Rare earth) with high degrees of site order. Substitution of B-site Fe^{3+}/Re^{5+} with Mn^{2+}/Re^{6+} has dramatic effects on the magnetic structure, producing a highly frustrated system and suggesting that further experimentation with cation substitution in this structure type may yield additional new phases with interesting phenomena due to competing magnetic orders. These results have been published in Chemistry of Materials (*Complex Ferrimagnetism and Magnetoresistance Switching in Ca-Based Double Double and Triple Double Perovskites*)[147] and appended data on $CaMnMnReO_6$ is provided in '**Appendix D**'.

Chapter 7. Final Conclusions & Further Work

The chapters in this thesis focus on: Chapter 3 - Mn_2FeReO_6, the first all transition metal (TM) double perovskite; Chapter 4 - $Ca_xMn_{2-x}FeReO_6$, a series of perovskite-type materials (of which Mn_2FeReO_6 is one end member), the central member of this series (where x = 1.0) is a double double perovskite that exhibits a simultaneous 1:1 A and B-site cation order; Chapter 5 - $Ca(Mn_{0.5}Cu_{0.5})FeReO_6$, a perovskite similar to the x = 1.0 material of the $Ca_xMn_{2-x}FeReO_6$ series but with partial triple double order. Cation order includes three distinct A-cation sites occupied by Ca, (Mn/Cu) and (Cu/Mn) in addition to 1:1 B-site cation order; Chapter 6 - $CaMnMnReO_6$ is an example of another double double perovskite with simultaneous 1:1 A and B-site cation orders, and while the Fe/Re materials possess G-type ferrimagnetism and magnetic order above room temperature, this Mn/Re material possesses a low-temperature antiferromagnetic spin ordering of B-site Mn/Re, with a subsequent perpendicular ferromagnetic order of A-site Mn, indicating that these orders are mutually frustrated.

Mn_2FeReO_6: This material is notable as the first all TM double perovskite, synthesised at 11 GPa and 1400 °C and found to adopt a highly distorted monoclinic $P2_1/n$ structure with a small B-antisite disorder of 2.3(4) % for a slow cooled sample. A high T_c of 520 K is found, corresponding to the onset of Fe/Re G-type antiferromagnetism in the *ac*-plane. There is evidence of antiferromagnetic A-site Mn^{2+} spin order at ~175 K, which possesses components along all three axes. Another transition is observed at ~75 K, corresponding to a further tilt of the Fe/Re spin

structure on to the *a*-axis as well as an additional antiferromagnetic component of Fe/Re order along the *b*-axis. This coincides with an unusual switch in the magnetoresistance (MR) of this material, where negative MR is measured above the transition (-19 % at 100 K and 7 T) and positive MR is found below the transition (+265 % at 20 K and 7 T). This can be explained by a switch in the dominant mechanism of MR from negative intergrain tunnelling at high temperatures to positive bulk MR from a modification of the spin structure, reducing the polarisation of the material, when subjected to applied fields at low temperatures. Mn_2FeReO_6 also has a record magnetisation amongst double perovskites of 4.8 μ_B f.u.$^{-1}$ at 2 K and 7 T (the magnetisation actually peaks at 5.0 μ_B f.u.$^{-1}$ at 75 K and 7 T, due to the reduced moment at lower temperatures from the antiferromagnetic component of Fe/Re spin order along the *b*-axis). The magnetisation in Mn_2FeReO_6 is likely enhanced from the moment provided by the magnetic structure of Fe/Re alone by the presence of fluctuating Mn^{2+} spins which are aligned by the applied field. The proximity of the low-temperature ordering transition in Mn_2FeReO_6 (~75 K) to the boiling point of liquid N_2 (77 K), a cheap cryogen, could yield useful applications for this material.

$Ca_xMn_{2-x}FeReO_6$: Syntheses of $Ca_xMn_{2-x}FeReO_6$ with nominal values of x = 0.5, 1.0 and 1.5 have yielded products with values of x determined by neutron diffraction to be x = 0.17, 0.74, 1.0 and 1.73. While Mn_2FeReO_6 and Ca_2FeReO_6 (end members of this series) adopt monoclinic $P2_1/n$ structures, the nominal x = 1.0 synthesis, at 10 GPa and 1400 °C, is found to produce a structure with combined 1:1 columnar A and rock salt B-site cation orders. A small B-antisite disorder of 3.0(1) % is found by synchrotron X-ray diffraction. A-sites in this structure consist of 10-

coordinate Ca^{2+} and 4-coordinate Mn^{2+} (in two separate sites, one tetrahedral and the other square planar). A small quantity of Fe (12(4) %) is also found on the 4-coordinate A-sites. The magnetic structure of this material is found to have spins collinear with the *c*-axis, where G-type ferrimagnetism of B-site Fe/Re has an onset of T_c = 500 K and a ferrimagnetic order of A-site Mn occurs at ~70 K. The magnetisation of this material saturates at 4.3 μ_B f.u.$^{-1}$ (at 10 K and 7 T). Notably, negative MR is seen in this material down to 20 K (-32 % at 20 K and 7 T), unlike the MR switch seen in Mn_2FeReO_6 at 75 K. This suggests that the antiferromagnetic component of Fe/Re spin order present in Mn_2FeReO_6 is not present here in $CaMnFeReO_6$, as not only is the A-site Mn^{2+} spin order diluted by Ca^{2+} but there is a fundamentally different structure type observed. The nominal x = 0.5 syntheses of this series have yielded phase mixtures of a monoclinic $P2_1/n$ phase with x = 0.17 and a tetragonal $P4_2/n$ phase with x = 0.74. These phases are qualitatively similar to x = 0 and x = 1.0, respectively. Synthesis of materials with nominal x = 1.5 yields a monoclinic $P2_1/n$ structure, with x = 1.73, qualitatively similar to that of x = 2.

$Ca(Mn_{0.5}Cu_{0.5})FeReO_6$: The structure type discovered in the nominal x = 1 material of the $Ca_xMn_{2-x}FeReO_6$ series has been exploited in the synthesis of $Ca(Mn_{0.5}Cu_{0.5})FeReO6$ at 10 GPa and 1400 °C. As the A-site Mn^{2+} in the x = 1.0 structure was found to have alternating tetrahedral and square planar coordinations, half of the Mn^{2+} has been substituted by Cu^{2+}, with the aim of producing a triple double perovskite material with tetrahedrally coordinated Mn^{2+} and square planar Cu^{2+} ordered across A-sites, while Ca^{2+} and Fe^{3+}/Re^{5+} still occupy the 10-coordinate A-sites and B/B′-sites, respectively. While products of these syntheses were found to be quite

varied, a set of these products were found to possess a partial order of Mn/Cu on tetrahedra and Cu/Mn on square planes in an approximate 3:2 ratio by neutron diffraction. Compared to $CaMnFeReO_6$, this partial triple double perovskite possesses an enhanced magnetisation of 4.8 μ_B f.u.$^{-1}$ (vs. 4.3 μ_B f.u.$^{-1}$), an enhanced B-site G-type ferrimagnetic ordering temperature of T_c = 560 K (vs. T_c = 500 K) and an enhanced A-site ferrimagnetic ordering temperature of ~160 K (vs. ~70 K). This is found by neutron diffraction to be largely due to the lack of a magnetic moment found on the square planar A-site. While this site is predominantly Cu^{2+} ($3d^9$, $S = {}^1/_2$), a large quantity of Mn^{2+} ($3d^5$, $S = {}^5/_2$) is present on this site, and one would expect a detectable magnetic moment if this site were magnetically ordered, suggesting that spin order on this site is frustrated. The magnetic structure of $Ca(Mn_{0.5}Cu_{0.5})FeReO_6$ is found to be similar to that of $CaMnFeReO_6$. However, square planar sites (antiparallel to the magnetisation in $CaMnFeReO_6$) possess zero moment, explaining the enhancement of magnetisation in $Ca(Mn_{0.5}Cu_{0.5})FeReO_6$. Another significant change between $CaMnFeReO_6$ and $Ca(Mn_{0.5}Cu_{0.5})FeReO_6$ is bulk metallic behaviour found in the partial triple double perovskite, alongside positive MR at high temperatures and negative MR below ~40 K. The onset of this MR switch appears to be ~70 K, and the metallic nature of this material suggests that high-temperature positive MR may be due to paramagnetic Mn^{2+}/Cu^{2+} promoting the spin scattering of charge carriers, with low-temperature negative MR explained by a reduction of this effect through A-site magnetic ordering.

$CaMnMnReO_6$: Samples of $CaMnMnReO_6$ made at 10 GPa and 1400 °C also exhibit the double double perovskite structure type, with simultaneous 1:1 columnar

A-site and rock salt B-site cation orders. A small amount of B-antisite order (4.0(1) %) is found by neutron diffraction, as well as 5.4(2) % Mn on the 10-coordinate A-site. A charge state of $Ca^{2+}Mn^{2+}Mn^{2+}Re^{6+}O_6$ is found for this material by BVS, unlike the formal charge states of $A^{2+}A'^{2+}Fe^{3+}Re^{5+}O_6$ found for the Fe/Re materials previously discussed. $CaMnMnReO_6$ has successive magnetic transitions at 120 K (antiferromagnetic B-site order) and at 100 K (ferromagnetic A-site order). These orders seem to be highly mutually frustrated. B-site spin order consists of antiferromagnetic layers, with spins oriented in the *ab*-plane that rotate by ±90° about the *c*-axis with each successive layer such that spins in each layer are perpendicular to those in layers above and below. A-site spin order consists of magnetic order perpendicular to all B-site spins in the form of a ferromagnetic arrangement parallel to the *c*-axis. The saturated magnetisation of this material is 3.4 μ_B f.u.$^{-1}$ (at 3 K and 7 T), with large coercive fields emerging at temperatures below 40 K ($\mu_0 H_c$ = 1.3 T at 3 K, $\mu_0 H_c$ = 0.11 T at 40 K). These large coercive fields are likely to be due to electron localised states in $CaMnMn^{2+}Re^{6+}O_6$, compared to the delocalised states in the $AA'Fe^{3+}Re^{5+}O_6$ materials with small coercive fields.

Summary: The synthesis and analysis of materials in this thesis has demonstrated again that high-pressure synthesis is a powerful means of generating new magnetic oxides. It is possible to force small Mn^{2+} cations to occupy the A-sites of these perovskite-type structures using high pressures, replacing the common non-magnetic alkaline earth metals Ba, Sr or Ca by magnetic transitional metal cations. These A-site magnetic cations can cause dramatic changes in the properties of these materials, such as the magnetoresistance switching transition due to frustration

between A-site Mn^{2+} and B-site Fe^{3+}/Re^{5+} spin orders in Mn_2FeReO_6. While high pressure can be used to access these highly distorted perovskite structures with small A-site cations, it can also be used to generate new structure types, demonstrated in the form of materials like $CaMnFeReO_6$, with simultaneous A and B-site cation orders. This structure type appears to be extremely flexible with regards to the charge distribution and cations it can accommodate, with three distinct formal charge states currently demonstrated in the form of $R^{3+}Mn^{2+}Mn^{2+}Sb^{5+}O_6$,[64] $Ca^{2+}Mn^{2+}Fe^{3+}Re^{5+}O_6$ and $Ca^{2+}Mn^{2+}Mn^{2+}Re^{6+}O_6$.

In addition to this double double perovskite structure, a further partial triple double order is seen in the $Ca^{2+}(Mn_{0.5}Cu_{0.5})^{2+}Fe^{3+}Re^{5+}O_6$ material, with the further order occurring between Mn^{2+} and Cu^{2+} across tetrahedra and square planes. These syntheses are found to be quite varied. However, this is not entirely unexpected from the complexity of the structures demanded of these syntheses with five different cations, as well as difficulty in reproducing the exact pressure and temperatures used from synthesis to synthesis. A greater degree of cation order across these sites could potentially be achieved by exploiting differences in cation size and/or charge states between the cations intended to occupy them. However, promoting cation order may be difficult to achieve in this manner due to both of these sites being 4-coordinate and with similar A_{TD}/A_{SP}–O bond lengths. Enhancing the degree of cation order could be achieved by considering cations with different ligand field stabilisation energies, utilising the different coordination environments of these sites.

Further Work: Materials of this type could be explored by many different research pathways. One area of research could be to attempt the synthesis of other double perovskite materials with A-site Mn^{2+} similar to Mn_2FeReO_6, but with B-site cation variation, such as substitution of Fe with other 3*d* transition metal cations in the form of Mn_2BReO_6. Only Mn_2FeReO_6 and Mn_2MnReO_6 have been synthesised thus far as examples of all transition metal double perovskites.[99,100,134,143] Another possibility for further research is the substitution of Re for other 4*d*/5*d* B′ cations that are present in other half metallic double perovskites in A = Ca, Sr and Ba materials, such as B′ = Mo or Os, which are known to lead to half metallic behaviour through their couplings to 3*d* transition metals. It is noted that Mn_2FeMoO_6 has been synthesised previously and determined to crystallise as a Ni_3TeO_6-type (NTO-type) material rather than a double perovskite.[90] However, utilising the double double perovskite structure type and substituting Re^{5+} (r_{Re} = 0.58 Å) for Mo^{5+} (r_{Mo} = 0.61 Å) may stabilise the perovskite structure type rather than the NTO-type, as the cation size difference between 10-coordinate Ca^{2+} (r_{Ca} = 1.23 Å) and 4-coordinate Mn^{2+} (r_{Mn} = 0.66 Å) may force the columnar A-site ordered structure to be favoured (e.g. in the form of $CaMnFeMoO_6$).[85]

Other substitution possibilities using this double double perovskite structure type may be interesting avenues to pursue, such as substitution of non-magnetic Ca^{2+} by rare earth cations that are known to occupy the 10-coordinate A-sites as ‘R’ in $RMnMnSbO_6$,[64] or by substitution of 4-coordinate Mn^{2+} (r_{Mn} = 0.66 Å) by other small magnetic cations, such as 4-coordinate Fe^{2+} (r_{Fe} = 0.63 Å).[85] A small proportion of Fe^{2+} (12(4) %) is noted to be present on A-sites in $CaMnFeReO_6$ and a precedent for

substitution of Mn^{2+} with Fe^{2+} in this columnar A-site order between Ca^{2+} and Mn^{2+} is already present in the form of $CaMnTi_2O_6$ and $CaFeTi_2O_6$.[55,56] Modifications to stabilise the tetrahedral/square planar cation order in the triple double perovskite of general form $AA'_{0.5}A''_{0.5}BB'O_6$ could be made by altering the identity of A′ and/or A″. An additional charge and/or size difference between these cations would be required to promote cation order, for example using cations such as Zn^{2+}, known to commonly adopt tetrahedral environments in crystalline materials such as ZnS and which possesses an ionic radius of 0.6 Å.[85] Silver is reported to adopt a square planar coordination in Ag_3O_4,[148] with oxidation states of Ag^{2+} and Ag^{3+}. The latter, rather unusual, oxidation state of Ag^{3+} possesses an ionic radius of 0.67 Å,[85] similar to the 0.66 Å ionic radius of square planar Mn^{2+} in the double (and triple) double perovskite structures described in this thesis. These A-site modifications in the double (or triple) double perovskite structure type could be combined with the aforementioned B-site modifications, creating a vast number of structures that may exist and be realised by high-pressure-synthesis techniques.

Chapter 8. Bibliography

1 S. A. Wolf, D. D. Awschalom, R. A. Buhrman, J. M. Daughton, S. von Molnár, M. L. Roukes, A. Y. Chtchelkanova and D. M. Treger, *Science.*, 2001, **294**, 1488–1495.

2 P. M. Woodward, *Acta Crystallogr. Sect. B Struct. Sci.*, 1997, **53**, 32–43.

3 R. H. Mitchell, *Perovskites: Modern and Ancient*, Almaz Press, 2002.

4 J. Hutton and R. J. Nelmes, *J. Phys. C Solid State Phys.*, 1981, **14**, 1713–1736.

5 E. J. Cussen and P. D. Battle, *Chem.Mater.*, 2000, **12**, 831–838.

6 B. J. Kennedy, C. J. Howard and B. C. Chakoumakos, *J. Phys. Condens. Matter*, 1999, **11**, 1479–1488.

7 J. M. Reddy, J. L. Bernstein and S. C. Abrahams, *J. Phys. Chem. Solids*, 1966, **27**, 997–1012.

8 A. M. Glazer, *Acta Crystallogr. Sect. B Struct. Crystallogr. Cryst. Chem.*, 1972, **28**, 3384–3392.

9 C. J. Howard and H. T. Stokes, *Acta Crystallogr. Sect. B Struct. Sci.*, 1998, **54**, 782–789.

10 H. A. Jahn and E. Teller, *Proc. R. Soc. A*, 1937, **161**, 220–235.

11 H. A. Kramers, *Physica*, 1934, **1**, 182–192.

12 J. B. Goodenough, *Phys. Rev.*, 1955, **100**, 564–573.

13 J. B. Goodenough, *J. Phys. Chem. Solids*, 1958, **6**, 287–297.

14 J. Kanamori, *J. Phys. Chem. Solids*, 1959, **10**, 87–98.

15 G. Toulouse, in *Modern Trends in the Theory of Condensed Matter: Proceedings of the XVI Karpacz Winter School of Theoretical Physics*, 1980, vol. 115, pp. 195–203.

16 J. Vannimenus and G. Toulouse, *J. Phys. C Solid State Phys.*, 1977, **10**, L537–L542.

17 M. Mekata, *Phys. Today*, 2003, **56**, 12–13.

18 S. T. Bramwell and M. J. Harris, *J. Phys. Condens. Matter*, 1998, **10**, L215–L220.

19 I. Dzyaloshinsky, *J. Phys. Chem. Solids*, 1958, **4**, 241–255.

20 T. Moriya, *Phys. Rev.*, 1960, **120**, 91–98.

21 J. M. D. Coey, M. Viret and S. von Molnár, *Adv. Phys.*, 1999, **48**, 167–293.

22 G. H. Jonker and J. H. Van Santen, *Physica*, 1950, **16**, 337–349.

23 J. H. Van Santen and G. H. Jonker, *Physica*, 1950, **16**, 599–600.

24 G. H. Jonker, *Physica*, 1956, **22**, 707–722.

25 J. Volger, *Physica*, 1954, **20**, 49–66.

26 S. Jin, T. H. Tiefel, M. McCormack, H. M. O'Bryan, L. H. Chen, R. Ramesh and D. Schurig, *Appl. Phys. Lett.*, 1995, **67**, 557–559.

27 *A. Fert and P. Grünberg - Nobel Prize in Physics 2007 - Advanced Information*, Class for Physics of the Royal Swedish Academy of Sciences.

28 J. Z. Liu, I. C. Chang, S. Irons, P. Klavins, R. N. Shelton, K. Song and S. R. Wasserman, *Appl. Phys. Lett.*, 1995, **66**, 3218.

29 C. Zener, *Phys. Rev.*, 1951, **82**, 403–405.

30 C. Zener, *Phys. Rev.*, 1951, **81**, 440–444.

Chapter 8. Bibliography

31 C. Zener, *Phys. Rev.*, 1951, **83**, 299–301.

32 N. G. Park, *Mater. Today*, 2015, **18**, 65–72.

33 Y. Yang and J. You, *Nature*, 2017, **544**, 155–156.

34 V. Gonzalez-Pedro, E. J. Juarez-Perez, W. S. Arsyad, E. M. Barea, F. Fabregat-Santiago, I. Mora-Sero and J. Bisquert, *Nano Lett.*, 2014, **14**, 888–893.

35 E. Edri, S. Kirmayer, S. Mukhopadhyay, K. Gartsman, G. Hodes and D. Cahen, *Nat. Commun.*, 2014, **5**, 3461.

36 C. H. Teh, R. Daik, E. L. Lim, C. C. Yap, M. A. Ibrahim, N. A. Ludin, K. Sopian and M. A. Mat Teridi, *J. Mater. Chem. A*, 2016, **4**, 15788–15822.

37 F. Bella, G. Griffini, J.-P. Correa-Baena, G. Saracco, M. Gratzel, A. Hagfeldt, S. Turri and C. Gerbaldi, *Science.*, 2016, **354**, 203–206.

38 W. Meissner and R. Ochsenfeld, *Naturwissenschaften*, 1933, **21**, 787–788.

39 *Superconducting Maglev Technology*, Central Japan Railway Company, 2017.

40 J. Bardeen, L. N. Cooper and J. R. Schrieffer, *Phys. Rev.*, 1957, **106**, 162.

41 M. K. Wu, J. R. Ashburn, C. J. Torng, P. H. Hor, R. L. Meng, L. Gao, Z. J. Huang, Y. Q. Wang and C. W. Chu, *Phys. Rev. Lett.*, 1987, **58**, 908–910.

42 J. Harada, J. D. Axe and G. Shirane, *Acta Crystallogr.*, 1970, 608.

43 G. Shirane, R. Pepinsky and B. C. Frazer, *Acta Crystallogr.*, 1956, **9**, 131.

44 R. E. Cohen, *Nature*, 1992, **358**, 136–138.

45 N. A. Hill, *J. Phys. Chem. B*, 2000, **104**, 6694–6709.

46 N. A. Spaldin and M. Fiebig, *Science.*, 2005, **309**, 391–392.

47 S. Vasala and M. Karppinen, *Prog. Solid State Chem.*, 2015, **43**, 1–36.

48 Y. Long, *Chinese Phys. B*, 2016, **25**, 078108.

49 G. King and P. M. Woodward, *J. Mater. Chem.*, 2010, **20**, 5785.

50 P. M. Woodward, T. Vogt, D. E. Cox, A. Arulraj, C. N. R. Rao, P. Karen and A. K. Cheetham, *Chem. Mater.*, 1998, **10**, 3652–3665.

51 V. Caignaert, F. Millange, M. Hervieu, E. Suard and B. Raveau, *Solid State Commun.*, 1996, **99**, 173–177.

52 M. T. Anderson and K. R. Poeppelmeier, *Chem. Mater.*, 1991, **3**, 476–482.

53 M. C. Knapp and P. M. Woodward, *J. Solid State Chem.*, 2006, **179**, 1076–1085.

54 M. Ducau, K. S. Suh, J. Senegas and J. Darriet, *Mater. Res. Bull.*, 1992, **27**, 1115–1123.

55 A. Aimi, D. Mori, K. Hiraki, T. Takahashi, Y. J. Shan, Y. Shirako, J. Zhou and Y. Inaguma, *Chem. Mater.*, 2014, **26**, 2601–2608.

56 K. Leinenweber and J. Parise, *J. Solid State Chem.*, 1995, **114**, 277–281.

57 G. King, S. Thimmaiah, A. Dwivedi and P. M. Woodward, *Chem. Mater.*, 2007, **19**, 6451–6458.

58 G. King, L. M. Wayman and P. M. Woodward, *J. Solid State Chem.*, 2009, **182**, 1319–1325.

59 T. Sekiya, T. Yamamoto and Y. Torii, *Bull. Chem. Soc. Jpn.*, 1984, **57**, 1859–1862.

60 M. A. Arillo, J. Gómez, M. L. López, C. Pico and M. L. Veiga, *J. Mater. Chem.*, 1997, **7**, 801–806.

61 M. C. Knapp, PhD Thesis: The Ohio State University, 2006.

62 M. L. Lopez, M. L. Veiga and C. Pico, *J. Mater. Chem.*, 1994, **4**, 547–550.

63 M. A. Arillo, J. Gómez, M. L. López, C. Pico and M. L. Veiga, *Solid State Ionics*, 1997, **95**, 241–248.

64 E. Solana-Madruga, Á. M. Arévalo-López, A. J. Dos Santos-García, E. Urones-Garrote, D. Ávila-Brande, R. Sáez-Puche and J. P. Attfield, *Angew. Chemie - Int. Ed.*, 2016, **55**, 9340–9344.

65 C. J. Howard, B. J. Kennedy and P. M. Woodward, *Acta Crystallogr. Sect. B Struct. Sci.*, 2003, **59**, 463–471.

66 D. Iwanaga, Y. Inaguma and M. Itoh, *Mater. Res. Bull.*, 2000, **35**, 449–457.

67 P. Battle, J. Goodenough and B. Price, *J. Solid State Chem.*, 1983, **46**, 234–244.

68 D. E. Cox and A. W. Sleight, *Acta Crystallogr. Sect. B Struct. Crystallogr. Cryst. Chem.*, 1979, **35**, 1–10.

69 R. J. Cava, B. Batlogg, J. J. Krajewski, R. Farrow, L. W. Rupp, A. E. White, K. Short, W. F. Peck and T. Kometani, *Nature*, 1988, 332, 814–816.

70 D. G. Hinks, B. Dabrowski, J. D. Jorgensen, A. W. Mitchell, D. R. Richards, S. Pei and D. Shi, *Nature*, 1988, **333**, 836–838.

71 P. Szabó, P. Samuely, L. N. Bobrov, J. Marcus, C. Escribe-Filippini and M. Affronte, *Phys. C Supercond. its Appl.*, 1994, **235**–**240**, 1873–1874.

72 K. Kobayashi, T. Kimura, H. Sawada, K. Terakura and Y. Tokura, *Nature*, 1998, **395**, 677–680.

73 O. Chmaissem, R. Kruk, B. Dabrowski, D. E. Brown, X. Xiong, S. Kolesnik, J. D. Jorgensen and C. W. Kimball, *Phys. Rev. B*, 2000, **62**, 14197.

74 D. Serrate, J. M. De Teresa and M. R. Ibarra, *J. Phys. Condens. Matter*, 2007, **19**, 023201.

75 T. Fix, D. Stoeffler, Y. Henry, S. Colis, A. Dinia, T. Dimopoulos, L. Bär and J. Wecker, *J. Appl. Phys.*, 2006, **99**, 08J107.

76 M. Bibes, K. Bouzehouane, A. Barthélémy, M. Besse, S. Fusil, M. Bowen, P. Seneor, J. Carrey, V. Cros, A. Vaurès, J.-P. Contour and A. Fert, *Appl. Phys. Lett.*, 2003, **83**, 2629.

77 N. Kumar, P. Misra, R. K. Kotnala, A. Gaur and R. S. Katiyar, *J. Phys. D. Appl. Phys.*, 2014, **47**, 065006.

78 H. Kato, T. Okuda, Y. Okimoto, Y. Tomioka, K. Oikawa, T. Kamiyama and Y. Tokura, *Phys. Rev. B*, 2002, **65**, 144404.

79 H. Wu, *Phys. Rev. B*, 2001, **64**, 125126.

80 D. Serrate, J. M. De Teresa, P. A. Algarabel, J. Galibert, C. Ritter, J. Blasco and M. R. Ibarra, *Phys. Rev. B*, 2007, **75**, 165109.

81 J. M. De Teresa, D. Serrate, J. Blasco, M. R. Ibarra and L. Morellon, *Phys. Rev. B*, 2004, **69**, 1–10.

82 K. Oikawa, T. Kamiyama, H. Kato and Y. Tokura, *J. Phys. Soc. Japan*, 2003, **72**, 1411–1417.

83 A. S. Wolf, J. M. Jackson, P. Dera, V. B. Prakapenka and W. E. T. Al, *J. Geophys. Res. B Solid Earth*, 2015, **120**, 7460–7489.

84 W. A. Bassett, *High Press. Res.*, 2009, **29**, 163–186.

85 R. D. Shannon, *Acta Crystallogr. Sect. A*, 1976, **32**, 751–767.

86 V. M. Goldschmidt, *Naturwissenschaften*, 1926, **14**, 477–485.

87 Y. Syono, S.-I. Akimoto and Y. Endoh, *J. Phys. Chem. Solids*, 1970, **32**, 243–249.

Chapter 8. Bibliography

88 M. R. Li, D. Walker, M. Retuerto, T. Sarkar, J. Hadermann, P. W. Stephens, M. Croft, A. Ignatov, C. P. Grams, J. Hemberger, I. Nowik, P. S. Halasyamani, T. T. Tran, S. Mukherjee, T. S. Dasgupta and M. Greenblatt, *Angew. Chemie - Int. Ed.*, 2013, **52**, 8406–8410.

89 M. R. Li, M. Croft, P. W. Stephens, M. Ye, D. Vanderbilt, M. Retuerto, Z. Deng, C. P. Grams, J. Hemberger, J. Hadermann, W. M. Li, C. Q. Jin, F. O. Saouma, J. I. Jang, H. Akamatsu, V. Gopalan, D. Walker and M. Greenblatt, *Adv. Mater.*, 2015, **27**, 2177–2181.

90 M. R. Li, M. Retuerto, D. Walker, T. Sarkar, P. W. Stephens, S. Mukherjee, T. S. Dasgupta, J. P. Hodges, M. Croft, C. P. Grams, J. Hemberger, J. Sánchez-Benítez, A. Huq, F. O. Saouma, J. I. Jang and M. Greenblatt, *Angew. Chemie - Int. Ed.*, 2014, **53**, 10774–10778.

91 I. D. Brown, *The Chemical Bond in Inorganic Chemistry: The Bond Valence Model*, Oxford University Press, 2002.

92 A. M. Arévalo-López and J. P. Attfield, *Phys. Rev. B - Condens. Matter Mater. Phys.*, 2013, **88**, 1–6.

93 M. Markkula, A. M. Arevalo-Lopez, A. Kusmartseva, J. A. Rodgers, C. Ritter, H. Wu and J. P. Attfield, *Phys. Rev. B - Condens. Matter Mater. Phys.*, 2011, **84**, 1–5.

94 A. Prodi, E. Gilioli, A. Gauzzi, F. Licci, M. Marezio, F. Bolzoni, Q. Huang, A. Santoro and J. W. Lynn, *Nat. Mater.*, 2004, **3**, 48–52.

95 S. V. Ovsyannikov, A. M. Abakumov, A. A. Tsirlin, W. Schnelle, R. Egoavil, J. Verbeeck, G. Van Tendeloo, K. V. Glazyrin, M. Hanfland and L. Dubrovinsky, *Angew. Chemie - Int. Ed.*, 2013, **52**, 1494–1498.

96 Y. Akizuki, I. Yamada, K. Fujita, N. Nishiyama, T. Irifune, T. Yajima, H. Kageyama and K. Tanaka, *Inorg. Chem.*, 2013, **52**, 11538–11543.

97 W. Chen, M. Mizumaki, H. Seki, M. S. Senn, T. Saito, D. Kan, J. P. Attfield and Y. Shimakawa, *Nat. Commun.*, 2014, **5**, 3909.

98 A. J. Dos Santos-García, C. Ritter, E. Solana-Madruga and R. Sáez-Puche, *J. Phys. Condens. Matter*, 2013, **25**, 206004.

99 A. M. Arévalo-López, F. Stegemann and J. P. Attfield, *Chem. Commun.*, 2016, **147**, 2–4.

100 M. R. Li, J. P. Hodges, M. Retuerto, Z. Deng, P. W. Stephens, M. C. Croft, X. Deng, G. Kotliar, J. Sánchez-Benítez, D. Walker and M. Greenblatt, *Chem. Mater.*, 2016, **28**, 3148–3158.

101 H. P. S. Corrêa, I. P. Cavalcante, D. O. Souza, E. Z. Santos, M. T. D. Orlando, H. Belich, F. J. Silva, E. F. Medeiro, J. M. Pires, J. L. Passamai, L. G. Martinez and J. L. Rossi, *Ceramica*, 2010, **56**, 193.

102 C. N. R. Rao and J. Gopalakrishnan, *New directions in solid state chemistry*, Cambridge University Press, 1st edn., 1986.

103 H. Huppertz, *Zeitschrift Fur Krist.*, 2004, **219**, 330–338.

104 C. J. M. Rooymans, in *Preparative Methods in Solid State Chemistry*, ed. P. Hagenmuller, Academic Press, 1972.

105 J. B. Goodenough, J. A. Kafalas and J. M. Longo, in *Preparative Methods in Solid State Chemistry*, ed. P. Hagenmuller, Academic Press, 1972.

106 D. Walker, M. A. Carpenter and C. M. Hitch, *Am. Mineral.*, 1990, **75**, 1020–1028.

107 J. Hernlund, K. Leinenweber, D. Locke and J. A. Tyburczy, *Am. Mineral.*, 2006, **91**, 295–305.

108 *William H. Bragg and William L. Bragg - Nobel Prize in Physics 1915 - Presentation Speech*, Royal Swedish Academy of Sciences.

109 D. S. Sivia, *Elementary Scattering Theory*, Oxford University Press, 1st edn., 2011.

110 The European Synchrotron Radiation Facility, *The Purple Book: Science and Technology Programme 2008-2017*, The European Synchrotron Radiation Facility, Grenoble, 2007.

111 The Institut Laue-Langevin, *The Yellow Book: Guide to neutron research facilities at the ILL*, Grenoble, 2008.

112 The ISIS Neutron and Muon Source, *Annual Review 2015*, Didcot, 2015.

113 *James Chadwick - Nobel Prize in Physics 1935 - Presentation Speech*, Royal Swedish Academy of Sciences.

114 U.S. Department of Energy, *The First Reactor - Fermi's Own Story*, 1982.

115 *Clifford G. Shull and Bertram N. Brockhouse - Nobel Prize in Physics 1994 - Press Release*, Royal Swedish Academy of Sciences.

116 J. Beringer et al., *(Particle Data Group), PR*, 2012, **D86**, 010001.

117 S. M. Bennington, A. C. Hannon and S. E. Rogers, *The ISIS Neutron and Muon Facility Neutron Training Course*, Didcot, 2006.

118 The Institut Laue-Langevin, *Neutron Data Booklet*, Grenoble, 2nd edn., 2003.

119 T. C. Hansen, P. F. Henry, H. E. Fischer, J. Torregrossa and P. Convert, *Meas. Sci. Technol.*, 2008, **19**, 034001.

120 L. C. Chapon, P. Manuel, P. G. Radaelli, C. Benson, L. Perrott, S. Ansell, N. J. Rhodes, D. Raspino, D. Duxbury, E. Spill and J. Norris, *Neutron News*, 2011, **22**, 22–25.

121 A. Baszczuk, B. Dabrowski, S. Kolesnik, O. Chmaissem and M. Avdeev, *J. Solid State Chem.*, 2012, **186**, 240–246.

122 H. Rietveld, *J. Appl. Crystallogr.*, 1969, **2**, 65–71.

123 G. Caglioti, A. Paoletti and F. P. Ricci, *Nucl. Instruments*, 1958, **3**, 223–228.

124 J. Rodríguez-Carvajal and F. Bourée, *EPJ Web Conf.*, 2012, **22**, 00010.

125 J. Rodriguez-Carvajal, *Phys. B Phys. Condens. Matter*, 1993, **192**, 55–69.

126 M. Müller, R. E. Dinnebier, A. C. Dippel, H. T. Stokes and B. J. Campbell, *J. Appl. Crystallogr.*, 2014, **47**, 532–538.

127 W. G. Jenks, S. S. H. Sadeghi and J. P. Wikswo Jr, *J. Phys. D. Appl. Phys.*, 1997, **30**, 293.

128 M. N. Baibich, J. M. Broto, A. Fert, F. N. Van Dau, F. Petroff, P. Etienne, G. Creuzet, A. Friederich and J. Chazelas, *Phys. Rev. Lett.*, 1988, **61**, 2472.

129 G. Binasch, P. Grünberg, F. Saurenbach and W. Zinn, *Phys. Rev. B*, 1989, **39**, 4828–4830.

130 A. Rogalev, K. Ollefs and F. Wilhelm, in *X-Ray Absorption and X-Ray Emission Spectroscopy*, John Wiley & Sons, Ltd, Chichester, UK, 2016, pp. 671–694.

131 B. T. Thole, P. Carra, F. Sette and G. Van Der Laan, *Phys. Rev. Lett.*, 1992, **68**, 1943–1946.

132 P. Carra, B. T. Thole, M. Altarelli and X. Wang, *Phys. Rev. Lett.*, 1993, **70**, 694–697.

133 U. Fano, *Phys. Rev.*, 1969, **178**, 131–136.

134 A. M. Arévalo-López, G. M. McNally and J. P. Attfield, *Angew. Chemie Int. Ed.*, 2015, **54**, 12074–12077.

135 K. H. Hong, G. M. McNally, M. Coduri and J. P. Attfield, *Zeitschrift für Anorg. und Allg. Chemie*, 2016, **642**, 1355–1358.

136 K. Momma and F. Izumi, *J. Appl. Crystallogr.*, 2011, **44**, 1272–1276.

137 D. D. Sarma, P. Mahadevan, T. Saha-Dasgupta, S. Ray and A. Kumar, *Phys. Rev. Lett.*, 2000,

85, 2549–2552.

138 O. Erten, O. N. Meetei, A. Mukherjee, M. Randeria, N. Trivedi and P. Woodward, *Phys. Rev. Lett.*, 2011, **107**, 1–4.

139 O. N. Meetei, O. Erten, A. Mukherjee, M. Randeria, N. Trivedi and P. Woodward, *Phys. Rev. B*, 2013, **87**, 165104, 1–7.

140 O. Erten, O. N. Meetei, A. Mukherjee, M. Randeria, N. Trivedi and P. Woodward, *Phys. Rev. B*, 2013, **87**, 165105, 1–7.

141 D. R. Parker, M. A. Green, S. T. Bramwell, A. S. Wills, J. S. Gardner and D. A. Neumann, *J. Am. Chem. Soc.*, 2004, **126**, 2710–2711.

142 H. Li, Y. Xiao, B. Schmitz, J. Persson, W. Schmidt, P. Meuffels, G. Roth and T. Brückel, *Sci. Rep.*, 2012, **2**, 750.

143 M. R. Li, M. Retuerto, Z. Deng, P. W. Stephens, M. Croft, Q. Huang, H. Wu, X. Deng, G. Kotliar, J. Sánchez-Benítez, J. Hadermann, D. Walker and M. Greenblatt, *Angew. Chemie - Int. Ed.*, 2015, **54**, 12069–12073.

144 F. Kanamaru, H. Miyamoto, Y. Mimura, M. Koizumi, M. Shimada, S. Kume and S. Shin, *Mater. Res. Bull.*, 1970, **5**, 257–261.

145 H. Taguchi, M. Sonoda and M. Nagao, *J. Solid State Chem.*, 1998, **137**, 82–86.

146 M. Sikora, C. Kapusta, M. Borowiec, C. J. Oates, V. Prochazka, D. Rybicki, D. Zajac, J. M. De Teresa, C. Marquina and M. R. Ibarra, *Appl. Phys. Lett.*, 2006, **89**, 89–92.

147 G. M. McNally, Á. M. Arévalo-López, P. Kearins, F. Orlandi, P. Manuel and J. P. Attfield, *Chem. Mater.*, 2017, **29**, 8870–8874.

148 T. Jia, X. Zhang, T. Liu, F. Fan, Z. Zeng, X. G. Li, D. I. Khomskii and H. Wu, *Phys. Rev. B*, 2014, **89**, 245117.

Appendix A. – Additional Results for Mn_2FeReO_6

A.1. Magnetic Information, Mn_2FeReO_6

Additional magnetic information is supplied in this section. **Fig. A.1** shows the field cooled (FC) and zero-field cooled (ZFC) plots of magnetisation versus temperature for Mn_2FeReO_6, under field strengths of 0.5 T. The inset shows the derivative of ZFC and FC plots in the region 50-350 K, with two small anomalies at 210 and 285 K.

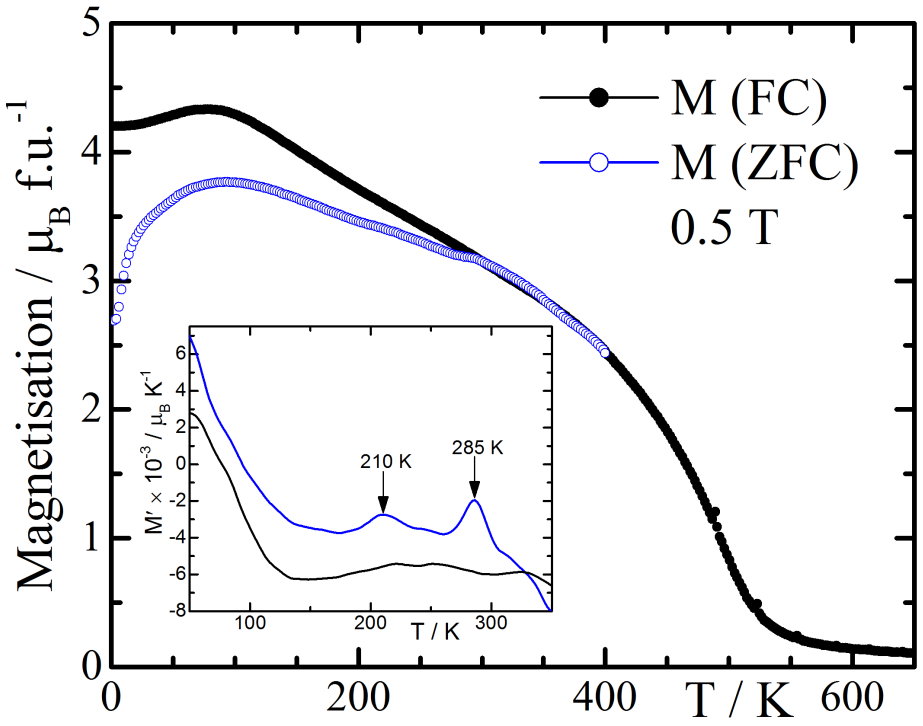

Figure A.1 | *Zero-field cooled (ZFC) and field cooled magnetisation versus temperature for Mn_2FeReO_6, with their derivatives shown in the inset between 50-350 K.*

Appendix A. Mn_2FeReO_6

Table A.1 contains alternative magnetic symmetry operations to those given by BasIreps in **Table 3.3**, that also describe the magnetic structure of Mn_2FeReO_6 but using definitions from Isotropy.[126] Further details of magnetic structure solution are provided in '*2.2.7 – Magnetic Symmetry Analysis*'.

Table A.1 | Irreducible representations and the basis vectors for Mn^{2+}, Fe^{3+} and Re^{5+} spin ordering in Mn_2FeReO_6 using the $\boldsymbol{k}$ = (0 0 0) propagation vector in space group $P2_1/n$.[126]

IrRep:	**Γ_1^+**					**Γ_2^+**				
Mag. mode:	A1		A2		A3	A1		A2		A3
Atom	m_x	m_z	m_x	m_z	m_y	m_x	m_z	m_x	m_z	m_y
Mn1, Mn2 [a]	-	-	-	+	+	-	-	-	+	+
Mn3, Mn4 [a]	+	+	+	-	+	-	-	-	+	-
Mag. Mode:	A_g1		A_g2		A_g3	A_g1		A_g2		A_g3
Atom	m_x	m_z	m_x	m_z	m_y	m_x	m_z	m_x	m_z	m_y
Fe1, Re1 [b]	+	+	+	-	+	-	-	-	+	-
Fe2, Re2 [b]	-	-	-	+	+	-	-	-	+	+

[a] Mn1=(0.490, 0.560, 0.755); Mn2=(0.510, 0.440, 0.245); Mn3=(0.010, 0.060, 0.745); Mn4=(0.990, 0.940, 0.255). For Mn order, magnetic modes used are Γ_1^+A1, Γ_1^+A2 and Γ_2^+A3. Coefficients for Γ_1^+A1 and Γ_1^+A2 are negative.

[b] Fe1=(0, ½, 0); Re1=(½, 0, 0); Fe2=(½, 0, ½); Re2=(0, ½, ½). For Fe and Re order, magnetic modes $\Gamma_2^+A_g1$ and $\Gamma_2^+A_g2$ are used for magnetic structure refinement in the high-temperature regime. In the low-temperature regime $\Gamma_2^+A_g3$ is also used (antiferromagnetic component along the *b*-axis). Coefficients for $\Gamma_2^+A_g1$ are negative for Fe, while coefficients for $\Gamma_2^+A_g2$ are negative for Re. Coordinates listed here are at 1.5 K.

A.2. WISH Results, Mn_2FeReO_6

Additional plots of data from refinements of WISH data on Mn_2FeReO_6 are supplied in this section, from results that are tabulated in **Tables A.4-A.7**. These plots include the variation with temperature of: Mn_2FeReO_6 lattice parameters (**Fig. A.2**), Fe–O (**Fig. A.3**) and Re–O (**Fig. A.4**) bond lengths, Fe–O–Re bond angles (**Fig. A.5**), fractional coordinates for O1, O2, O3 and Mn (**Fig. A.6**, **A.7**, **A.8** and **A.10**, respectively), and Mn–O bond lengths (**Fig. A.9**).

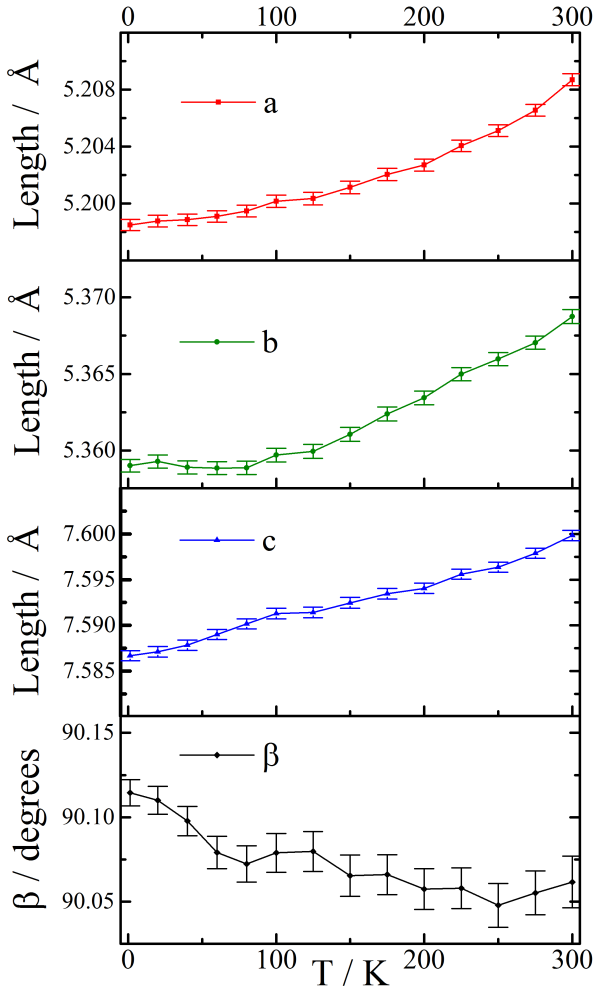

Figure A.2 | *Temperature variation of Mn_2FeReO_6 lattice parameters: a, b, c and β, from refined WISH data.*

Appendix A. Mn_2FeReO_6

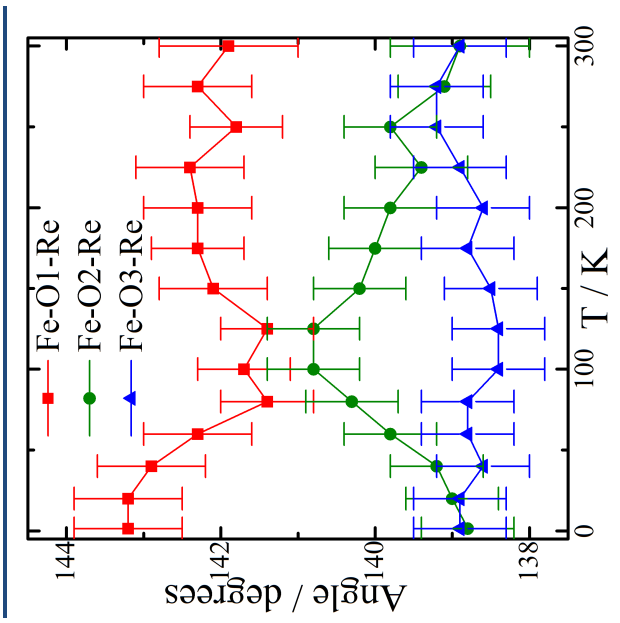

Figure A.5 | *Mn_2FeReO_6: temperature variation of Fe–O–Re bond angles from refined WISH data.*

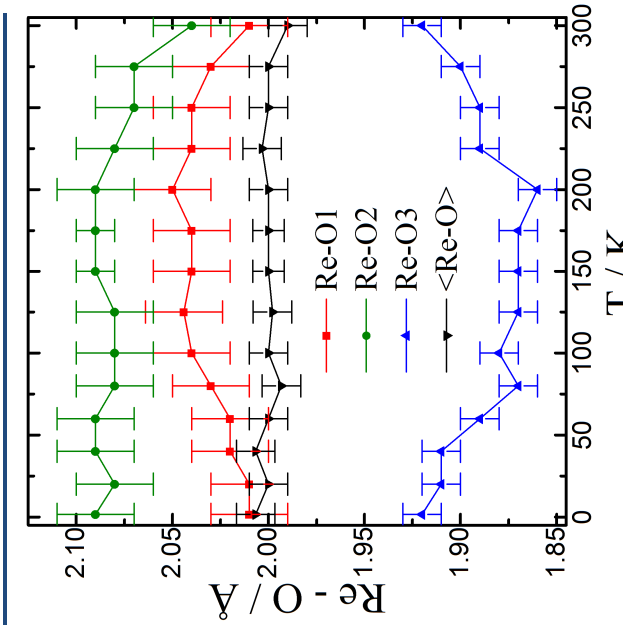

Figure A.4 | *Mn_2FeReO_6: temperature variation of Re–O bond lengths from refined WISH data.*

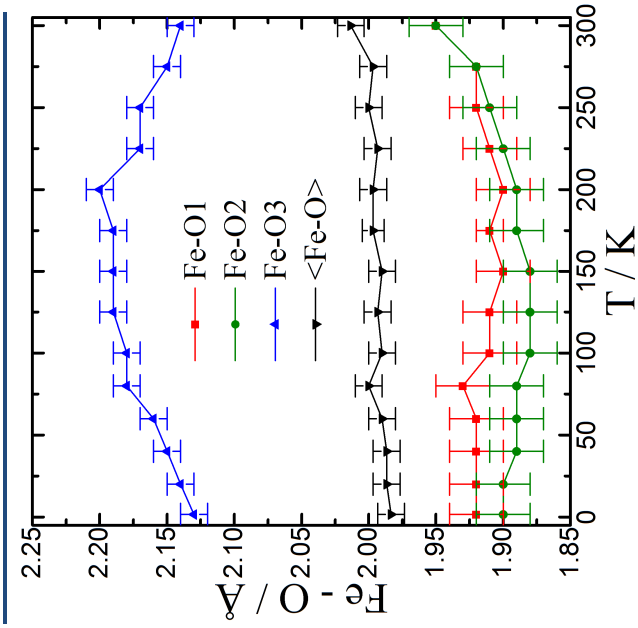

Figure A.3 | *Mn_2FeReO_6: temperature variation of Fe–O bond lengths from refined WISH data.*

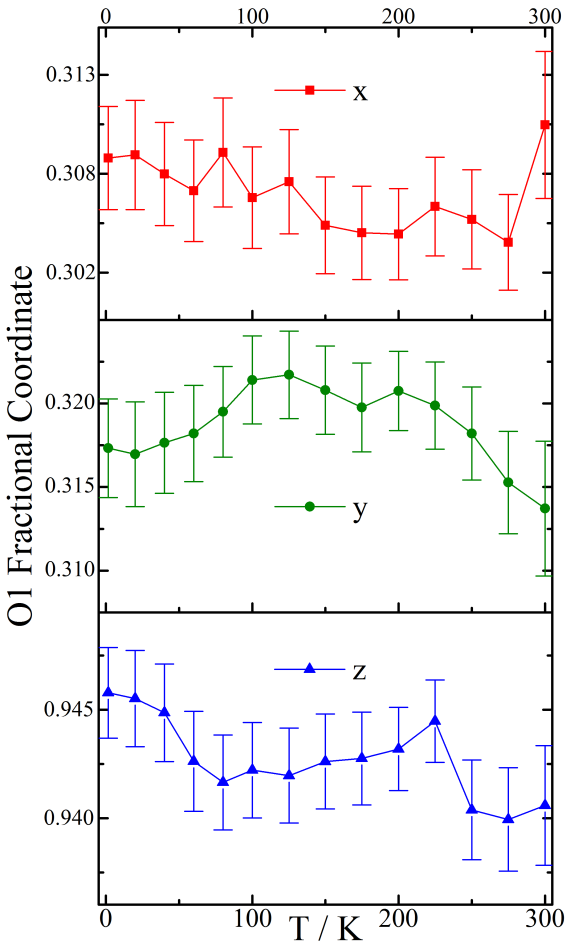

Figure A.6 | *Mn_2FeReO_6: O1 fractional coordinates versus T.*

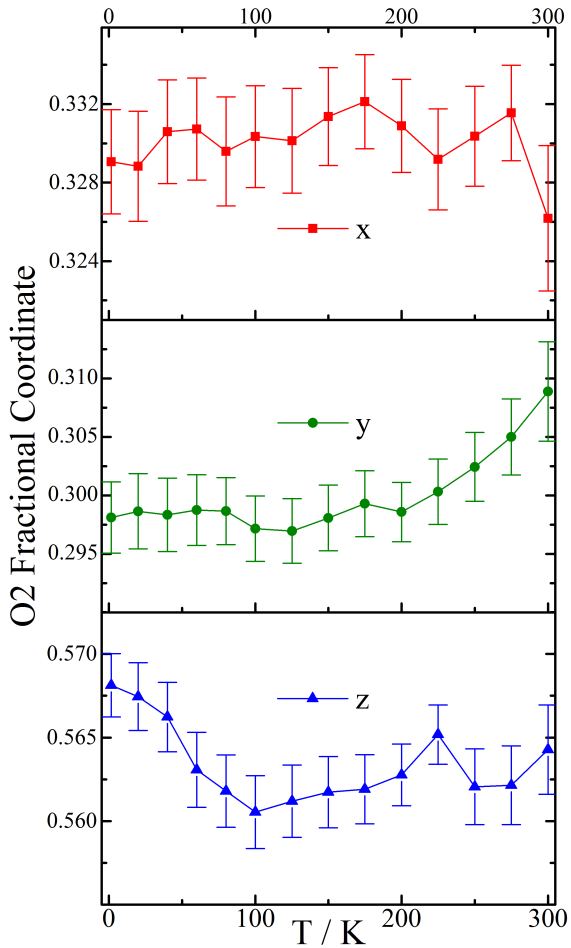

Figure A.7 | *Mn_2FeReO_6: O2 fractional coordinates versus T.*

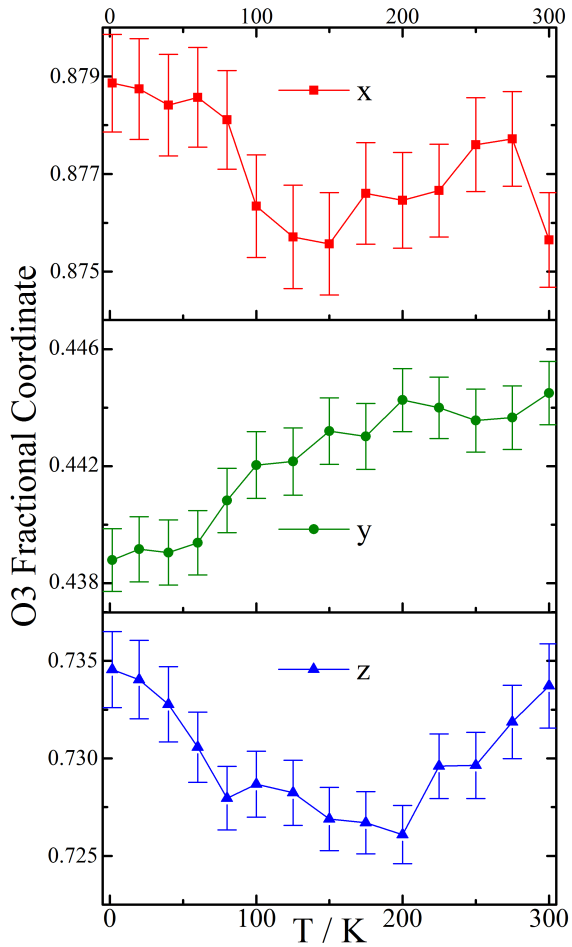

Figure A.8 | *Mn_2FeReO_6: O3 fractional coordinates versus T.*

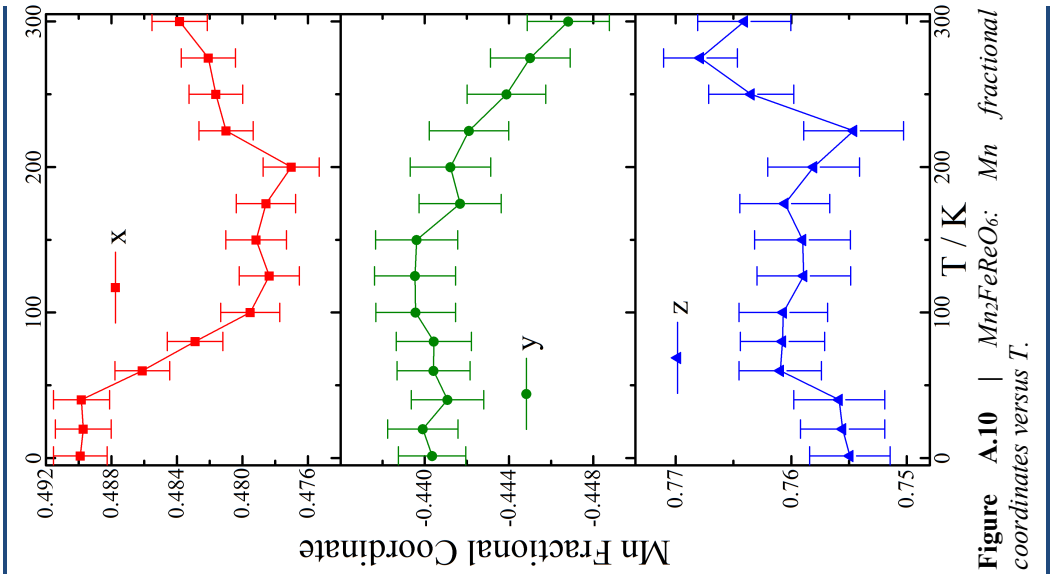

Figure A.10 | *Mn_2FeReO_6: Mn fractional coordinates versus T.*

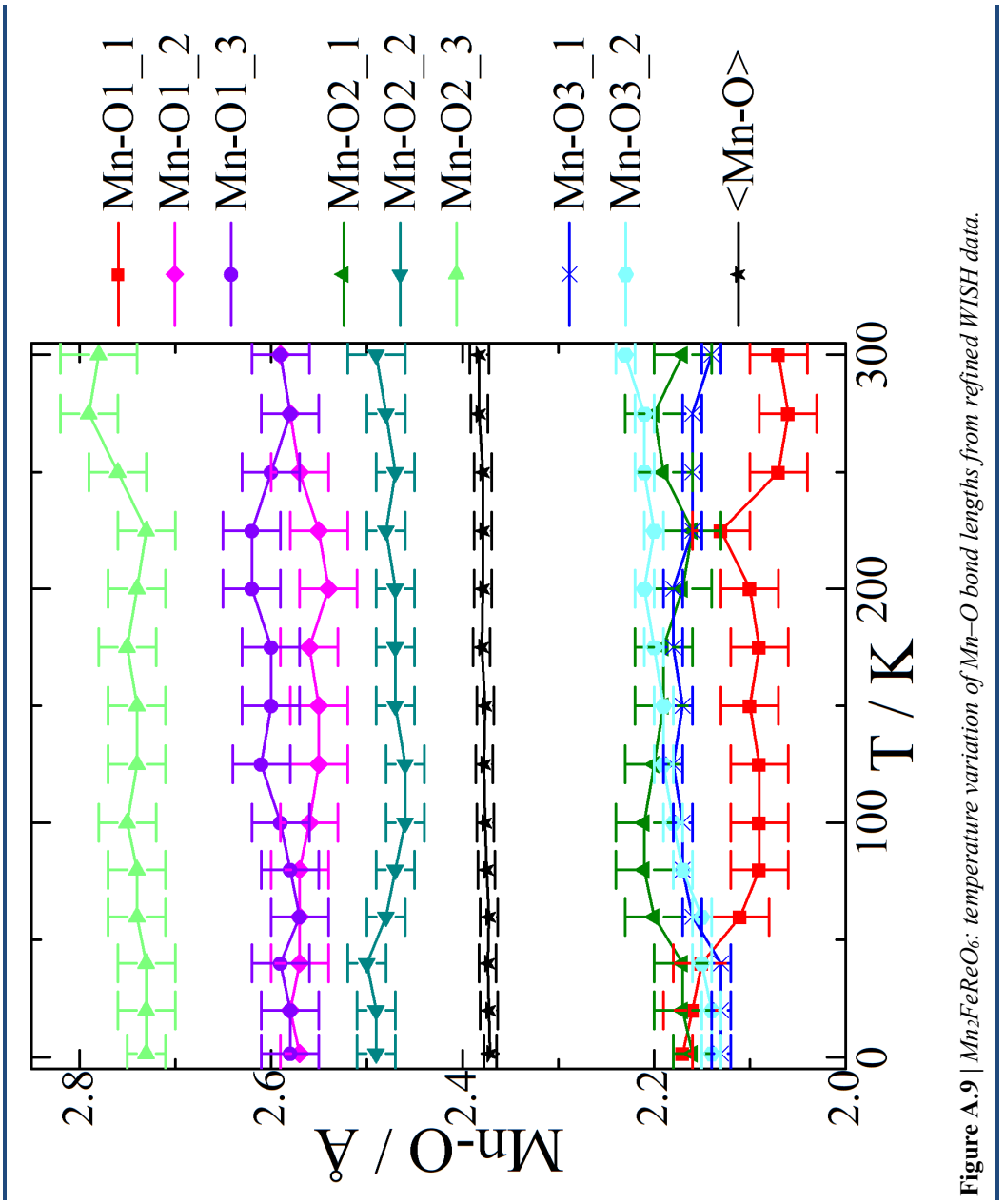

Figure A.9 | *Mn_2FeReO_6: temperature variation of Mn–O bond lengths from refined WISH data.*

Appendix B. Additional Results for $Ca_xMn_{2-x}FeReO_6$

Additional data in the form of plots of results from Rietveld refinements of $Ca_xMn_{2-x}FeReO_6$ (nominal x = 1.0, 1.5 and 0.5), using data collected on the WISH diffractometer at the ISIS Neutron Facility are shown in this section. Tetragonal and monoclinic phases are denoted here with 'T-' or 'M-' preceding their formula. For the tetragonal $P4_2/n$ phases of x = 1.0 (T-$Ca(Mn_{0.88(4)}Fe_{0.12})FeReO_6$, **Fig. B.1-B.7**) and x = 0.5 (T-$(Ca_{0.74(2)}Mn_{0.26})MnFeReO_6$), **Fig. B.16-B.22**), the thermal variation of A–O, Fe–O and Re–O bond lengths, Fe–O–Re bond angles, and fractional coordinates for O1, O2 and O3 are plotted. For the monoclinic $P2_1/n$ phases of x = 1.5 (M-$(Ca_{1.73(8)}Mn_{0.27})FeReO_6$, **Fig B.8-B.15**) and x = 0.5 M-$(Ca_{0.17(3)}Mn_{1.83})FeReO_6$, **Fig. B.23-B.30**) the thermal variation of A-site fractional coordinates are plotted in addition to the same parameters above that were plotted for the tetragonal phases.

B.1. WISH Plots, x = 1.0 – T-$Ca(Mn_{0.88(4)}Fe_{0.12})FeReO_6$

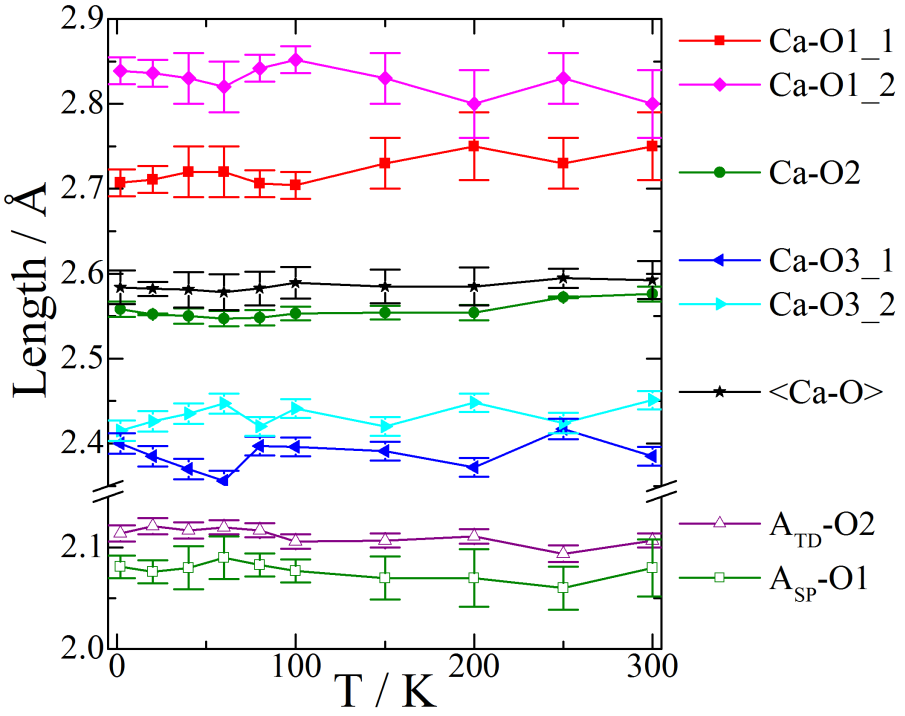

Figure B.1 | *T-$Ca(Mn_{0.88(4)}Fe_{0.12})FeReO_6$: temperature variation of Ca–O, A_{TD}–O2 and A_{SP}–O1 bond lengths from refined WISH data.*

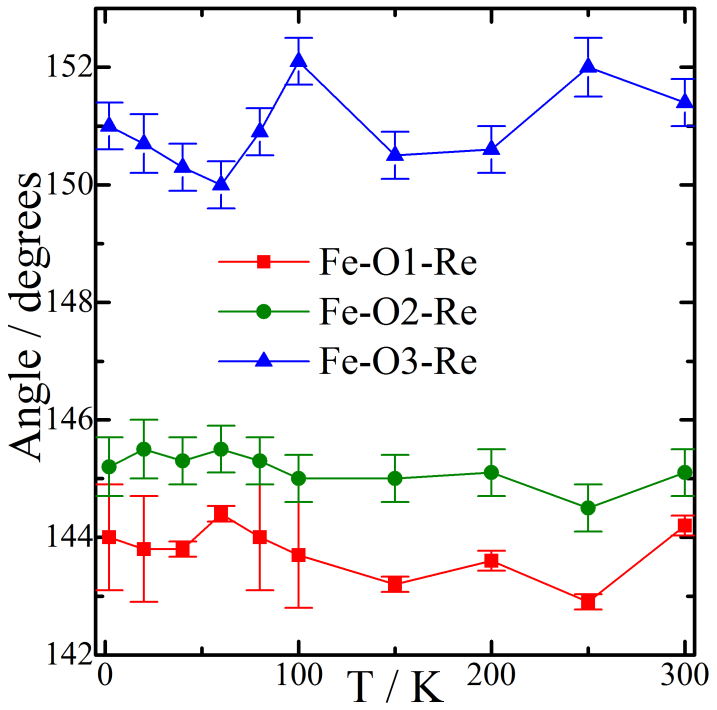

Figure B.2 | *T-$Ca(Mn_{0.88(4)}Fe_{0.12})FeReO_6$: thermal variation of Fe–O–Re bond angles from refined WISH data.*

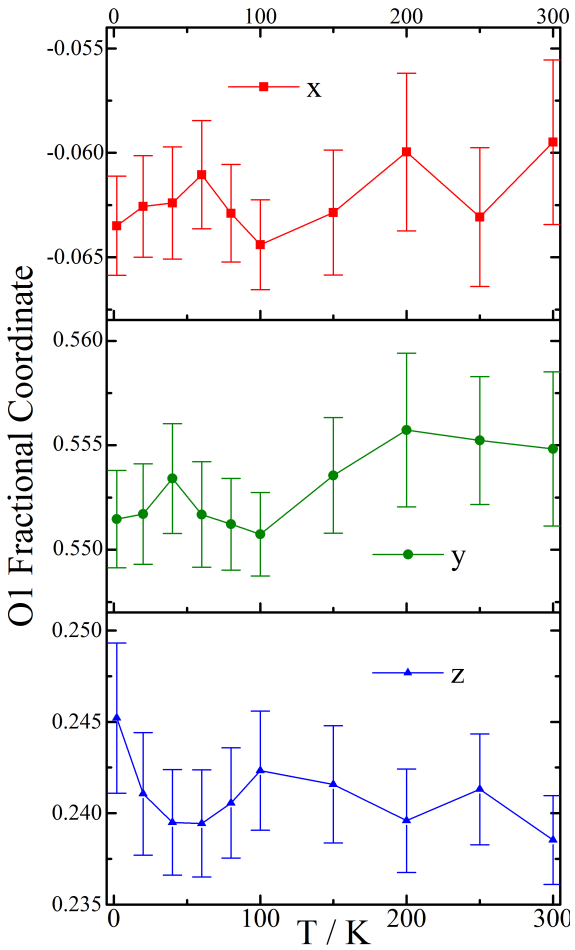

Figure B.3 | *T-Ca(Mn$_{0.88(4)}$Fe$_{0.12}$)FeReO$_6$: O1 fractional coordinates versus T.*

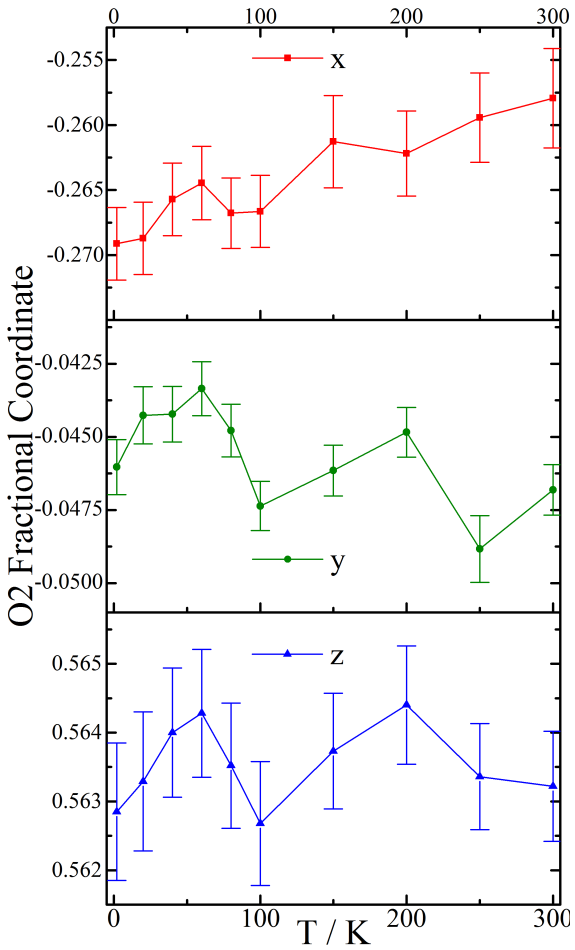

Figure B.4 | *T-Ca(Mn$_{0.88(4)}$Fe$_{0.12}$)FeReO$_6$: O2 fractional coordinates versus T.*

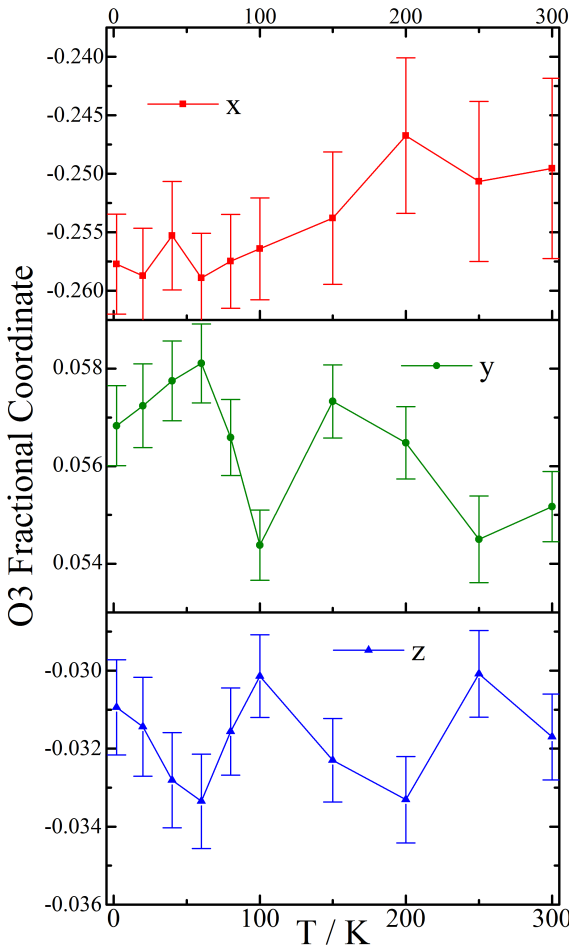

Figure B.5 | *T-Ca(Mn$_{0.88(4)}$Fe$_{0.12}$)FeReO$_6$: O3 fractional coordinates versus T.*

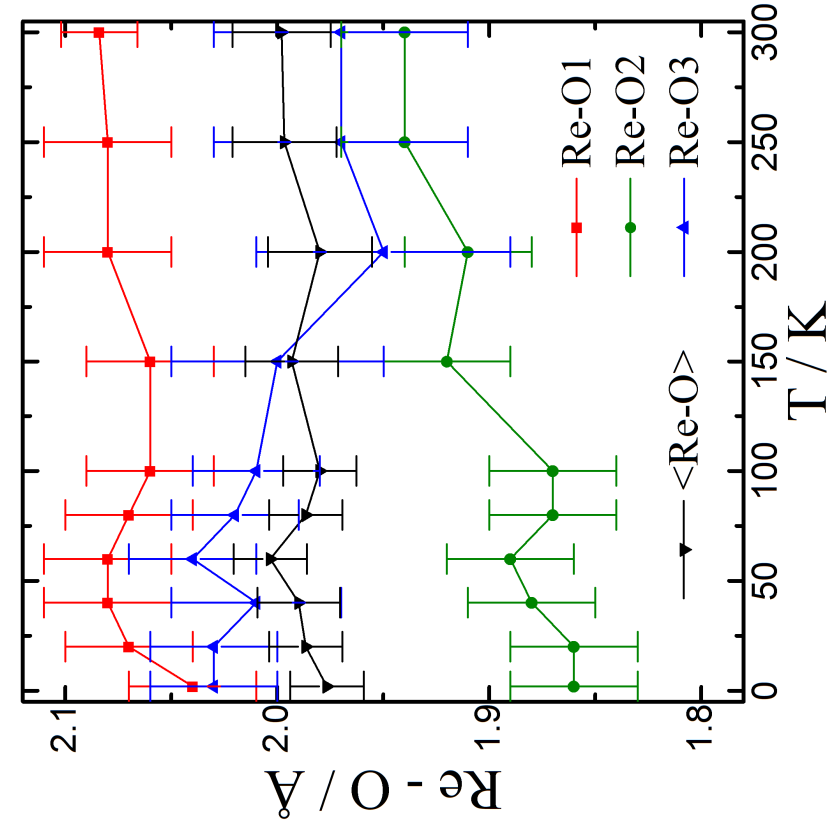

Figure B.7 | *T-Ca(Mn$_{0.88(4)}$Fe$_{0.12}$)FeReO$_6$: temperature variation of Re–O bond lengths from refined WISH data..*

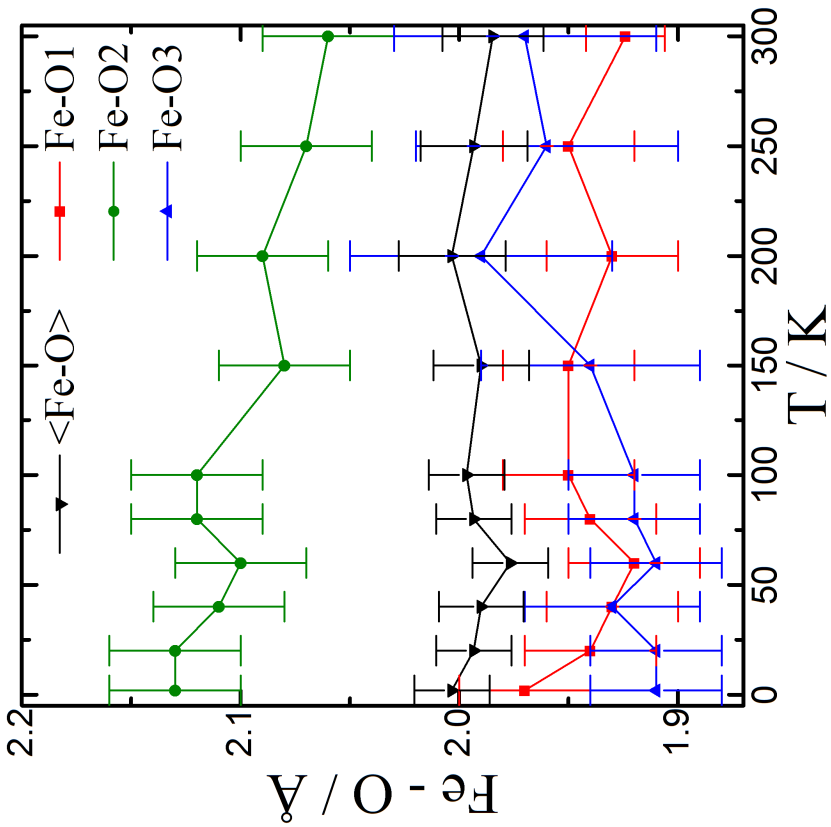

Figure B.6 | *T-Ca(Mn$_{0.88(4)}$Fe$_{0.12}$)FeReO$_6$: temperature variation of Fe–O bond lengths from refined WISH data.*

B.2. WISH Plots, x = 1.5 – M-$(Ca_{1.73(8)}Mn_{0.27})FeReO_6$

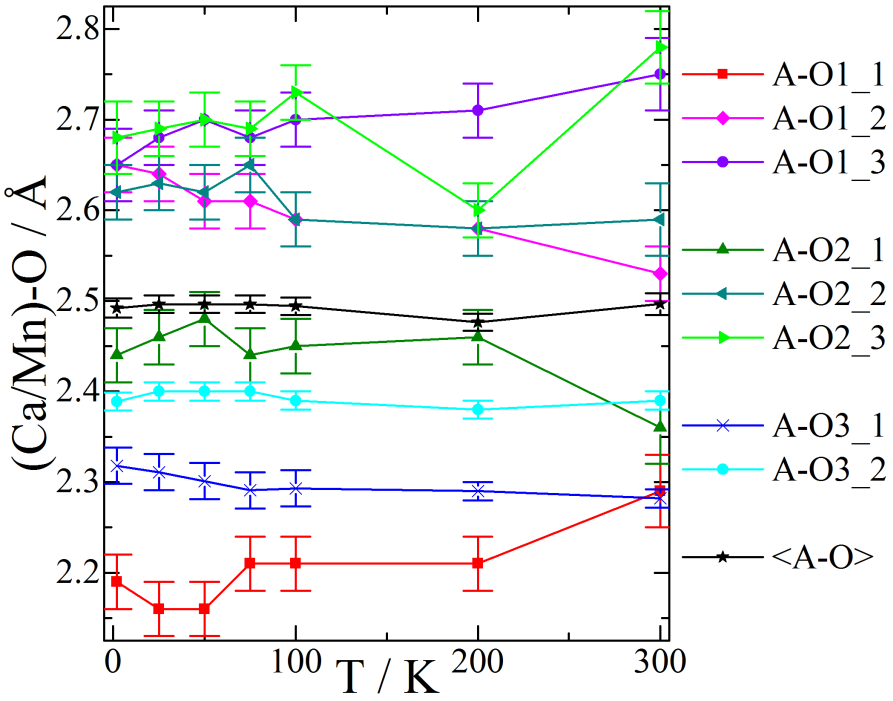

Figure B.8 | *M-$(Ca_{1.73(8)}Mn_{0.27})FeReO_6$: thermal variation of (Ca/Mn)–O bond lengths from refined WISH data.*

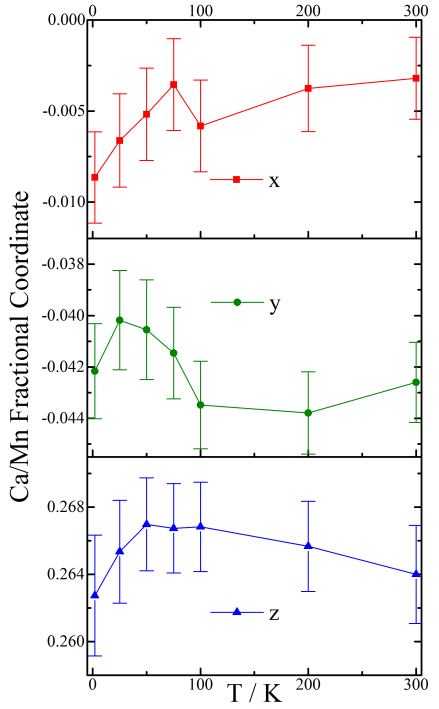

Figure B.9 | *M-$(Ca_{1.73(8)}Mn_{0.27})FeReO_6$: (Ca/Mn) fractional coordinates versus T.*

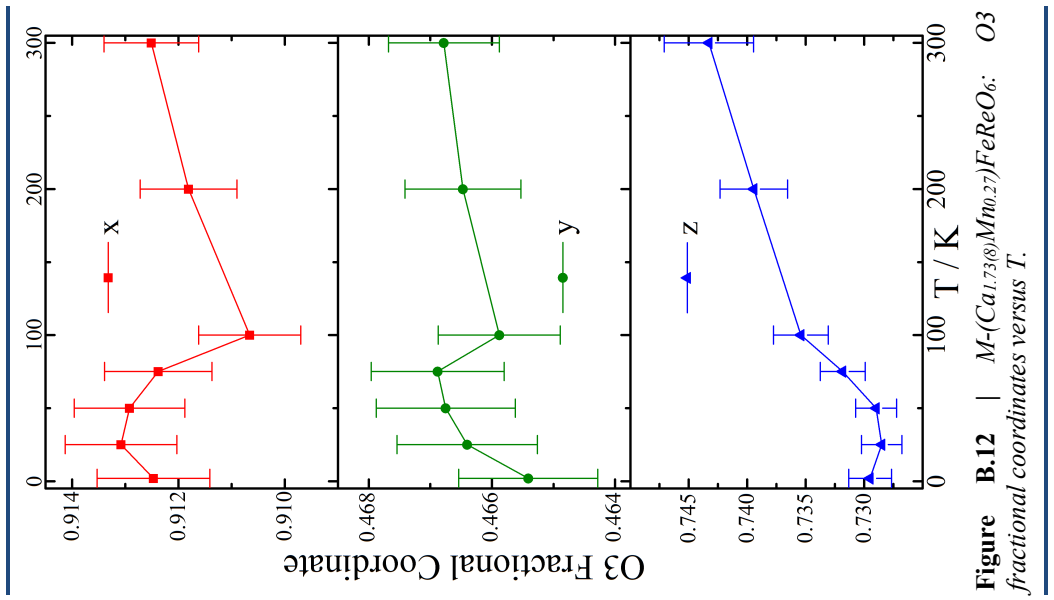

Figure B.12 | *M-($Ca_{1.73(8)}Mn_{0.27}$)$FeReO_6$: O3 fractional coordinates versus T.*

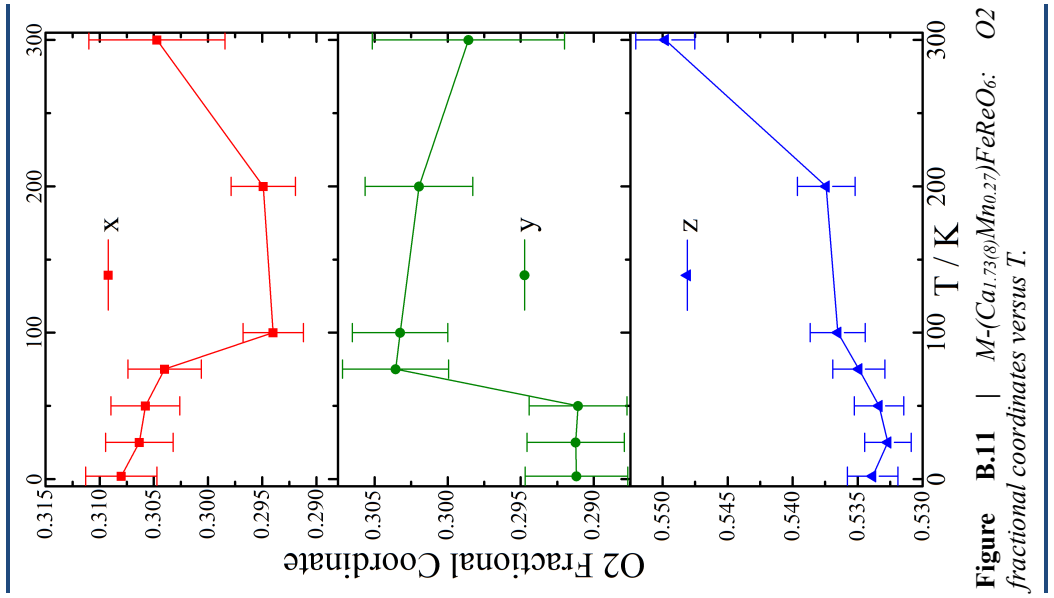

Figure B.11 | *M-($Ca_{1.73(8)}Mn_{0.27}$)$FeReO_6$: O2 fractional coordinates versus T.*

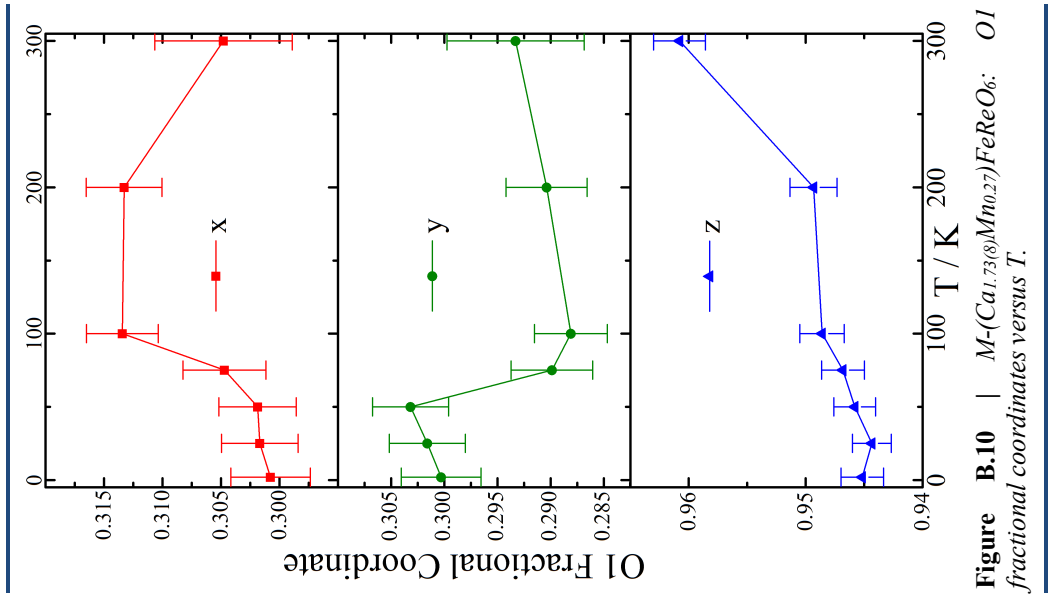

Figure B.10 | *M-($Ca_{1.73(8)}Mn_{0.27}$)$FeReO_6$: O1 fractional coordinates versus T.*

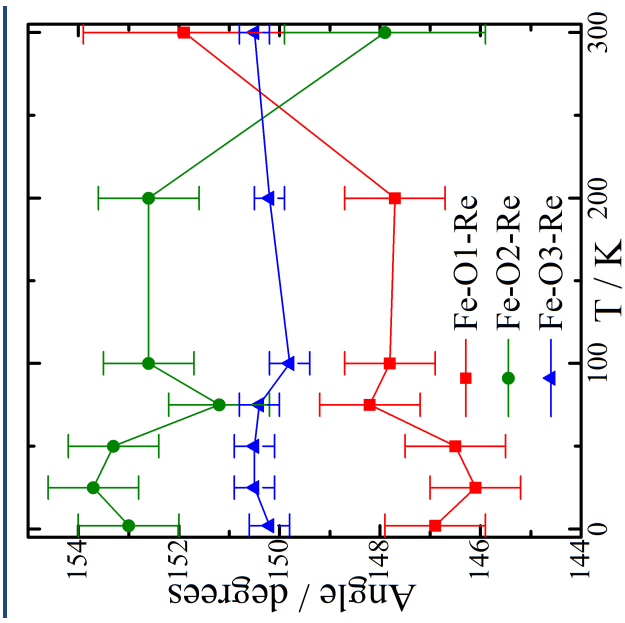

Figure B.15 | *M-($Ca_{1.73(8)}Mn_{0.27}$)$FeReO_6$: temperature variation of Fe–O–Re bond angles from refined WISH data.*

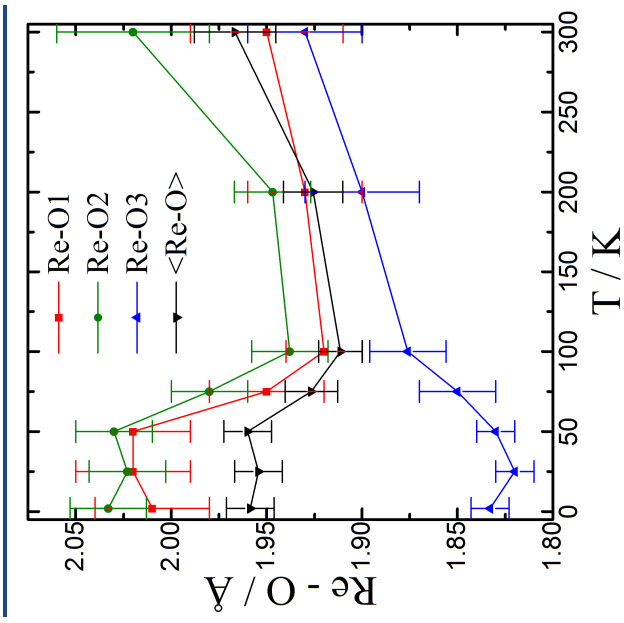

Figure B.14 | *M-($Ca_{1.73(8)}Mn_{0.27}$)$FeReO_6$: temperature variation of Re–O bond lengths from refined WISH data.*

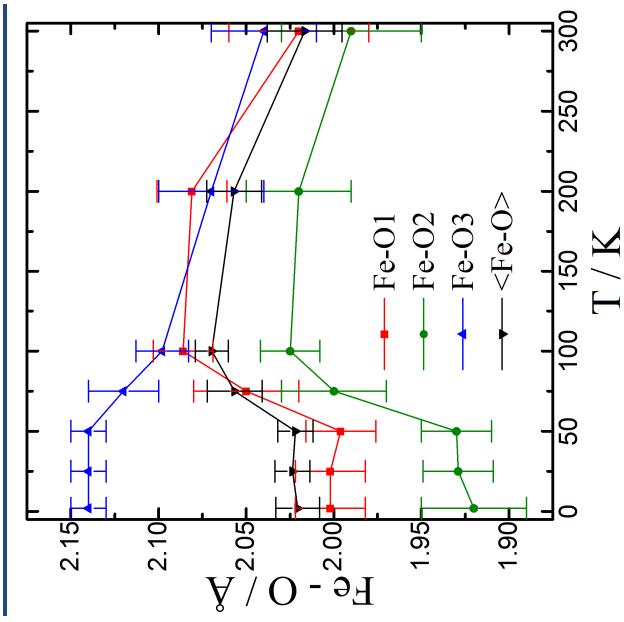

Figure B.13 | *M-($Ca_{1.73(8)}Mn_{0.27}$)$FeReO_6$: temperature variation of Fe–O bond lengths from refined WISH data.*

B.3. WISH Results, x = 0.5 – T-$(Ca_{0.74(2)}Mn_{0.26})MnFeReO_6$

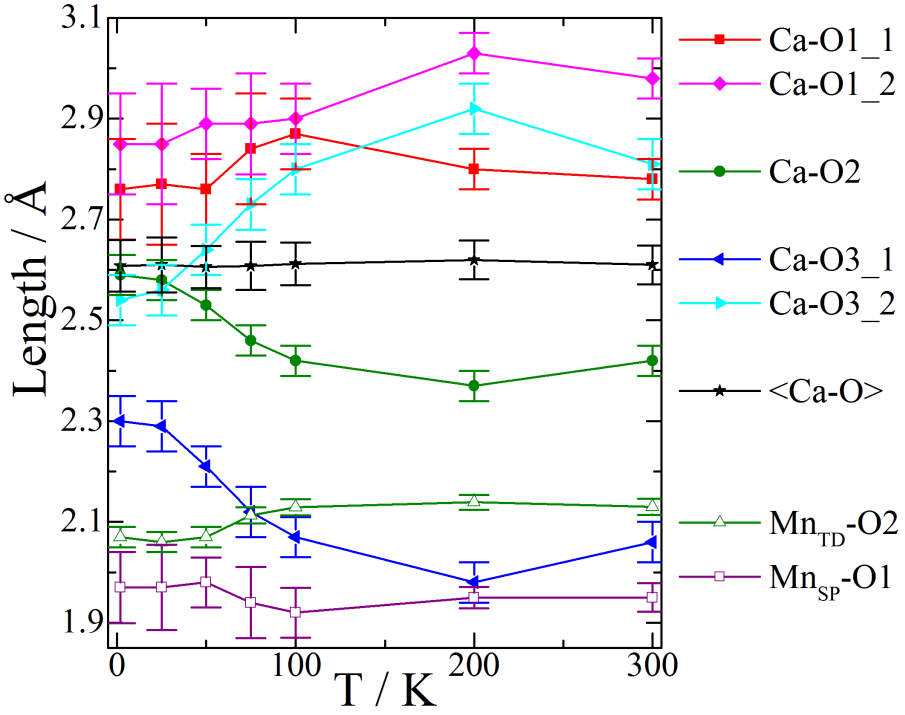

Figure B.16 | *T-$(Ca_{0.74(2)}Mn_{0.26})MnFeReO_6$: temperature variation of Ca–O, A_{TD}–O2 and A_{SP}–O1 bond lengths from refined WISH data.*

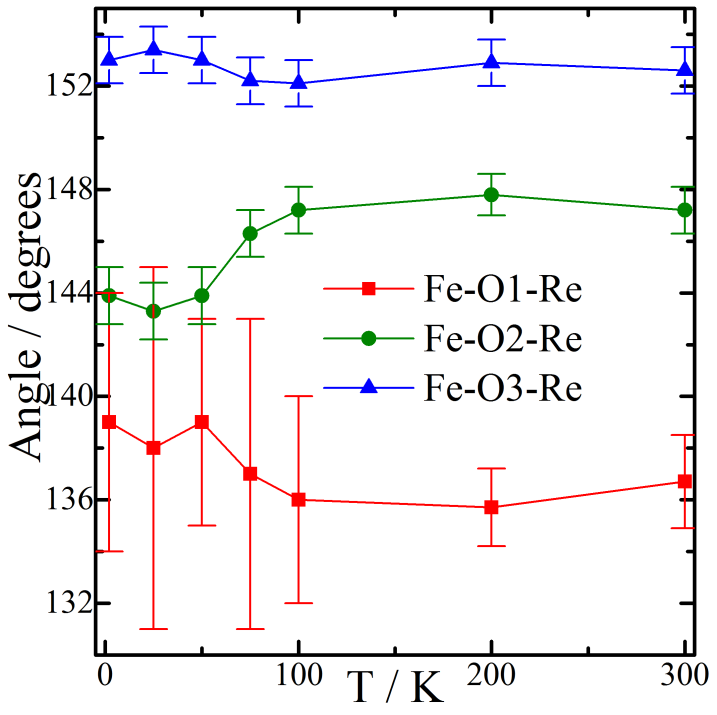

Figure B.17 | *T-$(Ca_{0.74(2)}Mn_{0.26})MnFeReO_6$: temperature variation of Fe–O–Re bond angles from refined WISH data.*

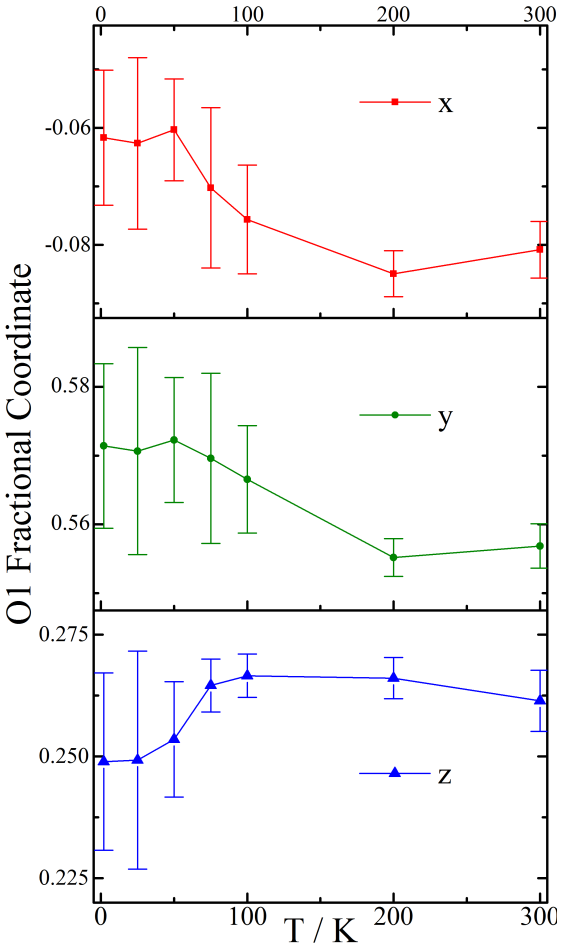

Figure B.18 | *T-($Ca_{0.74(2)}Mn_{0.26}$)MnFeReO$_6$: O1 fractional coordinates versus T.*

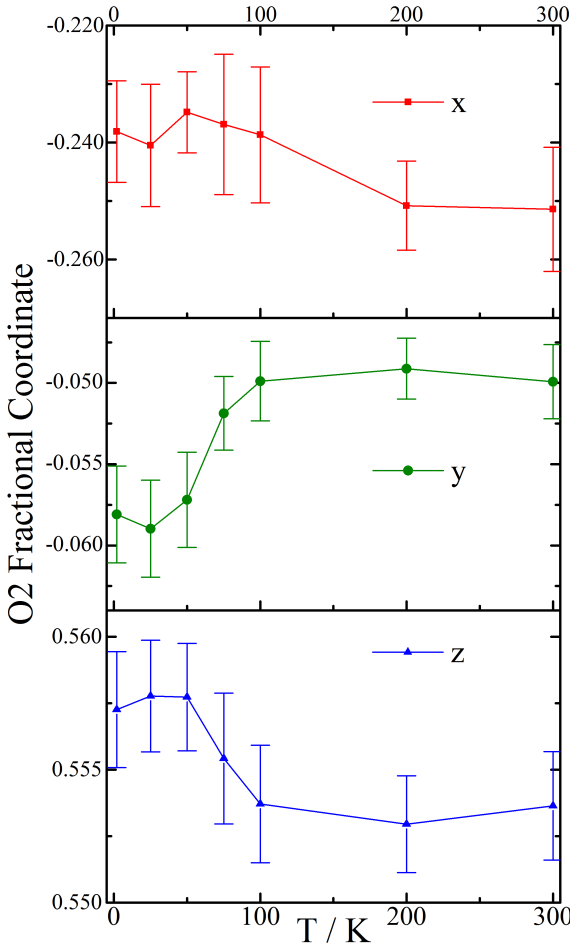

Figure B.19 | *T-($Ca_{0.74(2)}Mn_{0.26}$)MnFeReO$_6$: O2 fractional coordinates versus T.*

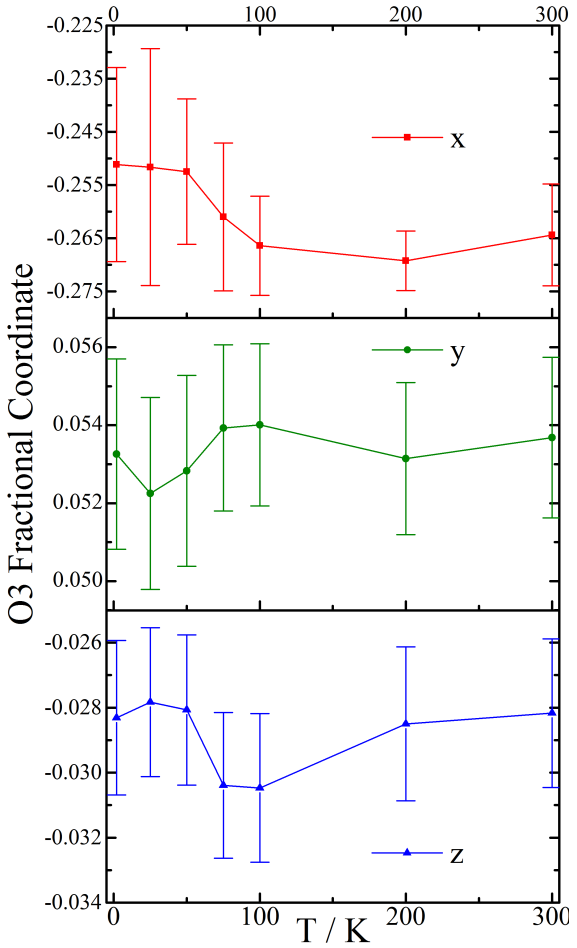

Figure B.20 | *T-($Ca_{0.74(2)}Mn_{0.26}$)MnFeReO$_6$: O3 fractional coordinates versus T.*

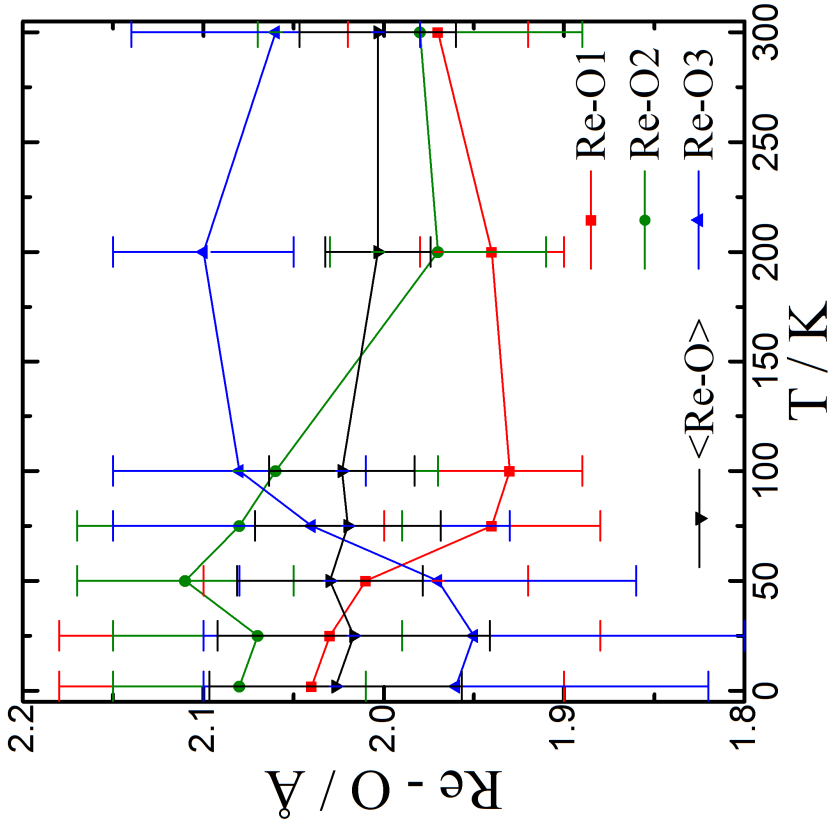

Figure B.22 | *T-$(Ca_{0.74(2)}Mn_{0.26})MnFeReO_6$: temperature variation of Re–O bond lengths from refined WISH data.*

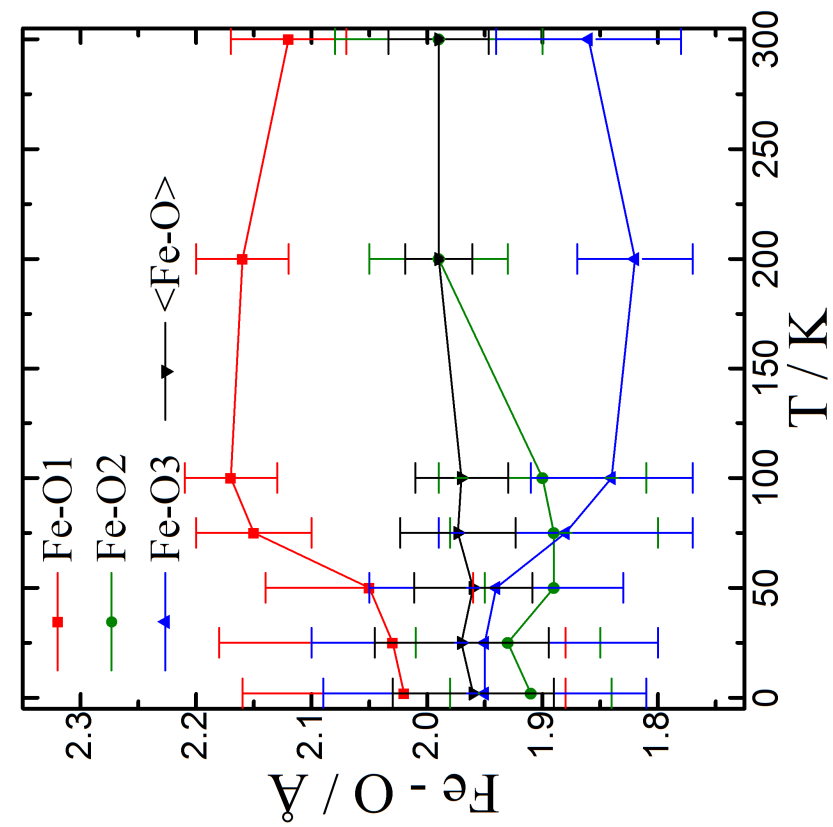

Figure B.21 | *T-$(Ca_{0.74(2)}Mn_{0.26})MnFeReO_6$: temperature variation of Fe–O bond lengths from refined WISH data.*

B.4. WISH Results, x = 0.5 – M-($Ca_{0.17(3)}Mn_{1.83}$)$FeReO_6$

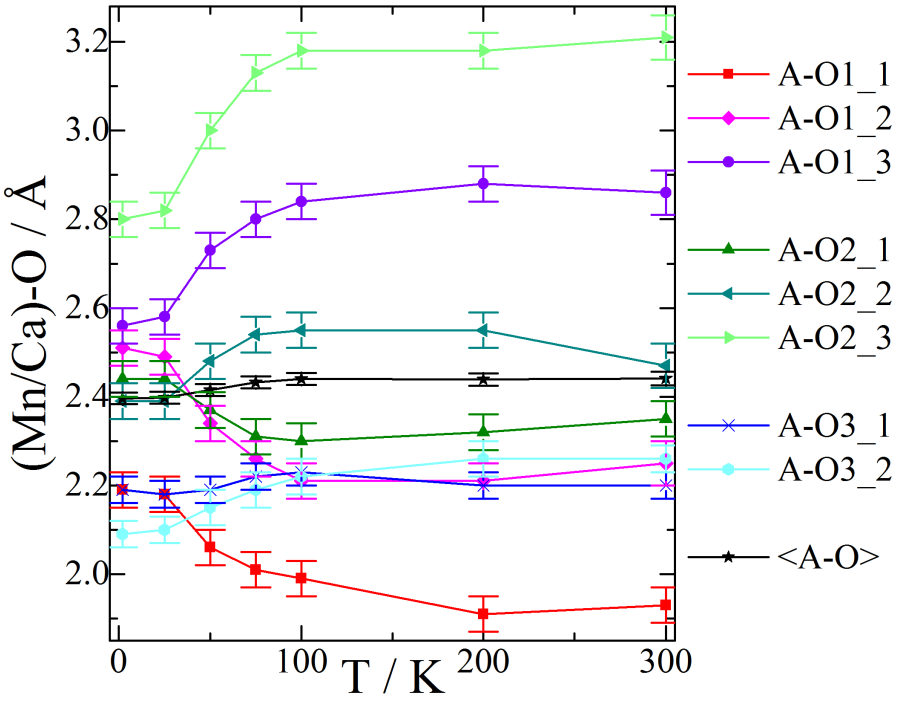

Figure B.23 | *M-($Ca_{0.74(2)}Mn_{0.26}$)$MnFeReO_6$: temperature variation of (Mn/Ca)–O bond lengths from refined WISH data.*

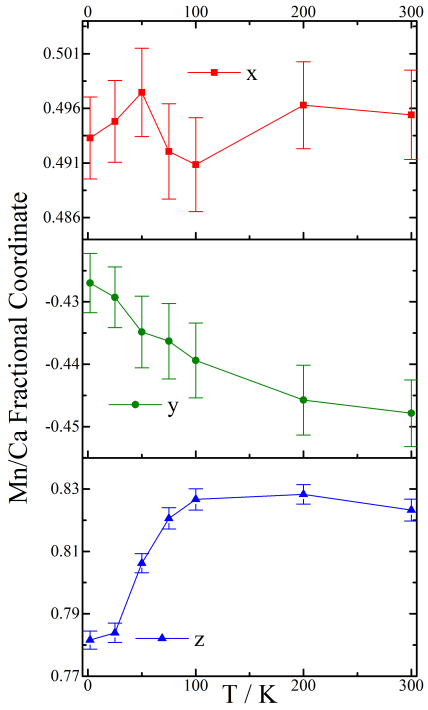

Figure B.24 | *M-($Ca_{0.74(2)}Mn_{0.26}$)$MnFeReO_6$: (Mn/Ca) fractional coordinates versus T.*

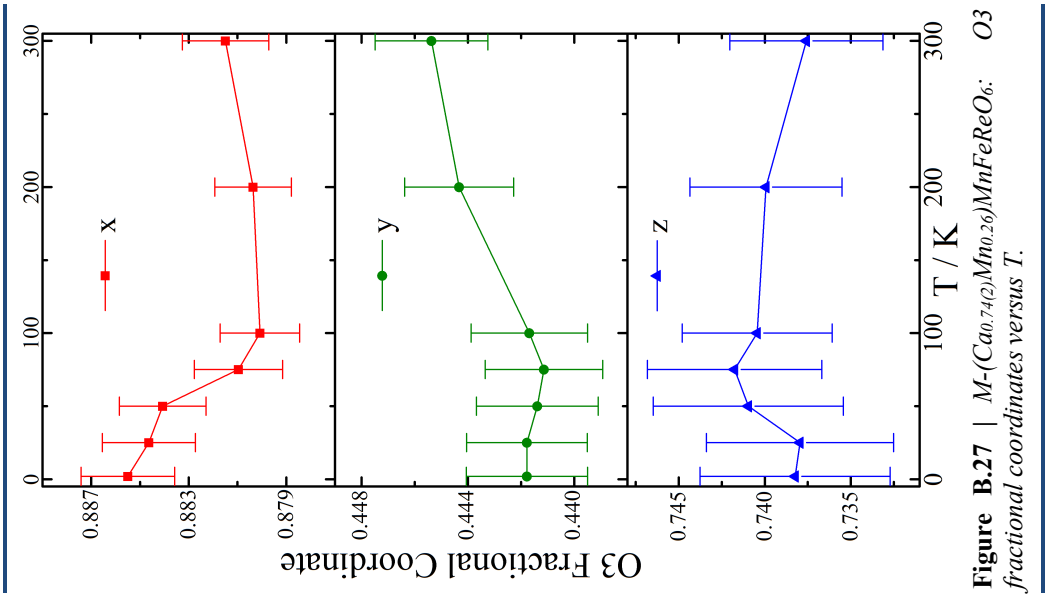

Figure B.27 | *M-($Ca_{0.74(2)}Mn_{0.26}$)MnFeReO$_6$: O3 fractional coordinates versus T.*

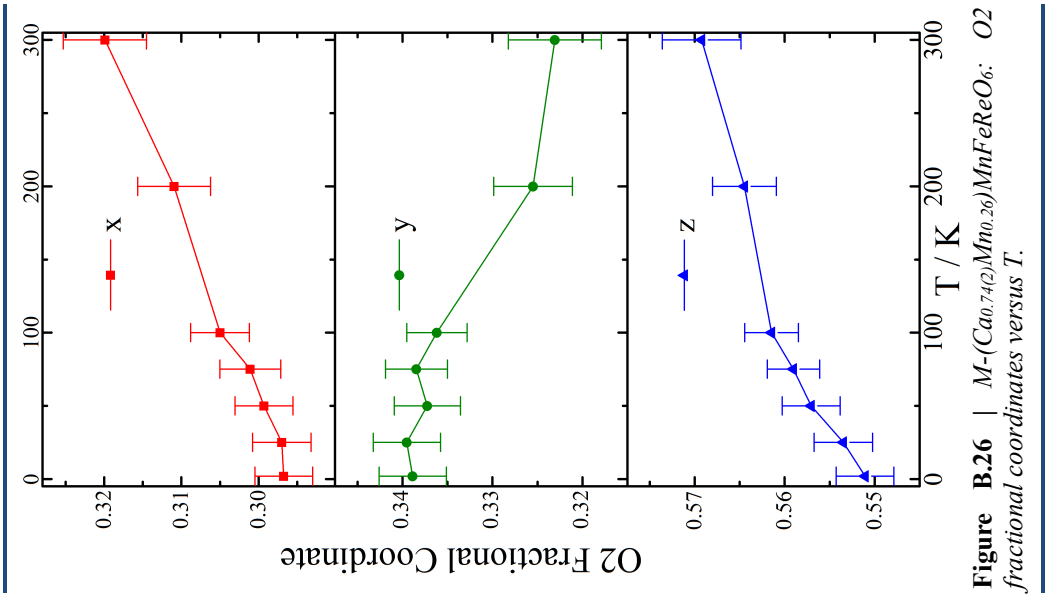

Figure B.26 | *M-($Ca_{0.74(2)}Mn_{0.26}$)MnFeReO$_6$: O2 fractional coordinates versus T.*

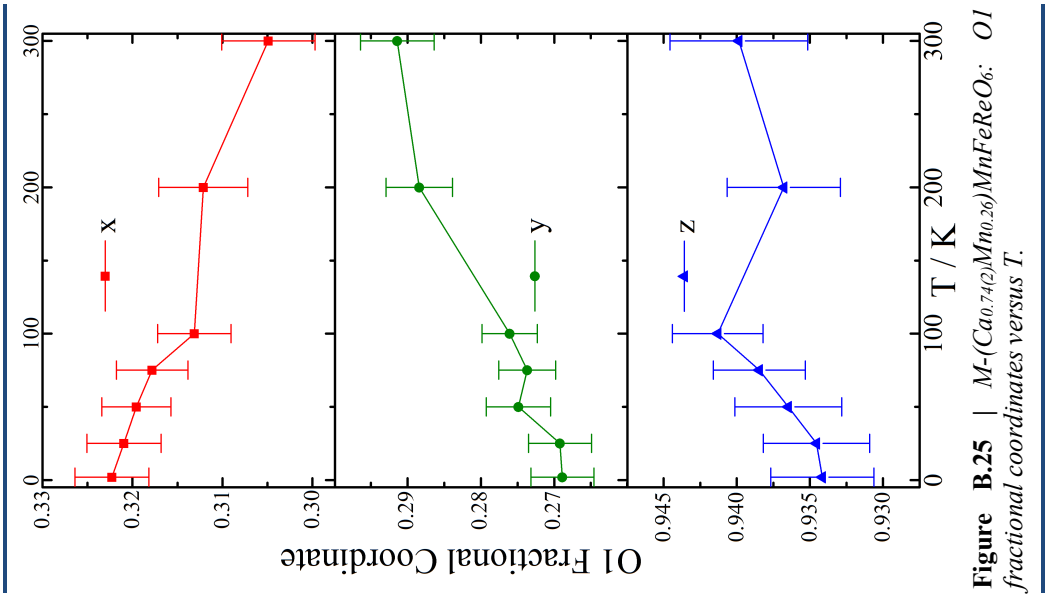

Figure B.25 | *M-($Ca_{0.74(2)}Mn_{0.26}$)MnFeReO$_6$: O1 fractional coordinates versus T.*

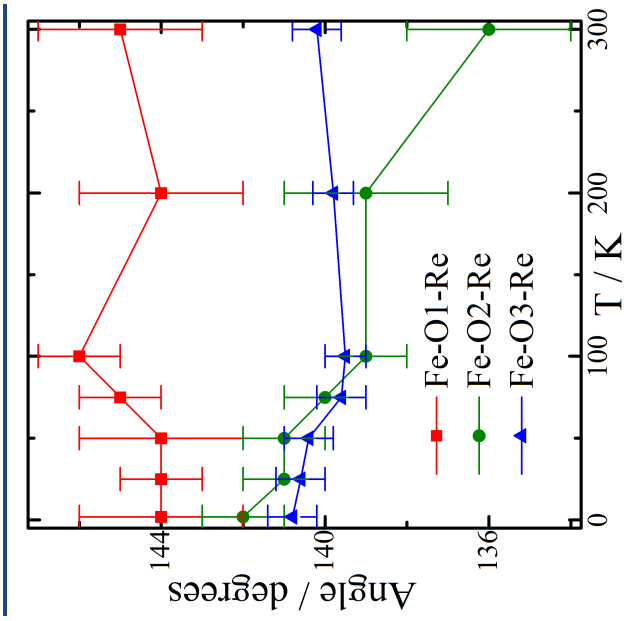

Figure B.30 | *M-($Ca_{0.74(2)}Mn_{0.26}$)MnFeReO$_6$: thermal variation of Fe–O–Re bond angles from refined WISH data.*

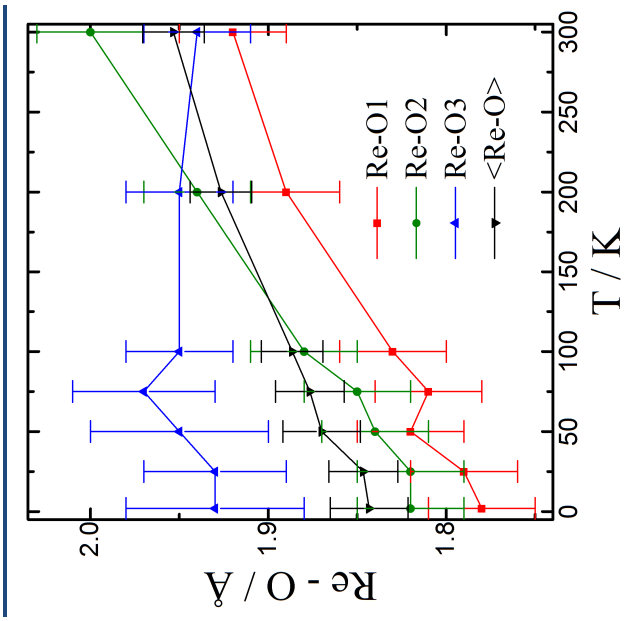

Figure B.29 | *M-($Ca_{0.74(2)}Mn_{0.26}$)MnFeReO$_6$: thermal variation of Re–O bond lengths from refined WISH data.*

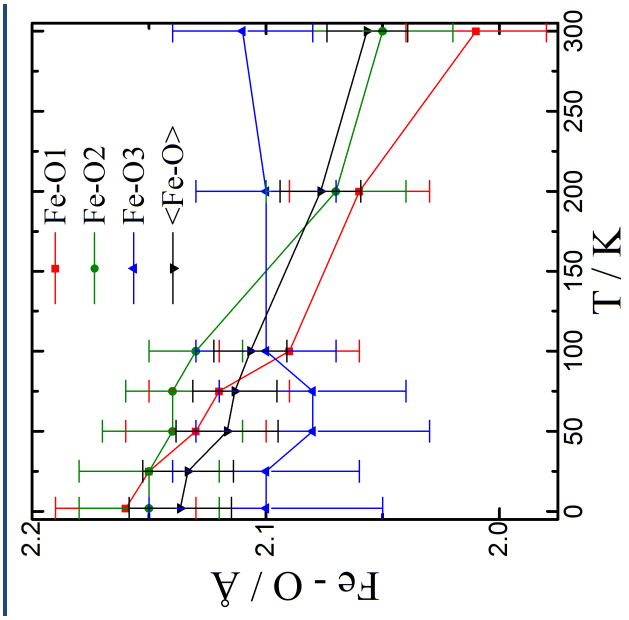

Figure B.28 | *M-($Ca_{0.74(2)}Mn_{0.26}$)MnFeReO$_6$: thermal variation of Fe–O bond lengths from refined WISH data.*

Appendix C. Additional Results for $Ca(Mn_{0.5}Cu_{0.5})FeReO_6$

Additional data for $Ca(Mn_{0.5}Cu_{0.5})FeReO_6$ is supplied in this section. **Fig. C.1** shows zero-field cooled as well as field cool magnetisation, measured in magnetic fields of 0.5 T. Plots of results obtained from refinements of neutron diffraction data obtained on $Ca(Mn_{0.5}Cu_{0.5})FeReO_6$ from the WISH diffractometer at the ISIS Neutron Facility are shown in **Fig. C.2-C.6**, including Ca–O, A_{TD}–O and A_{SP}–O bond lengths, Fe–O–Re bond angles, as well as fractional coordinate variations for O1, O2 and O3.

C.1. Magnetic Information, $Ca(Mn_{0.5}Cu_{0.5})FeReO_6$

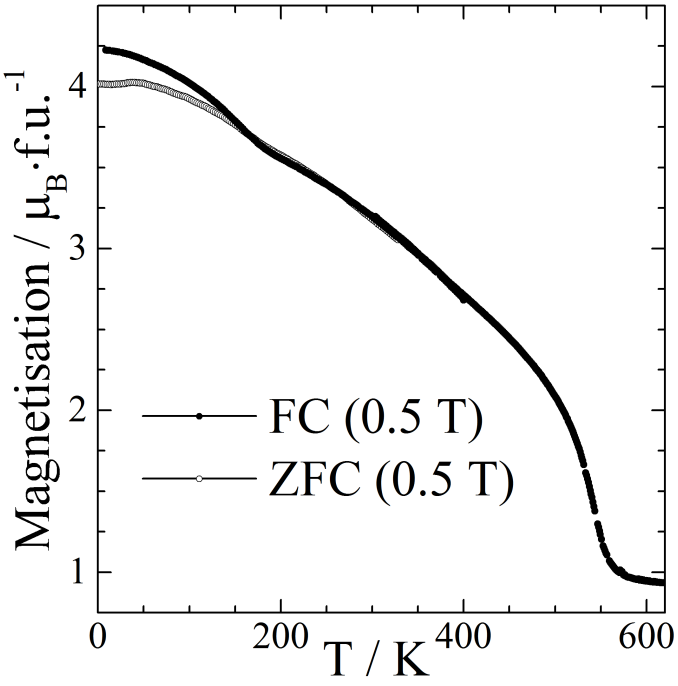

Figure C.1 | *Zero-field cooled (ZFC) and field cooled magnetisation versus temperature for $Ca(Mn_{0.5}Cu_{0.5})FeReO_6$.*

C.2. WISH Results, $Ca(Mn_{0.5}Cu_{0.5})FeReO_6$

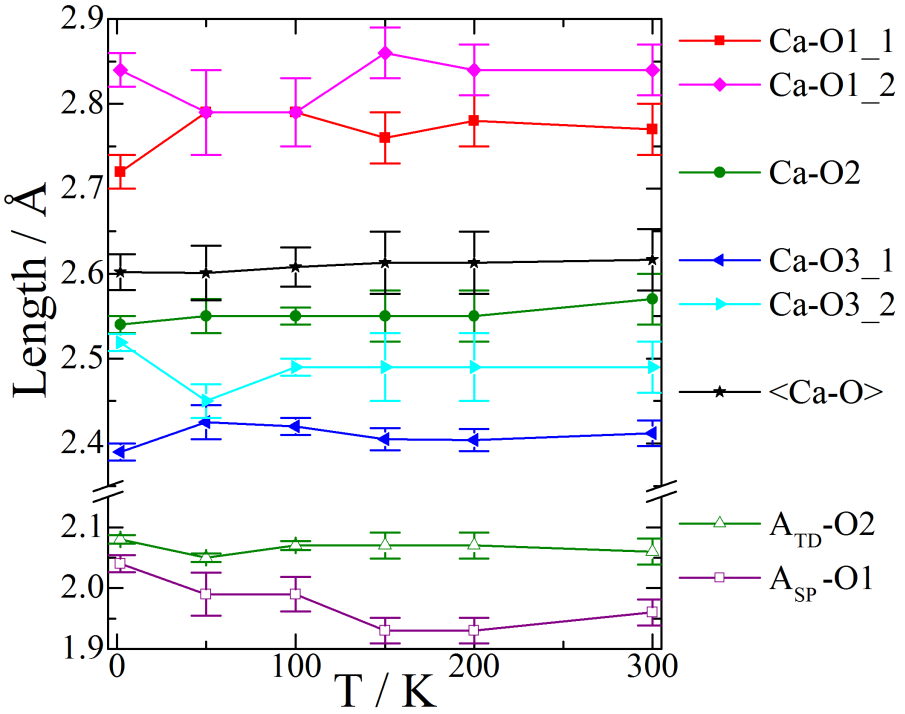

Figure C.2 | *$Ca(Mn_{0.5}Cu_{0.5})FeReO_6$: Temperature variation of Ca–O, A_{TD}–O2 and A_{SP}–O1 bond lengths from refined WISH data.*

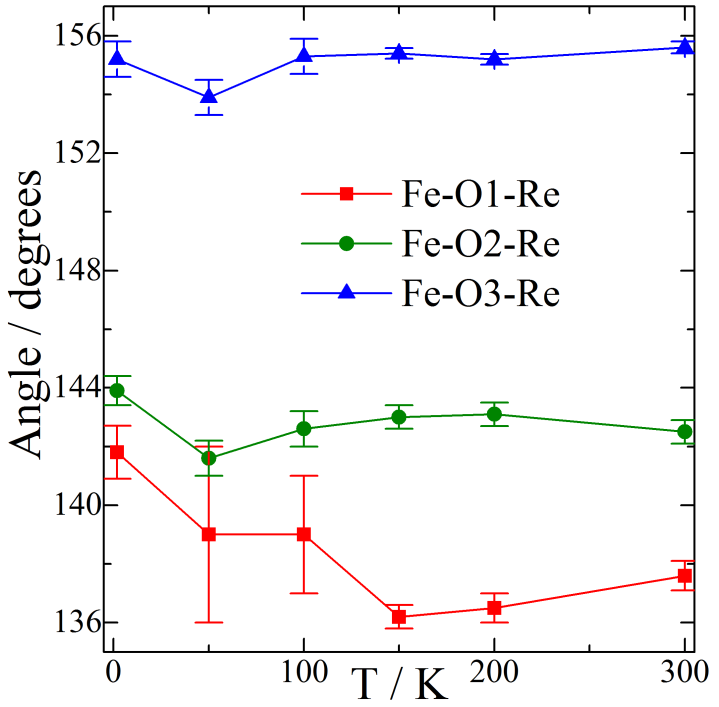

Figure C.3 | *$Ca(Mn_{0.5}Cu_{0.5})FeReO_6$: Temperature variation of Fe–O–Re bond angles from refined WISH data.*

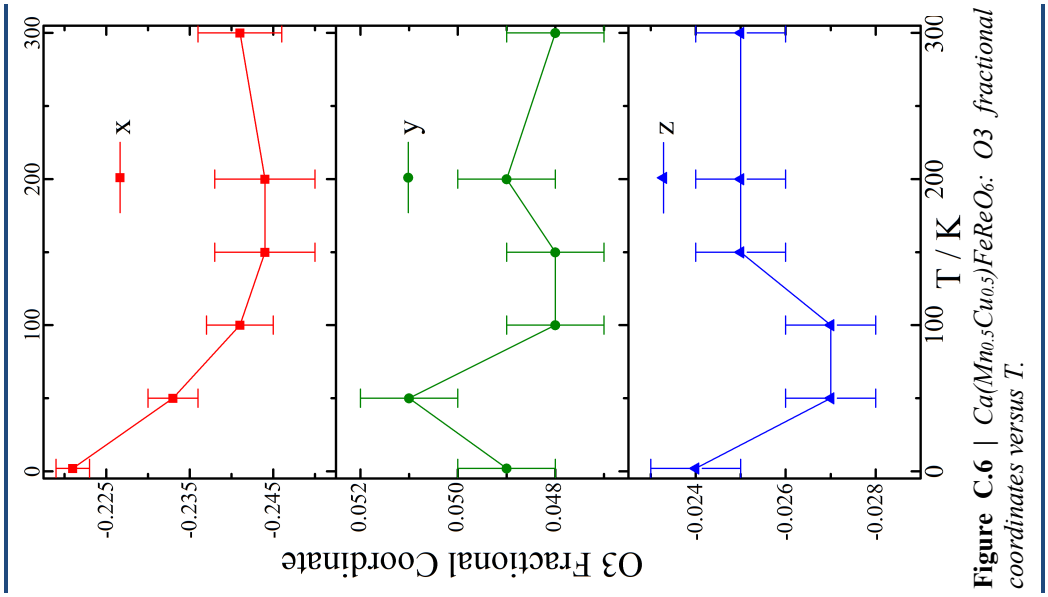

Figure C.6 | *$Ca(Mn_{0.5}Cu_{0.5})FeReO_6$: O3 fractional coordinates versus T.*

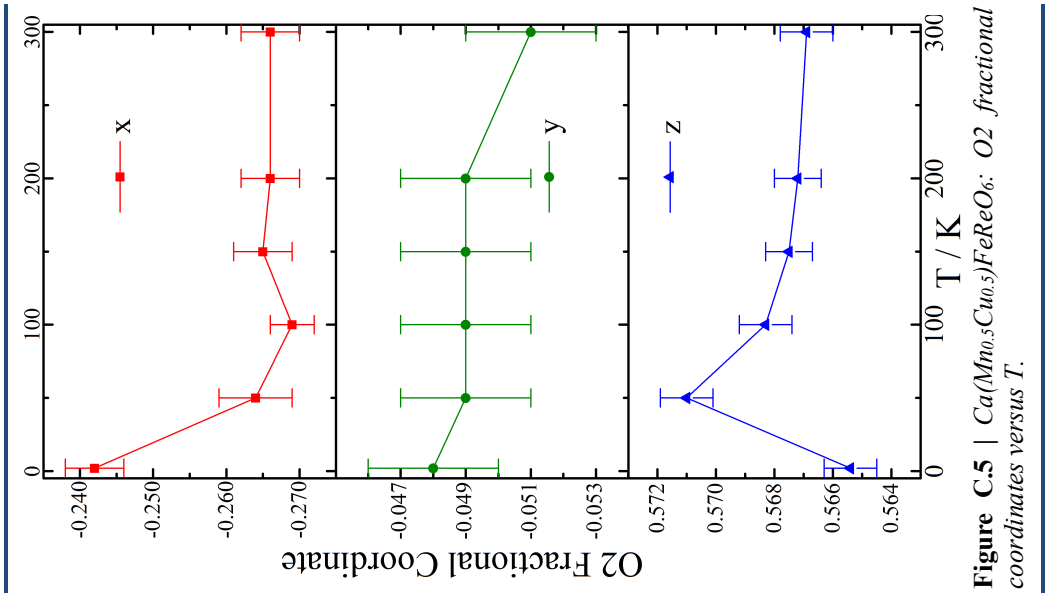

Figure C.5 | *$Ca(Mn_{0.5}Cu_{0.5})FeReO_6$: O2 fractional coordinates versus T.*

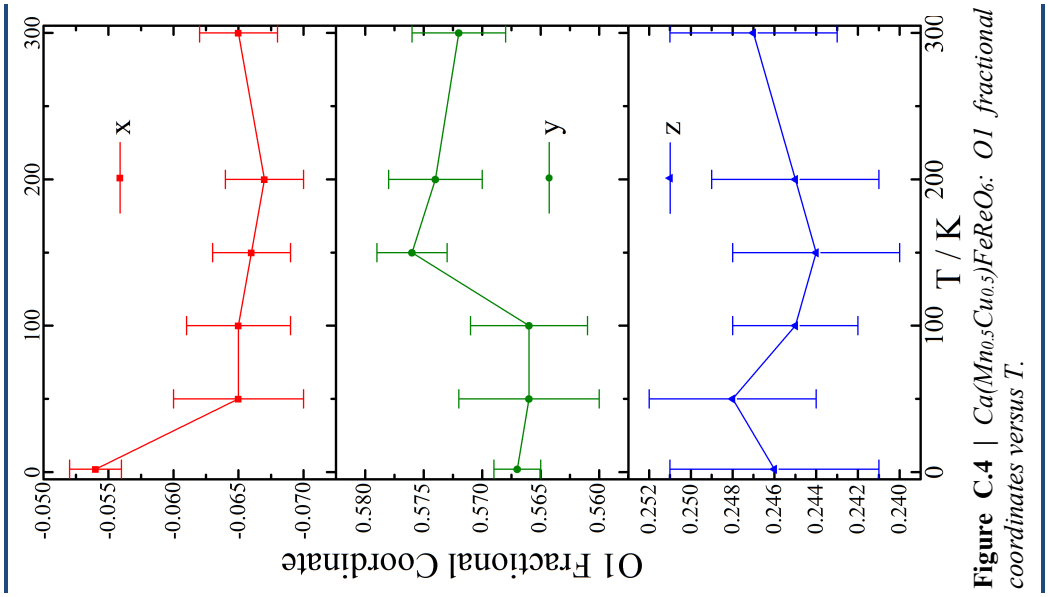

Figure C.4 | *$Ca(Mn_{0.5}Cu_{0.5})FeReO_6$: O1 fractional coordinates versus T.*

Appendix D. Additional Results for $CaMnMnReO_6$

Additional data for $CaMnMnReO_6$ is supplied in this section. **Fig. D.1** shows zero-field cooled and field cooled magnetisation in lower applied fields than shown in '**Chapter 6. $CaMnMnReO_6$ – Large Coercivity and Mutually Frustrated A and B-site Spin Orders in a Double Double Perovskite**'. Plots of data obtained from refinements of neutron data acquired using the WISH diffractometer at the ISIS Neutron Facility are shown in **Fig. D.2-D.6**, including Ca–O, Mn_{TD}–O2 and Mn_{SP}–O1 bond lengths, MnB–O–Re bond angles, as well as the fractional coordinate variations for O1, O2 and O3.

D.1. Magnetic Information, $CaMnMnReO_6$

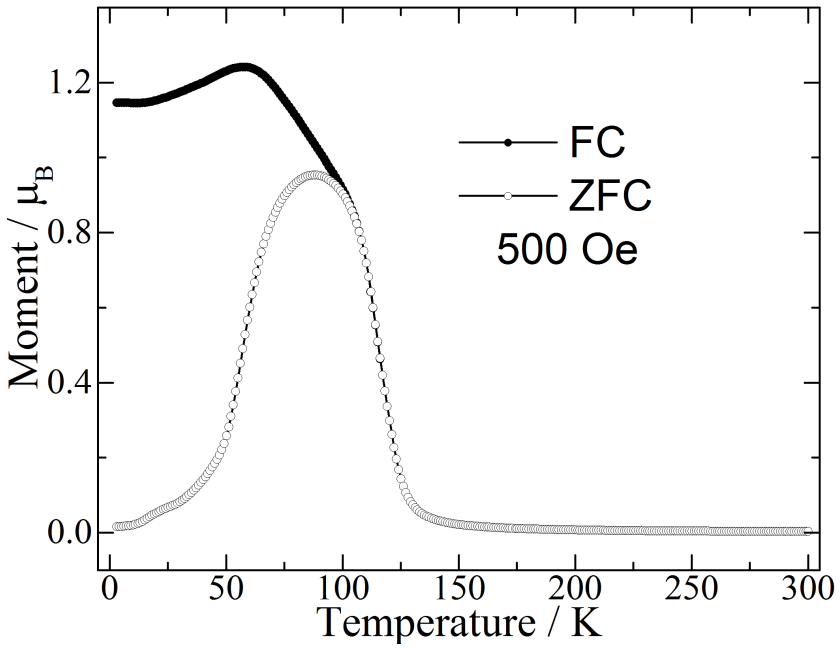

Figure D.1 | *Zero-field cooled (ZFC) and field cooled magnetisation versus temperature for $CaMnMnReO_6$ measured in a low applied field of 500 Oe.*

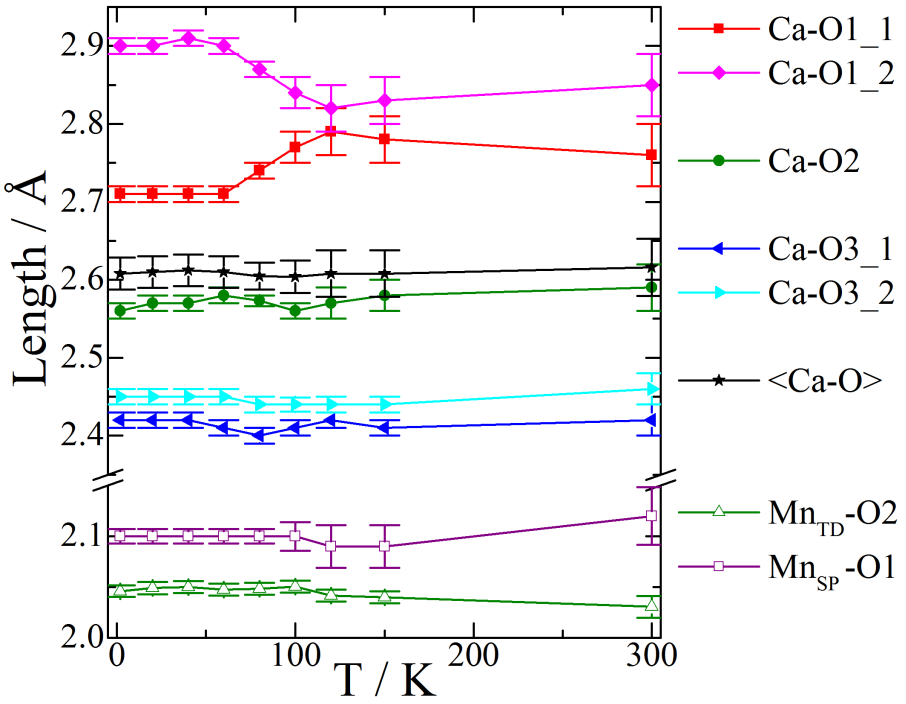

Figure D.2 | *$CaMnMnReO_6$: Temperature variation of Ca–O, Mn_{TD} and Mn_{SP} bond lengths from refined WISH data.*

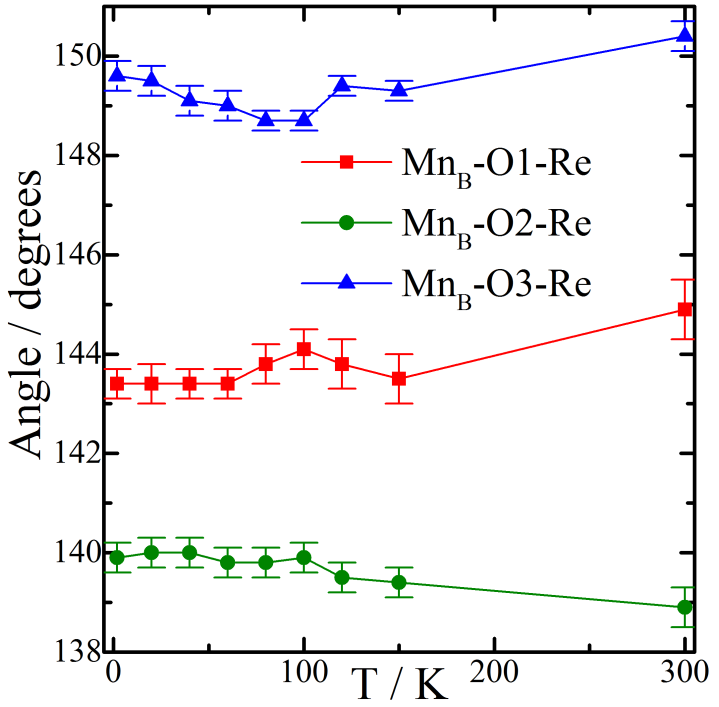

Figure D.3 | *$CaMnMnReO_6$: Temperature variation of Mn–O–Re bond angles from refined WISH data.*

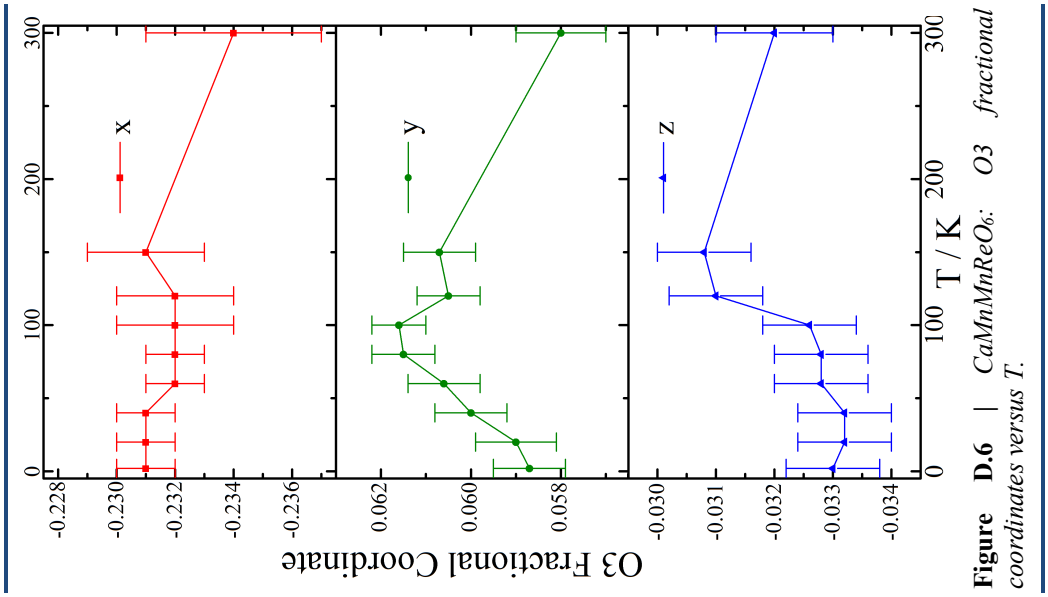

Figure D.6 | *CaMnMnReO₆: O3 fractional coordinates versus T.*

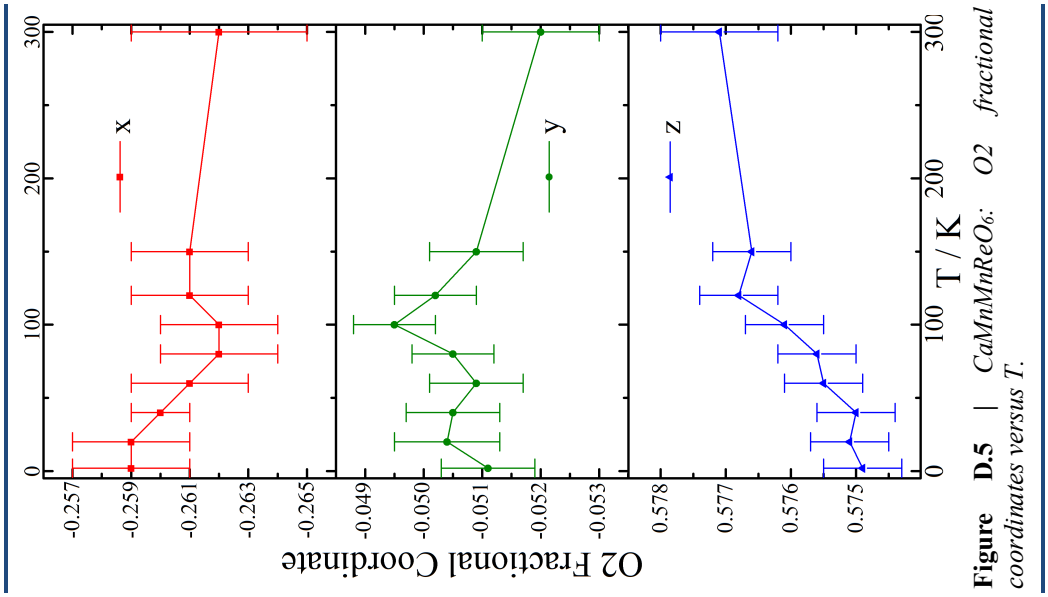

Figure D.5 | *CaMnMnReO₆: O2 fractional coordinates versus T.*

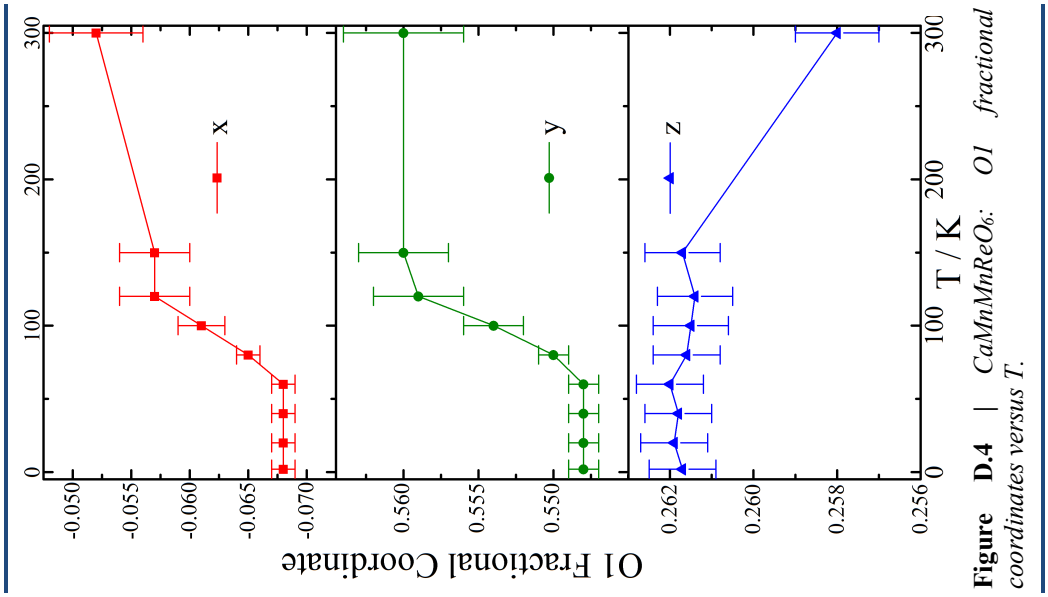

Figure D.4 | *CaMnMnReO₆: O1 fractional coordinates versus T.*

Publications

Publication I.

Large Magnetization and Frustration Switching of Magnetoresistance in the Double-Perovskite Ferrimagnet Mn_2FeReO_6

Angel M. Arévalo-López, Graham M. McNally and J. Paul Attfield.

Reprinted with permission from *Angewandte Chemie - International Edition*, 2015, **54**, 12074-12077.

DOI: 10.1002/anie.201506540

Publication II.

Complex Ferrimagnetism and Magnetoresistance Switching in Ca-Based Double Double and Triple Double Perovskites

Graham M. McNally, Ángel M. Arévalo-López, Padraig Kearins, Fabio Orlandi, Pascal Manuel and J. Paul Attfield.

Reprinted with permission from *Chemistry of Materials*, 2017, **29**, 8870-8874.

DOI: 10.1021/acs.chemmater.7b03556

Angewandte
Communications

Perovskite Phases

International Edition: DOI: 10.1002/anie.201506540
German Edition: DOI: 10.1002/ange.201506540

Large Magnetization and Frustration Switching of Magnetoresistance in the Double-Perovskite Ferrimagnet Mn_2FeReO_6

*Angel M. Arévalo-López, Graham M. McNally, and J. Paul Attfield**

Abstract: *Ferrimagnetic $A_2BB'O_6$ double perovskites, such as Sr_2FeMoO_6, are important spin-polarized conductors. Introducing transition metals at the A-sites offers new possibilities to increase magnetization and tune magnetoresistance. Herein we report a ferrimagnetic double perovskite, Mn_2FeReO_6, synthesized at high pressure which has a high Curie temperature of 520 K and magnetizations of up to 5.0 μ_B which greatly exceed those for other double perovskite ferrimagnets. A novel switching transition is discovered at 75 K where magnetoresistance changes from conventional negative tunneling behavior to large positive values, up to 265 % at 7 T and 20 K. Neutron diffraction shows that the switch is driven by magnetic frustration from antiferromagnetic Mn^{2+} spin ordering which cants Fe^{3+} and Re^{5+} spins and reduces spin-polarization. Ferrimagnetic double perovskites based on A-site Mn^{2+} thus offer new opportunities to enhance magnetization and control magnetoresistance in spintronic materials.*

Around 650 $A_2BB'O_6$ double perovskite oxides with an alternating (rocksalt) order of B and B′ cations are known.[1] An important subgroup are ferrimagnetic, spin-polarized conductors which combine large-spin 3d transition-metal B cations and small-spin 4d or 5d B′ ions,[2] for example Fe^{3+} (spin $S=5/2$) and Mo^{5+} ($S=1/2$) in Sr_2FeMoO_6.[3] Strong antiferromagnetic coupling between B and B′ spins leads to ferrimagnetism with a Curie temperature of $T_C=410$ K, and half-metallicity with a high degree of spin polarization P results. The predicted magnetization per double-perovskite formula unit is $M=4\ \mu_B$ and the highest reported value for non-magnetic A-cations is $M=4.1\ \mu_B$ for $Sr_2Fe(Mo_{0.6}W_{0.4})O_6$.[4] Ferrimagnetic double perovskites show large, low-field tunneling magnetoresistance (TMR) effects which have been exploited in spintronic devices, such as magnetic tunnel junctions.[5,6] Magnetoresistance ($MR=[R(H)-R(0)]/R(0)$ for resistances R measured in magnetic field H and at $H=0$) is given by $MR=-P^2M^2/(1+P^2M^2)$ in a simple TMR model,[2] so new materials with large values of P and M are desirable.

Ferrimagnetic double perovskites synthesized at ambient pressure have relatively large non-magnetic A^{2+} (A = Ca, Sr, Ba) cations. However, high pressure can be used to introduce smaller, magnetic, transition-metal cations at perovskite A-sites, and $Ca_{0.5}Cu_{1.5}FeReO_6$ (the 134 type quadruple perovskite $CaCu_3Fe_2Re_2O_{12}$ where 75 % of the A-sites contain $S=1/2$ Cu^{2+} ions with 1:3 cation order) was recently reported to have an enhanced $M=4.35\ \mu_B$ and a high $T_C=560$ K, although with modest $MR=-4\,\%$ at 5 T and 10 K.[7] High pressure stabilizes $S=5/2$ Mn^{2+} ions at the A sites of a few perovskites, such as $MnVO_3$[8] and the double perovskite Mn_2FeSbO_6,[9] both of which have low-temperature incommensurate antiferromagnetic spin orders, and the 134 types ζ-Mn_2O_3[10] and $MnCu_3V_4O_{12}$.[11] We have explored possible Mn^{2+}-based ferrimagnetic double perovskites and we report herein the new material Mn_2FeReO_6 which shows large M and a novel MR switching transition.

Mn_2FeReO_6 was synthesized at high pressure (11 GPa) and temperature (1400 °C). Experimental details are in Supporting Information. Powder X-ray- and neutron-diffraction fits (Figure 1) show that this new material has a mono-

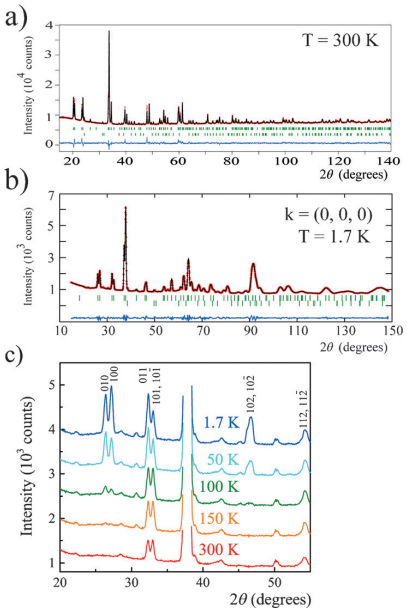

Figure 1. a) Fit to the room-temperature X-ray profile of Mn_2FeReO_6, lower reflection markers are for 1.5 wt % of ReO_2 impurity. b) Fit of crystal and magnetic structure models to 1.7 K neutron data. c) Low-angle neutron-diffraction profiles with magnetic diffraction peaks indexed. Appearance of peaks below 150 K evidences onset of antiferromagnetic Mn spin order, and changes between 100 and 50 K mark the 75 K reorientation transition driven by magnetic frustration.

[*] Dr. A. M. Arévalo-López, G. M. McNally, Prof. J. P. Attfield
Centre for Science at Extreme Conditions (CSEC) and
School of Chemistry, University of Edinburgh
Mayfield Road, Edinburgh EH9 3JZ (UK)
E-mail: j.p.attfield@ed.ac.uk

Supporting information for this article is available on the WWW under http://dx.doi.org/10.1002/anie.201506540. Open data for this article are at http://dx.doi.org/10.7488/ds/288.

clinically distorted double-perovskite structure similar to that of Ca_2FeReO_6.[2] Mn, Fe, and Re are highly ordered over the three $A_2BB'O_6$ cation sites, with only Mn at A sites and a very small antisite disorder (which is important for obtaining a high P) of 1.4% for Fe/Re at B/B′ sites. This material is the first double-perovskite with magnetic transition-metal cations at all positions; $S = 5/2$ Mn^{2+} at the A-sites, and $S = 5/2$ Fe^{3+} and $S = 1$ Re^{5+} at B and B′ sites.

Magnetization measurements in Figure 2 reveal that Mn_2FeReO_6 has a high $T_C = 520$ K, comparable with 530 K

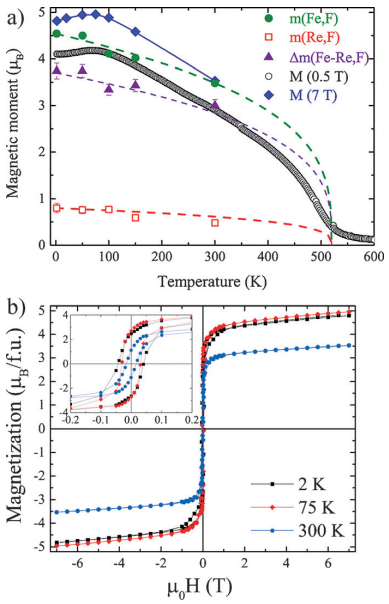

Figure 2. a) Temperature dependence of magnetization M per Mn_2FeReO_6 unit. Measurements at 0.5 T were collected during warming, and 7 T points are from hysteresis data such as in (b). Antiparallel Fe and Re moments m from neutron analysis and their net difference are also shown with Brillouin function fits (dashed lines). b) Magnetization-field hysteresis loops. The low-field inset shows a small magnetic anisotropy with a coercive field of 43 mT at 2 K.

for Ca_2FeReO_6 and 560 K for $Ca_{0.5}Cu_{1.5}FeReO_6$.[2,7] The observed magnetizations for Mn_2FeReO_6 exceed those for other ferrimagnetic double perovskites at high and low field strengths. $M = 3.5$ μ_B at 300 K and 7 T exceeds room-temperature values for all other double-perovskite ferrimagnets, and the maximum $M = 5.0$ μ_B at 75 K is a record in this materials class. Magnetic fields of 30 T were used to obtain saturated M up to 3.3 μ_B for other A_2FeReO_6 (A = Ca, Sr, $Sr_{0.5}Ba_{0.5}$) double perovskites,[12] but Mn_2FeReO_6 could offer spectacular magnetizations up to a theoretical $M = 13$ μ_B if $S = 5/2$ Mn^{2+} spins are aligned with the $S = 5/2$ Fe^{3+} spins, antiparallel to $S = 1$ Re^{5+}, at similar high fields. Although high-field M is enhanced by alignment of fluctuating Mn^{2+} spin components, it is notable that remnant values (at zero field during cycling as shown in the inset to Figure 2b) of $M_r = 2.8$ μ_B at 75 K and 1.1 μ_B at 300 K also exceed those of other double-perovskite

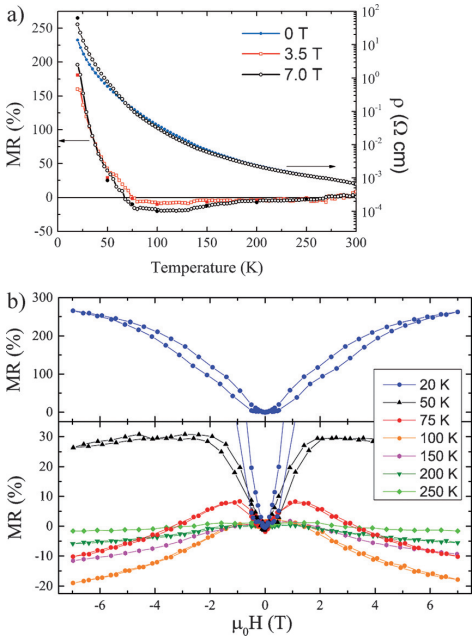

Figure 3. a) Temperature dependence of zero-field and 7 T resistivities for Mn_2FeReO_6, and of magnetoresistance MR at fields of 3.5 and 7 T, showing the switching transition at 75 K. Open MR points are from R–T measurements at constant H, and closed points are from MR–H data in (b). b) Variations of MR for magnetic field cycled between +7 and −7 T, with the large positive response at 20 K shown in the upper panel.

ferrimagnets, which typically have $M_r < 2$ μ_B at 5 K and $\ll 1$ μ_B at 300 K.[2]

Resistivity measurements in Figure 3a reveal bulk semiconducting behavior for a ceramic pellet of Mn_2FeReO_6. This behavior is consistent with the change from metallicity to semiconductivity as A^{2+} cation size decreases from Ba to Ca in ceramic A_2FeReO_6 samples,[2] as Mn is even smaller than Ca. Ca_2FeReO_6 undergoes a metal to insulator (semiconductor) transition at 140 K driven by orbital ordering of the $5d^2$ Re^{5+} states.[13] Our neutron refinements reveal elongated ReO_6 octahedra consistent with Jahn–Teller distortion at 2–300 K (see Supporting Information), so it is likely that Mn_2FeReO_6 has an orbitally ordered insulating ground state, with any insulator to metal transition occurring only above 300 K. The Mn_2FeReO_6 pellet shows negative high-field MR which increases on cooling to $MR = -19\%$ at 7 T and 100 K, but MR takes large positive values below a sharp discontinuity at 75 K. This crossover is unprecedented in ferrimagnetic double perovskites where negative MR is consistently observed. MR–H data in Figure 3b show that the positive contribution emerges at low fields and high temperatures, increases near the transition ($MR = 8\%$ at 1 T at 75 K), and is dominant at low temperatures with $MR = 265\%$ at 7 T and 20 K. Hence, Mn_2FeReO_6 does not show large low-field magnetoresistances at room temperature

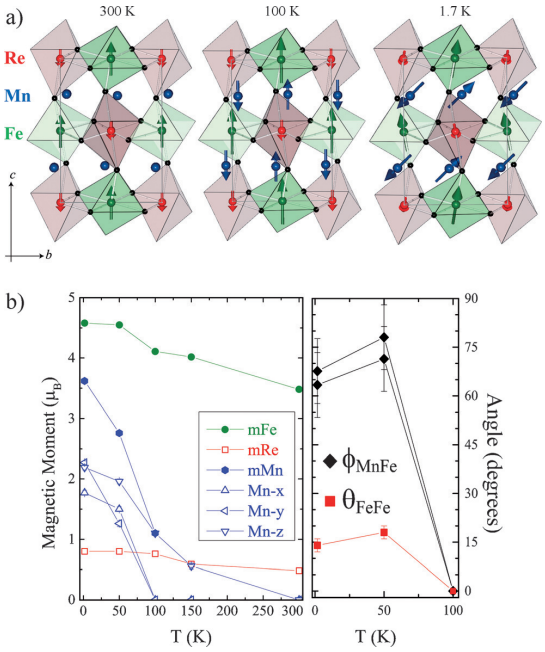

Figure 4. a) Magnetic orders in Mn_2FeReO_6 at representative temperatures, spins shown by arrows. b) Temperature variations of the total ordered Fe, Re, and Mn moments and of the Mn *x*, *y*, and *z* components. Variations of canting angles φ_{MnFe} (where the angle between Mn and Fe spins that are antiparallel at 100 K is 180°–φ_{MnFe}) and the Fe–Fe spin canting angle θ_{FeFe} are also shown.

despite a large *M*, as the positive *MR* contribution largely cancels the negative TMR effect.

Three spin-ordering regimes (Figure 4a) have been discovered in Mn_2FeReO_6 from analysis of magnetic neutron diffraction (Figure 1), as described in Supporting Information. The antiparallel order of the Fe^{3+} and Re^{5+} moments at 300 K is like those in other ferrimagnetic double perovskites, and there is no measurable moment at the Mn sites. However, at 150 and 100 K additional magnetic reflections reveal a partial antiferromagnetic order of the Mn spins, collinear with the Fe and Re moments. This result shows that Mn-O-Mn interactions are antiferromagnetic. Changes in the magnetic peaks between 100 and 50 K reveal that the *MR* switch is associated with a magnetic reorientation transition at $T_M = 75$ K, below which Mn_2FeReO_6 has non-collinear magnetic order with spin components in *x*, *y*, and *z* directions (Figure 4). This reflects competition between Mn-O-Mn, Fe-O-Re, and Mn-O-Fe/Re exchange interactions that introduces magnetic frustration. Neighboring Mn and Fe spins that are antiparallel above T_M become canted by approximately 70°, showing that symmetric Heisenberg exchange is largely frustrated and weaker antisymmetric (Dzyaloshinskii–Moriya) interactions favoring perpendicular orientation are influential below T_M. Mn moments are antiferromagnetically aligned but the Fe order is no longer purely ferromagnetic, with spins in successive *ab*-plane layers canted by $\theta_{FeFe} \approx 15°$ (Figure 4). The rise in antiferromagnetic Mn order below $T_M = 75$ K reduces the fluctuating Mn^{2+} spin components and the field-induced magnetization, as seen in Figure 2a.

We have also synthesized the double-perovskite (CaMn)-$FeReO_6$ (results are in Supporting Information) which demonstrates that dilution of Mn^{2+} with non-magnetic Ca^{2+} ions suppresses the Mn^{2+} spin-ordering transition and the *MR* switch. *MR* is negative to low temperatures with $MR = -32\%$ at 7 T and 20 K comparable to values of double perovskites, such as Sr_2FeMoO_6 which has −30% at 7 T and 4 K.[2]

Antiferromagnetic Mn^{2+} spin order would be completely frustrated with respect to ferrimagnetic Fe–Re order in a cubic double perovskite, but the monoclinic symmetry of Mn_2FeReO_6 breaks the equivalence of couplings of Fe or Re to spin-up and spin-down Mn^{2+} neighbors. Hence the antiferromagnetically ordered Mn spin components observed at 100 and 150 K couple to the Fe and Re spin order and enhance ferrimagnetism, as evidenced by high M_r and spin polarization. The enhancement is evidenced by a slight change of magnetization slope (Figure 2a) and increase in high-field *MR* (Figure 3a) below around 200 K. The broadness of these features suggests that Mn spin order may be induced by local interactions with ferrimagnetic Fe and Re moments, rather than through a spontaneous transition within the Mn spin sublattice. This is consistent with the collinear order of a small ordered Mn^{2+} moment, (e.g. 1.1 μ_B at 100 K) in this regime.

The magnetic transition at $T_M = 75$ K marks the onset of spontaneous Mn^{2+} spin order and frustration leads to a non-collinear magnetic structure with canting of Fe^{3+} spins. In double-exchange models of ferrimagnetic $A_2FeB'O_6$ double perovskites,[14] the probability of electron hopping between cations depends on the alignment of their core spins as $\cos(\theta_{FeFe}/2)$,[15,16] so the experimentally observed canting of $\theta_{FeFe} \approx 15°$ only corresponds to a 1% decrease in electron hopping. However, the sharp switch in *MR* at T_M shows that the effects of antiferromagnetism are amplified by magnetic fields, probably through increased Fe spin canting, and neutron measurements in applied fields will be needed to verify this. The positive *MR* is intrinsic to the bulk material, in contrast to the negative TMR which is an interfacial effect. Thermal changes between positive and negative MR regimes are only known in a few materials, such as the spinel $Zn_{0.95}Cu_{0.05}Cr_2Se_4$, through change of conduction mechanism at a 25 K ferromagnetic transition,[17] and at 50 K in GdSi from effects of Gd 4f-spin transitions on magnetopolarons,[18] but the mechanism in Mn_2FeReO_6 is very different and arises from coexistence of ferrimagnetic conducting FeRe and antiferromagnetic Mn spin networks in the same phase.

In conclusion, this study shows that novel ferrimagnetic double perovskites with magnetic transition metals at all cation sites can be synthesized at high pressure.[19] A very high degree of Mn/Fe/Re order over the three $A_2BB'O_6$ cation sites is observed in Mn_2FeReO_6. The large $S = 5/2$ spin of Mn^{2+} significantly enhances magnetization—Mn_2FeReO_6 has the highest reported remnant and high field values for a double perovskite despite antiferromagnetic interactions between Mn spins. This Mn antiferromagnetism introduces an intrinsic positive MR effect that tends to cancel out the

negative low-field TMR at ambient temperatures, and becomes dominant below a $T_M = 75$ K spin reorientation transition where magnetic frustration leads to spin canting. Further exotic magnetoresistance or other spintronic phenomena may be generated from couplings between spin, lattice, and charge degrees of freedom in other Mn-based double perovskites. Although high pressures are required for the bulk synthesis of these materials, epitaxial stabilization may enable thin films to be deposited for device applications, as demonstrated for the multiferroic double perovskite Bi_2MnNiO_6.[20]

Acknowledgements

We acknowledge EPSRC and STFC for support and the provision of beam time at ILL. We thank C. Ritter (ILL) for assistance with neutron-diffraction experiments.

Keywords: ferrimagnetic double perovskites · high-pressure chemistry · magnetic properties · magnetoresistance · perovskite phases

How to cite: *Angew. Chem. Int. Ed.* **2015**, *54*, 12074–12077
Angew. Chem. **2015**, *127*, 12242–12245

[1] S. Vasala, M. Karppinen, *Prog. Solid State Chem.* **2014**, *43*, 1–36.
[2] D. Serrate, J. M. De Teresa, M. R. Ibarra, *J. Phys. Condens. Matter* **2007**, *19*, 023201.
[3] K.-I. Kobayashi, T. Kimura, H. Sawada, K. Terakura, Y. Tokura, *Nature* **1998**, *395*, 677–680.
[4] A. P. Douvalis, M. Venkatesan, J. M. D. Coey, M. Grafoute, J.-M. Greneche, R. Suryanarayanan, *J. Phys. Condens. Matter* **2002**, *14*, 12611–12627.
[5] M. Bibes, K. Bouzehouance, A. Barthelemy, M. Besse, *Appl. Phys. Lett.* **2003**, *83*, 2629–2631.
[6] N. Kumar, P. Misra, R. K. Kotnala, A. Gaur, R. S. Katiyar, *J. Phys. D* **2014**, *47*, 065006.
[7] W.-t. Chen, M. Mizumaki, H. Seki, M. S. Senn, T. Saito, D. Kan, J. P. Attfield, Y. Shimakawa, *Nat. Commun.* **2014**, *5*, 3909.
[8] M. Markkula, A. M. Arévalo-López, A. Kusmartseva, J. A. Rodgers, C. Ritter, H. Wu, J. P. Attfield, *Phys. Rev. B* **2011**, *84*, 094450.
[9] A. J. Dos Santos-García, C. Ritter, E. Solana-Madruga, R. Sáez-Puche, *J. Phys. Condens. Matter* **2013**, *25*, 206004.
[10] S. V. Ovsyannikov, A. M. Abakumov, A. A. Tsirlin, W. Schnelle, R. Egoavil, J. Verbeeck, G. Van Tendeloo, K. Glazyrin, M. Hanfland, L. Dubrovinsky, *Angew. Chem. Int. Ed.* **2013**, *52*, 1494; *Angew. Chem.* **2013**, *125*, 1534.
[11] K. Shiro, I. Yamada, N. Ikeda, K. Ohgushi, M. Mizumaki, R. Takahashi, N. Nishiyama, T. Inoue, T. Irifune, *Inorg. Chem.* **2013**, *52*, 11538–11543.
[12] J. M. De Teresa, J. M. Michalik, J. Blasco, P. A. Algarabel, M. R. Ibarra, C. Kapusta, U. Zeitler, *Appl. Phys. Lett.* **2007**, *90*, 252514.
[13] K. Oikawa, T. Kamiyama, H. Kato, Y. Tokura, *J. Phys. Soc. Jpn.* **2003**, *72*, 1411–1417.
[14] D. D. Sarma, P. Mahadevan, T. Saha-Dasgupta, S. Ray, A. Kumar, *Phys. Rev. Lett.* **2000**, *85*, 2549–2552.
[15] O. Erten, O. N. Meetei, A. Mukherjee, M. Randeria, N. Trivedi, P. Woodward, *Phys. Rev. Lett.* **2011**, *107*, 257201.
[16] O. N. Meetei, O. Erten, A. Mukherjee, M. Randeria, N. Trivedi, P. Woodward, *Phys. Rev. B* **2013**, *87*, 165104.
[17] D. R. Parker, M. A. Green, S. T. Bramwell, A. S. Wills, J. S. Gardner, D. A. Neumann, *J. Am. Chem. Soc.* **2004**, *126*, 2710–2711.
[18] H. Li, Y. Xiao, B. Schmitz, J. Persson, W. Schmidt, P. Meuffels, G. Roth, T. Brückel, *Sci. Rep.* **2012**, *2*, 750.
[19] Note added in proof. While this manuscript was under review we became aware of a closely related study: M. R. Li, M. Retuerto, Z. Deng, P. W. Stephens, M. Croft, Q. Huang, H. Wu, X. Deng, G. Kotliar, J. Sánchez-Benítez, J. Hadermann, D. Walker, M. Greenblatt *Angew. Chem. Int. Ed.* **2015**, *54*, DOI:10.1002/anie.201506456; *Angew. Chem.* **2015**, *127*, DOI:10.1002/ange.201506456
[20] M. Saikai, A. Masuno, D. Kan, M. Hashisaka, K. Takata, M. Azuma, M. Takano, Y. Shimakawa, *Appl. Phys. Lett.* **2007**, *90*, 072903.

Received: July 15, 2015
Published online: August 26, 2015

CHEMISTRY OF MATERIALS
Cite This: Chem. Mater. 2017, 29, 8870-8874
Article
pubs.acs.org/cm

Complex Ferrimagnetism and Magnetoresistance Switching in Ca-Based Double Double and Triple Double Perovskites

Graham M. McNally,[†] Ángel M. Arévalo-López,[†] Padraig Kearins,[†] Fabio Orlandi,[‡] Pascal Manuel,[‡] and J. Paul Attfield*[,†]

[†]Centre for Science at Extreme Conditions (CSEC) and School of Chemistry, University of Edinburgh, Peter Guthrie Tait Road, Edinburgh EH9 3FD, U.K.

[‡]STFC Rutherford Appleton Lab, ISIS Facility, Harwell Science and Innovation Campus, Didcot OX11 0QX, U.K.

Supporting Information

ABSTRACT: Cation ordering in ABO_3 perovskites can lead to interesting and useful phenomena such as ferrimagnetism and high magnetoresistance by spin polarized conduction in Sr_2FeMoO_6. We used high pressures and temperatures to synthesize the cation ordered $AA'BB'O_6$ perovskites $CaMnFeReO_6$, $CaMnMnReO_6$, and $Ca(Mn_{0.5}Cu_{0.5})FeReO_6$. These have columnar A/A′ and rocksalt B/B′ cation orders, as found in the recently discovered double double perovskite $MnNdMnSbO_6$, and partial Mn/Cu order over tetrahedral and square planar A′ sites in $Ca(Mn_{0.5}Cu_{0.5})FeReO_6$ demonstrates that triple double cation order is possible. Neutron diffraction reveals complex ferrimagnetic orders in all three materials; $CaMnFeReO_6$ and $Ca(Mn_{0.5}Cu_{0.5})FeReO_6$ have large room temperature magnetizations with low temperature switching of magnetoresistance in the latter material, and $CaMnMnReO_6$ displays a high coercivity of 1.3 T at low temperatures.

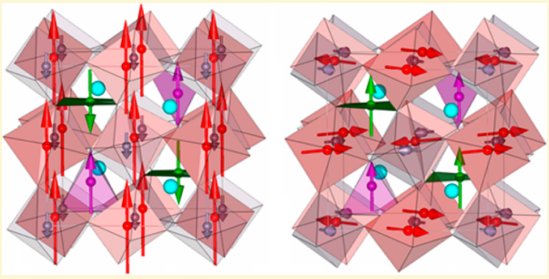

The ABX_3 perovskite structure is notable for giving rise to many materials with outstanding properties and for the ability to accommodate many structural variations through cation order.[1] In double perovskites of the form $A_2BB'O_6$,[2] rocksalt order of 3d large spin B cations with small spin 4d or 5d B′ cations can result in strong ferrimagnetism and half metallicity such as in Sr_2FeMoO_6 (SFMO).[3] This has a high Curie temperature (T_C = 410 K) and spin polarized conduction, resulting in large, low-field tunnelling magnetoresistance (TMR, where magnetoresistance is MR = $[\rho(H) - \rho(0)]/\rho(0)$ for resistivities ρ measured in magnetic field H and at H = 0). Substitution of other cations such as A-site Ca or Ba and B-site Mo or Re gives rise to materials with similar properties.[4−7]

Recent studies have shown that high pressure synthesis can be used to stabilize small magnetic transition-metal ions such as Mn^{2+} at the A-sites of perovskites in place of large, nonmagnetic cations like Ca^{2+} and Sr^{2+}.[8−10] This introduces a source of A-site magnetism that may change or improve the functionality of these materials. The double perovskite Mn_2FeReO_6 has room temperature ferrimagnetism similar to that of SFMO but with enhanced magnetization and an unusual MR switching transition at low temperatures (~75 K), where MR switches from negative to positive.[11,12] Mn_2FeSbO_6 and Mn_2MnReO_6 both have complex low temperature antiferromagnetic orders.[13−15]

Double perovskites have also been reported in the form $AA'B_2O_6$ with columnar A-site order such as $CaATi_2O_6$ (A = Mn and Fe)[17,18] and, in addition, it was found that a new double double cation order is stabilized in the series $MnRMnSbO_6$ (R = La, Pr, Nd, and Sm) with 1:1 columnar A-site and rocksalt B-site orders.[19] Here, we report that this structural type is surprisingly versatile, as $CaABReO_6$-type materials $CaMnFeReO_6$ (CMFR) and $CaMnMnReO_6$ (CMMR) synthesized at high pressure have the same double double perovskite structure (space group $P4_2/n$, Figure 1), and that a further partial triple double cation order of three cations over A-sites and two over B-sites is achieved in $Ca(Mn_{0.5}Cu_{0.5})FeReO_6$ (CMCFR). These materials all have different complex ferrimagnetic orders with up to four spin sublattices present.

Polycrystalline ~15 mg samples of $CaMnFeReO_6$, $CaMnMnReO_6$, and $Ca(Mn_{0.5}Cu_{0.5})FeReO_6$ were prepared by high pressure−temperature synthesis at 10 GPa and 1673 K in a Walker-type multianvil module. Variable temperature powder neutron diffraction (PND) data were collected from 60 mg aggregates of several samples of each material using the WISH diffractometer at the ISIS Neutron Facility. Powder synchrotron X-ray diffraction (PSXRD) data were also collected for $CaMnFeReO_6$ at the ALBA facility, and a small crystal of $Ca(Mn_{0.5}Cu_{0.5})FeReO_6$ was analyzed by single crystal X-ray diffraction (SCXRD). Magnetic properties were characterized by magnetization measurements up to temperatures of 650 K in

Received: August 22, 2017
Revised: September 25, 2017
Published: September 25, 2017

DOI: 10.1021/acs.chemmater.7b03556
Chem. Mater. 2017, 29, 8870−8874

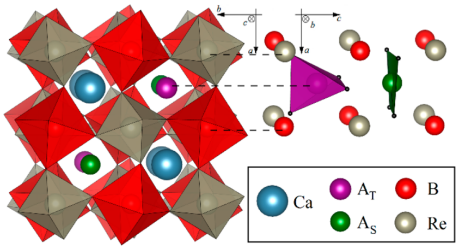

Figure 1. Double/triple double perovskite structure of $CaABReO_6$ materials in space group $P4_2/n$. Large Ca and small A_T/A_S cations are ordered in columns with the latter alternating between tetrahedral A_T and square planar A_S sites, as shown in the upper right view. BO_6 and ReO_6 octahedra order in a rocksalt arrangement and are tilted in system $a^+a^+c^-$ following Glazer notation.[16]

fields up to 7 T. Experimental details are outlined in the Supporting Information.

CMFR was previously reported to be a semiconducting ferrimagnet with T_C = 500 K, saturated magnetization μ_{sat} = 4.3 μ_B per formula unit (f.u.) and negative MR down to −32% at 20 K and 7 T.[11] This material was originally proposed to be a 1:1 solid solution between the double perovskites Ca_2FeReO_6 and Mn_2FeReO_6, both of which have a monoclinically distorted $P2_1/n$ structure with Ca/Mn disordered over the A-sites. However, we find that this model gives very poor fits to our PND data, whereas the $P4_2/n$ double double perovskite structure accounts for the neutron intensities well (Figure 2a). Hence, $CaMnFeReO_6$ is identified as the first Ca-based material to adopt the $MnRMnSbO_6$ type double double perovskite structure, and this discovery inspired the synthesis of the other materials reported here. Structural and magnetic parameters for $CaMnFeReO_6$ are summarized in Table 1.

There is a very high degree of B cation order with only 3.0(1)% Fe/Re antisite disorder obtained by PSXRD structure refinement. Ca^{2+} occupies the 10-coordinate A-sites, and Mn^{2+} predominantly occupies the 4-coordinate A_T and A_S sites, although some Fe occupancy (8(3)% and 16(3)%, respectively) was found by PND, yielding a structural formula of $Ca(Mn_{0.88}Fe_{0.12})FeReO_6$ and allowing a small amount (<1%) of $MnFe_3O_5$ to be detected. PND shows that at 300 K, $CaMnFeReO_6$ has magnetic order of only Fe^{3+} ($3d^5$, $S = {}^5/_2$) and Re^{5+} ($5d^2$, S = 1) spins in a collinear G-type ferrimagnetic arrangement like that found in SFMO and similar double perovskites. Magnetization measurements in Figure 4a show that this order occurs below T_B = 500 K (we write the Curie temperature as T_B = 500 K to emphasize that only the B-site spins order below this transition) and a second transition is observed at low temperatures. This coincides with the appearance of new magnetic peaks in PND data below T_A = 70 K, and these are fitted by a second ferrimagnetic order of up A_T and down A_S site Mn^{2+} ($3d^5$, $S = {}^5/_2$) spins as shown in Figure 3a. The magnitudes of A_T and A_S moments were found to be very similar and were constrained to be equal. Temperature variations of the refined moments are shown in Figure 4a; the net moment of 3.63(1) μ_B f.u.$^{-1}$ at 2 K agrees well with the saturated magnetization of 4.3 μ_B f.u.$^{-1}$ from the M–H hysteresis measurement at 10 K in Figure 3c. A-site spin order has a magnetoelastic effect on the lattice as the c-axis thermal expansion changes from negative to positive on warming through the transition, as shown in the inset to Figure 4a. The ferrimagnetic A-site order of Mn^{2+} spins appears

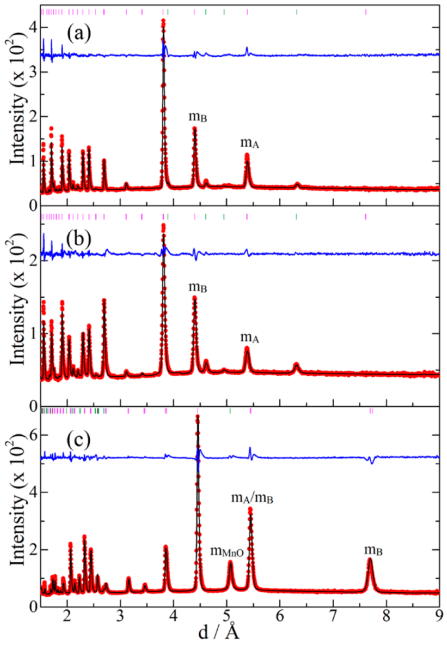

Figure 2. Rietveld fits to PND data at 2 K from the WISH diffractometer at the ISIS Neutron Facility (average of banks 2 and 9). The major phase (nuclear and magnetic) in each pattern is represented by magenta tick marks, with the minor impurity phases represented by green tick marks. Significant magnetic intensities are marked by *m*. (a) $CaMnFeReO_6$ and (b) $Ca(Mn_{0.5}Cu_{0.5})FeReO_6$ both show $MnFe_3O_5$ as a magnetic impurity,[20] fit as an intensity matching le Bail phase. (c) $CaMnMnReO_6$ with an MnO impurity (3.6(2)%).

to reinforce the Fe/Re ferrimagnetic order, leading to a large negative tunnelling MR of −32% at 20 K and 7 T.[11] This is in contrast to the double perovskite Mn_2FeReO_6, where frustration between antiferromagnetic Mn-spin order and the Fe/Re ferrimagnetism leads to a low temperature switch from negative to positive MR.[11,12]

The presence of distinct tetrahedral A_T and square planar A_S-sites within the double double perovskite structure in Figure 1 suggests that two different transition-metal cations might be ordered over these positions, and hence CMCFR was investigated with the aim of ordering Mn^{2+}/Cu^{2+} cations at A_T/A_S-sites based on the stability of Cu^{2+} in square planar coordination. Single crystal structural analysis confirmed that this material has the $P4_2/n$ structure with a high degree of B-site Fe/Re order and only Ca at the Ca site. Refinements of Cu/Mn occupancies (Table 1) over square planar and tetrahedral sites using PND and SCXRD show that a partial order is achieved with 60% Cu at A_S-sites in both analyses and 77% occupancy of Mn at A_T by SCXRD, the difference between A_T occupancy by SCXRD and PND likely indicates that a higher degree of order is promoted during crystal growth. Although the degree of ordering is small, it does verify the principle that two metals may be ordered over the A_T/A_S-sites of the $P4_2/n$ structure to generate triple double perovskites, where three and two cations are respectively ordered over the A and B-sites of the ABO_3 lattice. It is notable that four different transition metals (Mn, Fe, Cu, and Re) as well as Ca are at least

DOI: 10.1021/acs.chemmater.7b03556
Chem. Mater. 2017, 29, 8870–8874

Table 1. Summary of Structural and Magnetic Parameters for the Three $CaABReO_6$ Double/Triple Double Perovskites in This Study[a]

		CMMR	CMFR	CMCFR
	a/Å	7.7136(7)	7.6311(5)	7.618(1)
	c/Å	7.7430(8)	7.6266(7)	7.629(1)
	B-antisite/%	4.0(1)	3.0(1)[b]	1.3(5)[b]
occ A_S/%	PND	100 Mn	84(3) Mn/16 Fe	60(1) Cu/40 Mn
	SCXRD			61(4) Cu/39 Mn
occ A_T/%	PND	100 Mn	92(3) Mn/8 Fe	64(1) Mn/36 Cu
	SCXRD			77(4) Mn/23 Cu
BVS	A[c]	1.7	1.6	1.8
	B	2.3	3.3	2.7
	Re	4.9	4.2	4.9
	T_B/K	120	500	560
	T_A/K	100	70	160
	m_{sat}/μ_B (MvH)	3.4	4.3	4.8
	m_{sat}/μ_B (NPD)	2.70(6)	3.63(1)	4.78(4)
	H_c/μ_0T	1.3	0.04	0.06

[a]Lattice parameters and bond valence sums (BVS) at 300 K and occupancies of A_S and A_T sites. BVS and B-antisite disorder are from refinements of PND data unless stated otherwise. [b]B-antisite disorder for CMFR obtained from PSXRD and by SCXRD for CMCFR. [c]Mean BVS for A_T and A_S sites.

partially ordered in the structure of $Ca(Mn_{0.5}Cu_{0.5})FeReO_6$. As in CMFR, a trace of $MnFe_3O_5$ (<1%) was found by PND.

The magnetic properties of CMCFR are similar to those described above for CMFR, as shown in Table 1 and Figures 3a and 4b. CMCFR has higher temperatures for Fe/Re spin order at T_B = 560 K and at T_A = 160 K for A-site magnetic order. Weaker magnetoelastic effects at T_A are seen in CMCFR than in CMFR, probably due to dilution and disorder effects from replacing $S = {}^5/_2$ Mn^{2+} by $S = {}^1/_2$ Cu^{2+}. No significant magnetic moment was found at the square planar A_S sites in initial refinements, suggesting that Mn/Cu disorder frustrates spin order at this site, and so the moment was fixed to zero. The 2 K A_T moment refines to 2.70(6) μ_B, which is close to the ideal value of 3.2 μ_B for alignment of 64% Mn^{2+} $S = {}^5/_2$ spins. The predicted m_{sat} of 4.8 μ_B from the 2 K neutron refinement agrees perfectly with the measured value from magnetization measurements. This is second only to the value of 5.0 μ_B for Mn_2FeReO_6 among double perovskite materials with rocksalt order of transition-metal cations.[11]

The resistivity of a sintered pellet of CMCFR is ~0.01 Ωcm, indicative of metallic behavior, but with a small increase on cooling (equivalent to an activation energy of 3 meV) that is likely due to grain boundary resistances (Figure 3d). MR is positive at high temperatures, which is unusual in A_2FeReO_6 double perovskites, but begins to decrease below 70 K before becoming negative below 40 K. This suggests that paramagnetic Mn^{2+}/Cu^{2+} at A_T/A_S-sites promotes spin-scattering of carriers that increases in applied field with reduction of this effect below T_A enabling the negative TMR mechanism to dominate. Hence, Cu-substitution into CMFR to give CMCFR promotes metallicity and leads to an increase in both ordering temperatures and saturated magnetization.

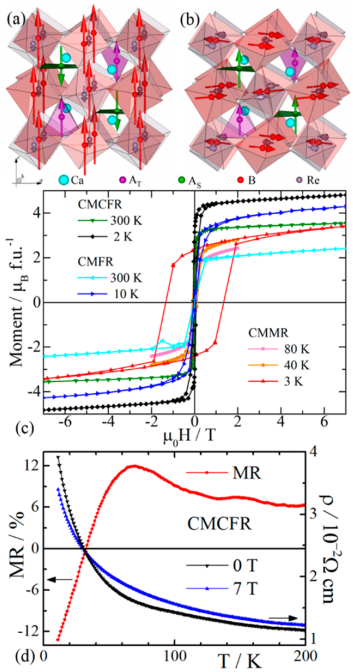

Figure 3. (a) Spin structure of $CaMnFeReO_6$, with k = (0 0 0) propagation vector, showing ferrimagnetic G-type ordering of the Fe/Re sublattice along the c-axis and the collinear antiferromagnetic Mn A-site sublattice with Mn_T orientating parallel to Fe and Mn_S antiparallel. $Ca(Mn_{0.5}Cu_{0.5})FeReO_6$ possesses a similar spin structure; however, no moment on the A_S-site can be detected by NPD. (b) Spin structure of $CaMnMnReO_6$ also has k = (0 0 0) with ferromagnetic A-site order and antiferromagnetic order of the Mn_B spins placed at 45° to the a,b-axes. Each successive plane has a ±90° rotation of the Mn_B spins around the c-axis. (c) Field dependence of the magnetization of CMFR, CMMR, and CMCFR at various temperatures. (d) Resistivity in 0 and 7 T fields and the derived MR for CMCFR.

Fe^{3+} and Re^{5+} are present at the B-sites in the above materials, but the double perovskites Ca_2MnReO_6[21] and Mn_2MnReO_6[12] are found to have Mn^{2+} and Re^{6+}, so the composition CMMR was investigated to discover if the same charge configuration can be stabilized in the $P4_2/n$ double double perovskite arrangement. This phase was successfully synthesized with a small 3.6(2)% impurity of MnO, and structure refinement against PND data reveals a high degree of cation order with 4.0(1)% of Mn/Re antisite disorder and also 5.4(2)% Mn occupancy of the Ca site. The BVS[22] for B-site Mn confirms the $Ca^{2+}Mn^{2+}Mn^{2+}Re^{6+}O_6$ configuration, although there is little Re^{5+}/Re^{6+} discrimination by BVS. Magnetic order in $CaMnMnReO_6$ is evidenced by an increase in magnetization below ~125 K, and two transitions were found from analysis of PND data at T_B = 120 K and T_A = 100 K (Figure 4c). B-site spins lie in the ab-plane, and successive antiferromagnetic layers are rotated by 90° to adjacent layers in the c-direction (Figure 3b). PND also shows that the A-site Mn^{2+} square planar and tetrahedral moments order ferromagnetically parallel to the c-axis below T_A = 100 K. The perpendicular orientation of A-site to B-site moments shows that their orders are mutually frustrated. The net magnetization resulting from the A-site Mn^{2+} spins is predicted to be the refined A-site moment of 2.7

DOI: 10.1021/acs.chemmater.7b03556
Chem. Mater. 2017, 29, 8870−8874

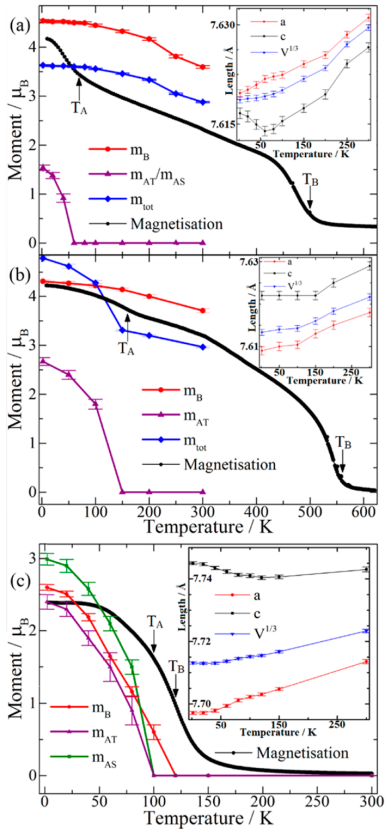

Figure 4. Magnetization versus temperature (field cooled, 5000 Oe) data of (a) CaMnFeReO6, (*b*) $Ca(Mn_{0.5}Cu_{0.5})FeReO_6$, and (c) $CaMnMnReO_6$. Magnetic moments *m* are obtained from variable temperature PND. Combined total moments (m_{tot}) from A- and B-sites for $CaMnFeReO_6$ and $Ca(Mn_{0.5}Cu_{0.5})FeReO_6$ (including Re moments) are shown; m_{AS} is zero for $Ca(Mn_{0.5}Cu_{0.5})FeReO_6$ and constrained to be equal and opposite to m_{AT} for $CaMnFeReO_6$. Insets: Thermal dependence of the lattice parameters *a*, *c*, and $V^{1/3}$ for $CaABReO_6$.

μ_B f.u.$^{-1}$, which is comparable to the measured magnetization 3.4 μ_B f.u.$^{-1}$ at 2 K and 7 T. *M*−*H* hysteresis loops for $CaMnMnReO_6$ in Figure 3c show that a large coercive field develops at low temperatures, up to 1.3 T at 3 K. Similar behavior has been reported in some other Re-based double perovskites such as $Sr_{2-x}Ca_xFeReO_6$, which can show coercivity of up to 2 T that was attributed to magnetic anisotropy of Re^{5+} ions.[6] However, in our $CaABReO_6$ double double perovskites, the high coercivity is observed only for CMMR based on Re^{6+} and not for the Re^{5+} materials CMFR and CMCFR. The difference most likely arises from electron delocalization in the latter spin-polarized ferrimagnetic materials, whereas CMMR has electron-localized Re^{6+} states. Coupling of magnetization to the lattice in CMMR is evidenced by magnetoelasticity below T_B = 120 K, similar to that of CMFR above.

The above results show that the recently discovered $P4_2/n$ double double perovskite structure has a versatile chemistry as three different $AA'BB'O_6$ charge configurations are now exemplified by $R^{3+}Mn^{2+}Mn^{2+}Sb^{5+}O_6$,[19] $Ca^{2+}Mn^{2+}Fe^{3+}Re^{5+}O_6$, and $Ca^{2+}Mn^{2+}Mn^{2+}Re^{6+}$ O_6 with high degrees (>90%) of A/A′ and B/B′ cation ordering in all cases. In addition, this structure type offers the possibility of derived triple double perovskites by further order of two species over the tetrahedral and square planar sites within the A′ cation column. This pattern of charge ordering was recently reported in RMn_3O_6 (R = Gd−Tm and Y),[23] and the partial triple double order of five different cations is demonstrated here in $Ca(Mn_{0.5}Cu_{0.5})FeReO_6$.

This study also demonstrates that varied magnetic and electronic properties can be generated in double double perovskites with all of the present materials showing separate spin ordering transitions for the A- and B-site cations. CMFR is remarkable as a double ferrimagnet with ferrimagnetic order of antiparallel Fe and Re spins below T_B = 500 K and a second ferrimagnetic order of opposed inequivalent tetrahedral and square planar Mn spins below T_A = 70 K. CMFR and CMCFR preserve the ferrimagnetism and high Curie transition temperatures (500−600 K) of simple spin-polarized A_2FeReO_6 double perovskites (A = Ca, Sr, and Ba) but enhance the saturated magnetization from ∼3 μ_B up to 4.8 μ_B in CMCFR. CMCFR is metallic with an unusual switch from positive to negative MR on cooling. CMMR has very different magnetic order with antiferromagnetism of B-site spins but ferromagnetic order in the A-site Mn columns. In conclusion, high pressure synthesis is likely to generate many further new materials in this double double, and even triple double, perovskite family, with notable magnetic or other physical properties.

■ ASSOCIATED CONTENT

Supporting Information

The Supporting Information is available free of charge on the ACS Publications website at DOI: 10.1021/acs.chemmater.7b03556.

Experimental section, crystal structures, magnetic data, Rietveld fits, and MR measurements. Open data for this article are at http://dx.doi.org/10.7488/ds/2221 (PDF)

■ AUTHOR INFORMATION

Corresponding Author

*E-mail: j.p.attfield@ed.ac.uk.

ORCID

Fabio Orlandi: 0000-0001-6333-521X

J. Paul Attfield: 0000-0001-9763-3987

Notes

The authors declare no competing financial interest.

■ ACKNOWLEDGMENTS

We acknowledge EPSRC, the Royal Society, and STFC for support and the provision of beam time at the ISIS Neutron Source. We also acknowledge the help of Dr. O. Vallcorba and Dr. C. Popescu during synchrotron X-ray beam time on BL04-MSPD at ALBA.

■ REFERENCES

(1) King, G.; Woodward, P. M. Cation Ordering in Perovskites. *J. Mater. Chem.* **2010**, *20*, 5785.

(2) Vasala, S.; Karppinen, M. A2BB'O6 Perovskites: A Review. *Prog. Solid State Chem.* **2015**, *43*, 1−36.

(3) Kobayashi, K.-I.; Kimura, T.; Sawada, H.; Terakura, K.; Tokura, Y. Room-Temperature Magnetoresistance in an Oxide Material with an Ordered Double-Perovskite Structure. *Nature* **1998**, *395*, 677−680.

DOI: 10.1021/acs.chemmater.7b03556
Chem. Mater. 2017, 29, 8870−8874

(4) Lue, C. S.; Kuo, Y.-K.; Horng, S.-N.; Peng, S. Y.; Cheng, C. Nuclear and Magnetic Structural Properties of Ba_2FeMoO_6. *Phys. Rev. B: Condens. Matter Mater. Phys.* **2005**, *71*, 64202.
(5) Michalik, J. M.; De Teresa, J. M.; Blasco, J.; Algarabel, P. A.; Ibarra, M. R.; Kapusta, C.; Zeitler, U. Temperature Dependence of Magnetization under High Fields in Re-Based Double Perovskites. *J. Phys.: Condens. Matter* **2007**, *19*, 506206.
(6) Serrate, D.; De Teresa, J. M.; Algarabel, P. A.; Galibert, J.; Ritter, C.; Blasco, J.; Ibarra, M. R. Colossal Magnetoresistance in $Ca_xSr_{2-x}FeReO_6$ Double Perovskites due to Field-Induced Phase Coexistence. *Phys. Rev. B: Condens. Matter Mater. Phys.* **2007**, *75*, 165109.
(7) Prellier, W.; Smolyaninova, V.; Biswas, A.; Galley, C.; Greene, R. L.; Ramesha, K.; Gopalakrishnan, J. Properties of the Ferrimagnetic Double Perovskites A_2FeReO_6 (A = Ba and Ca). *J. Phys.: Condens. Matter* **2000**, *12*, 965−973.
(8) Ovsyannikov, S. V.; Abakumov, A. M.; Tsirlin, A. A.; Schnelle, W.; Egoavil, R.; Verbeeck, J.; Van Tendeloo, G.; Glazyrin, K. V.; Hanfland, M.; Dubrovinsky, L. Perovskite-like Mn_2O_3: A Path to New Manganites. *Angew. Chem., Int. Ed.* **2013**, *52*, 1494−1498.
(9) Arévalo-López, A. M.; Attfield, J. P. Weak Ferromagnetism and Domain Effects in Multiferroic $LiNbO_3$-Type $MnTiO_3$-II. *Phys. Rev. B: Condens. Matter Mater. Phys.* **2013**, *88*, 1−6.
(10) Markkula, M.; Arevalo-Lopez, A. M.; Kusmartseva, A.; Rodgers, J. A.; Ritter, C.; Wu, H.; Attfield, J. P. Incommensurate Spin Order in the Metallic Perovskite $MnVO_3$. *Phys. Rev. B: Condens. Matter Mater. Phys.* **2011**, *84*, 1−5.
(11) Arévalo-López, A. M.; McNally, G. M.; Attfield, J. P. Large Magnetization and Frustration Switching of Magnetoresistance in the Double-Perovskite Ferrimagnet Mn_2FeReO_6. *Angew. Chem., Int. Ed.* **2015**, *54*, 12074−12077.
(12) Li, M. R.; Retuerto, M.; Deng, Z.; Stephens, P. W.; Croft, M.; Huang, Q.; Wu, H.; Deng, X.; Kotliar, G.; Sánchez-Benítez, J.; Hadermann, J.; Walker, D.; Greenblatt, M. Giant Magnetoresistance in the Half-Metallic Double-Perovskite Ferrimagnet Mn_2FeReO_6. *Angew. Chem., Int. Ed.* **2015**, *54*, 12069−12073.
(13) Dos Santos-García, A. J.; Ritter, C.; Solana-Madruga, E.; Sáez-Puche, R. Magnetic and Crystal Structure Determination of Mn_2FeSbO_6 Double Perovskite. *J. Phys.: Condens. Matter* **2013**, *25*, 206004.
(14) Arévalo-López, A. M.; Stegemann, F.; Attfield, J. P. Competing Antiferromagnetic Orders in the Double Perovskite Mn_2MnReO_6 (Mn_3ReO_6). *Chem. Commun.* **2016**, *52*, 5558−5560.
(15) Li, M. R.; Hodges, J. P.; Retuerto, M.; Deng, Z.; Stephens, P. W.; Croft, M. C.; Deng, X.; Kotliar, G.; Sánchez-Benítez, J.; Walker, D.; Greenblatt, M. Mn_2MnReO_6: Synthesis and Magnetic Structure Determination of a New Transition-Metal-Only Double Perovskite Canted Antiferromagnet. *Chem. Mater.* **2016**, *28*, 3148−3158.
(16) Momma, K.; Izumi, F. VESTA 3 for Three-Dimensional Visualization of Crystal, Volumetric and Morphology Data. *J. Appl. Crystallogr.* **2011**, *44*, 1272−1276.
(17) Leinenweber, K.; Parise, J. High-Pressure Synthesis and Crystal Structure of $CaFeTi_2O_6$, a New Perovskite Structure Type. *J. Solid State Chem.* **1995**, *114*, 277−281.
(18) Aimi, A.; Mori, D.; Hiraki, K.; Takahashi, T.; Shan, Y. J.; Shirako, Y.; Zhou, J.; Inaguma, Y. High-Pressure Synthesis of A -Site Ordered Double Perovskite $CaMnTi_2O_6$ and Ferroelectricity Driven by Coupling of A -Site Ordering and the Second-Order Jahn−Teller Effect. *Chem. Mater.* **2014**, *26*, 2601−2608.
(19) Solana-Madruga, E.; Árévalo-López, Á. M.; Dos Santos-García, A. J.; Urones-Garrote, E.; Ávila-Brande, D.; Sáez-Puche, R.; Attfield, J. P. Double Double Cation Order in the High-Pressure Perovskites $MnRMnSbO_6$. *Angew. Chem., Int. Ed.* **2016**, *55*, 9340−9344.
(20) Hong, K. H.; McNally, G. M.; Coduri, M.; Attfield, J. P. Synthesis, Crystal Structure, and Magnetic Properties of $MnFe_3O_5$. *Z. Anorg. Allg. Chem.* **2016**, *642*, 1355−1358.
(21) Corrêa, H. P. S.; Cavalcante, I. P.; Souza, D. O.; Santos, E. Z.; Orlando, M. T. D.; Belich, H.; Silva, F. J.; Medeiro, E. F.; Pires, J. M.; Passamai, J. L.; Martinez, L. G.; Rossi, J. L. Synthesis and Structural Characterization of the Ca_2MnReO_6 Double Perovskite. *Ceramica* **2010**, *56*, 193.
(22) Brown, I. D. *The Chemical Bond in Inorganic Chemistry: The Bond Valence Model*; Oxford University Press: Oxford, 2002.
(23) Zhang, L.; Matsushita, Y.; Yamaura, K.; Belik, A. A. Five-Fold Ordering in High-Pressure Perovskites RMn_3O_6 (R = Gd−Tm and Y). *Inorg. Chem.* **2017**, *56*, 5210−5218.

DOI: 10.1021/acs.chemmater.7b03556
Chem. Mater. 2017, 29, 8870−8874